IMPER: Characterization of the Wind Field over a Large Wind Turbine Rotor

Final report

Schmidt Paulsen, Uwe; Wagner, Rozenn

Publication date:
2012

Document Version
Publisher's PDF, also known as Version of record

IMPER: Characterization of the Wind Field over a Large Wind Turbine Rotor-Final report

DTU Wind Energy Report E

Uwe Schmidt Paulsen, Rozenn Wagner
DTU Wind Energy Report E-0002(EN)
January 2012

DTU Wind Energy
Department of Wind Energy

Author: Uwe Schmidt Paulsen, Rozenn Wagner
Title: IMPER: Characterization of the Wind Field over a Large Wind Turbine Rotor-Final report
Department: DTU Wind Energy

DTU Wind Energy Report E-0002(EN)
January 2012

Abstract:

A modern wind turbine rotor with a contemporary rotor size would easily with the tips penetrate the air between 116 m and 30 m and herby experience effects of different wind. With current rules on power performance measurements such as IEC 61400-121 the reference wind speed is measured at hub height, an oversimplification of the wind energy power over the rotor disk area is carried out.

The project comprised a number of innovative and coordinated measurements on a full scale turbine with remote sensing technology and simulations on a 500 kW wind turbine for the effects of wind field characterization.

The objective with the present report is to give a short overview of the different experiments carried out and results obtained within the final phase of this project.

ISSN 0106-2840
ISBN 978-87-92896-00-1

Contract no.:
33032-0106

Project no.:
1125005-01/43056

Sponsorship:

Cover :

Pages:333
Tables:6
References:42

Technical University of Denmark
Frederiksborgvej 399
4000 Roskilde
Denmark
Telephone +45 46775024
bcar@dtu.dk
www.vindenergi.dtu.dk

Contents

Preface

This report is the final publishable report in the project "Improved Performance Measurements; Characterization of the Wind Field over a large wind turbine rotor", funded by the Danish Energy Research Programme EFP-2006 under contract Journal nr:33032-0106. The project (under acronym IMPER) was carried out in the period from March 2006 to Dec 2009 in cooperation with Risøs DTU, Siemens Wind Power and Vestas Wind Systems. In 2010 IMPER was revised and continued by Risø DTU until Dec 2011.

The project comprised a number of innovative and coordinated measurements on a full scale turbine with remote sensing technology and simulations on a 500 kW wind turbine for the effects of wind field characterization.

The objective with the present report is to give a short overview of the different experiments carried out and results obtained within the final phase of the project.

Articles, reports and works carried out in the course of the project are listed in the present report.

Uwe Schmidt Paulsen

DTU, February 2012

1 Introduction

The use of a single hub-height mounted anemometer is already today considered inadequate for characterizing the wind conditions a huge turbine rotor encounters as it spirals through a large portion of the atmospheric boundary layer. As future wind turbines become even bigger, performance results based on a single hub height measurement will result in even bigger uncertainties and faulty estimates. Measurements at hub height require an assumption of the wind profile as a function of height above ground. But this method fails to describe the incoming flow field and the influence of parameters such as turbulence intensity, wind shear, and wind direction changes on the turbine performance. The performance of contemporary, and forthcoming even larger turbines requires development of new "distributed" measurement methods in the rotor plane to replace the hitherto use of a single hub-height wind measurement. This again requires the use of remote sensing instrumentation in the form of LIDAR and SODAR measurements in order to acquire wind measurements over the whole rotor profile, free of met tower influence effects and the difficulties and expenses associated with the met tower installation.

The following graphs illustrate the essentials on the subject. A time trace shows the mean wind speeds at the National Test Site at Høvsøre, collected on March 28, 2007:

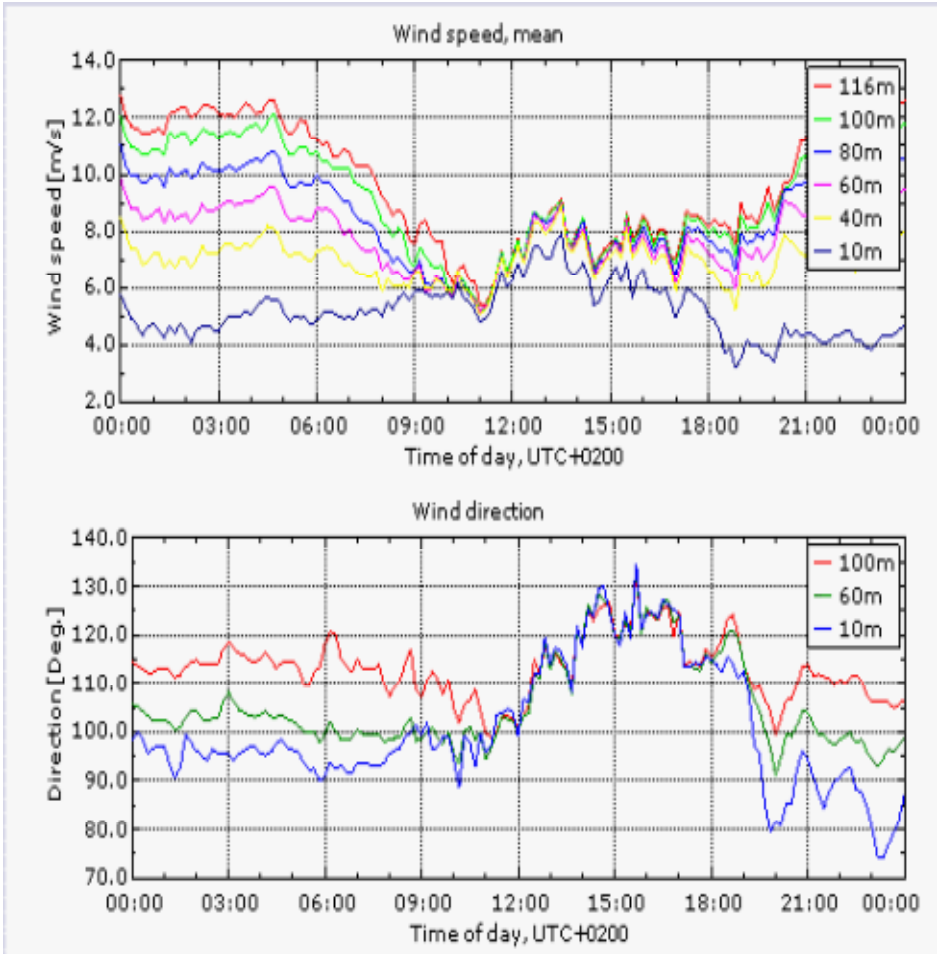

The wind conditions are stable during night and the cup anemometers in the different heights show a fine layered wind, in contrary to the situation at noon. Now, the wind

is unstable or near neutral and has a well-mixed, turbulent structure. A modern wind turbine rotor with a contemporary rotor size would easily with the tips penetrate the air between 116 m and 30 m and herby experience the above mentioned effects of different wind. With current rules on power performance measurements such as IEC 61400-121 the reference wind speed is measured at hub height, an oversimplification of the wind energy power over the rotor disk area is carried out.

2 Objectives and approach

2.1 Objectives

The objective of this project is to improve on the current practice in performance evaluation to use a single point measurement of wind speed as a representative measurement for the entire rotor disk area. This will be achieved through:
An evaluation of the influence of wind field characteristics (turbulence, wind shear wind veer) which influence the performance of large wind turbines:

- Developing a new method to characterize the performance of large wind turbines in flat terrain, taking into account the wind field measurement covering the complete rotor area.
- Creating the background to improve the accuracy in wind potential measurement methods.
- Contributing to further development and use of remote sensing methods in wind energy in order to improve the energy yield and reduce the financial risk.
- Extending the above method for performance measurements from flat to slightly complex terrain.

2.2 Approach

The complexity of the problem and the use of cup anemometers, in particular when extending from analyzing power curves in flat over to complex terrain is found to require a condensed literature survey on previous works on the use of cup anemometers and how to derive the power curve. Recommendations and findings are found in Chapter3.

Much work and activities has been performed within IMPER, in particular the work carried out in[3.1] , and the PhD thesis[3.2] on the characterization of the wind field effects on wind turbine rotors and the use of remote sensing. Findings from these investigations are to some extend been experimentally duplicated in order to provide data with statistical confidence.

A differentiated approach to analyze the rotor power in further details has been re-introduced here and applied to the 500 kW wind turbine in Chapter 5. The site and experimental conditions are described in Chapter 4. Under these conditions data are analyzed to embrace power curve and loads analysis on the rotor.
A wind turbine and wind model has been implemented to quantify the effects of the wind characterisation, as shown in Chapter 6.
Further the use of remote sensing is used to confirm earlier studies in IMPER are made in Chapters 8-8.3, and conclusions are made for an outlook on further activities in this field.

3 Wind characterisation over a large rotor disk area- few retrospective findings

Condensed findings are performed from the following references, which are by no means exhaustive. The amount of literature and the diverseness of the different topics addressed in this field make it difficult in providing a full picture to the topic.

The report on "Accuracy of power curve measurements" from 1986 provides a good introduction to the diversity of challenges concerned with deriving a power curve[3.3], in particular under clause 'precise'. Some themes on reaching comparability, is on how to interpret the wind measurements with a wind turbine in a landscape and a measurement setup, how to utilize measurement procedures that makes sense, and recommendations how to provide 'good' estimates.

Previous results from a study on cup anemometry in "Wind Turbine Power Performance Verification in Complex Terrain and Wind Farms"[3.4] are used:
"The vector scalar wind speed definition in relation to power curve measurements is based on the assumption, that the important wind parameters are all the wind components U_x, U_y, U_z. The measured average wind speed becomes: The vector scalar wind speed definition in relation to power curve measurements is based on the assumption, that the important wind parameters are all the wind components Ux, Uy, Uz. The measured average wind speed becomes:

$$U_{vector} = \int_0^T \sqrt{U_X^2(t) + U_Y^2(t) + U_Z^2(t)}dt = \sqrt{U^2 + W^2}$$

The horizontal wind speed definition is based on the assumption, that the important wind parameters are the horizontal components. The measured average wind speed is therefore:

$$U_{horiz} = \int_0^T \sqrt{U_X^2(t) + U_Y^2(t)}dt = U$$

The longitudinal wind speed definition is based on the assumption that the wind turbine only responds to average longitudinal (and horizontal) wind, in which only the components in the longitudinal direction φ are taken into account:

$$U_{long} = \int_0^T \sqrt{U_X^2(t) + U_Y^2(t)}\cos(Ar\tan(U_X / U_Y) - \phi)dt$$

"The 'energy equivalent' wind speed, U, is the equivalent non-turbulent flow speed that yields the same energy flux through a unit-area perpendicular to the mean flow direction as the real flow"(Frandsen, cited in [3.4])

The power in the wind per unit swept area is:

$$P = \overline{q \cdot (U+u)} = \tfrac{1}{2}\rho \cdot \overline{((U+u)^2 + v^2 + w^2) \cdot (U+u)}$$
$$= \tfrac{1}{2}\rho \cdot \overline{(U^3 + 3U^2u + U(3u^2 + v^2 + w^2) + u(u^2 + v^2 + w^2))}$$

And where q is the kinetic energy
From the formula of the power, the energy equivalent wind speed can be ex-pressed as:

$$U_{energy} = \left(\overline{((U+u)^2 + v^2 + w^2) \cdot (U+u)}\right)^{1/3}$$

Since $\overline{u} = 0 \Rightarrow \overline{3U^2 u} = 0$, and since $\overline{u(u^2+v^2+w^2)}$ is one order of magnitude less than the remaining terms, and therefore set to zero, the expression reduces to:

$$P \approx \tfrac{1}{2}\rho \cdot \left(U^3 + 3U\overline{u^2} + U\overline{v^2} + U\overline{w^2}\right) = \tfrac{1}{2}\rho \cdot U^3 \left(1 + 3\frac{\overline{u^2}}{U^2} + \frac{\overline{v^2}}{U^2} + \frac{\overline{w^2}}{U^2}\right).$$

With

$$\sigma_v^2 = \overline{v^2},\ \sigma_w^2 = \overline{w^2} \text{ and } \sigma_u^2 = \overline{u^2}$$

P turns out to:

$$P \approx \tfrac{1}{2}\rho \cdot U^3 \left(1 + 3\frac{\sigma_u^2}{U^2} + \frac{\sigma_v^2}{U^2} + \frac{\sigma_w^2}{U^2}\right).$$

With the usual definition of turbulence intensity Ti, and depending if to adopt variations in v and w directions the expression is:"
P α (1+3 Ti^2)(mainly turbulence towards turbine) or P α (1+5 Ti^2)(isotropic turbulence)

In the same report, following conclusions are made:
"Cup anemometers show systematic turbulence dependent differences in field comparisons

- Neither the RISØ nor the Thies cup anemometer has any "ideal" angular characteristics for "Horizontal" or "Vector" instruments
- The difference in measured wind speed between the two definitions "vector" and "horizontal" is quite low (about 1% at 20% turbulence), and is not the explanation to the high differences shown in the field comparisons
- Angular response is not enough to explain the differences of the cup-anemometers in field comparisons.
- Dynamic overspeeding is a substantial factor that must be taken into account
- Dynamic overspeeding of cup-anemometers is more complex than previously thought. For an adequate analysis, a non-dimensional torque curve must be provided
- The RISØ cup anemometer seems to have a little negative overspeeding at 10% turbulence, but increasing positive overspeeding at higher turbulence intensities.
- The Thies cup-anemometer seems to have substantially higher overspeeding than the RISØ cup anemometer, which must be an important part of the explanation of the high differences in field comparisons
- Cup anemometers should, apart from field comparisons, be classified according to a classification system, and based on an analysis of their friction dependency, angular response and dynamic overspeeding effects under well-defined ranges of external climatic conditions. A classification system is proposed in the CLASSCUP project
- Such a classification system should be widely adopted in the wind energy community, and it should be used to estimate operational uncertainties in power performance measurements (uncertainty uV2,i in the power performance measurement standard IEC 61400-121)
- The definition of the measured wind speed should with respect to inclined flow be based on the following considerations:
  1. Influence of flow inclination (sloped terrain and without turbulence)
  2. Influence of turbulence on the wind turbine and the wind speed sensor .."

In the same report, code and experimental validation of the power reduction from yaw misalignment is shown in Figure 1. The report concludes:" The reduction of

power with the yaw angle is almost the same as for inclined airflow. The difference is the wind shear, and the effect is very low. For the pre-sent analysis we can make the assumption that misalignment of the flow relative to the rotor axis is cos related for yaw, tilt and slope angles. Under this assumption, it is possible to make some simple calculations of the consequences of different ways of performing performance measurements in different kinds of terrain."

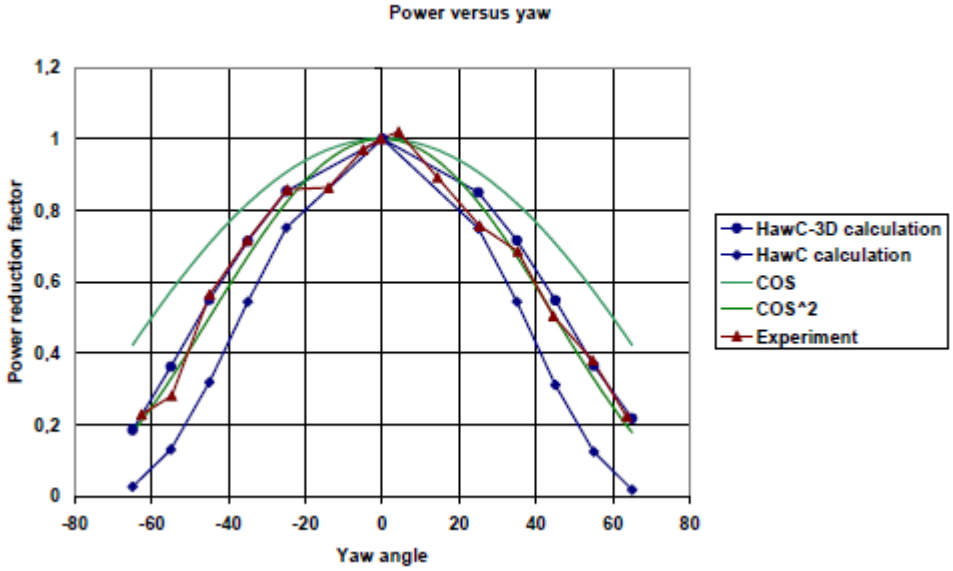

Figure 1 Yaw error effect on the power curve

Following these arguments, a coordinate on the power curve should be {U $\text{Cos}(\gamma\text{angle}^2)^{-1/3}$,P $\text{Cos}(\gamma\text{angle}^2)$}, where angle is a term originating from [i]flow inclination, [ii]rotor tilt angle or/and [iii]yaw error. The relation has been elaborated on a set of data and results are shown in Figure 2. ".. For a defined "ideal site", as described in IEC 61400-12, Ref. 1, the maximum average slope is 3°. Including the influence of a tilting angle of 5°, this leads to AEP differences of -0.95% and -0.70% differences for the vector scalar and horizontal definitions, respectively. Realistically, the flow might at an "ideal site" be 5°, which leads to AEP differences of -1.8% and -1.1%, respectively. At these slope angles, the verification of performance seems to give small problems".

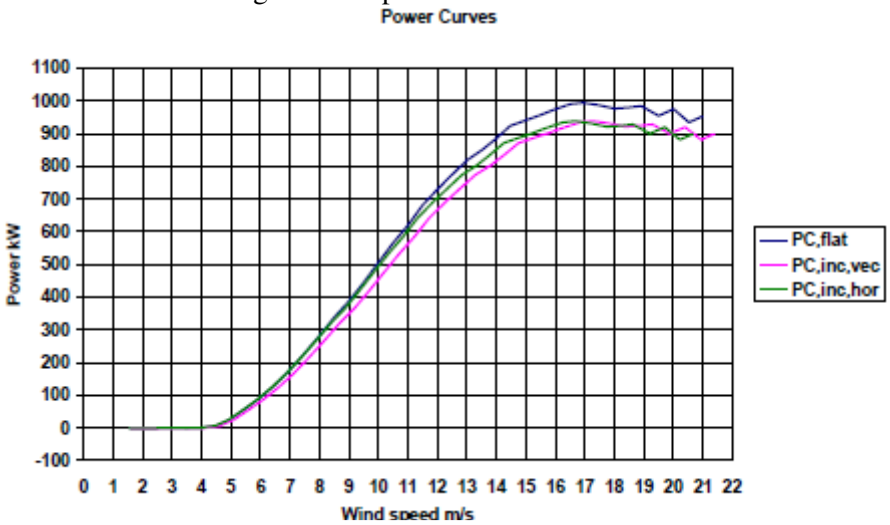

Figure 2 Simulation of different degrees of inclined flow.

On the turbulence effects on cup anemometers the report says: “Cup anemometers are influenced by turbulence in two ways; overspeeding and angular characteristics. Overspeeding might increase the reading by several percent, as has been shown earlier, but in the present study it is not taken into account. It could be argued that the overspeeding in flat and sloped terrain cancels out in when AEP from the power curves are subtracted.” On the indirect effects of turbulence effects on the cup anemometer it is stated:
“The turbulence changes the flow inclination to the cup anemometer, and over a period of 10 minutes, changes the signal, except if it has ideal characteristics for the defined measured wind speed. If a cup anemometer has flat angular characteristics and the defined wind speed is the vector scalar wind speed, then it has no dependency on turbulence.”

From this study and the example for the Risø cup anemometer response in Figure 3 it is clear that cup anemometers are sensitive to turbulence through altering the local flow conditions for the cup and thereby changes the cup response with a shape in the proximity of +-15 degrees close to a $\cos^2$ relationship.

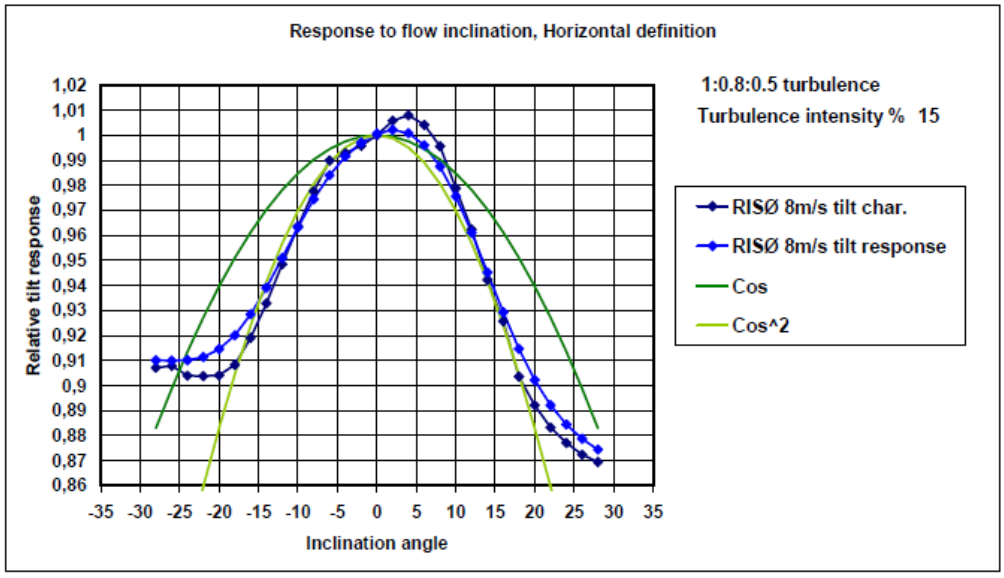

Figure 3Angular response characteristics of RISØ cup anemometer with horizontal wind speed definition, σ_u:σ_v:σ_w ≈1:0.8:0.5

A study on inclined flow effects on the power performance has been made by means of a nacelle anemometer(note: assumption is here Thies type) and reported [3.5], concluding with: ..” In a lot of cases the power curve based on the nacelle anemometer is consistent with the met mast measured power curve in terms of the annual energy production. Typical uncertainties of power curve measurements according to the IEC standard are 5-8 % in flat terrain and 6-12 % in complex terrain (inclusive site calibration with two masts).The differences found between the AEP from the nacelle and the AEP from mast measurements were in the range of only 1 % in moderately complex terrain.

In conclusion a change of the AEP is expected to happen in the range of 6%(flat terrain) to 10%(moderate complex terrain), which again is surrounded with uncertainty on the inherited influences from the cup anemometers on flow angle and turbulence.

Wind shear is a main driver in power performance measurements. As pointed out [POWASS] the energy flux P or turbulent kinetic energy(TKE) over a rotor area depends on the shear factor, as shown in Figure 4 .

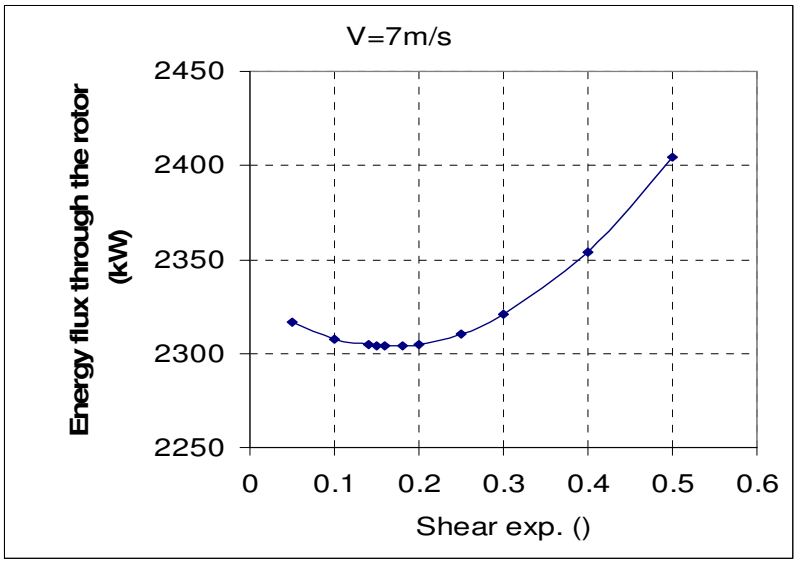

Figure 4 Energy flux vs. shear factor

In [3.6] the empirical knowledge of turbulent wind variations are studied by means of looking at the main contributions from the wind variations. It is shown, that the flapwise load under given design conditions of constant rpm and twist is driven by the fluctuating wind component u along with the average wind U. In essence the relative variation of the flapwise loading (σMy/My) under these assumptions is proportional to turbulence intensity Ti (σu/U). In other words the aerodynamic loading of the rotor is a footprint of the variability of the wind. A similar argument is used in[3.7] to analyze spectra performed in a rotating frame of reference. In the paper it is shown that wind shear is clearly visible.
This issue is followed up in the present analysis and has been an argument to apply the chosen experimental method.

There are quite a number of contributions to the scope of IMPER, and only few to be mentioned here: studies on the influence of atmospheric turbulence [3.8, 3.9, 3.10, 3.11], in complex terrain[3.12], an explanation of the physics for the origin of wind, and seasonal wind variations at the Danish National Test Site[3.13]. A summary of practical experience has been found in a description on field measurements carried out at about 126 different places in USA with SODARs[3.14]. In the paper, routine analysis includes plotting mean profiles by wind direction sector and by hour of day and fit data with a power law, screening of transient events such as front passages, low-level jets and circulation flow (mountain/valley, sea breeze) and is shown in Table 1 .

Table 1 Factors affecting the shape of the wind profile, from[14]

Meteorological:	**Site:**
Stability (hour, season)	Slope steepness, aspect
Low-level jets	Upslope vs. downslope
Frontal passage	Vegetation (roughness, stability)
Local circulations (mountain/valley, sea breeze, etc.)	

The authors suggest assessing / detecting the wind profiles with the following measures[3.14]:

- Shear—change in horizontal wind speed with height
  Friction velocity (u*), roughness length (z0), displacement height
- Directional shear (degrees of rotation)
  Directional shear (along- and cross-wind component shear)
- Flow inclination– vertical/horizontal
- Turbulence Intensity

The crosses indicate we will look into the data at the Risø Campus for the effects on power performance. In the paper, effort is made on to stress that wind profiles represented by a point measurement is not adequate for the power in the entire rotor disk, and a weighting by means of $\sum \rho A_i \, Cos^2(\Delta\theta) U^3_i$ as suggested [3.14]. Here P_i is the power calculated for the i^{th} layer, A_i is the area of the rotor disk and $\Delta\theta$ the difference between wind directions of layer relative to hub height wind direction.

From the investigation, following results seem in general valuable:

Inflow angle by hour of day

Temporal variations due to circulation effect in particular in mountainous areas (upslope/down slope pattern) with slopes as much as 10 degrees (3-4 % on power reduction as per $cos^2(10º)$.

Directional shear by hour of day

A variation of the wind direction by clockwise 0.2-0.5 Degrees/m in the rotor plane in particular early morning hours is observed, and with effects more pronounced at low wind speeds (cases above 5 m/s have also been observed), see Figure 5. Applying a Cos^2 method to these findings, 2-3% power loss is expected.

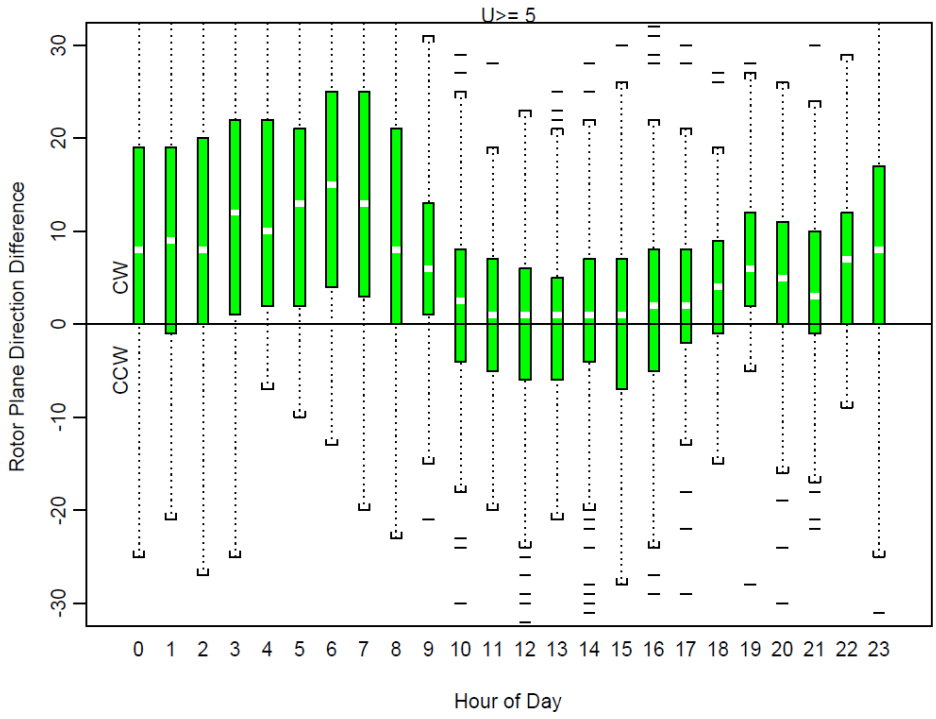

Figure 5 Wind direction differences (veer) between 40m and 120m. From[3.14]

Time varying horizontal wind shear

Temporal variations are observed on the mean wind profiles with positive and negative shear, changing the integrated power typically to a 5% loss.

Directional shear

A height –time representation of wind direction has been presented in the paper showing results from a site with thermal circulation within the rotor area. Shifts occur during the day, moving the profiles down towards mid-day.

Some closing words are made here on the rotor conditions, where factors like roughness of the rotor blades(including tip) affect the aerodynamic performance as shown in [3.15], and the condition of other aerodynamic devices such as vortex generators and stall strips.

The wind turbine in use is described in 4.2 and the aerodynamic devices are known to be in good conditions. However, blades have undergone natural exposure to wind and pollutants, and hereby aggregated roughness built up. We have here ignored to quantify the equivalent roughness-they are as shown minor in effect.

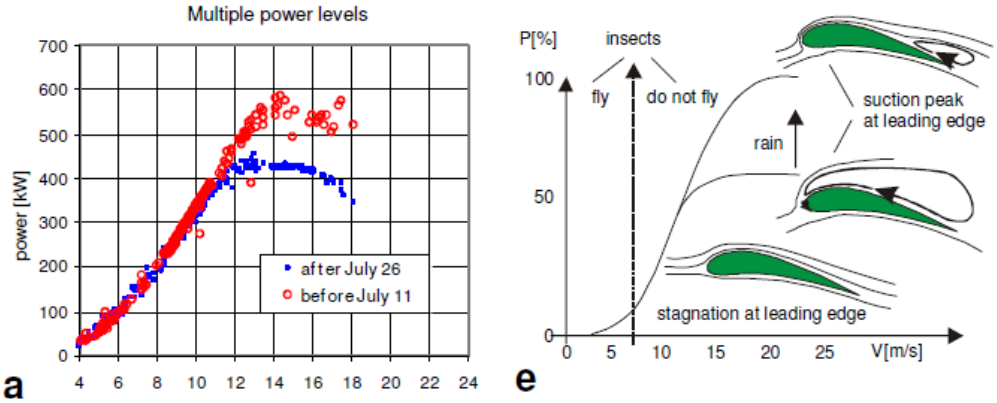

Figure 6 Effect of roughness for wind turbine power performance, a: power curves based on two measured roughness conditions, and e: flow stages around profile

3.1 References

3.1. Wagner, R. et al. The Influence of the Wind Speed Profile on Wind Turbine Performance Measurements Wind Energy 2009; 12:348–362

3.2. Wagner R. Accounting for the speed shear in wind turbine power performance measurement, Risø-PhD-58(EN), 155pp, 2010

3.3. Christensen, C.J. et al: Accuracy of power curve measurements Risøs-M-2632 133pp, 1986

3.4. Pedersen, T.F. et al. Wind Turbine Power Performance Verification in Complex Terrain and Wind Farms Risø R-1330

3.5. Axel, A.: Power performance Verification In EWEC99 Procedings.

3.6. Jensen, N.O., and Frandsen, S. Atmospheric turbulence structure in relation to wind generator design, in EWEA Proceedings of wind energy system Amsterdam 1978, paper C1

3.7. Connell JR, George RL Accurate Correlation of wind turbine response with wind speed using a new characterization of turbulent wind, journal of solar wind Eng. Vol 109 pp321-329, 1987

3.8. Albers, A. et al.: Influence of Meteorogical variables on measured wind turbine power curves, paper 163, pp7, In Proceedings EWEC 2007

3.9. Walter, K. et al.: Speed and Direction Shear in the Stable Nocturnal Boundary Layer, J. Sol Eng 2009 Vol131 2009 , 11013-1 – 11013-7
3.10. Summer, J. And Masson, C. : Influence of Atmospheric stability on wind turbine power performance curves, J. Sol. Ener Eng 2006 Vol128 p531-538
3.11. Sathe, A.: Influence of different wind profiles due to varying atmospheric stability on the fatigue life of wind turbines 2007 J. Phys.: Conf. Ser. 75 012056
3.12. Rareshide, E. : Effects Of Complex Wind Regimes On Turbine Performance, GH 2009
3.13. Nielsen, J.N. On the application of a numerical model to simulate the coastal boundary layer, Risø-PhD-39(EN),111 pp 2008
3.14. Moore, K. E.: Classifying rotor span shear profile variability and improving wind turbine production prediction
3.15. Corten, P. And Veldkamp, H. Insects can halve power. NATURE VOL 412 pp 42/43 www.nature.com, 2001

4 Description of the experimental facility

4.1 Site

The Wind turbine is geographically located at the Risø Campus, about 6 km North of Roskilde as shown on Figure 7. The wind turbine is placed on the foundation no 4, in a rather gentle sloping terrain towards the area 'Bløden' on the west side of the Roskilde firth. The free undisturbed inflow is from the dominant westerly wind direction.

Figure 8 shows an overview of the site with position of wind turbine, and meteorological mast(283 Deg).

Figure 9 shows the ambient turbulence intensity at the met mast. The influence of the open water is shown as a low turbulence intensity area with about 8-10 % turbulence intensity, and increases towards the south and north to about 20-30% in intensity.

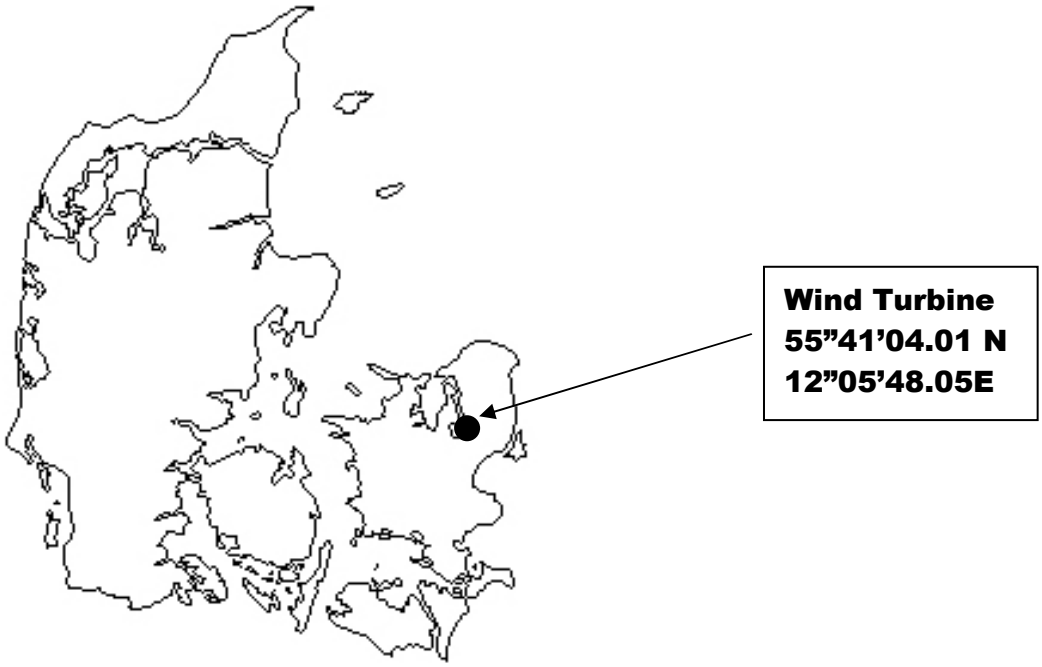

Figure 7: Location of turbine

Figure 8 Top:Map of DTU, Campus Risø and wind turbine(mark) ,and met mast-turbine direction(283Deg), from [4.15].Below: a westerly view from the nacelle.

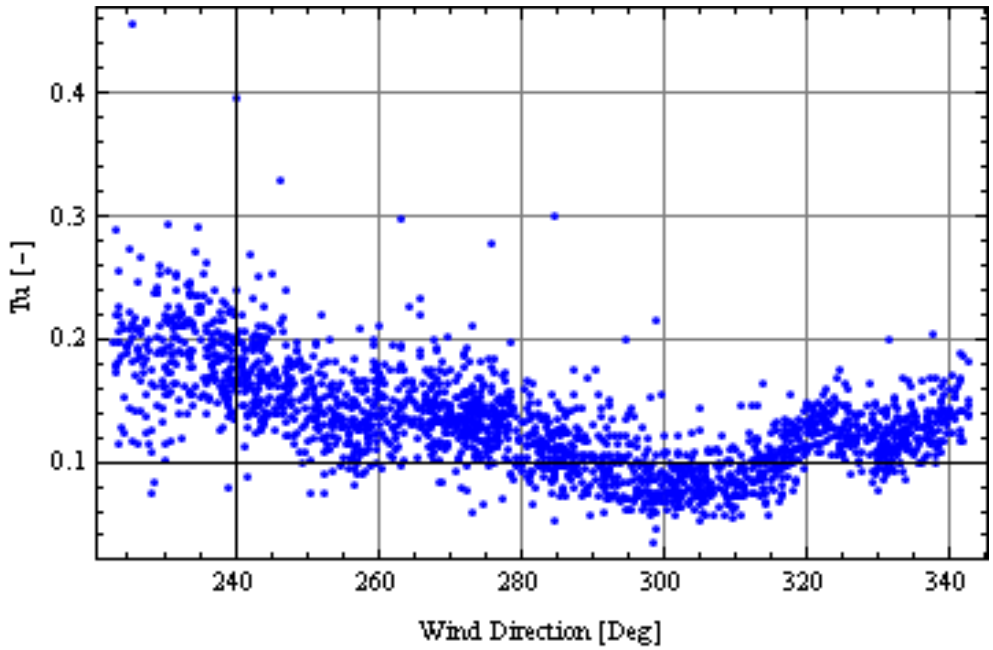

Figure 9 Site turbulence measured at 36magl measured with a cup anemometer

4.2 Wind Turbine Description

The test wind turbine, which is located at Risø Campus, Roskilde, is a traditional Danish three-bladed stall regulated Nordtank, NTK 500/41 wind turbine – see specifications in Table 2. Figures in brackets reflect results from post survey on turbine specs. The turbine is primarily used for energy production and tests and it is serviced on commercial conditions.

Figure 10 Photo of NTK500/41 wind turbine

Table 2: Nordtank NTK 500/41 specifications.

Identification No.	92-500
Rotor	
Rotor Diameter	41.1m
Swept area	1320 m²
Rotational Speed:	27.1 rpm
Measured tip angle:	-0.2º±0.2º

Tilt	2º
Coning	0º
Blades	
Blade type:	LM 19.1
Blade profile[s]	NACA 63-4xx & NACA FF-W3, equipped with vortex generators.
Blade length:	19.04 m
Blade chord:	0.265 – 1.630 m
Blade twist:	0.02 – 20.00 degrees
Air brakes	Pivotal blade tips, operated in FS-mode
Drive train	
Mechanical brake	High speed shaft, operated in FS-mode
Power regulation	Passive aerodynamic stall
Gearbox	Flender; ratio 1:55.35
Generator	Siemens 500 kW, 4 poles, 690 V
Tower	
Type	Conical steel tube, h=33.8 m
Hub height	36.0 m
Masses:	
Blade weight:	1960 kg (2249 kg incl. Extender and bolts)
Rotor incl. hub	9030 kg (9846 kg)
Tower head mass	24430 kg (25246kg)
Tower mass	22500 kg

The turbine was installed in 1992 with a 37 m diameter rotor, which in 1994 was substituted with a 41 m diameter rotor in combination with a rotor speed reduction to limit the power output. The wind turbine has been subjected to tests, modifications and investigations during 1992- 1999 with a short list of references [5.2,5.3,5.4,5.6,5.6]. There have been load measurements on the wind turbine drive train [5.7], and load simulations on a 600 kW gearbox design similar to the present wind turbine gearbox [5.8].

4.3 Grid connection

The wind turbine is connected to a local 400 V grid, designed for test of smaller wind turbines. The 400 V is supplied from the public 10 kV grid through a 1000 kVA, 10/ 0.4 kV transformer that is presently shared between the 500 kW Nordtank wind turbine and a 100 kW Tellus wind turbine.
The Nordtank wind turbine is rated to 690 V, and therefore an additional 800 kVA, 0.4 / 0.69 kV transformer is installed to increase the voltage. The principal electric connection diagram is shown in Figure 11.

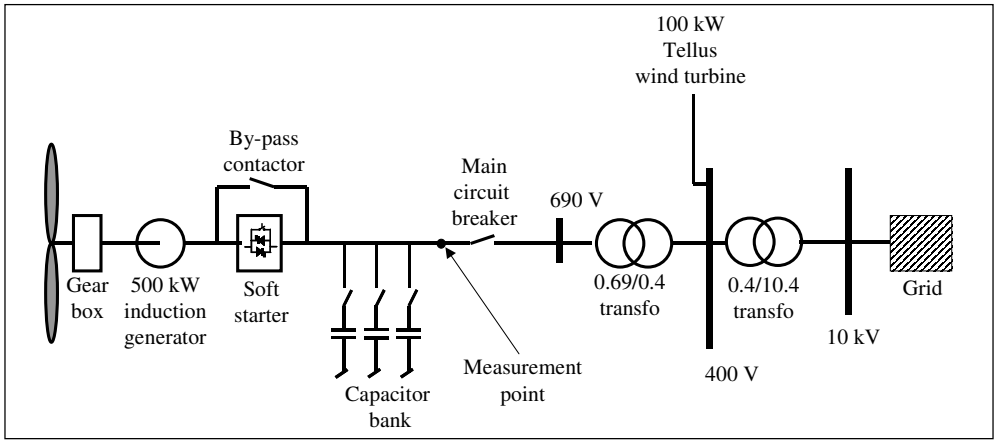

Figure 11: Connection diagram of 500 kW Nordtank in Risø.

A frequency converter system has been designed and implemented allowing the wind turbine to operate at variable grid frequency. This wind turbine operation mode can be switched to from stall regulated mode by means of a by-pass contactor as seen on Figure 11.

4.4 Instrumentation

Presently the experimental facility is instrumented as described in the following:
A meteorological mast is placed 2½ rotor diameters in westerly direction from the wind turbine. The mast is equipped for measurement of wind speed at hub height, wind direction, air temperature, air barometric pressure and air humidity. The installation is made in accordance with the recent IEC recommendations for both power performance [5.10] and structural load measurements [5.11] and [5.12,5.13].

Dedicated instrumentation devices such as the spinner anemometer and the 5-hole pitot system were planned to be implemented on the wind turbine for their potentials in revealing detailed information on the inflow at the rotor disk. Unable to implement them in service the description of the sensors are mentioned.

The structural loads are monitored by strain gauges mounted at the blade root, on the main shaft, at the tower top and at the tower bottom. The instrumented locations are detailed below:

4.5 Blades

The load signals from the reference blade includes bending moments at the blade root, measured by strain gauges mounted on the blade root steel extenders, as shown on Figure 12. The gauge installation enables measurements of both flap-wise and edge-wise bending moments in a rotating reference system.

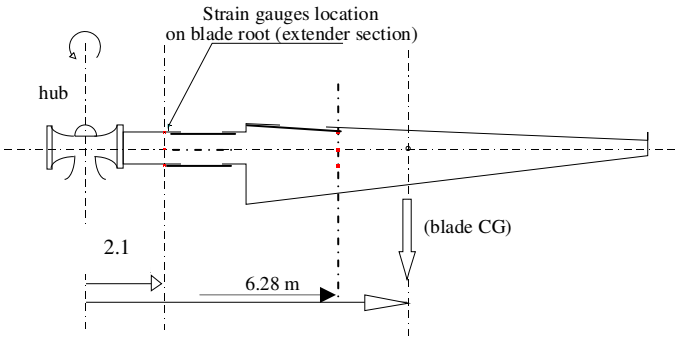

Figure 12: Structural load measurements in the blade root at radius 2.1 m.

4.6 Rotor and drive train

The load measurement on the main shaft includes a torque sensor in front and right after the main bearings, and two bending moments at a position behind the hub/main shaft flange – in a rotating reference system, as shown on Figure 13 . The gauge location enables measurements of bending moments in two directions, perpendicular to each other in a rotating reference system. The two bending moments combined with the rotor position are used to determine the rotor bending moments in yaw and tilt direction - in a nacelle reference system.

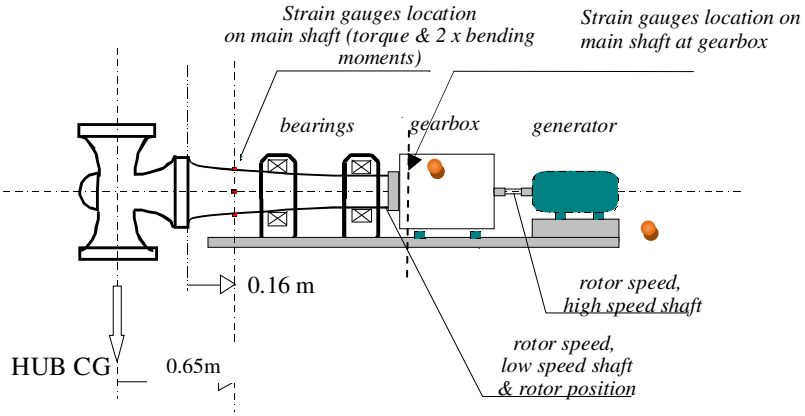

Figure 13: Structural load measurements on the main shaft.

Additionally accelerometers are positioned on the gearbox and on the rear of the nacelle, see Figure 14.

Figure 14 Left: Accelerometers on gearbox corner, and right- in the rear of the nacelle

4.7 Spinner

A spinner anemometer has been installed in order to provide detailed information about the interaction between wind flow towards the turbine, and the turbine yaw response and the effect of this difference on the power performance. The instrument is a prototype and has not worked properly in the period. The standard way of deriving the information was used with wind direction from the sonic anemometer at the met mast, and the nacelle position.

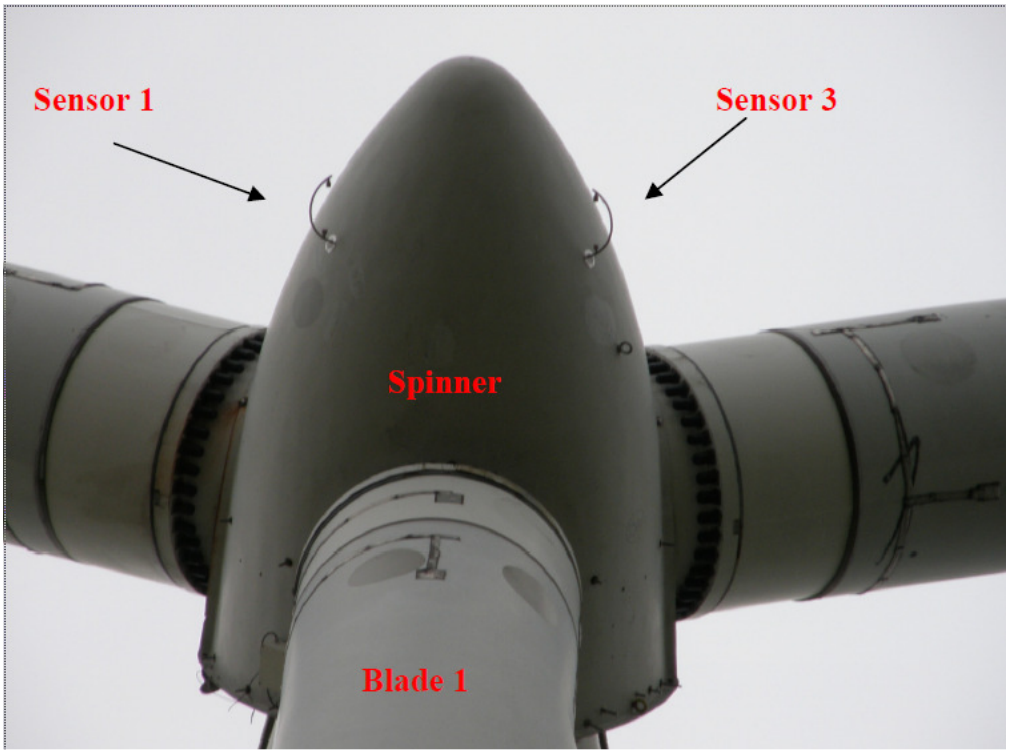

Figure 15 Photo showing spinner anemometer sensors 1 and 3 and 2 (hidden)

4.8 5-hole pitot

In 5.14 the use of a 5-hole pitot system was introduced to derive an aerodynamic power curve and to be able to show differences in vertical as well as horizontal inflow wind. A data acquisition system and a similar 5-hole pitot system see Figure 16, built for the PSO aerial sensors project, was planned here to be used in a similar manner as in [5.15], but it was not finalized to a technically acceptable quality. However, where the spinner anemometer is a dedicated instrument for providing

control of the effects of inflow and nacelle position, the 5-hole pitot tube sensor is dedicated for research of the interaction between inflow and the rotor output (power performance).

Figure 16 Photo of the manufactured 5-hole pitot system for inflow measurements on the rotor blade

4.9 Lidars

Two different LIDAR systems were put in service for IMPER: QinetiQ Zephyr continuous LIDAR system and a pulse LIDAR developed at the University of Stuttgart (SWE) equipped with a optic system for multivariate points scanning option, see Figure 17.

Figure 17 SWE LIDAR(left) and QinetiQ Zephyr LIDAR from Natural Power(right)

The SWE LIDAR was used for wake studies and has been used to profile the upwind conditions at the site. This has been achieved by stopping the turbine, yawing it 180 deg and letting the SWE LIDAR facing the wind and the mast. The wind turbine has been stopped several times during summer and autumn 2011:

- To study wake effect on a neighbouring turbine.
- To carry out profiling of the upstream wind conditions shore-mast

Ground based LIDARs(QinetiQ) Figure 17, right were operating successfully and installed in March 2011, with first one unit installed at the shore, as indicated approximately with a mark in Figure 18 (position 1). A second LIDAR was set in operation at a position 2, and the unit from position 1 was then moved into position 3, after the unit at position 2 was with failure. Details are shown in chapter 8 .

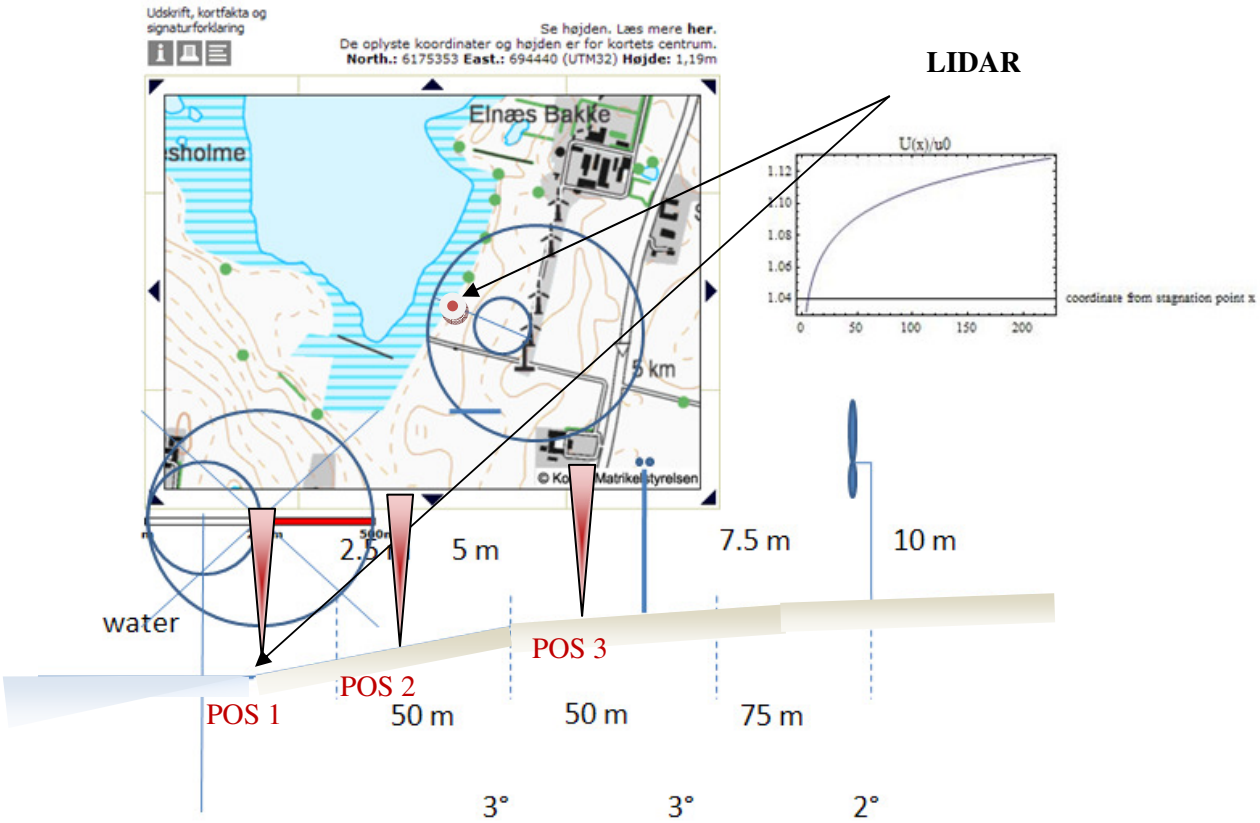

Figure 18 Overview sketch of site with location of LIDARs, and a rough estimation of the wind speed increase at the met mast, by means of potential flow solution of ideal flow approaching a 6 Deg symmetrical wedge.

4.10 Turbine tower

The tower loads includes torque at the tower top and bending moments in two directions at the tower bottom, as shown on Figure 19 in a (fixed) tower reference system.

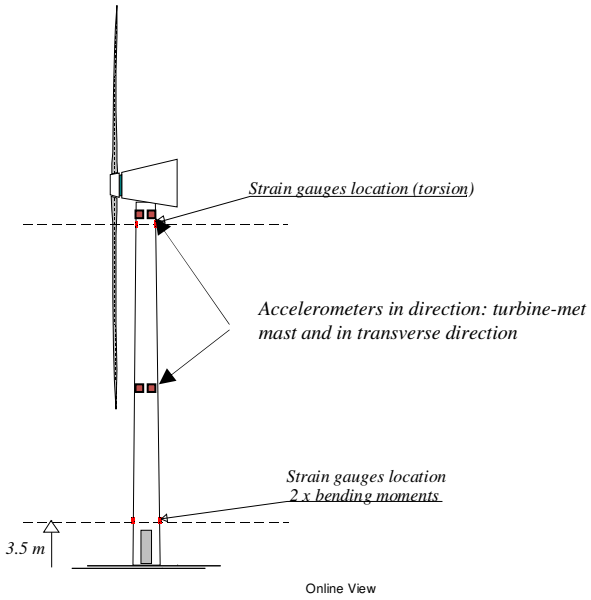

Figure 19: Structural load measurements on the welded tubular steel tower.

An overview of the signals, the type and sensor conversion principle is given in Table 6 see appendix.

4.11 Meteorological mast

The mast was reconfigured for wind speed instrumentation up to 57 magl. A sketch of the instrumentation of the mast and configuration is shown in Figure 20.

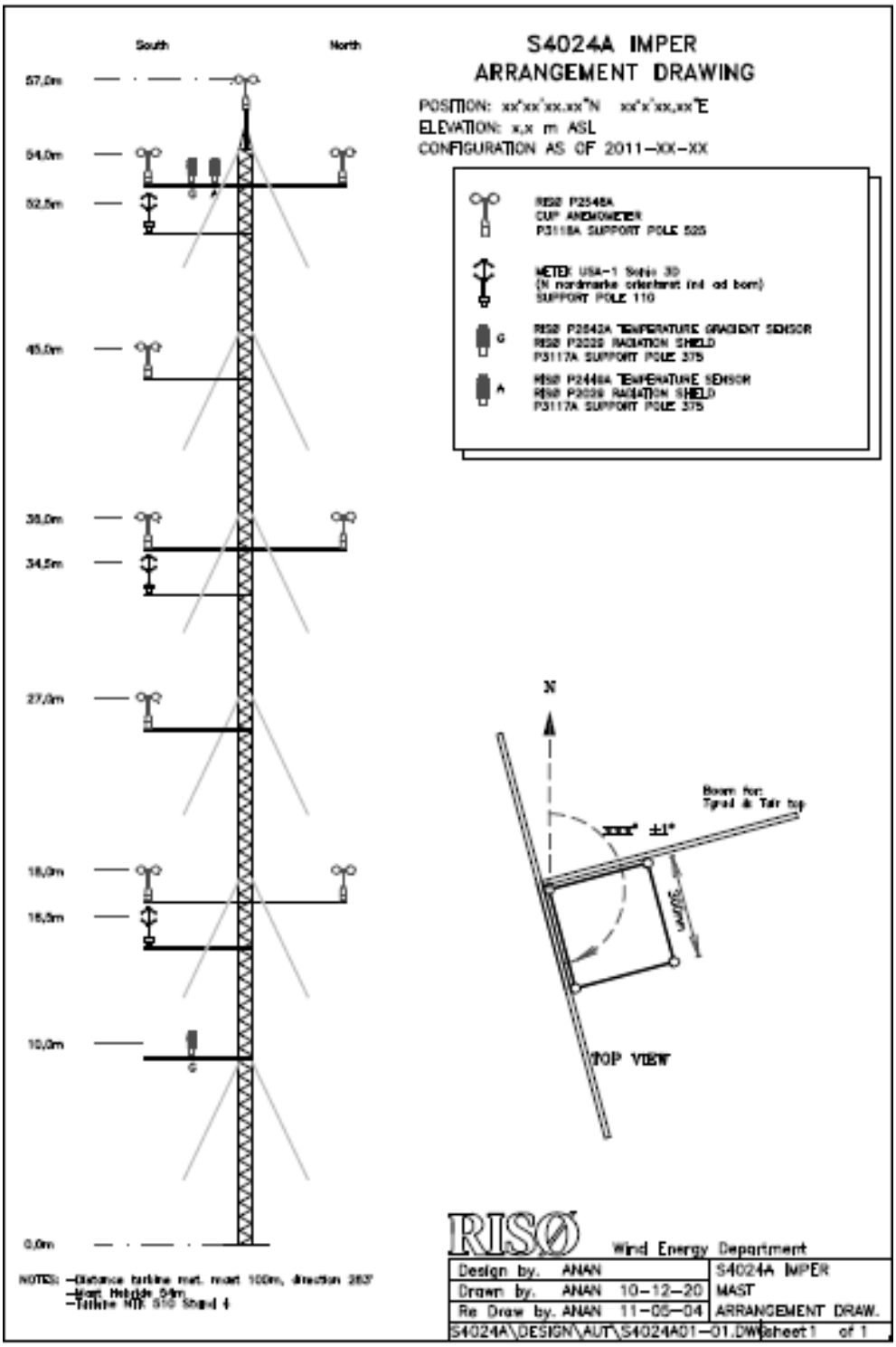

Figure 20 IMPER met mast instrumentation

4.12 Data Acquisition

A PC-based data acquisition system has been designed to monitor and collect data from the wind turbine sensors – see *Figure 21*.

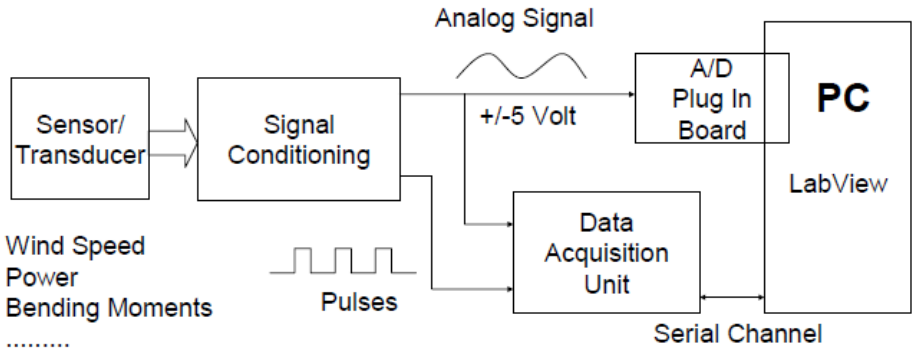

Figure 21: Overall load monitoring data acquisition system (35 Hz)

The output signals from all sensors are conditioned to the +/- 5 V range. Analogue signals are either continuously varying (strain gauges, temperature…), digital types such as train of pulses (rotational speed, anemometer…) or on/off levels (status signals for brake, blade tips and generator modes). All signals - except outputs from voltage and current transformers - are connected to one of three RISØ P2558A data acquisition units (DAU), each of which provides 16 analogue input channels and 6 general-purpose digital input channels [5.17]. The analogue inputs are converted into 16-bit quantities. Data from all channels are assembled in a binary telegram, each data occupying 16 bits. The telegram is preceded by two synchronization bytes and it is succeeded by two check-sum bytes. The whole telegram is transmitted to the PC over a RS232 serial channel at a rate of 38400 Baud. The sampling rate at the DAUs is set to 35 Hz so new telegrams are created and send 35 times per second per channel. One DAU is installed in the bottom of the wind turbine tower, another in the nacelle and the last one is mounted on the hub – it is rotating and transmitting data over a RF-link. The serial channel from each DAU is connected to the PC over a multi-port serial plug-in board. Even a 35 Hz scan rate is high when considering meteorological conditions, but appropriate for mechanical phenomena, and it is far too slow when studying the impact of the wind turbine on the power grid or mechanical loading in the drive train. The facility allows switching to a fast scanning system for studying mechanical and electrical interactions, but this is not used here. The data acquisition system is build up around a standard desktop PC and connected to the Internet and thereby to DTU from where it can be operated remotely.

To build up complete documentation of the wind turbine behaviour, data acquisition is carried out constantly. Dedicated measurement software DaQWin™ has been developed under LabVIEW©. The data streams received on the serial channels from the DAUs are read, error checked and the measured values are derived from the data telegrams. Data are assembled in 10-minutes time series and statistics such as mean, standard deviation, maximum and minimum values are calculated. The whole time series and the statistics – with a time stamp added – are stored on disk in ASCII-format.

4.13 Calibration and measured signals

The signals are calibrated in comparison with known sources. The strain gauge signals are calibrated by applying known loads on the structure schematically as shown in Figure 22. This is carried out on regular intervals. Details in the calibration procedure are shown in [5.18, 5.19].
There are regularly checks carried out on these signals; these are categorized as to idling at constant rotational speed at low wind speed as in Figure 23 and in Figure 24, and as yawing of the turbine 360 Deg around the horizon with results as in Figure 25 and with applied scaling the result shown in Figure 26.

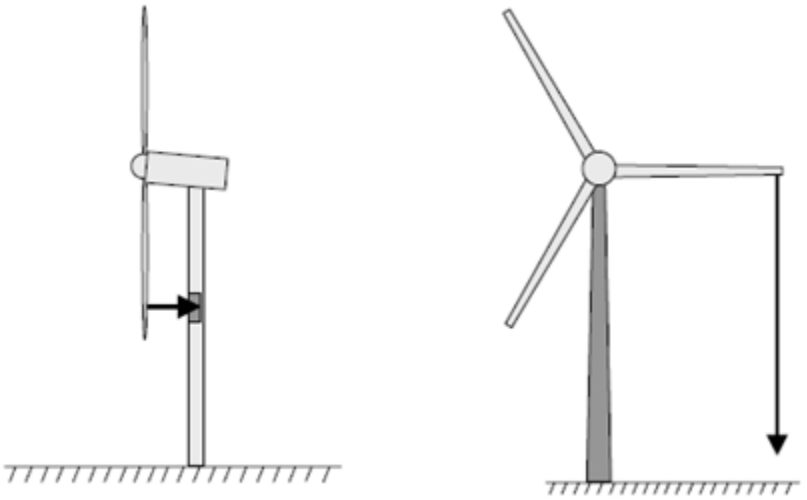

Figure 22 Rotor load calibration: Flapwise loads(left), Edgewise loads(right)[]

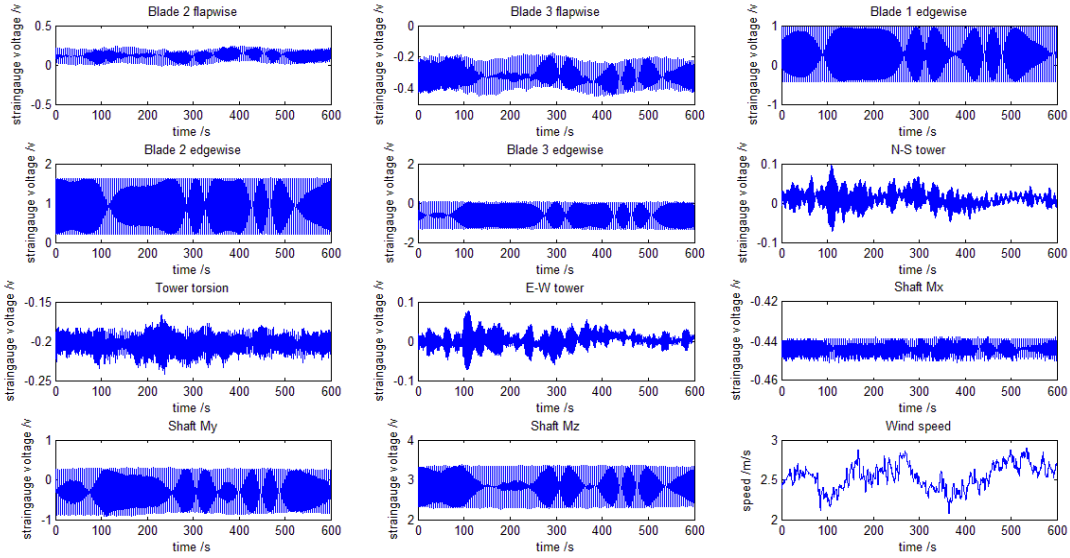

Figure 23 Idling of rotor at low wind speeds

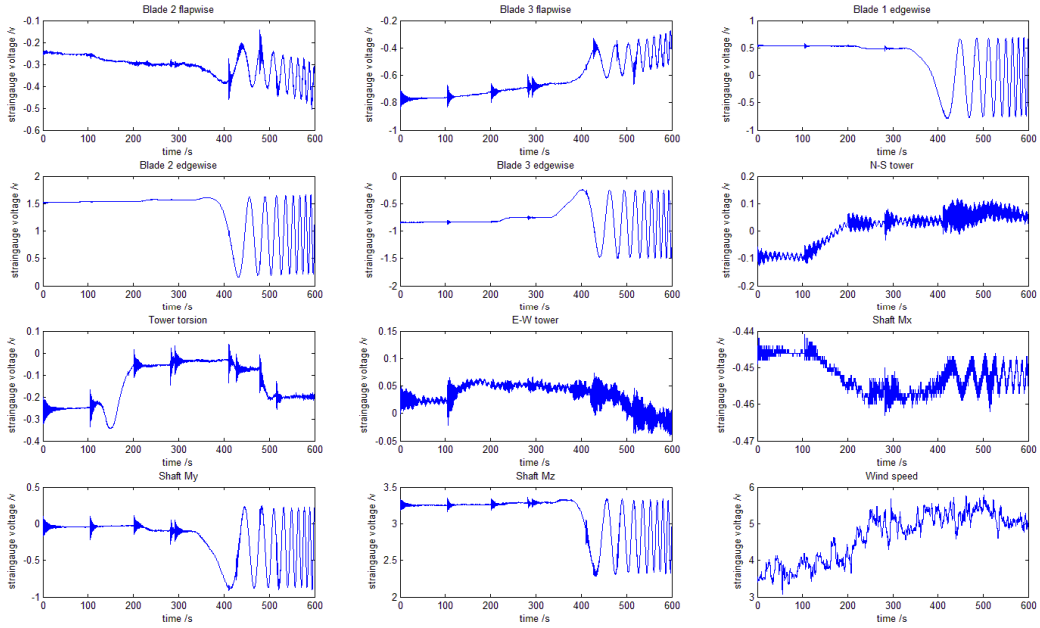

Figure 24: Wind turbine start sequence at low to medium wind speed

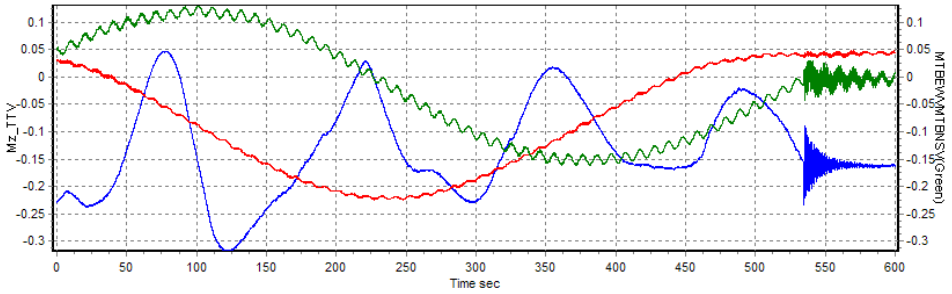

Figure 25: Mz_TT (Blue), MTBEW (Red) and MTBNS (Green) during 360° yaw test performed 28-07-2010

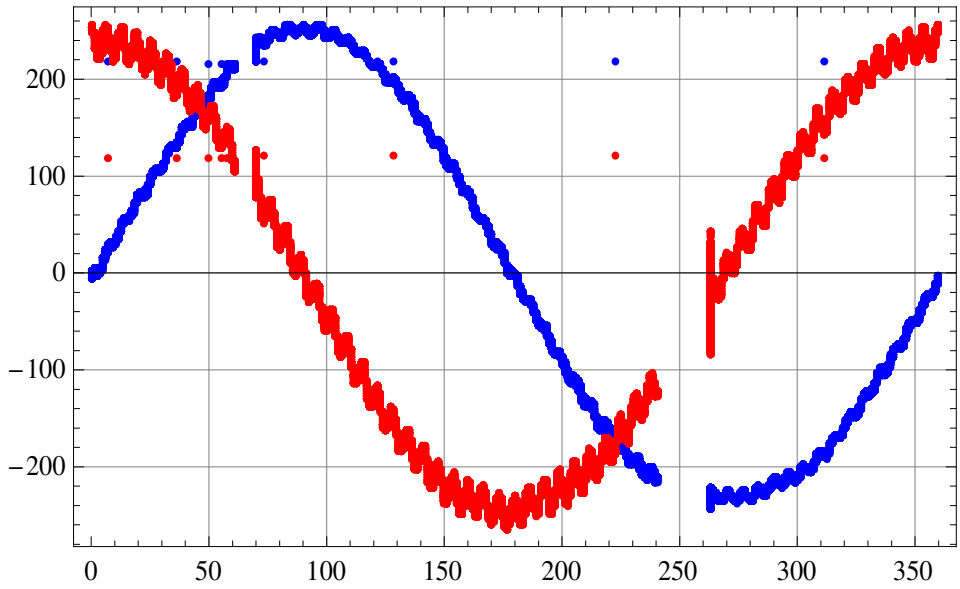

Figure 26MTBNS (Red), MTBEW (Blue) with physical scaling in kNm vs. nacelle position, in Deg. From yaw test 28-07-2010

The measurement signals with the complete gain and offset values are listed in Table 3.

Table 3 Signals with Gain and offset values for scaling

Ind	*Signal*	*Description*	*Gain*	*Offset*	*Units*
4	Mz_TT	Tower top torsion	-272.087	-121.079	[kNm]
5	MT_B_EW	Tower Bottom Bending moment,EW	1841.92	155.7	[kNm]
6	MT_B_NS	Tower Bottom Bending moment,NS	1782.25	31.4	[kNm]
7	Pe_net	Electrical Net Power	1	0	[kW]
8	AC_T_x1	Acceleration tower top x	2.212389	-4.77655	[g]
9	AC_T_y1	Acceleration Tower top y	2.227171	-7.34967	[g]
10	AC_B_x2	Acceleration Tower bot x	2.207506	-5.85872	[g]
11	AC_B_y2	Acceleration tower bot y	2.325581	-5.97674	[g]
12	IO_tip	Status of deployed blade tips	1	0	[-]
13	IO_brk	Status of brake activated	1	0	[-]
14	IO_gen	Status of generator on	1	0	[-]
15	IO_stl	Status of constant speed\variable speed	1	0	[-]
16	Precip	Precipitation	1	0	[-]
17	DAU_#0	Status DAU_#0	1	0	[-]
18*	WDC_Met	WDC_Met	1	0	[V]
19*	WDS_Met	WDS_Met	1	0	[V]
20*	WDD_Met	WDD_Met	1	0	[Deg]
21	Yaw	Nacelle position	1	0	[Deg]
22	RotAzi	Rotor Azimuth position	1	0	[Deg]
23	Rot_LLS	Rotor main shaft speed	1	0	[RPM]
24	Rot_HSP	Generator shaft speed	1	0	[RPM]
25	WS_Nac	Wins speed, nacelle	1	0	[m/s]
26	AC_GBx	Acceleration Gearbox forth\back	2.212389	-4.86062	[g]
27	AC_GBy	Acceleration Gearbox sideway	2.267574	-5.38549	[g]
28	AC_GBz	Acceleration Gearbox up\down	2.257336	-5.17381	[g]
29	AC_Nacx	Acceleration Nacelle forth\back	2.227171	-4.70379	[g]
30	AC_Nacy	Acceleration Nacelle sideways	2.217295	-4.19734	[g]
31	AC_Nacz	Acceleration Nacelle up\down	2.309469	-4.65127	[g]
32	Q_Shft2	Rotor Shaft torque main rotor#2	-613.648	1809.503	[kNm]
33*	Q_Shft3	Rotor Shaft torque High speed	11.79288	4.6755	[kNm]
34	DAU_#14	Status DAU_#14	1	0	[-]
35	WDR_Nac	Wind Direction reference signal Nacelle	1	0	[V]
36	WDS_Nac	Wind Direction viper signal Nacelle	1	0	[V]
37	WDD_Nac	Wind Direction(derived) Nacelle	1	0	[Deg]
38	Mx_NR	Main Rotor shaft torque	193.2	-87.8548	[kNm]

39	My_NR	Main rotor shaft bending 0-180 Degrees	108.2142	32.14643	[kNm]
40	Mz_NR	Main rotor shaft bending 90-270 Degrees	-117.738	333.7142	[kNm]
41	Mx11	Edgewise bending moment, blade 1	-169.865	79.25246	[kNm]
42	My11	Flapwise bending moment, blade 1	-142.72	-84.0623	[kNm]
43	Mx31	Edgewise bending moment, blade 3	-164.488	-97.9374	[kNm]
44	My31	Flapwise bending moment, blade 3	-143.756	25.85806	[kNm]
45	Mx21	Edgewise bending moment, blade 2	157.7466	-263.939	[kNm]
46	My21	Flapwise bending moment, blade 2	109.27	50.85978	[kNm]
47	DAU_#07	Status DAU_#07	1	0	[-]
48	SST_nac	Status Sonic nacelle	1	0	[-]
49	SSH_nac	Status heat Sonic nacelle	1	0	[-]
50	SX_nac	Vector Sonic nacelle x-direction	1	0	[m/s]
51	SY_nac	Vector Sonic nacelle y-direction	1	0	[m/s]
52	SZ_nac	Vector Sonic nacelle z-direction	1	0	[m/s]
53	ST_nac	Air temperature Sonic nacelle	1	0	[Deg C]
54	SHD_nac	Horizontal wind Direction Sonic nacelle	1	0	[Deg]
55	S3S_nac	Speed Sonic nacelle	1	0	[m/s]
56	SVD_nac	Tilt angle Sonic nacelle	1	0	[Deg]
57*	Spsp_Av	Spsp_Av	1	0	[m/s]
58*	Spyw_Av	Spyw_Av	1	0	[-]
59*	Spin_Av	Spin_Av	1	0	[-]
60*	Sp_sped	Sp_sped	1	0	[m/s]
61*	Sp_yaw	Sp_yaw	1	0	[Deg]
62*	Sp_incl	Sp_incl	1	0	[-]
63*	Sp_temp	Sp_temp	1	0	[Deg C]
64*	Spspd_Q	Spspd_Q	1	0	[-]
65*	Spacc_Q	Spacc_Q	1	0	[-]
66*	Spcal_Q	Spcal_Q	1	0	[-]
67*	Sp_Stat	Sp_Stat	1	0	[-]
68	SST_525	Status Sonic@52.5m	1	0	[-]
69	SX_525	Speed Vector x-direction@52.5m	1	0	[m/s]
70	SY_525	Speed Vector y-direction@52.5m	1	0	[m/s]
71	SZ_525	Speed Vector z-direction@52.5m	1	0	[m/s]
72	ST_525	Air temperature Sonic@52.5m	1	0	[Deg C]
73	S3S_525	Speed Sonic@52.5m	1	0	[m/s]
74	SHD_525	Horizontal wind Direction@52.5m	1	0	[Deg]
75	SVD_525	Tilt angle 52.5m	1	0	[Deg]
76	SST_345	Status Sonic@34.5m	1	0	[-]
77	SX_345	Speed Vector x-direction@ 34.5m	1	0	[m/s]
78	SY_345	Speed Vector y-direction@34.5m	1	0	[m/s]

79	SZ_345	Speed Vector z-direction@34.5m	1	0	[m/s]
80	ST_345	Air temperature Sonic@34.5m	1	0	[Deg C]
81	S3S_345	Speed Sonic@34.5m	1	0	[m/s]
82	SHD_345	Horizontal wind Direction@34.5m	1	0	[Deg]
83	SVD_345	Tilt angle@34.5m	1	0	[Deg]
84	SST_165	Status Sonic@16.5m	1	0	[-]
85	SX_165	Speed Vector x-direction@16.5m	1	0	[m/s]
86	SY_165	Speed Vector y-direction@16.5m	1	0	[m/s]
87	SZ_165	Speed Vector z-direction@16.5m	1	0	[m/s]
88	ST_165	Air temperature Sonic@16.5m	1	0	[Deg C]
89	S3S_165	Speed Sonic@16.5m	1	0	[m/s]
90	SHD_165	Horizontal wind Direction@16.5m	1	0	[Deg]
91	SVD_165	Tilt angle@16.5m	1	0	[Deg]
92	DAU_1_	Status DAU_1_	1	0	[-]
93	WS57	Wind speed cup@57m	1	0	[m/s]
94	WS54_N	Wind speed cup@54m North	1	0	[m/s]
95	WS54_S	Wind speed cup@54m South	1	0	[m/s]
96	WS_36_N	Wind speed cup@ 36m North	1	0	[m/s]
97	WS_36_S	Wind speed cup@36m South	1	0	[m/s]
98	Tdiff_54_10	Air Temperature Difference between 54m and 10m	1	0	[Deg C]
99	Tabs_54	Air Temperature@54m	1	0	[Deg C]
100	BMet_2m	Air Barometric Pressure Metmast @2m	1	0	[hPa]
101	DAU_2	Status DAU_2	1	0	[-]
102	WS_18_N	Wind speed cup@18 m North	1	0	[m/s]
103	WS_18_S	Wind speed cup@18 m South	1	0	[m/s]
104	WS_27_S	Wind speed cup@27 m South	1	0	[m/s]
105	WS_45_S	Wind speed cup@45 m South	1	0	[m/s]

* only listed for completion not in operation

4.14 Field experiences

The instrumentation was originally designed and partially carried out during 2006, and finished by 2007. The Nordtank turbine was then under repair from 2008 to 2009. Here the rotor was taken down for rotor blade repairs: refurbishment of tips, repair of surface cracks, and renewing the blade vortex generators which were broken. During spring the rotor was installed without blade strain gauges. During summer the strain gauges on the blades were installed. In July 2010 the system was ready for loads calibration, but a fault in blade No 1 flapwise instrumentation was discovered. In connection with the re-establishment of blade 1 strain gauges, the installations on the blade have shown drifting problems due to water ingress. Even after during 2010 and onwards, blade strain gauges are prone to drifting-even when considering that mounting are executed with the same quality procedures 'as usual'.

In late fall 2010 the preparations for extending the mast instrumentation to contain cups and sonic devices for IMPER, as shown in Figure 20. The cup anemometers at heights of 27 magl and at 45 magl have been installed to provide a better capability

to profile the wind. The mast was fully operational by March 2011, but suffered a week of downtime due to a failure caused by mice destroying the fibre optic cable.

The nacelle has been modified in late 2010 to carry a platform for the SWE LIDAR as shown in Figure 17, left.

5 Extended power performance measurements approach

5.1 Methodology

Analysis of data is carried out on the power performance according to the recommendations of IEC 61400-121[5.10] and on loads according to IEC 61400-13[5.11]. The recommended practices[5.13] on load cycles and counting techniques are used to categorize conditions defining a capture matrix with respect to:

- normal power production
- normal power production plus occurrences of faults
- parked conditions
- normal transients events and
- other than normal transients events

In the present analysis the normal production condition was particularly selected for further analysis for loads and performance studies.

The data are post processed on a time series basis with a accredited code *posttime.exe*, filtered according to the selection criteria and normalized with a accredited code *easy06082004.exe* as per power- and loads standards, and for statistical properties with *MsExcel2003©*.
The time series are in parallel processed and stored in a database environment allowing analyzing the statistical properties of the data with *MySql© and MathematicaV7©*.

The fatigue loads are evaluated using the Rainflow counting method (RFC). The RFC results in a load spectrum with information regarding the number of load cycles with a certain magnitude. The load spectrum was calculated for every 10-minute period. This procedure took place immediately after the end of each 10-minute sampling period (as a background operation) and simultaneously with the sampling of the next data set. The original result is a two dimensional vector consisting of the magnitudes of loads and the number of times these magnitudes appeared during those ten minutes. From these numbers the equivalent load corresponding to an equivalent predefined number of load cycles was calculated.

The RFC method is described in detail in Ref. [5.11] and the fundamental assumption is that the Palmgren-Miner damage rule applies. This rule states that, it is possible to accumulate the fatigue damage experienced by a component with the use of a simple linear method and thus obtain information on the total fatigue damage in a certain time period. The RFC is here performed using 50 range levels between minimum and maximum of the signals and a jitter filter size of one range level After the RFC load spectrum is established for an average of ten-minutes it is converted into an equivalent load range L_{eq} , and an equivalent number of load cycles N_{eq} ,

which together should have the same damaging effect as the original RFC load spectrum for the time period of the 10 minutes. Thus two numbers Leq and Neq can express the fatigue damage in a ten-minute period finally. N_{eq} has in this case, been selected arbitrarily equal to 600 in order to match one second. With N_{eq} selected as constant all information on the fatigue damage is expressed as L_{eq}, defined as:

$$L_{eq} = \left[\frac{\sum_i R_i^m \cdot n_i}{N_{eq}} \right]^{1/m}$$

where R_i is the magnitude of the range level (i) and n_i the number of times this range level appeared.
The exponent (1/m) is the slope of the material Wöhler curve and the summation is carried out over the total number of ranges (i=50) in the Rainflow spectrum. L_{eq} is in the present case calculated for m=12 for strain gauges on the blades, m=8 for strain gauges on the shaft and m=4 for strain gauges on the tower. The method has been performed on 35 Hz sampled data sets.

5.2 Selection of data

While the 35 Hz data acquisition system runs on an automatic mode, regular data collections are provided and forwarded for processing on a server for data base processing (statistics) and for time series. A comprehensive analysis of statistical data from the Nordtank data base has been performed here, and the measurements are covering a period from April to November 2011. A refinement of the data selection is carried out to reflect the following criteria:

- The measurement period covers the period May 29 15:40 to September 30 24:00 2011, in all 1792 10- minutes data
- All westerly wind direction sectors within the measurement period, i.e. between 223° to 343°.(sector +-60 Deg from base 283 Deg)
- Run duration equal to 600 sec.
- Wind turbine available ($IO_{brk} = 0$)
- No failure on the test equipment
- No turbulence selection/specification
- No fault, no maintenance or no manual shut down on the wind turbine(fail free=0)
- No still stand of the wind turbine($IO_{gen} = 1$)

5.3 Loads and performance analysis

Derived signals were generated in the post processing process to provide the following channels shown in the overview of Table 4:

Table 4 Derived channels overview

Ind	Variable	Name/description	Gain	offset	SI-unit
106	Airdens	Air density	1	0	[kg/m3]

107	WindDir	Wind Direction	1	0	[Deg]
108	Yaw_Dir	Nacelle position	1	0	[Deg]
109	Yaw_err	WindDir minus Yaw_Dir	1	0	[Deg]
110	Mx11_MR	Blade bending moment(edge),Blade 1, mean removed	1	0	[kNm]
111	MyNr_MR	Shaft Bending moment, mean removed	1	0	[kNm]
112	MzNr_MR	Shaft Bending moment, mean removed	1	0	[kNm]
113	Omega_L	Rotor speed, main rotor shaft	1	0	[rad/s]
114	ShtPm_L	Mechanical power, main rotor shaft	1	0	[kW]
115	Omega_H	Rotor shaft speed, generator	1	0	[rad/s]
116	My21_MR	Blade bending moment(Flap),Blade 2, mean removed	1	0	[kW]
117	MzNf	Rotor yaw moment	1	0	[kNm]
118	MyNf	Rotor tilt moment	1	0	[kNm]
119	Mx_TB	Tower Roll bending moment	1	0	[kNm]
120	My_TB	Tower Tilt moment	1	0	[kNm]
121	WS_54M	Wind speed cup 54m	1	0	[m/s]
122	WS_36M	Wind speed cup 36 m	1	0	[m/s]
123	WS_18M	Wind speed cup 18 m	1	0	[m/s]
124	WS_SHR	Wind shear exponent weighted over 18m,27m,36m, 45m, 54m	1	0	[1/s]
125	Mx11_OR	Blade bending moment (edge),Blade 1, mean removed	1	0	[kNm]
126	Mx21_OR	Blade bending moment (edge),Blade 2, mean removed	1	0	[kNm]
127	Mx31_OR	Blade bending moment (edge),Blade 3, mean removed	1	0	[kNm]
128	My11_OR	Blade bending moment (Flap),Blade 1, reference to Blade 2	1	0	[kNm]
129	My21_OR_ref	Blade bending moment (Flap),Blade 2, reference	1	0	[kNm]
130	My31_OR	Blade bending moment (Flap),Blade 3,reference to Blade 2	1	0	[kNm]
131	WSM_54M	WSM_54M	1	0	[m/s]
132	WS_W_36	Wind speed@ 36m (average of north, south)	1	0	[m/s]
133	WDdiff_525_165	Wind Direction difference between 52.5m and 16.5m)	1	0	[Deg]
1	Mx11	RFC Mx11	1	0	[kNm]
2	My11	RFC My11	1	0	[kNm]
3	Mx21	RFC Mx21	1	0	[kNm]
4	My21	RFC My21	1	0	[kNm]
5	Mx31	RFC Mx31	1	0	[kNm]
6	My31	RFC My31	1	0	[kNm]
7	MTBEW	RFC MTBEW	1	0	[kNm]
8	MTBNS	RFC MTBNS	1	0	[kNm]
9	MzNf	RFC MzNf	1	0	[kNm]
10	MyNf	RFC MyNf	1	0	[kNm]
11	Mx_TB	RFC Mx_TB	1	0	[kNm]

12	My_TB	RFC My_TB	1	0	[kNm]
13	Mz_TT	RFC Mz_TT	1	0	[kNm]

Mx11_OR, Mx21_OR and Mx31_OR are intended to suppress offset drifting of the strain gauges by removing the mean value of the series. My11_OR, My21_OR and My31_OR are referred to My21 signal because this has been the most stable throughout the period with little zero drifting. However it is by far not standard to correct in this way; the normal is to conduct measurements at 'no wind' conditions as reference. WSM_54M means a geometric means of wind speed sensor south and north, and WSW_36 is the area weighted wind speed (e.g. $A^{-1}\sum A_i u_i$) of the cups at 18magl, 27, 36, 45, 54 and 57 magl.
The last 13 channels are expressing Rainflow counting to be applied in the analysis results.

5.4 Results from post processing time series

The results are provided in the appendix and gives an overview of the channels plotted (average, standard deviation, minimum and maximum) as functions of average 10 minute wind speed at 36 m.

The blade moments discussed are corrected for zero drift; a simple correlation of mean values (power versus flapwise bending moment) is used to manipulate the curves from the original line inherited with drifting to a common, unbiased reference.

The filtered data covers a period from 20110704 13:00 to 20110913 11:40, expressing the applied filters mentioned previously. The plots show the signals with the wind turbine power ranging from cut in to stall conditions, at about 16 m/s.

A final remark: the analysis is provided for test conditions where the wind turbine is exposed to a free wind, which inherently is without any mechanical turbulence from other turbines. In other words, the natural turbulence is without footprints from processes that structures the wind in a certain pattern.

5.4.1 Wind direction difference over the rotor disk area

In the following plots the 35 hz observed wind direction difference at 52.5m and at 16.5m differences (e.g.) over the rotor disk area is presented; Figure 27 shows the overall observed distribution.

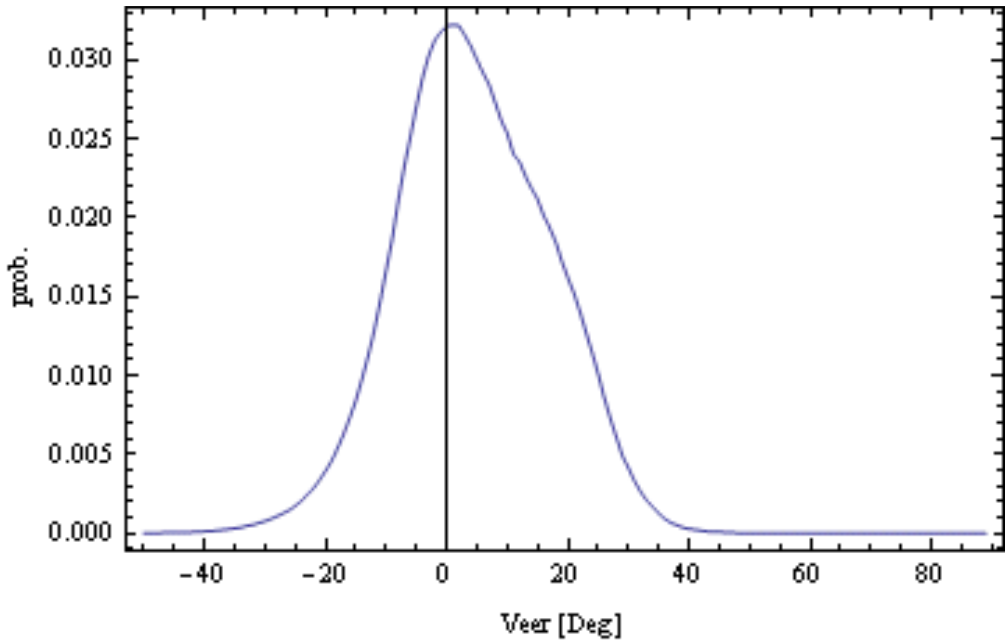

Figure 27 Wind direction difference, in average during the period

About the distribution within 10 minutes itself, there is more variation than indicated in Figure 34; in average the distribution of wind direction difference over the rotor disk area is as indicated in Figure 27, with an average veer of -0.5 Deg and a range of almost 70 Degrees. It is also within this band from -20 to 20 Deg where most the power is produced from the wind turbine. However during the measurement period substantial variation in veer has been observed as shown in Figure 28.
The observations show that during the day and night the wind direction pattern changes, as indicated in Figure 29, and in Figure 30. The wind speeds are 5 m/s±0.25m/s and 8 m/s±0.25m/s, respectively. It is likely that there is a yearly variation of this pattern, but in absence of long term measurements this is open.

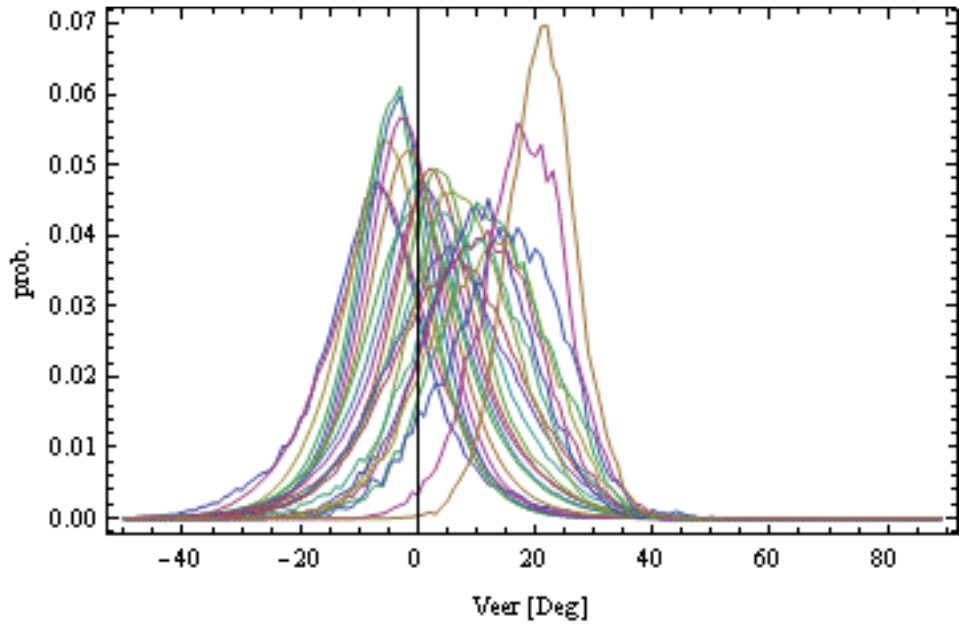

Figure 28 Distribution of wind direction differences within 10 minutes during the period into 27 curves. The bin width is 1 Degree.

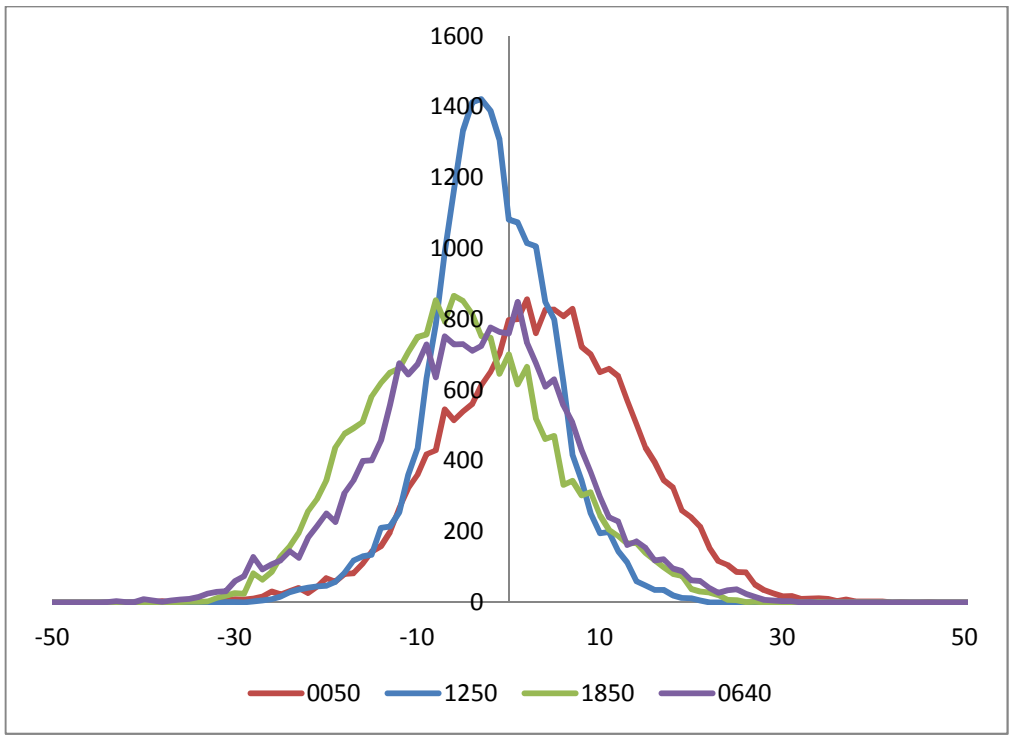

Figure 29 Wind direction distribution(counts) over the rotor disk at 5 m/s, at different timings. Each of the runs corresponds to each 21000 counts.

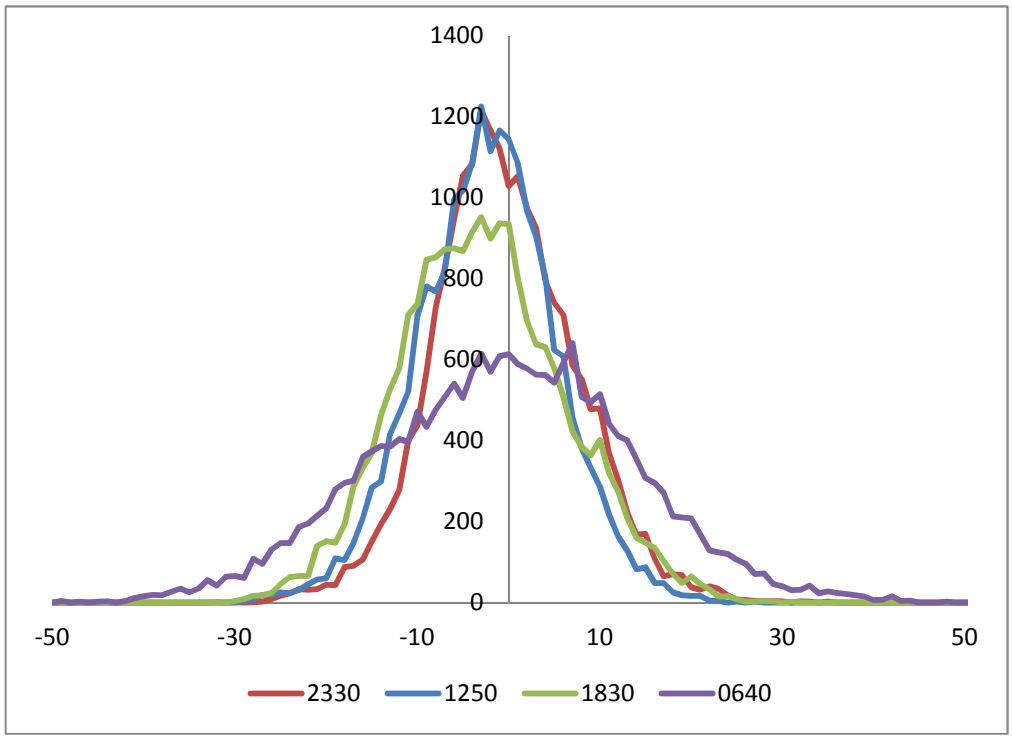

Figure 30 Wind direction distribution(counts) over the rotor disk at 8 m/s, at different timings

Figure 31 shows again a cycle of the variation during a whole day and night, on the basis of all time series analysed.

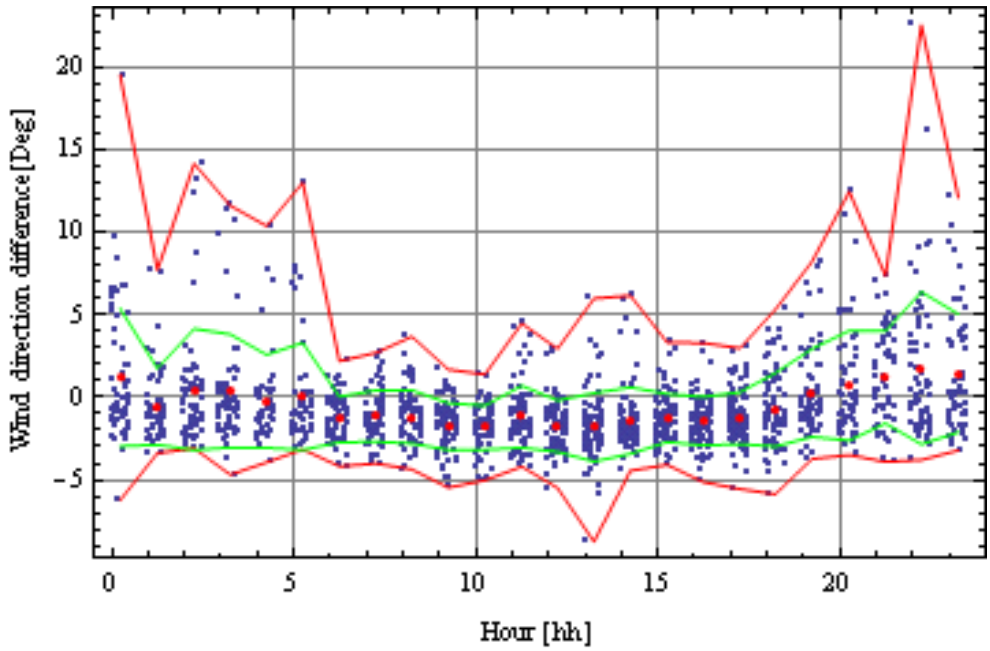

Figure 31 Wind direction difference over the rotor disk area from the time series

5.5 Results from analysing MySQL Nordtank database

The Nordtank database was used to derive correlations between different parameters as explained in the introductory chapters. The analysis describes wind characteristic parameters (nocturnal variations, stability, and turbulence), and wind turbine output from a point of view where the wind turbine extracts power as reacts to the inflow in a structural way. The results are presented in the following:

With the applied filtering, the data are distributed statistically more or less even over the period, as indicated in Figure 32.

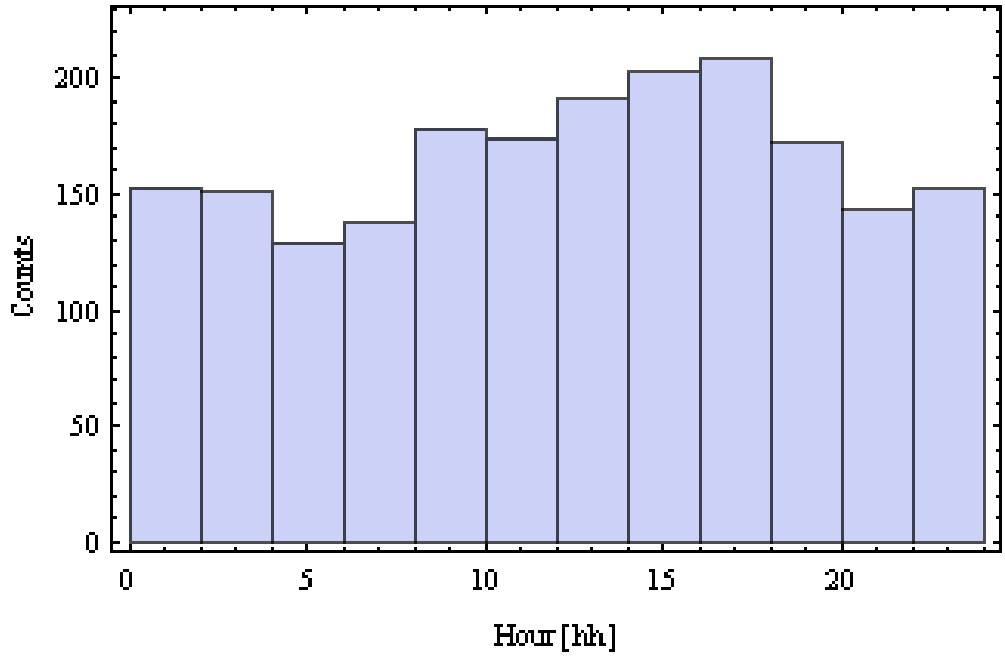

Figure 32 Histogram of the data on a daily cycle

5.5.1 Turbulence

Figure 33 shows the turbulence intensity during the entire measurement period and can be fitted nicely by applying $F(\Gamma(1+2/k)/\Gamma(1+1/k)^2 - \langle u^2\rangle/\langle u\rangle^2 \equiv 0)$ with result (A,k)=(4.34,1.680).

The day-night variation of turbulence intensity is shown in Figure 35. During night there is more stable conditions in the ABL, and during day time the wind is characterized as to unstable or near neutral conditions [5.22].

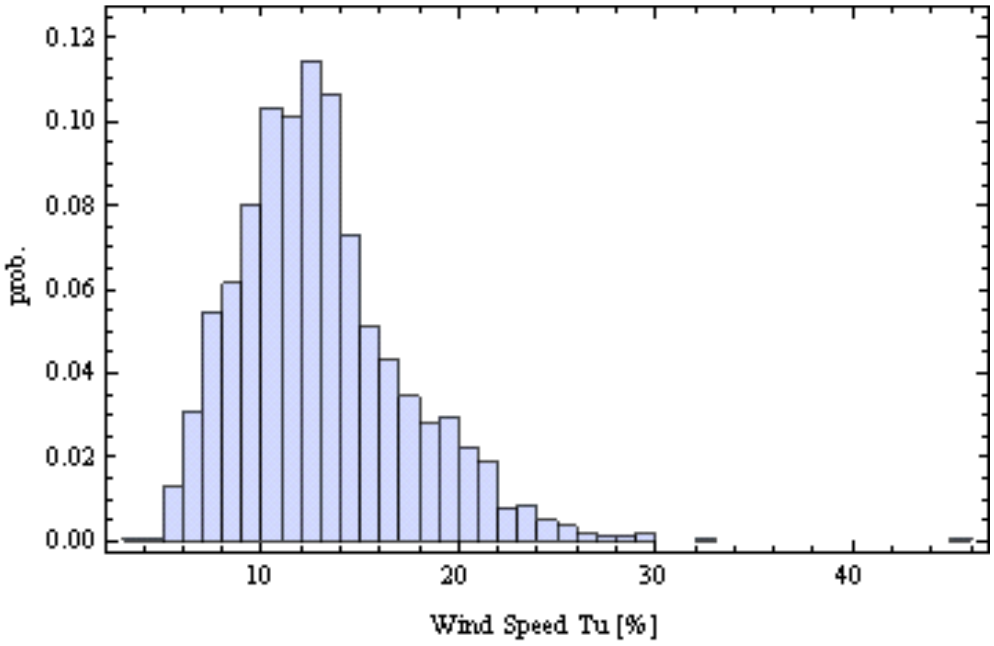

Figure 33 PDF of the turbulence intensity during the measurement period

5.5.2 Flow towards and over the rotor disk area

Figure 34 shows the distribution of the 10 minutes data, and with a similar fitting procedure than for the wind speed, the Weibull distribution is fitted nicely with the data.

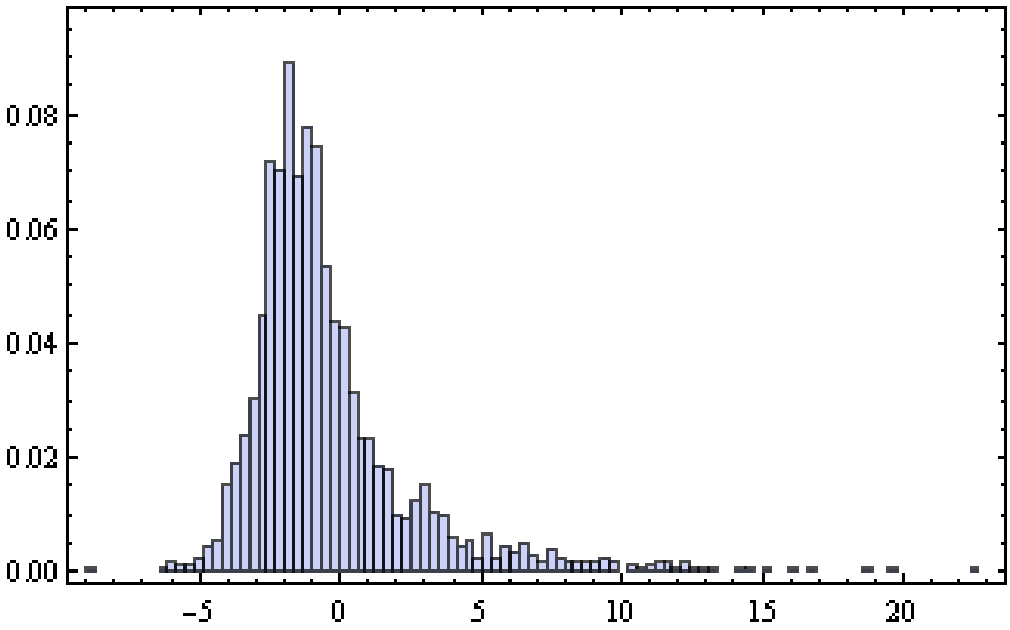

Figure 34Wind veer (WD@52.5m-WD@16.5m). 10 min- average values distribution over the rotor disk Weibull fit A,k(9.07,3.219)

Figure 35 shows the difference in wind direction measured at 52.5m and at 16.5m with Sonics, here shown as 10 minute averages over the day and night time. In connection to turbulence it also shows that the nocturnal wind is characterized as less turbulent than at noon, with the higher extend of energy radiated from the sun to the soil and with a more unstable classified wind.
It also means that horizontal direction changes are to be expected over stable ABL during night and that a well mixed ABL show less variance during mid-day.

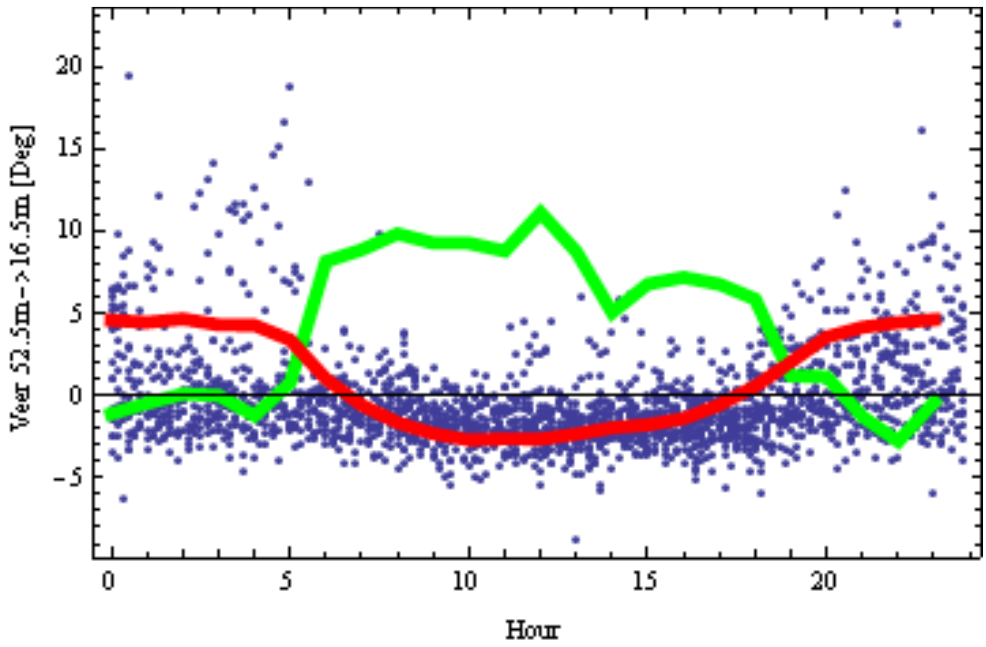

Figure 35Direction difference over the rotor disk area(scatter 10 minutes data) and Temperature difference diff54_10m(red solid line, scaled arbitrarily), and Tu(green solid line, scaled arbitrarily) on an hourly basis

Figure 36 shows the veer relationship with the wind direction, and it is obvious that the low turbulence from the direction of the open fjord is providing a situation with a lump of air with more or less unchanged wind direction differences over the rotor. In comparison the landscape towards south reflects variations, likely governed by the more hilly countours.

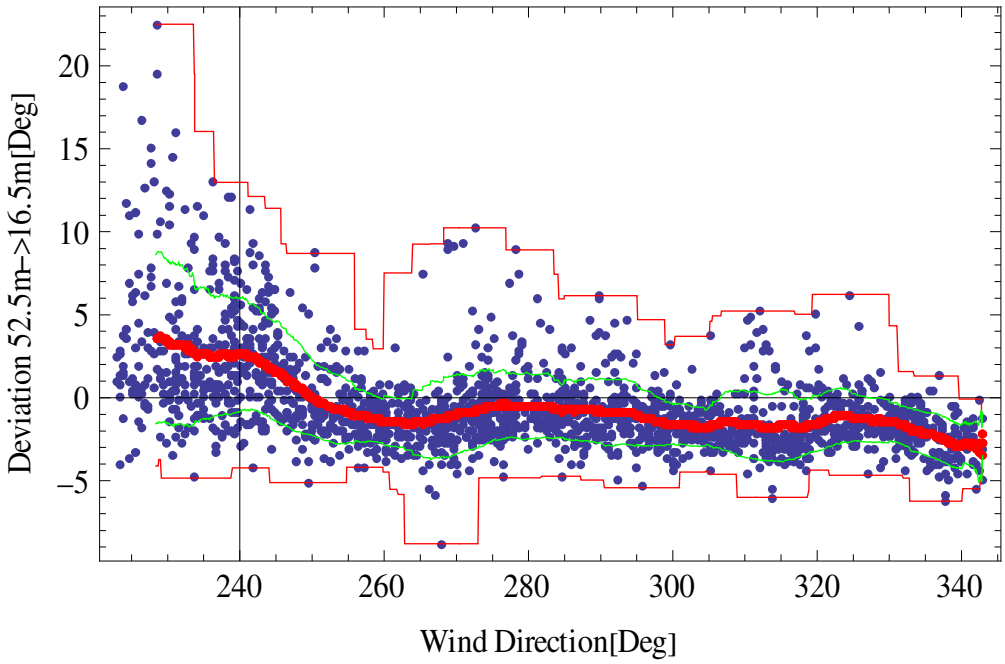

Figure 36 Veer vs. wind direction (scatter) and 10 deg bins (thick red line) ±1 stdev (green line), max-min with red thin line

The sonic instrumentation provided inflow measurements with regard to mean horizontal directional changes(Figure 37) , mean inclination (divergence from vertical, Figure 38) and the mean air temperature profile(Figure 39). The temperature profile was unexpected and particular analysis of the instrumentation showed as in Figure 40, that the deviations between the temperature readings are about 1.8 DegC compared to the reference Tabs@54magl.
On the discussion of instrumentation uncertainty we have uncertainty on the installation(e.g. verticality) connected with the observations, and the flow distrortion and mast deflections at the sensor positions. A verticality of 1 Deg seems to be to be technically difficult though, but achievable. In this perspective results are to be connected to uncertainties which will rules out definite differences observed.

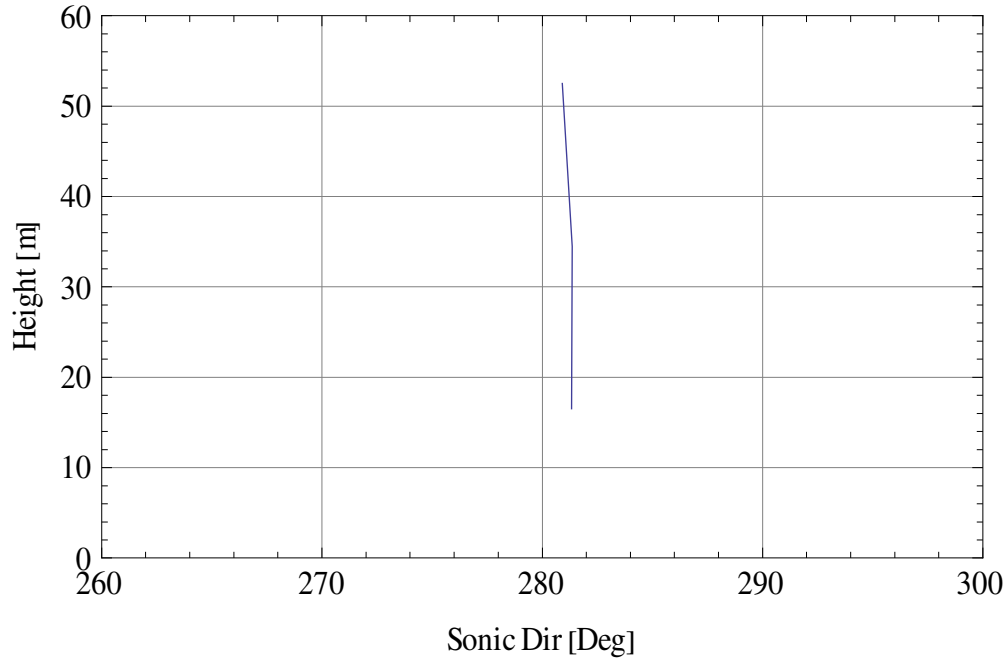

Figure 37 Mean value of horizontal direction over height

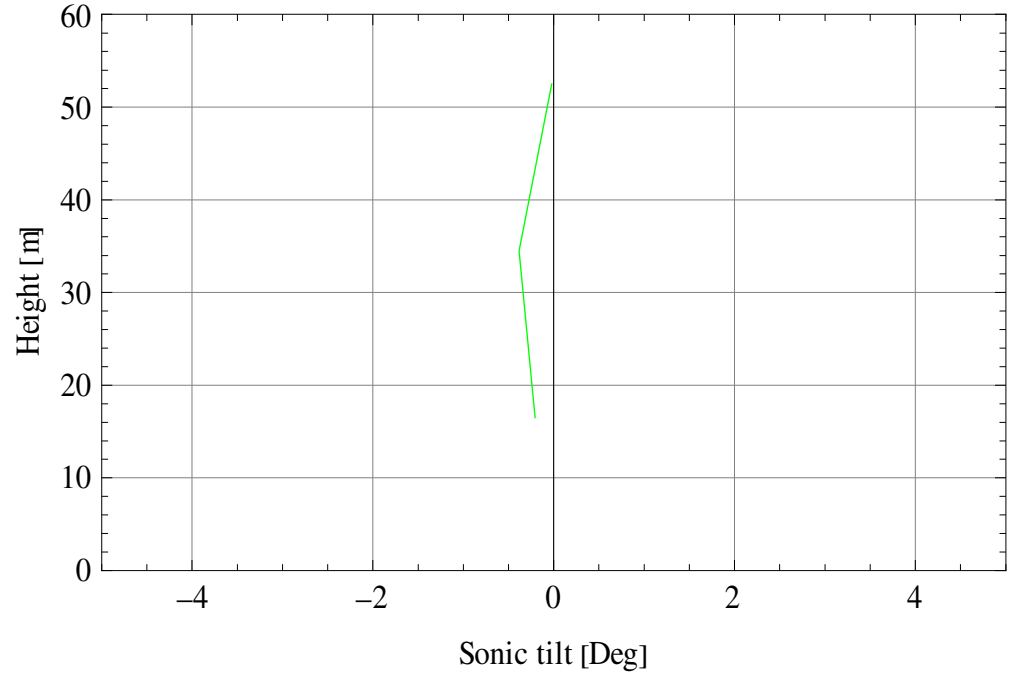

Figure 38Flow inclination (tilt) over height

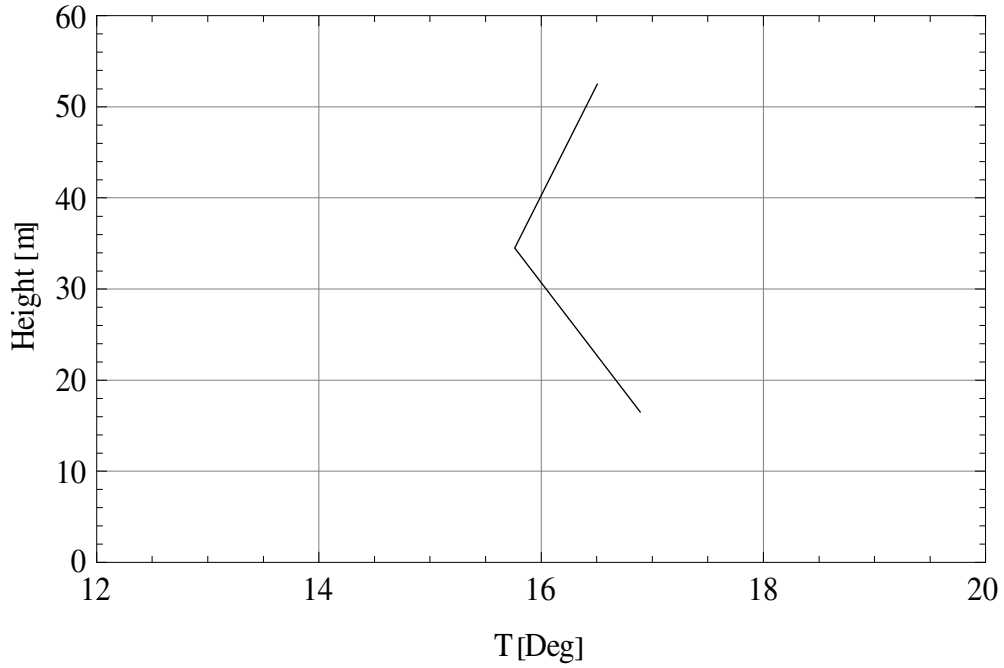

Figure 39 Air temperature over height

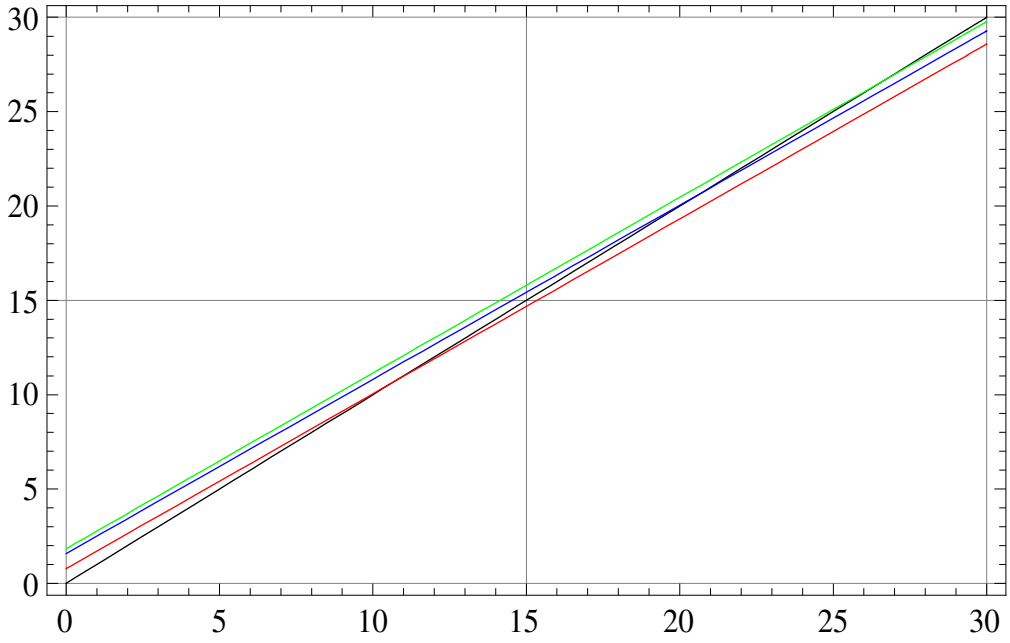

Figure 40Fit of Sonic temperature@34.5m (red), @52.5m (blue) and @16.5m(green) as function of sonic temperature ST_52_5(referenced to Tabs@54magl)

Figure 41 shows a comparison between the mean values from cup anemometers and from the three Sonics during the period, and through the observed temperature difference of the sonic anemometer at 16.5m it could be obvious that the measurements from this particular sonic is different to what it should be.

The cup anemometers have been analyzed to derive a wind signal which takes into account the vertical shear over the rotor disk, and Figure 42 shows a comparison of the weighted wind speed with the point measurement at 36 m. The spread of this

ratio at lower wind speeds is more remarkable than the ratios observed at higher wind speeds.

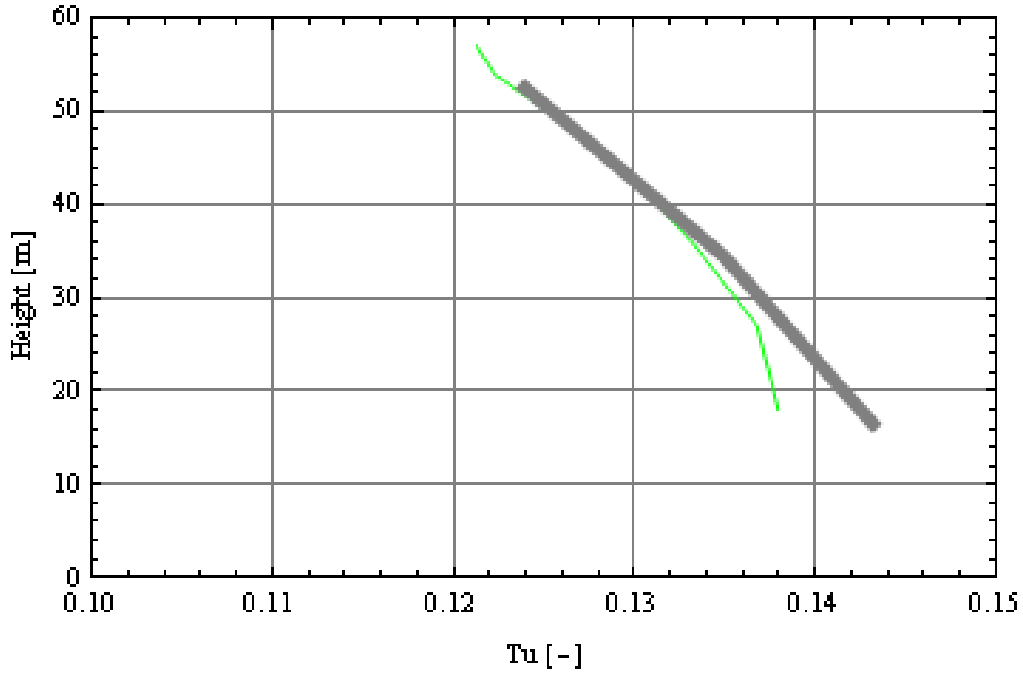

Figure 41Comparison of cup anemometers(green line) and Sonics(gray line)

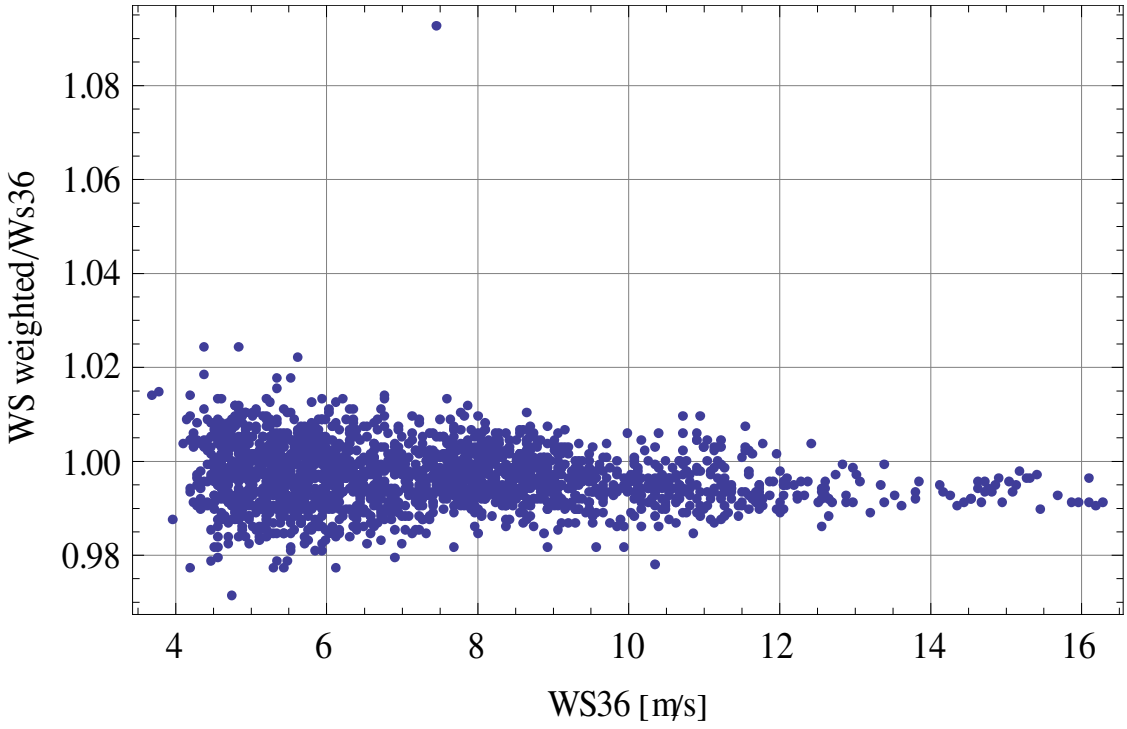

Figure 42Weighted wind speed ratio vs. wind speed at hub height, cups

5.5.3 Vertical Shear

Figure 43 is reflecting that the speed data over the rotor disk area have been transformed into a power law fit ≈ $U(z)=U(z_{ref})\cdot(z/z_{ref})^{\alpha}$, and that the exponent α is an expression of the wind characterisation with respect to vertical shear.

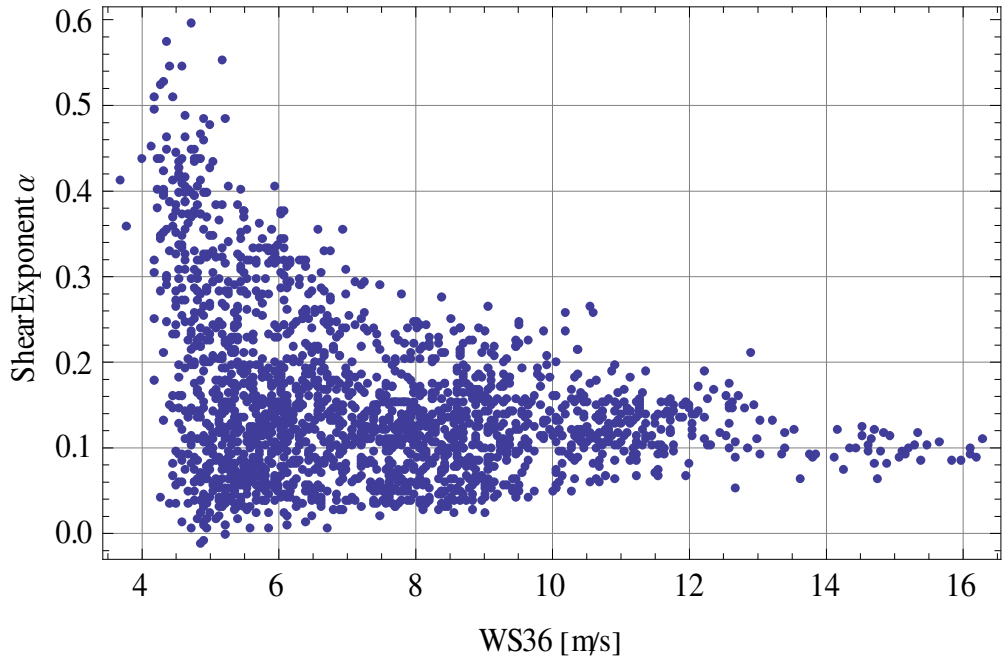

Figure 43 Wind shear vs. wind speed at hub height, cups

Figure 43 is a result of this analysis for the period, and shows that particular curviness is obtained at low wind speeds. Figure 44 demonstrates the effect the different wind profiles during night and day cycles in the period. In conclusion the night variation is an expression for more stable boundary layer than the wind characteristics during day between 6 and 18. The ABL is in this way described to be similar to what has been experienced in this project with analysis of the wind over MMW turbines with very large rotor disk areas, such as the turbines at Høvsøre [3.1, 3.2].
A comparison with a power law shows, that measurements derived from the cup anemometers are comparable to different cases of shear exponent, as shown in Figure 45. In the fit the mean values have been adjusted to fit with the mean values, shown in blue. The different shear cases are typical mean values from the classification of the shear into ($\alpha \leq 0.15$, $0.15 < \alpha \leq 0.3$, $\alpha > 0.3$). A variation with approximately 5.5 m/s between minima and maxima of the same readings are observed in the same plot. Additionally the standard deviation observed is more or less constant, which is close to the standard assumption, as shown in Figure 41($\sigma u(z) \approx$ constant => Turbulence intensity Tu(z) decreases with increasing z).
At Høvsøre, observations of low level jets and the interaction between external and internal boundary layer have complicated analysis of wind possessing deviating, conditional determined turbulence intensity shapes and wind profiles[3.13].

At the present site, turbulence variability during day-night cycles was mentioned in Figure 35 as one of the effects associated with wind directional changes over the rotor disk area, and Figure 46 explains the physical basis on the temperature difference between air and the air layers close to the soil.

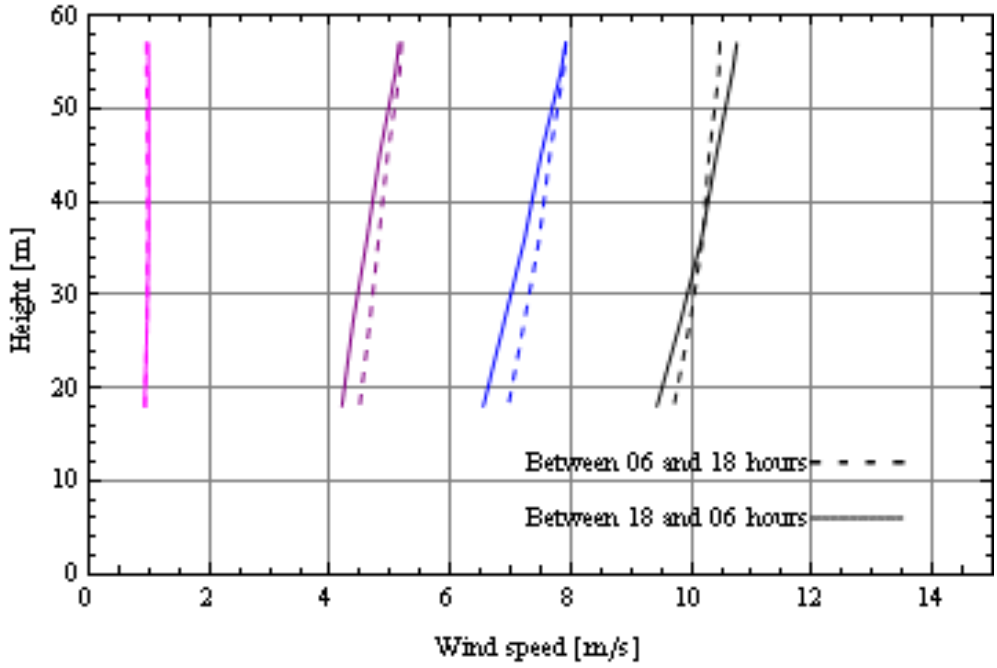

Figure 44 Measured diurnal wind profile cycle

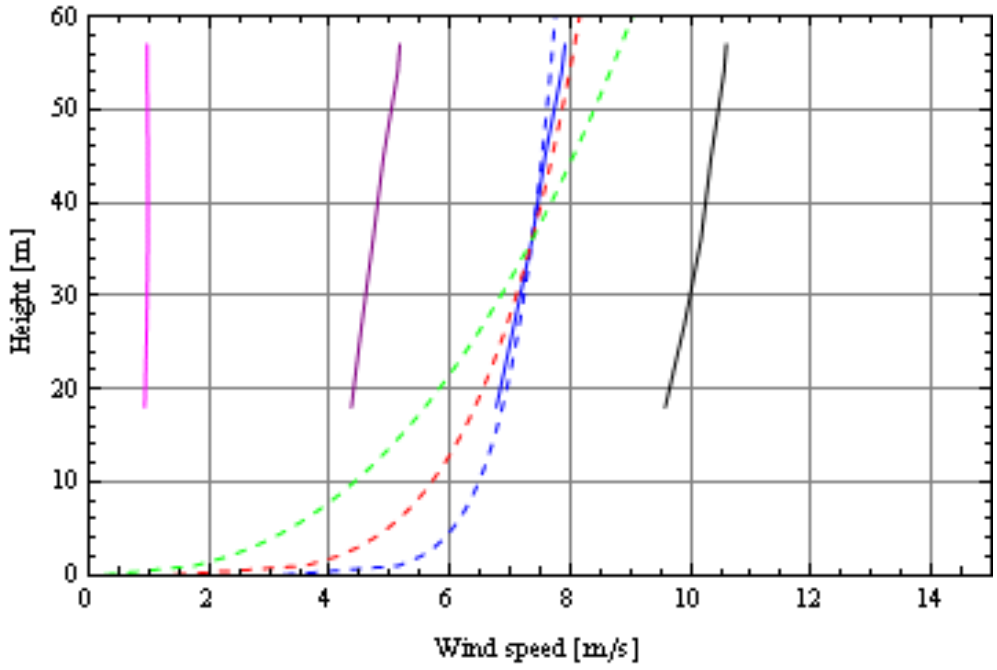

Figure 45 Mean values of average(solid blue line), standard deviation(purple), minimum(brown) and maximum(black) wind speed in comparison with different synthetic shear cases based on power law $U(z)=U(z_{ref})\cdot(z/z_{ref})^{\alpha}$*, Green:*$\alpha=0.4$*, Red:*$\alpha=0.2$*, Blue:* $\alpha=0.1$*.* $z_{ref}=36m$

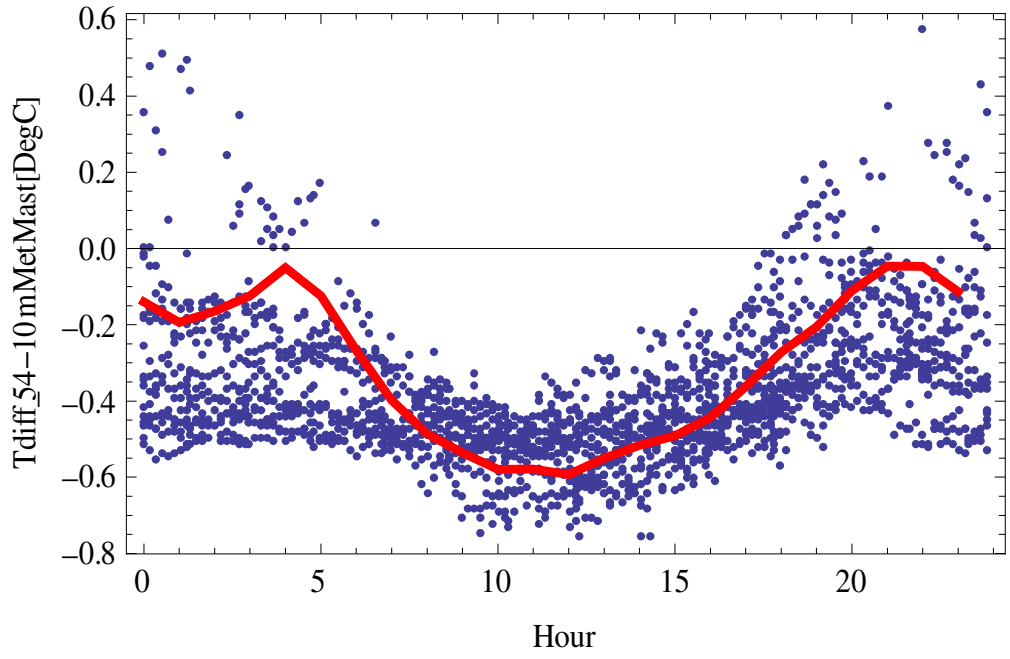

Figure 46 Temperature difference (scatter) and mean (line) development on an hourly basis

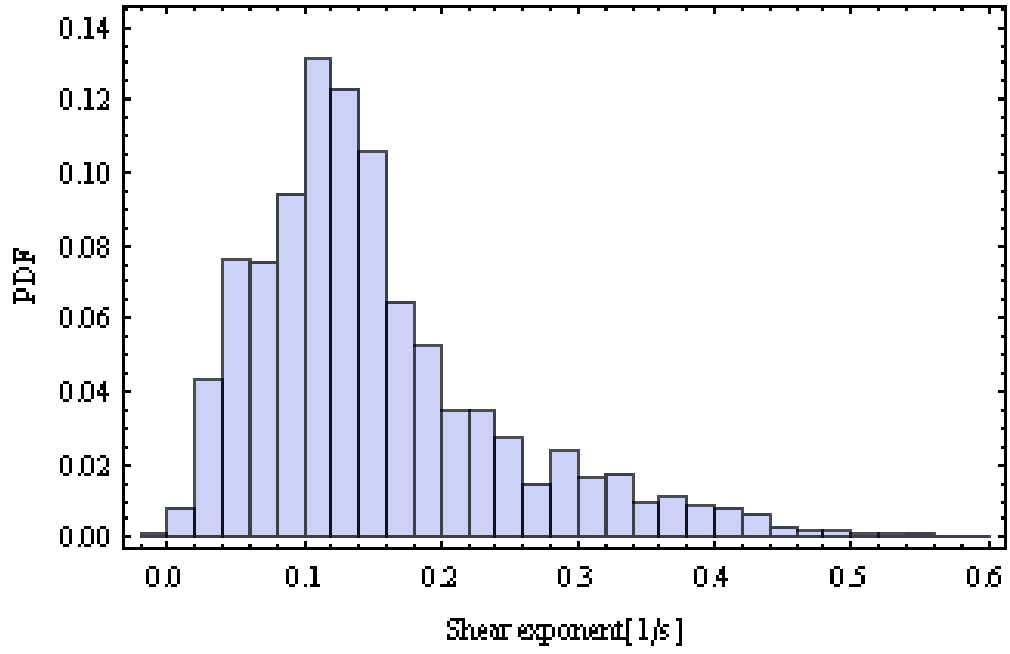

Figure 47Distribution of wind shear in the rotor disk area

5.5.4 Horizontal wind direction differences and Yaw error

Figure 48 shows the results for the wind turbine with the effect of yaw error. The almost constant yaw error results qualitatively in no significant difference of the power curve. The experience from simulations conclude on a Cos2 dependency with the yaw error; in the present cases of (-15..-10Deg, (-10..-5Deg) and (-5..0 Deg) they account with(-7%..-3%), (-3%..-0.7%) and less (-0.7%..0%), respectively.

Reductions of 7% at 6 m/s and 10 m/s are approximately 5 kW and 24 kW, respectively and are within the ranges measured. Later it is shown that the loads are increased with the effect of yaw misalignment. The conclusion to draw from this is that ideal flow conditions, e.g. wind turbine conditions with no yaw error, have not been reached under the present conditions.

Figure 49 shows in conclusion what have been observed in simulations (Figure 1), that power variability decreases with increasing turbulence intensity.

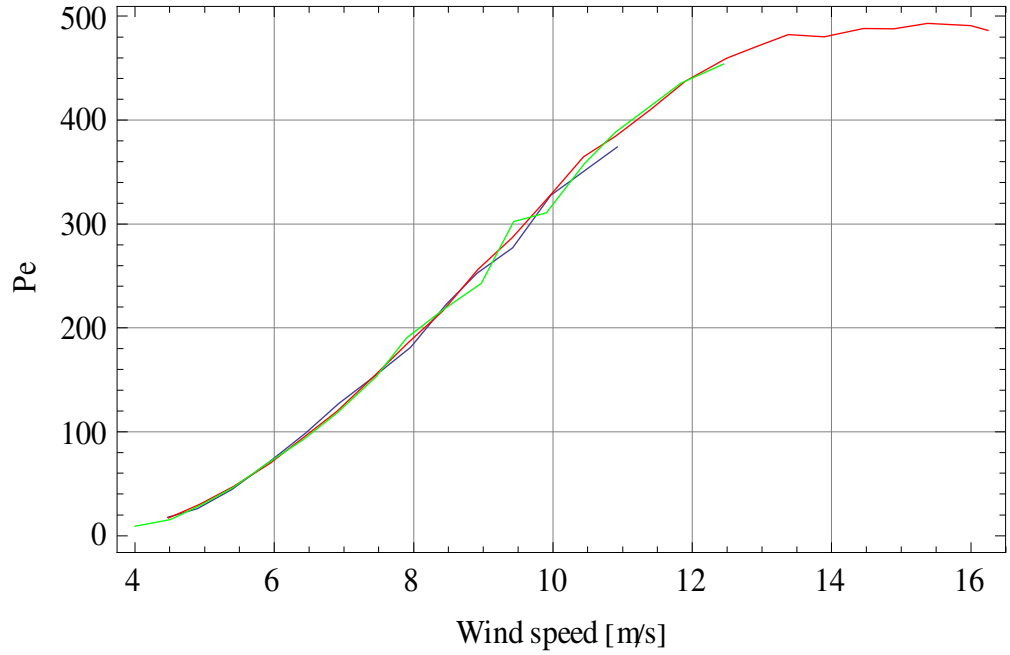

Figure 48 Density corrected power vs. wind speed at hub height, for different cases of yaw error (-15..-10 Deg, -10..-5 Deg, -5..0 Deg)

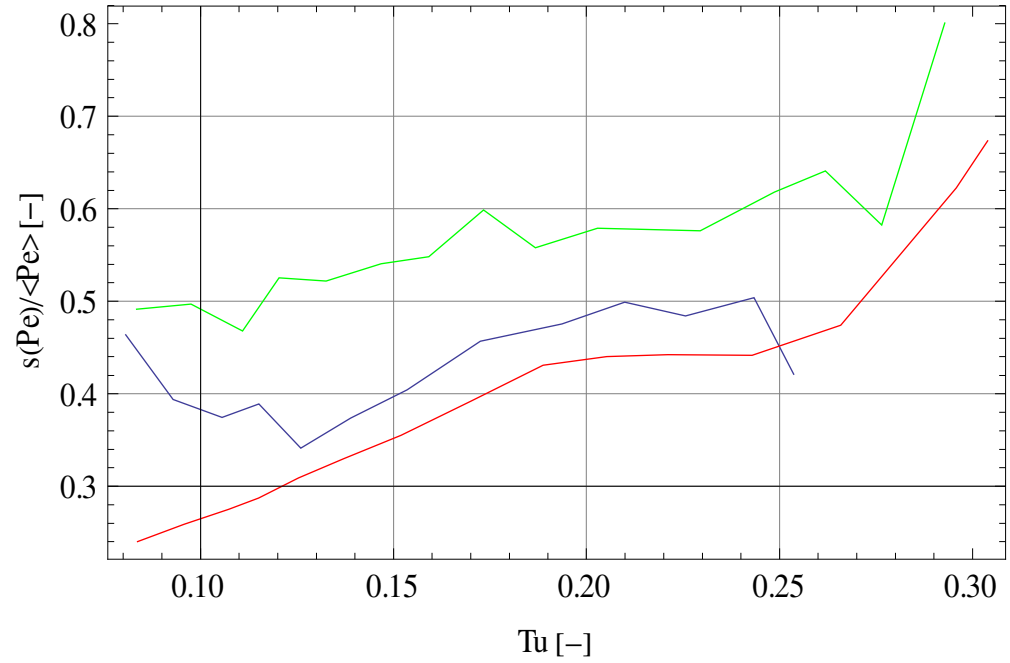

Figure 49 Power variability as function of turbulence for different cases of yaw error (-15..-10 Deg, -10..-5 Deg, -5..0 Deg)

5.5.5 Vertical shear effect and rotor performance

Figure 51 demonstrates the effect of shear for the wind turbine rotor. The shear is divided into classes α<=0.15, 0.15< α<=0.3 and α >0.3. From the figure the shear profile(as in Figure 45) with the least curvature is dominating in the lower wind speeds around cut-in, and the second largest class in the operating region of the turbine around maximum efficiency. The shear similar to a power law with the steepest curvature is to be found in the complete region from cut-in into deep stall region.

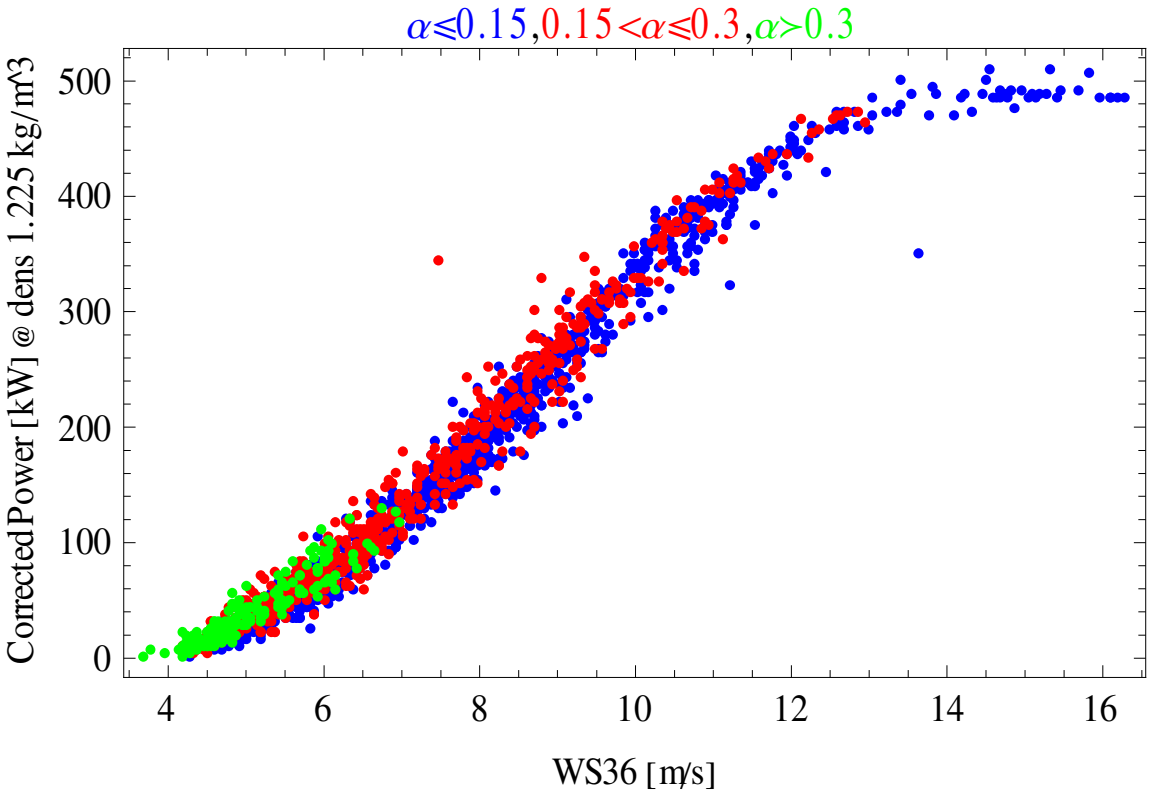

Figure 50Power vs. wind speed at hub height for different shear cases

The variation of the data within a band (point variation) is remarkable, significant and apparently uncorrelated with the wind speed at hub height. With the project objectives in mind, this may start speculations why we do not have a better correlation between power and wind speed. Anyway, dividing the power with ½ρ<U>^{3}A representing the dimensionless coefficient C_P, we see with Figure 51 that the scatter has not decreased significant. On the other side, Figure 52 demonstrates what simulation is able to predict, that lesser turbulence effects tends to decrease the efficiency for the conditions on the left hand side of maximum efficiency[3.2, 3.10]. Less turbulence is correlated as shown with more stable boundary layer(SBL). The wind profiles were as shown less steep.

For the discussion of the experimental results correlated with atmospheric turbulence, Figure 53 shows that a rotor is able to 'exploit' turbulence. The statistical significance decreases at high turbulence levels but tends to 'limit' the effects. At the moment we could state, that the rotor is unable to extract energy out of eddies beyond a certain size. However, turbulence intensities are connected with the ability to increase the relative energy capture as shown in Figure 54. Ideally the coordinates

$(1+Tu^2, 3Tu)$ should fit with the trend. As is shown in the fit, the statistical basis for fitting higher Tu is rather limited, and much scatter of the data at low Tu exists. The result is in comparable agreement with [3.10]. In conclusion there is yet no (new) explanation for why s(Pe)/<Pe> develops as it does.

A way to decrease the scatter of points around a coordinate (U, P) on the power curve is to incorporate the above 'fit', e.g. to replace average wind speed as $U(1+Tu^2)$, or to increase the energy over the rotor disk area as $½\rho U^3 A(1+3Tu^2)$ and to non dimension P with it. This effort on wind speed is made in Figure 55, and on C_P in Figure 56. It demonstrates to some extent to reduce the scatter compared to what was observed. Again the division of turbulence intensity into high (blue: above 0.2), medium(red: between 0.10 and 0.2) and low(green: under 0.10) shows that turbulence decrease rotor efficiency below C_P max, and for wind speed right of C_P max it increases the efficiency. Fitting the data with a weighted wind speed reflecting the vertical shear profile does not change essentially the above findings.

The question "Why does the power curve scatter, even we apply turbulence corrections etc" still remains.
One of the ideas to gain insight was to learn from the footprints of the structural signals. As mentioned in the introduction, in a simple rotor airfoil model, lift is more or less directed co-parallel with the wind direction [3.6, 3.7], and the turbulence is proportional to flapwise moment variability. In the rotation plane, edge wise bending moment variation are according to [3.6] an improvement for enhanced power due to turbulence[3.6, p C1-5].
Figure 57 shows the variability of edgewise bending moment with varying tip speed ratio (TSR) with low wind speeds from right to left. Under these conditions given, the results show that there is more potential to utilize energy at low wind speeds than at high wind speeds (low TSR), and that the function has a global minimum about TSR of 4.2.
Before entering the discussion of spectral analysis of the flapwise bending moments, this signal (Blade 2) is shown in Figure 58.

Another interesting feature with thrust is that this parameter multiplied with wind speed is proportional to power extracted from the wind; see Figure 59, with a more linear function than as seen in ordinary power curves. This relationship could be interesting to study on the variations in terms of power extraction and the interaction of the wind turbine itself(rotor filter function, tower deflection dependency). However to do so, there is substantial need to acquire stable strain gauge signals.

Figure 60 show the role of turbulence as it has importance on the loads over power ratio. The data set is not complete for describing high turbulence, but fairly a good trend is obtained from the plot: fewer loads are generated per power generated. However caution should be emphasized because it is a relative measure. Qualitatively the power generated increases with the wind speed and limits towards stalled conditions together with a smaller variance on power. Since the ratio increases heavily, the numerator must be limited by less variation of the flap wise loads(as can be seen in the appendix for corresponding blade loads). In conclusion the figure tells us that the decrease of turbulence intensity increases the loads over power output, e.g. there seems to be a basis for improving the power and reducing the loads in an aerodynamic optimisation process. If it is another way of stating that the aerodynamic lift has a improper variation along the blade is a question for specific simulations to be conducted.

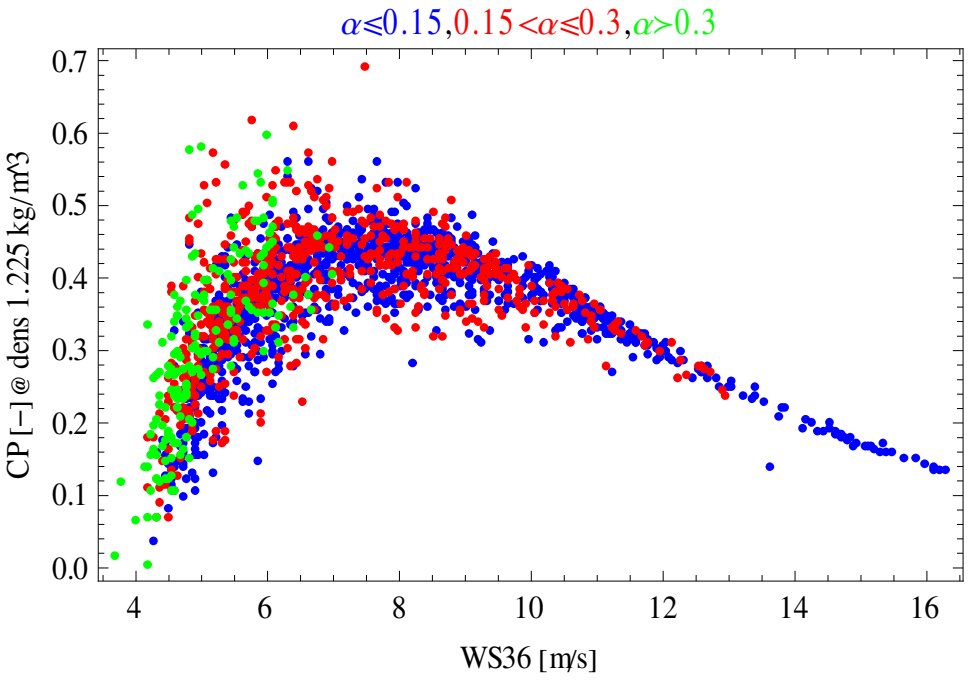

Figure 51Power coefficient vs. wind speed at hub height for different shear cases)

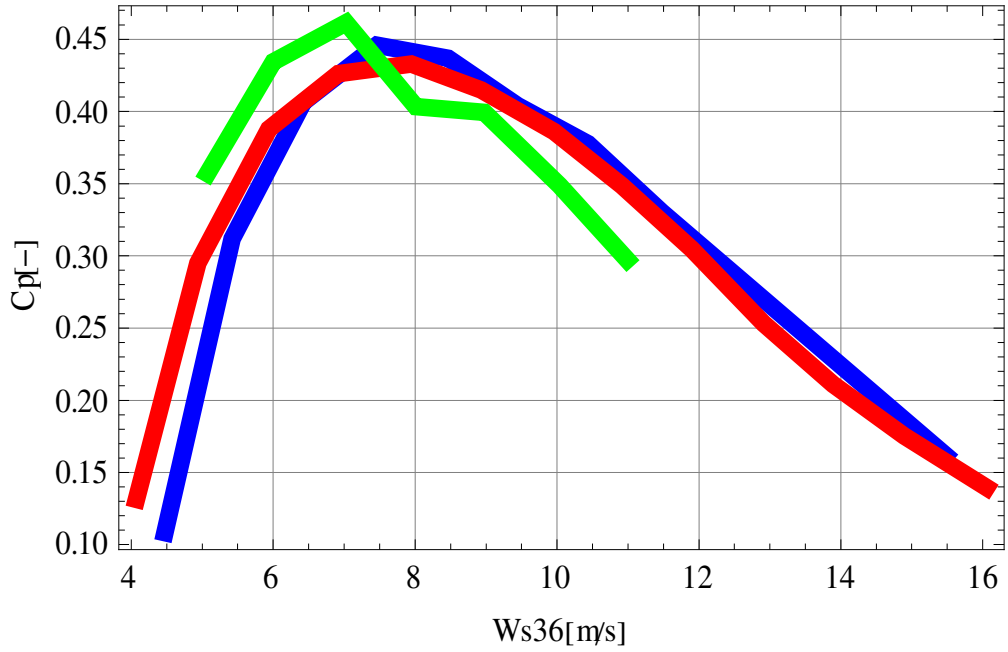

Figure 52 Cp versus wind speed (binned values) for three different turbulence classes (Green: Tu>0.2, Red: 0.1<Tu≤0.2, Blue: Tu≤0.1

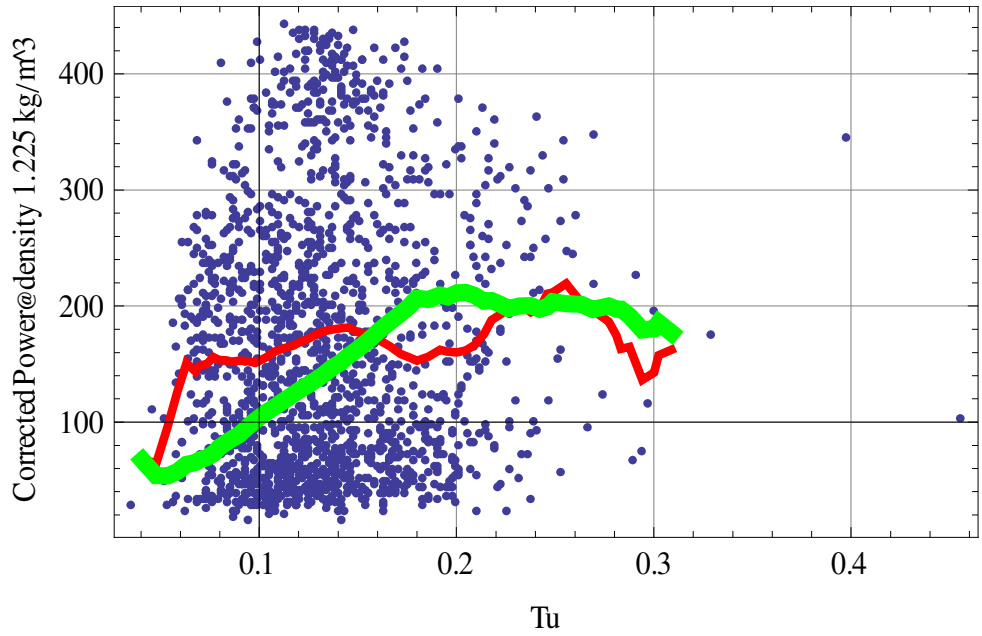

Figure 53 Power(scatter) and binned(red) and shear(green) trends vs. Turbulence intensity Tu (scaled for comparison)

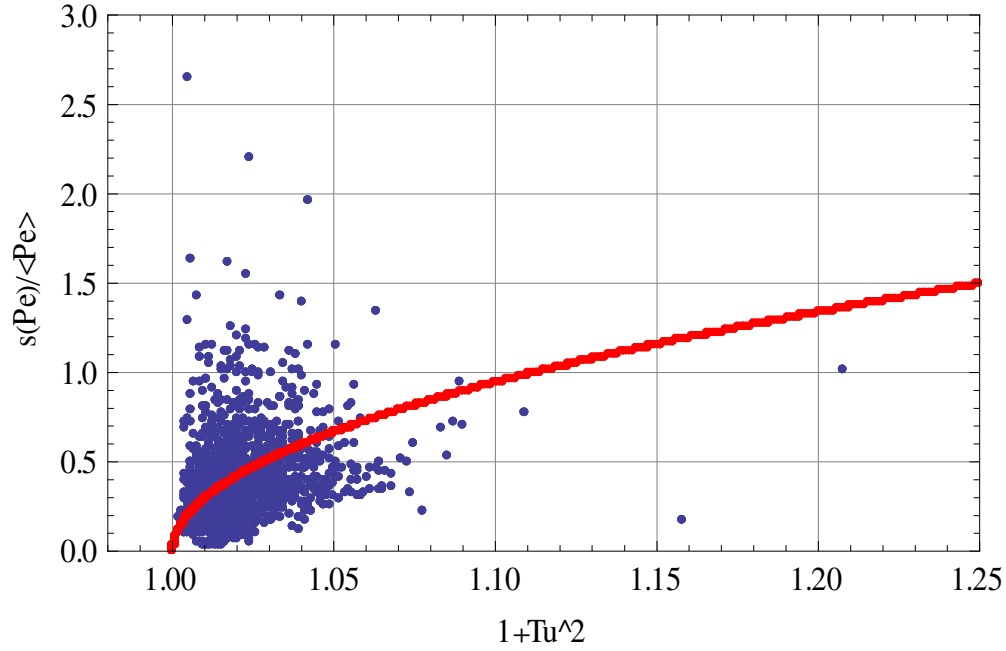

Figure 54 Power variability vs. Turbulence, and a (1+Tu^2, 3Tu) fit

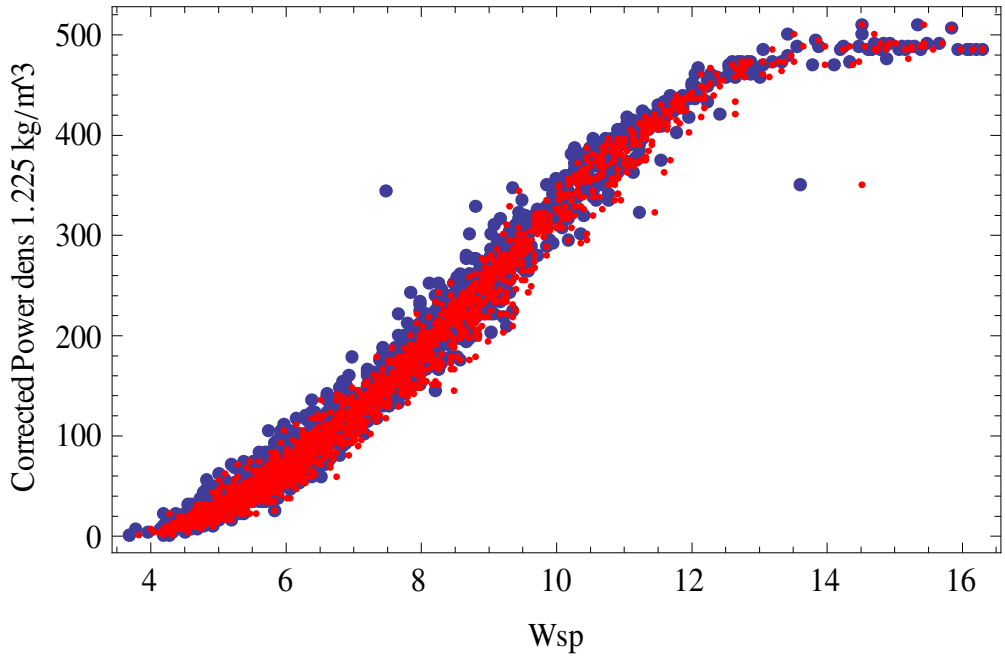

Figure 55Power corrected for density variations other than 1.225 kg/m^3, and wind speed corrected for turbulence effects(red dots)

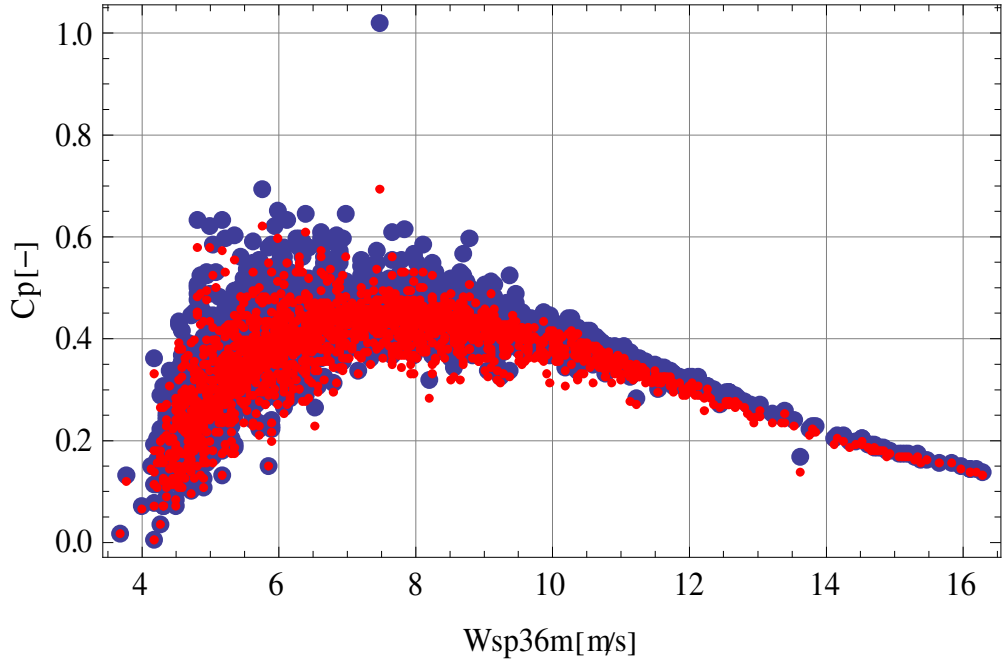

Figure 56 Power coefficient corrected for density variations other than 1.225 kg/m^3 without turbulence effect (blue dots) and with corrected (red dots)

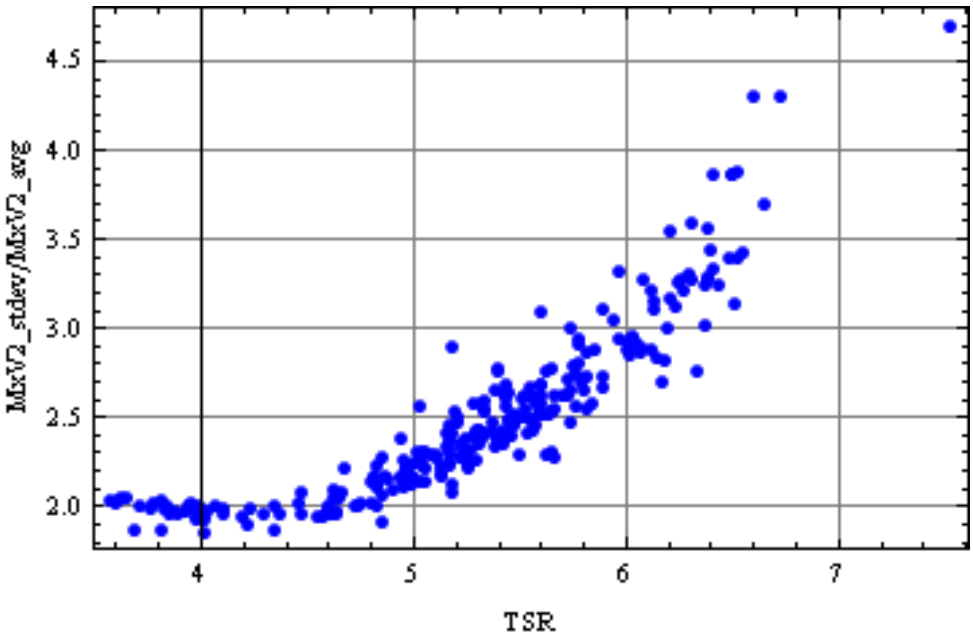

Figure 57 Edgewise moment variability vs. TSR

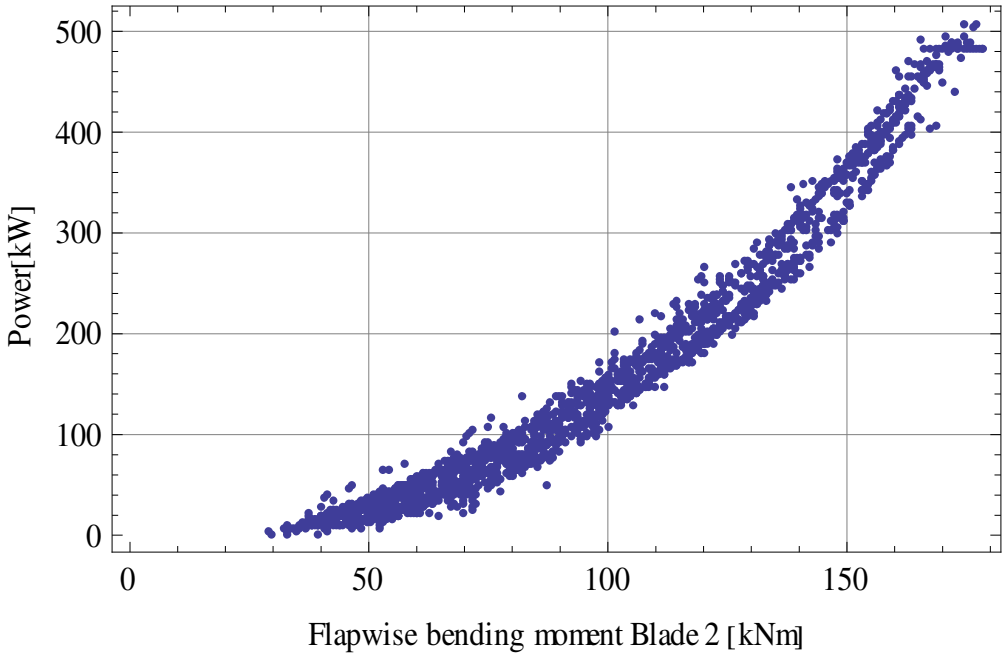

Figure 58 Measured flapwise bending moment

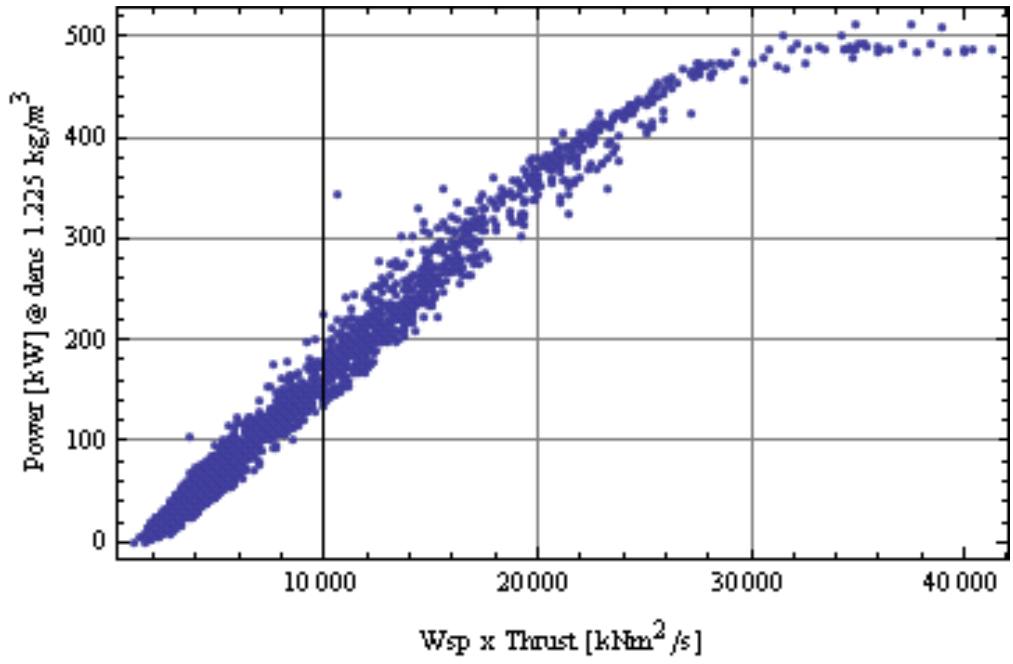

Figure 59 Corrected power vs. derived signal power= force x speed

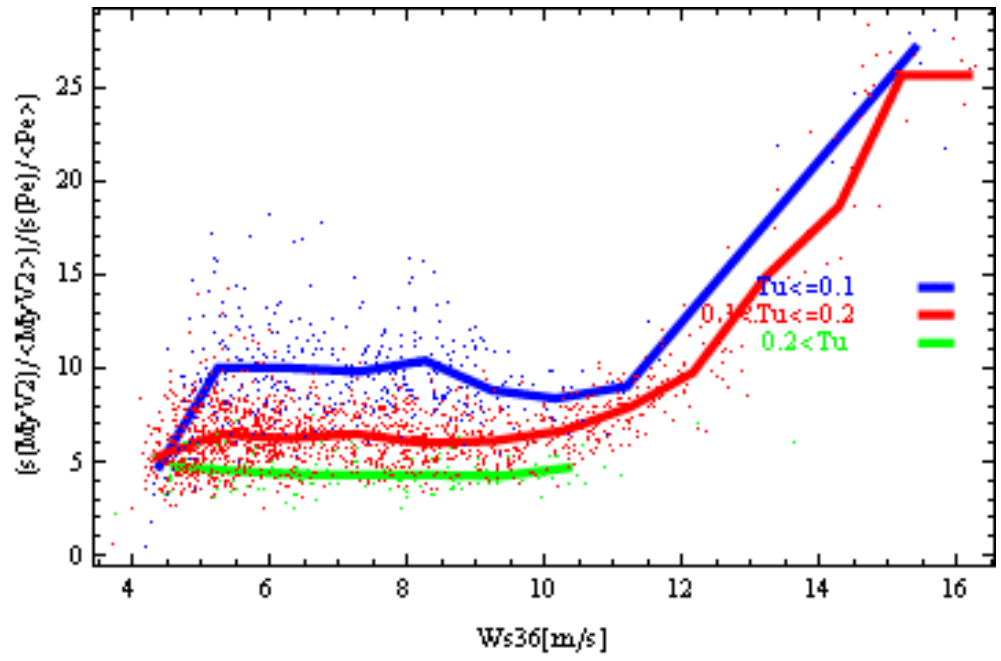

Figure 60 Loads over power ratio vs. wind speed for different turbulence intensity classes

5.6 Spectral analysis

The wind speed, flapwise bending and power signal are investigated with spectral methods to provide better understanding of the variability in power compared to wind speed.

In Figure 61 spectra of the wind speed 1(average wind speed of south and north cup anemometer at 36m) and 2(weighted wind speed) Blade 2 bending moment, blade 1 bending moment and blade 3 bending moment is shown as signal 3, 4, 5 and electrical power as signal 6.

A black vertical line is drawn to indicate the cup anemometer 3-dB threshold frequency, and the brown line to indicate the pulse each time a blade passes the tower.
Also a black line is indicating the -2/3 slope in the spectrum, as in classic wind spectra. The -5/3 line is omitted for comparison with the power signal and flap bending moment signals.

The plot show a strong connection between the structural signals and the power-a strong similarity exists compared to with the wind signal. The difference between the black and red line is not that typical; it seems that the weighted wind speed follows the 'unfiltered' part of the structural and power signal better.

On the discussion of the turbine signals 'rotational sampling' has been used to explain the effect of the spikes(peaks) evolving in the spectra. This part has to do with that the blades segment by segment penetrate part of the boundary layer with speed differences over the rotor disk area. The shear plays a particular role in contributing to the variance (area under the curve), and hence to the ordinate of the spectral power signal (electrical power P). Because the variations in wind affects the in plane driving torque variations(lateral) edgewise bending and power signal P, it also has a contribution to the longitudinal (flapwise bending moment) signal(indicated previously as proportional to σu/U).

Another difference is between power and structural signal that the power spectrum contains more area under the curve, and consequently more variance at low frequencies. One of the reasons for this is that variations of different kind of nature play a role in this. The turbulence spectrum such as Kaimal[5.22] shows a specific maximum and the area to the left of that normally is described with a decay towards higher frequencies where turbulence is governing.

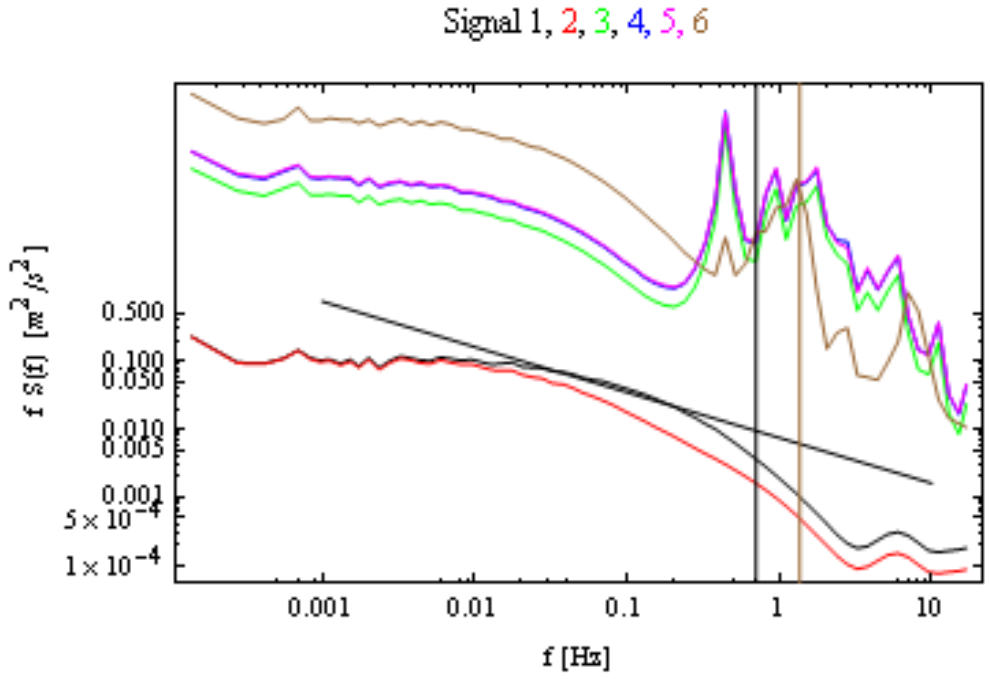

Figure 61 Spectra of main parameters: wind speeds(1,2) flapwise bending moment blade2, blade1,blade3(3,4,5) and power(6)

A 1st order description of what might happen with the wind turbine fluctuating power is to look at the flux in terms of spectral description can be found by looking again at

chapter 2.2 and derive the formula on the flux with longitudinal mean U and variation u(t):
$E(t)/½\rho=(U+u)^3$, which is expressed as:

$E(t)/½\rho=U^3+3Uu(t)^2+3u(t)U^2+u(t)^3$ with variables as shown functions of time t.

Now building the spectrum of E(t) to a first order on the basis of $3u(t)U^2$ gives

$$\omega S_E(\omega) \approx \omega \int 3u(t)U^2 d\omega$$
$$\approx \underline{(½\rho)^2\, 9\, U^4\, \omega\, S_u(\omega)}$$

With $\omega=2\pi f$ this can be compared with the spectra and shows that the variations add to the area under the spectra for the power signal in Figure 61.

The influences of night day variations are shown in Figure 62 to Figure 64. The selection is based only on 7 and 13 data sets within August of nocturnal and daylight situations, respectively. Averaging over longer periods than august, spectra are averaged out leaving no trend as below.

The influence of the conditions governed by nocturnal ABL situations during late afternoon, night and early morning between 18 and 06 is shown in Figure 62. As per Figure 44 the average profile during these hours is less steep and contributes to the power spectrum of the power signal (brown). This observation goes also for the other wind and flapwise bending signals.

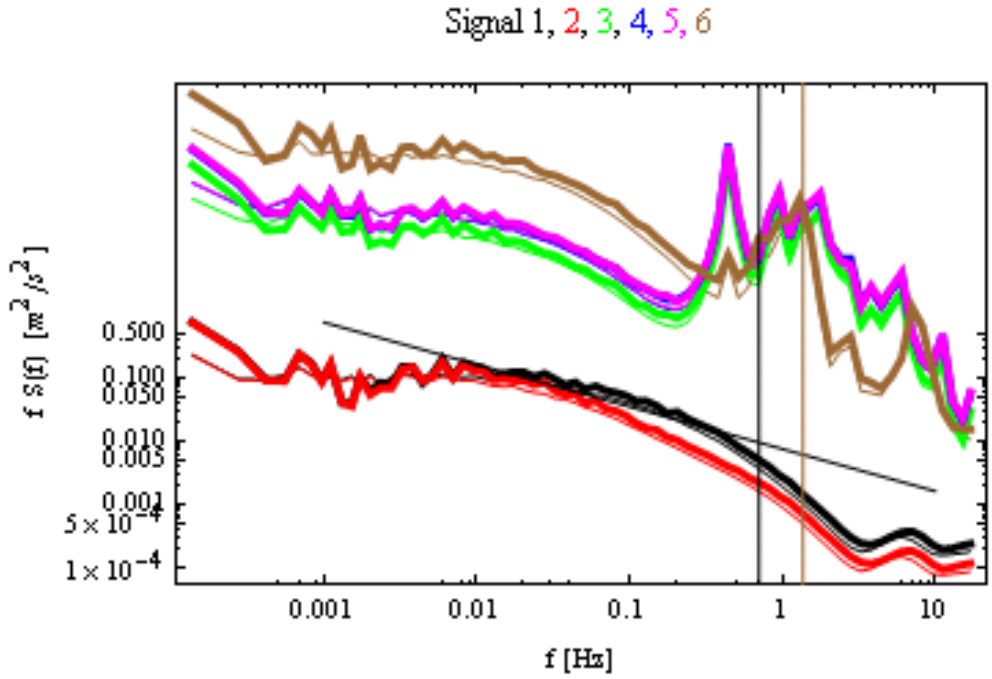

Figure 62 Influence of diurnal conditions between 18-06(stable)on power signal (thick brown)

The influence of the conditions governed by daylight ABL time series between 06 and 18 is shown in Figure 63. Due to the diurnal situation, the wind profile is steeper and lowers the area under the power spectrum of the signal.

Figure 64 shows both effects in comparison with the Kaimal spectrum. The Integral length was estimated with an arbitrary constant to fit the spectra of the power signal on a visual basis. The result of about 200 m tell that eddies in size are around 5 times the rotor diameter. At the same time the Kaimal spectrum shows the shape of the

turbulence spectrum, and that the low frequency variations are different(according to classical descriptions[5.21]: they decrease for increasing frequencies).

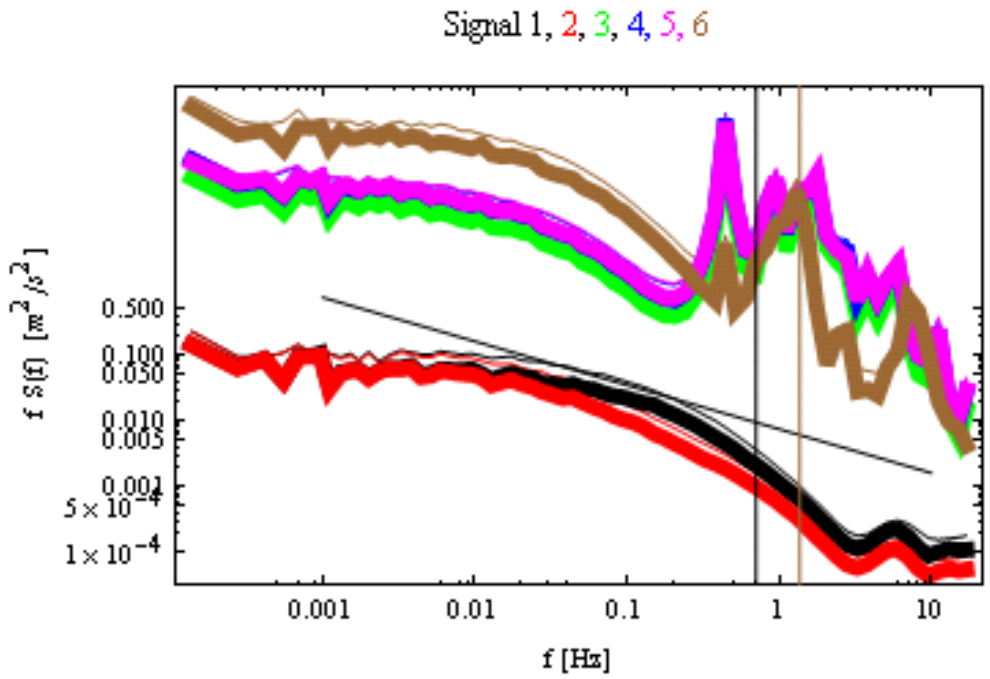

Figure 63 Influence of diurnal conditions between 06-18 (unstable) on power signal (thick brown)

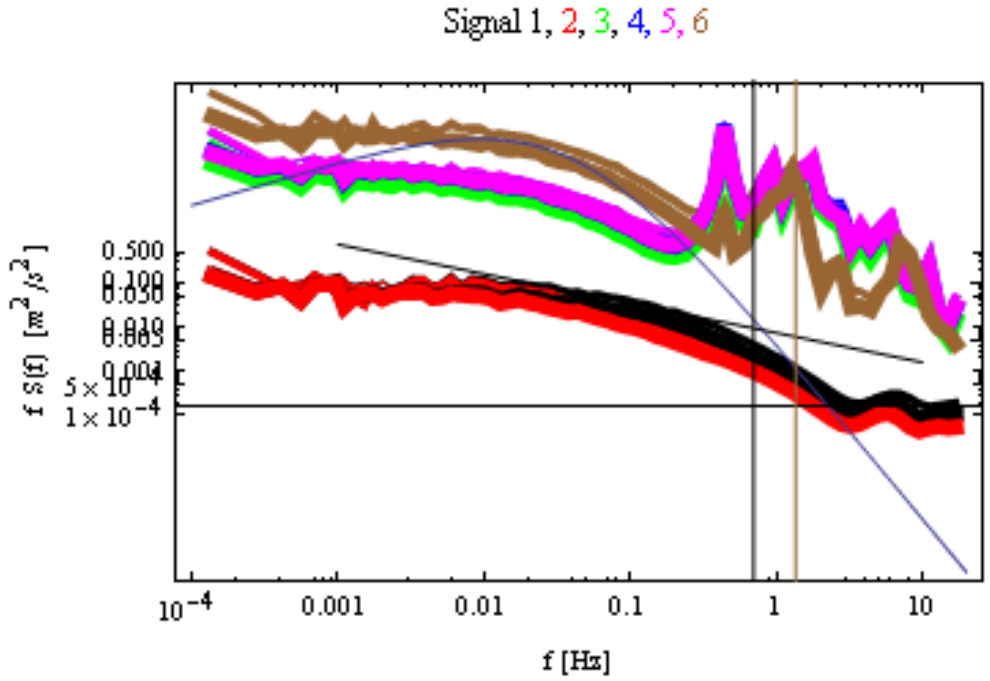

Figure 64Influence of stable and unstable conditions in comparison with Kaimal spectrum[5.22]. The integral length is determined as 204 m.

5.7 References

5.1. Diznabi, B.: Investigation of the flow relation to nacelle anemometry. Master Thesis MEK-FM-EP-2009-03, 136 pp, March 2009.

5.2. Vindmølleafprøvning Nordtank NTK 500/37, Måling af Effektkurve, Risø-I-731, September 1993.

5.3. Wind turbine Test, NORDTANK NTK 500/37, Risø-R-714, December 1994

5.4. Vindmølleafprøvning Nordtank NTK 500/41, Måling af Effektkurve, Risø-I-889, Maj 1995.

5.5. Accelerated Fatigue Testing of LM 19.1 Blades, Risø-R-1358, May 2003

5.6. Power curve measurements, Measurement Summary, No. 12.2, June 1995, NTK 500/41

5.7. Paulsen, U. : Work Package 1B.2 under the European Commission, Integrated Wind Turbine Design (UPWIND): Verification of long-term load measurement technique

5.8. Validation of Aeroelastic Model of Nordtank 500/37, Risø-R-1006, November 1997

5.9. Helgesen K.O., LabVIEW Data Acquisition exercise from 500 kW Wind Turbine, DTU-Oersted 2005

5.10. INTERNATIONAL STANDARD IEC 61400-121, Wind turbine generator systems – Part 121: Wind turbine power performance testing

5.11. Technical specification IEC TS 61400-13, Wind turbine generator systems – Part 13: Measurements of mechanical loads.

5.12. INTERNATIONAL STANDARD IEC 61000-4-7, Testing and measurement techniques –General guide on harmonics and interharmonics measurements and instrumentation, for power supply systems and equipment connected thereto

5.13. IEA Recommended Practices for wind turbine testing and evaluation; 3. FATIGUE CHARACTERISTICS.

5.14. Madsen, H.A. et al. : The DAN-AERO MW Experiments Final report 41pp, Risø R-1726(EN) DTU 2010

5.15. Giebel, G. Et al.: Autonomous Aerial Sensors for Wind Power Meteorology-A Pre project, 90 pp, Risøs-R-1798(EN) 2012.

5.16. Wagner, R. et al., Accounting for the speed shear in wind turbine power performance measurement, Wind Energy, 2011; 14:993--1004

5.17. DAU P2858 Data Acquisition Unit description, User manual. Risø 17-12-2001

5.18. Fischer, T. Leloudas G.: Calibration of Strain Gauges in the Nordtank Wind Turbine 29 pp Report DTU 2006

5.19. Larsen, E. And Holden, S.: Field Calibration Of The Strain-Gauges On A 500kw Wind Turbine pp47 DTU report 2010.

5.20. IEA Recommended Practices for Wind Turbine Testing and Evaluation, 3 Fatigue Characteristics, 2 editions. 1990

5.21. Stuhl, R.B. :An introduction to boundary layer meteorology ISBN 90-277-2768-6, 1988.

5.22. International Standard IEC 61400-1 Wind turbines –Part 1: Design requirements

6 Simulations on the 500 kW wind turbine

The aero elastic simulation tool HAWC2 (***H**orizontal **A**xis **W**ind turbine simulation **C**ode, version 2*) is a code designed for calculating wind turbine response in time domain. It has been developed at the aero elastic design research programme in the Wind Energy Department of the Risø National Laboratory.

The HAWC2 code is based on a multibody formulation where the turbine is subdivided into to a number of bodies interconnected by constraint equations. Within a body the calculations are linear, which is valid as long as deflections and rotations are small, whereas large deflections and rotations are accounted for through the coupling of bodies. Using too few bodies will therefore result in a reduction of non-linear problems into a linear.

The sign conventions are adapted from the user manual [1] and shown in Figure 65.

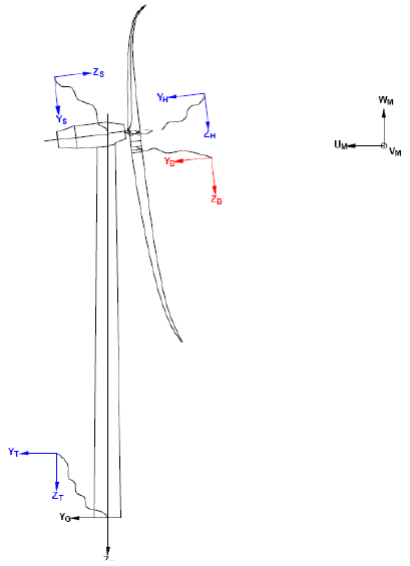

Figure 65 Illustration of coordinate system as result of user input[6.1]. There are two coordinate systems in black which are the default coordinate systems of global reference and default wind direction. The blue coordinate systems are main body coordinate systems attached to node 1 of the substructure, the orientation of these are fully determined by the user. The red coordinate systems are also defined by the user, but in order to make the linkage between aerodynamic forces and structure work these have to have the z from root to tip, x in chordwise direction and y towards the suction side.

In the structural model of the 500 kW Nordtank wind turbine [6.2] data of the blades and wind turbine were implemented.

6.1 Simulation cases selection

The simulation cases were generated by selecting cases from the real measurements collected from the mast and the wind turbine extending from April to November 2011. The filtering was made according to the description in 5.2.

6.1.1 Set up of HAWC2

The data remaining after filtering were binned according to the wind speed at hub height per bin of 1m/s from 4 to 16m/s. Within in each wind speed bin, the wind speed profiles were binned according to their shape (i.e. wind speed at the 4 other levels). This resulted in a various number of profiles bins for each wind speed bin. Finally, one profile was randomly chosen from each profile bin. 141 different profiles were thus obtained.

Each one of these profiles was the basis for a simulation case. The 2-dimentional 10-min mean wind speed vector at the 5 levels was given as input for the wind speed profiles through the "user-defined-shear" function; i.e. at each level the mean wind speed was combined to the mean direction deviation from the wind direction at hub height; thus characterizing both the shear and the veer. Similarly, the wind speed standard deviation was given at each level through the "user-defined-turbulence-shear".

Every simulation case were run with 10 turbulence seeds (with the Mann model of turbulence) in order to be statistically significant.

6.2 Results and comparison with experiments

Following channels shown in Table 5 are calculated, and for comparison with measurements a selection of these variables have been made. The statistics of the simulation cases have been carried out up to 11 m/s (the simulation above 11 m/s were not finalized due to a PC problem) and plotted with selected measured signals for comparison in this report.

There is a general fair agreement of computed variables against measured signals. Structural signals seems to be of difference, in particular the flapwise signals have higher outputs than measured.

In Figure 96 the estimated load over power sensitivity factor is by far comparable in levels with the measured ones shown in Figure 60. One difference is about on the gain of the flapwise bending moment which influences the variance over mean flapwise bending moment. In conclusion there is effort to do in finding the reasons for these particular differences between measurements and calculations.

Table 5 Calculated channels

Channel Variable Description	Unit	Describtion	X [m]	Y [m]	Z [m]
1 Time	s	Time			
2 Omega	rad/s	Rotor speed			
3 Ae rot. Torque	kNm	Aero rotor torque			
4 Ae rot. Power	kW	Aero rotor power			
5 Ae rot. Thrust	kN	Aero rotor thrust			
6 WSP gl. coo.,Vx	m/s	Free wind speed Vx, gl.	0.00	0.00	-14.00
7 WSP gl. coo.,Vy	m/s	Free wind speed Vy, gl.	0.00	0.00	-14.00
8 WSP gl. coo.,Vz	m/s	Free wind speed Vz, gl.	0.00	0.00	-14.00
9 WSP gl. coo.,Vx	m/s	Free wind speed Vx, gl.	0.00	0.00	-17.50
10 WSP gl. coo.,Vy	m/s	Free wind speed Vy, gl.	0.00	0.00	-17.50
11 WSP gl. coo.,Vz	m/s	Free wind speed Vz, gl.	0.00	0.00	-17.50
12 WSP gl. coo.,Vx	m/s	Free wind speed Vx, gl.	0.00	0.00	-26.50
13 WSP gl. coo.,Vy	m/s	Free wind speed Vy, gl.	0.00	0.00	-26.50
14 WSP gl. coo.,Vz	m/s	Free wind speed Vz, gl.	0.00	0.00	-26.50
15 WSP gl. coo.,Vx	m/s	Free wind speed Vx, gl.	0.00	0.00	-35.50
16 WSP gl. coo.,Vy	m/s	Free wind speed Vy, gl.	0.00	0.00	-35.50
17 WSP gl. coo.,Vz	m/s	Free wind speed Vz, gl.	0.00	0.00	-35.50
18 WSP gl. coo.,Vx	m/s	Free wind speed Vx, gl.	0.00	0.00	-44.50
19 WSP gl. coo.,Vy	m/s	Free wind speed Vy, gl.	0.00	0.00	-44.50
20 WSP gl. coo.,Vz	m/s	Free wind speed Vz, gl.	0.00	0.00	-44.50
21 WSP gl. coo.,Vx	m/s	Free wind speed Vx, gl.	0.00	0.00	-53.50
22 WSP gl. coo.,Vy	m/s	Free wind speed Vy, gl.	0.00	0.00	-53.50
23 WSP gl. coo.,Vz	m/s	Free wind speed Vz, gl.	0.00	0.00	-53.50
24 WSP gl. coo.,Vx	m/s	Free wind speed Vx, gl.	0.00	0.00	-56.50
25 WSP gl. coo.,Vy	m/s	Free wind speed Vy, gl.	0.00	0.00	-56.50
26 WSP gl. coo.,Vz	m/s	Free wind speed Vz, gl.	0.00	0.00	-56.50

Channel Variable Description	Unit	Description
27 Mx coo: tower	kNm	Moment, tower nodenr: 1, coo: tower base flange
28 My coo: tower	kNm	Moment, tower nodenr: 1, coo: tower base flange
29 Mz coo: tower	kNm	Moment, tower nodenr: 1, coo: tower base flange
30 Mx coo: tower	kNm	Moment, tower nodenr: 5, coo: tower middle flange
31 My coo: tower	kNm	Moment, tower nodenr: 5, coo: tower middle flange
32 Mz coo: tower	kNm	Moment, tower nodenr: 5, coo: tower middle flange
33 Mx coo: tower	kNm	Moment, tower nodenr: 8, coo: tower top flange
34 My coo: tower	kNm	Moment, tower nodenr: 8, coo: tower top flange
35 Mz coo: tower	kNm	Moment, tower nodenr: 8, coo: tower top flange
36 Fx coo: tower	kN	Force, tower nodenr: 8, coo: tower yaw bearing
37 Fy coo: tower	kN	Force, tower nodenr: 8, coo: tower yaw bearing
38 Fz coo: tower	kN	Force, tower nodenr: 8, coo: tower yaw bearing
39 Mx coo: shaft	kNm	Moment, shaft nodenr: 4, coo: shaft, sg

40	My coo: shaft	kNm	Moment, shaft nodenr: 4, coo: shaft, sg
41	Mz coo: shaft	kNm	Moment, shaft nodenr: 4, coo: shaft, sg
42	Mx coo: shaft	kNm	Moment, shaft nodenr: 5, coo: shaft main bearing
43	My coo: shaft	kNm	Moment, shaft nodenr: 5, coo: shaft main bearing
44	Mz coo: shaft	kNm	Moment, shaft nodenr: 5, coo: shaft main bearing
45	Mx coo: blade1	kNm	Moment, nodenr: 1, coo: blade1, root
46	My coo: blade1	kNm	Moment, nodenr: 1, coo: blade1, root
47	Mz coo: blade1	kNm	Moment, nodenr: 1, coo: blade1, root
48	Fx coo: blade1	kN	Force, nodenr: 1, coo: blade1, root
49	Fy coo: blade1	kN	Force, nodenr: 1, coo: blade1, root
50	Fz coo: blade1	kN	Force, nodenr: 1, coo: blade1, root
51	Mx coo: blade2	kNm	Moment, nodenr: 1, coo: blade2, root
52	My coo: blade2	kNm	Moment, nodenr: 1, coo: blade2, root
53	Mz coo: blade2	kNm	Moment, nodenr: 1, coo: blade2, root
54	Mx coo: blade3	kNm	Moment, nodenr: 1, coo: blade3, root
55	My coo: blade3	kNm	Moment, nodenr: 1, coo: blade3, root
56	Mz coo: blade3	kNm	Moment, nodenr: 1, coo: blade3, root

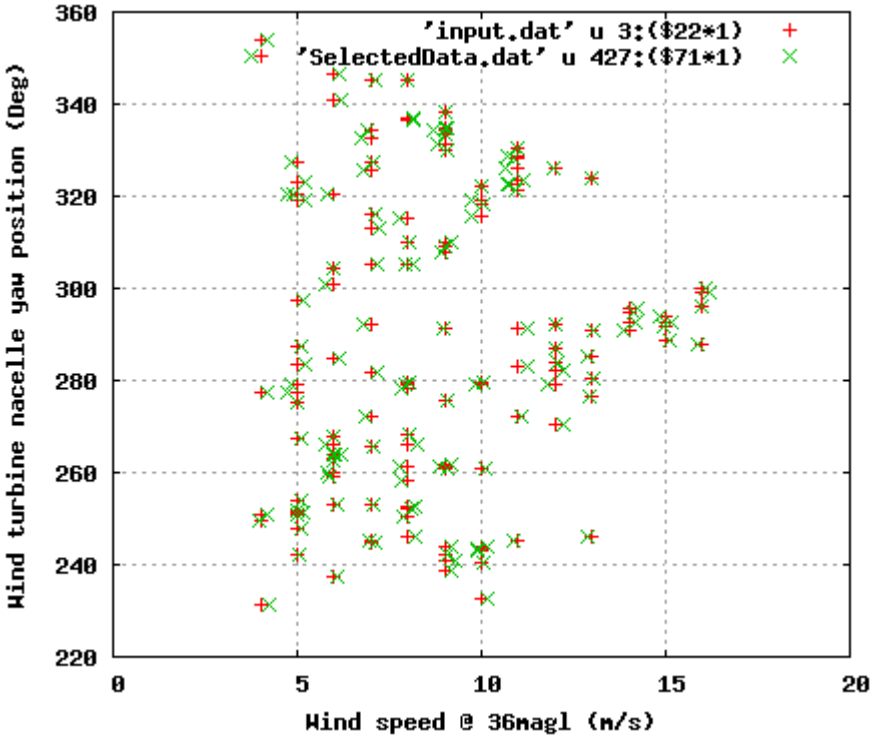

Figure 66 Mean Nacelle position

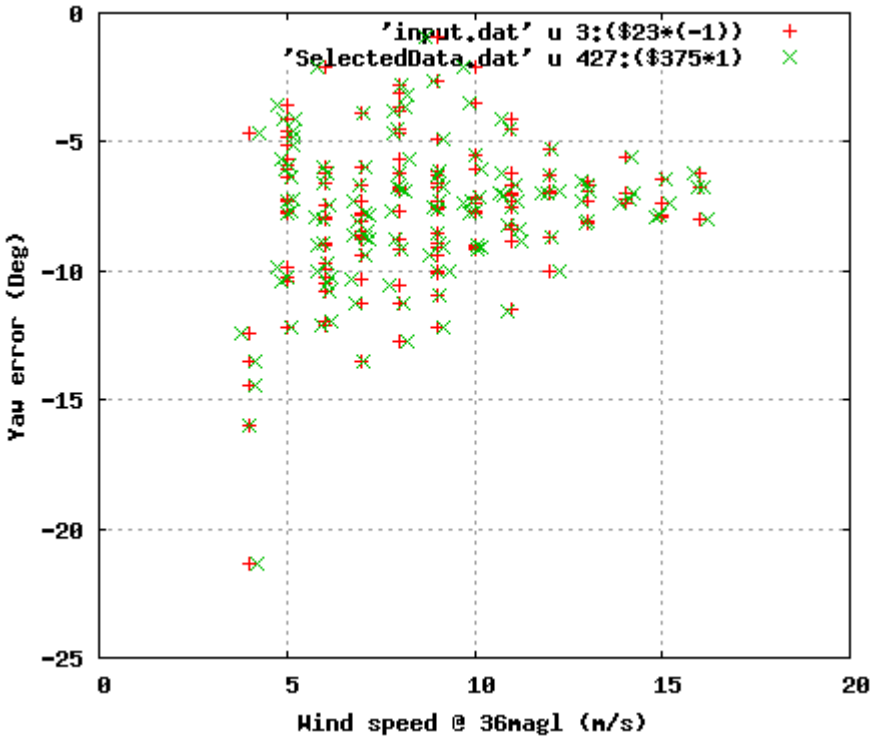

Figure 67 Mean Yaw error(wind direction-nacelle position)

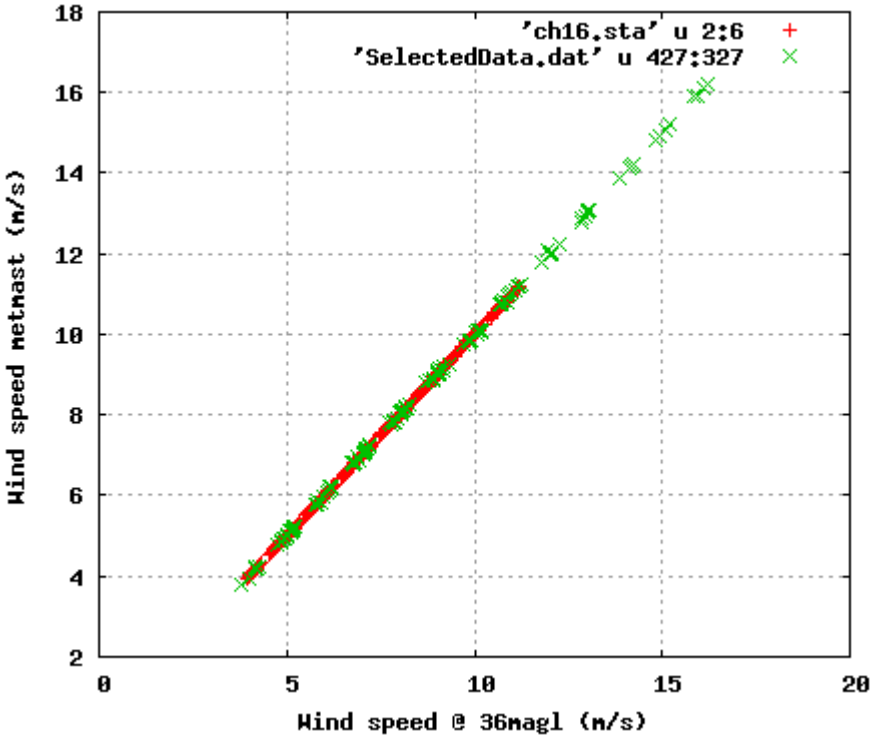

Figure 68 Mean Wind speed

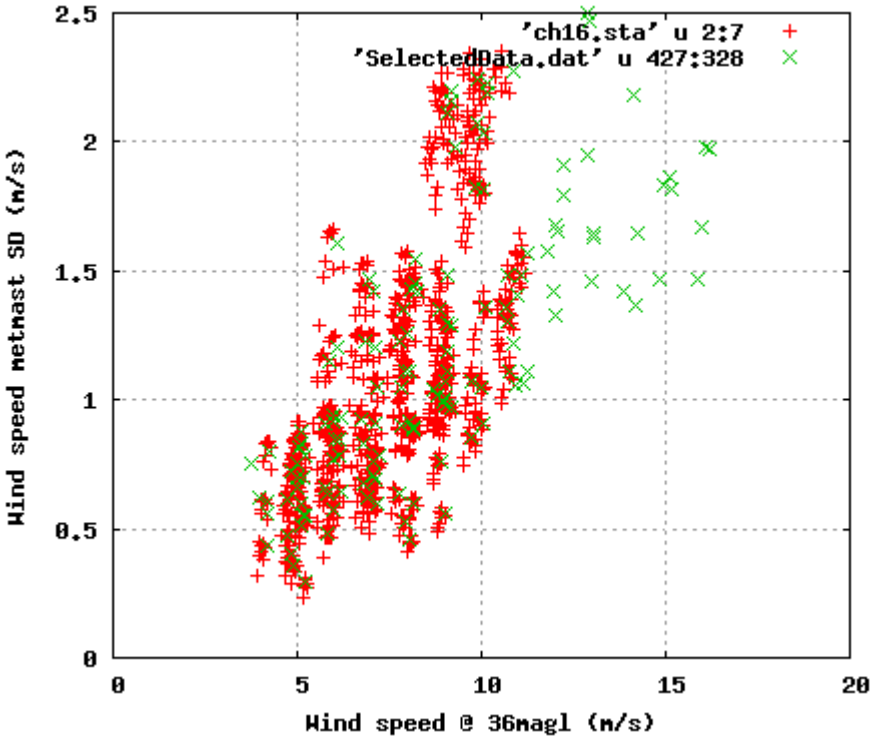

Figure 69Stdev wind speed

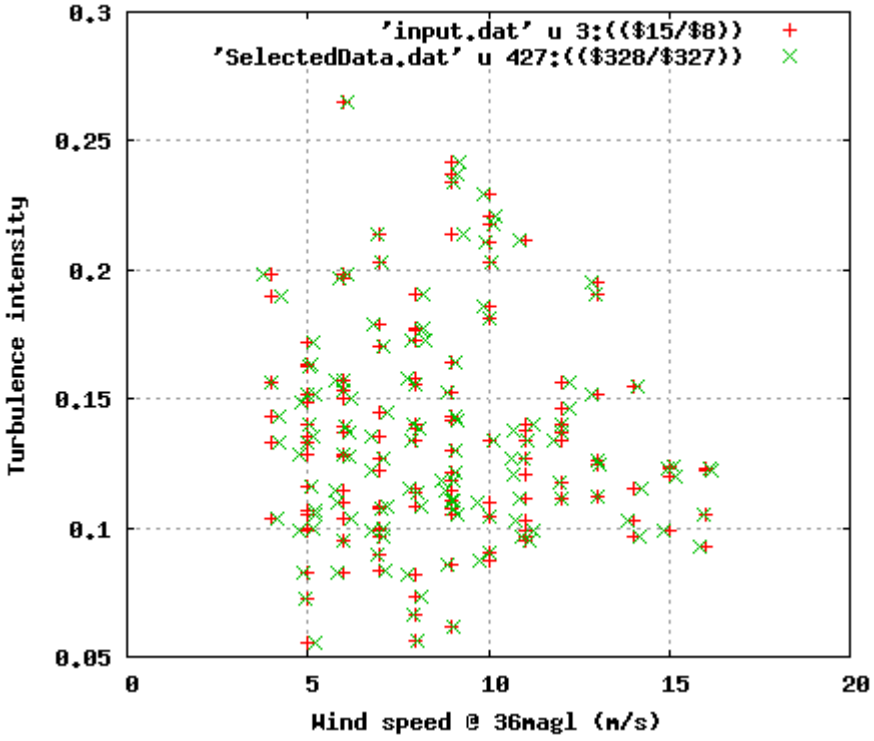

Figure 70 Mean Tu

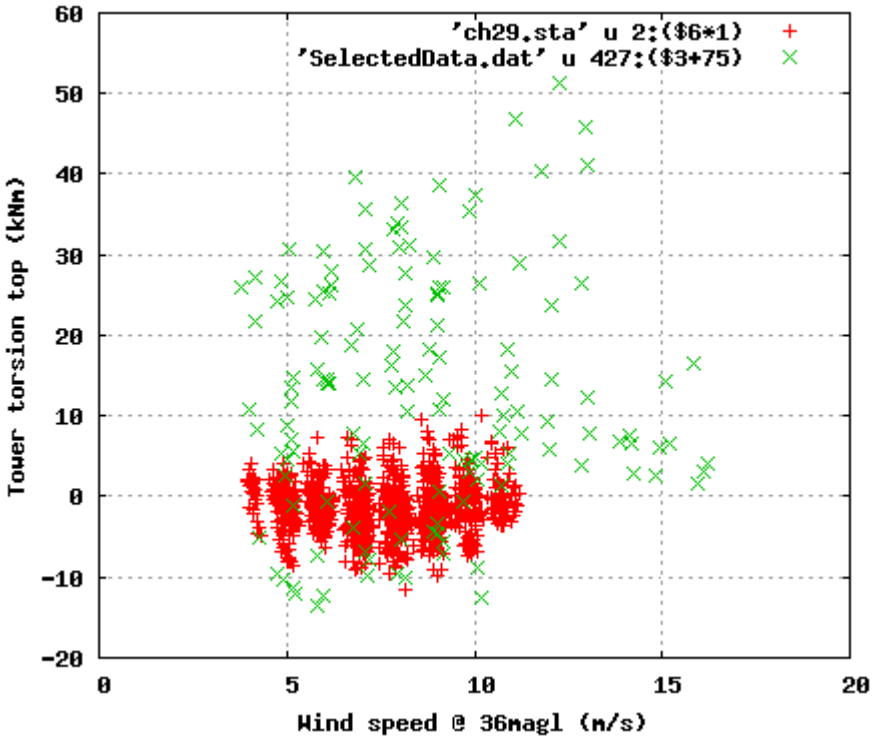

Figure 71 Mean Tower torsion

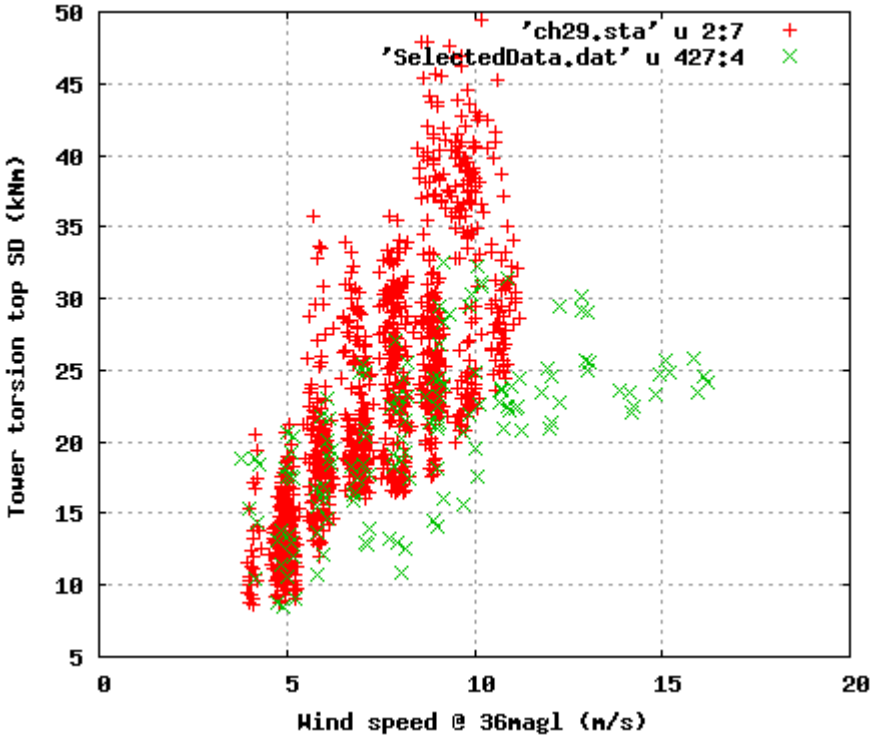

Figure 72 Stdev Tower torsion

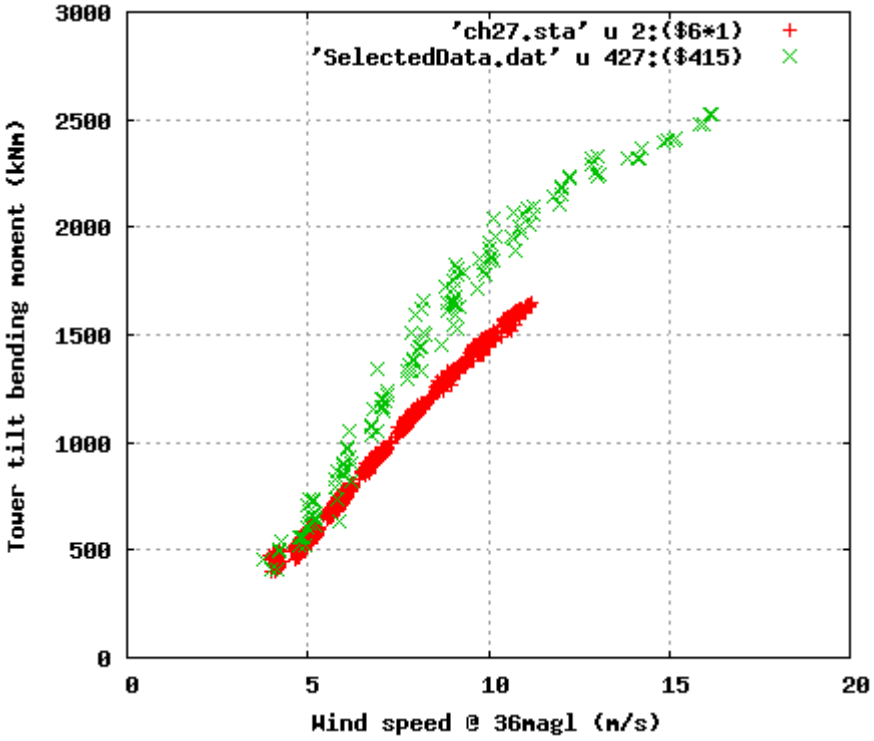

Figure 73 Mean Tilt moment

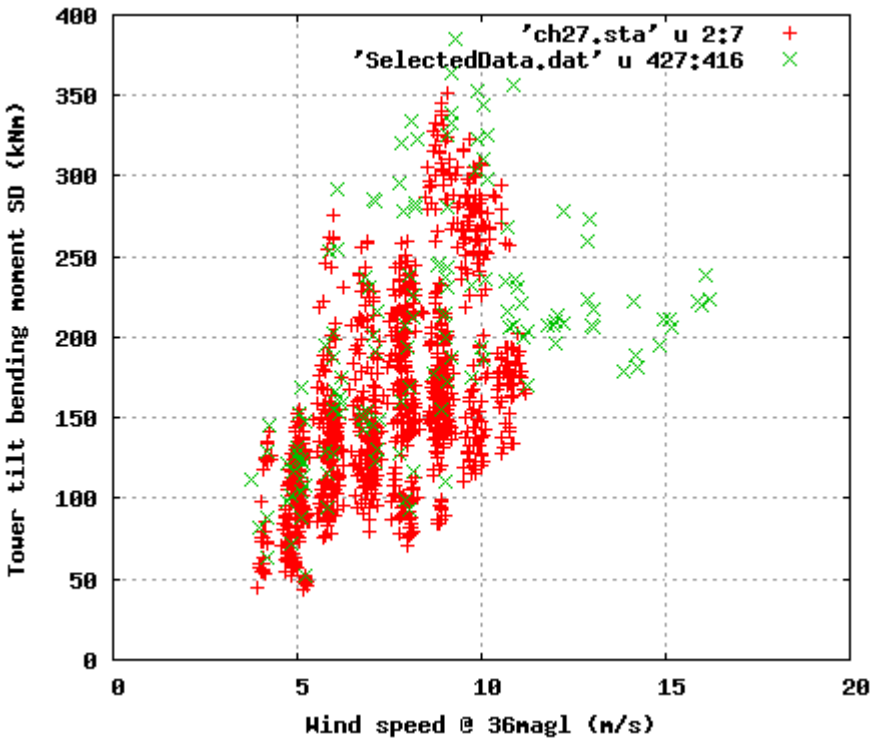

Figure 74 Stdev Tilt moment

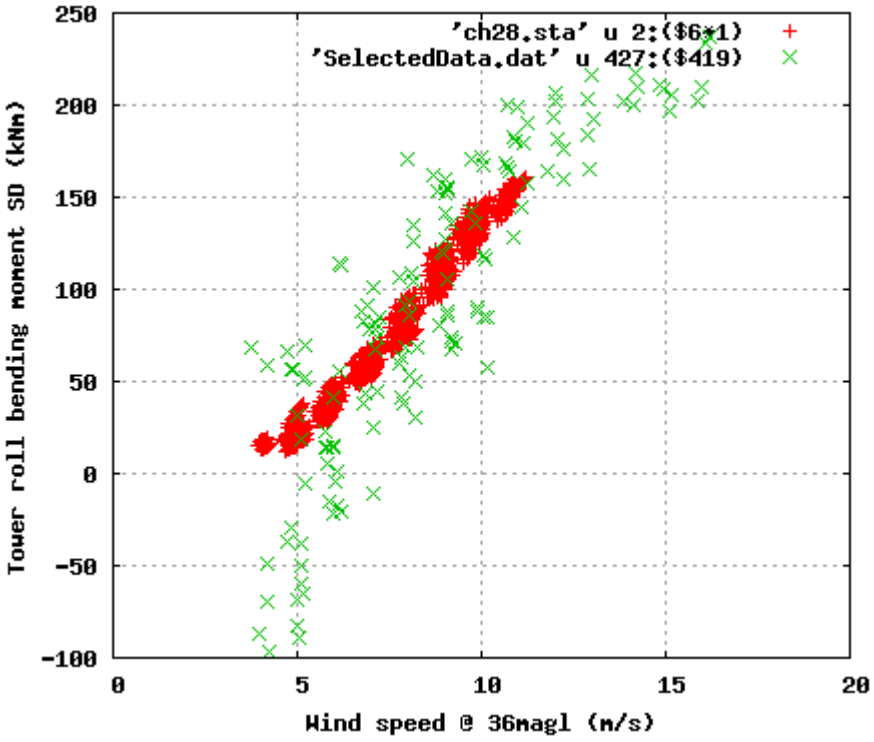

Figure 75Mean Tower roll bending moment

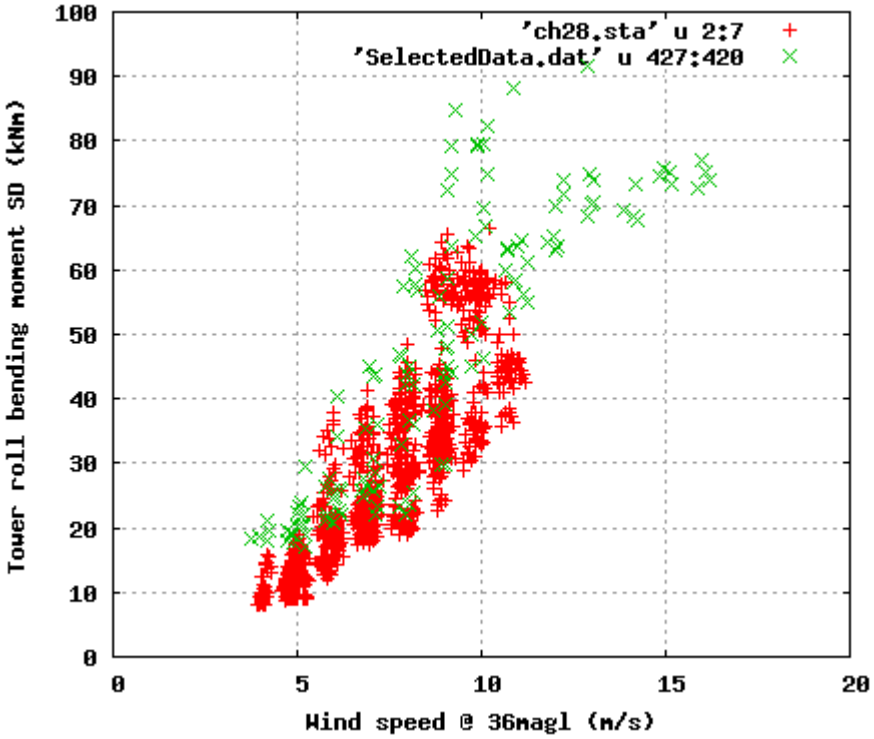

Figure 76 Stdev Tower roll bending moment

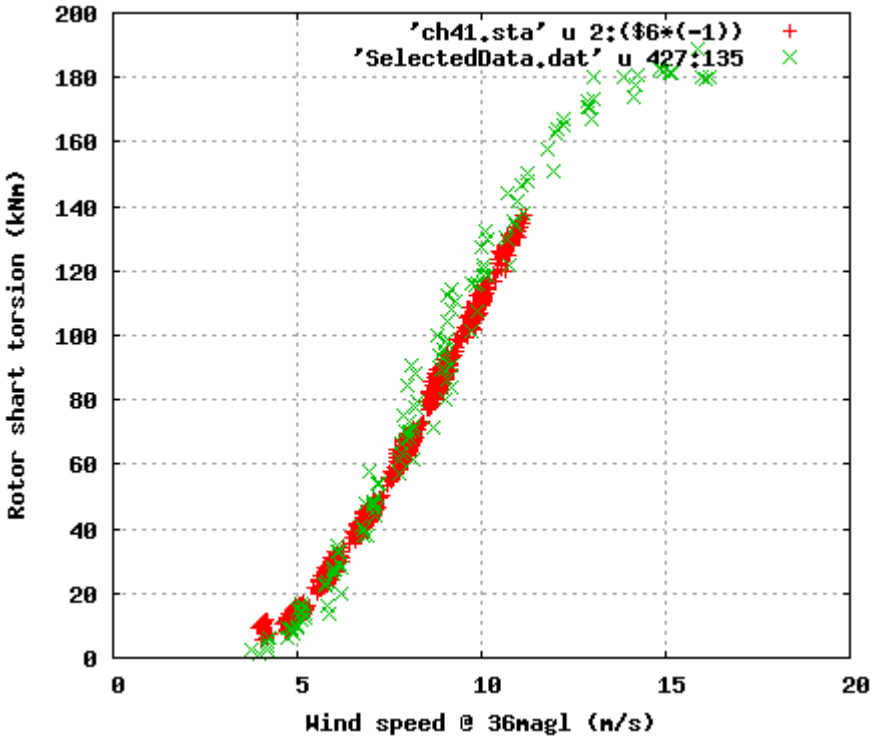

Figure 77Mean Rotor Shaft moment

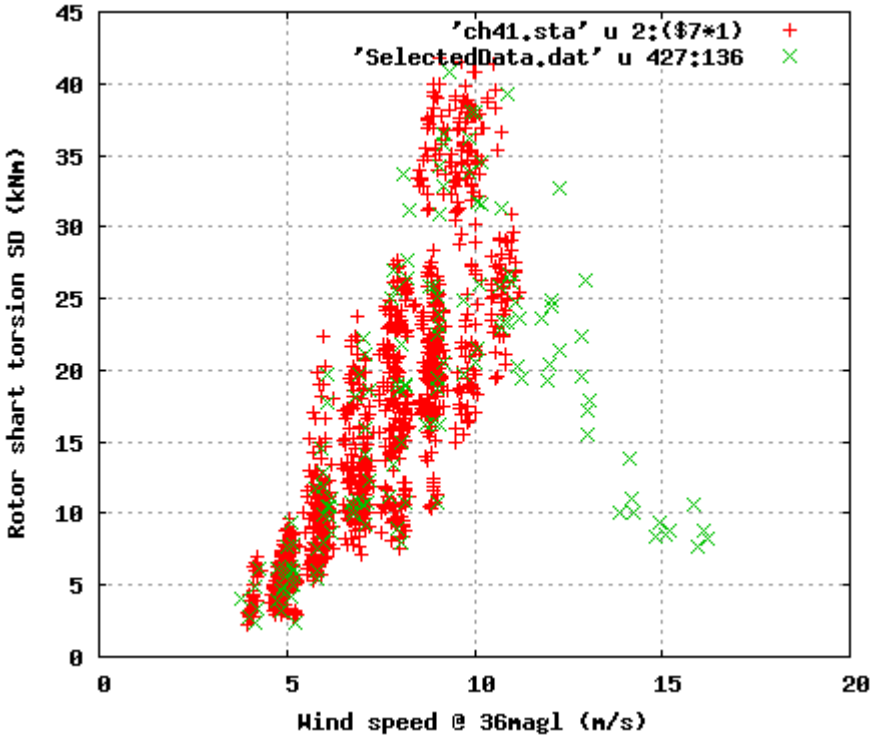

Figure 78 Stdev Rotor Shaft moment

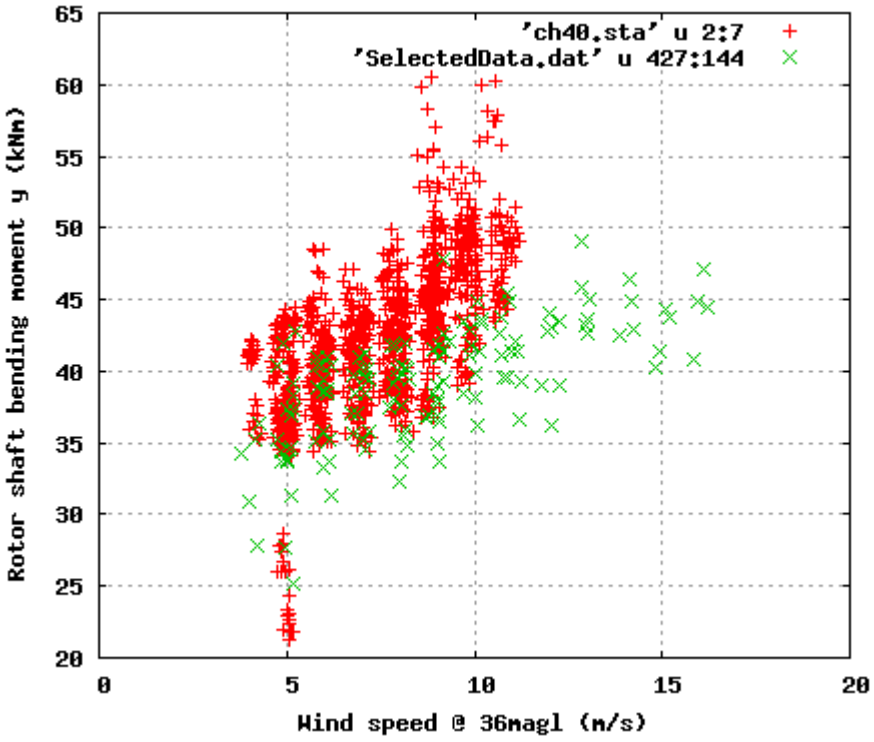

Figure 79 Mean rotor shaft bending

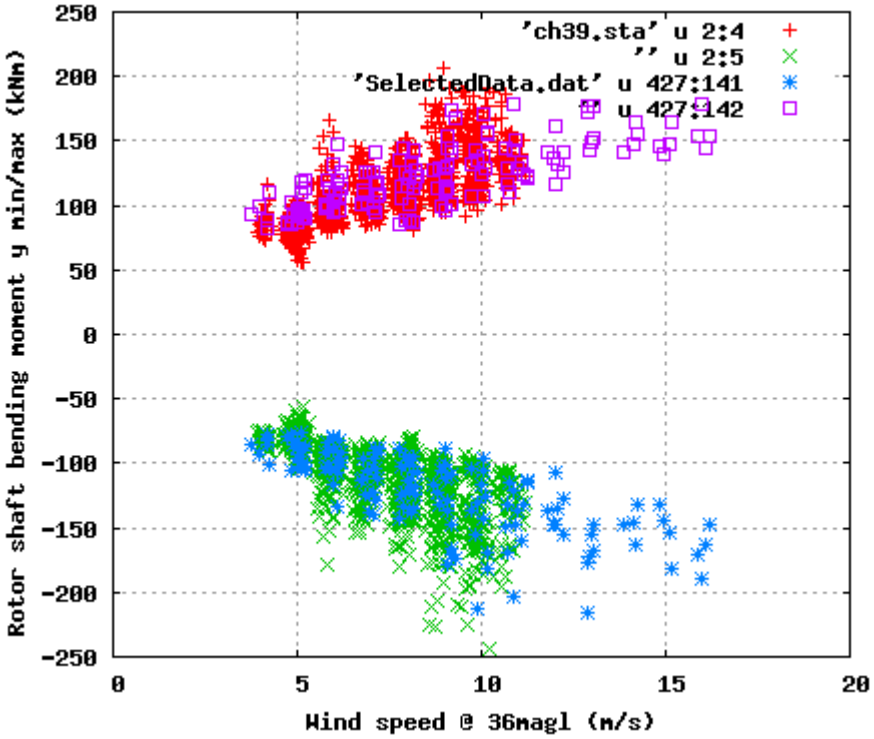

Figure 80 Min and Max rotor shaft bending

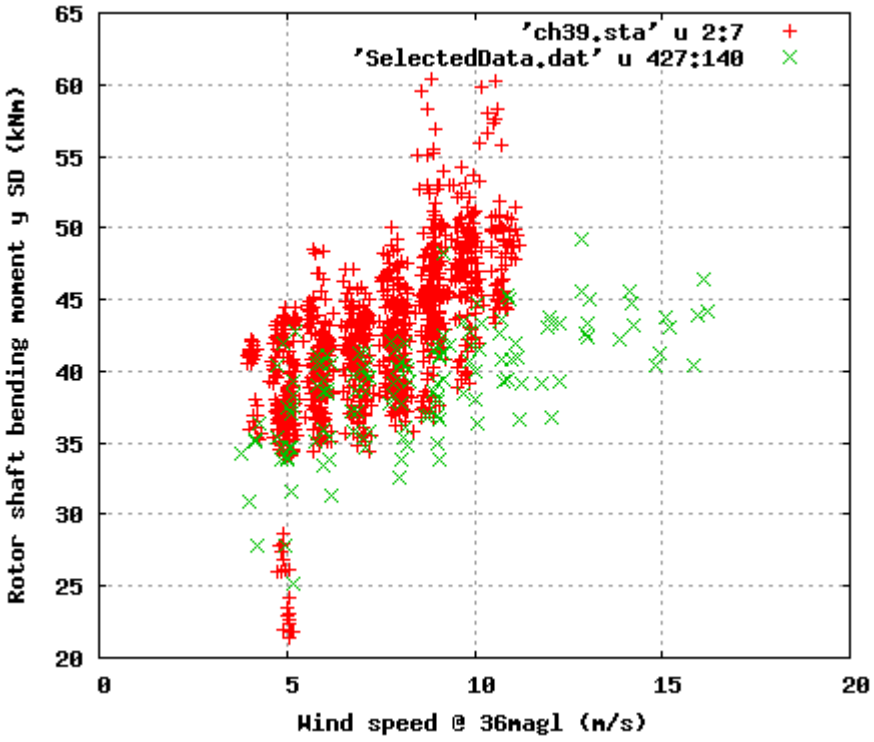

Figure 81Stdev Rotor shaft bending

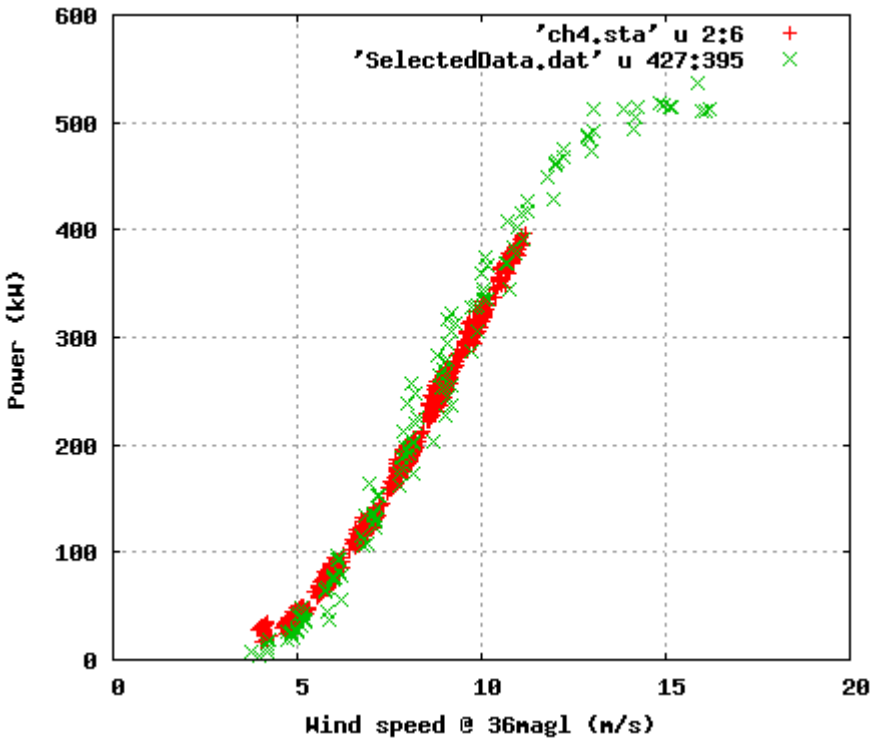

Figure 82 Mean Rotor Shaft Power

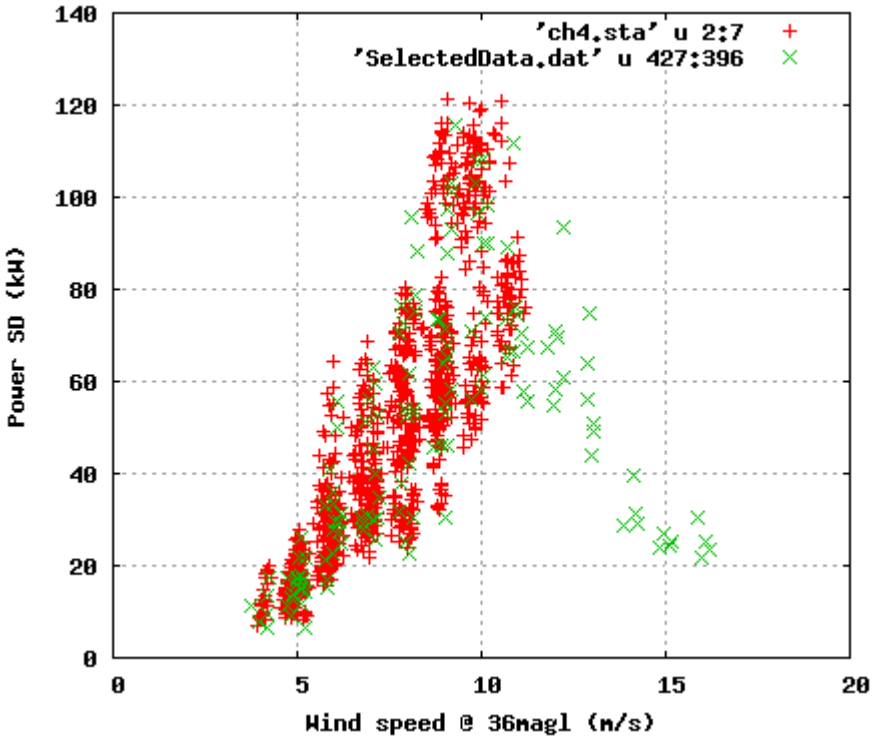

Figure 83 Stdev Rotor Shaft Power

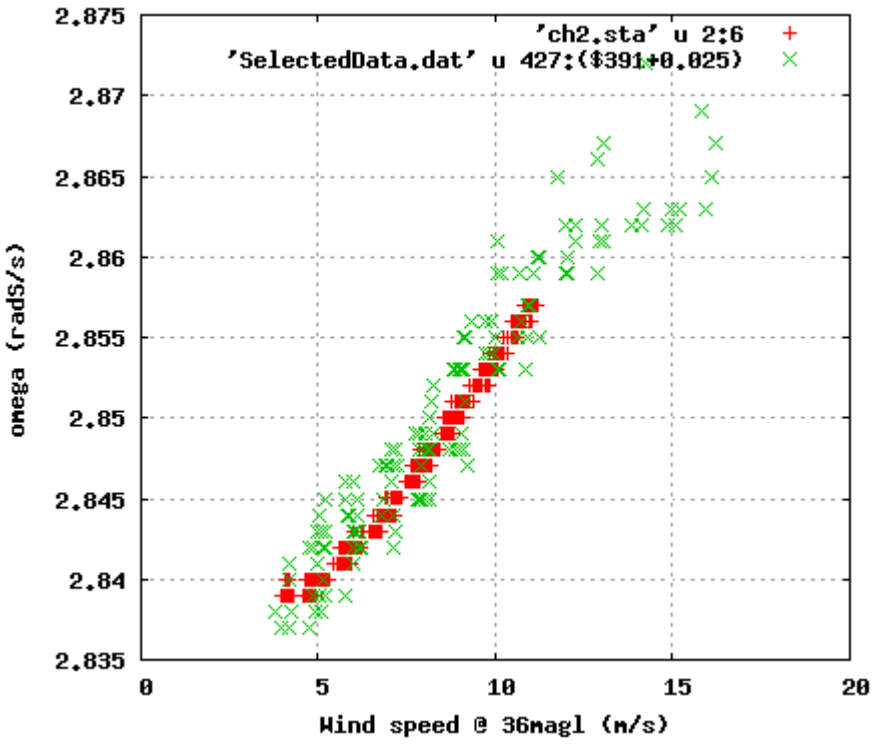

Figure 84 Mean RPM

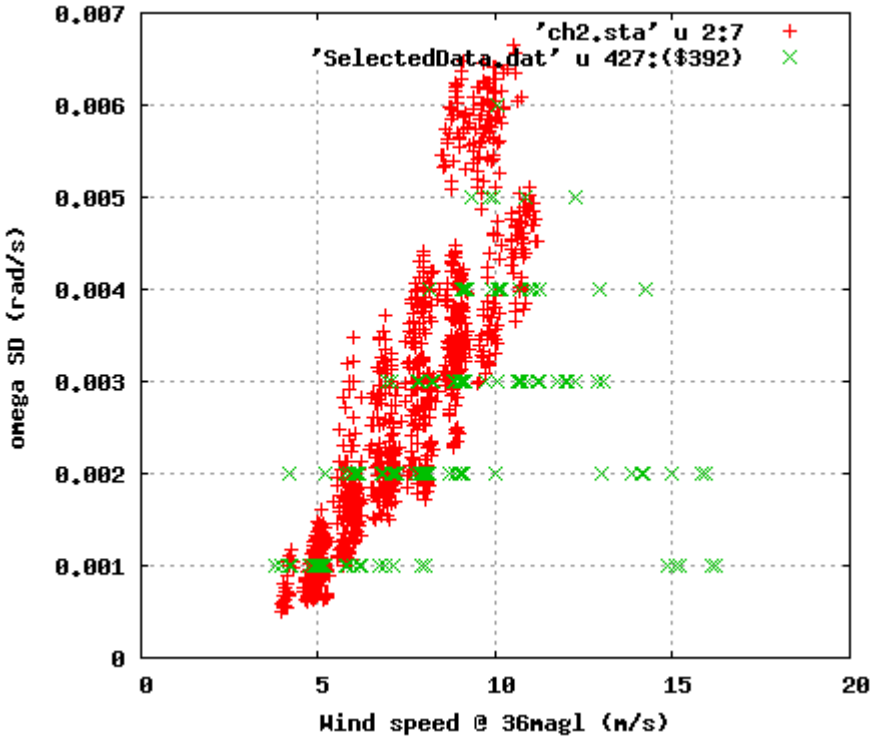

Figure 85 Stdev RPM

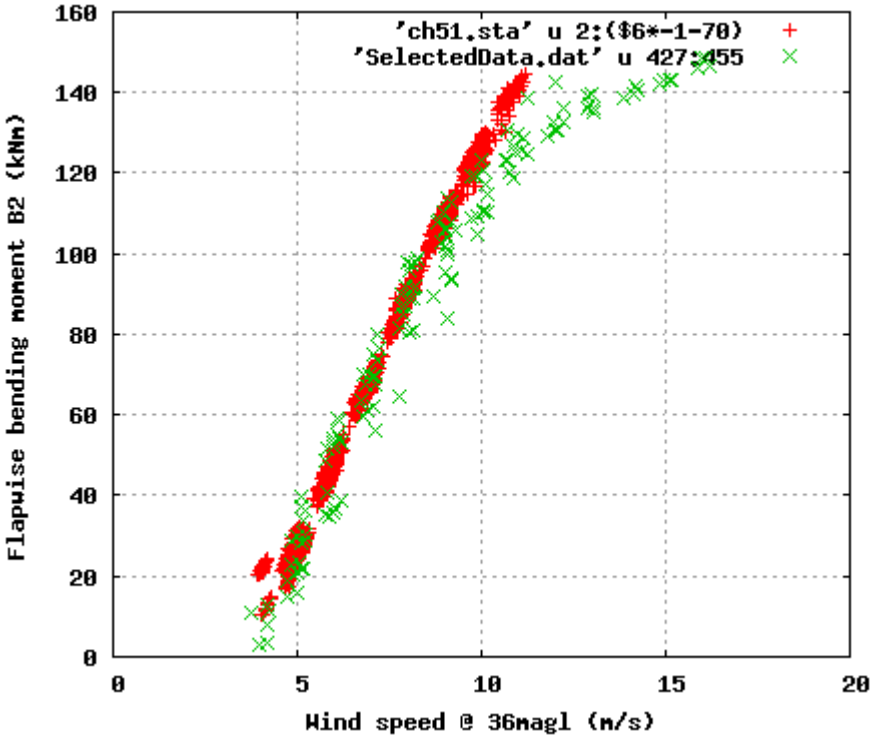

Figure 86 Mean Flapwise bending moment ref blade

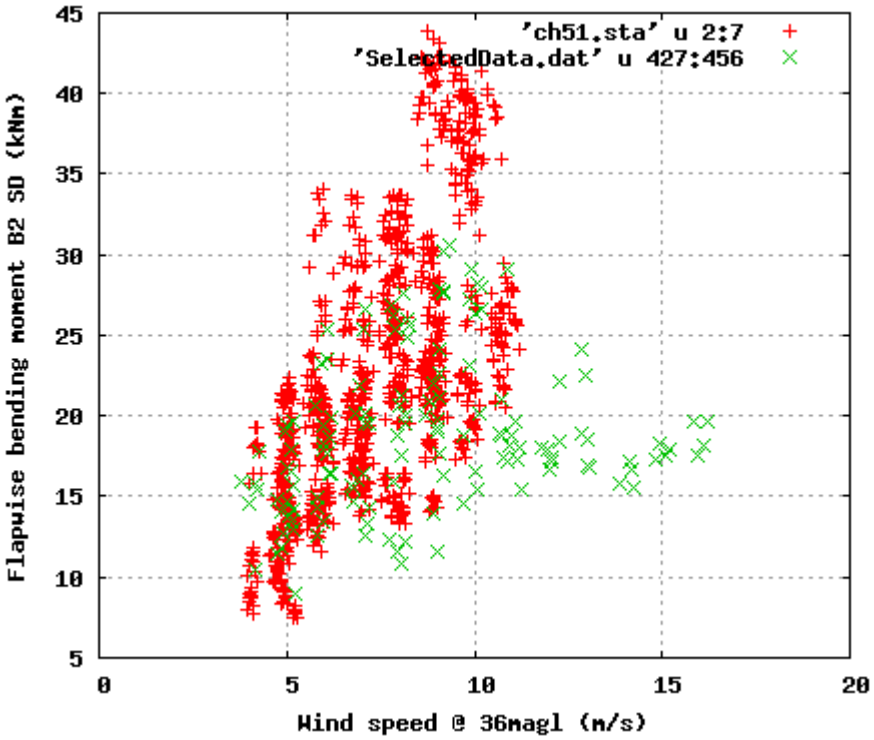

Figure 87Stdev Flapwise bending moment ref blade

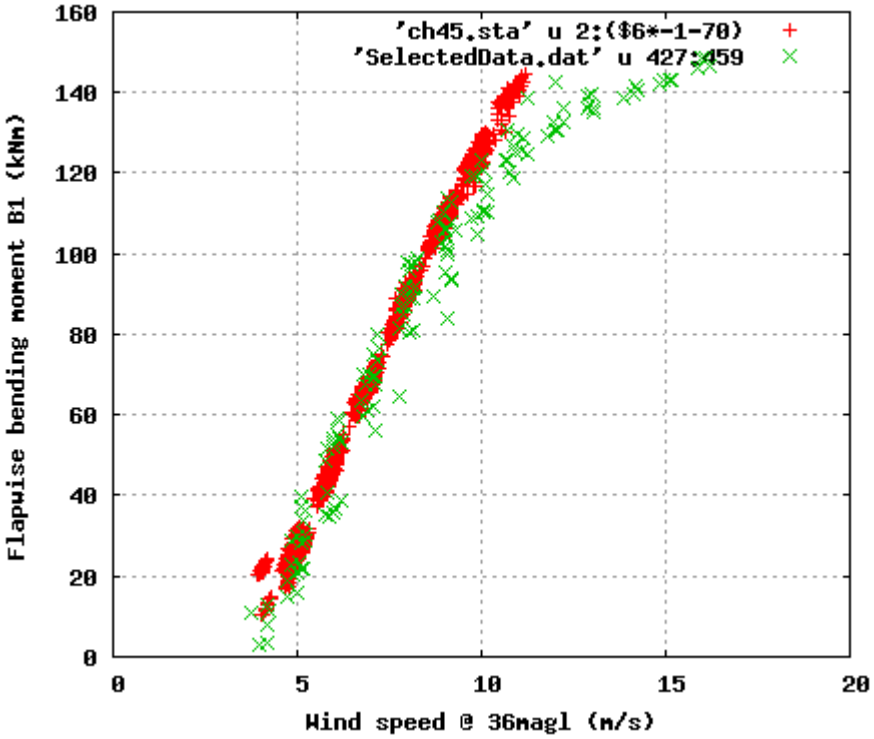

Figure 88 Mean Flapwise bending moment Blade 1

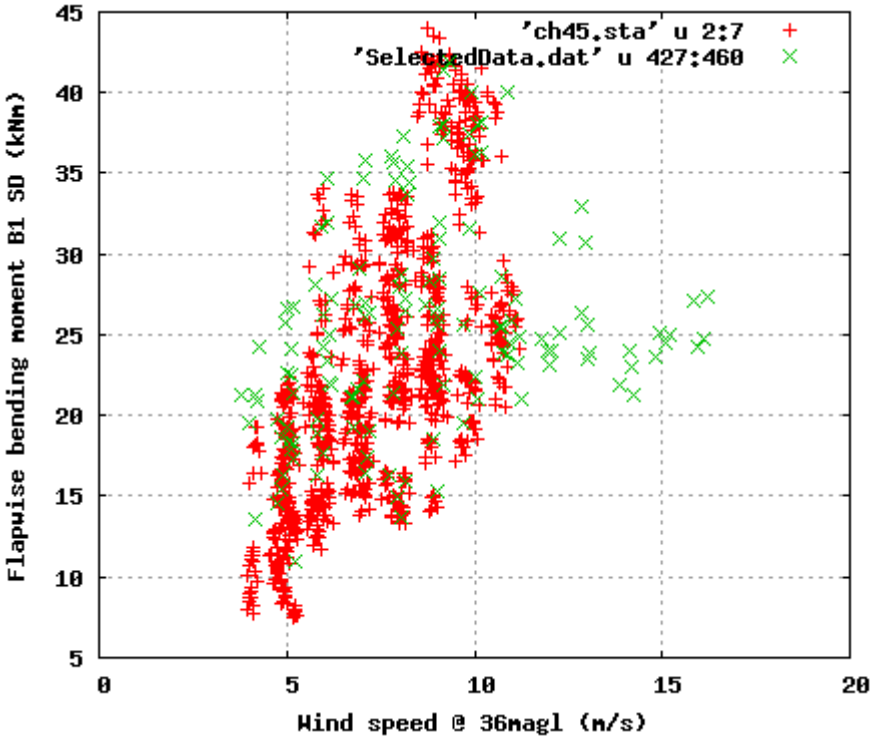

Figure 89 Stdev Flapwise bending moment Blade 1

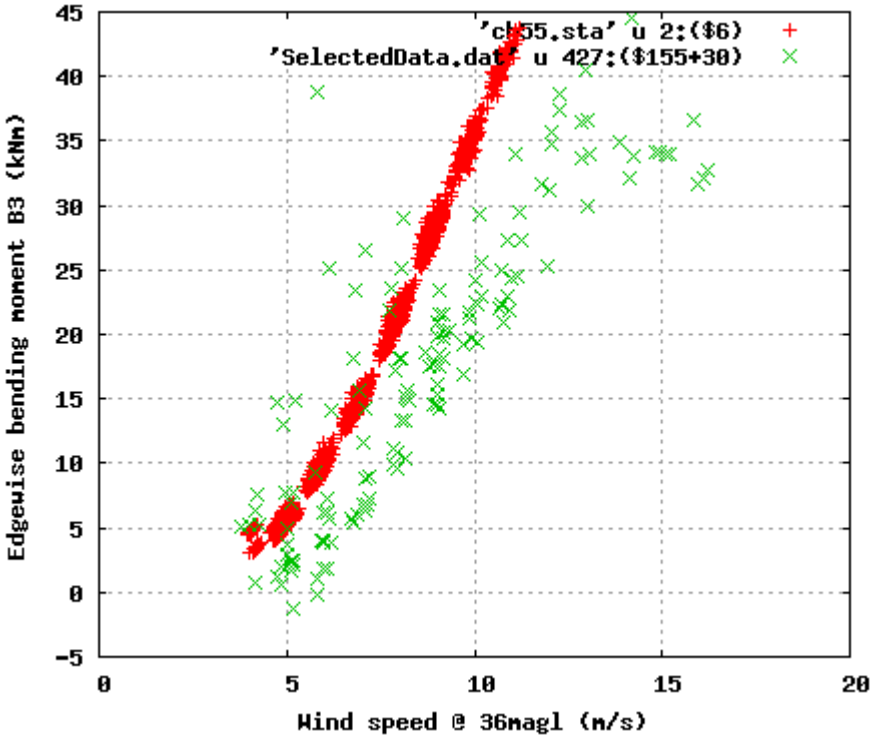

Figure 90 Mean Edgewise bending moment Blade 3

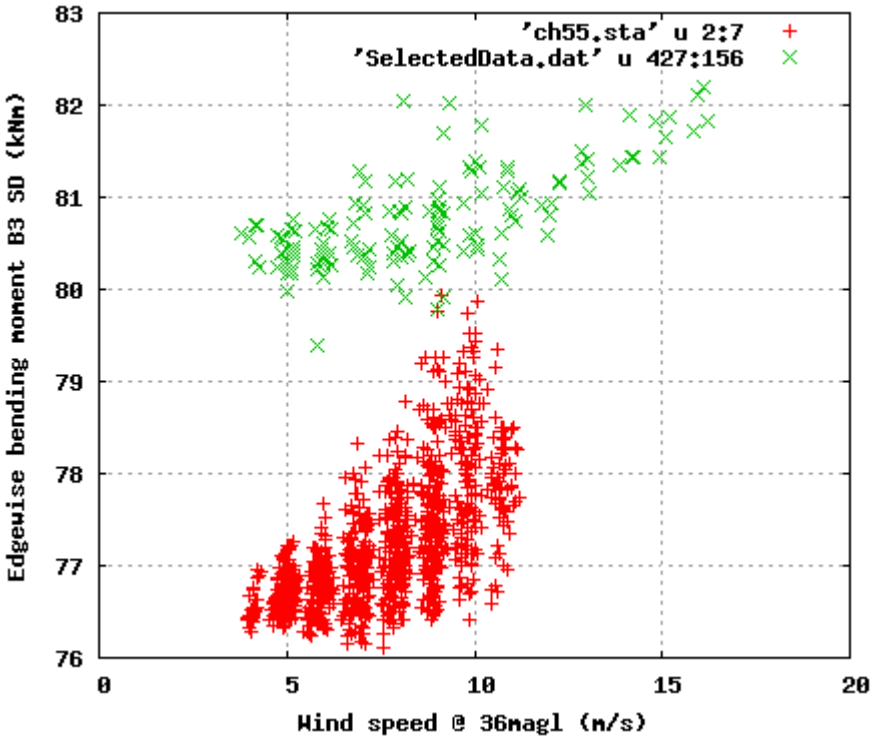

Figure 91Stdev Edgewise bending moment Blade 3

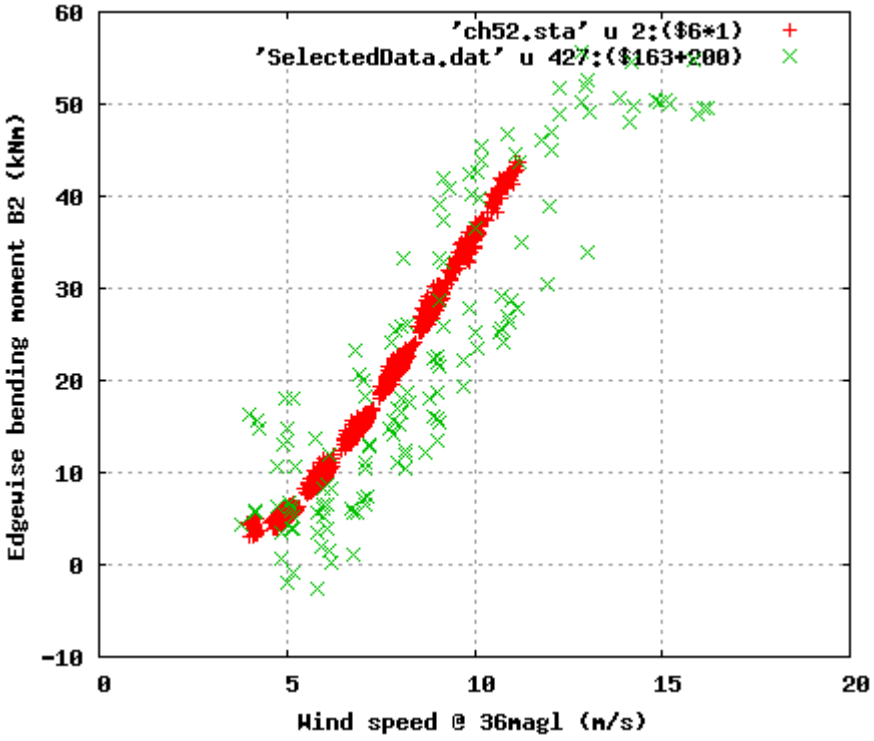

Figure 92Mean Edgewise bending moment ref blade

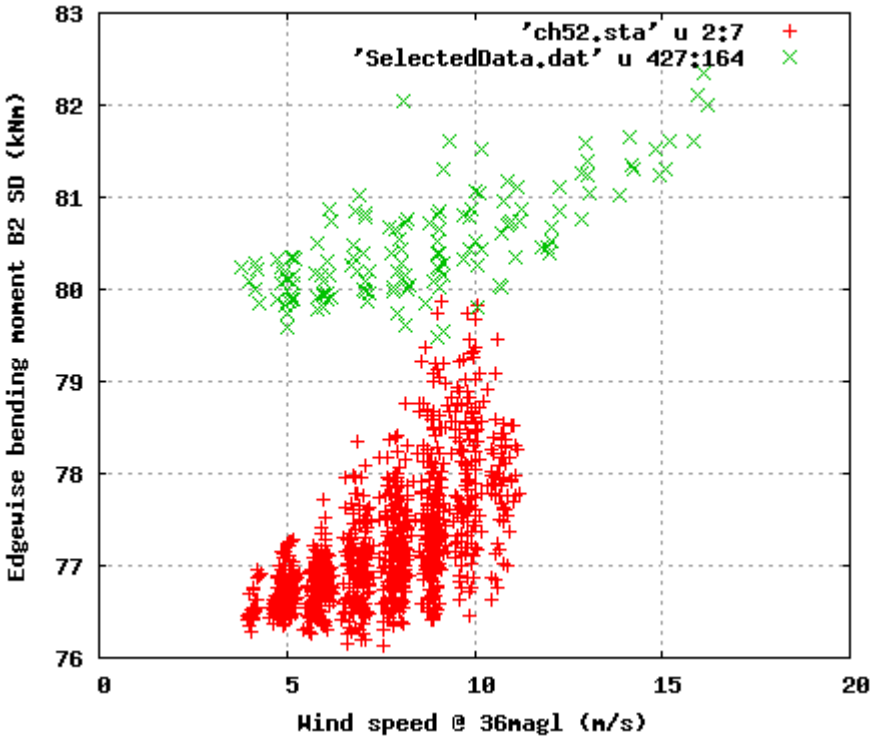

Figure 93Stdev Edgewise bending moment ref blade

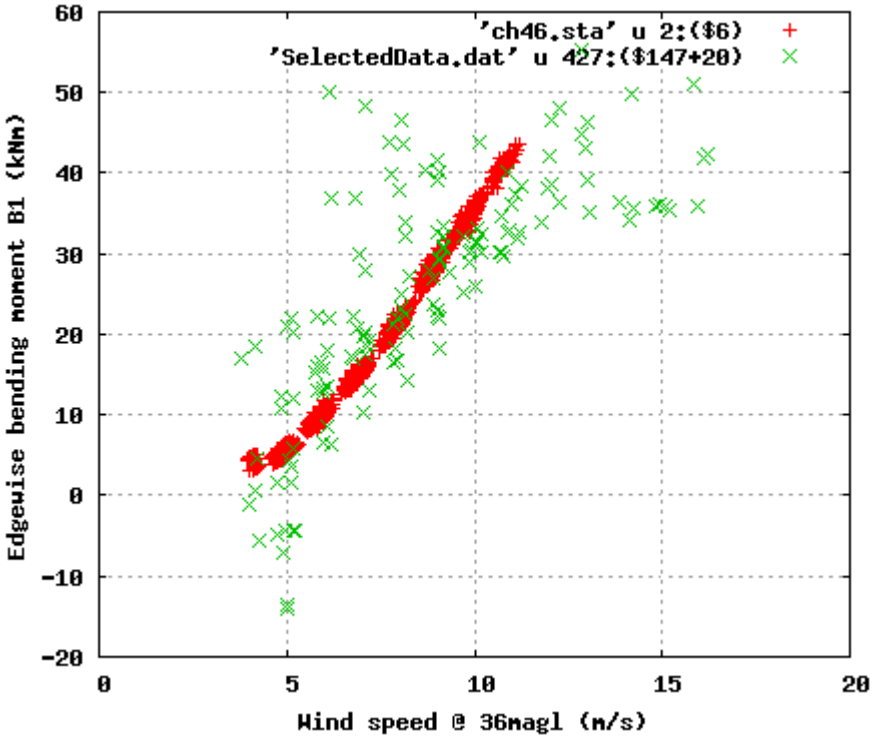

Figure 94Mean Edgewise bending moment Blade 1

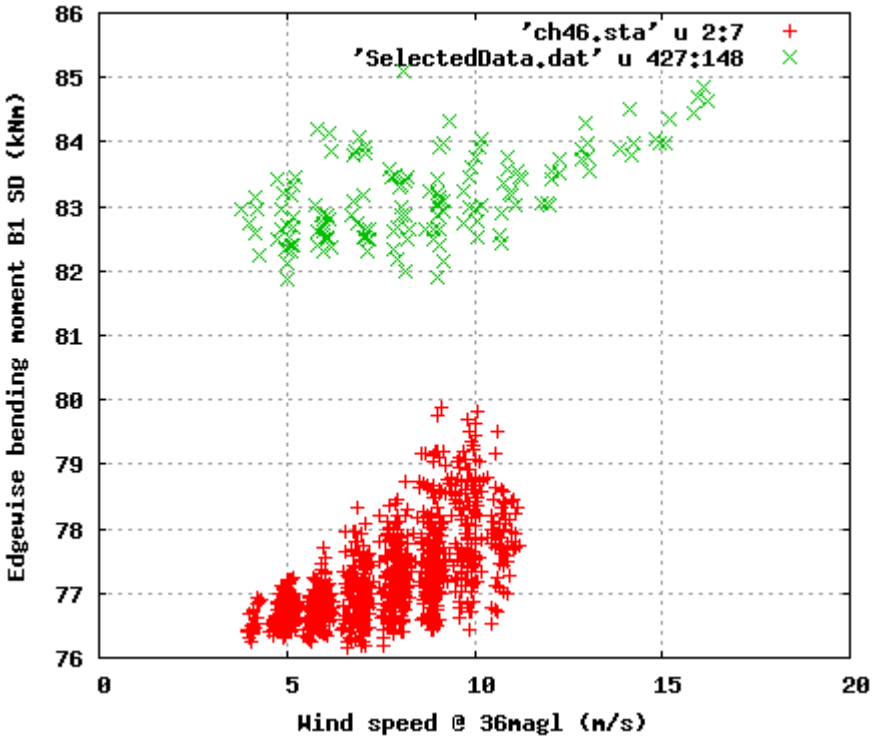

Figure 95Stdev Edgewise bending moment Blade 1

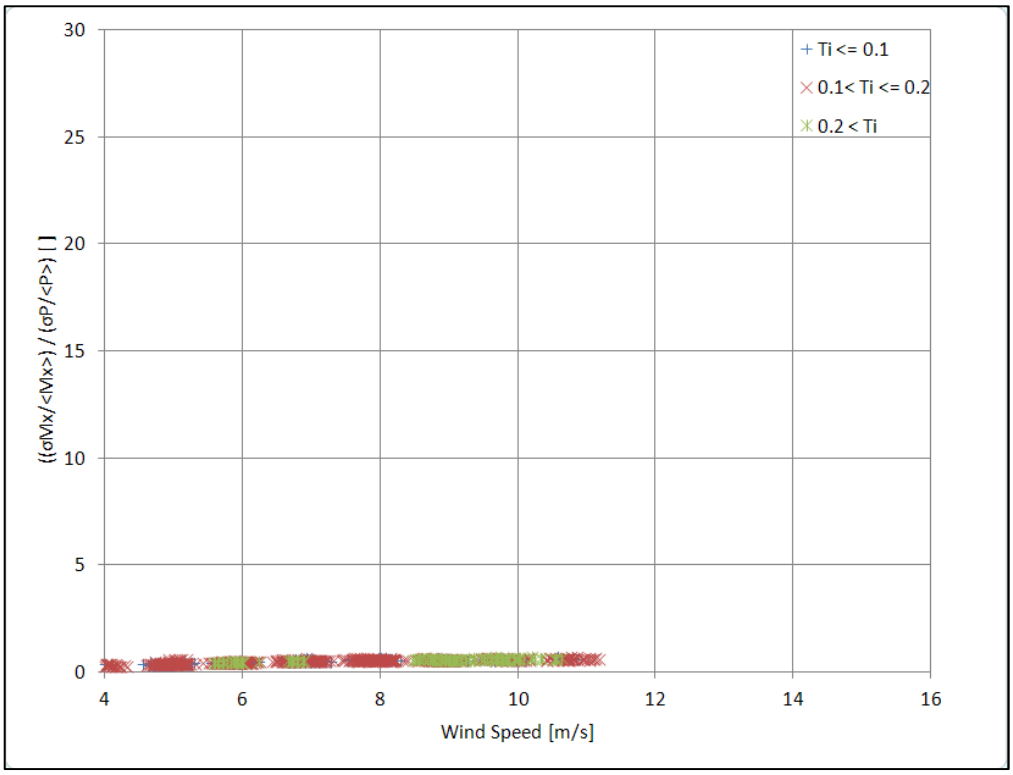

Figure 96 Estimated load over power sensitivity for different turbulence intensities

6.3 References

6.1. Larsen TJ. How 2 HAWC2, the user manual – version 1.4 Risø-R-report(EN), Risø National Laboratory, April 2006.

6.2. Morten Hansen. Data for aeroelastic modelling of the Nordtank 500 kW turbine with LM19.1 blades 2010 Risø report to be published

6.3. Larsen T.J., Description of the DLL regulation interface in HAWC. Risø-R-1290(EN), Risø National Laboratory, 2001.

7 Equivalent wind speed power curve for the Nordtank turbine

In [3.2], it was first shown that the wind speed profile has an influence on the measured power curve of a MMW wind turbine, secondly that the use of the equivalent wind speed accounting for the whole wind speed profile and defined by:

$$U_{eq} = \left(\sum_i U_i^3 \frac{A_i}{A} \right)^{1/3}$$

reduces the scatter due to the variation of the wind speed profile and results in a power curve almost independent of the shear. A similar analysis was achieved for the 500kW Nordtank wind turbine power curve.

7.1 Data

The analysis is based on the power curve measurement of the Nordtank wind turbine located at the Risø Campus test site between the 02-06-2011 and 19-01-2012. It is a 500kW wind turbine with a hub height of 36.5m and a rotor diameter of 41m. A met mast is located on the west side of the turbine (283 degrees) equipped with cup anemometers at 5 heights: 18m, 27m, 36m, 45m, 54m, boom mounted on the south side of the mast. It enabled us to measure the wind speed profile within the span of the rotor swept area. The wind direction was measured with a sonic anemometer at 34.5m. Wind directions within 250 and 300 degrees were considered. After selecting data, obtained with normal operation of the turbine and wind speed measurement status the dataset used for the analysis counts 3581 data.

7.2 Method

A similar analysis to that described in [3.2] was achieved for the Nordtank wind turbine power curve. The wind speed profiles were divided in 3 groups according to the shape of the profile, i.e. whether the profile is close to the power law or not, and if not if its kinetic energy flux (KEF_{eq}) defined as:

$$\mathrm{KEF} = \frac{1}{2}\rho \mathrm{U}_{\mathrm{eq}}^3 \mathrm{A} = \frac{1}{2}\rho \sum_i U_i^3 A_i$$

is under or overestimated by the wind speed at hub height (i.e. by $\mathrm{KEF}_{\mathrm{hub}} = \frac{1}{2}\rho \mathrm{U}_{\mathrm{hub}}^3 \mathrm{A}$). This was achived first by fitting the wind speed profile measured with the met mast to a power law and estinating the goodness of fit with the residual sum of square (RSS). The the profiles with a low RSS wer grouped depending on the ratio KEF_{eq} / KEF_{hub} (see [3.2] for more details). The categorization is as follow:

- Type 1: RSS<0.015 (value taken arbitrarily In order to have a good number of data of each type); i.e. profiles with a shape close to a power law;
- Type 2: RSS>0.015 and KEFeq/KEFhub smaller than the theoretical value of the ratio for a theoretical power law profile; i.e. profiles with a shape deviating from a power law and for which Uhub overestimates the KEF of the profile;
- Type 3: RSS>0.015 and KEFeq/KEFhub larger than the theoretical value of the ratio for a theoretical power law profile ; i.e. profiles with a shape

deviating from a power law and for which Uhub underestimates the KEF of the profile;

The first group of profile is shown in Figure 97 and all three groups together in Figure 98.

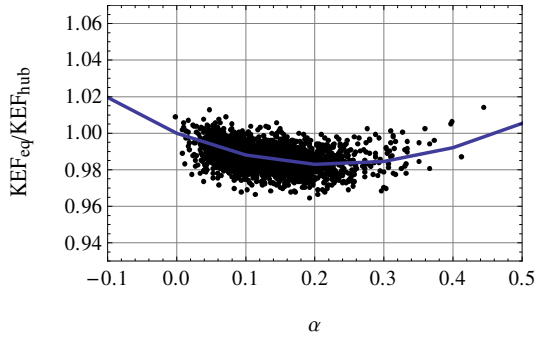

Figure 97 Ratio KEF_{eq}/KEF_{hub} vs. shear exponent (alpha) for theoretical power law profile (blue line) and for measured profile with an RSS<0.015 (type 1 profiles) in black.

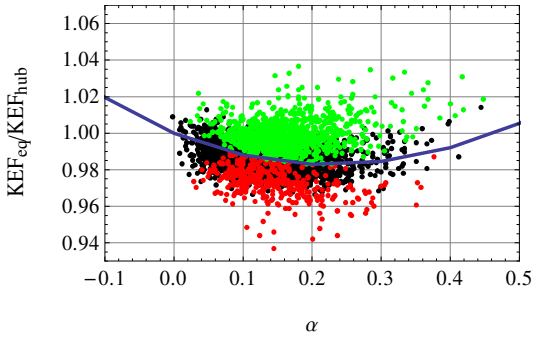

Figure 98Same figure as Figure 97 with in addition Ratio KEFeq/KEFhub vs. shear exponent (alpha) for type 2 profiles in red and type 3 profiles in green.

The power curve obtained, with the method of bins according to the IEC 61400-12-1 standard [5.10], were evaluated for the 3 groups of data separately, with wind speed at hub height on one hand (Figure 99) and the equivalent wind speed on the other hand (Figure 99).

7.3 Results

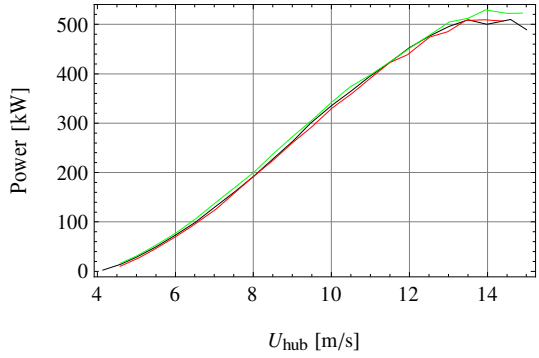

Figure 99 Mean power curve obtained with the wind speed at hub heights for the three types of profile: type 1 in black, type 2 in red and type 3 in green.

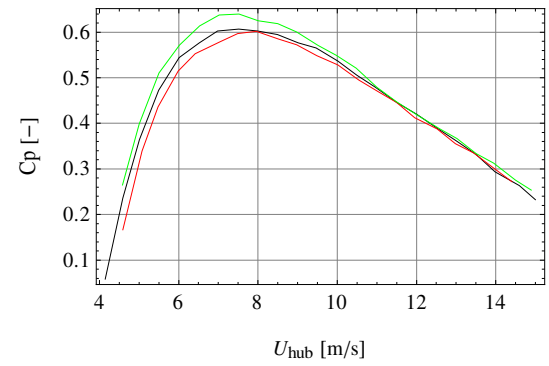

Figure 100 Mean Cp curve obtained with the wind speed at hub heights for the three types of profile: type 1 in black, type 2 in red and type 3 in green.

The various types of wind profiles result in three slightly different power curves. The difference is more obvious in the Cp curves. The power curve (and Cp curve) obtained with the type 2 profiles (red in Figure 99 and Figure 100) is "below" the others, which is in accordance with the profile categorization: the wind speed at hub height overestimates KEF_{eq} for this type of profile. Similarly the green curve is

above the others, as for type 3 profiles, the wind speed at hub height underestimates the KEF. This shows that the wind speed profile has an influence on the measured power curve, for small wind turbine (i.e below 1MW rated power) as for large MMW wind turbines. The turbine rotor span is smaller but hub height is also lower, therefore located where the shear is stronger.

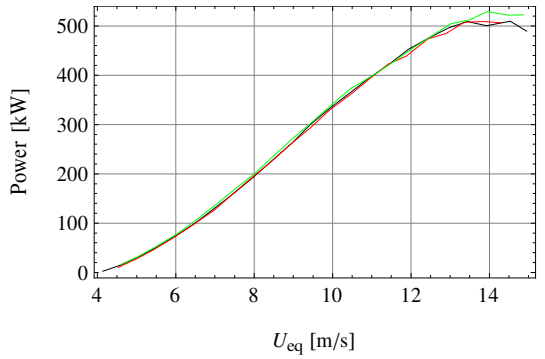

Figure 101 Mean power curve obtained with the equivalent wind speed for the three types of profile: type 1 in black, type 2 in red and type 3 in green.

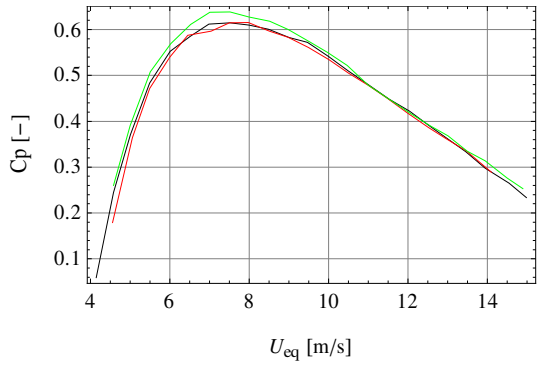

Figure 102 Mean Cp curve obtained with the equivalent wind speed for the three types of profile: type 1 in black, type 2 in red and type 3 in green

The power curve and Cp curves obtained with the equivalent wind speed are more similar to each other (see *Figure 101* and Figure 102). Both power curves for group 1 and 2 have moved slightly upwards toward the power curve for group 3, which has not changed very much. Moreover power curves for groups 1 and 2 are closer to each other.

The distributions of wind directions (Figure 103) and turbulence intensity (Figure 104) are very similar for type 1 and type 2. Therefore, the difference seen between the black and the red power curves in Figure 99 and Figure 100 are mainly due to the difference in wind speed shear. The equivalent wind speed method reduces most of the difference due to the shear. The average turbulence intensity is very similar for both dataset except for low wind speeds, as shown in Figure 105. This may explain the difference around low wind speeds in the power curve obtained with the equivalent wind speed in *Figure 101* and Figure 102 .

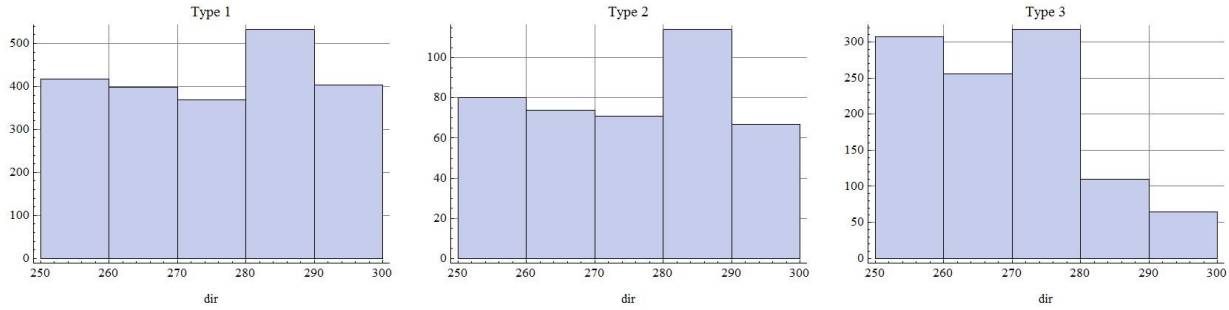

Figure 103 Wind direction distribution for each dataset.

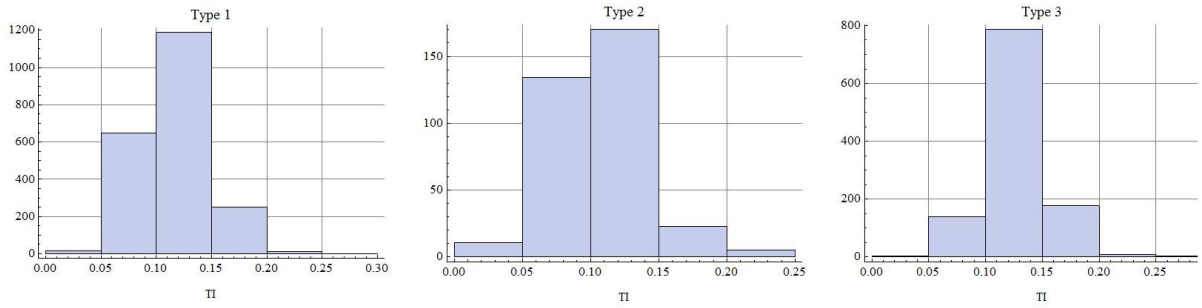

Figure 104 Turbulence intensity (TI) distribution for each dataset

On the other hand, the turbulence intensity distribution is quite different for group 3. The turbulence intensity is in average larger for this dataset than for the two others; except for wind speeds larger than rated speed (see Figure 106). Thus the power curve for group 3 is above the other 2 (i.e. it gives more energy) not only because of the shear but also because of the high turbulence intensity. This is probably why the power curve obtained with the equivalent wind speed (normalizing the shear effect) remains similar to that obtained with the wind speed at hub height.

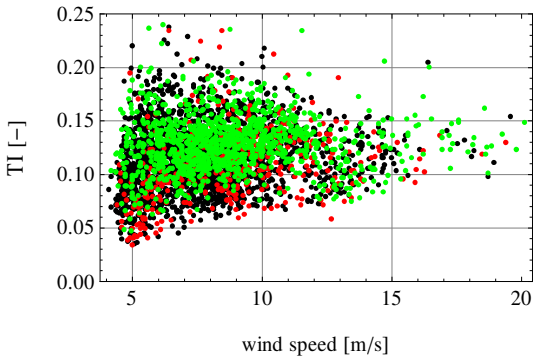

Figure 105 Turbulence intensity vs. wind speed for the three datasts: type 1 profiles in black, type 2 profiles in red and type 3 in green. Each dot is a 10 min value.

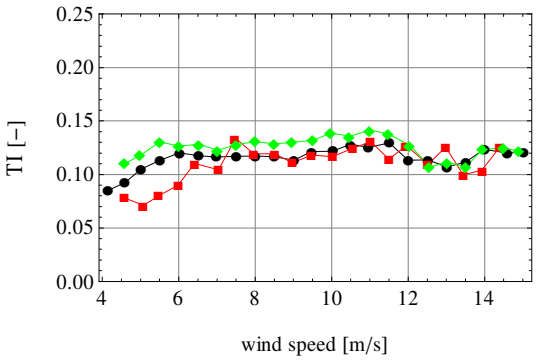

Figure 106 Wind speed bin averaged Turbulence intensity vs. the wind speed (at hub height) for each dataset.

The two power curves (Figure 107) are very similar. This is probably due to the fact that there are both profiles for which the KEF was underestimated by the wind speed at hub height and profiles for which it was overestimated. Therefore, on average, U_{hub} is close to U_{eq} for this power curve. However, it is not completely exact since a slight difference can be observed in the Cp curves. There are more profiles for which U_{hub} overestimates the KEF, therefore resulting in an underestimation of the Cp.
Figure 109(resp. Figure 110) shows that the using the equivalent wind speed in the power (resp. Cp) curve clearly reduces the scatter, therefore the uncertainty [3.2].

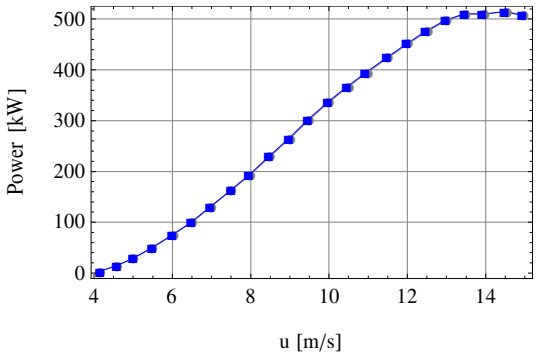

Figure 107 Bin averaged power curve obtained with the wind speed at hub height in gray and the equivalent wind speed in blue for the data together (i.e. all wind profiles)

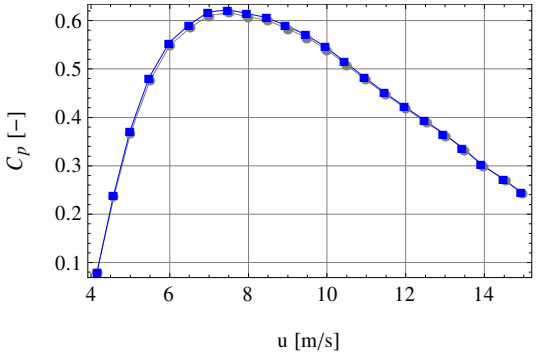

Figure 108 Bin averaged Cp curve obtained with the wind speed at hub height in gray and the equivalent wind speed in blue for the data together

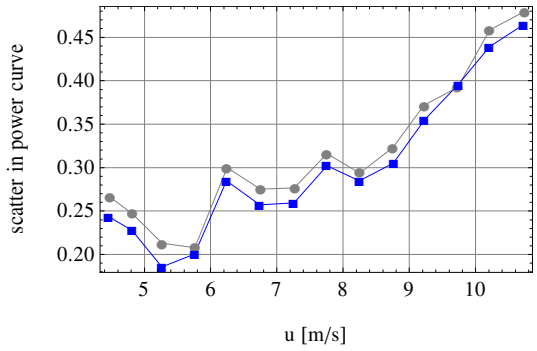

Figure 109 Scatter per bin for the power curve obtained with the wind speed at hub height in gray and the equivalent wind speed in blue for the data together

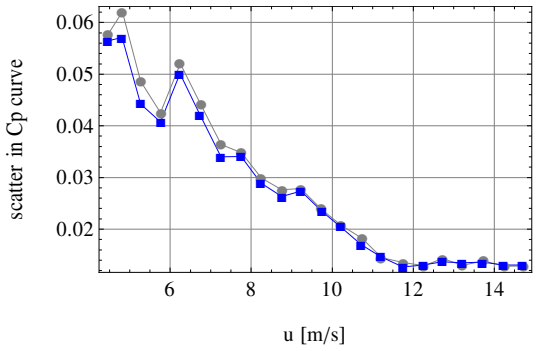

Figure 110 Scatter per bin for the Cp curve obtained with the wind speed at hub height in gray and the equivalent wind speed in blue for the data together

7.4 Conclusions

A similar analysis to what was done for a MMW wind turbine was achieved here for a 500kW turbine. It shows that shear can also significantly influence the power curve measurement of a small wind turbine. Furthermore, the results coincide with those obtained for the MMW wind turbine. Using the equivalent wind speed in the power curve reduce the differences between the power curves obtained for different types of wind profiles, therefore decrease the scatter in the measured power curve.
However, the profiles for which the energy was underestimated by the wind speed at hub height coincided, in this dataset, with larger turbulence intensity. The higher turbulence intensity is expected to increase the power output for low and medium wind speeds. Therefore some difference remained between he various power curves obtained for the different type of profiles.

Finally, contrary to the analysis made with the MWW wind turbine based on a dataset for which the KEF of most of the profiles was overestimated by the wind speed at hub height, the dataset used in the present analysis counted both profiles for which the KEF was overestimated by the equivalent wind speed. It results that the mean power curve obtained with the wind speed at hub height is very similar to that

obtained with the equivalent wind speed. It reinforces the conclusion that the difference between the 2 power curves depends on the wind speed profile distribution and therefore cannot be corrected for with a simple factor or the assumption of one profile representative for all the dataset. It strengths the necessity to measure the wind speed profile during the power curve measurement.

8 Speed profile evolution from the shore to the mast

As a part of the project a study on a lightly sloped terrain were conducted to investigate on the usefulness of LIDARS for power curve performance measurements.

8.1 Description of the measurement campaign

The measurements took place at the Risø DTU test site. The measurement campaign took place in several phases. First, one LIDAR (Z2) was placed next to a mast of 45 m (mast V27) in order to verify the LIDAR measurement accuracy. Secondly, the same LIDAR was installed near the shore on the west side (283 degrees) of the Nordtank turbine (in alignment with the turbine and the mast) in order to measure the wind speed profiles at this location and compare them to those measured by the mast in front of the turbine. When the mast was erected on the 29/04/2011, it was equipped with 4 cup anemometers (3 boom mounted on the south side at 18, 36, and 54m and one top mounted at 57m), and 3 sonic anemometers on the north side of the mast. Two complementary cup anemometers were added at 27 and 45m (boom mounted) about one month later.

In the meantime, a second LIDAR (Z107) was installed between the shore and the mast (at about 85m from the shore and 100 m from the nordtank mast). Later, this LIDAR was moved closer to the mast (61.5 m). Unfortunately this LIDAR stopped working on the 24/07/2011; it has not been possible to repair it before the end of the campaign.

The power supply of LIDAR Z2 got flooded (due to strong westerly winds) on the 10/08/2011. It was repaired a couple of days later. But the focus system got stuck on the 27/08/2011. After getting repaired, the LIDAR was placed next to the Nordtank mast (32 m) in order to correlate the LIDAR measurements with the mast measurements. An overview of the measurements available from the different instruments is given in Figure 111.

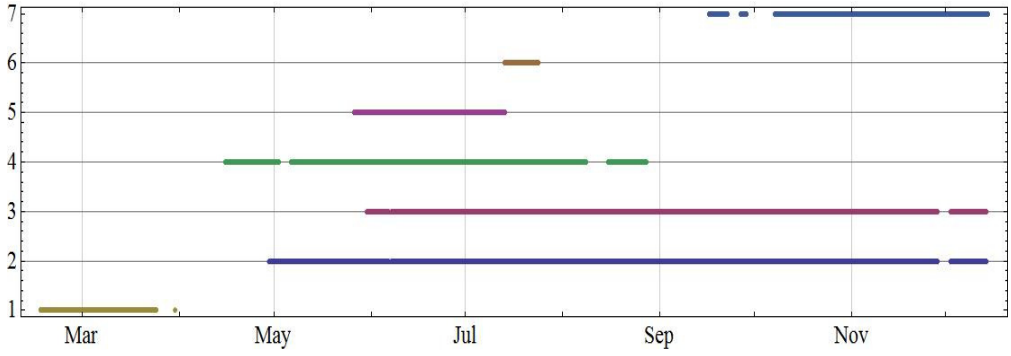

Figure 111 Overview of the measurements availability for the different instruments used in the measurement campaign: Yellow: Zephir 2 next to V27 mast

- *Blue: mast (3heights) (since 2011-04-29)*

- *Red: mast (5 heights) (since 2011-05-30)*

  (missing data are due to a power cut in June and broken fiber optics (by a mouse)that prevented data transfer between 2011-11-28 and 2011-12-02)
- *Green: Zephir 2 at the shore (2011-04-15 15:30 -- 2011-08-27 12:30; power supply got flooded on the 2011-08-10)*
- *Pink: Zephir 107 at the kink (2011-05-26 -- 2011-07-13)*
- *Orange: Zephir 107 in the slope (2011-17-13 -- 2011-07-24)*
- *Light Blue: Zephir 2 next to the Nordtank mast (from 2011-09-16 16:10)*

Both lidars used in this measurement campaign were Zephirs (from Natural Power) version 1. A Zephir is a continuous wave LIDAR that selects the measurement height by focusing the beam at the corresponding distance. It measures the radial speed at 50 positions around a circle, which are then fitted to a rectified cosine function. From this fit are retrieved the horizontal and vertical components of the wind speed as well as the wind direction [1]. These lidars are good at measuring at low ranges (from 10 to 150 m) but the wind speed measurements can be biased by the presence of low clouds and fog. The automatic (online) cloud correction has been used during the measurements for both units.

Both masts were instrumented with Risø cup anemometers. The calibration mast, situated at the V27 turbine, has a instrumentation shown in Figure 112.

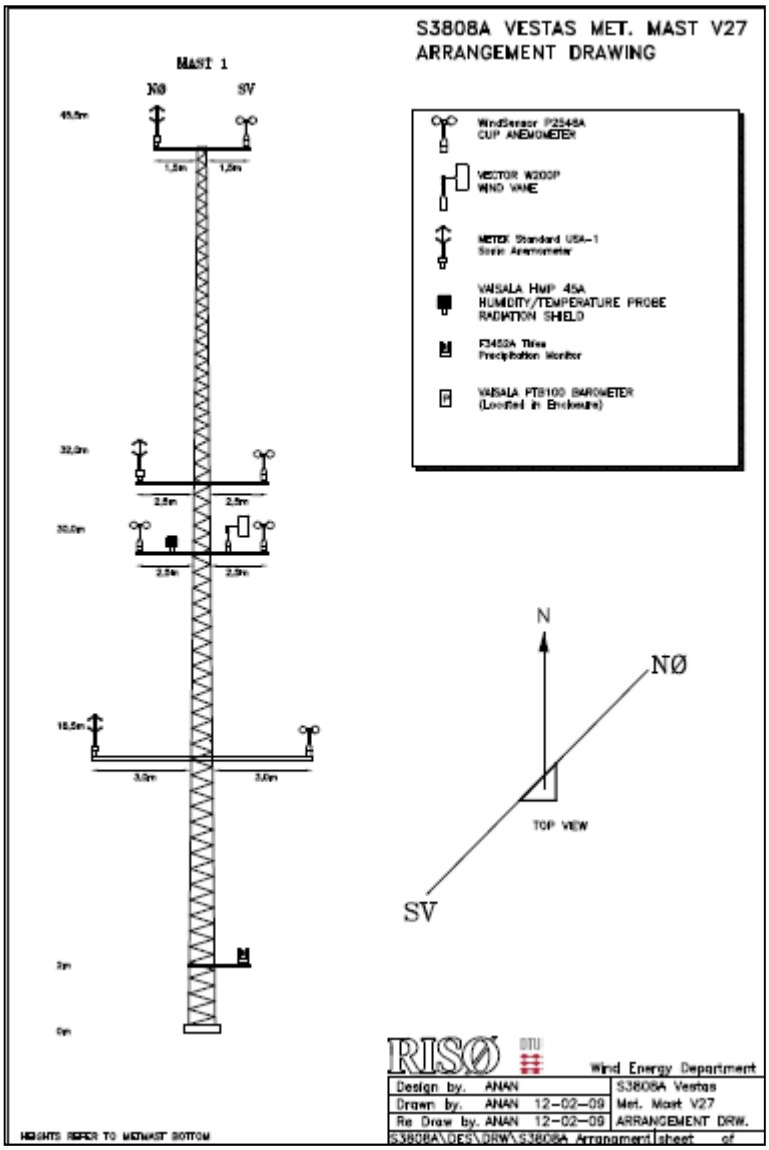

Figure 112 Met mast arrangement for LIDAR calibration

8.2 Verification Zephir unit 2 at mast V27

First of all, the first LIDAR (Z2) was placed next to the V27 mast in order to be compared with the cup measurements. The mast is equipped with 4 cup anemometers (3 boom-mounted, at 18.5, 30 and 32 m, on the south side of the mast, and one top mounted at 45 m). This mast is positioned on the west side of a V27 turbine. However during this comparison, the rotor of the turbine had been taken down, therefore the eastern wind sector can also be considered as free from major obstacles.

The sector used for the comparison was chosen such as the cup anemometers were outside the wake of the mast. Therefore the Northern sector had to be excluded (see Figure 2). The sector selected was 80 to 120 and 230 to 300 degrees.

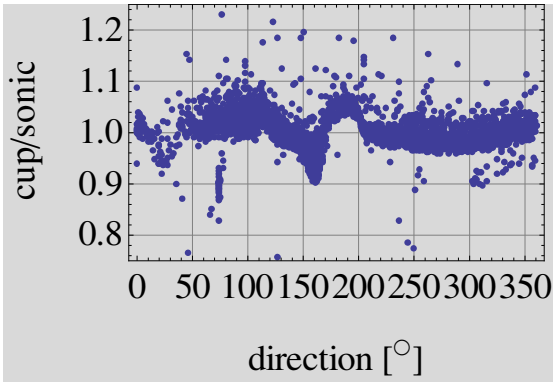

Figure 113 Ratio between the 10 min mean wind speed measured by the cup anemometer (south boom) and the sonic anemometer (north boom) at 32 m vs. the wind direction measure by the vane at 30m. The sector for which the cup anemometer is in the wake of the mast can be detected from this figure.

Figure 114 shows the linear regressions between the 10 min LIDAR wind speed and the corresponding cup anemometer measurements. In these graphs, all data within the selected wind sector with a wind speed above 4 m/s are considered. A Zephir LIDAR cannot measure low wind speed very accurately because of the RIN noise [7]. As a significant amount of outliers were remaining, further filtering had to be applied.

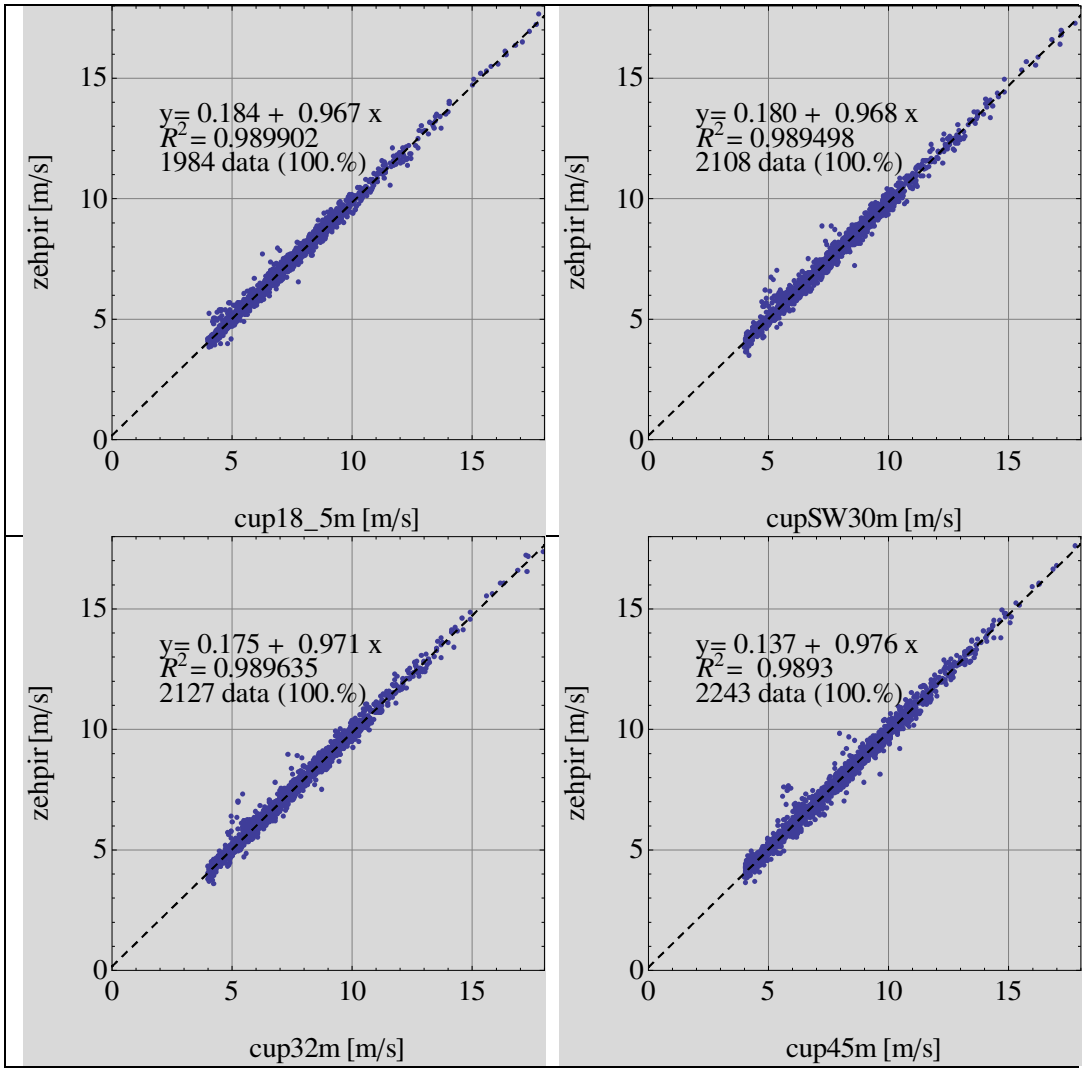

Figure 114 Comparison of the LIDAR (Z2) and the V27 mast cup anemometers for the selected wind sector (80˚-120˚ & 230˚-300˚) and the wind speed above 4 m/s.

Figure 115 shows once more the comparison and linear regressions between LIDAR and cup anemometer wind speed measurements at the same 4 heights. But, here the data were also filtered so that the "turb" parameter was below 0.1. "Turb" is defined as the residual in the cosine fit (so called figure of 8). This parameter gives an indication of the scatter in the figure of 8. A large scatter, that can be due to turbulence within the scanning circle, but also to noise in the measurements, or partial clouds, usually results in a bad fitting and in an error in the wind speed indication. Therefore excluding data for which the 10 minute value of turb exceeds 0.1 is a good compromise between the acceptable data with some turbulence and non-acceptable data.

All the obvious outliers seen in Figure 114 do not appear in Figure 115. The regression at every height presents a high coefficient of determination ($R^2 > 0.991$). However the gain shows a general underestimation by about 2% of the LIDAR wind speed indication compared to the cup anemometer. It was concluded that the LIDAR was functioning fairly well, but a comparison to the Nordtank mast would be necessary to complete the measurement campaign.

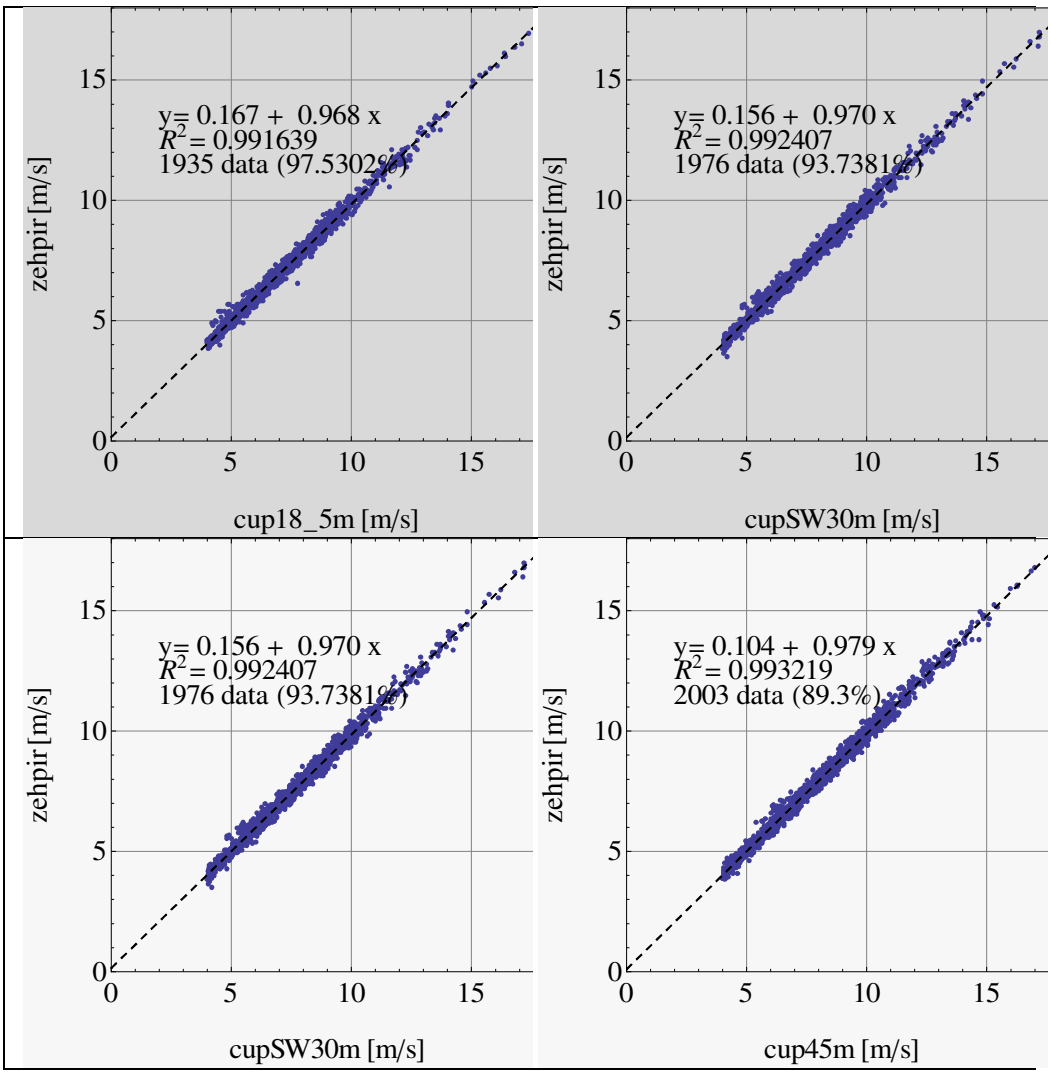

Figure 115 Comparison of the LIDAR (Z2) and the V27 mast cup anemometers for the selected wind sector (80˚-120˚ & 230˚-300˚) and the wind speed above 4 m/s with an additional flitering: "turb"<0.1

8.3 Comparison of the profiles

After the LIDAR verification, Z2 was installed right next to the shore at about 200m from the mast in the direction 283˚, therefore aligned with the mast and the turbine, the aim being to compare the wind speed profile at the shore and at the mast, to observe how it develops with the change of roughness and the slight slope until it arrives to the turbine.

In Figure 116 below, the mast profiles were binned according the wind speed at 36m, and for each wind speed bin are displayed the average wind speed profile measured by the mast, the average wind speed profile measured by the LIDAR at the shore and the average wind speed profile measured by the LIDAR a between the mast and the shore.

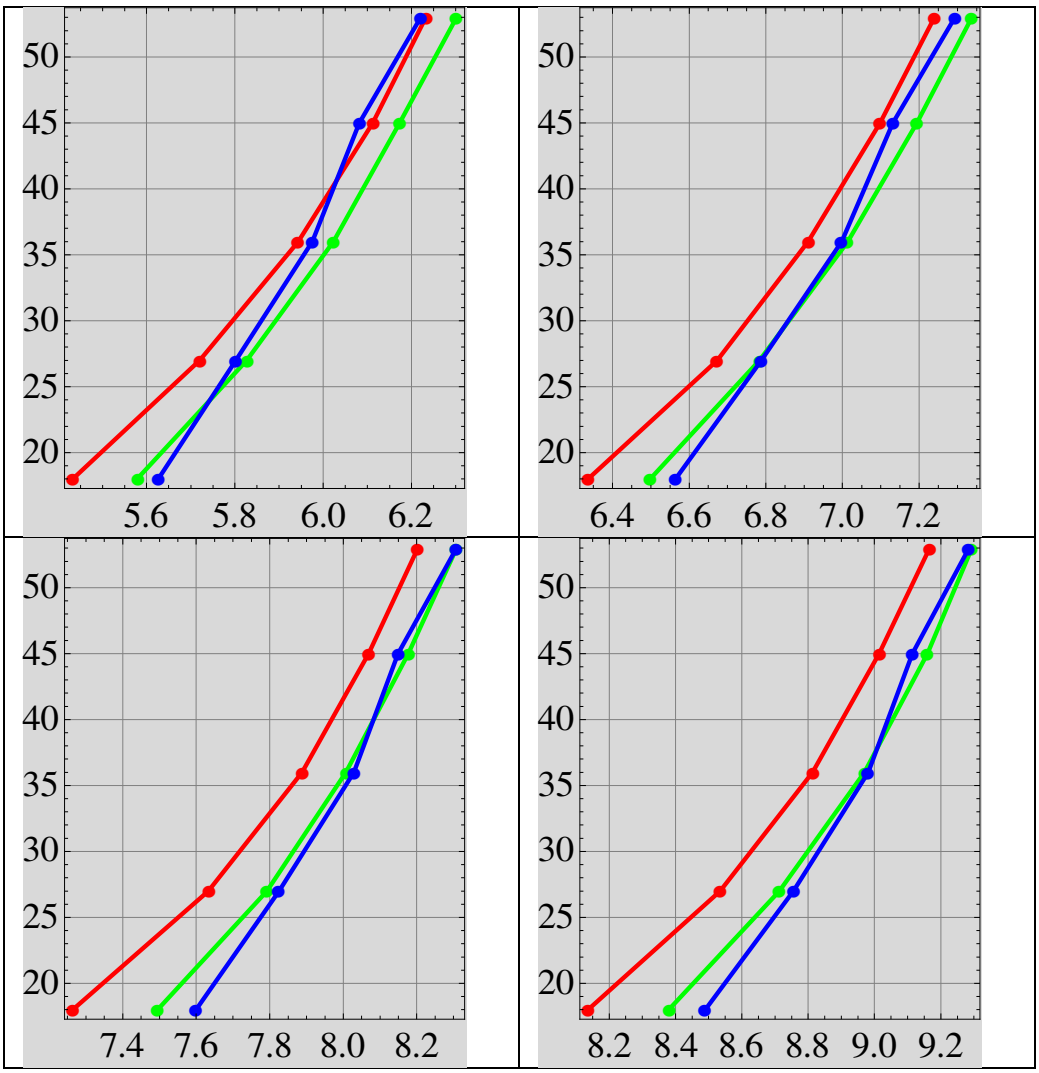

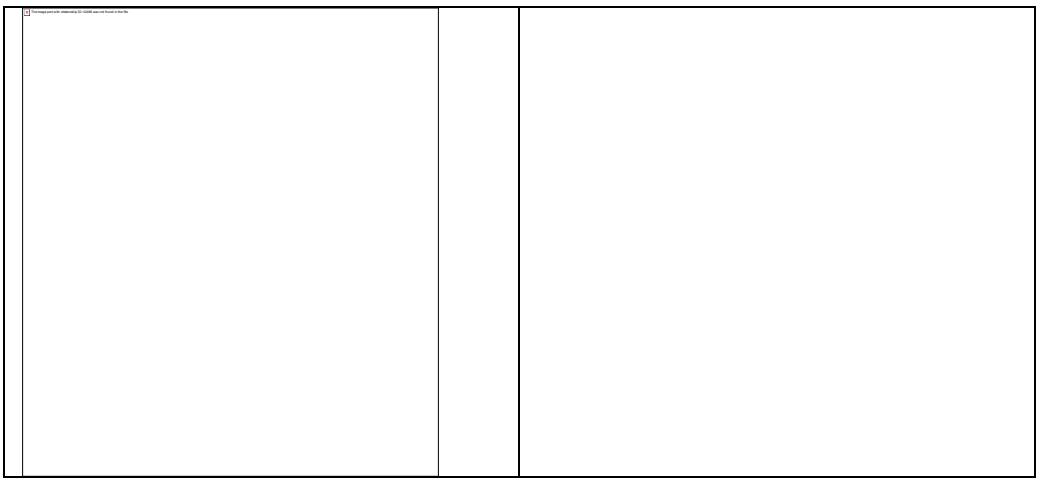

Figure 116 Average wind speed profiles measured by the mast (blue), the LIDAR Z2 at the shore (red) and the LIDAR Z107 at the kink between the change of slope between Z2 and the mast (green), for 6 different wind speed bins

The profiles measured by Z107 are, on average, closer to the mast profiles than those from Z2; which is expected since LIDAR Z107 is only 60m from the mast whereas Z2 is at about 200m. A large difference is observed between the shore LIDAR profile and the mast profile. The question raising then is whether this difference is due to a physical phenomena influencing the profile at the shore or to a bias inherent to the LIDAR measurements. It was therefore necessary to make a proper comparison of the LIDAR with Nordtank mast. In October, LIDAR Z2 was installed next to the mast (about 30 m to the west in order to be close enough but to avoid the disturbance that could be caused by the guy wires on the LIDAR measurements). The comparison of the 10 min mean wind speeds of the LIDAR Z2 and the cup anemometers at the various heights are displayed in the figure below.

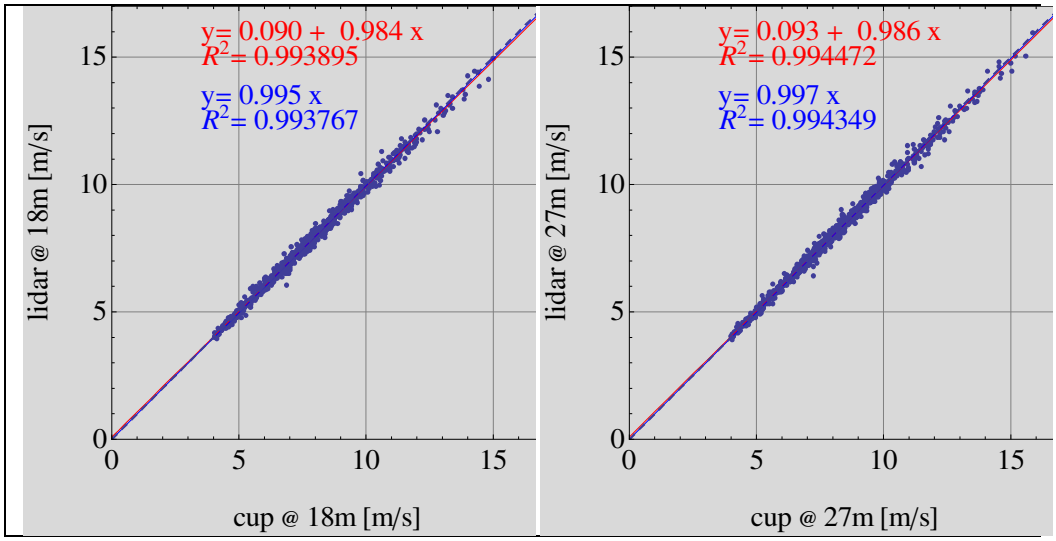

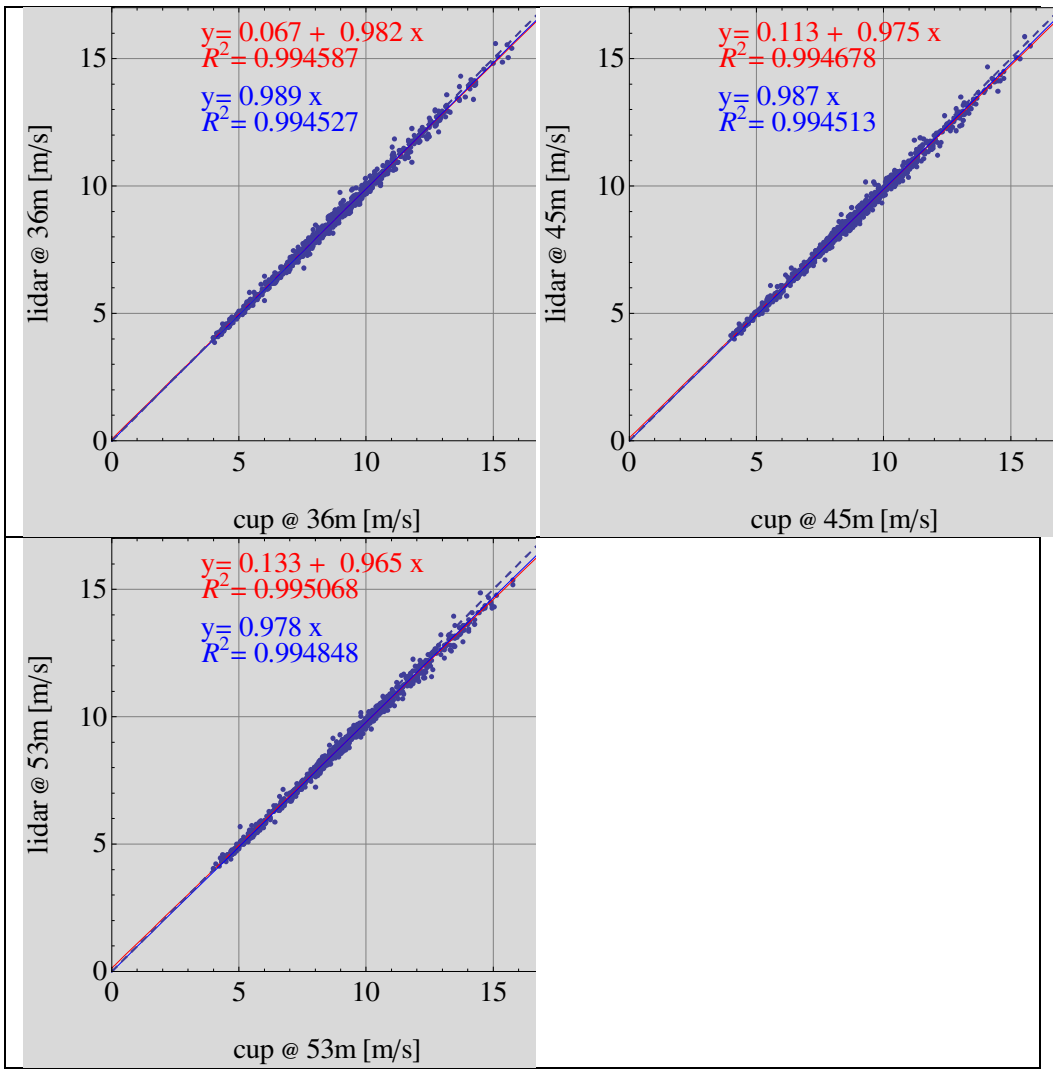

Figure 117 Comparison of the LIDAR Z2 at 30 m form the mast and the Nordtank mast cup anemometers (between) for the selected wind sector 250°-310° and the wind speed above 4 m/s and "turb"<0.1

We have used the inverse regression to correct the offset inherent to the LIDAR measurement. The regression applied to all LIDAR measurements are shown in Figure 118, and the profiles obtained with corrected wind speed for Z2 are shown in Figure 119.

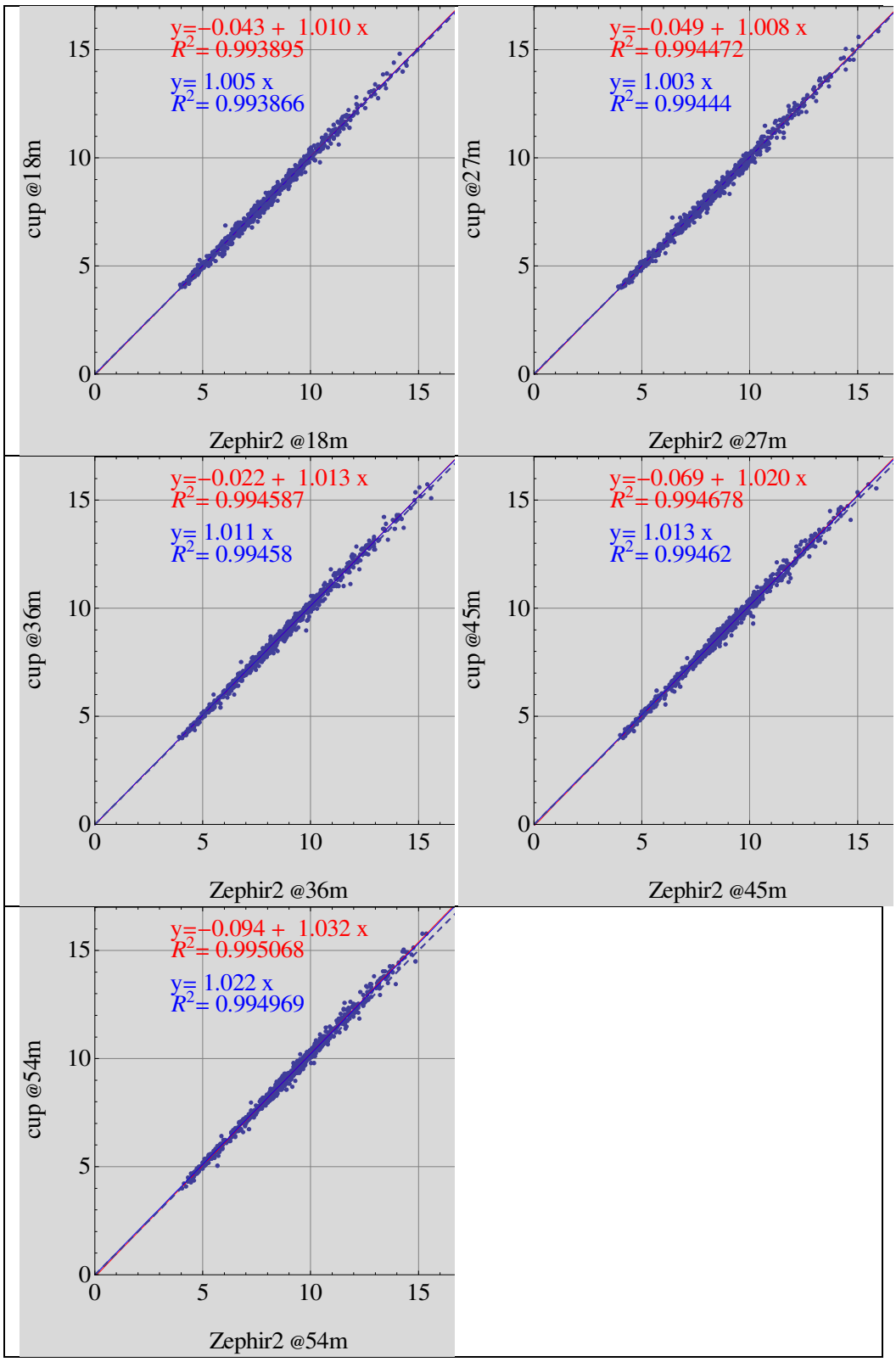

Figure 118 Regression between the LIDAR Z2 at 30 m from the mast and the Nordtank mast cup anemometers (between) for the selected wind sector 250°-310° and the wind speed above 4 m/s and "turb"<0.1

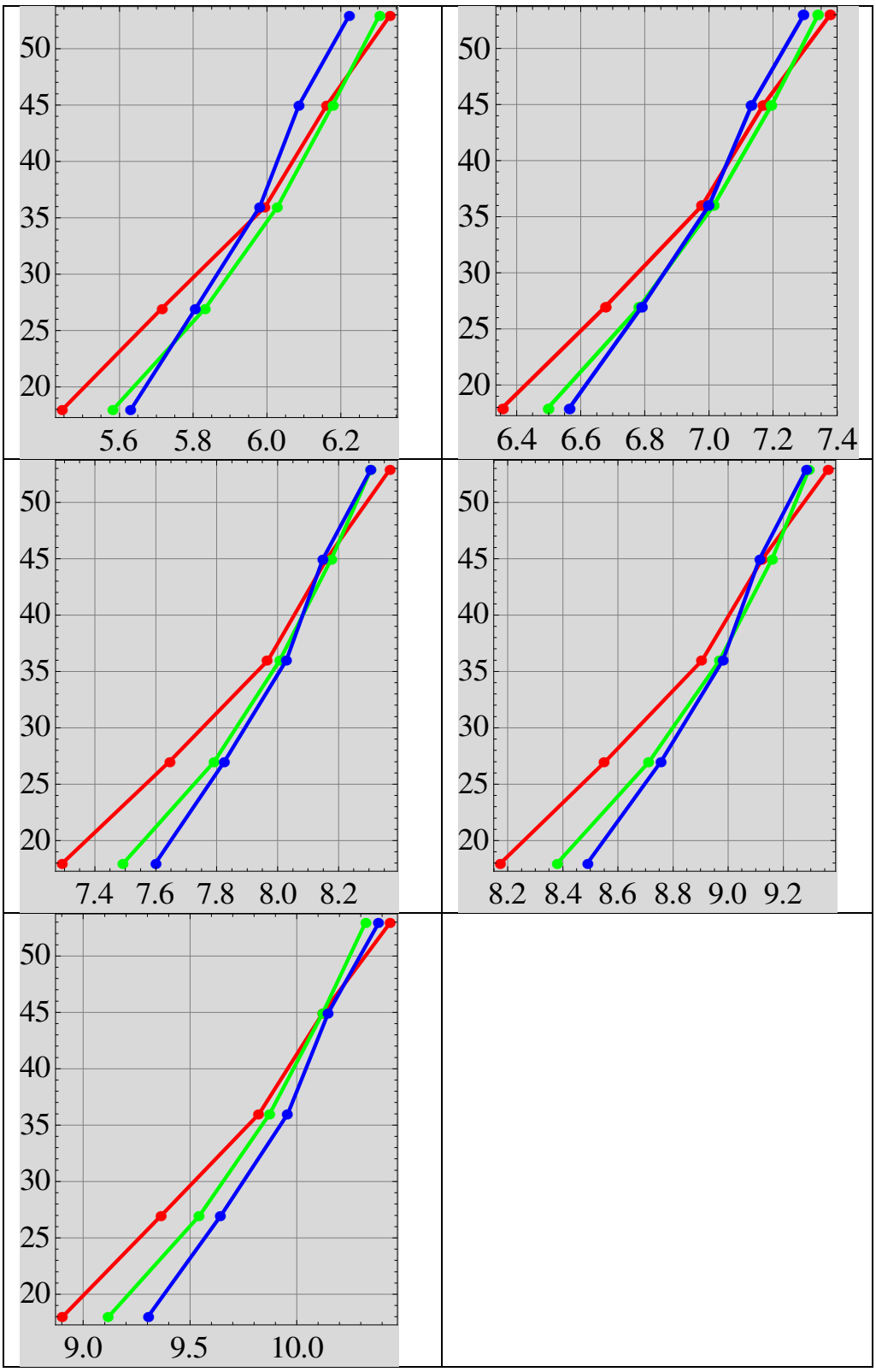

Figure 119 Average wind speed profiles measured by the mast (blue), the LIDAR Z107 at the kink between the change of slope between Z2 and the mast (green) and the LIDAR Z2 at the shore corrected according to the regression given in Figure 6 (red), for 5 different wind speed bins: from 6 to 10 m/s. A narrow wind sector was selected: 260˚-300˚.

The profiles from Z2 are then closer to those from Z107, especially above 36m. Below 36m, the wind speed is higher at the kink (Z107) and at the shore (Z2) and higher at the mast than at the kink. This is in accordance with a WAsP calculation presented in [8.2] which shows that the wind speed at the shore is expected to be about 5% lower than at the mast location. It would be due to a speed up effect due to the slope. As Z107 is closer to the mast the wind speed is also closer to that measured at the mast.

From 36m and above, the influence of the ground does influence the wind speed and the profiles at the 3 locations are rather similar; except for the 2 lower wind speed bins, the wind speed measured by the mast is lower than that measured by both LIDARS.

8.4 References

8.1. Hill C and Harris M, Remote Sensing (UpWind WP6) QinetiQ LIDAR Measurement Report, UpWind WP6 deliverable 6.1.1.

8.2. Paulsen US, The impact of the induced velocity in the near flow field of a horizontal axis wind turbine, Risø-M-2835.

8.5 Conclusions

The present analysis is by far neither completed nor exhaustive; factors shown in this report are influencing the effectiveness of the wind turbine to extract power. The nature of these factors is determined by the natural wind and the conditions defining it(surrounding area), and the wind turbine which utilizes the apparent wind. The amounts of data allow showing some specifics of the wind for this particular site in over the time span for the present study. The survey (barely also) indicates that other factors observed other places can impose other effects not necessarily matching with present observations, which makes the observation time too short. However, there is a major amount of existing data which should be used to compare the inflow and the rotor filtered output in terms of power. Such method should be based on analysis of the Reynolds stresses by means of met mast instrumentation and by looking into the output of LIDARS describing turbulent flow features.
As a contribution to inflow measurements, it is believed that the use of 5-hole pitot systems would benefit the analysis of improving power performance and the role of turbulence and wind characterisation.

In the report results from power measurements as well as structural signals have been shown.
It has been shown on the basis of the driving force, that the potential of extracting kinetic energy with a rotor is large (and unexploited) at wind conditions just above cut-in.
It is also suggested to conduct further analysis of the wind variability over a rotor disk via the flapwise bending moment signal, and with a variable that express the relative flapwise load ($\sigma My/\langle My \rangle$) over power ($\sigma P/\langle P \rangle$) efficiency factor.

The comparison of measurements and simulations shows, that the current model (structural and aerodynamic) agrees to a first order of comparison, but does not match the measured effects of natural turbulence experienced over the rotor disk in comparison with calculations, in particular with Figure 60.

A similar analysis to what was done for a MMW wind turbine was achieved here for a 500kW turbine. It shows that shear can also significantly influence the power curve measurement of a small wind turbine. Furthermore, the results coincide with those obtained for the MMW wind turbine. Using the equivalent wind speed in the power curve reduce the differences between the power curves obtained for different types of wind profiles, therefore decrease the scatter in the measured power curve.

8.6 Outlook

As mentioned more details are expected to show up by re-analysing the data and extending the data over a longer period to cover seasonal effects. Particular models containing a description as in [3.6] for a numerical approach of the wind characterisation would encourage comparing turbulence effects on a particular rotor, and the effects of rotor dynamics (rotor filter function).

On the measurement application point of view it would be very valuable from a research point of view to conduct inflow measurements with a 5-hole pitot system and one or two LIDAR systems simultaneously.

9 Acknowledgement

The Danish Ministry of Climate, Energy and Buildings, in particular the Danish Energy Agency are acknowledged for financial support. Also the Danish wind industry companies VESTAS Wind Systems A/S and Siemens Wind Power are appreciated for contributions and work throughout the project.

Many thanks to colleagues at DTU Wind Energy contributing with support and with discussions on the topics of IMPER, and technicians in the Test and Measurement program (TEM) for setting up the instrumentation- in particular Per Hansen for fixing the two LIDARS every time it was needed.

Andreas Waage Lopdrup Borgen, Engineering intern is greatly appreciated for his help in preparing plots and last revisions from the post processed data and simulations results.

Appendixes

Analysis results from post processing

In this annex, plots from the post processing of data as explained in 5.4 is presented. Each sensor is visualized by means of statistics representation in terms of wind speed at hub height, and typical time series with power spectra. Each sensor is represented with reference to the signal list.

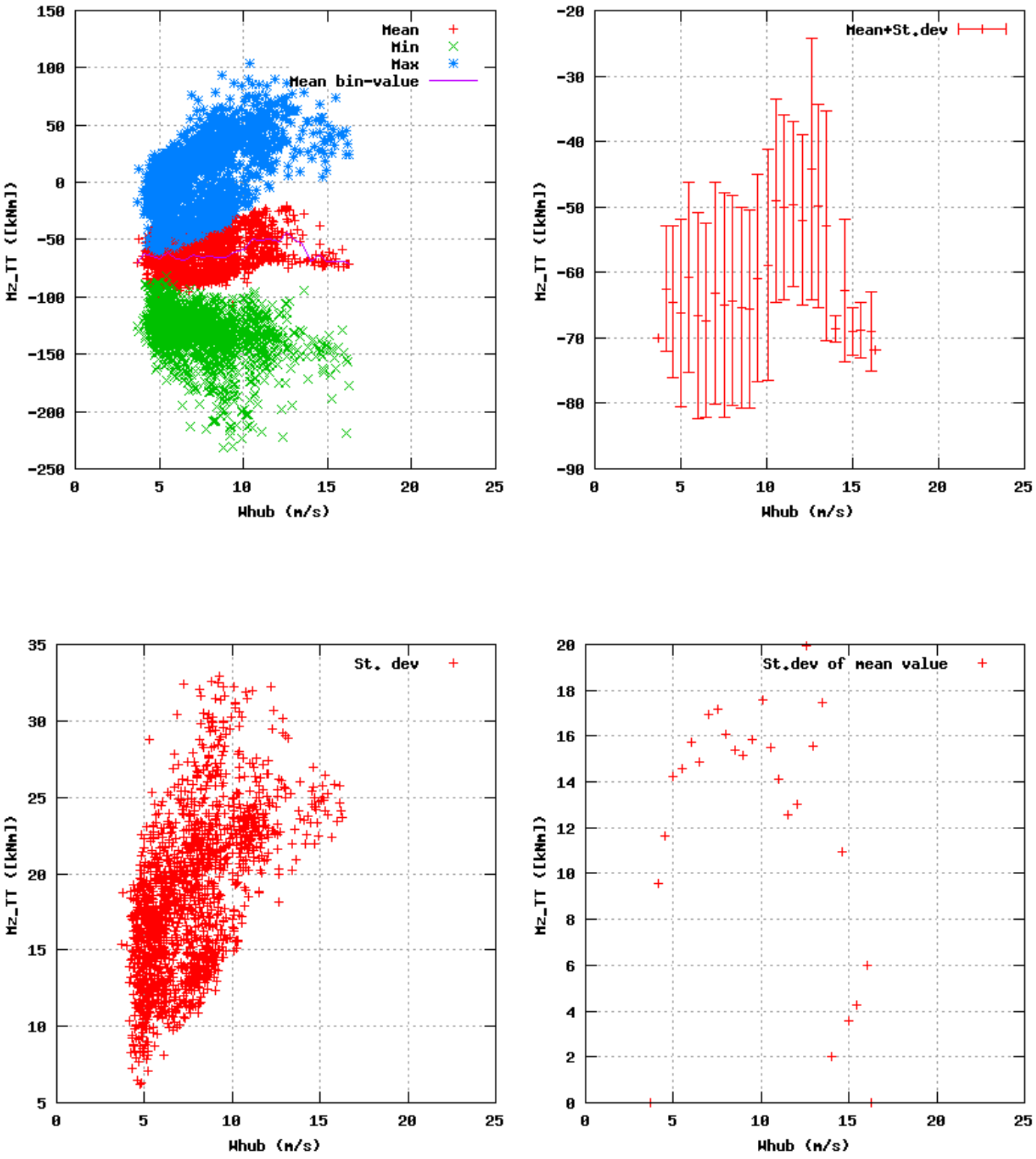

Figure 1a, Sensor 3: Tower torsion top Mz_TT versus wind speed
Input files: ntk500res.dat, stat_3.dat

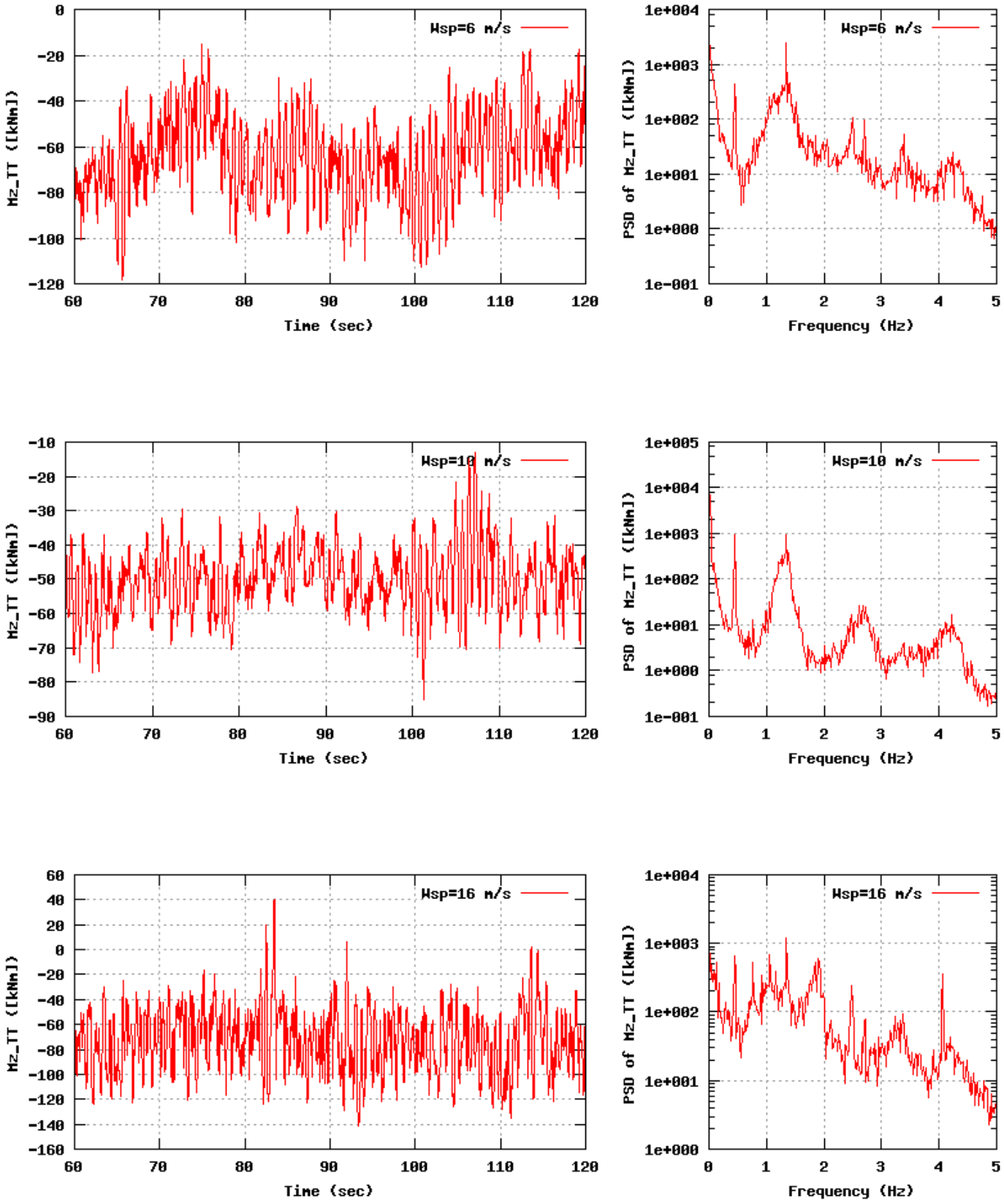

Figure 1b, Sensor 3: Tower torsion top Mz_TT versus time and frequency
Input files: m06.asc, m10.asc, m16.asc, m06.psd, m10.psd and m16.psd

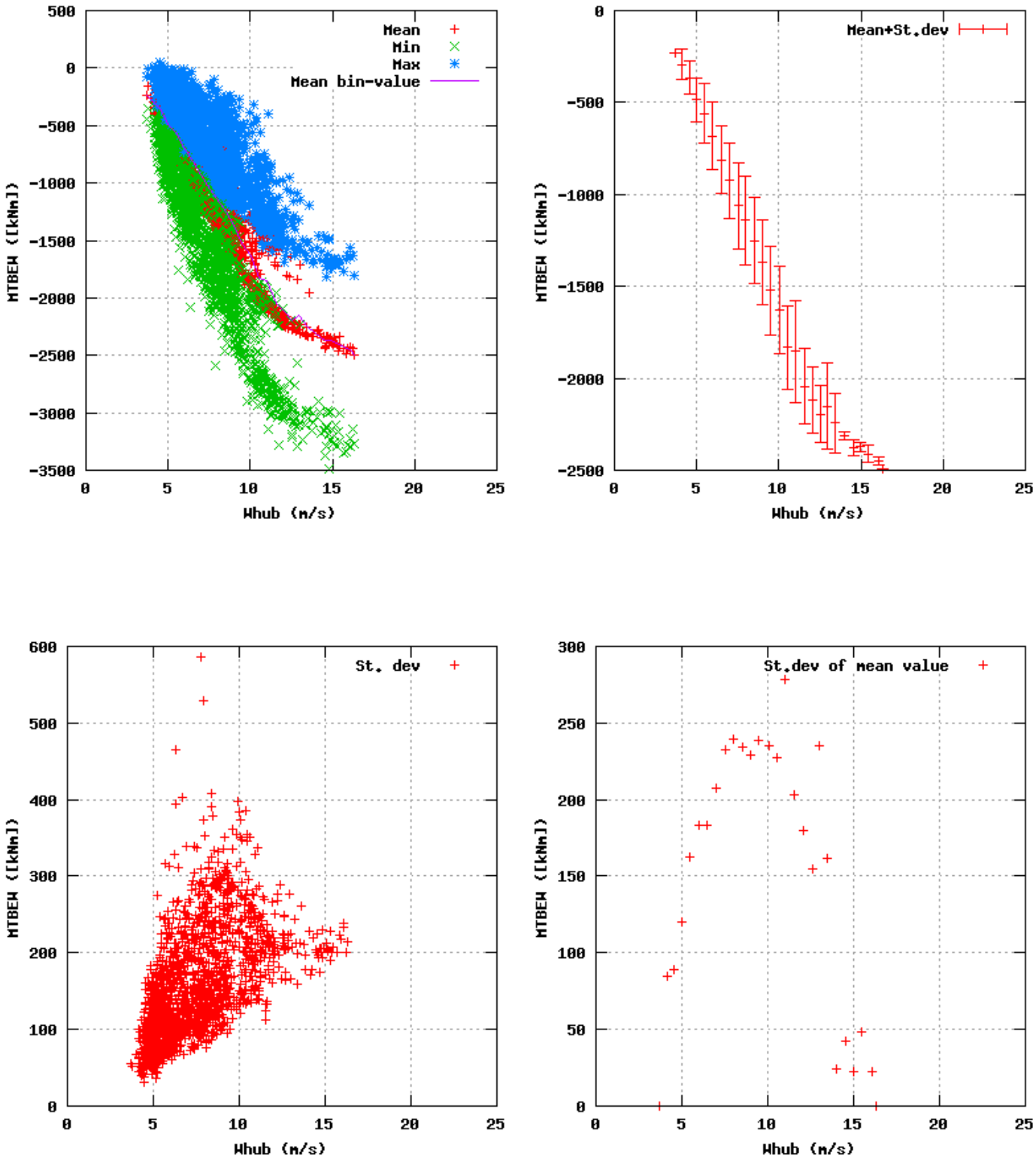

Figure 2a, Sensor 7: Tower bending bottom MTBEW versus wind speed
Input files: ntk500res.dat, stat_7.dat

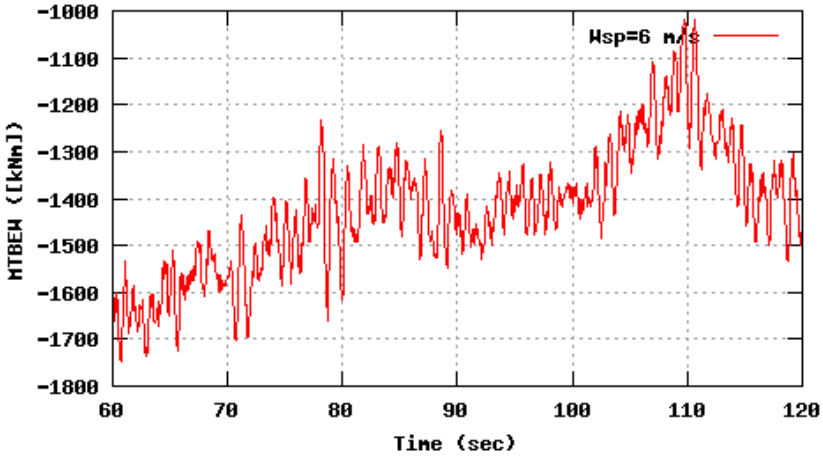

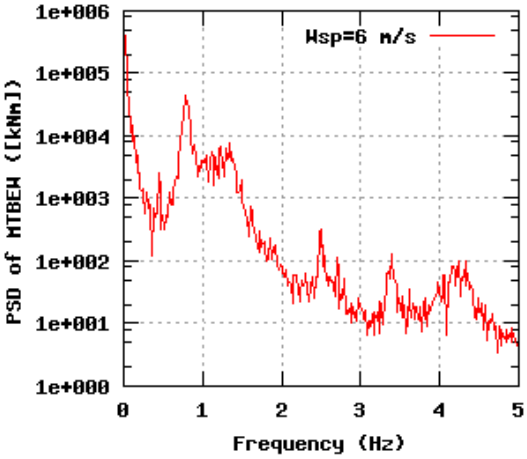

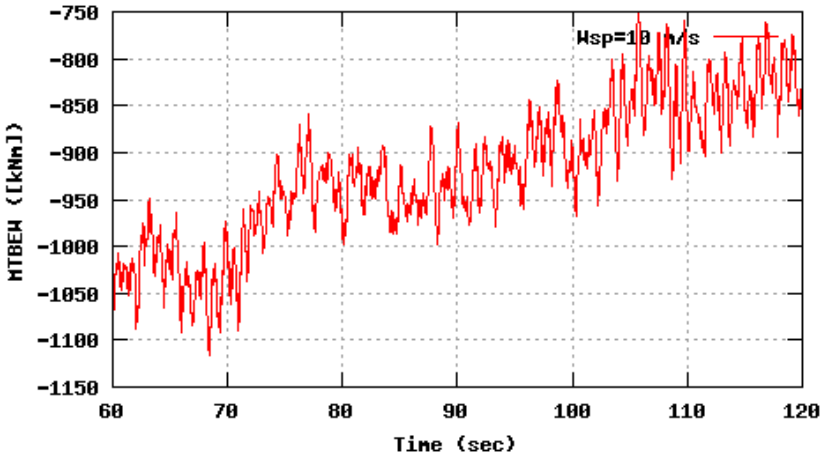

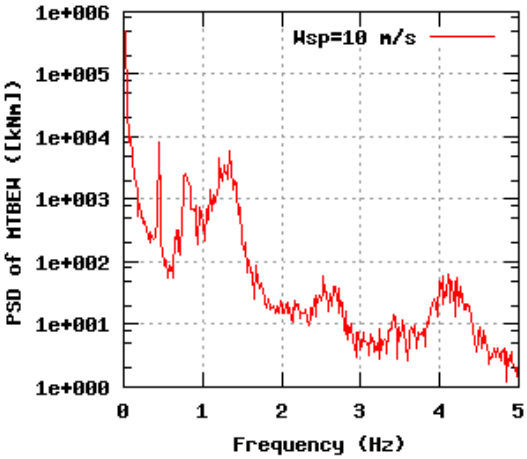

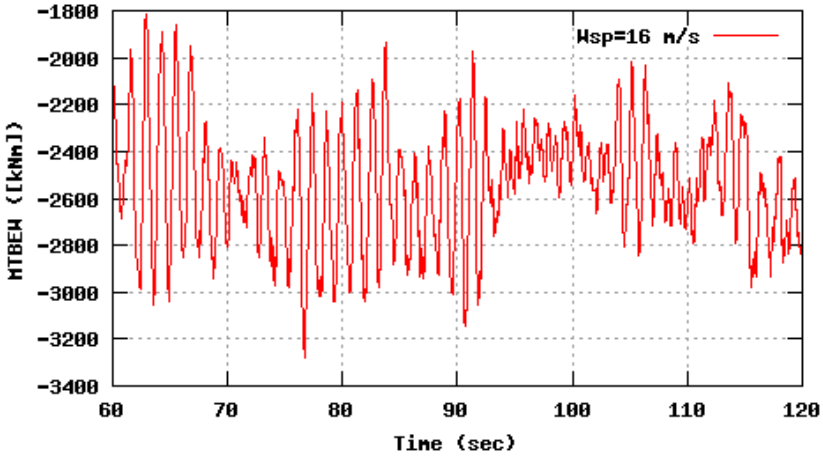

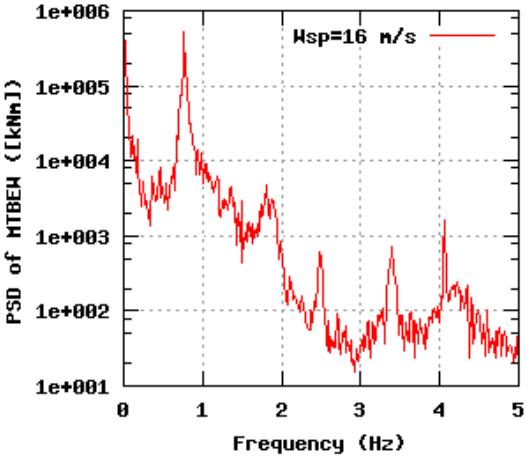

Figure 2b, Sensor 7: Tower bending bottom MTBEW versus time and frequency
Input files: m06.asc, m10.asc, m16.asc, m06.psd, m10.psd and m16.psd

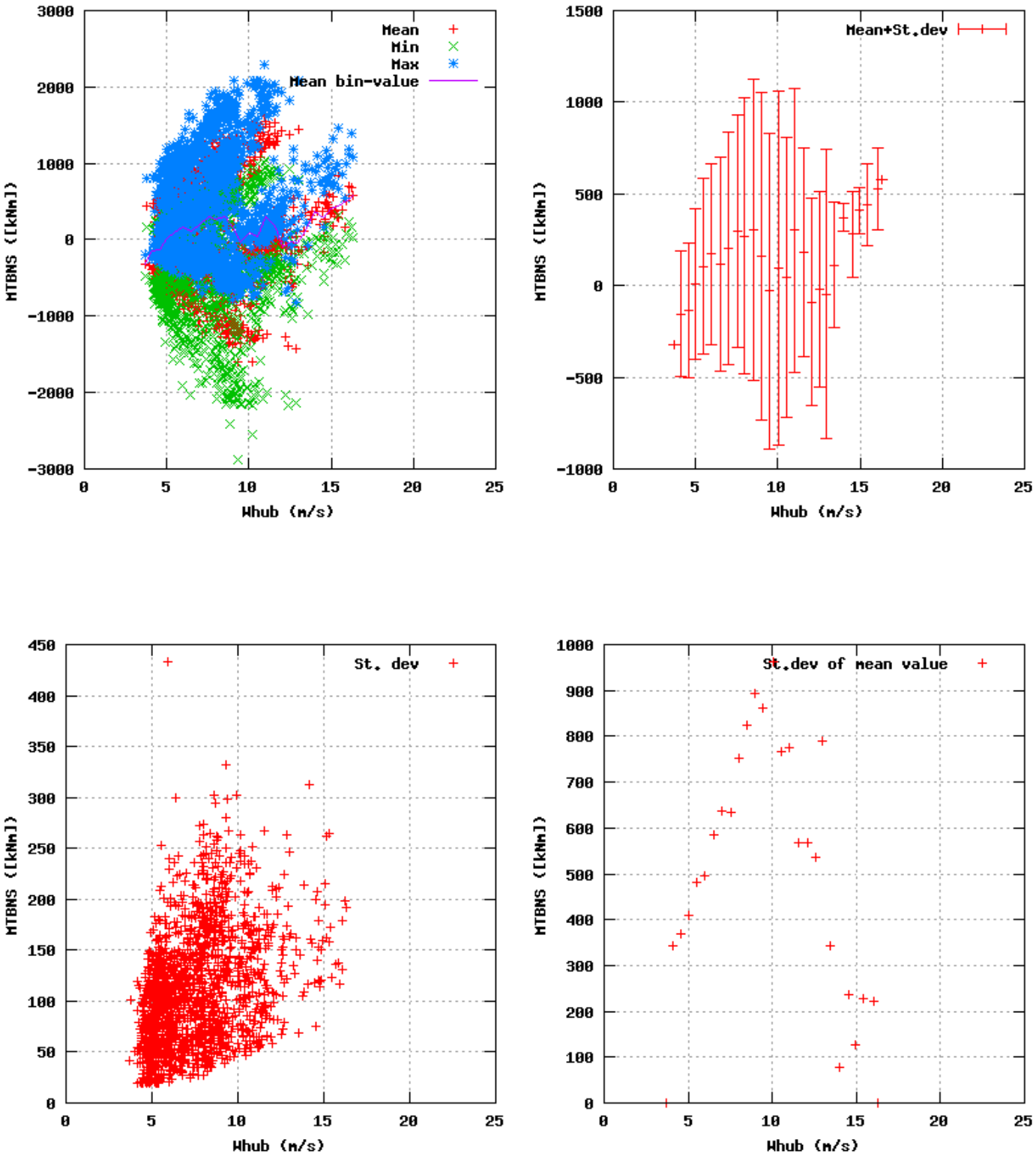

Figure 3a, Sensor 11: Tower bending bottom MTBNS versus wind speed
Input files: ntk500res.dat, stat_11.dat

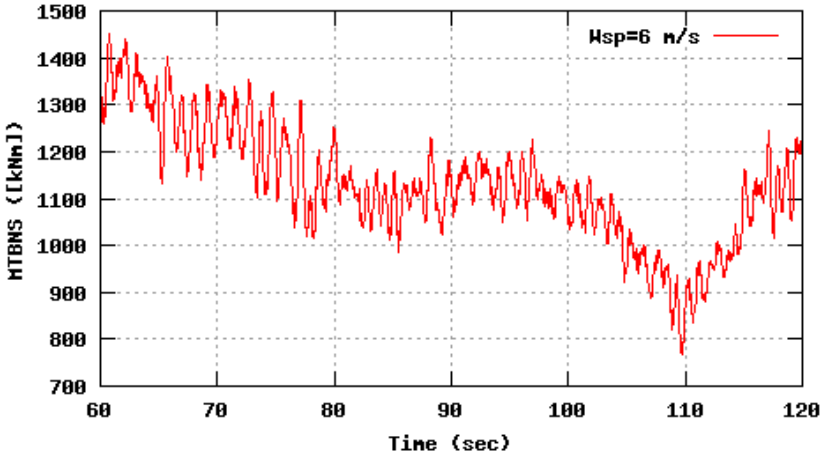

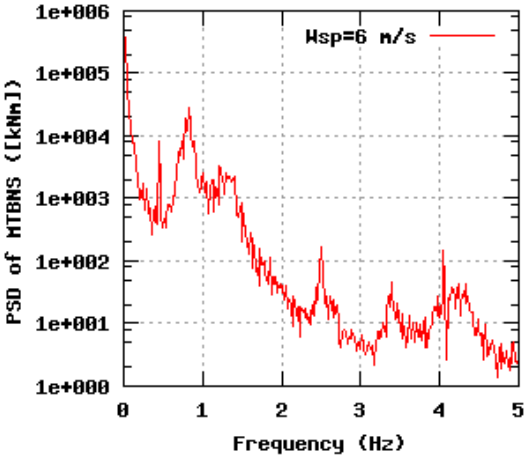

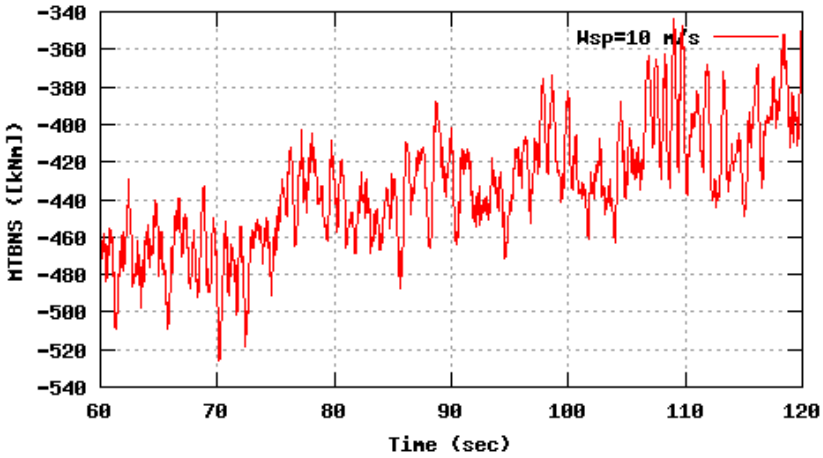

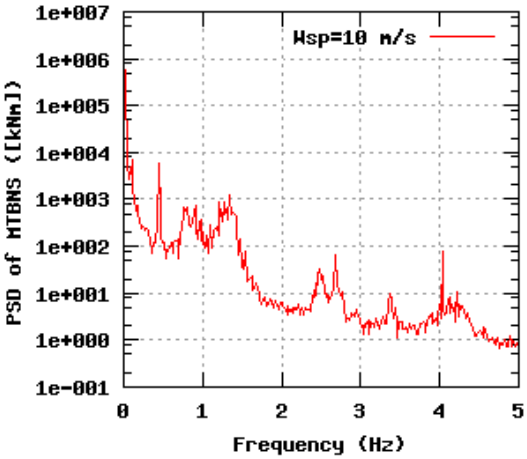

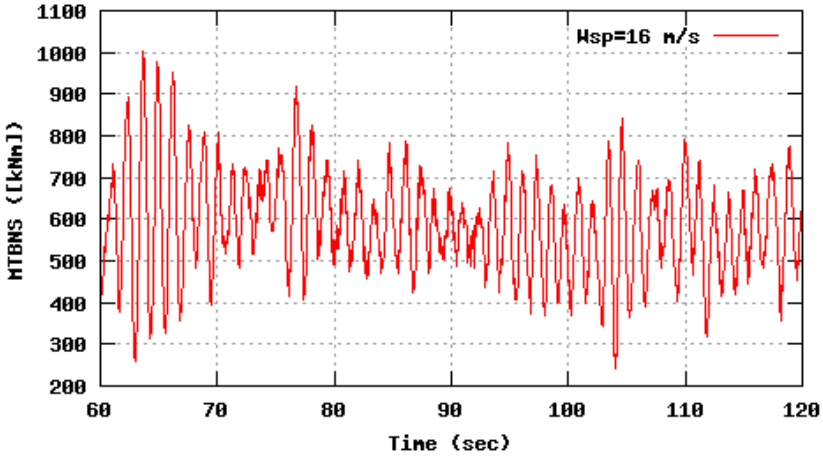

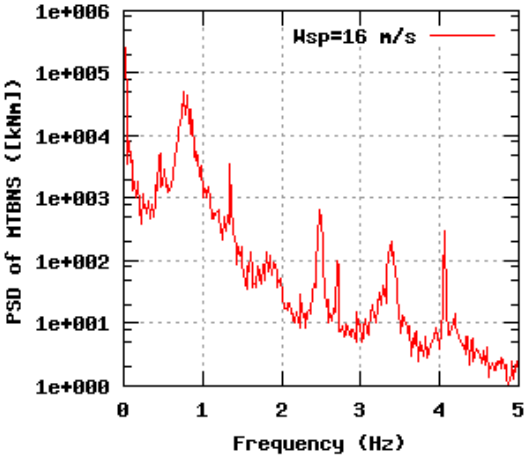

Figure 3b, Sensor 11: Tower bending bottom MTBNS versus time and frequency
Input files: m06.asc, m10.asc, m16.asc, m06.psd, m10.psd and m16.psd

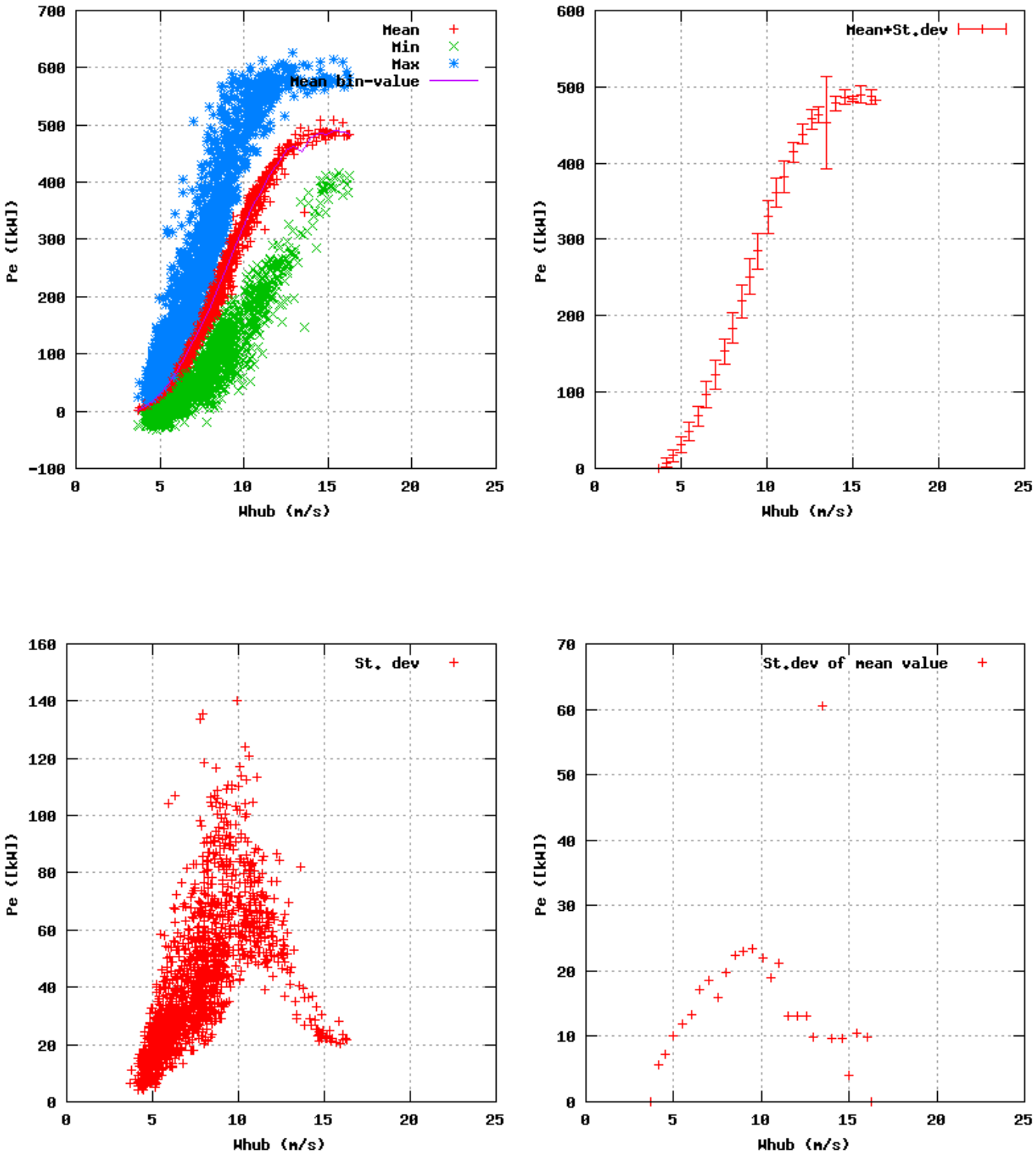

Figure 4a, Sensor 15: Electrical net power Pe versus wind speed
Input files: ntk500res.dat, stat_15.dat

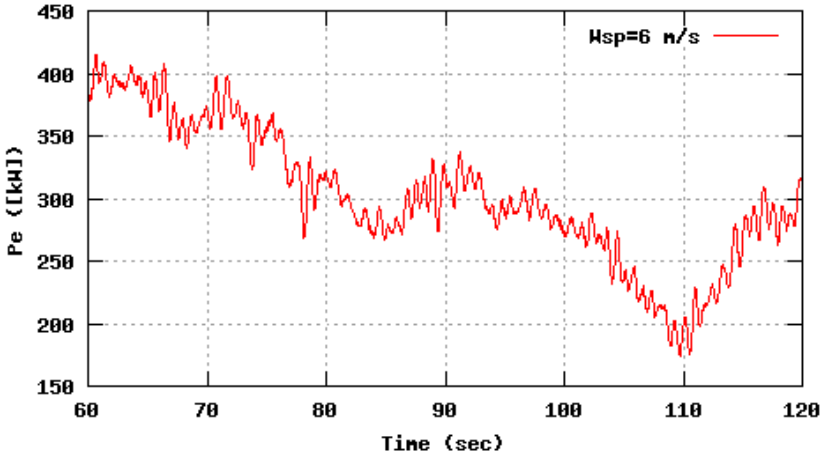

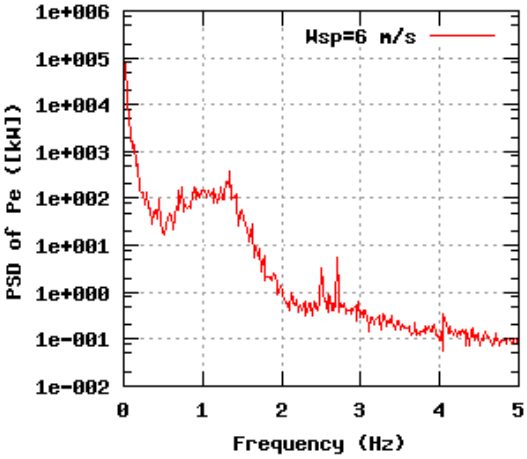

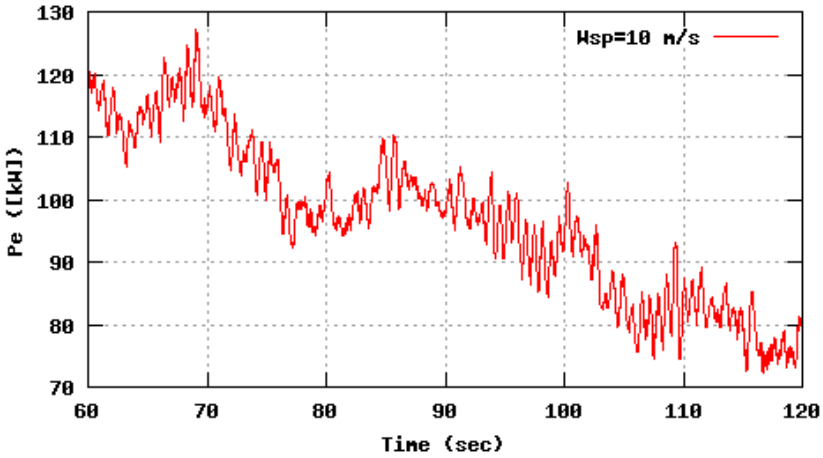

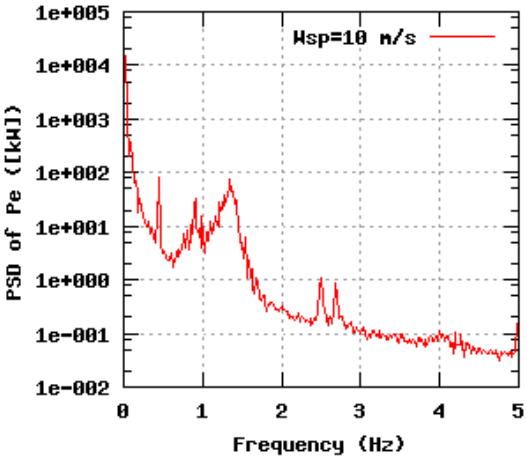

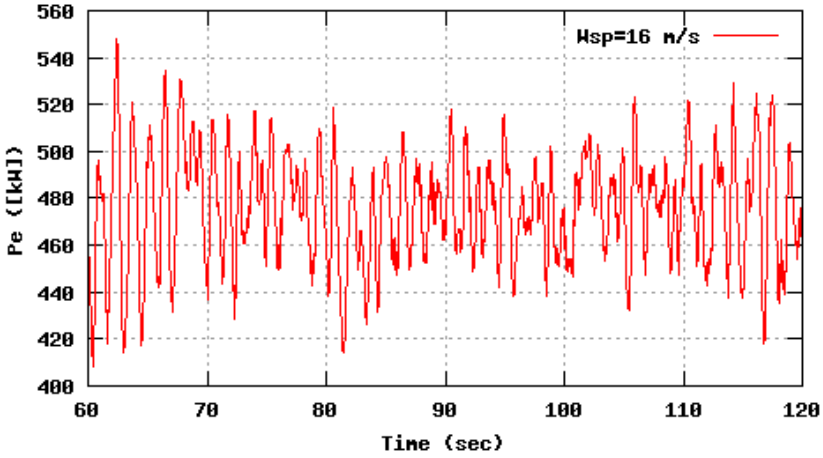

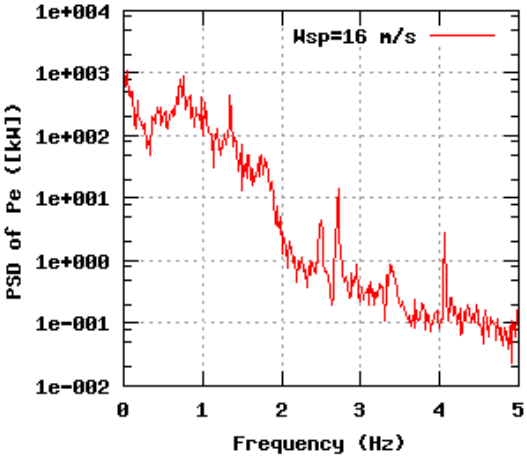

Figure 4b, Sensor 15: Electrical net power Pe versus time and frequency
Input files: m06.asc, m10.asc, m16.asc, m06.psd, m10.psd and m16.psd

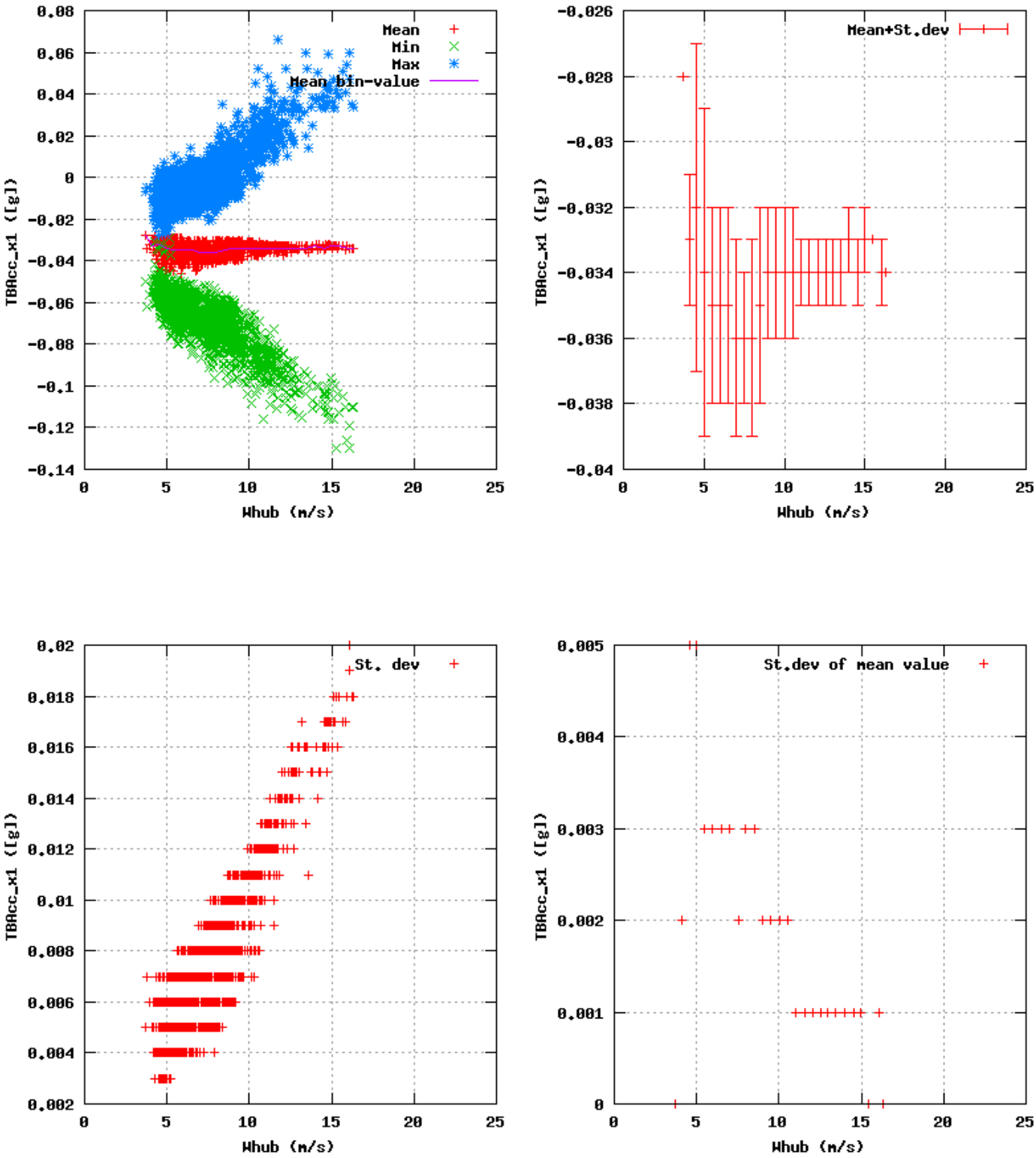

Figure 5a, Sensor 19: Tower accelleration 140 cm from top flange versus wind speed
Input files: ntk500res.dat, stat_19.dat

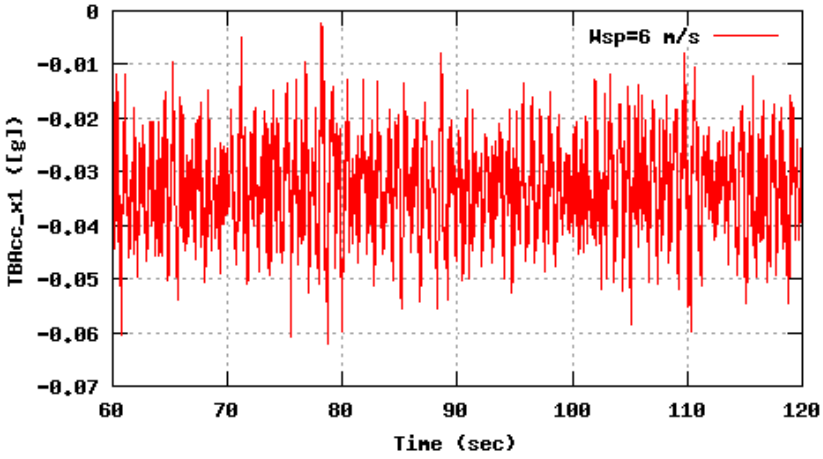

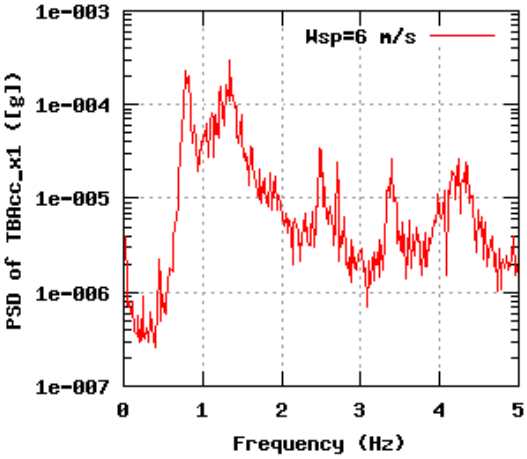

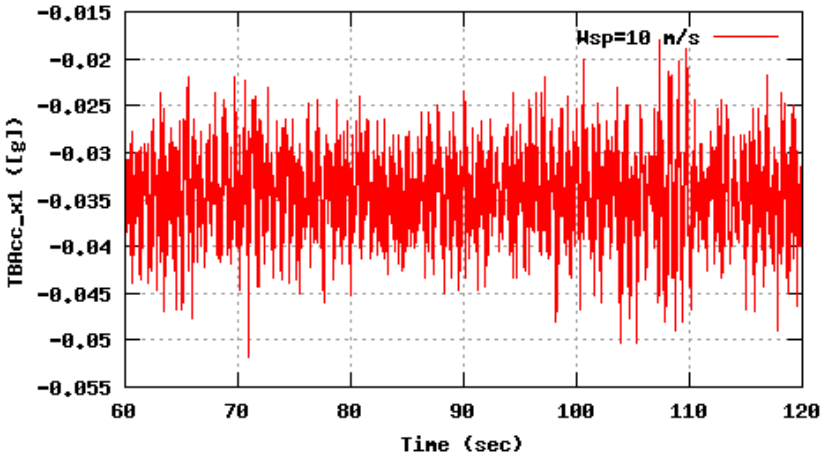

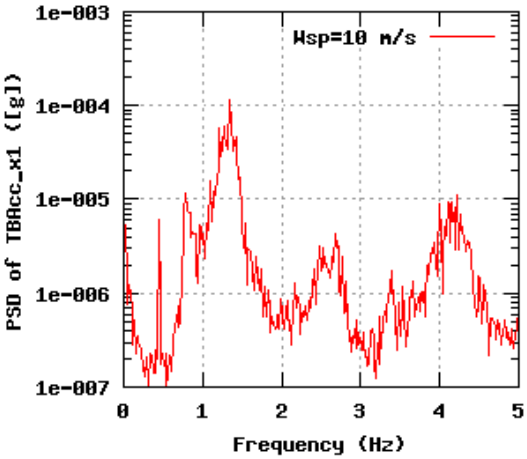

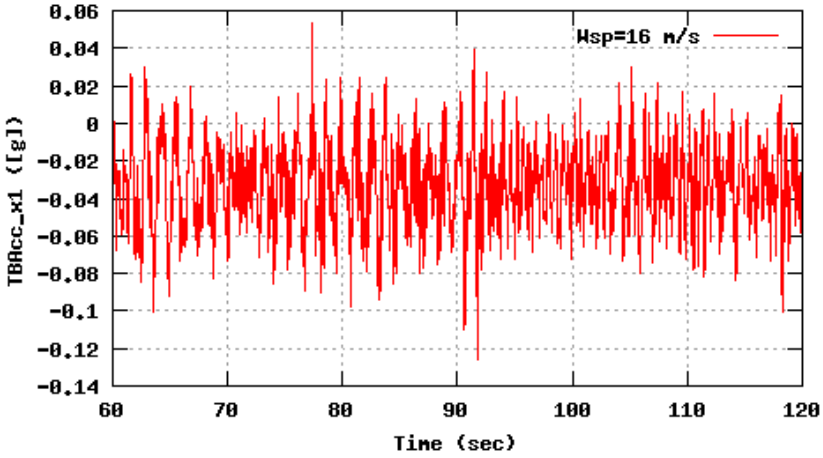

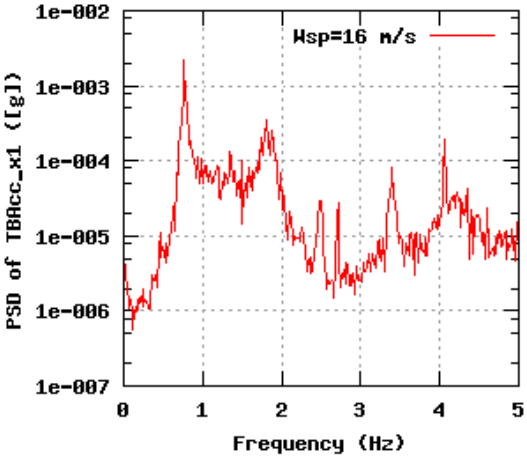

Figure 5b, Sensor 19: Tower accelleration 140 cm from top flange versus time and frequency
Input files: m06.asc, m10.asc, m16.asc, m06.psd, m10.psd and m16.psd

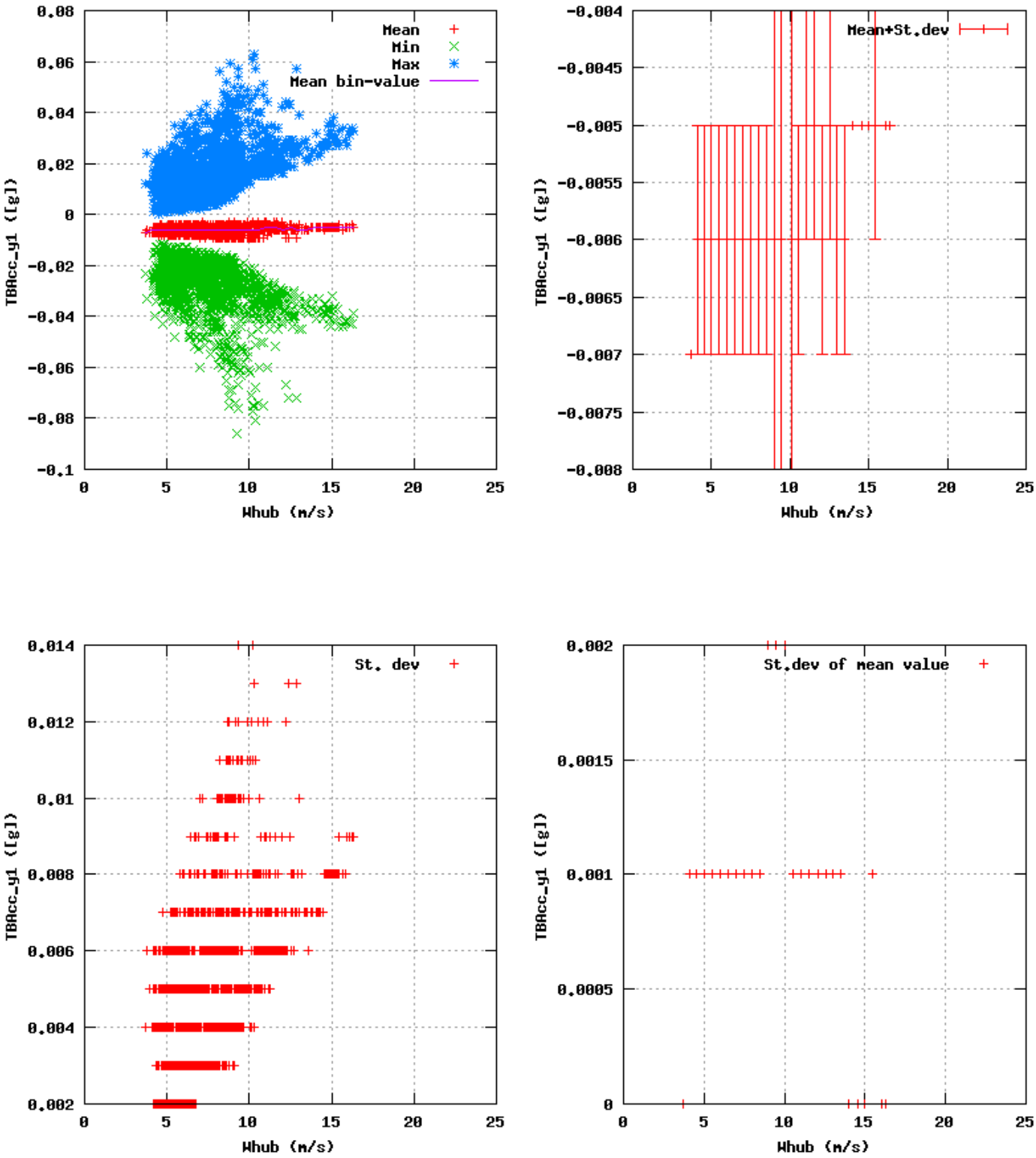

Figure 6a, Sensor 23: Tower accelleration 140 cm from top flange versus wind speed
Input files: ntk500res.dat, stat_23.dat

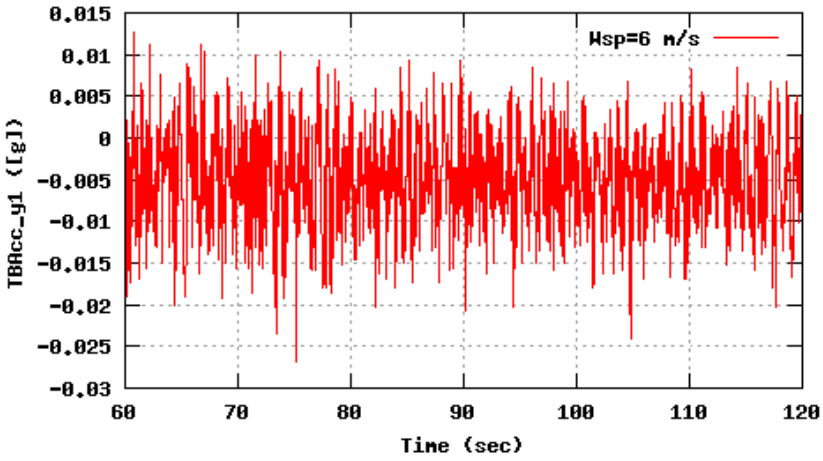

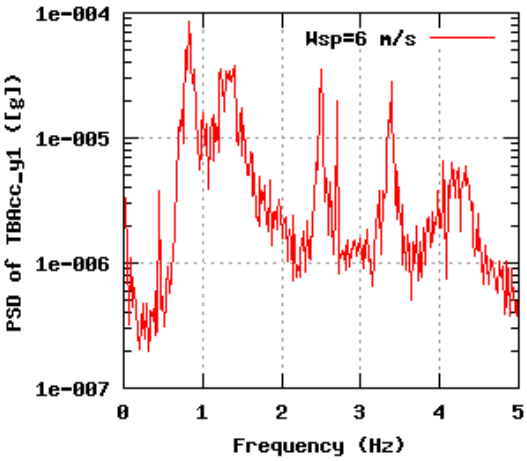

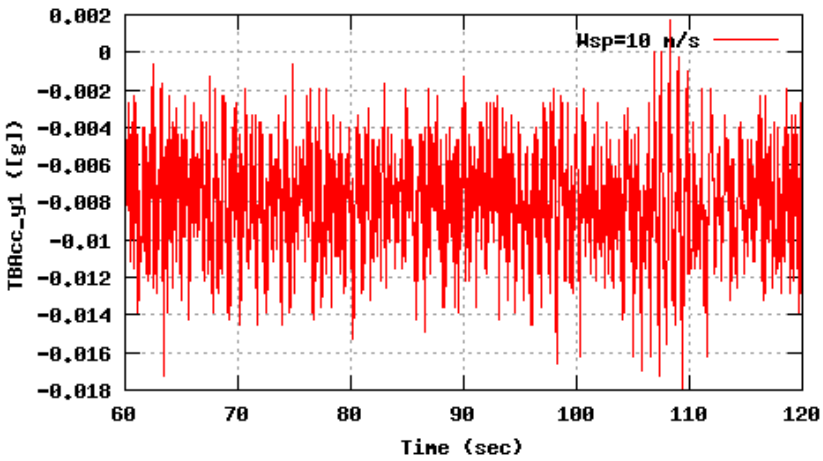

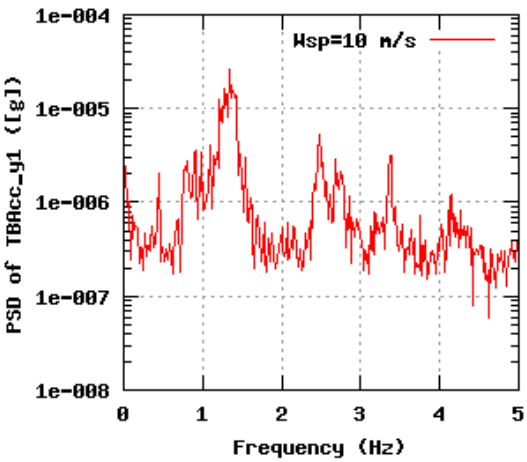

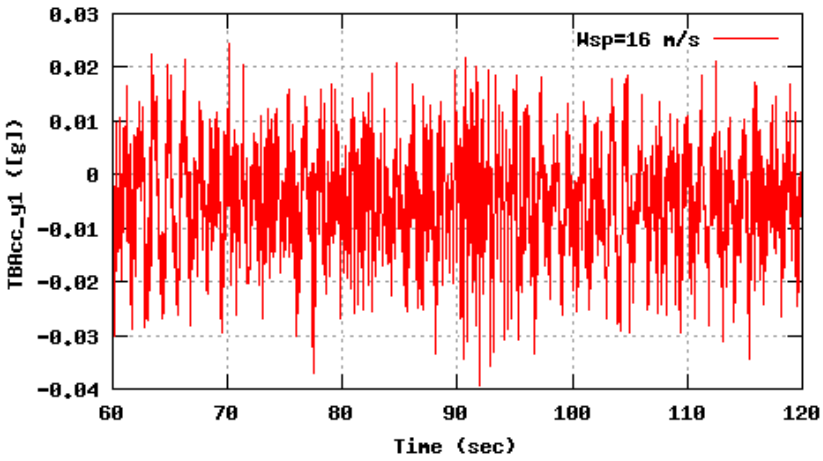

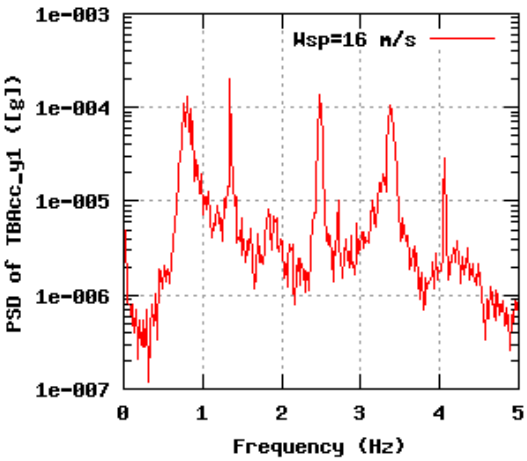

Figure 6b, Sensor 23: Tower accelleration 140 cm from top flange versus time and frequency
Input files: m06.asc, m10.asc, m16.asc, m06.psd, m10.psd and m16.psd

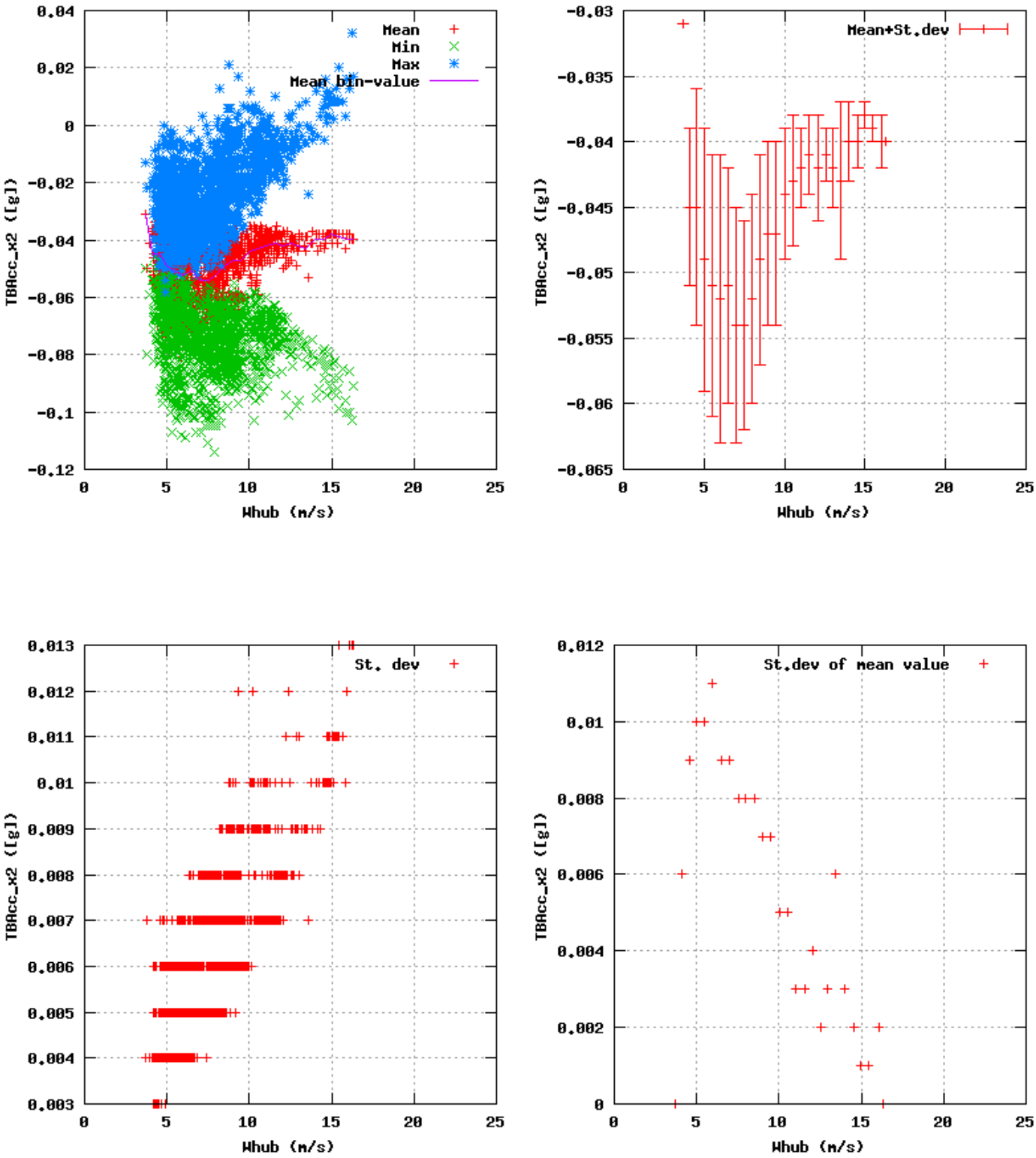

Figure 7a, Sensor 27: Tower accelleration 80 cm from flange and 1st repos versus wind speed
Input files: ntk500res.dat, stat_27.dat

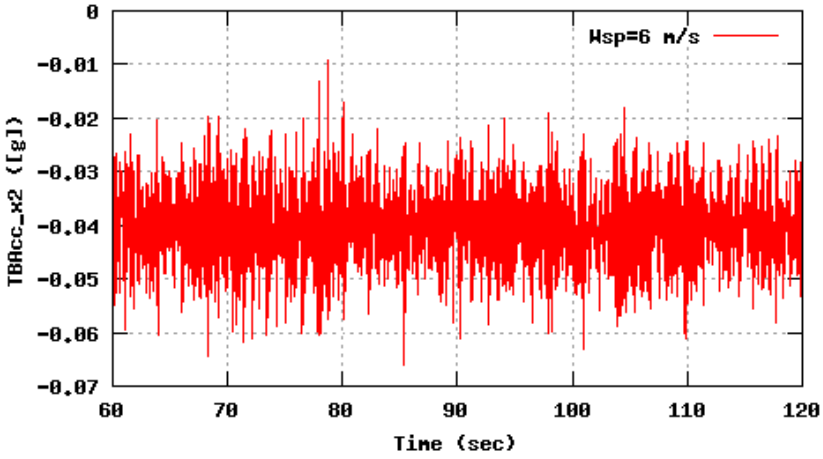

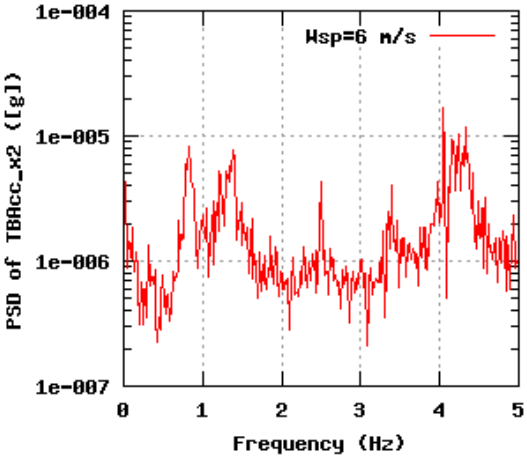

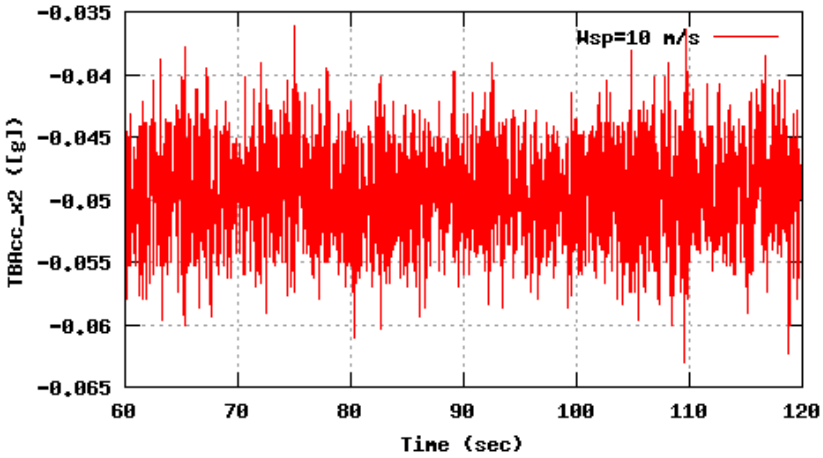

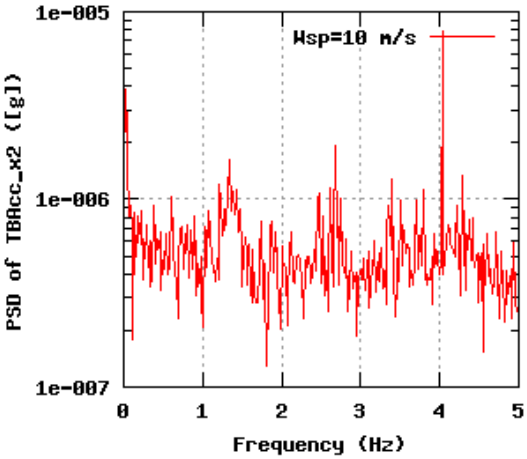

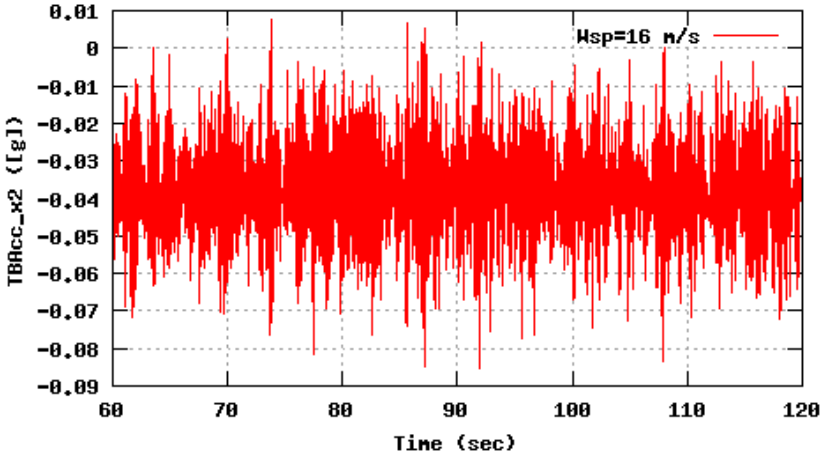

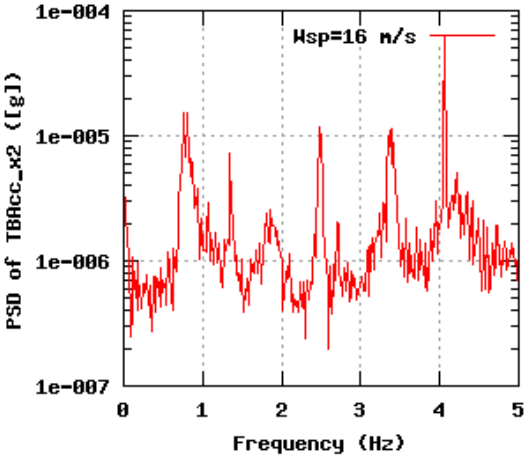

Figure 7b, Sensor 27: Tower accelleration 80 cm from flange and 1st repos versus time and frequency
Input files: m06.asc, m10.asc, m16.asc, m06.psd, m10.psd and m16.psd

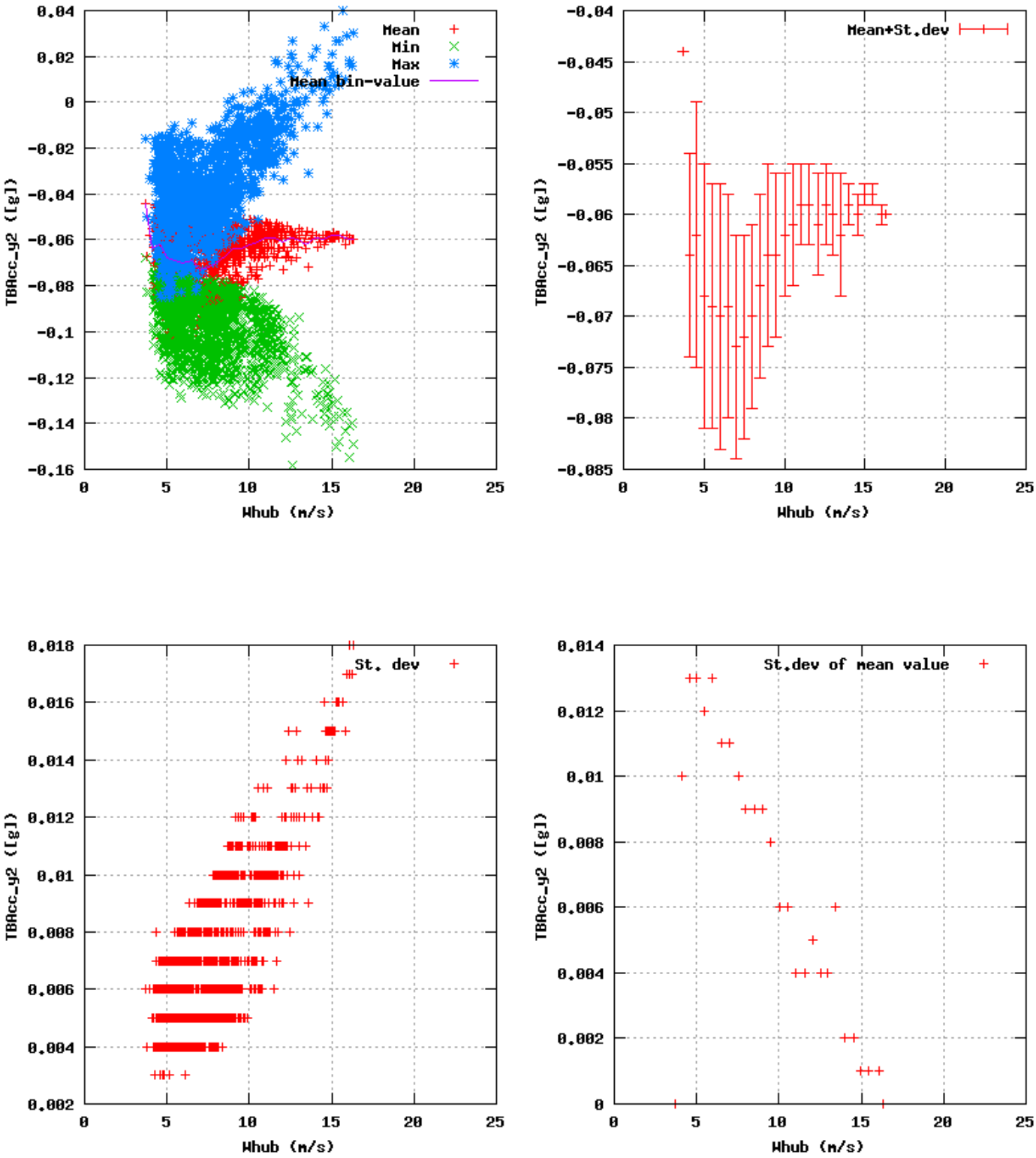

Figure 8a, Sensor 31: Tower accelleration 80 cm from flange and 1st repos versus wind speed
Input files: ntk500res.dat, stat_31.dat

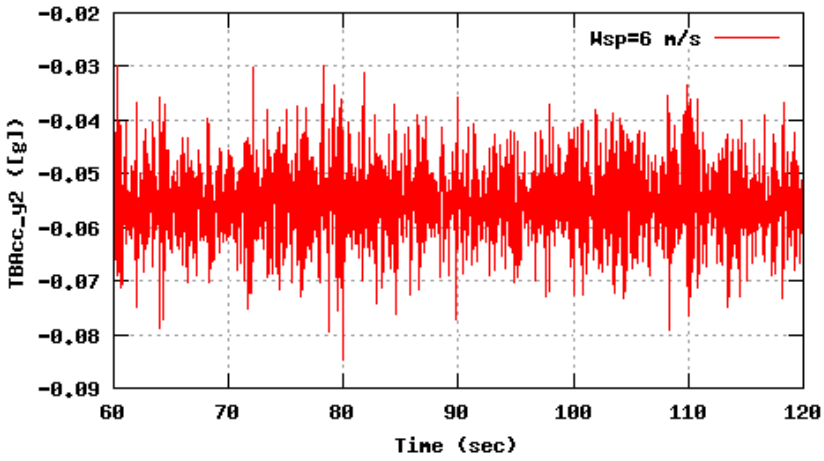

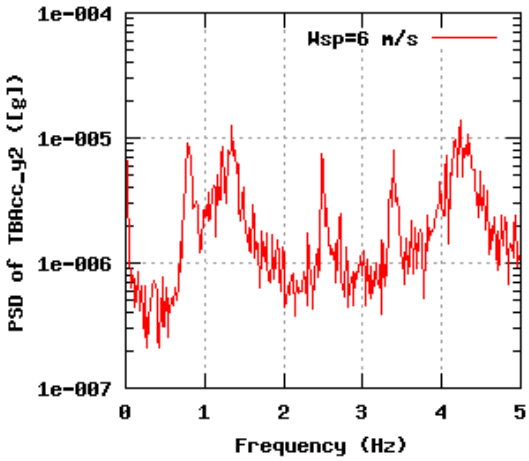

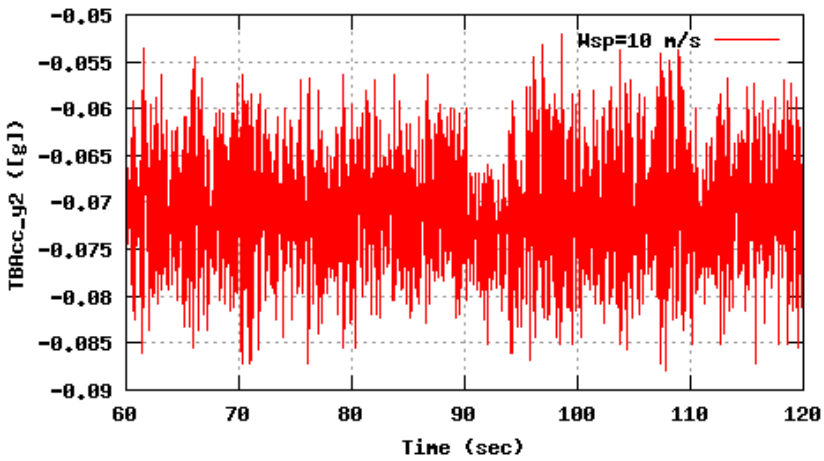

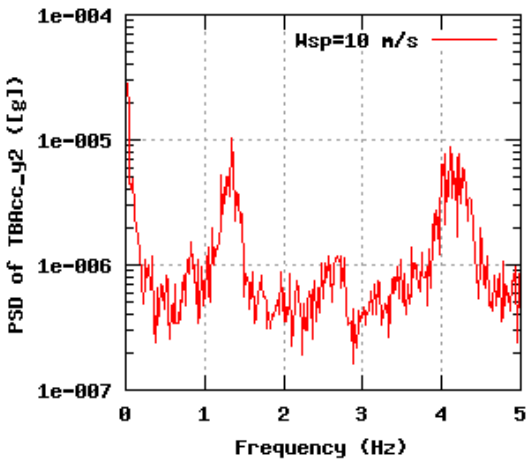

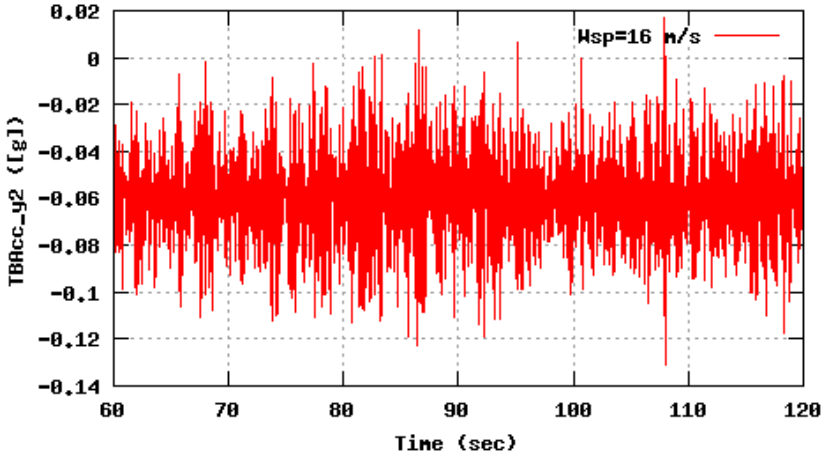

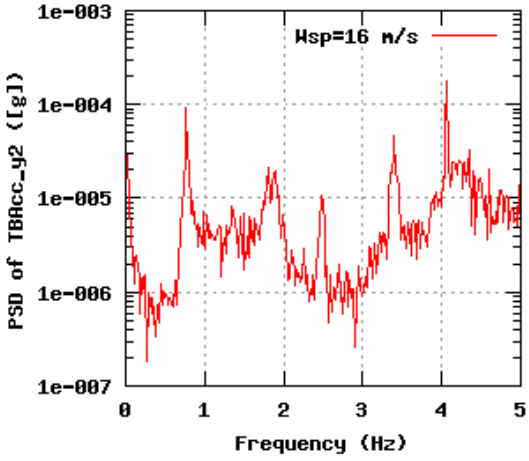

Figure 8b, Sensor 31: Tower accelleration 80 cm from flange and 1st repos versus time and frequency
Input files: m06.asc, m10.asc, m16.asc, m06.psd, m10.psd and m16.psd

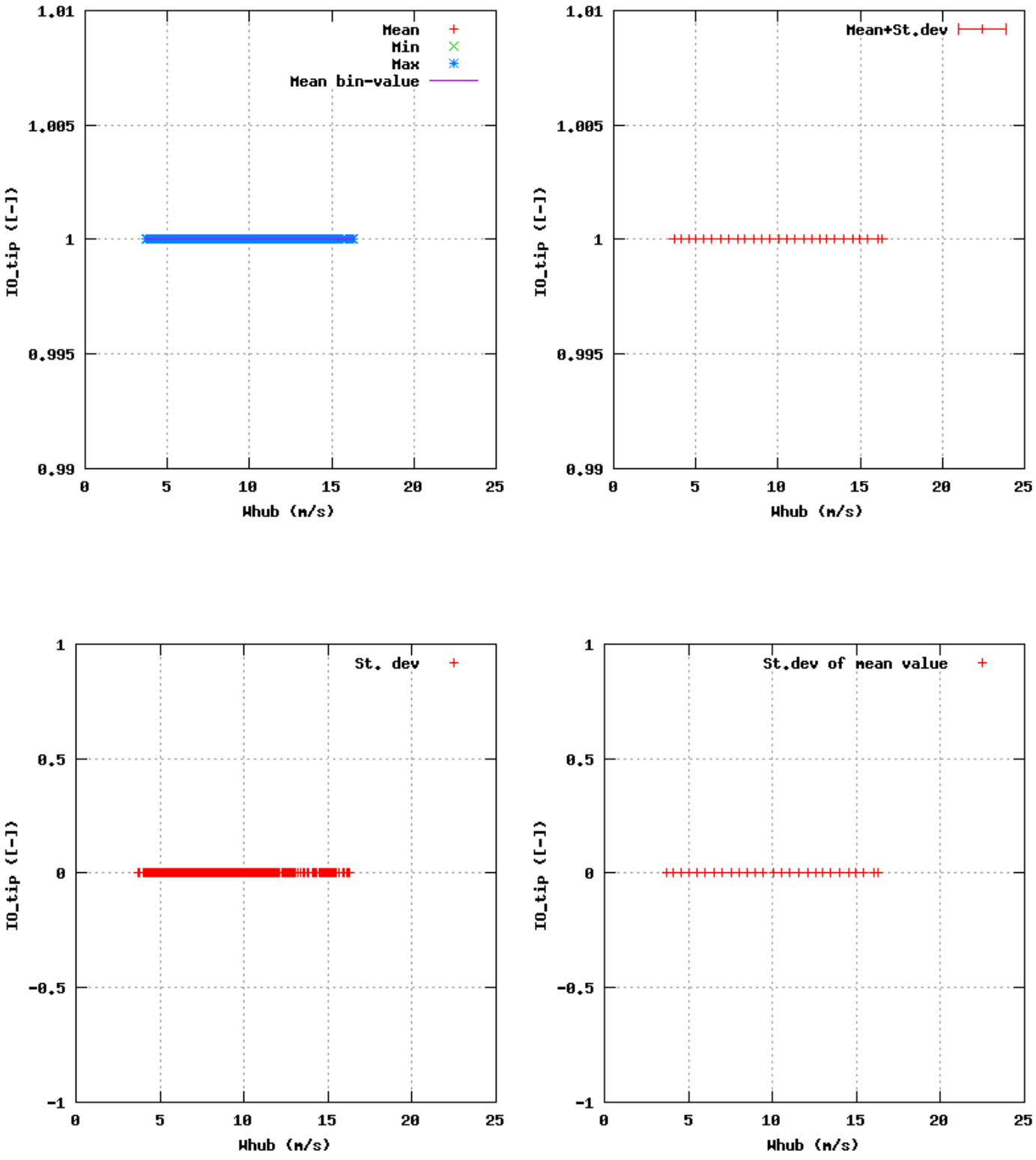

Figure 9a, Sensor 35: Controls:tip on/off IO_tip versus wind speed
Input files: ntk500res.dat, stat_35.dat

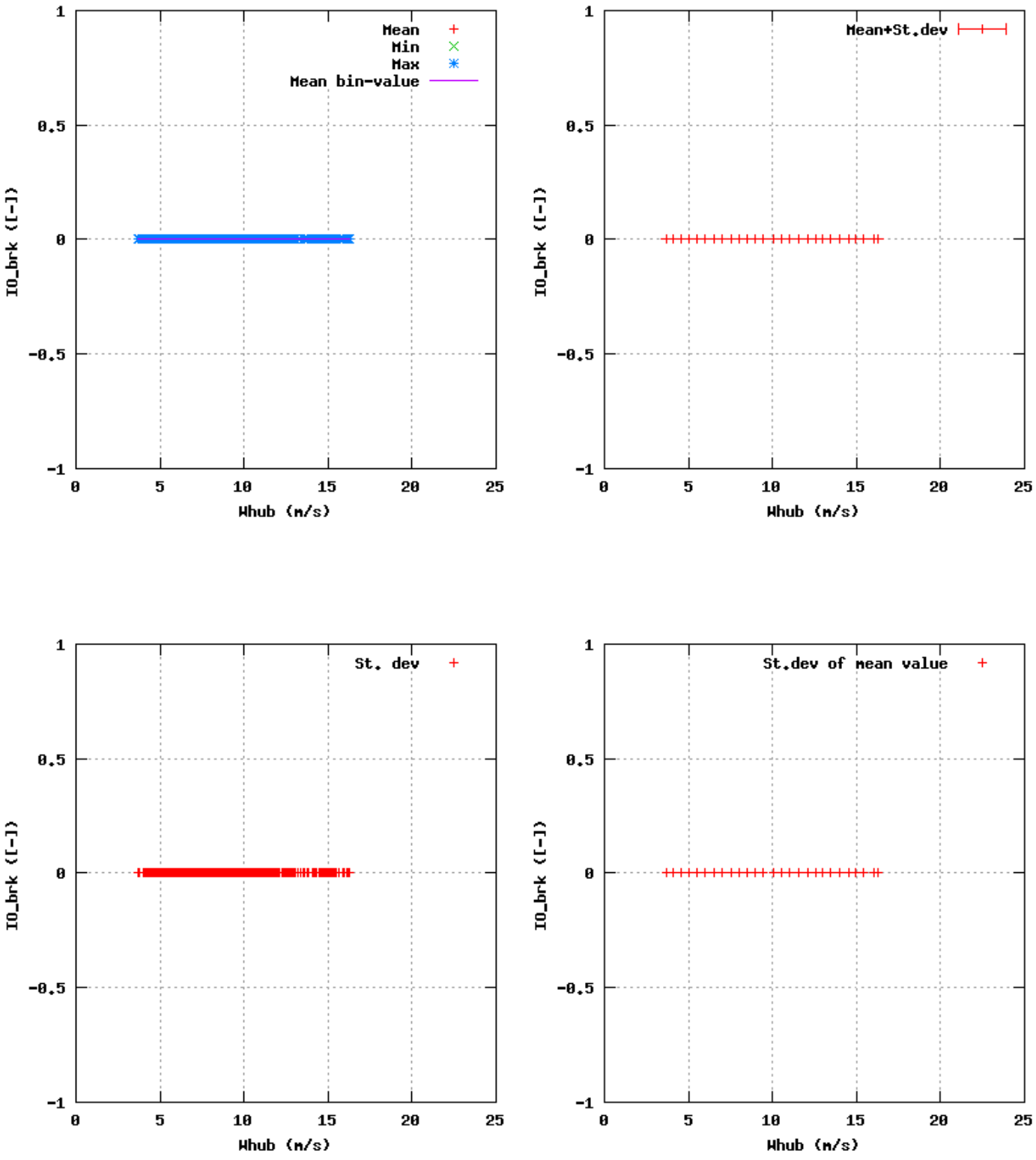

Figure 10a, Sensor 39: Controls:brake on/off IO_brk versus wind speed
Input files: ntk500res.dat, stat_39.dat

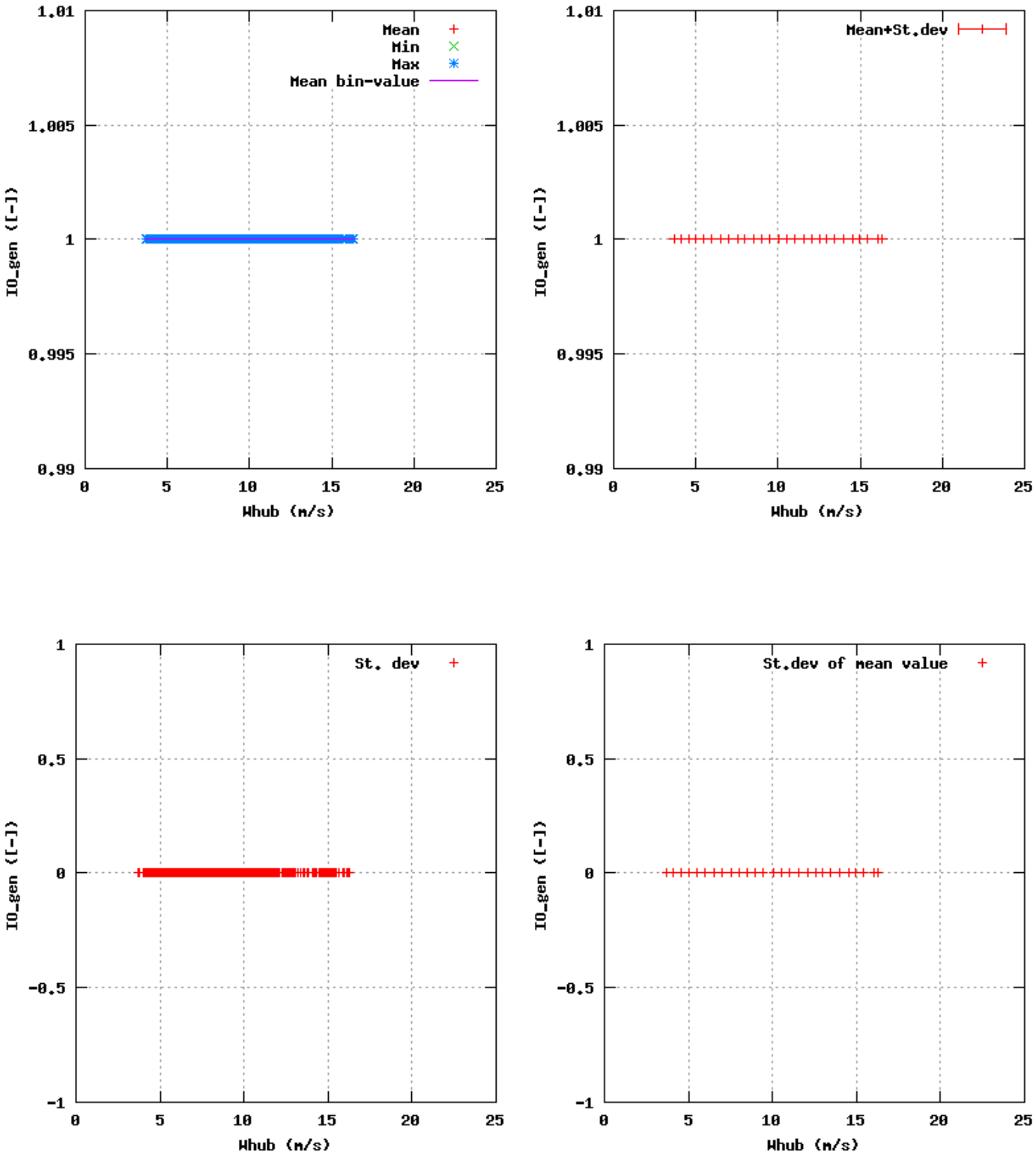

Figure 11a, Sensor 43: Controls:generator on/off IO_gen versus wind speed
Input files: ntk500res.dat, stat_43.dat

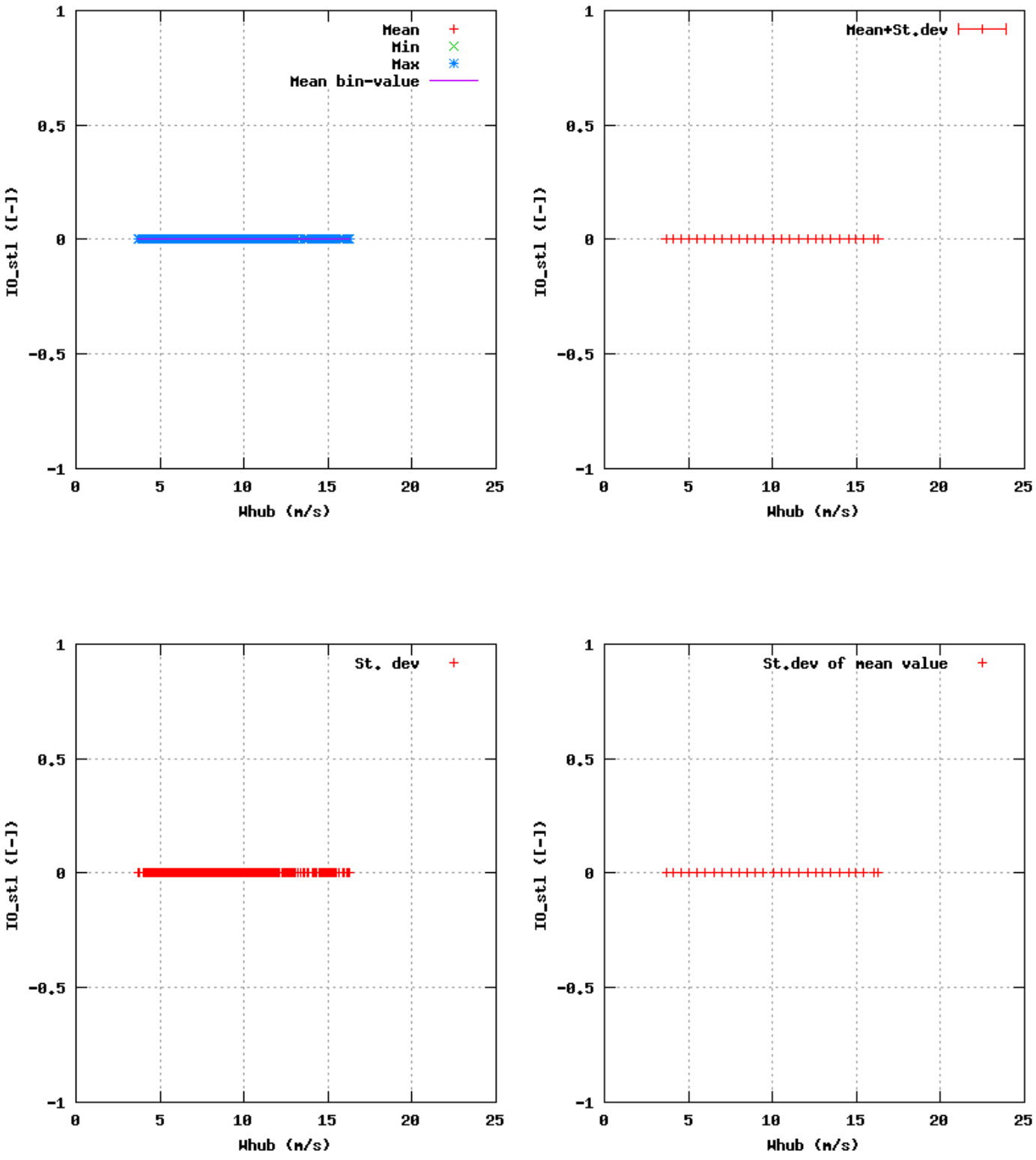

Figure 12a, Sensor 47: Controls:constant/variable speed on/off IO_stl versus wind speed
Input files: ntk500res.dat, stat_47.dat

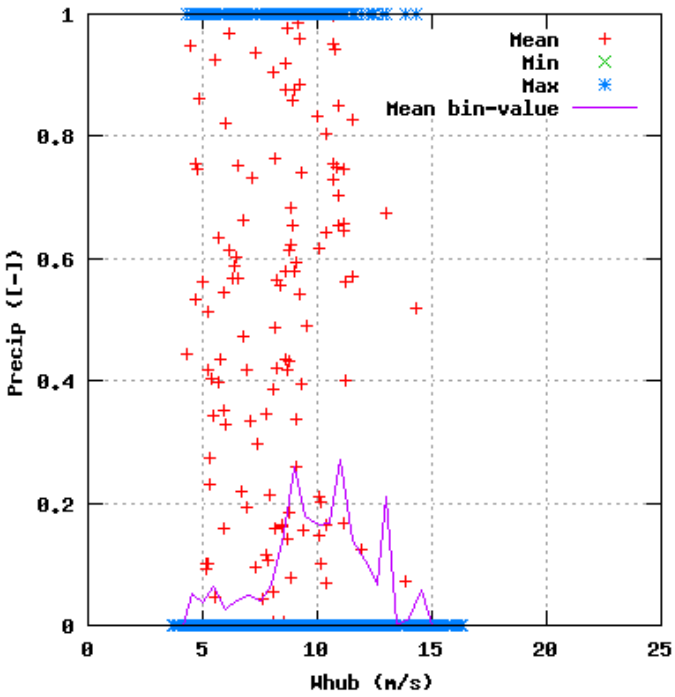

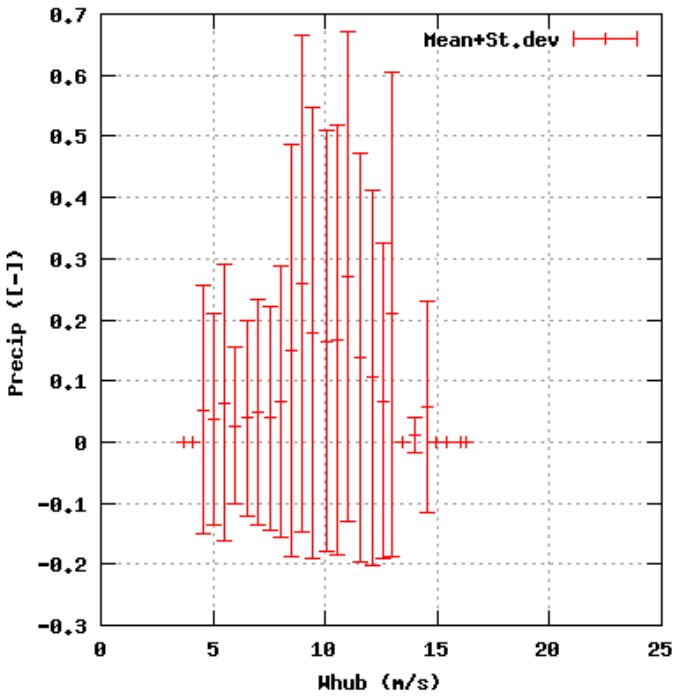

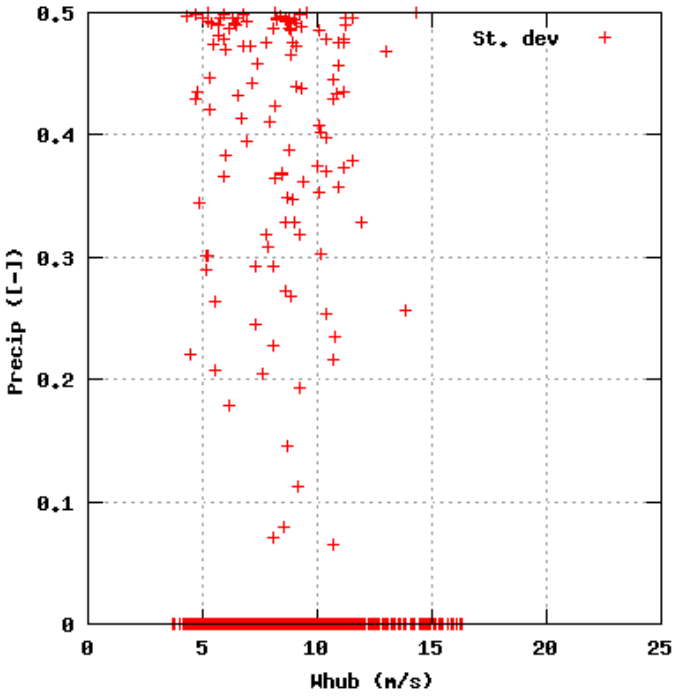

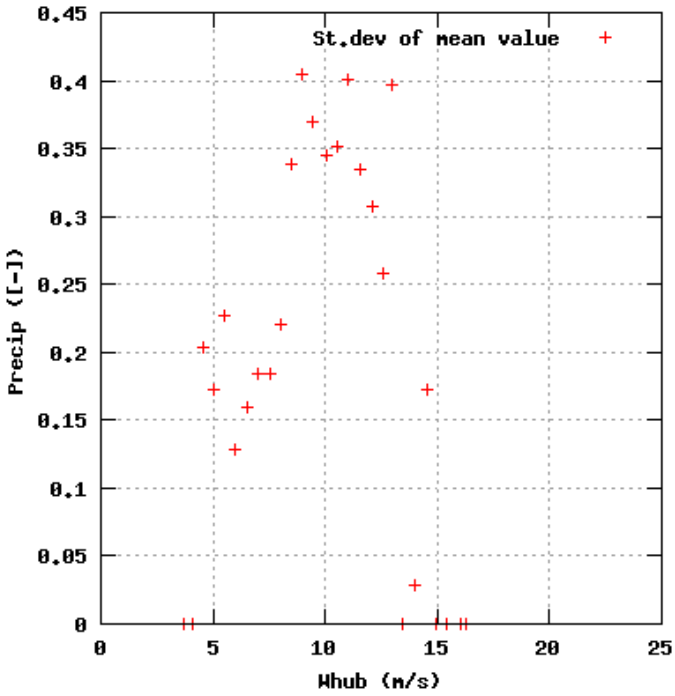

Figure 13a, Sensor 51: Precipitation versus wind speed
Input files: ntk500res.dat, stat_51.dat

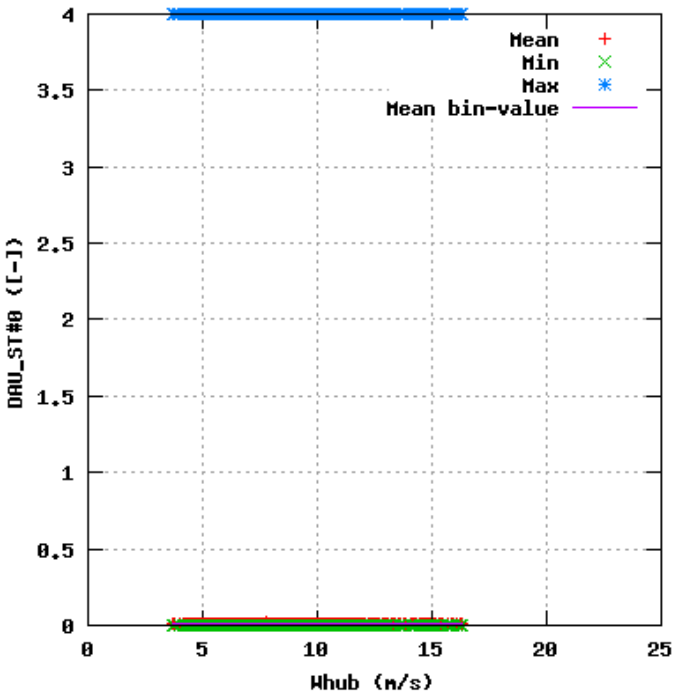

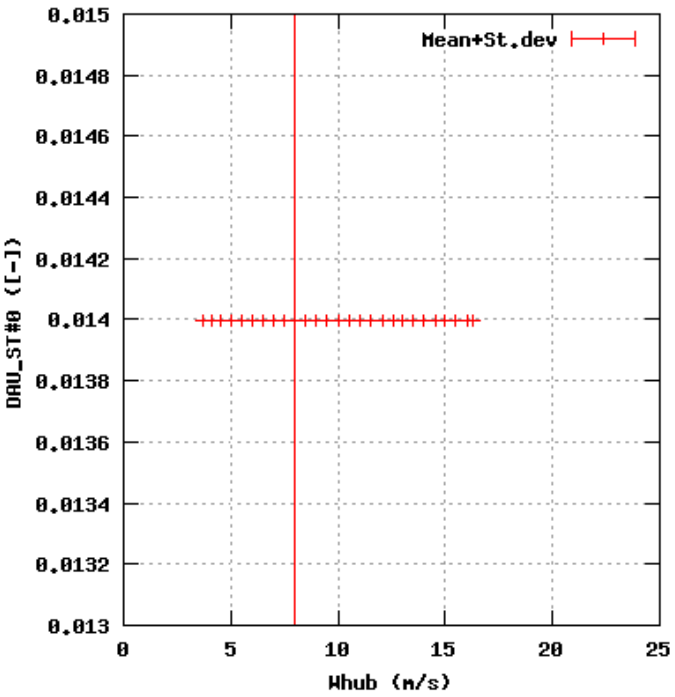

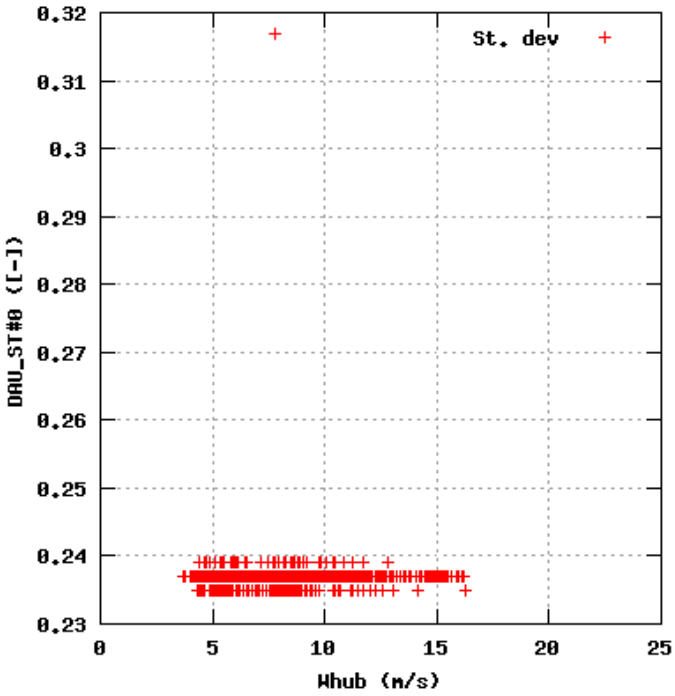

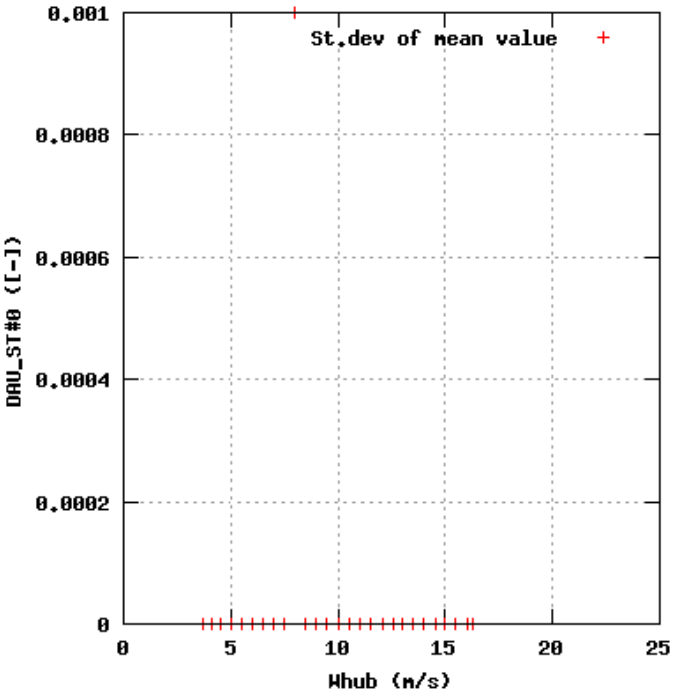

Figure 14a, Sensor 55: DAU_ST#0 versus wind speed
Input files: ntk500res.dat, stat_55.dat

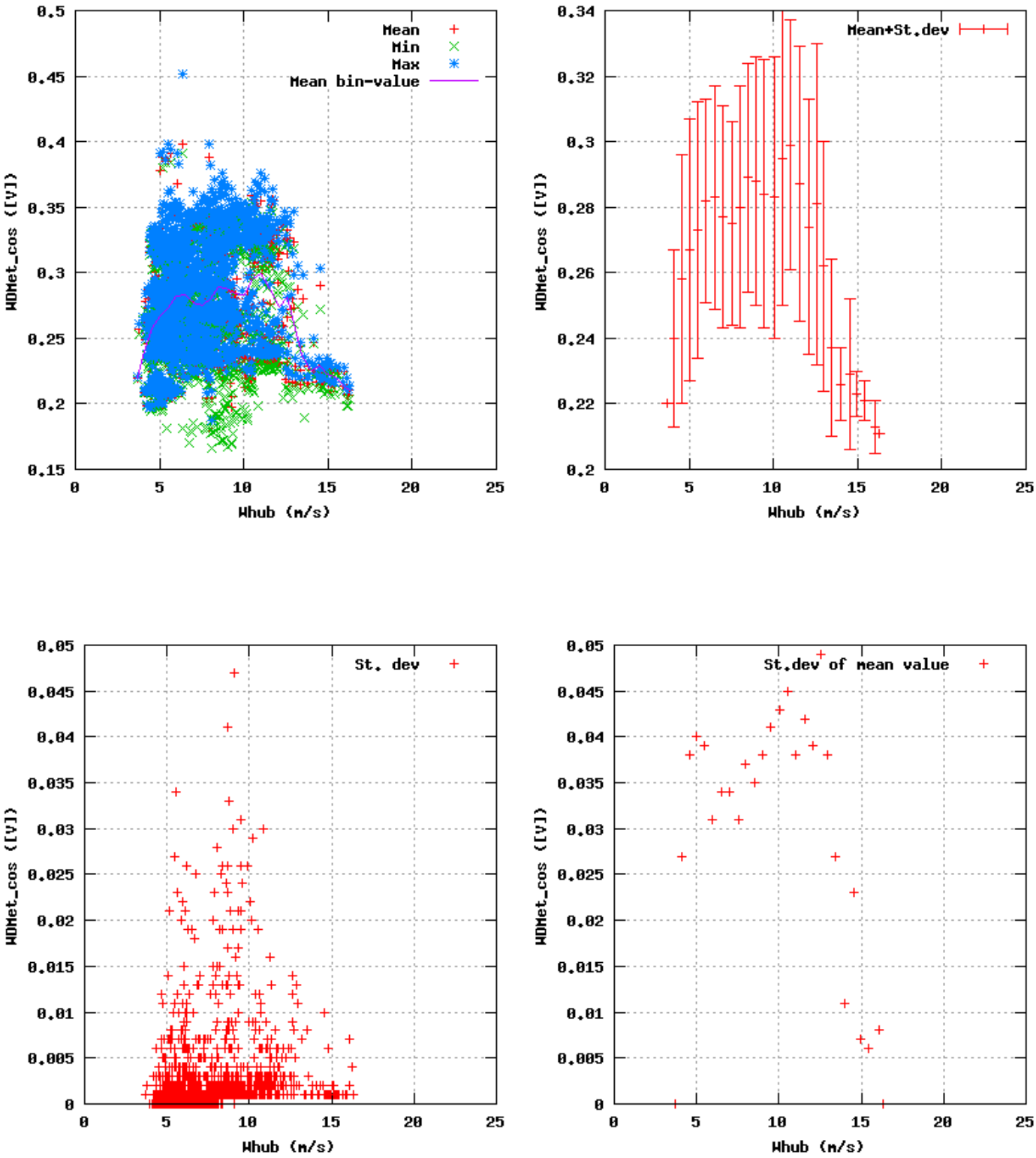

Figure 15a, Sensor 59: Metmast WDMet_cos versus wind speed
Input files: ntk500res.dat, stat_59.dat

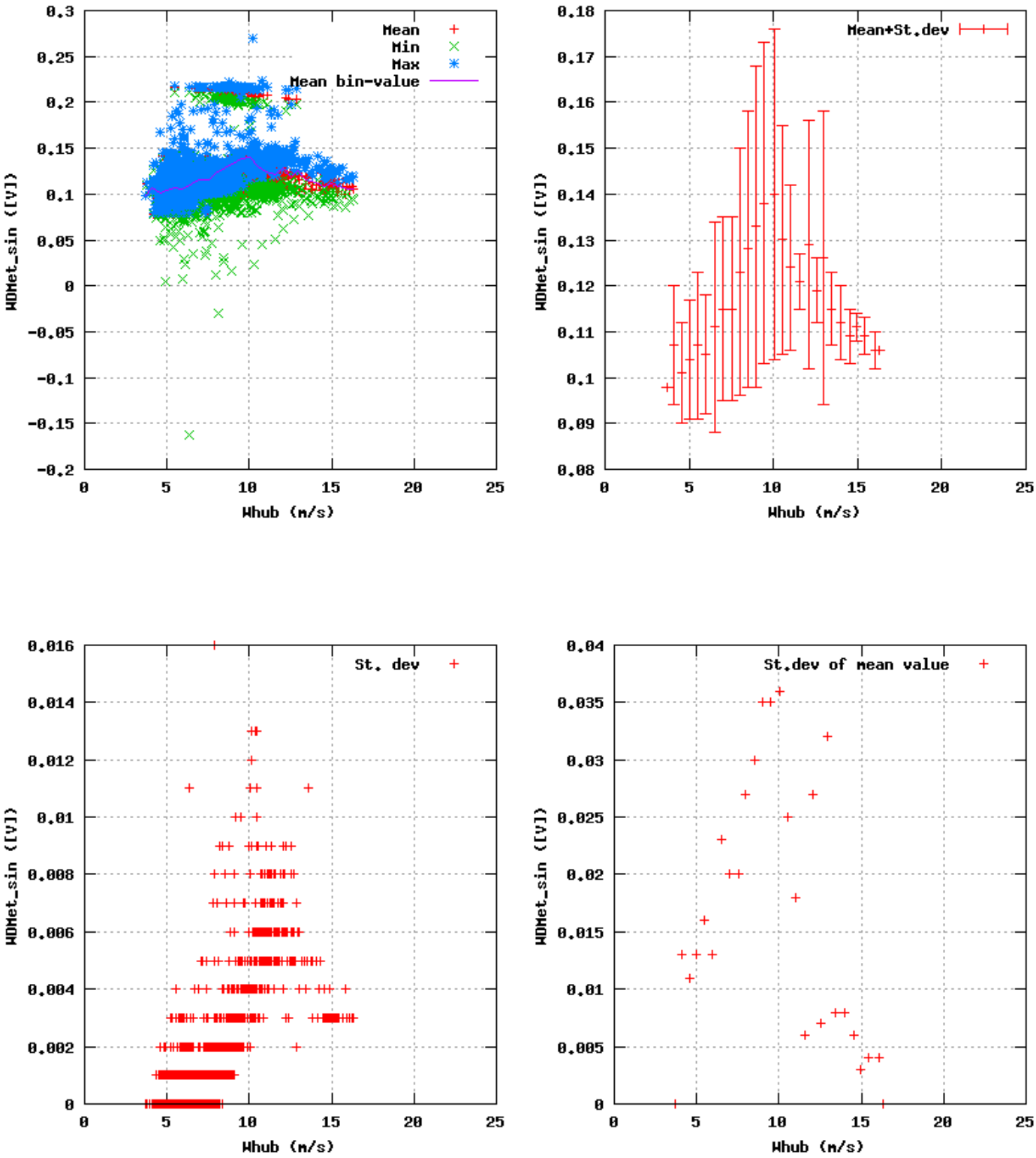

Figure 16a, Sensor 63: Metmast WDMet_sin versus wind speed
Input files: ntk500res.dat, stat_63.dat

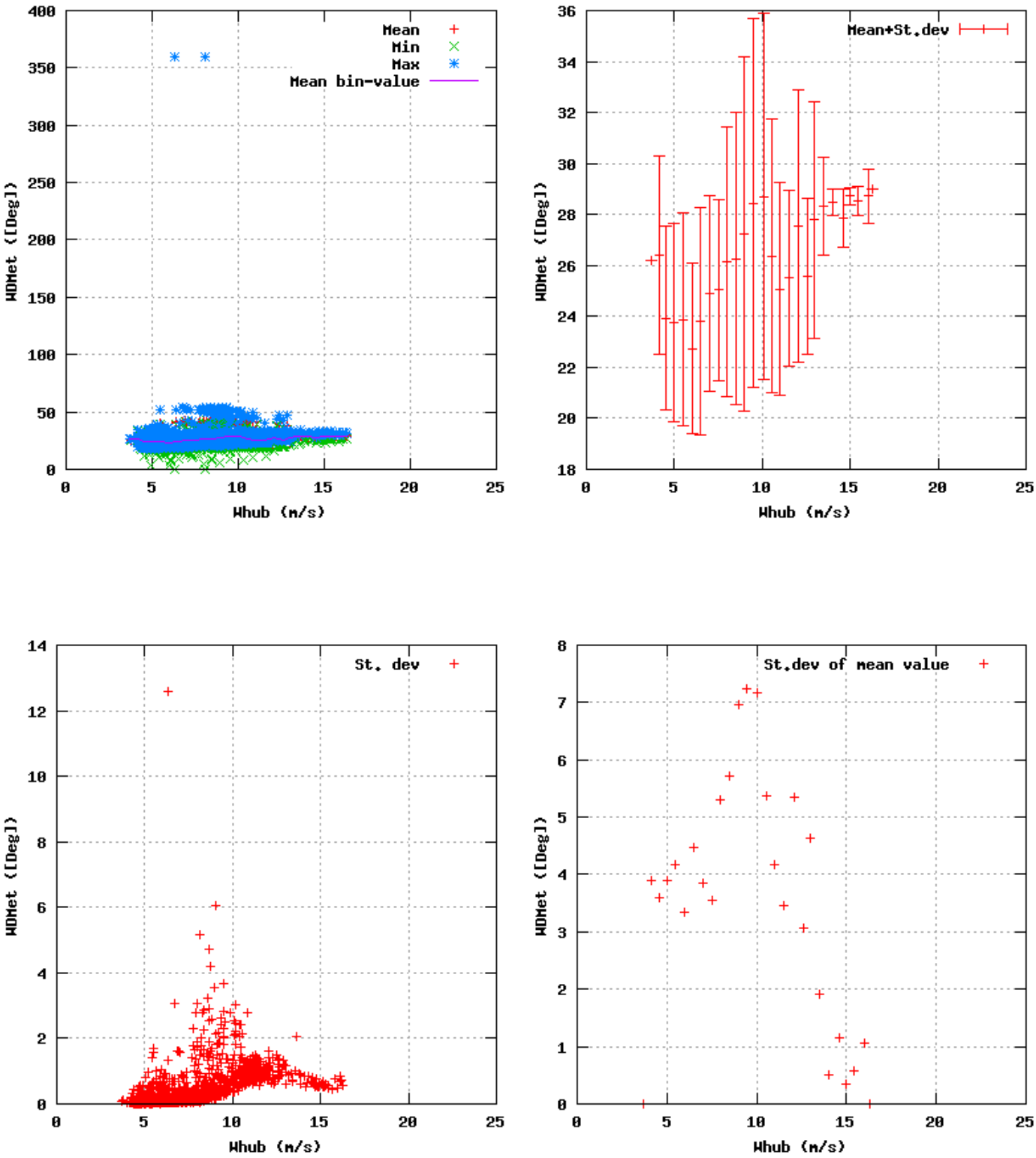

Figure 17a, Sensor 67: Metmast wind direction WDMet versus wind speed
Input files: ntk500res.dat, stat_67.dat

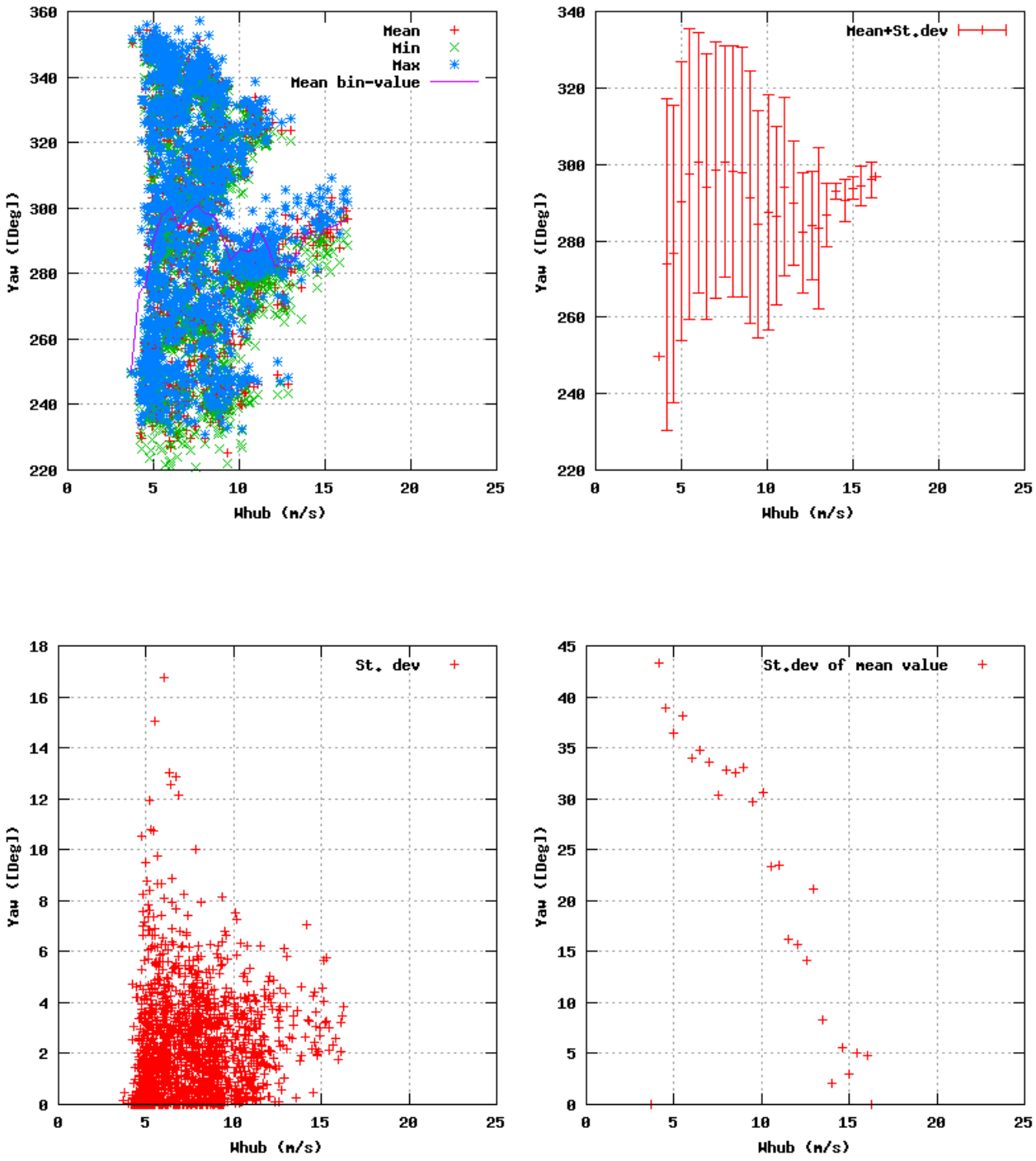

Figure 18a, Sensor 71: Wind turbine nacelle position Yaw versus wind speed
Input files: ntk500res.dat, stat_71.dat

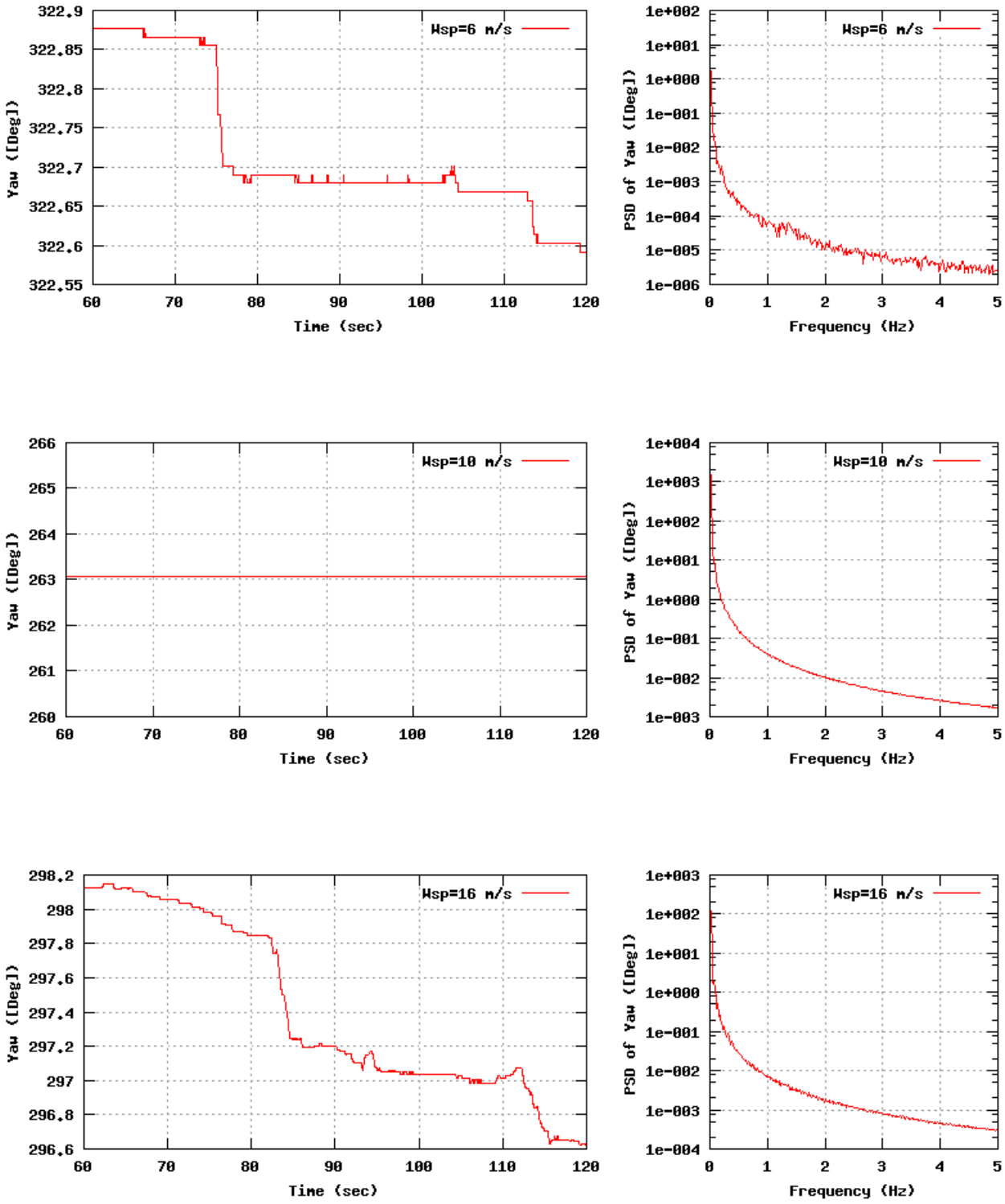

Figure 18b, Sensor 71: Wind turbine nacelle position Yaw versus time and frequency
Input files: m06.asc, m10.asc, m16.asc, m06.psd, m10.psd and m16.psd

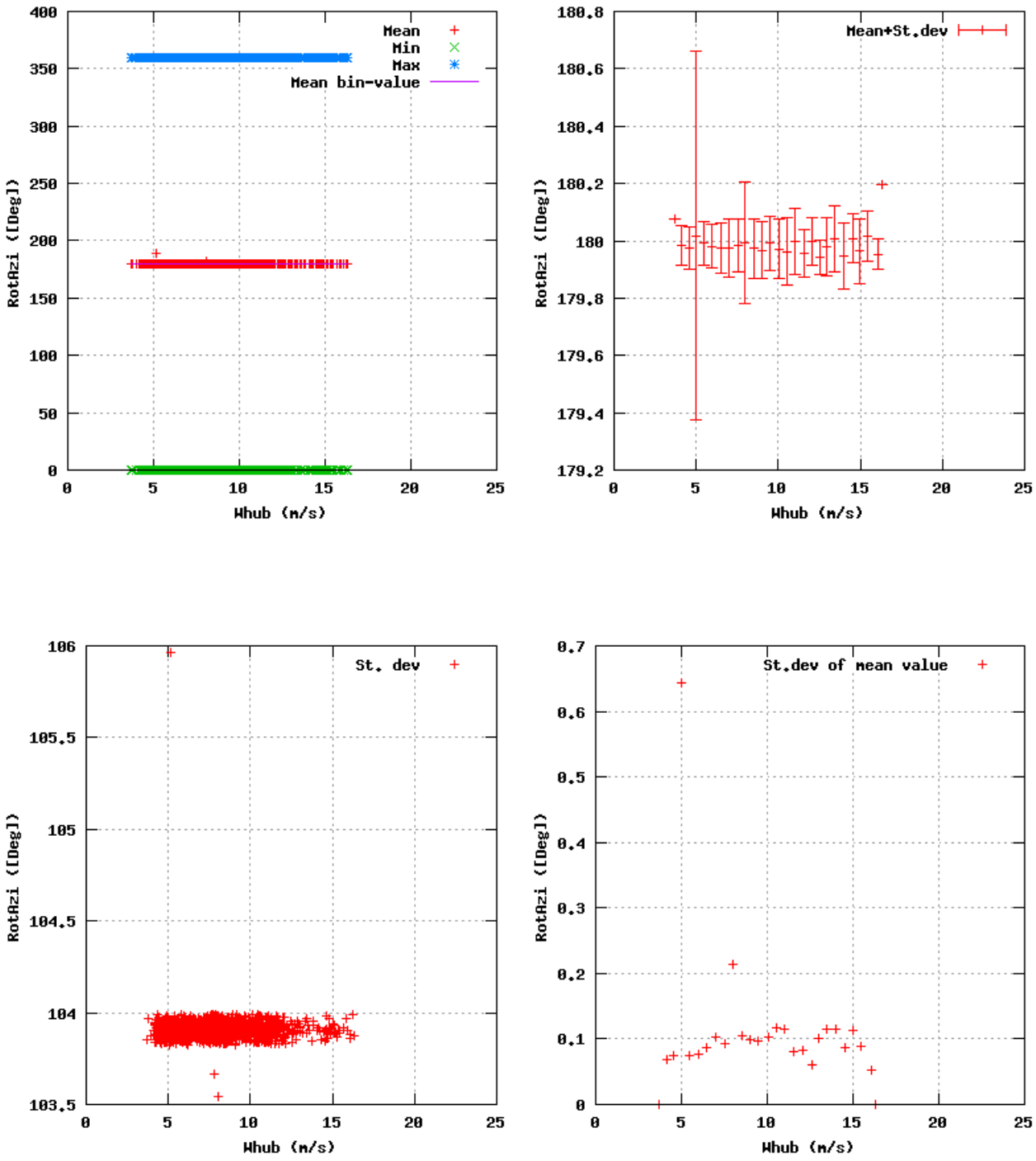

Figure 19a, Sensor 75: Rotor blade azimuth angle RotAzi versus wind speed
Input files: ntk500res.dat, stat_75.dat

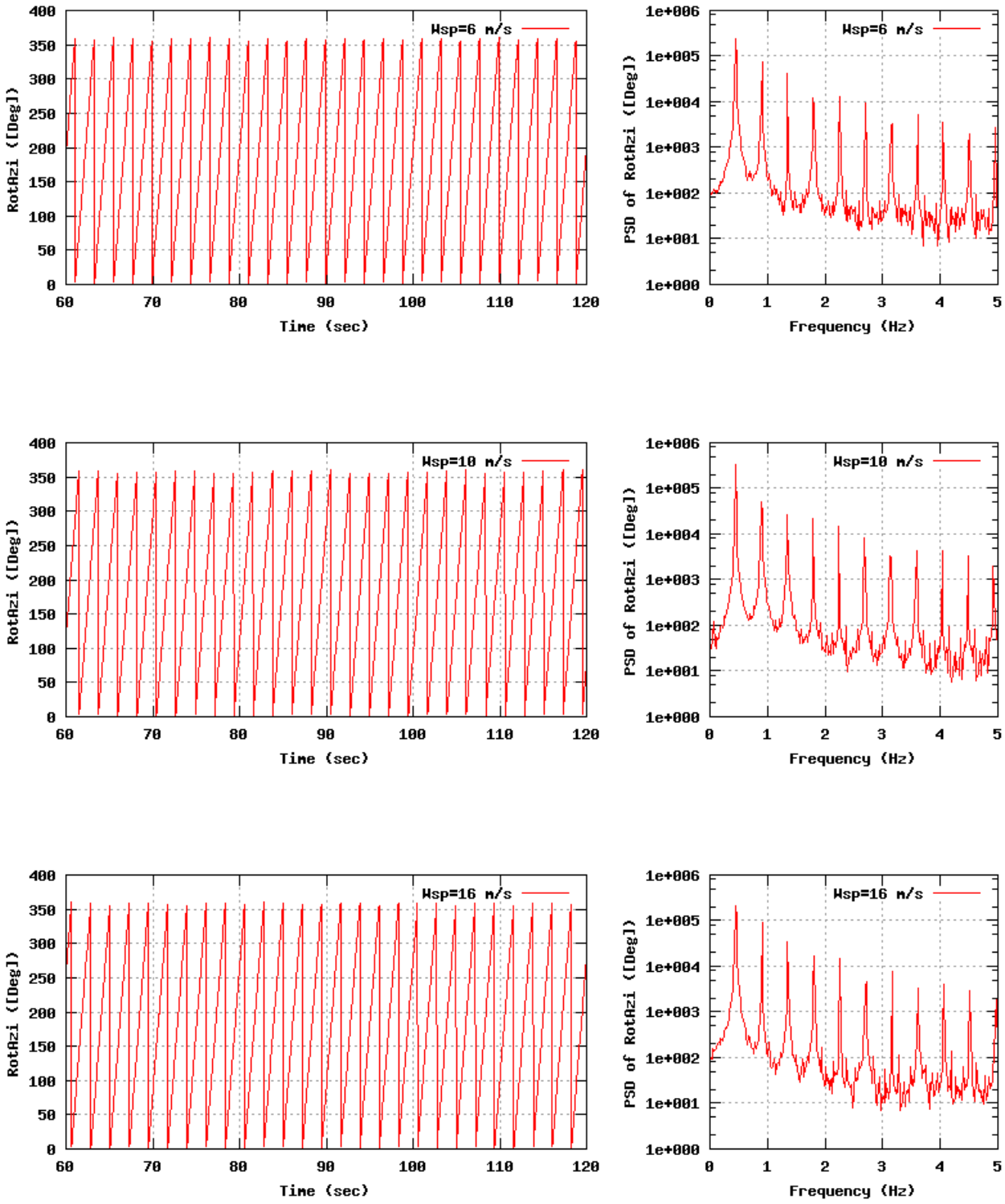

Figure 19b, Sensor 75: Rotor blade azimuth angle RotAzi versus time and frequency
Input files: m06.asc, m10.asc, m16.asc, m06.psd, m10.psd and m16.psd

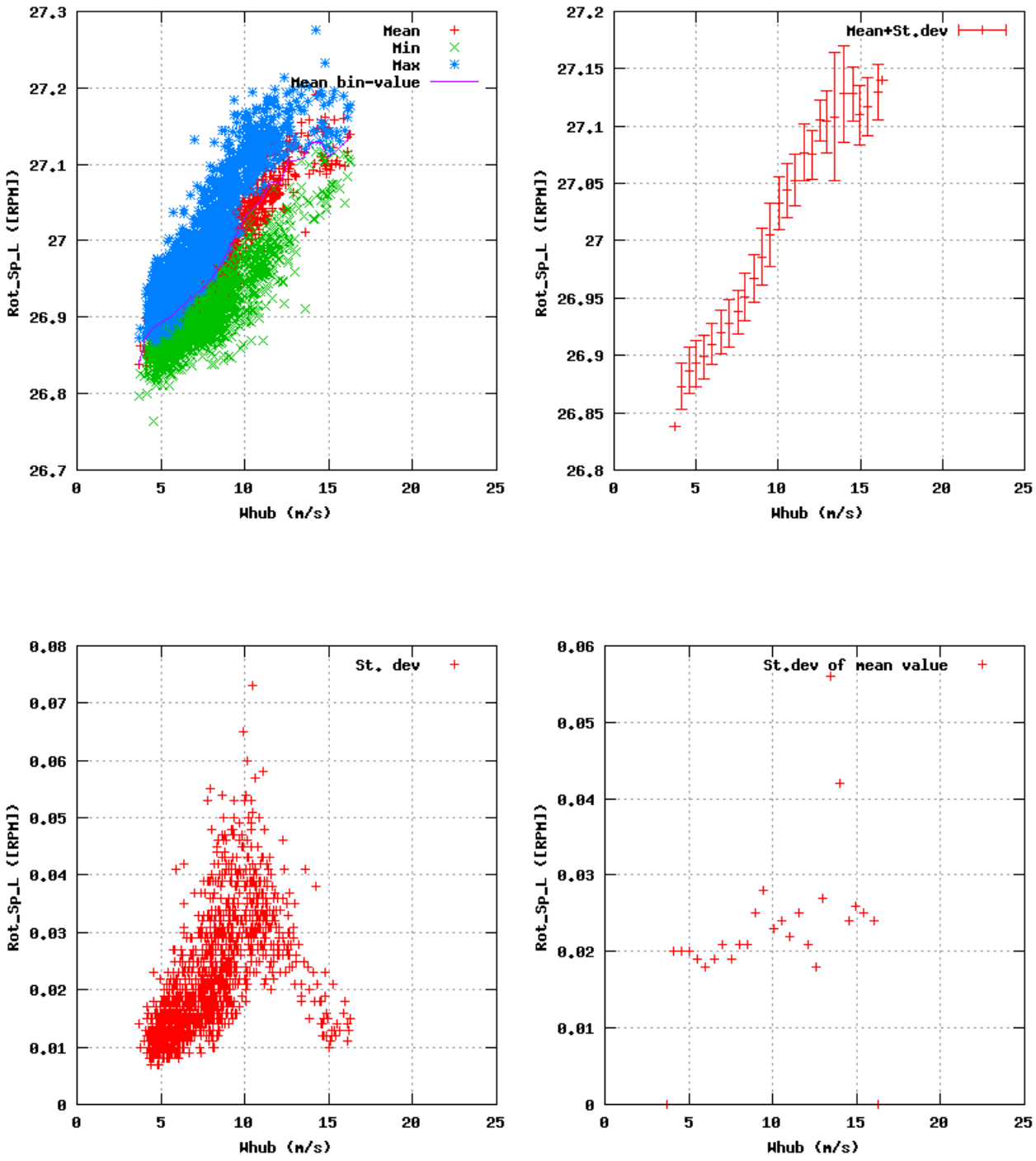

Figure 20a, Sensor 79: Rotor shaft speed LSS Rot_Sp_L versus wind speed
Input files: ntk500res.dat, stat_79.dat

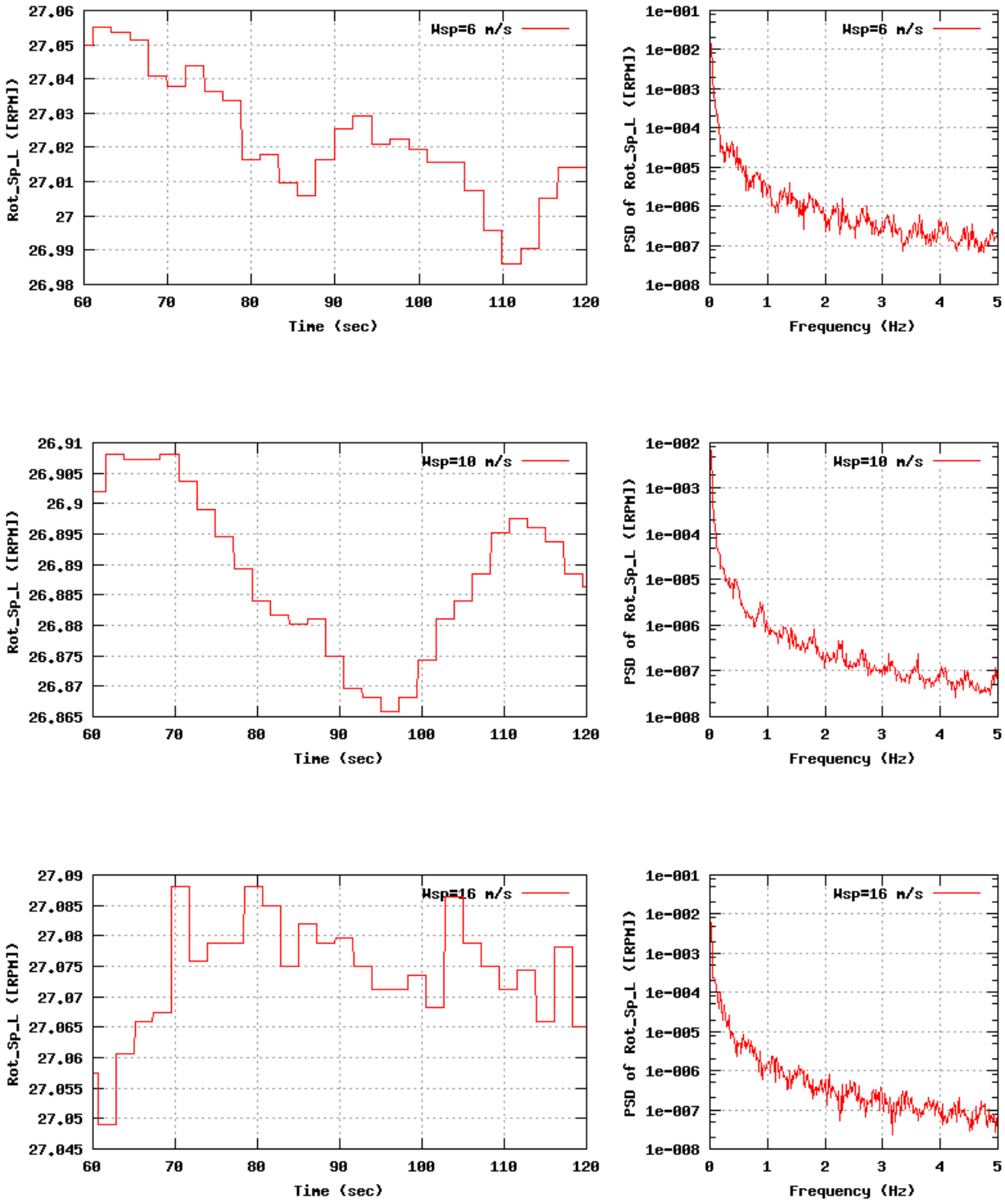

Figure 20b, Sensor 79: Rotor shaft speed LSS Rot_Sp_L versus time and frequency
Input files: m06.asc, m10.asc, m16.asc, m06.psd, m10.psd and m16.psd

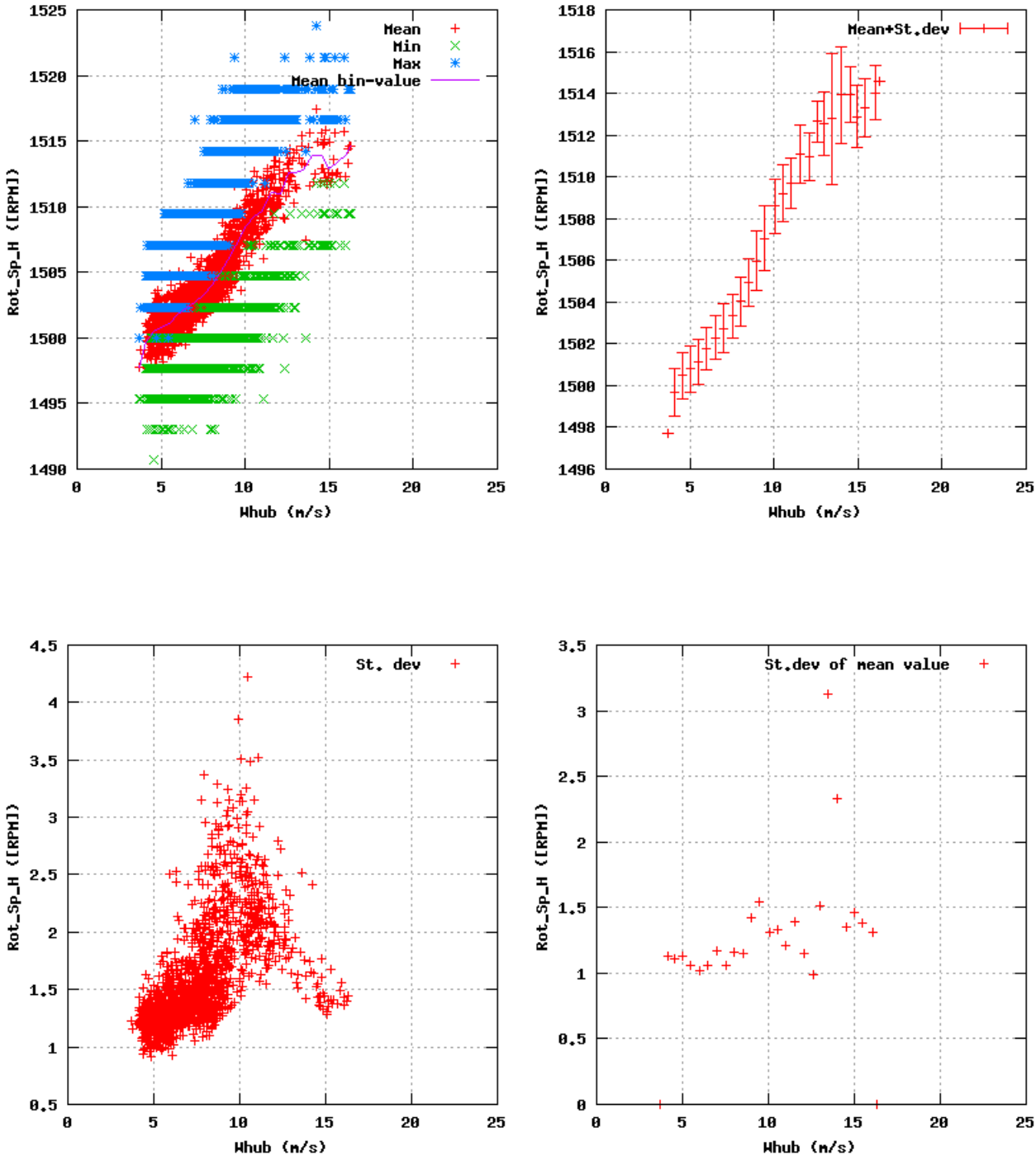

Figure 21a, Sensor 83: Rotor shaft speed HSS Rot_Sp_H versus wind speed
Input files: ntk500res.dat, stat_83.dat

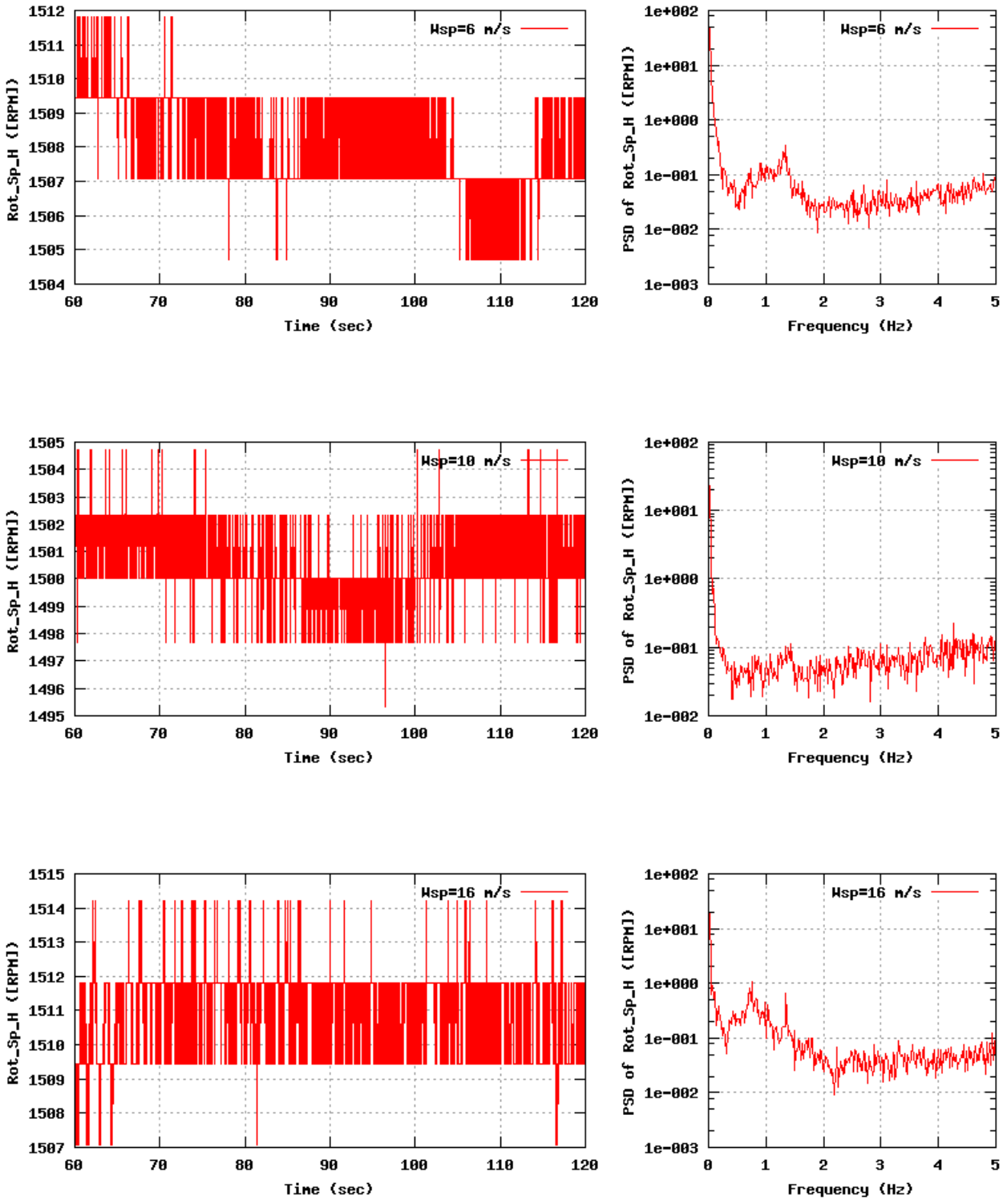

Figure 21b, Sensor 83: Rotor shaft speed HSS Rot_Sp_H versus time and frequency
Input files: m06.asc, m10.asc, m16.asc, m06.psd, m10.psd and m16.psd

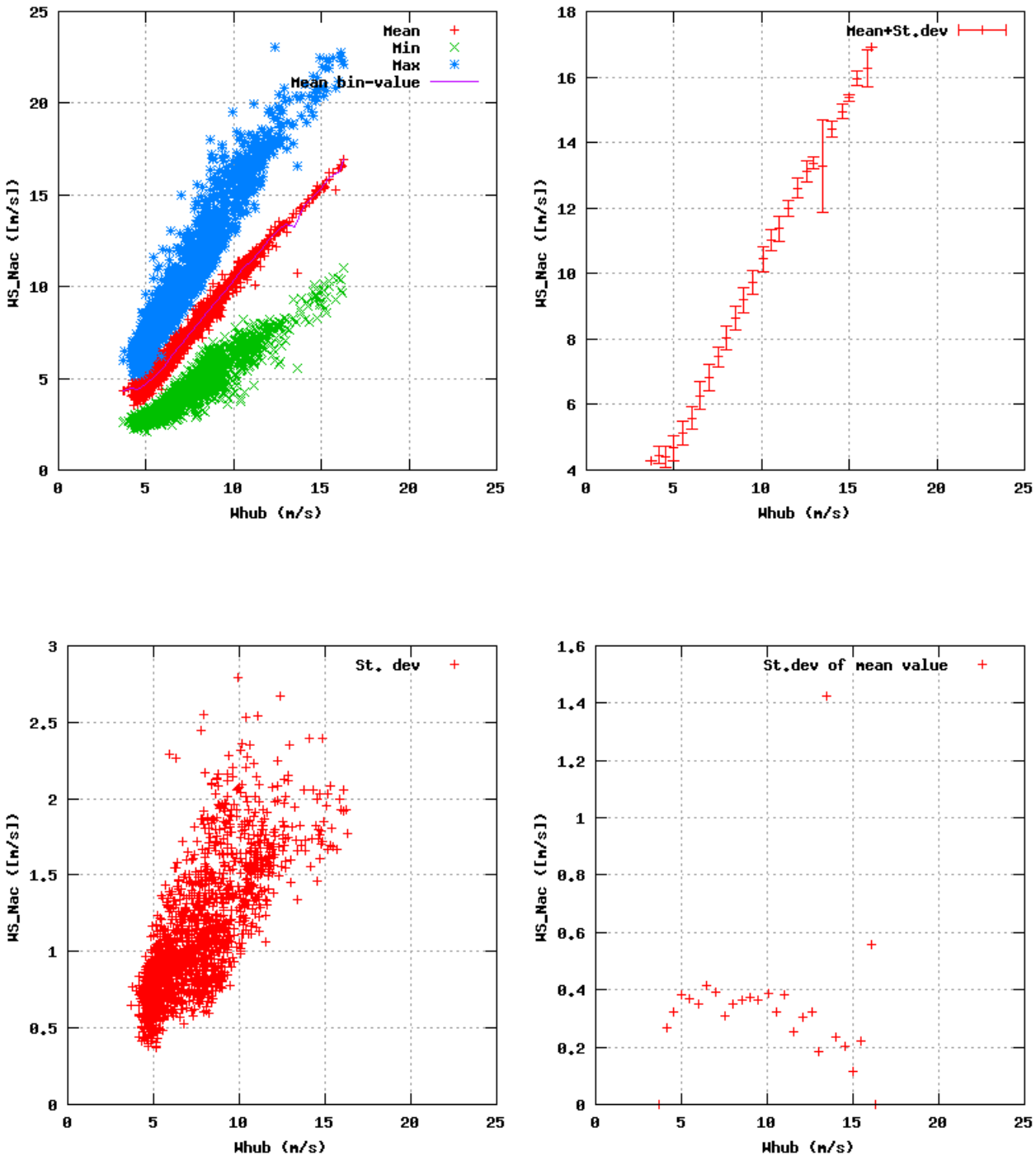

Figure 22a, Sensor 87: Wind speed WS_Nac versus wind speed
Input files: ntk500res.dat, stat_87.dat

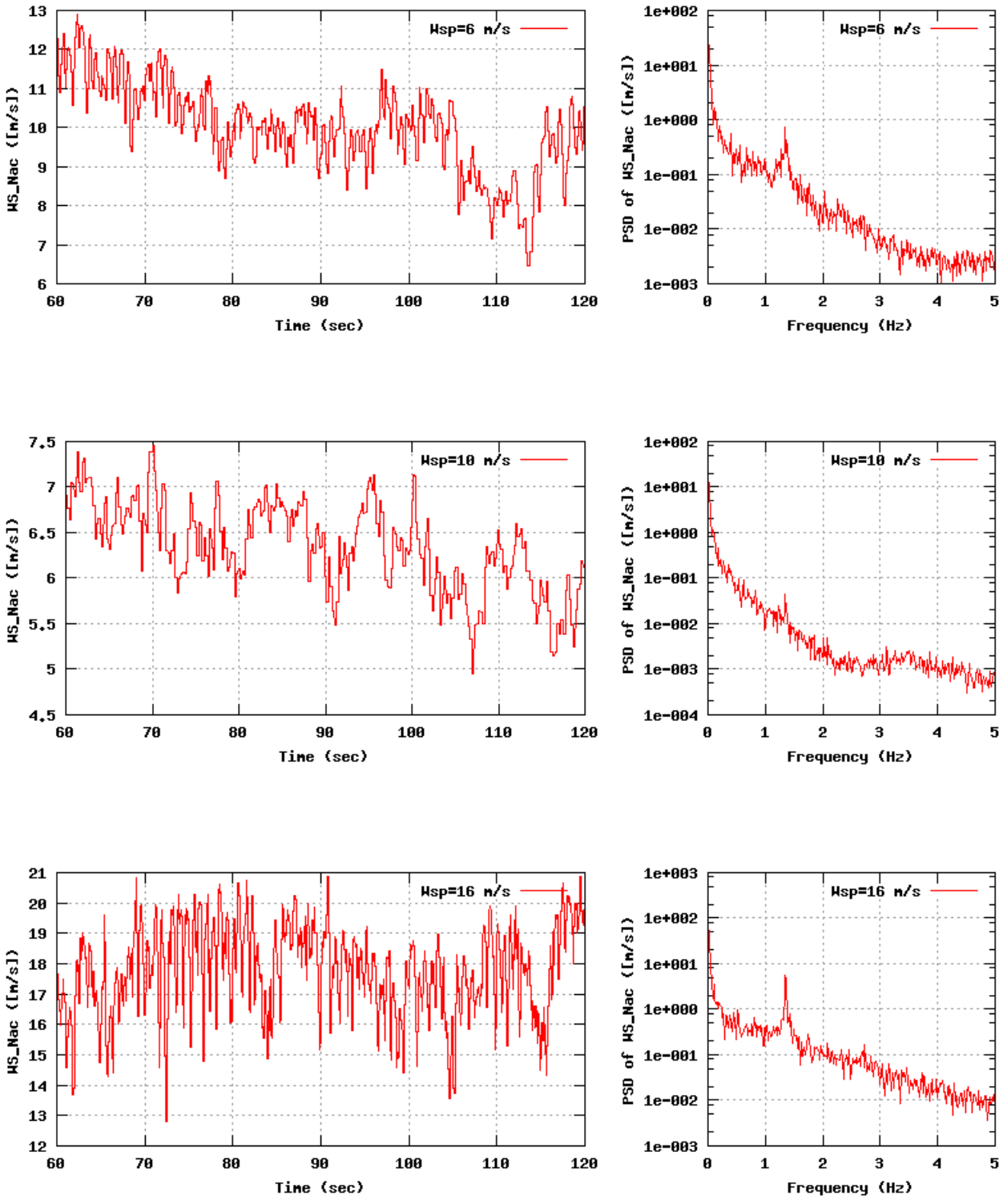

Figure 22b, Sensor 87: Wind speed WS_Nac versus time and frequency
Input files: m06.asc, m10.asc, m16.asc, m06.psd, m10.psd and m16.psd

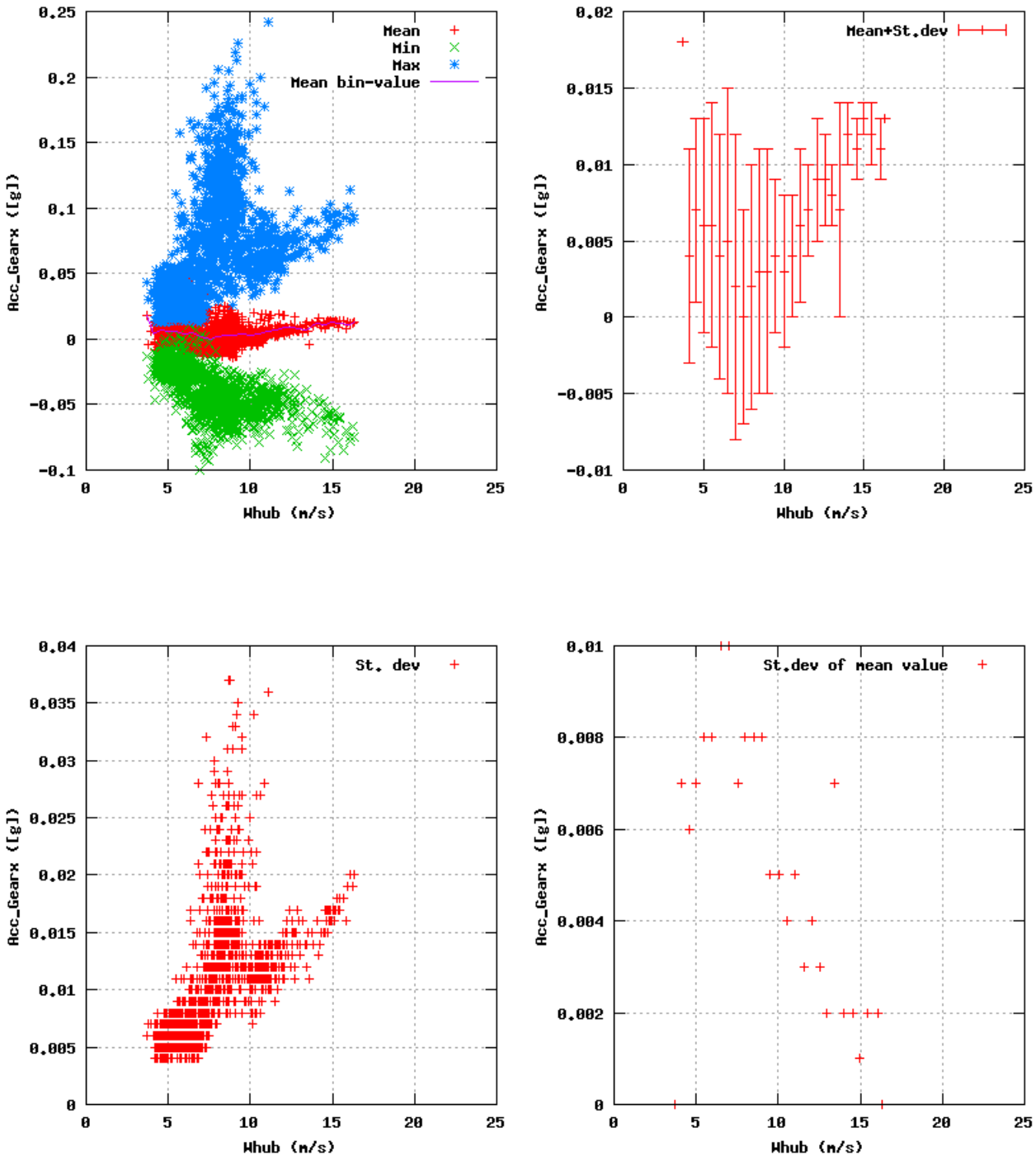

Figure 23a, Sensor 91: Acceleration gearbox Acc_Gearx versus wind speed
Input files: ntk500res.dat, stat_91.dat

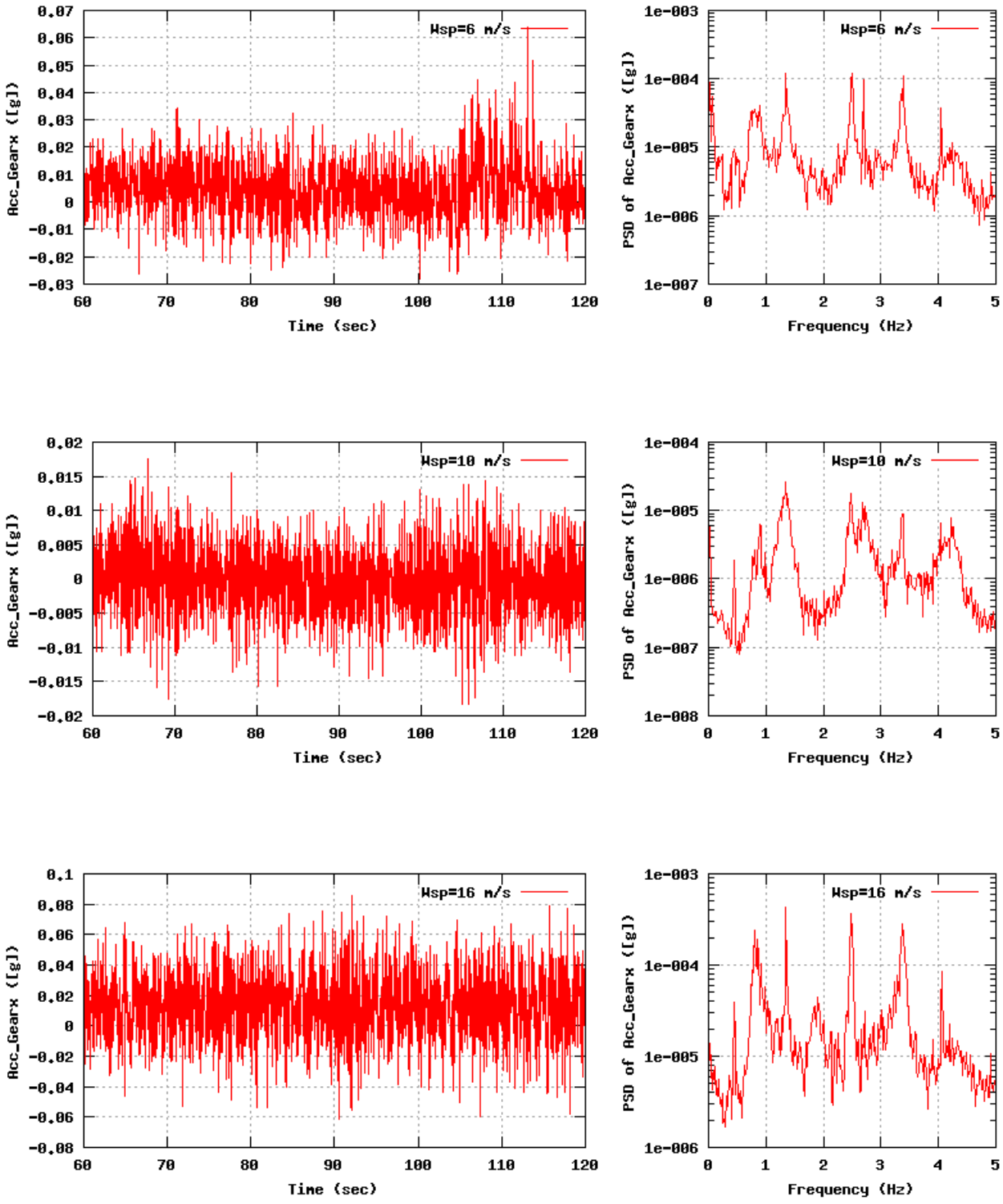

Figure 23b, Sensor 91: Acceleration gearbox Acc_Gearx versus time and frequency
Input files: m06.asc, m10.asc, m16.asc, m06.psd, m10.psd and m16.psd

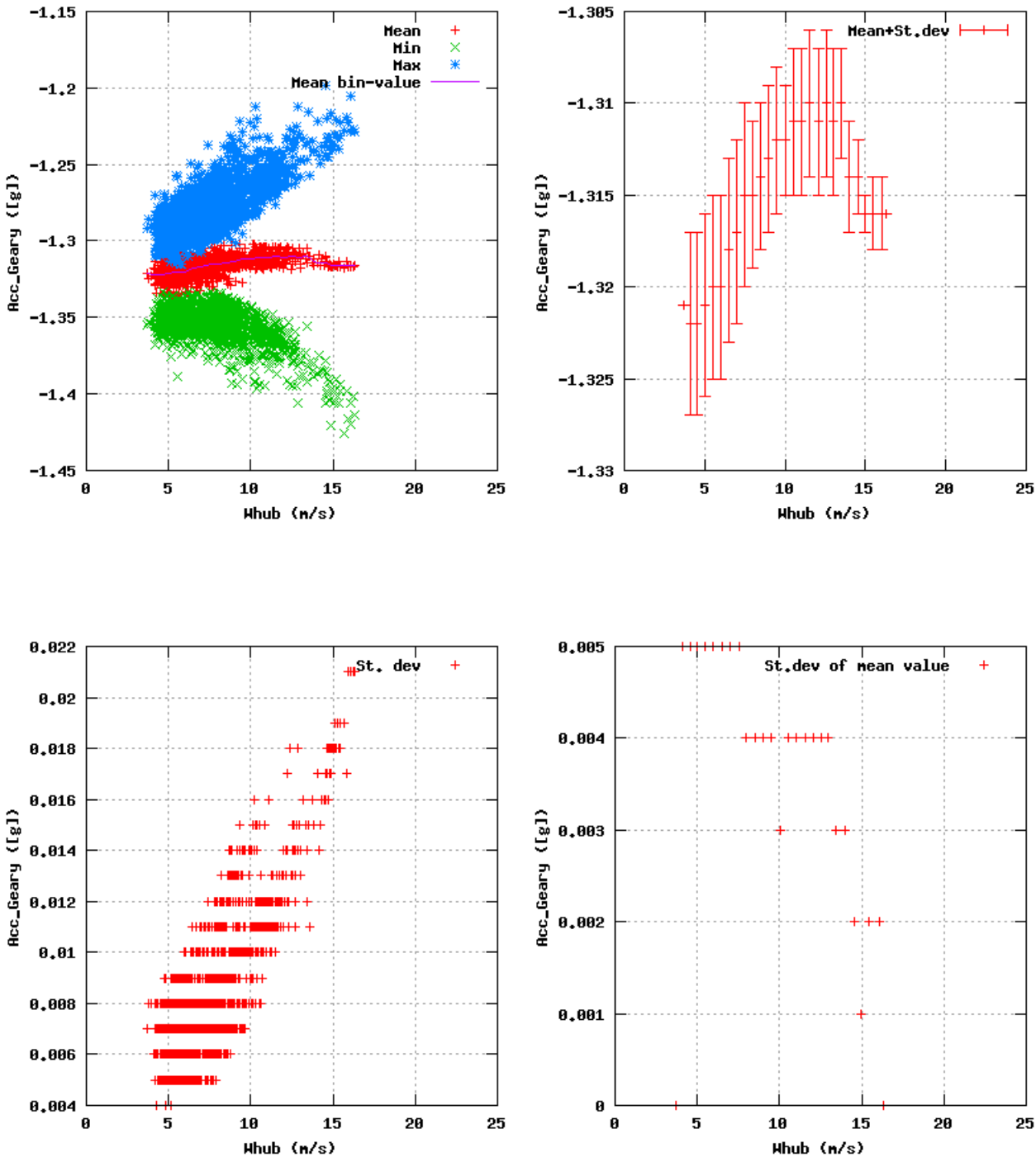

Figure 24a, Sensor 95: Acceleration gearbox Acc_Geary versus wind speed
Input files: ntk500res.dat, stat_95.dat

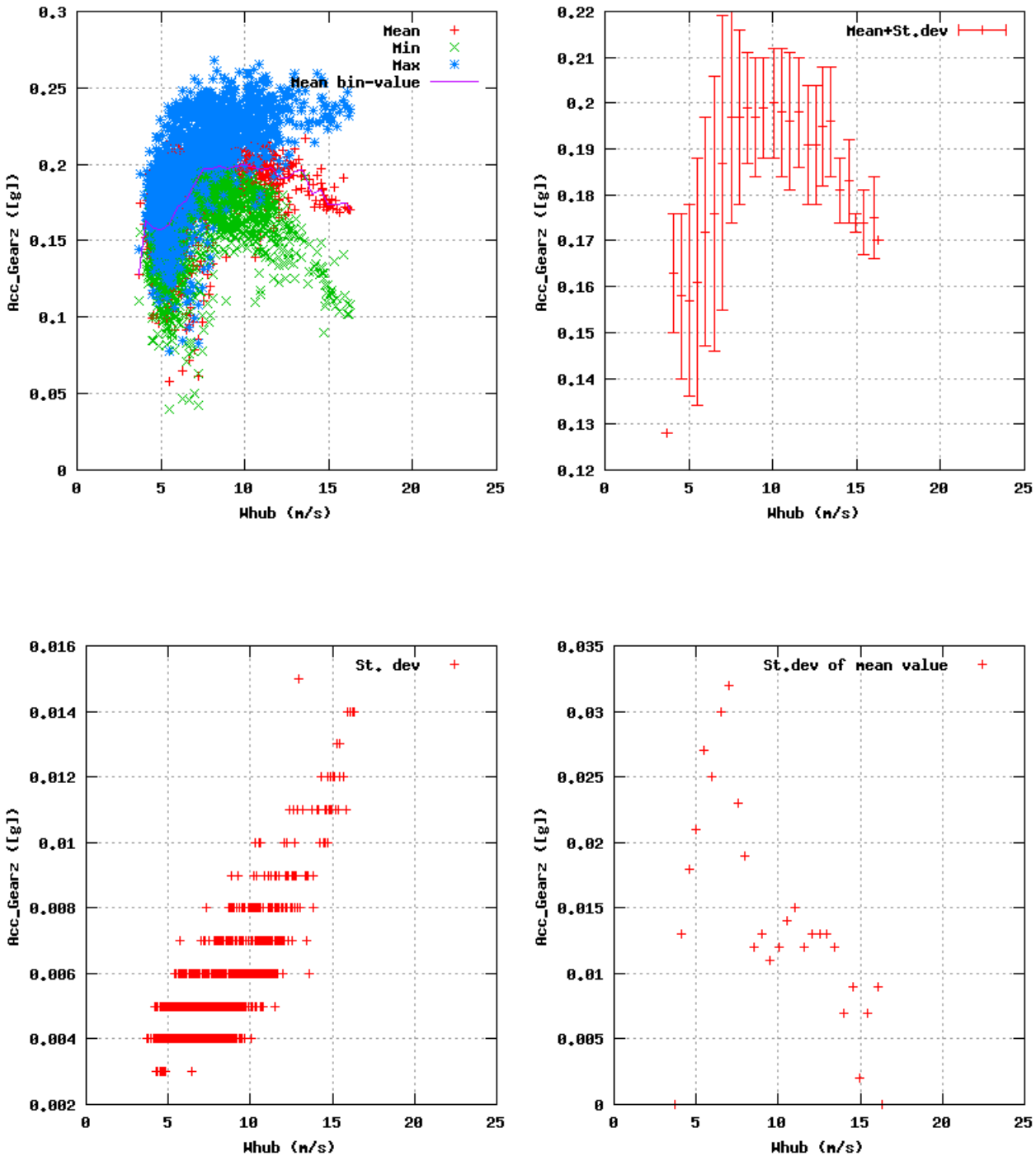

Figure 25a, Sensor 99: Acceleration gearbox Acc_Gearz versus wind speed
Input files: ntk500res.dat, stat_99.dat

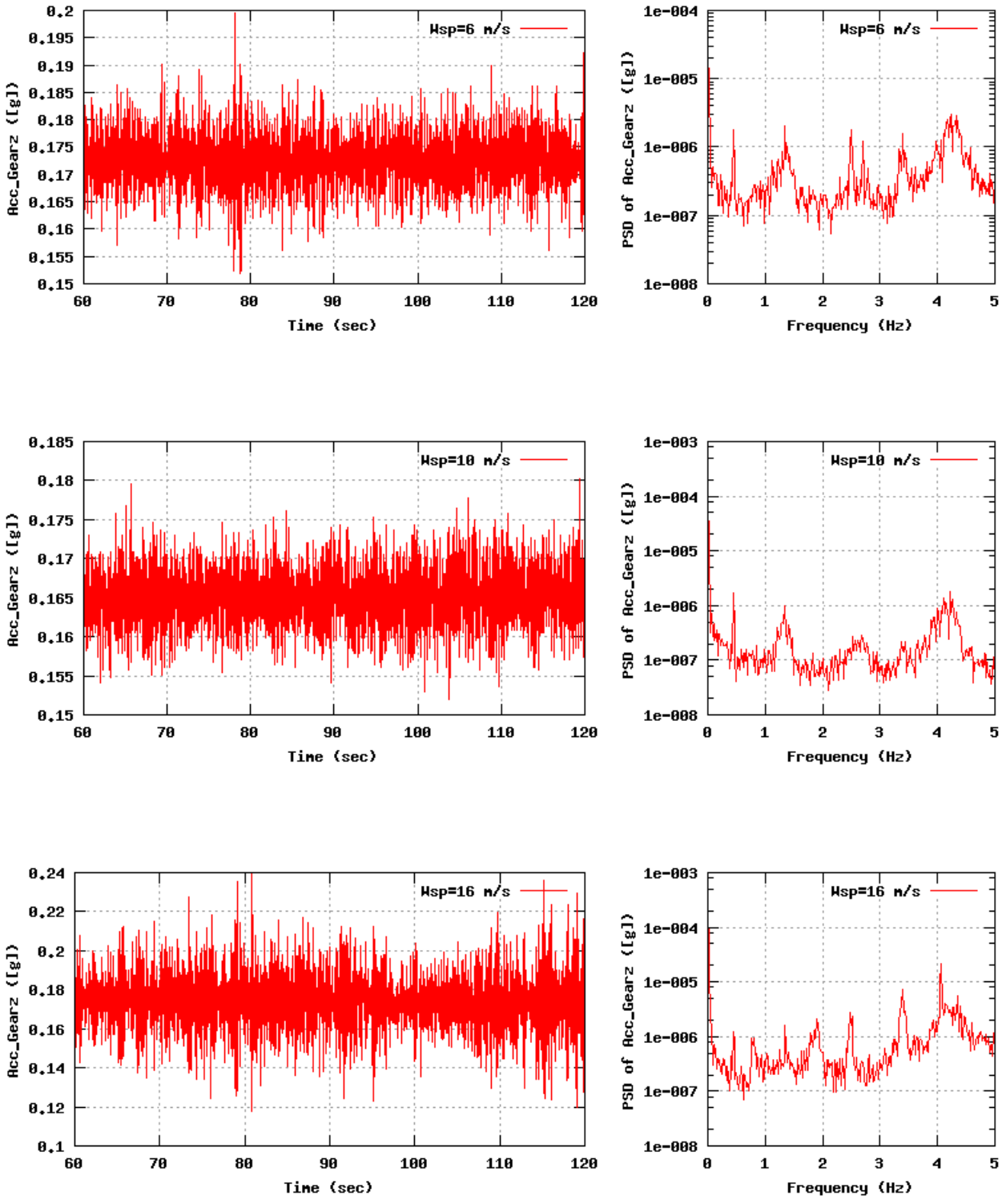

Figure 25b, Sensor 99: Acceleration gearbox Acc_Gearz versus time and frequency
Input files: m06.asc, m10.asc, m16.asc, m06.psd, m10.psd and m16.psd

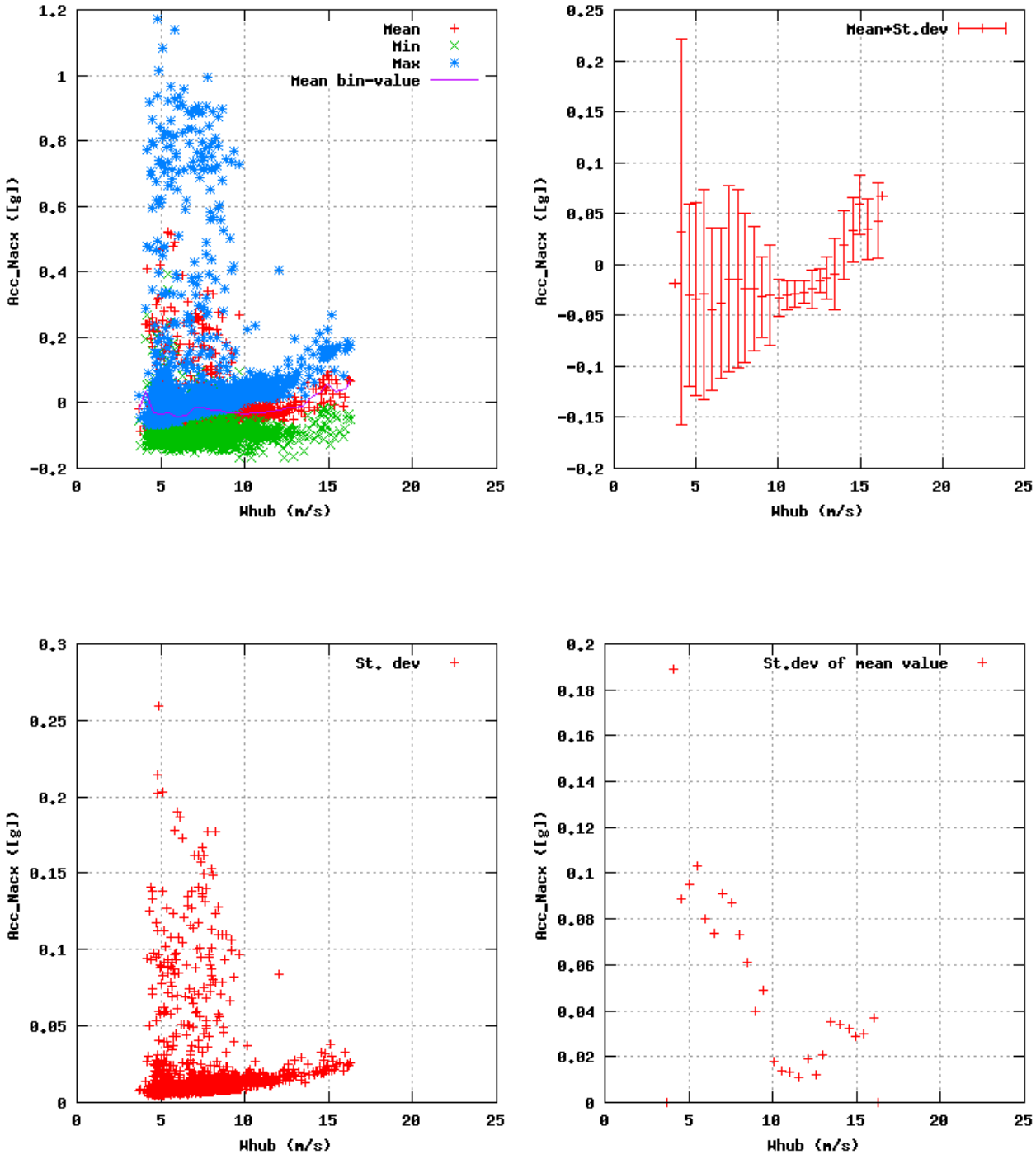

Figure 26a, Sensor 103: Acceleration nacelle leeward Acc_Nacx versus wind speed
Input files: ntk500res.dat, stat_103.dat

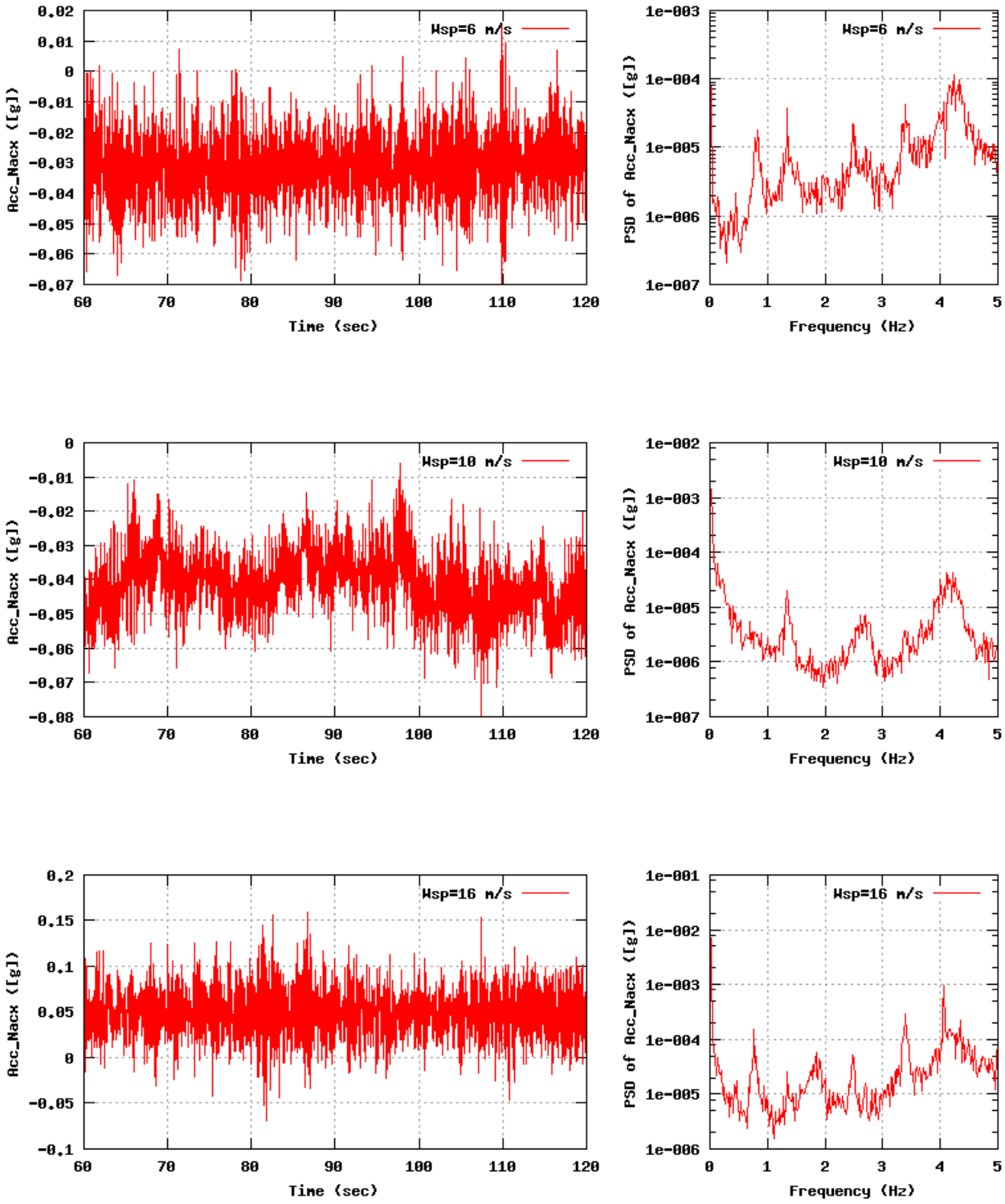

Figure 26b, Sensor 103: Acceleration nacelle leeward Acc_Nacx versus time and frequency
Input files: m06.asc, m10.asc, m16.asc, m06.psd, m10.psd and m16.psd

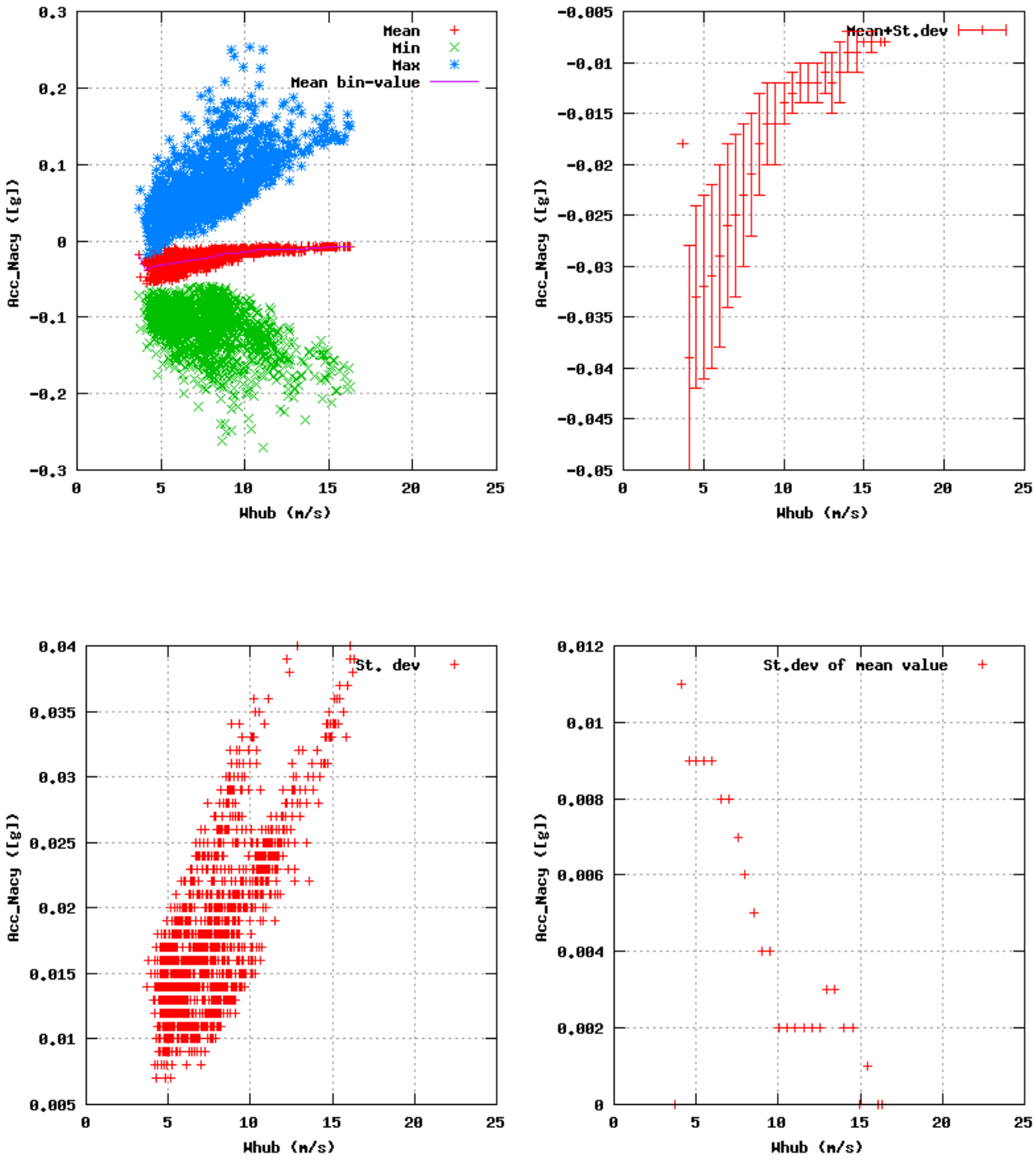

Figure 27a, Sensor 107: Acceleration nacelle leeward Acc_Nacy versus wind speed
Input files: ntk500res.dat, stat_107.dat

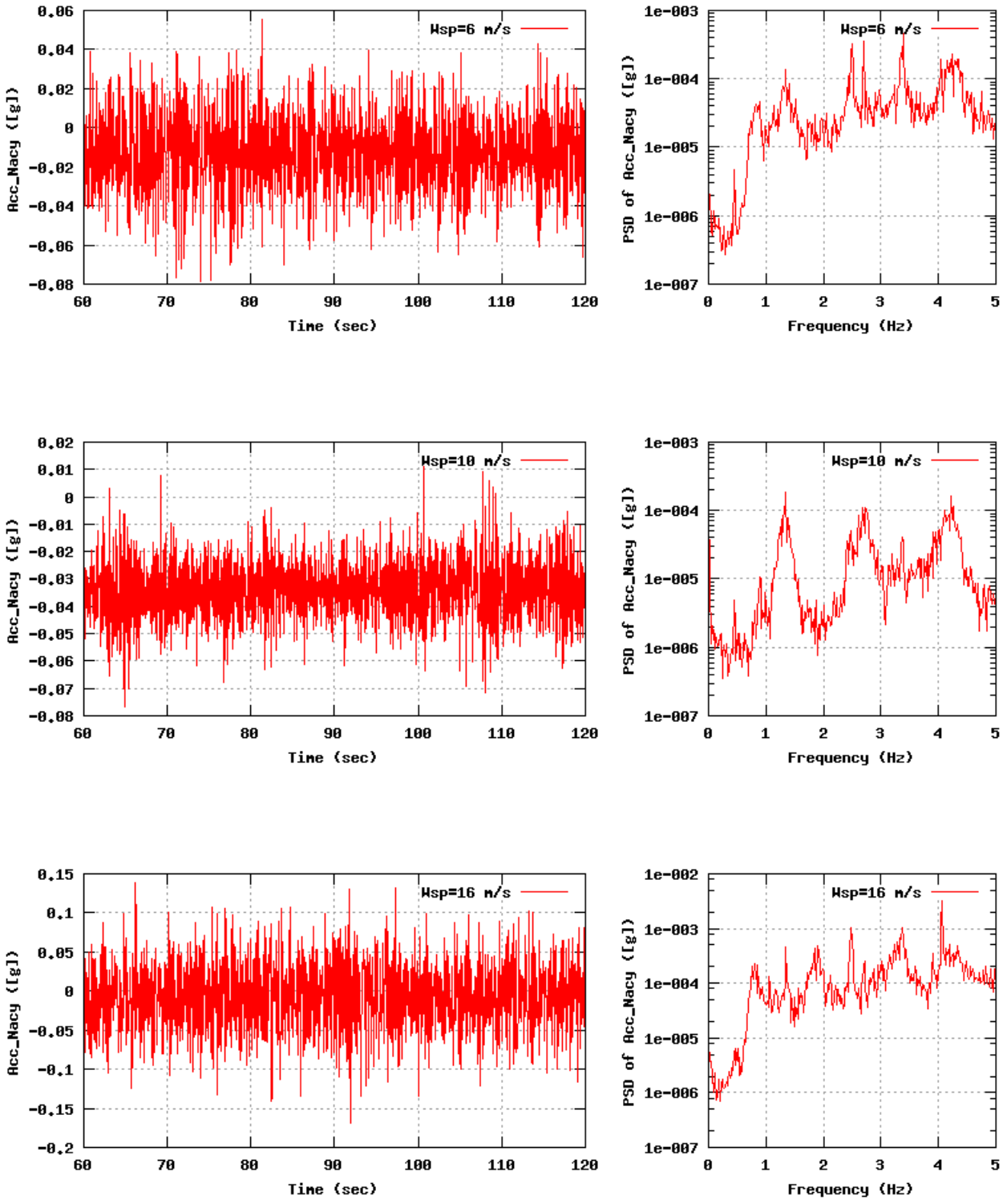

Figure 27b, Sensor 107: Acceleration nacelle leeward Acc_Nacy versus time and frequency
Input files: m06.asc, m10.asc, m16.asc, m06.psd, m10.psd and m16.psd

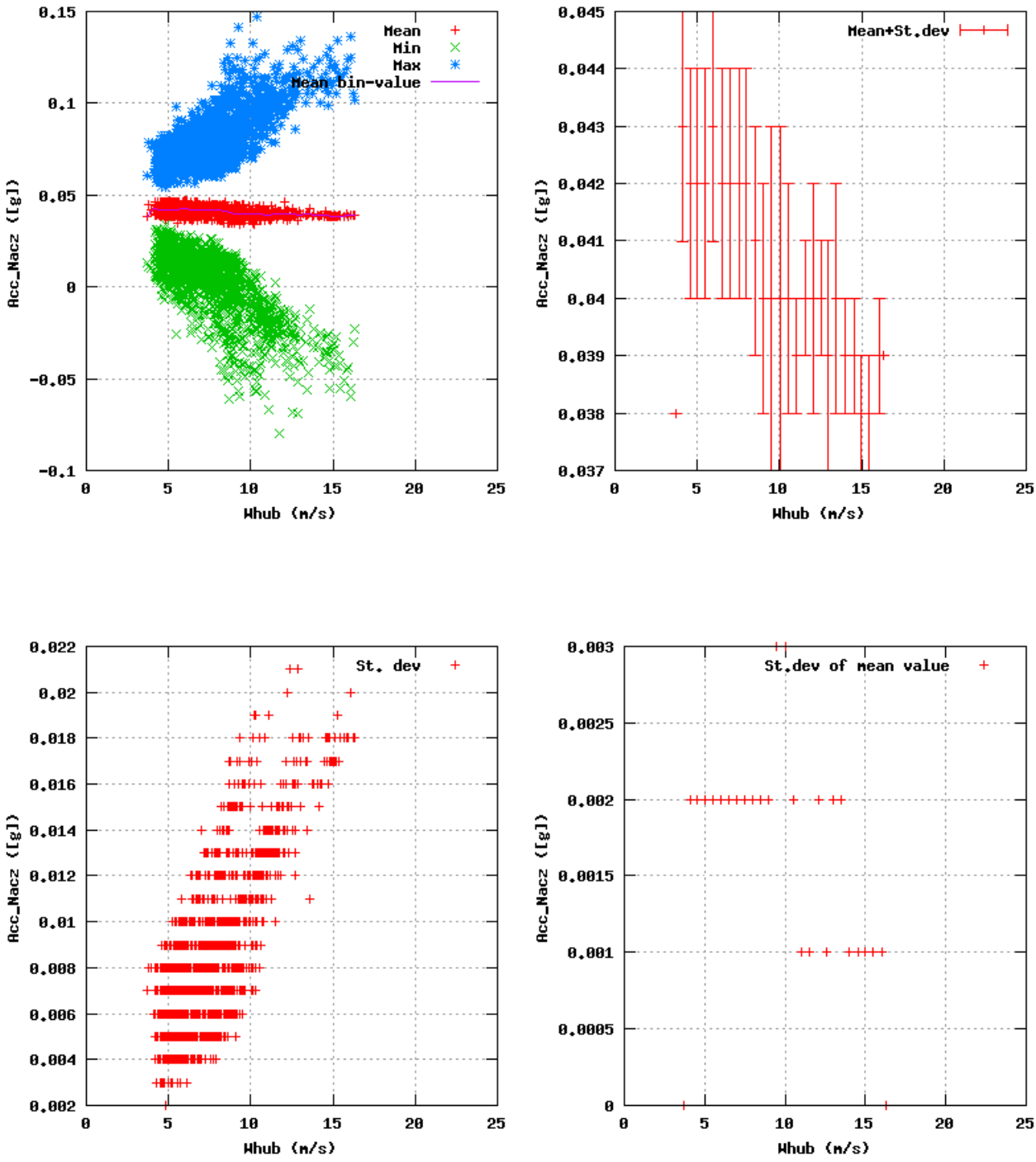

Figure 28a, Sensor 111: Acceleration nacelle leeward Acc_Nacz versus wind speed
Input files: ntk500res.dat, stat_111.dat

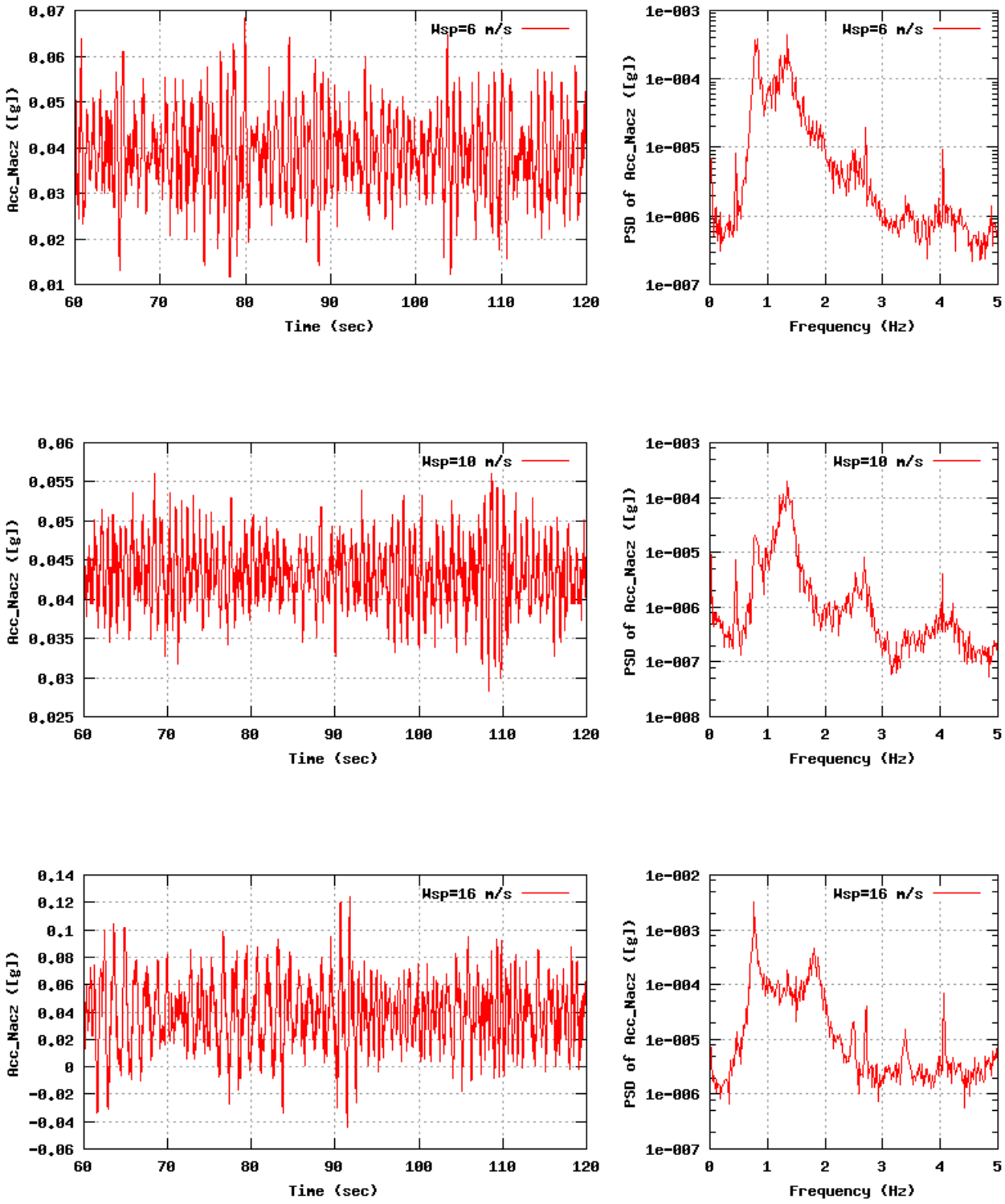

Figure 28b, Sensor 111: Acceleration nacelle leeward Acc_Nacz versus time and frequency
Input files: m06.asc, m10.asc, m16.asc, m06.psd, m10.psd and m16.psd

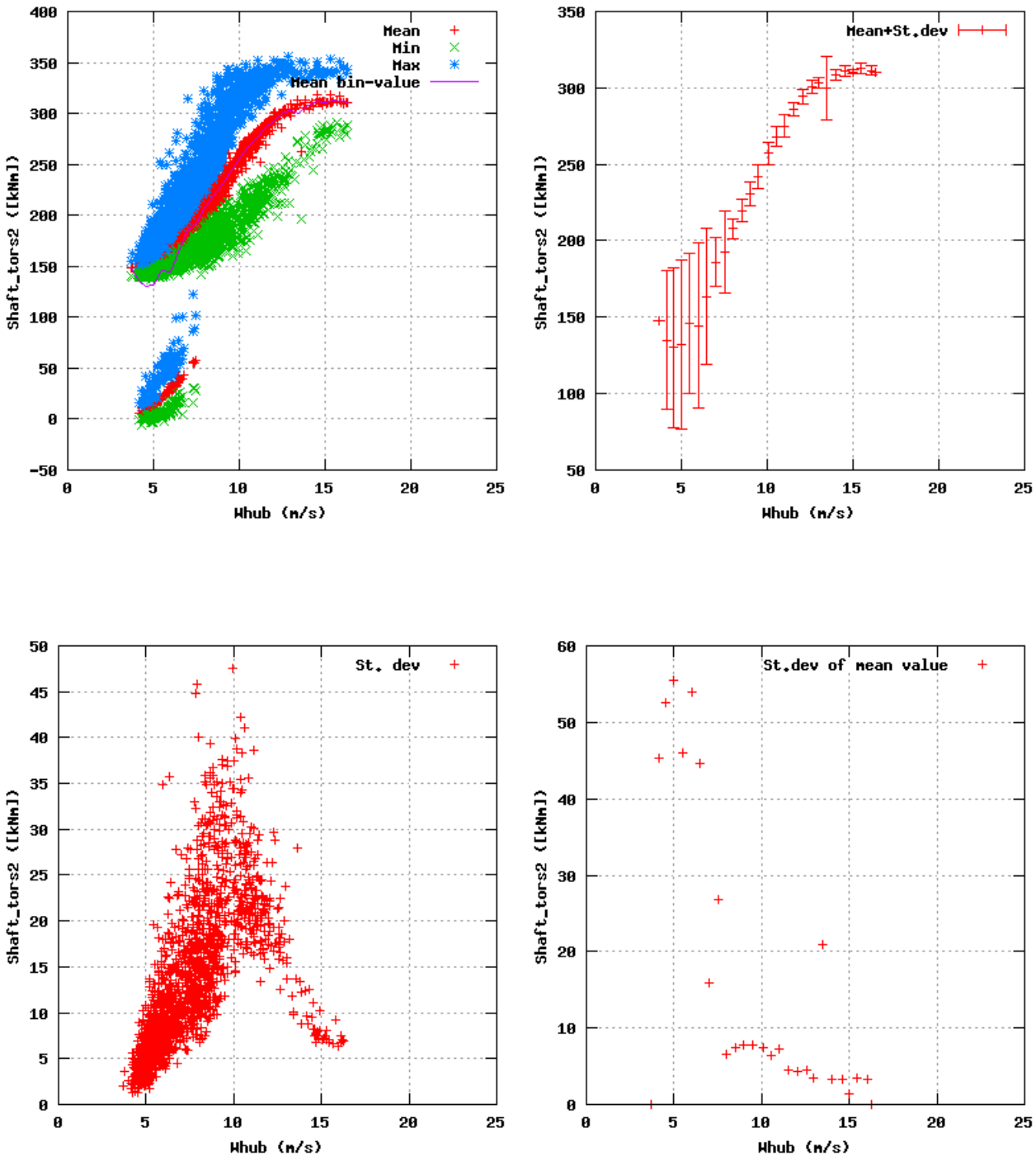

Figure 29a, Sensor 115: Rotor shaft torsion into gearbox Shaft_tors2 LSS versus wind speed
Input files: ntk500res.dat, stat_115.dat

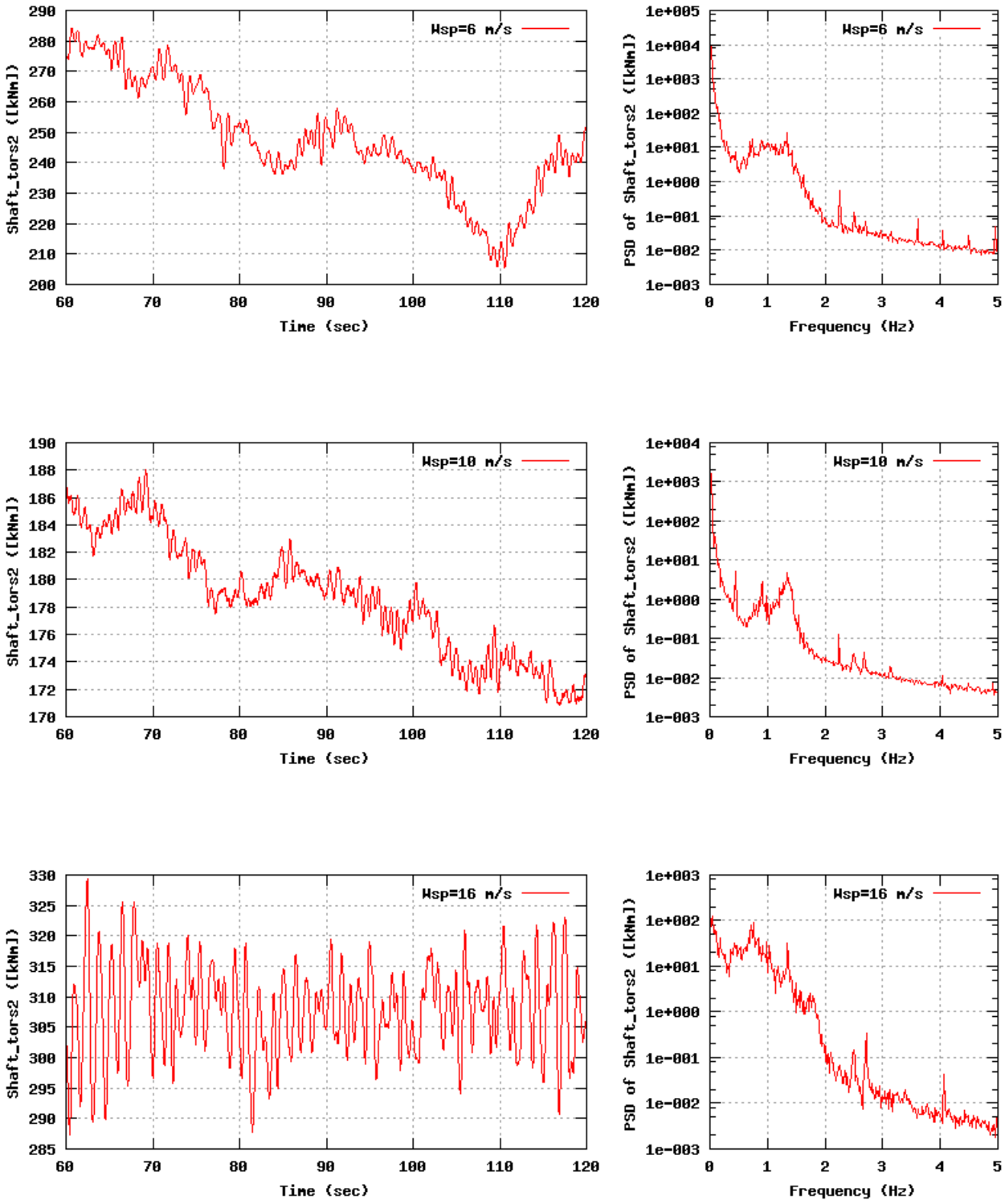

Figure 29b, Sensor 115: Rotor shaft torsion into gearbox Shaft_tors2 LSS versus time and frequency
Input files: m06.asc, m10.asc, m16.asc, m06.psd, m10.psd and m16.psd

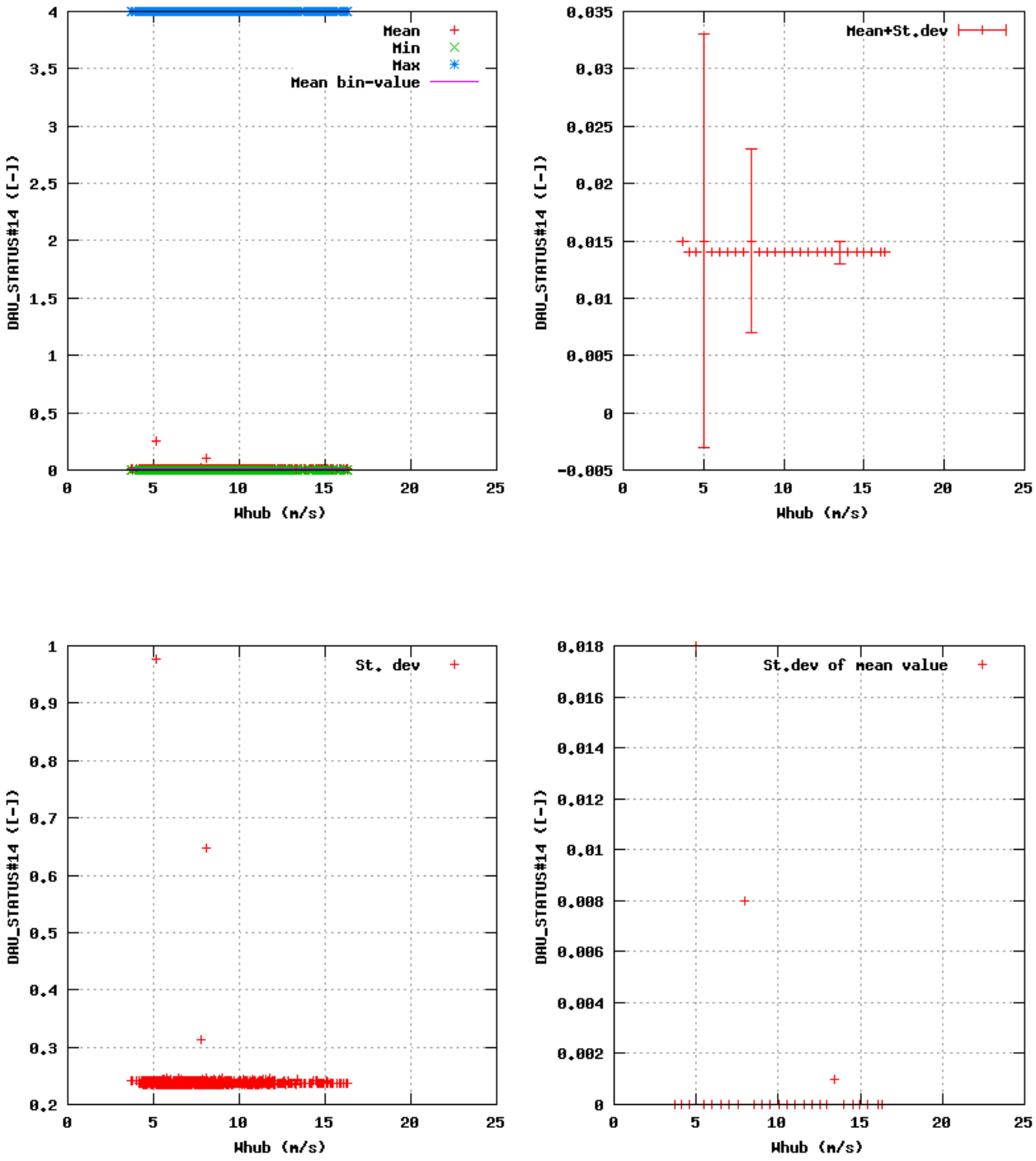

Figure 30a, Sensor 119: DAU_STATUS#14 versus wind speed
Input files: ntk500res.dat, stat_119.dat

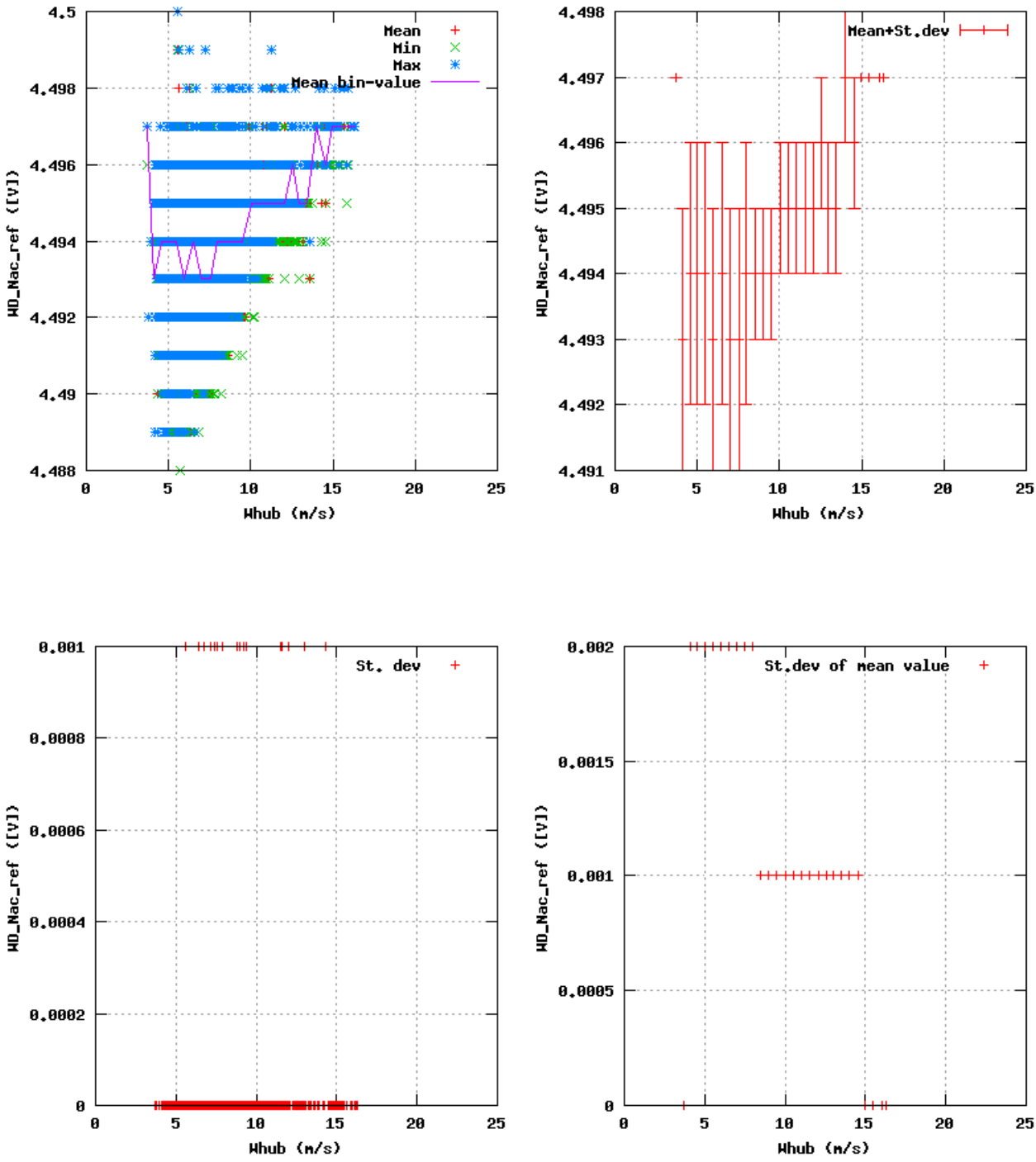

Figure 31a, Sensor 123: Wind direction nacelle WD_Nac_ref versus wind speed
Input files: ntk500res.dat, stat_123.dat

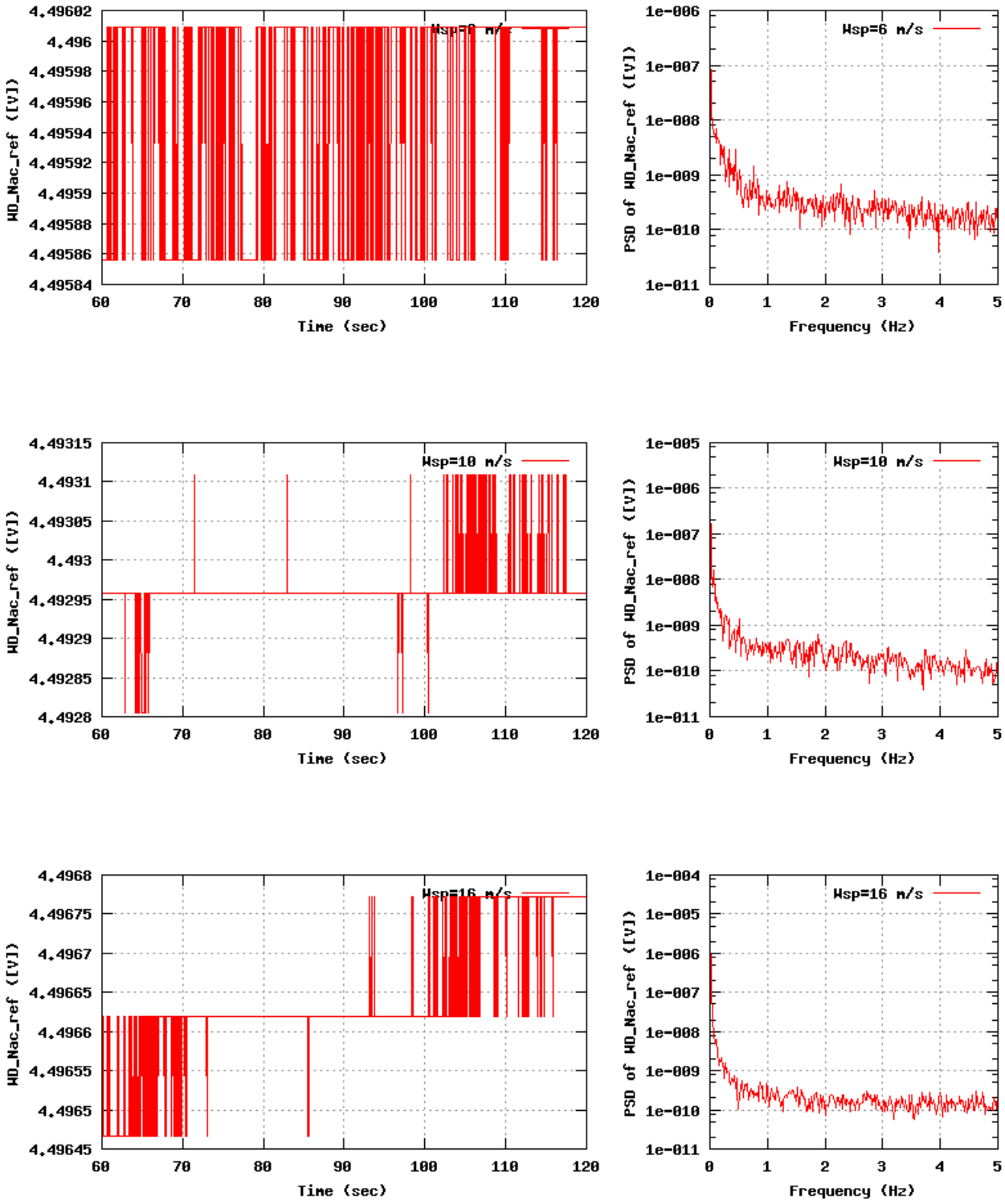

Figure 31b, Sensor 123: Wind direction nacelle WD_Nac_ref versus time and frequency
Input files: m06.asc, m10.asc, m16.asc, m06.psd, m10.psd and m16.psd

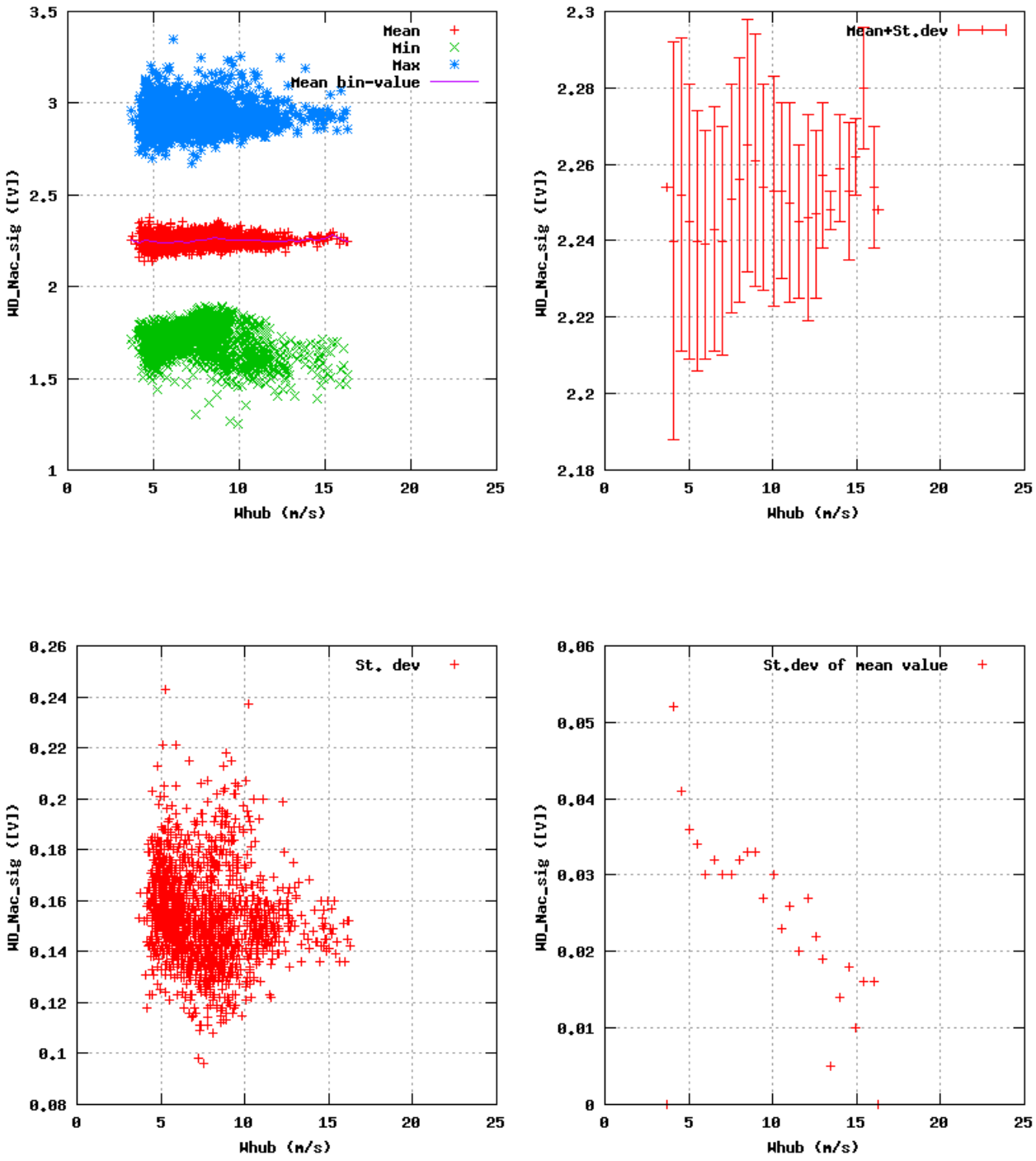

Figure 32a, Sensor 127: Wind direction nacelle WD_Nac_sig versus wind speed
Input files: ntk500res.dat, stat_127.dat

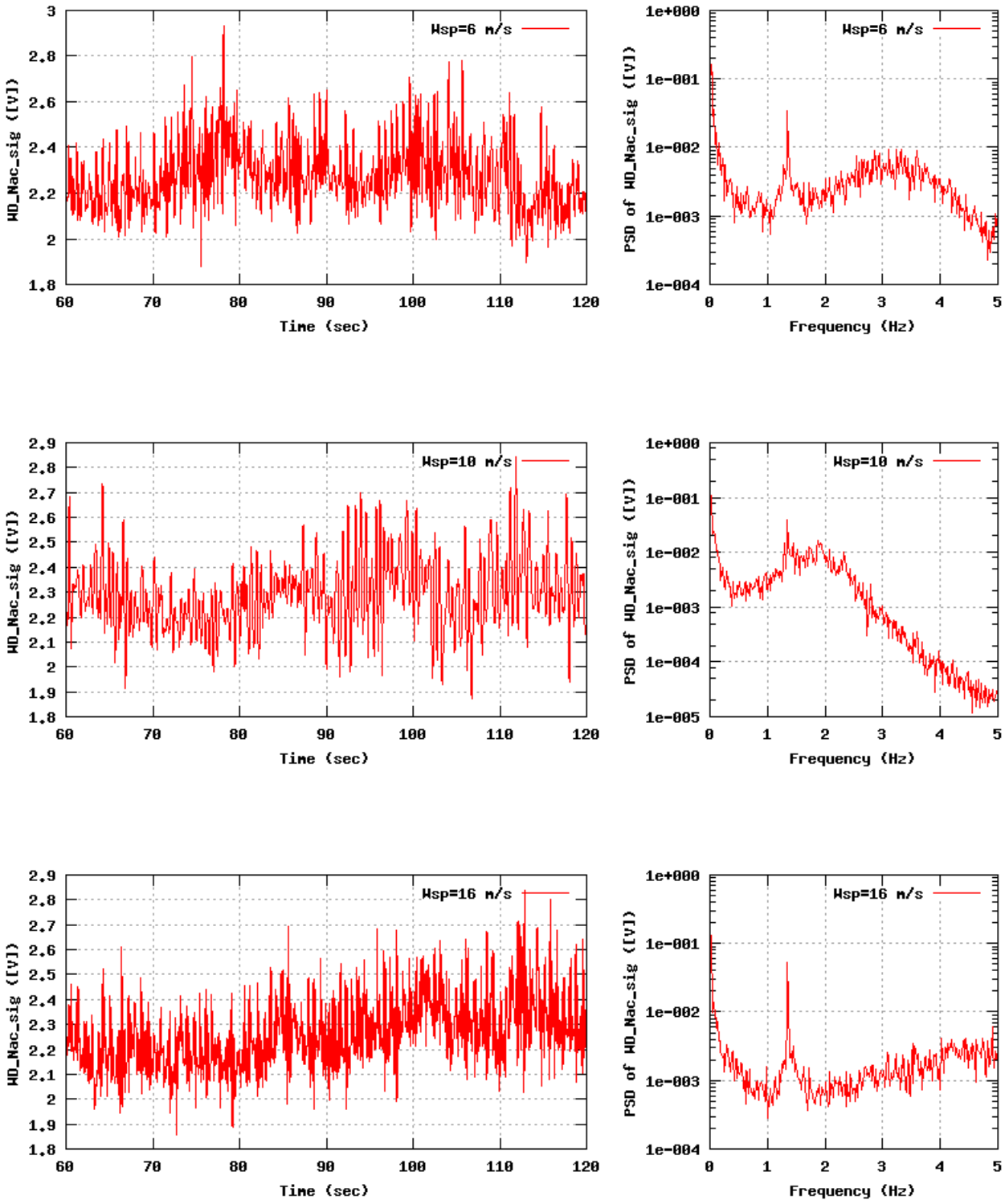

Figure 32b, Sensor 127: Wind direction nacelle WD_Nac_sig versus time and frequency
Input files: m06.asc, m10.asc, m16.asc, m06.psd, m10.psd and m16.psd

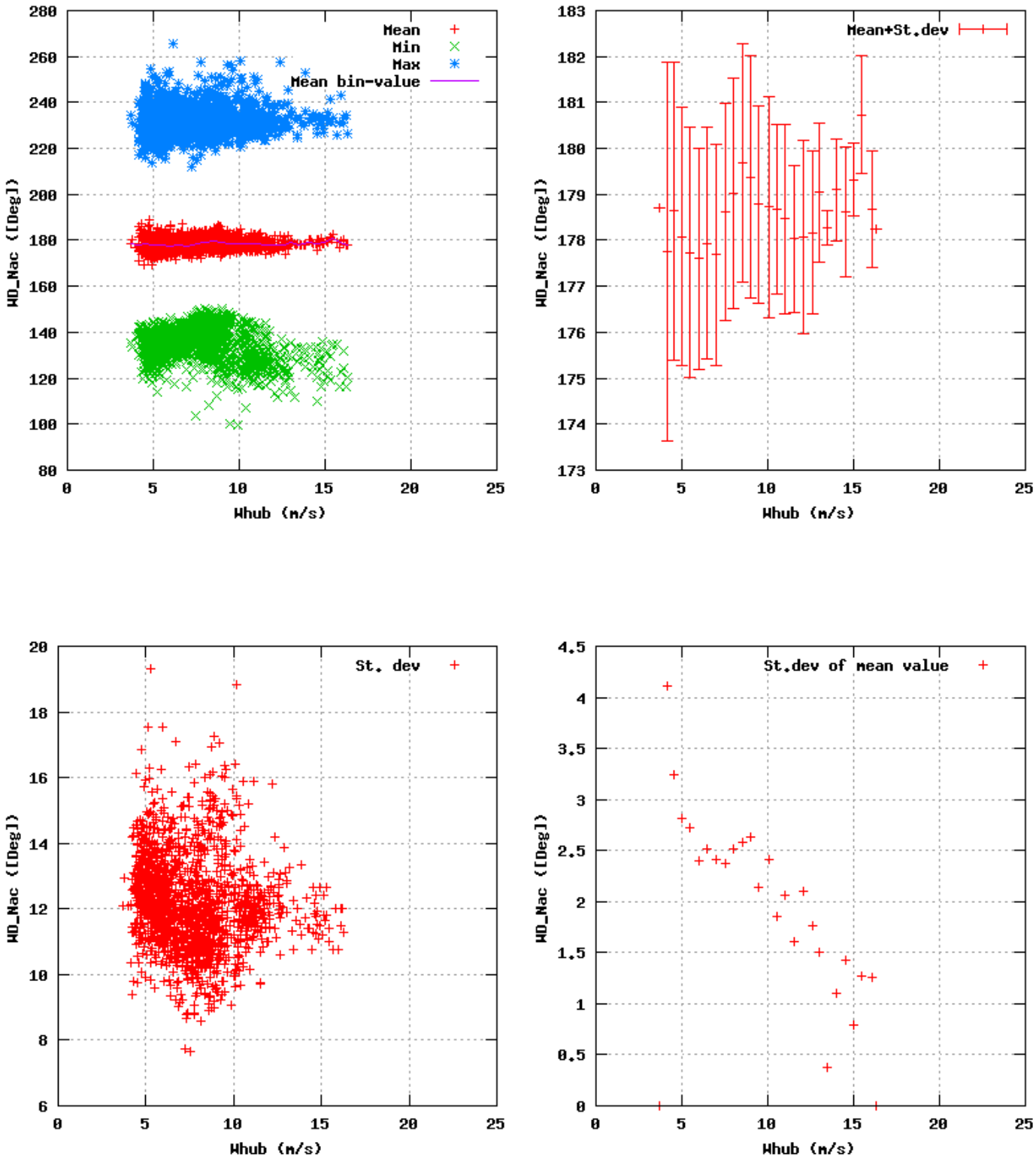

Figure 33a, Sensor 131: Wind direction nacelle versus wind speed
Input files: ntk500res.dat, stat_131.dat

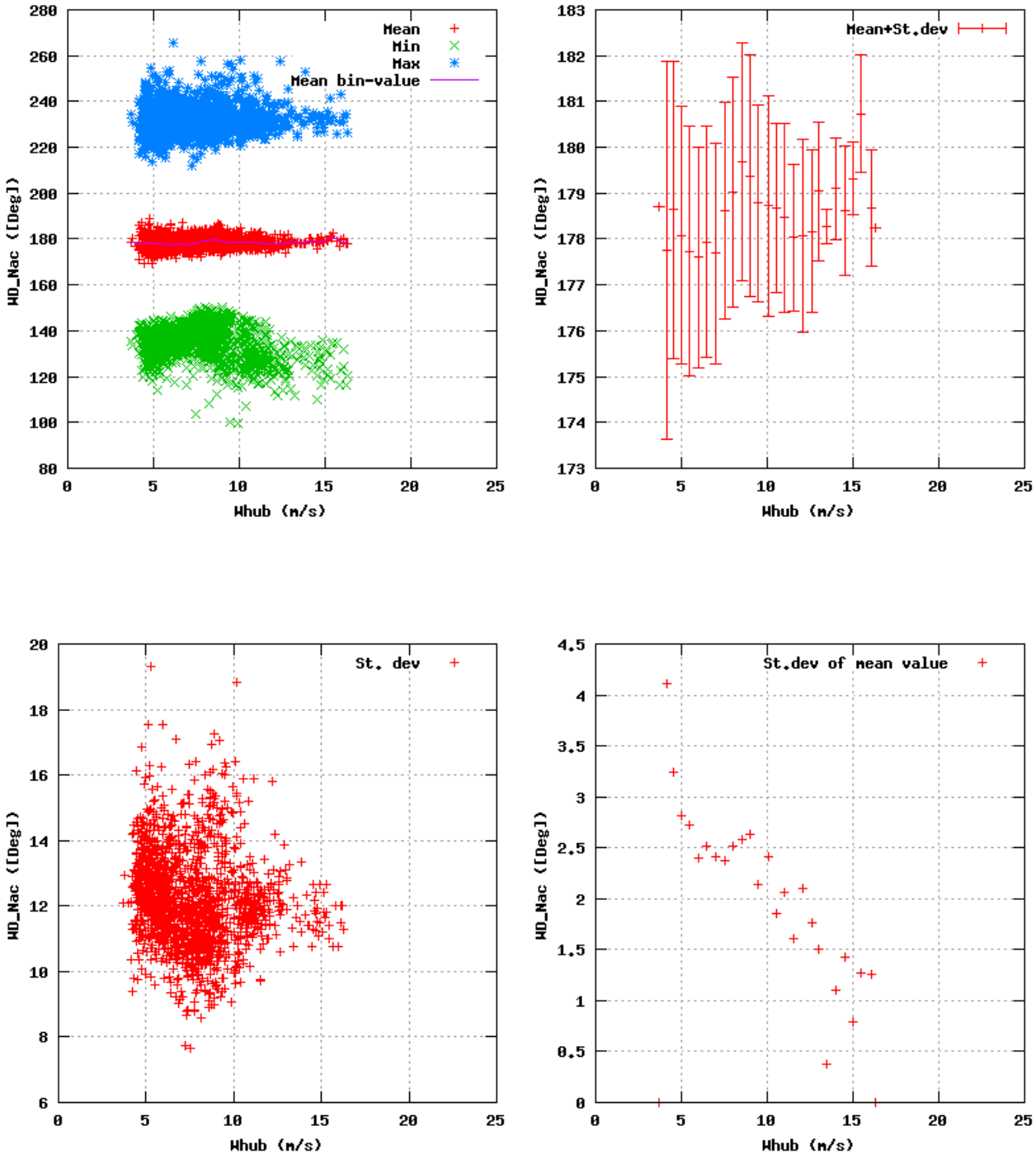

Figure 33a, Sensor 131: Wind direction nacelle versus wind speed
Input files: ntk500res.dat, stat_131.dat

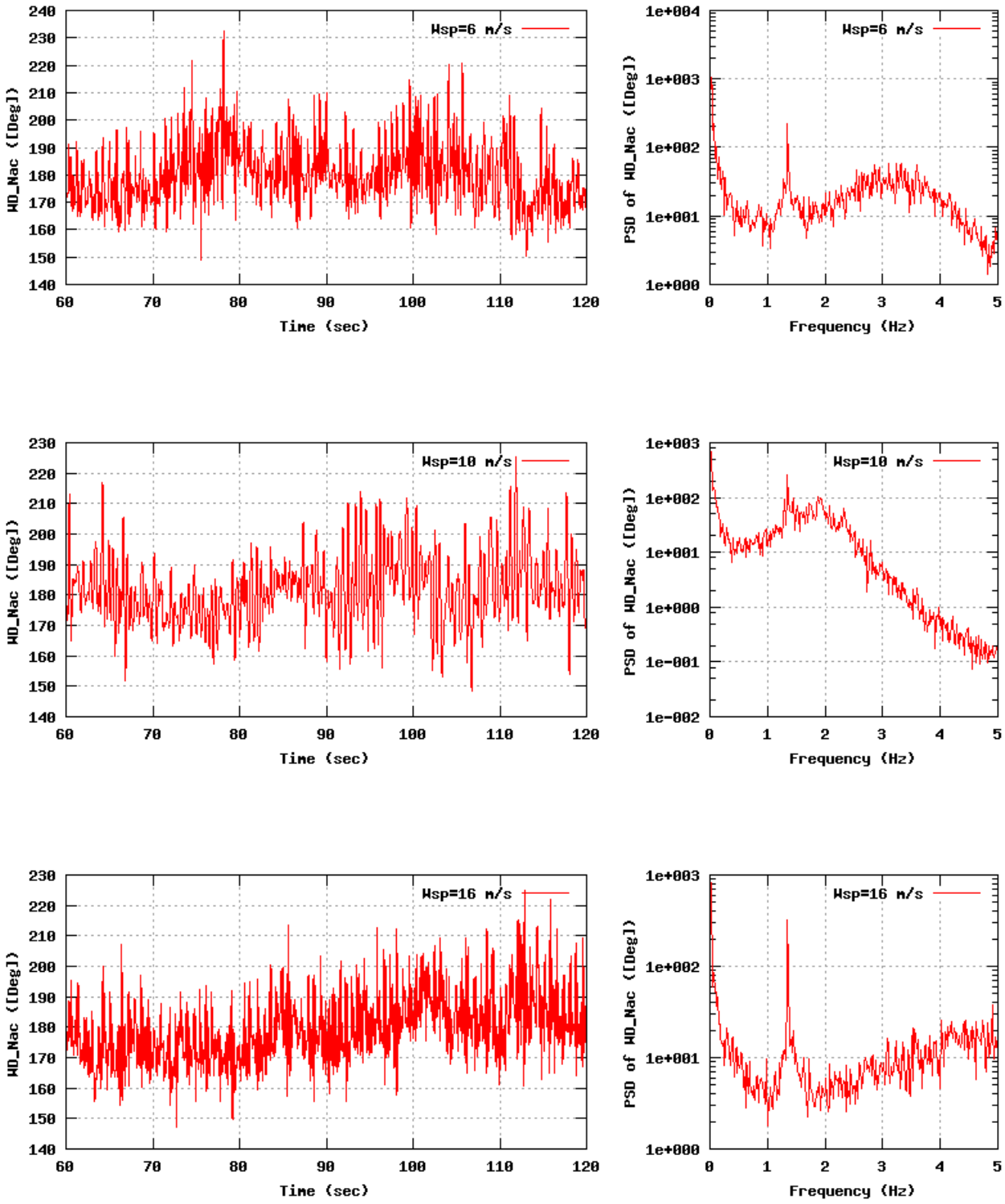

Figure 33b, Sensor 131: Wind direction nacelle versus time and frequency
Input files: m06.asc, m10.asc, m16.asc, m06.psd, m10.psd and m16.psd

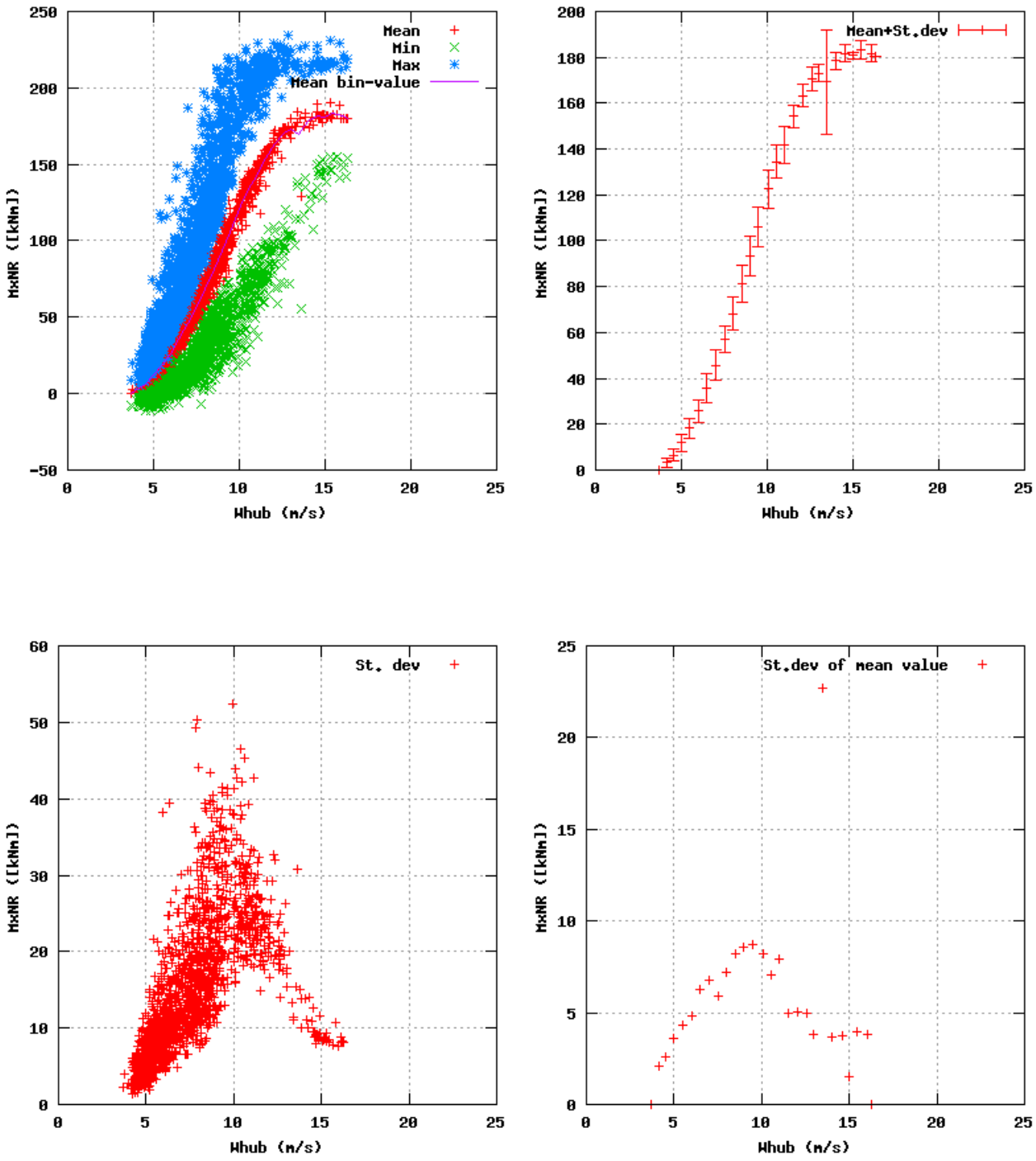

Figure 34a, Sensor 135: Rotor shaft torsion LSS versus wind speed
Input files: ntk500res.dat, stat_135.dat

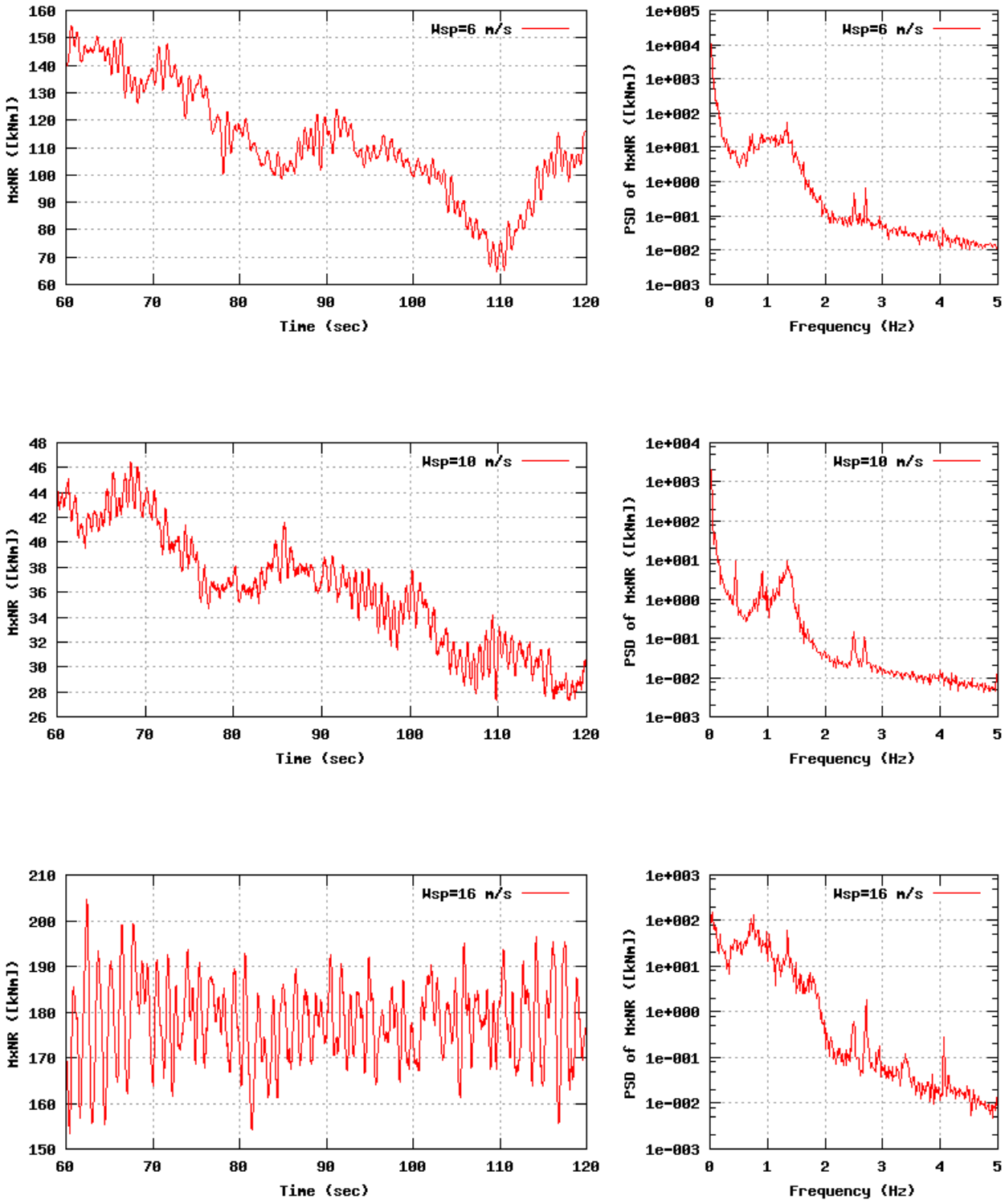

Figure 34b, Sensor 135: Rotor shaft torsion LSS versus time and frequency
Input files: m06.asc, m10.asc, m16.asc, m06.psd, m10.psd and m16.psd

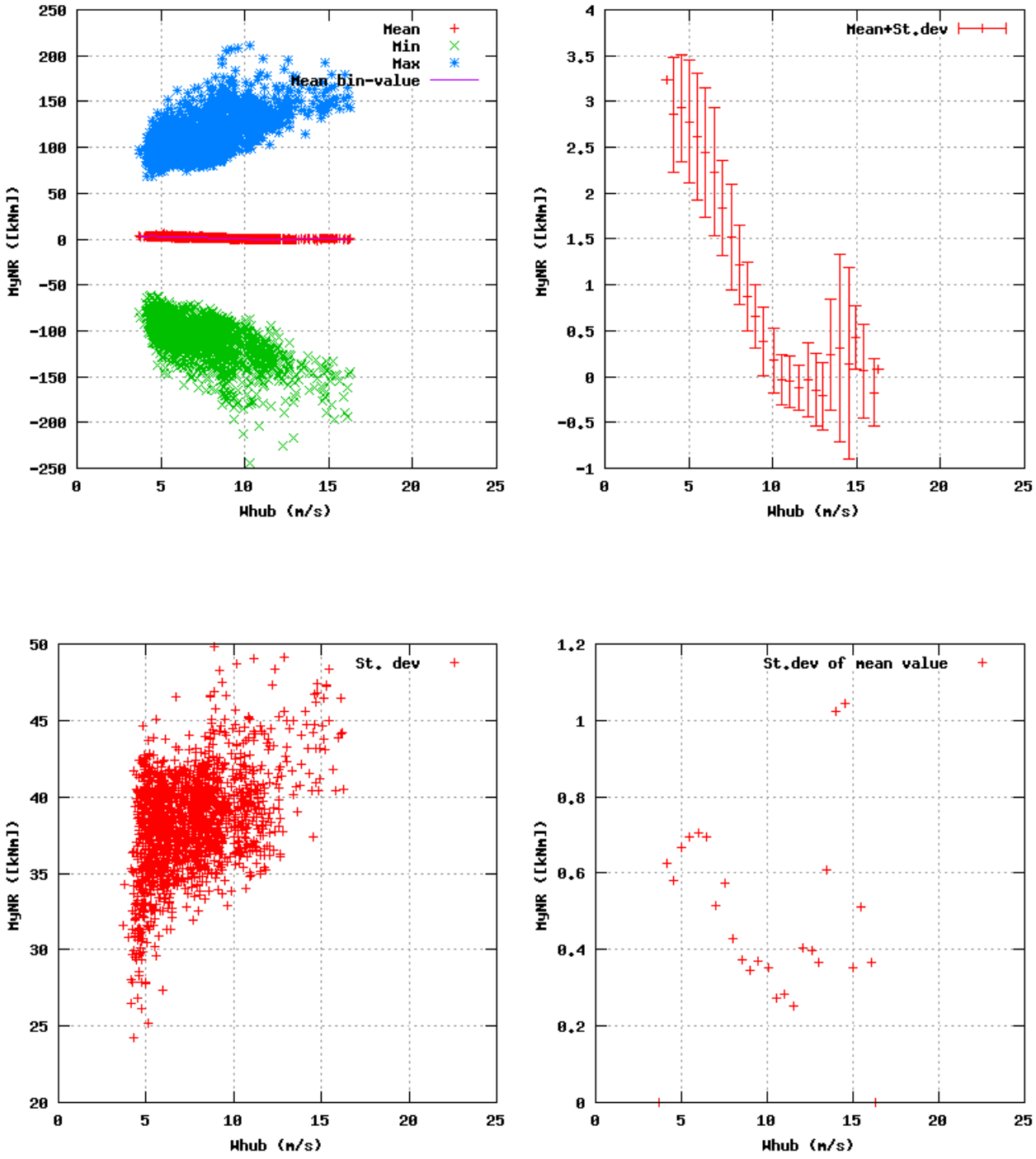

Figure 35a, Sensor 139: Rotor shaft bending moment y versus wind speed
Input files: ntk500res.dat, stat_139.dat

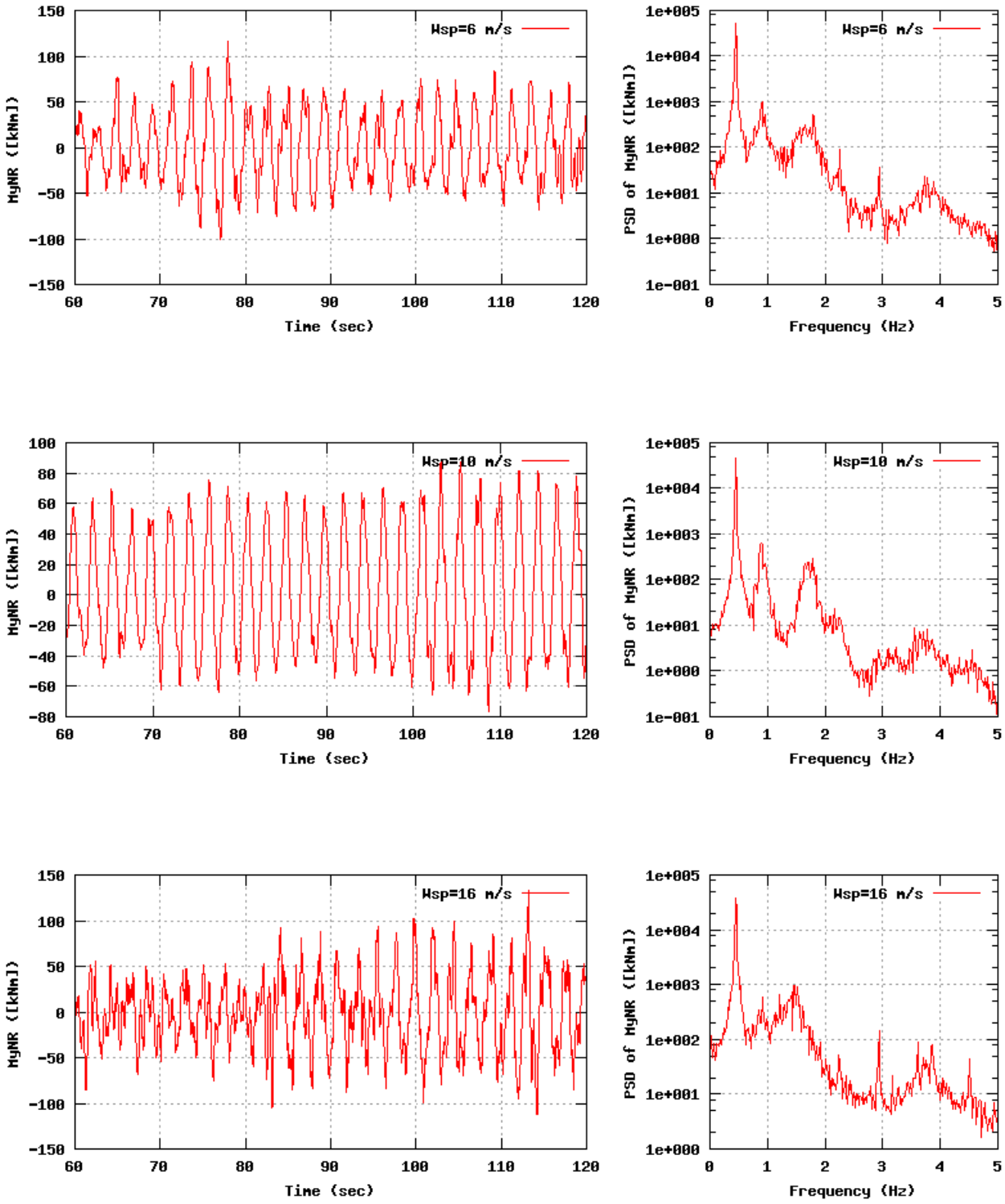

Figure 35b, Sensor 139: Rotor shaft bending moment y versus time and frequency
Input files: m06.asc, m10.asc, m16.asc, m06.psd, m10.psd and m16.psd

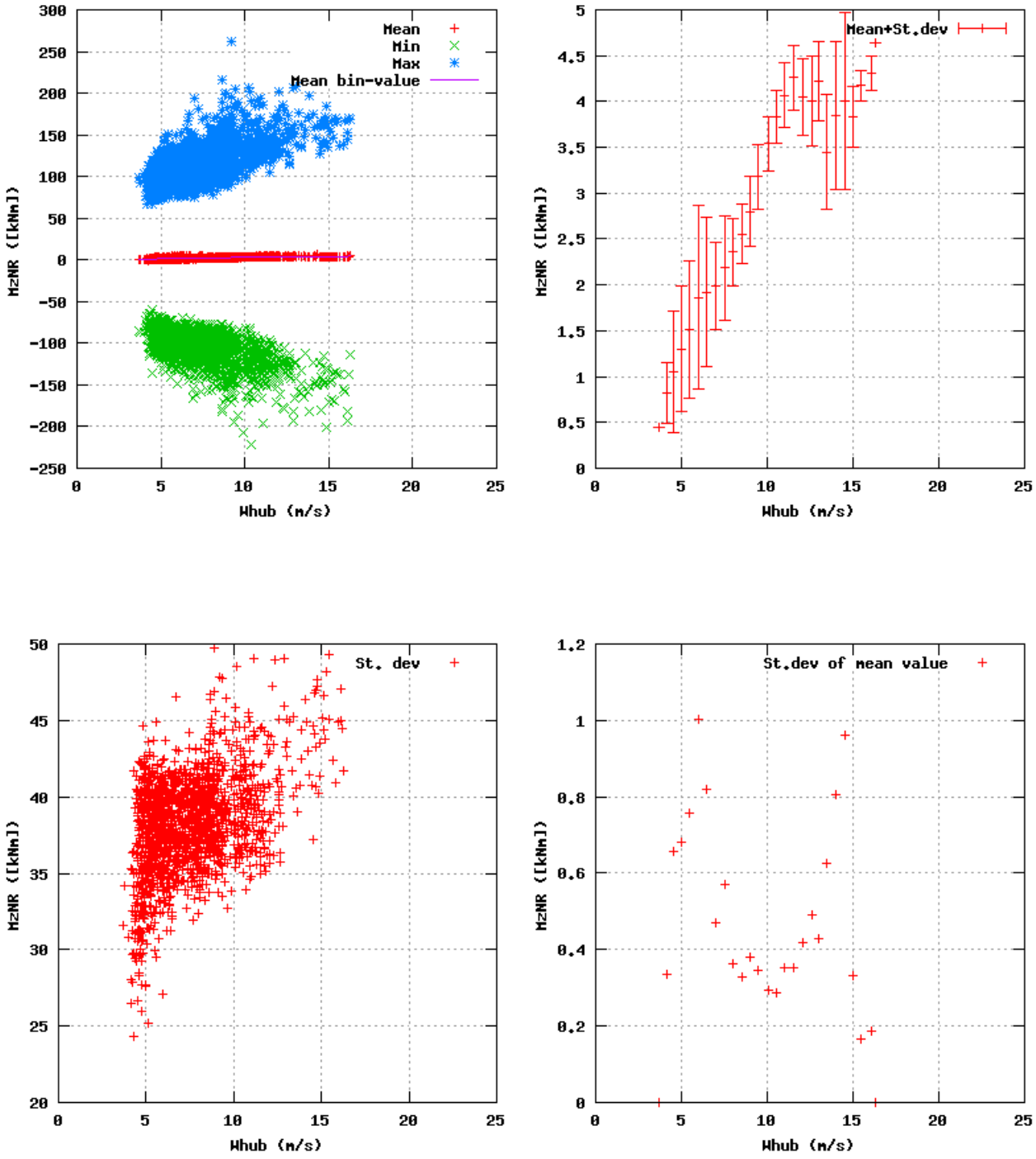

Figure 36a, Sensor 143: Rotor shaft bending moment z versus wind speed
Input files: ntk500res.dat, stat_143.dat

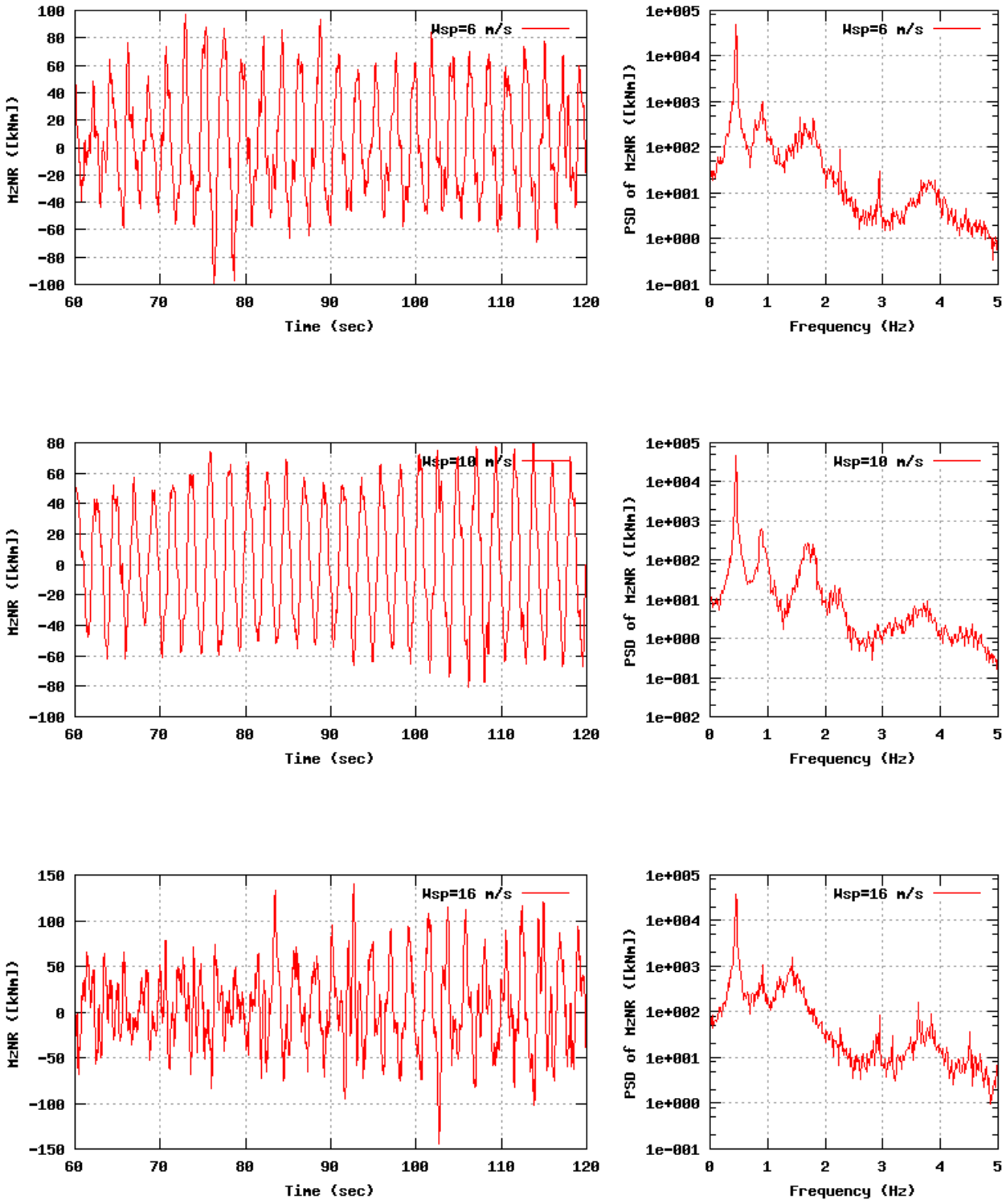

Figure 36b, Sensor 143: Rotor shaft bending moment z versus time and frequency
Input files: m06.asc, m10.asc, m16.asc, m06.psd, m10.psd and m16.psd

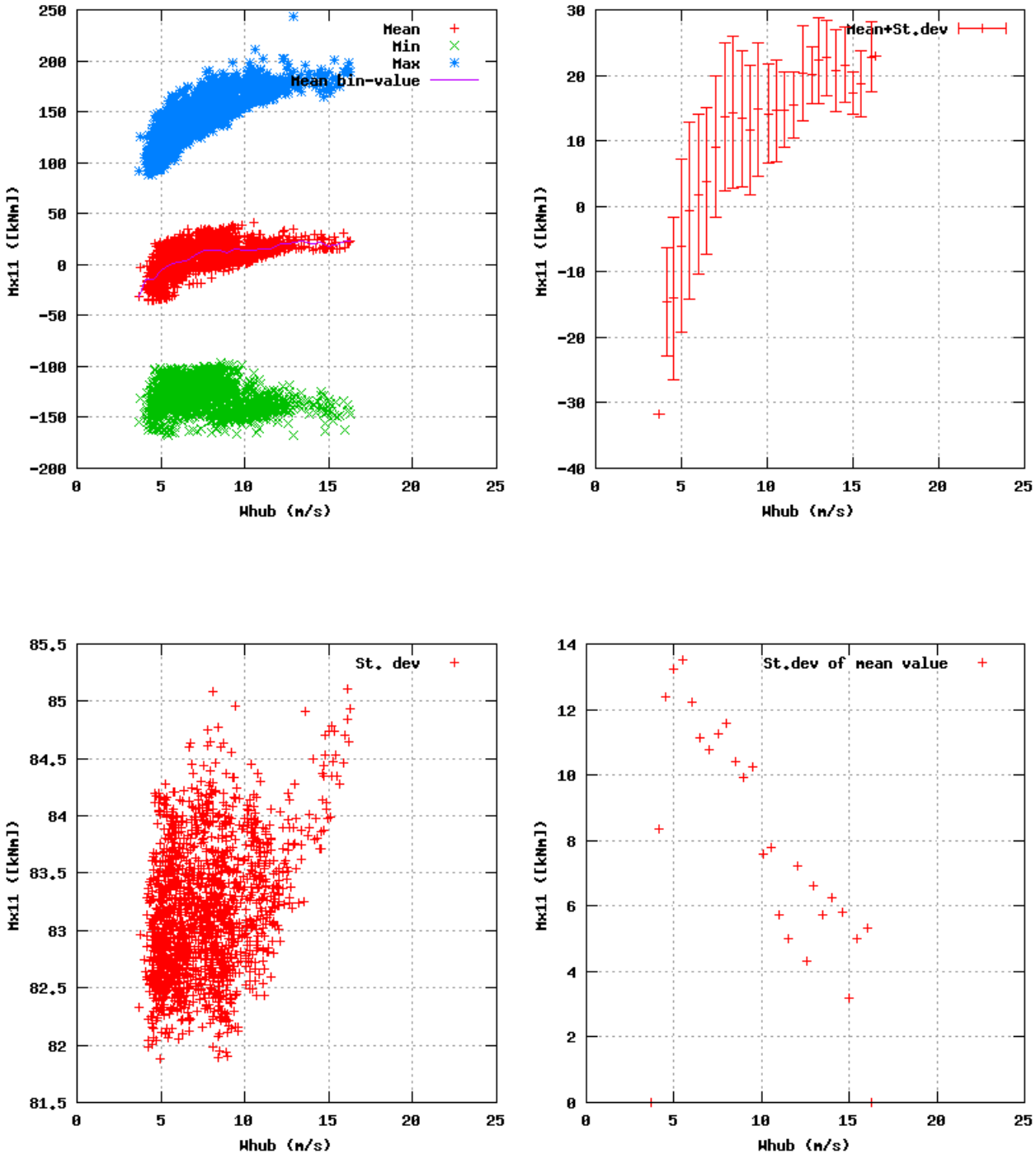

Figure 37a, Sensor 147: Edge bending moment B1 r=2.1m versus wind speed
Input files: ntk500res.dat, stat_147.dat

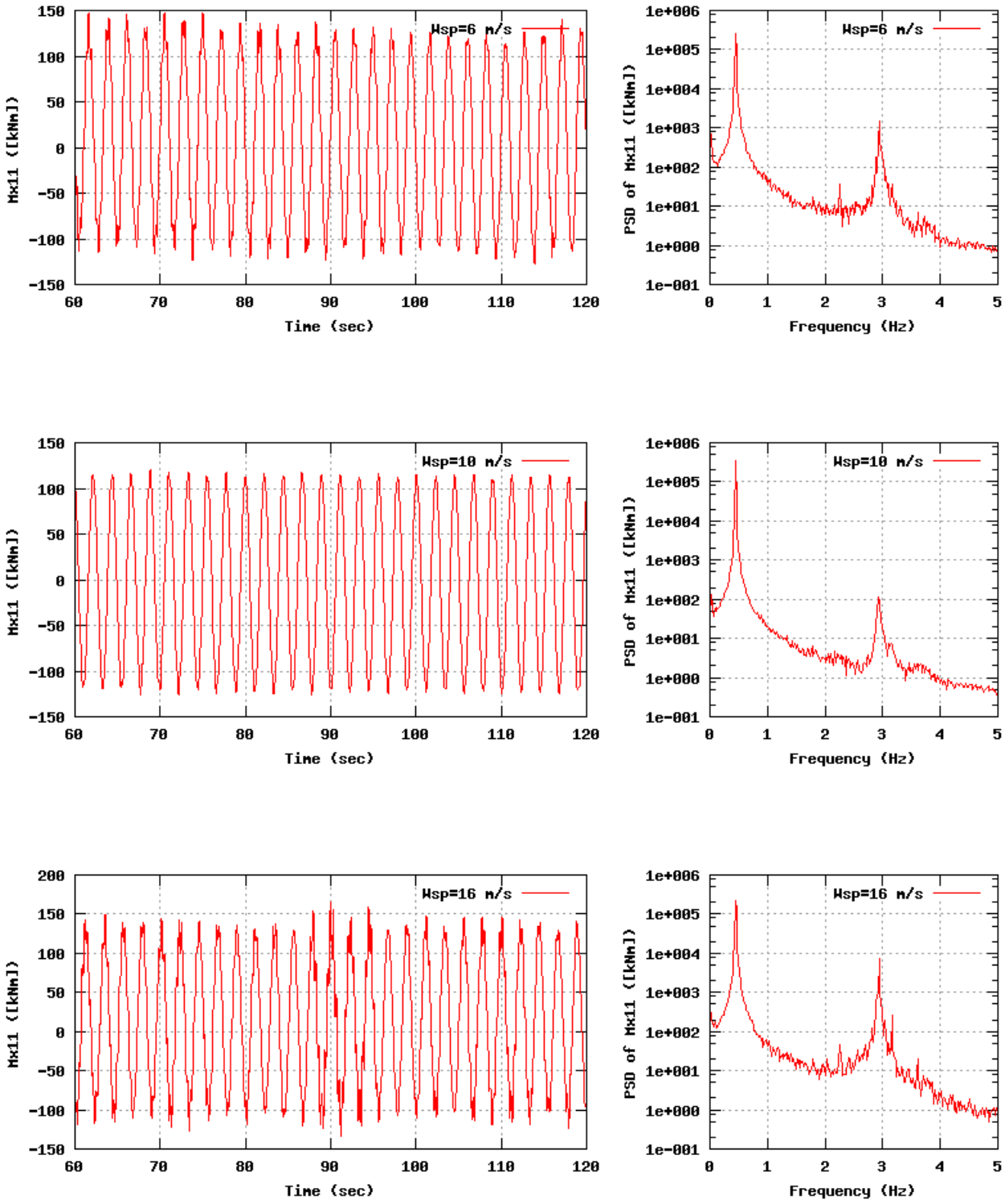

Figure 37b, Sensor 147: Edge bending moment B1 r=2.1m versus time and frequency
Input files: m06.asc, m10.asc, m16.asc, m06.psd, m10.psd and m16.psd

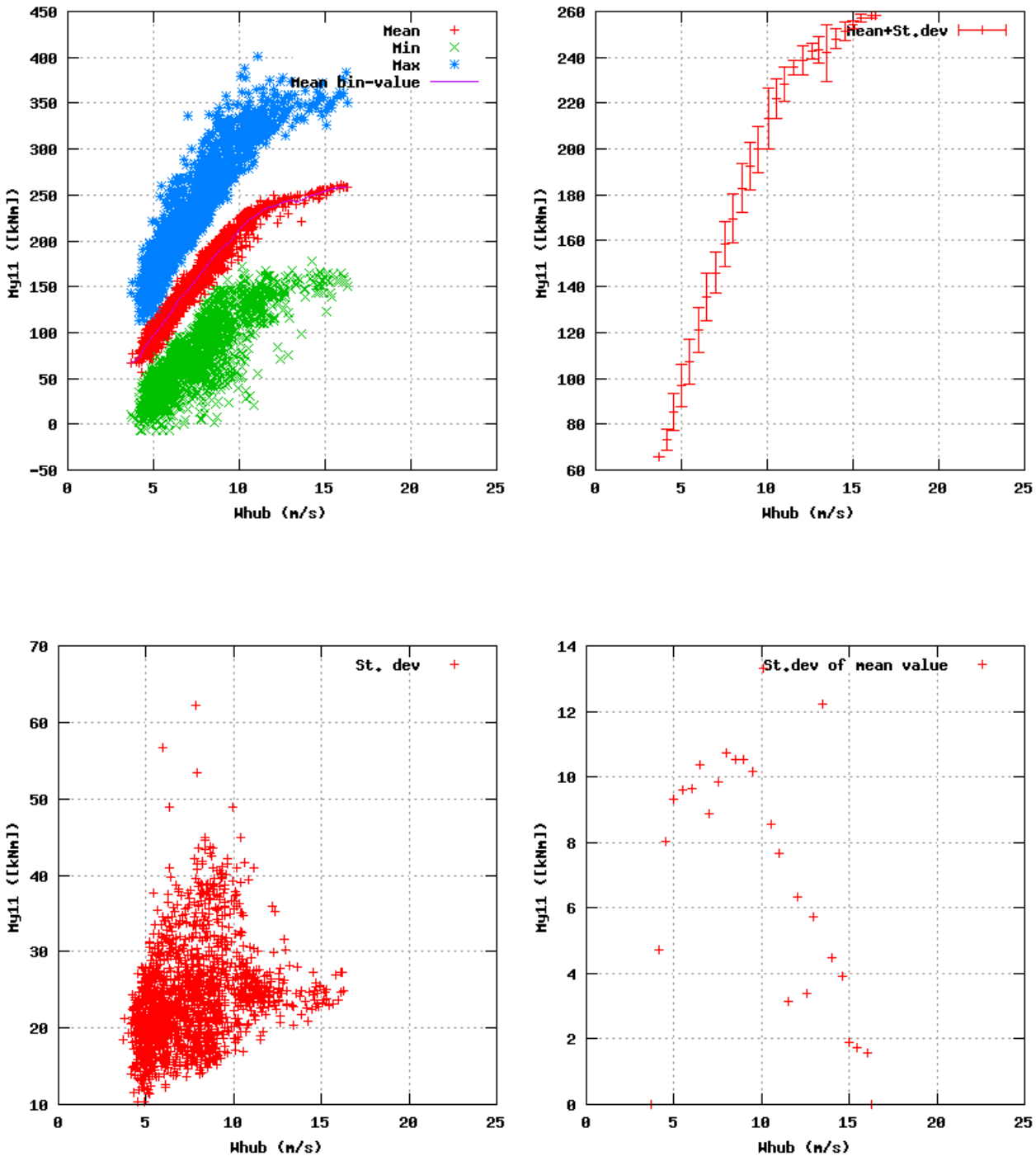

Figure 38a, Sensor 151: Flap bending moment B1 r=2.1m versus wind speed
Input files: ntk500res.dat, stat_151.dat

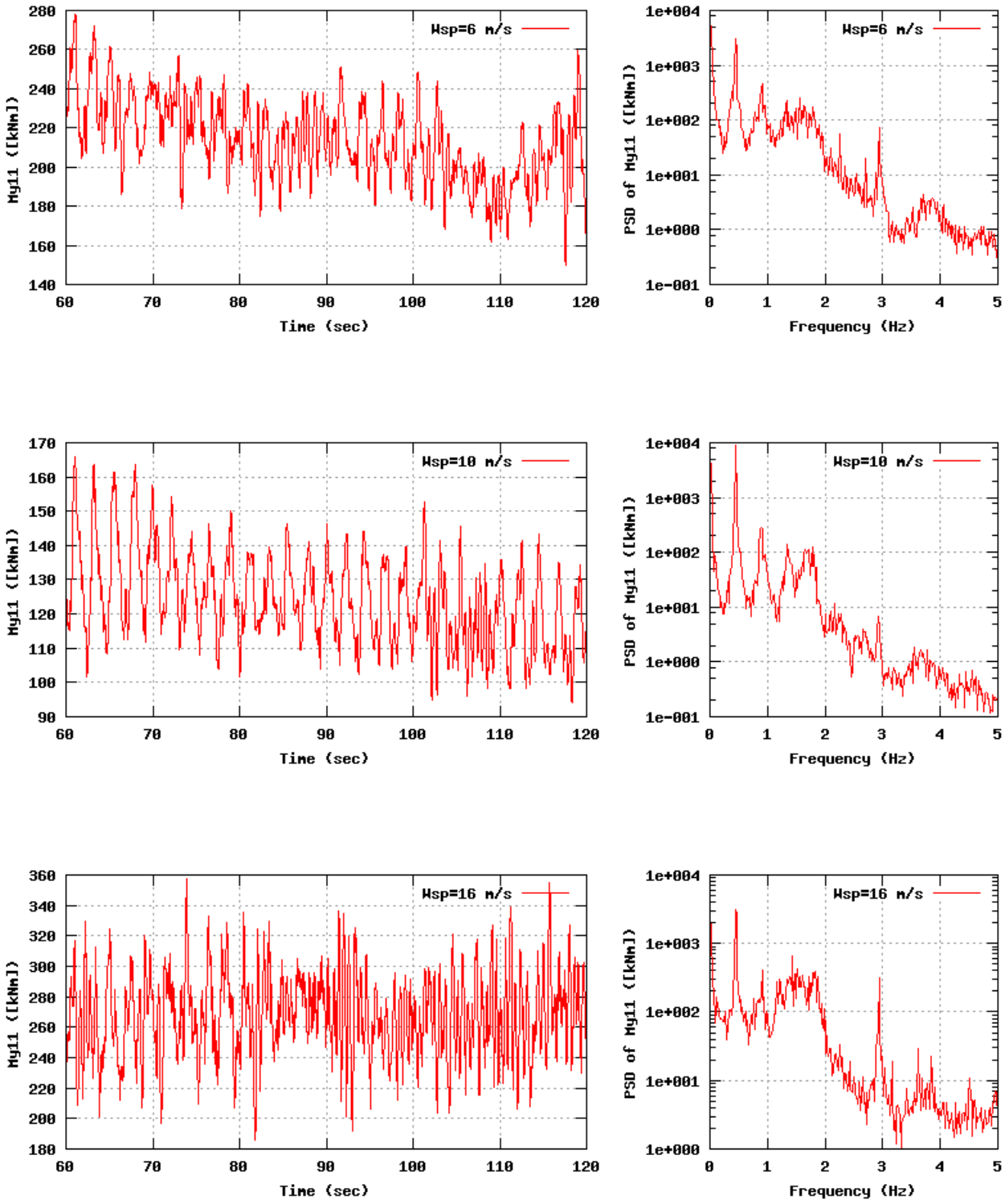

Figure 38b, Sensor 151: Flap bending moment B1 r=2.1m versus time and frequency
Input files: m06.asc, m10.asc, m16.asc, m06.psd, m10.psd and m16.psd

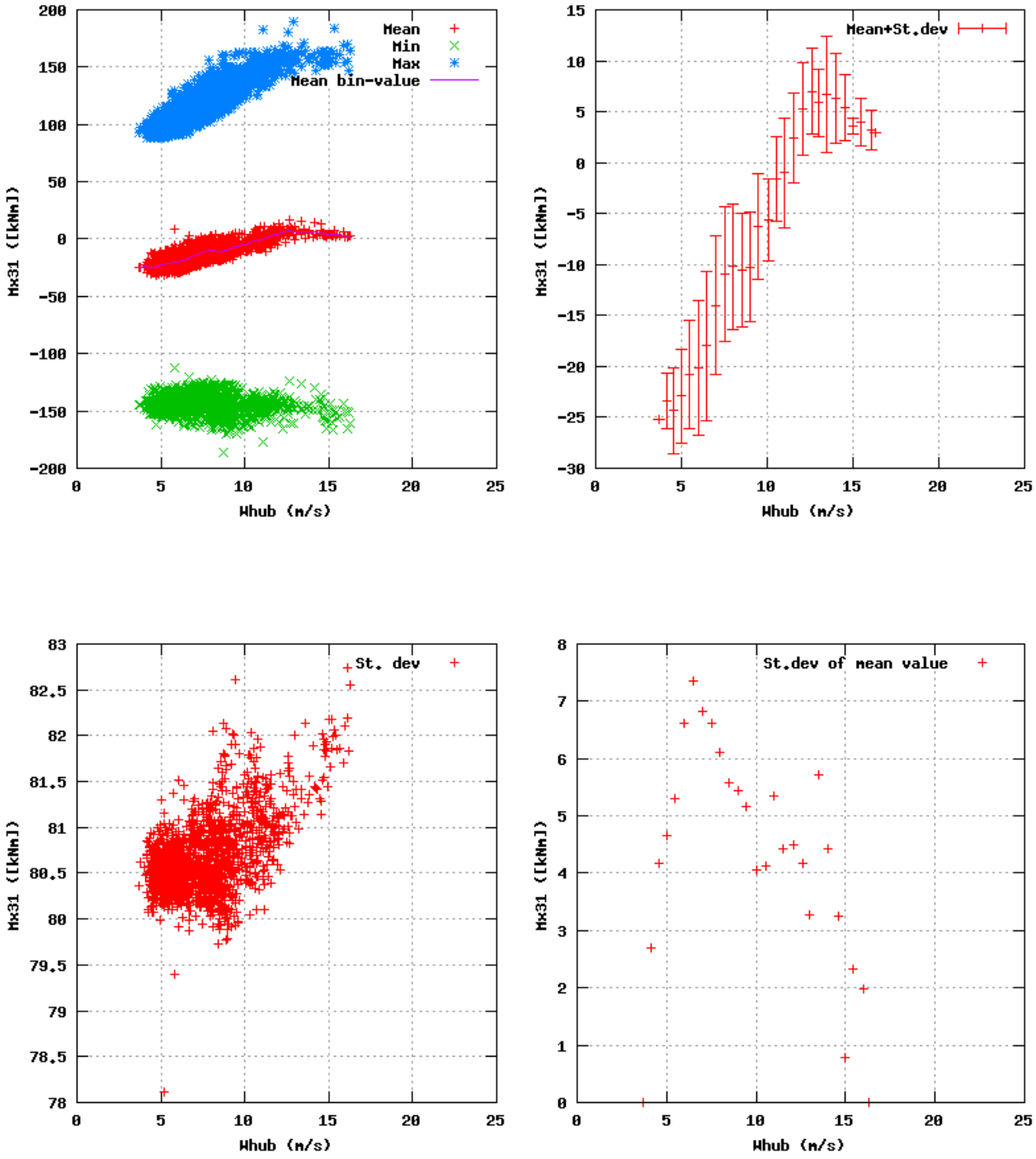

Figure 39a, Sensor 155: Edge bending moment B3 r=2.1m versus wind speed
Input files: ntk500res.dat, stat_155.dat

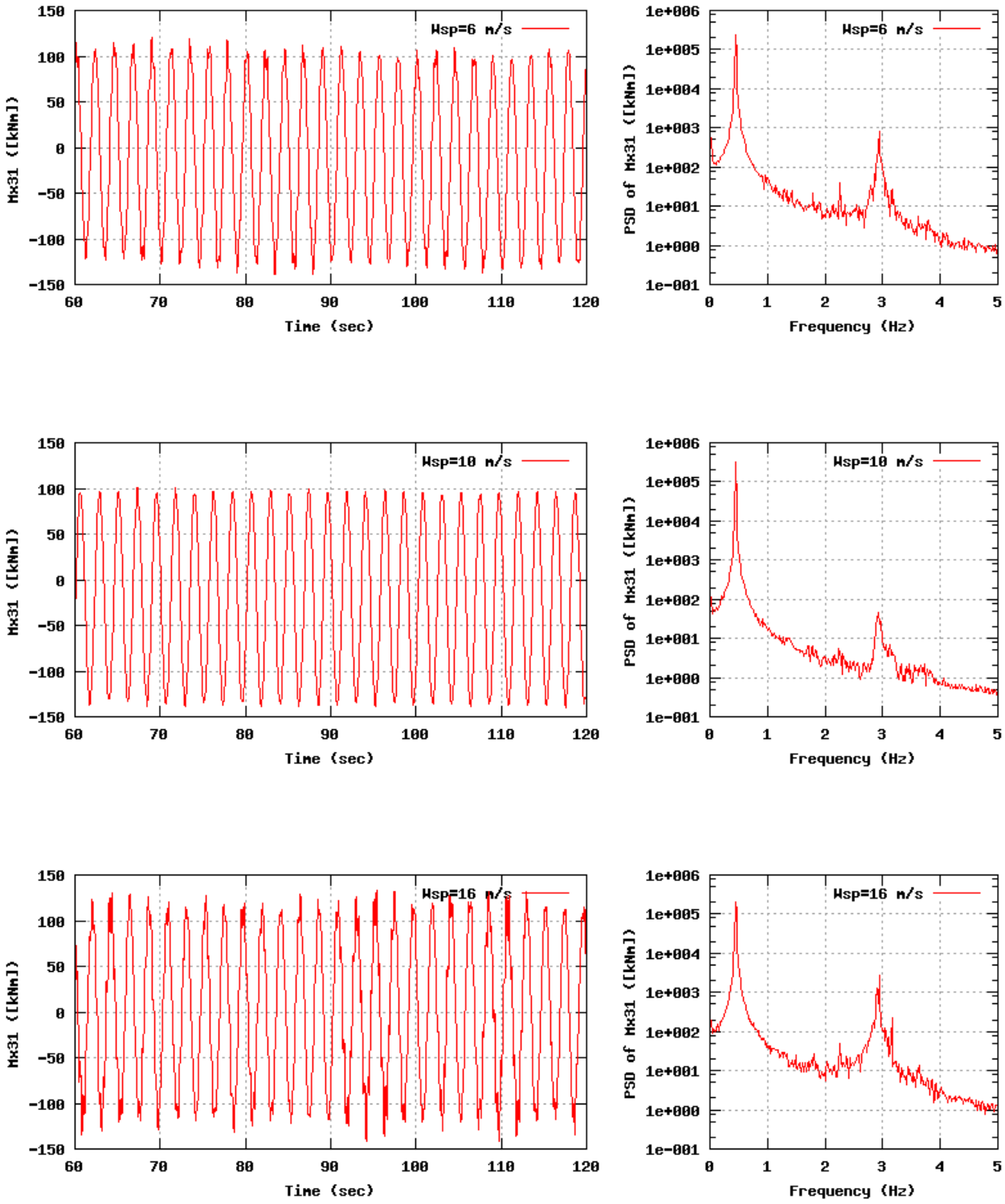

Figure 39b, Sensor 155: Edge bending moment B3 r=2.1m versus time and frequency
Input files: m06.asc, m10.asc, m16.asc, m06.psd, m10.psd and m16.psd

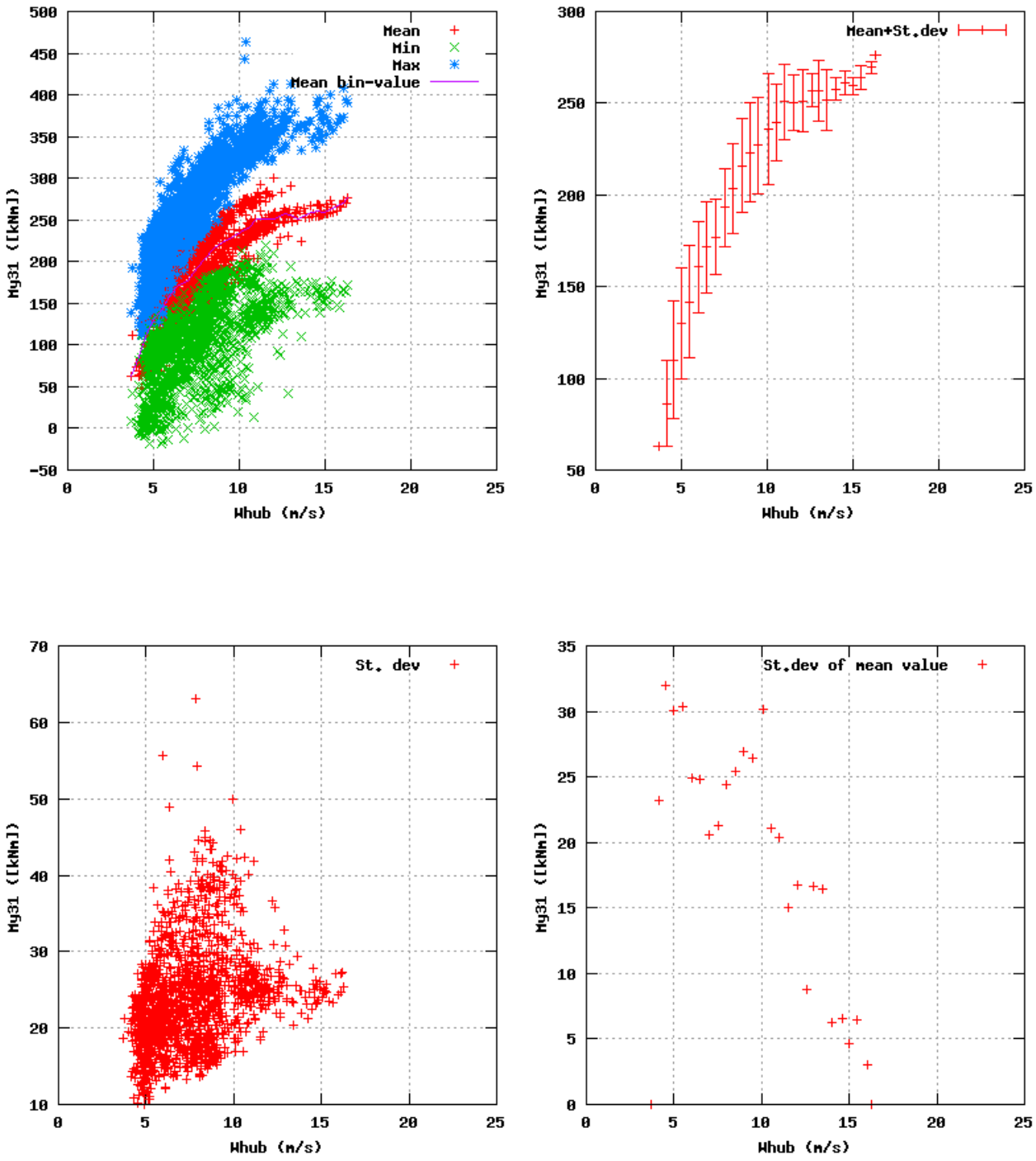

Figure 40a, Sensor 159: Flap bending moment B3 r=2.1m versus wind speed
Input files: ntk500res.dat, stat_159.dat

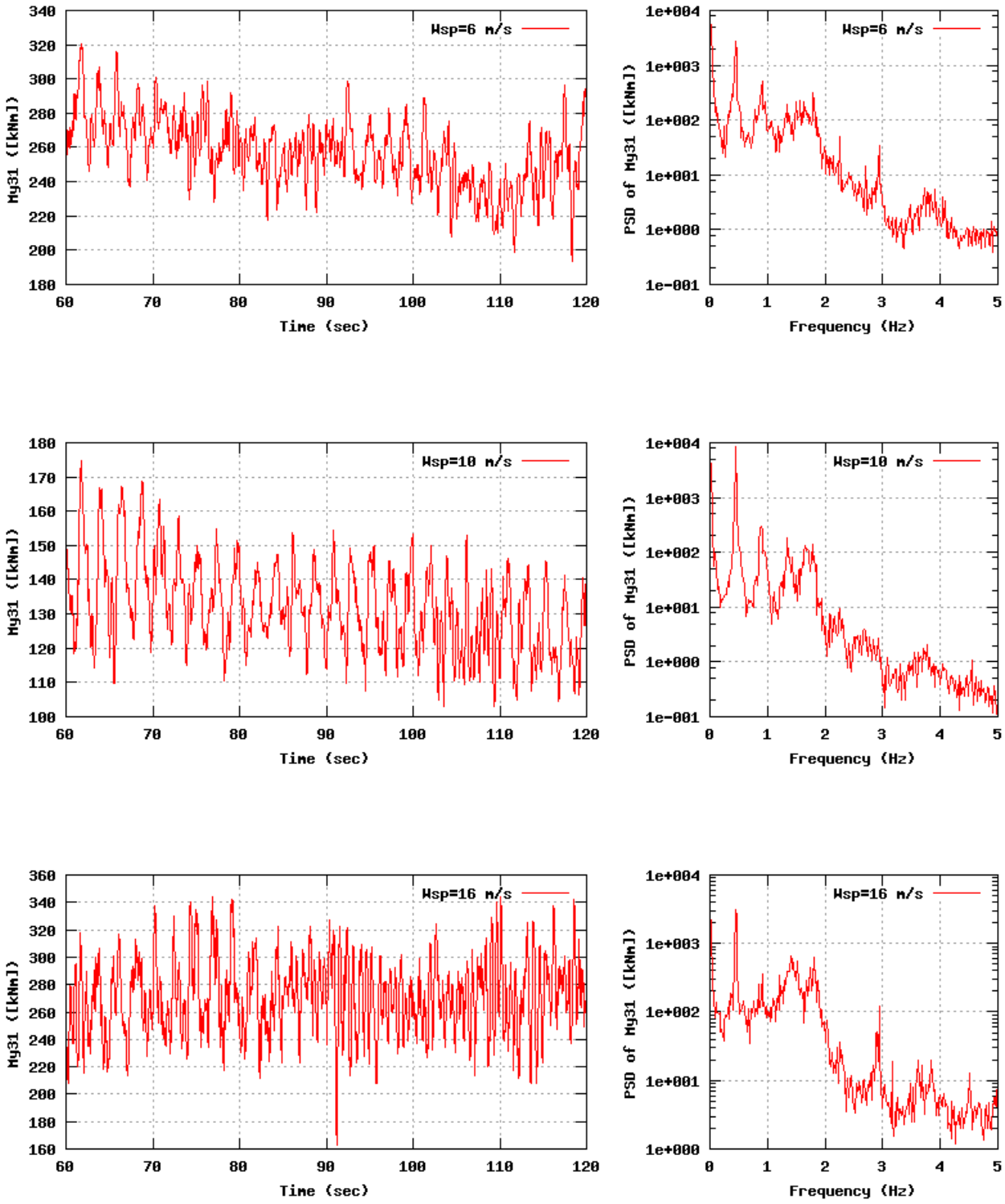

Figure 40b, Sensor 159: Flap bending moment B3 r=2.1m versus time and frequency
Input files: m06.asc, m10.asc, m16.asc, m06.psd, m10.psd and m16.psd

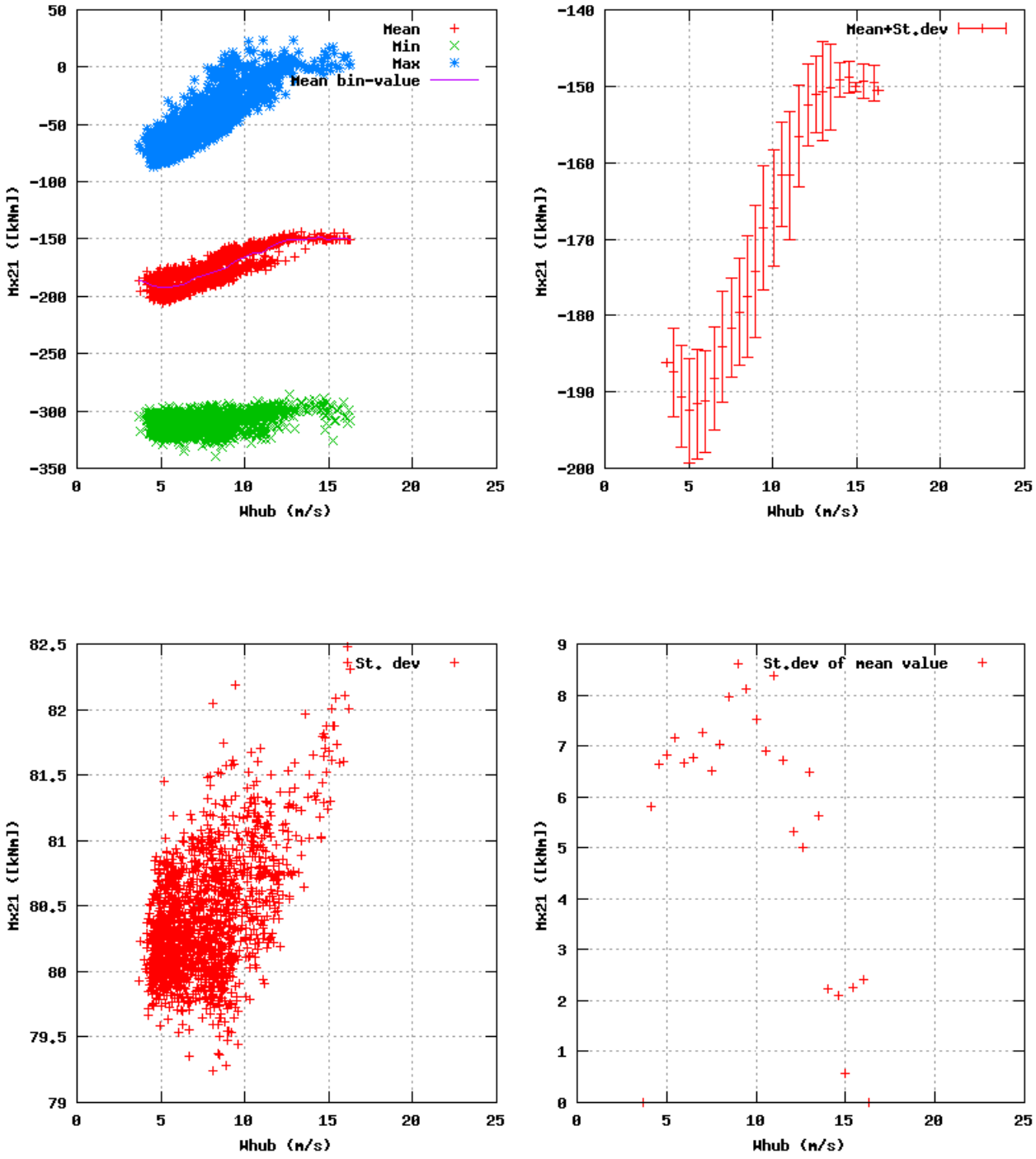

Figure 41a, Sensor 163: Edge bending moment B2 r=2.1m versus wind speed
Input files: ntk500res.dat, stat_163.dat

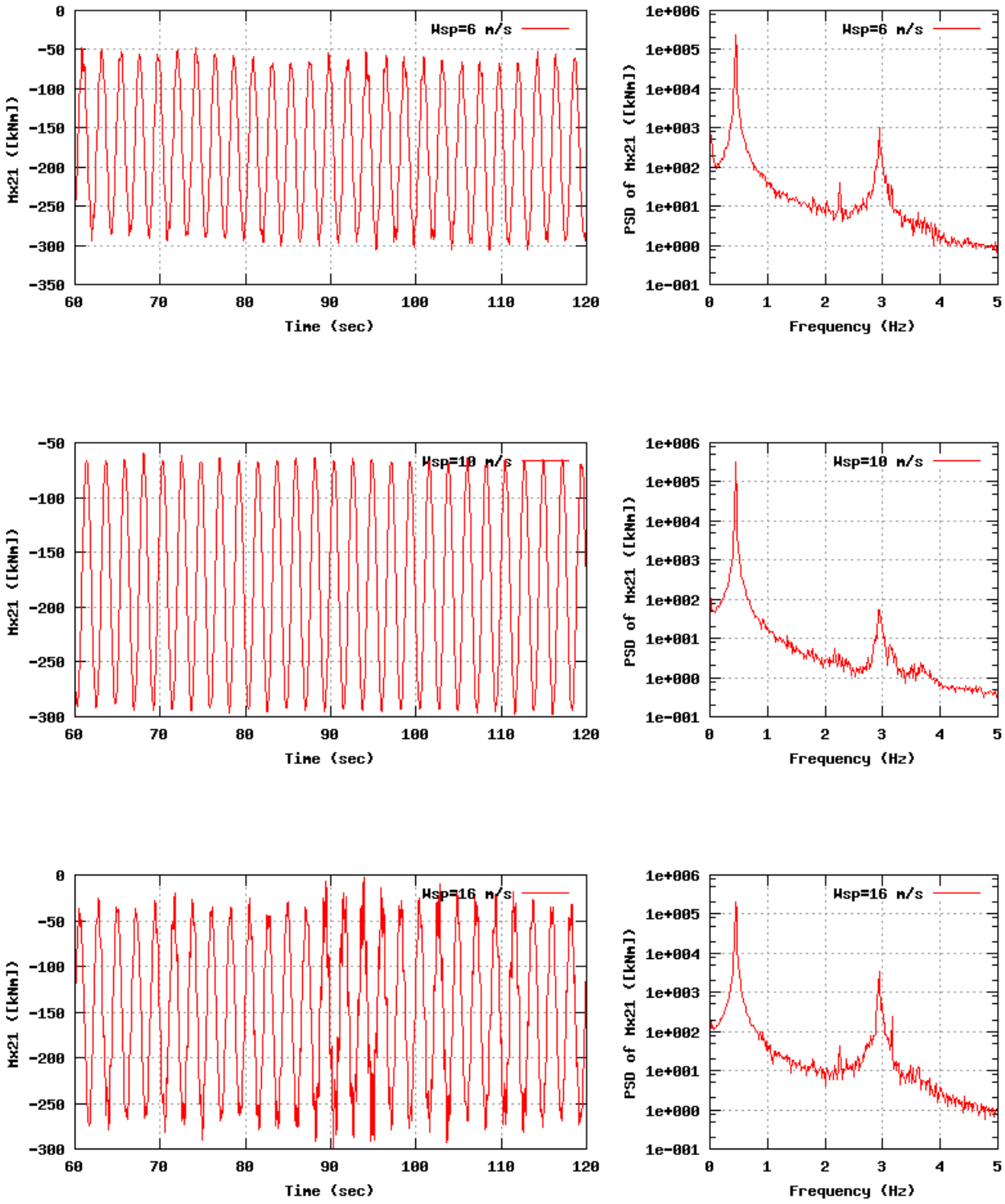

Figure 41b, Sensor 163: Edge bending moment B2 r=2.1m versus time and frequency
Input files: m06.asc, m10.asc, m16.asc, m06.psd, m10.psd and m16.psd

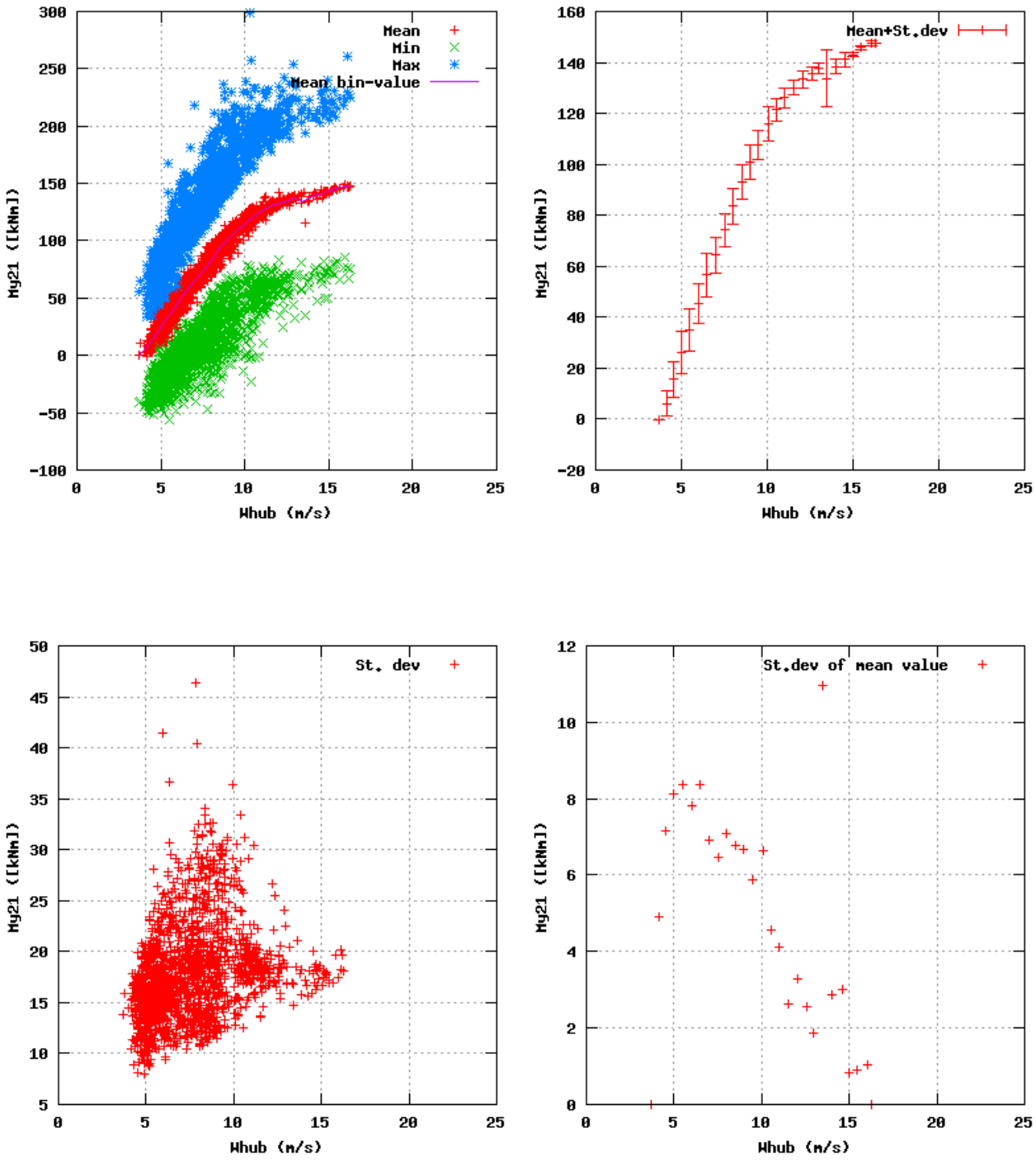

Figure 42a, Sensor 167: Flap bending moment B2 r=2.1m versus wind speed
Input files: ntk500res.dat, stat_167.dat

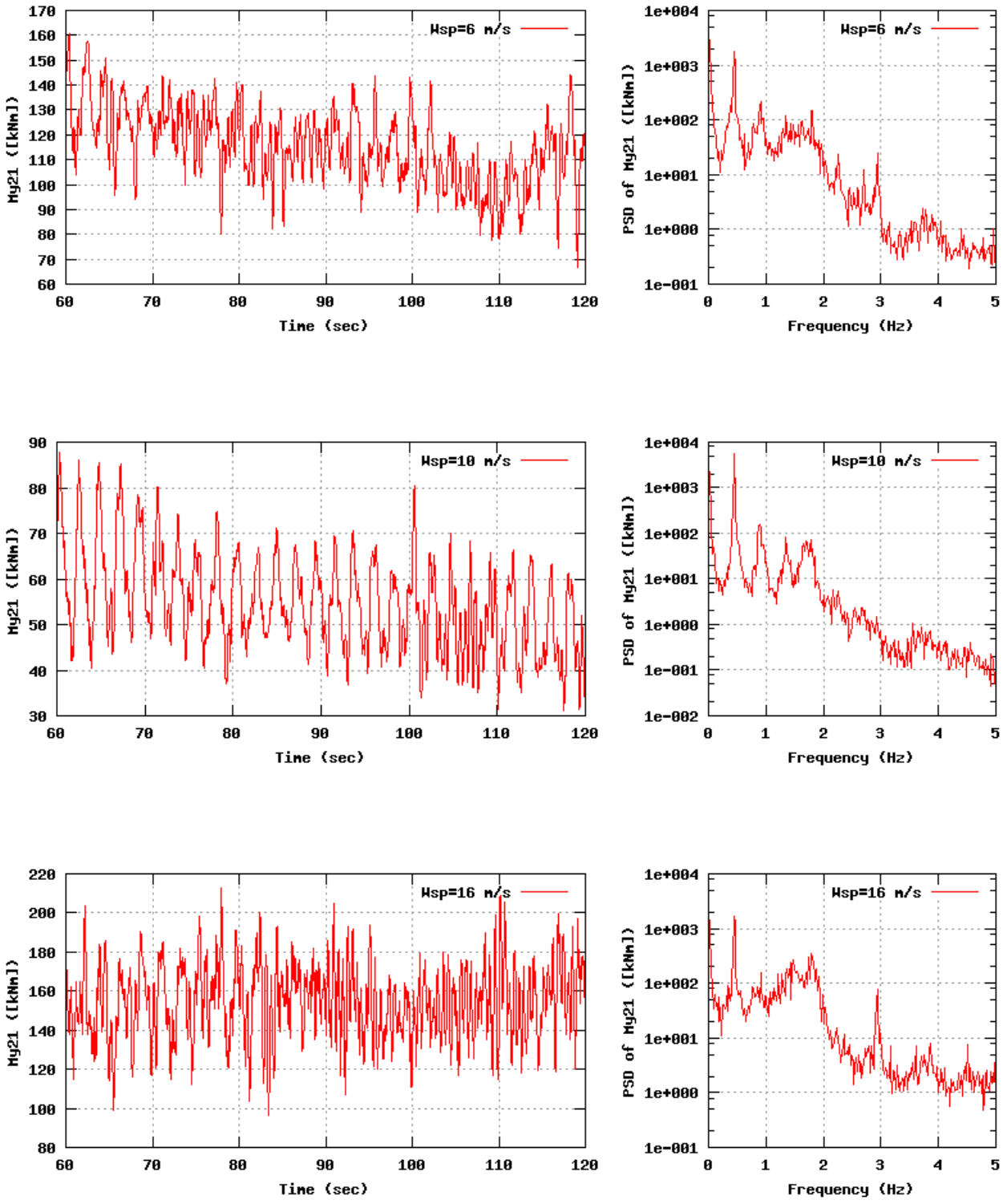

Figure 42b, Sensor 167: Flap bending moment B2 r=2.1m versus time and frequency
Input files: m06.asc, m10.asc, m16.asc, m06.psd, m10.psd and m16.psd

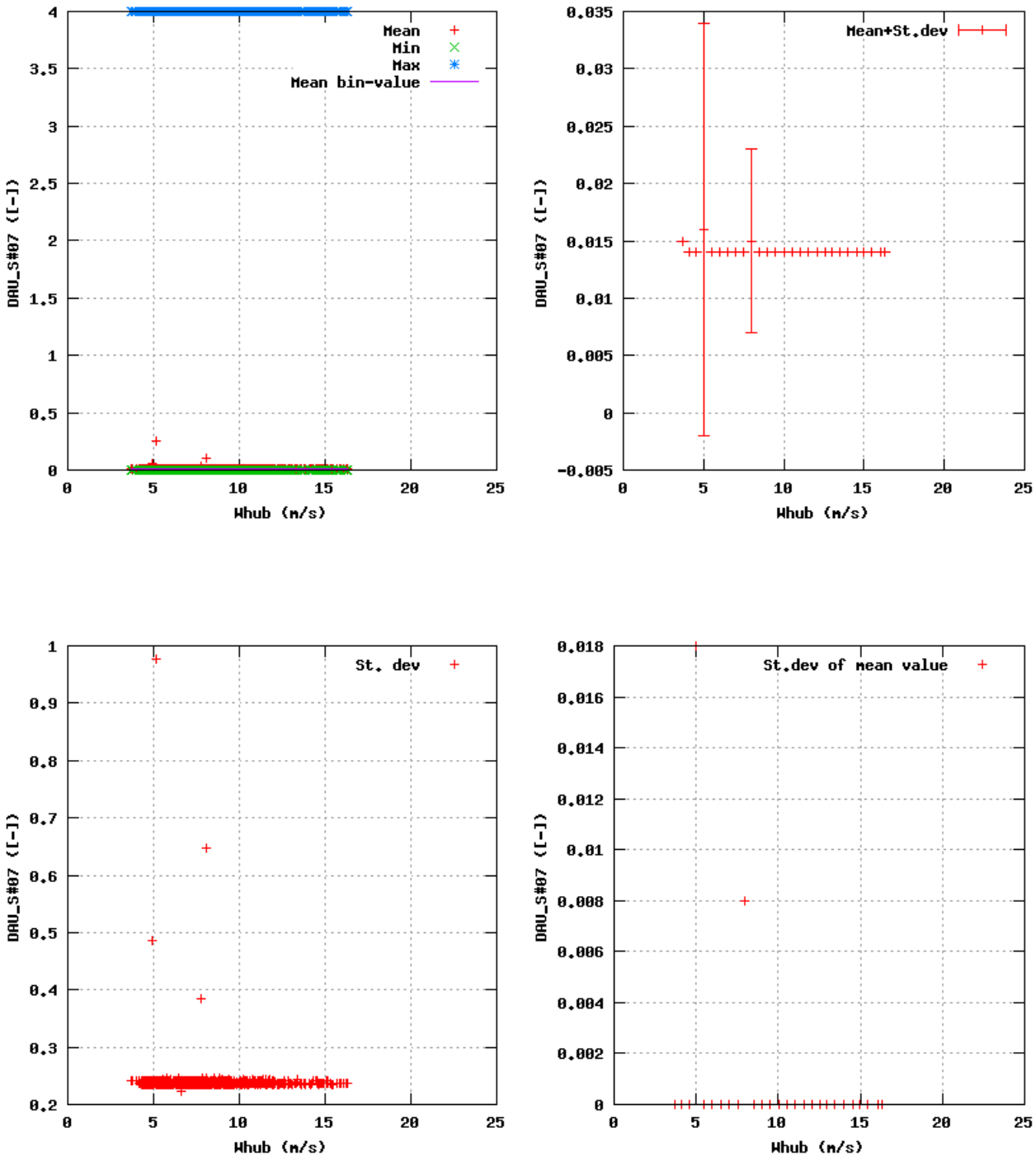

Figure 43a, Sensor 171: DAU_S#07 versus wind speed
Input files: ntk500res.dat, stat_171.dat

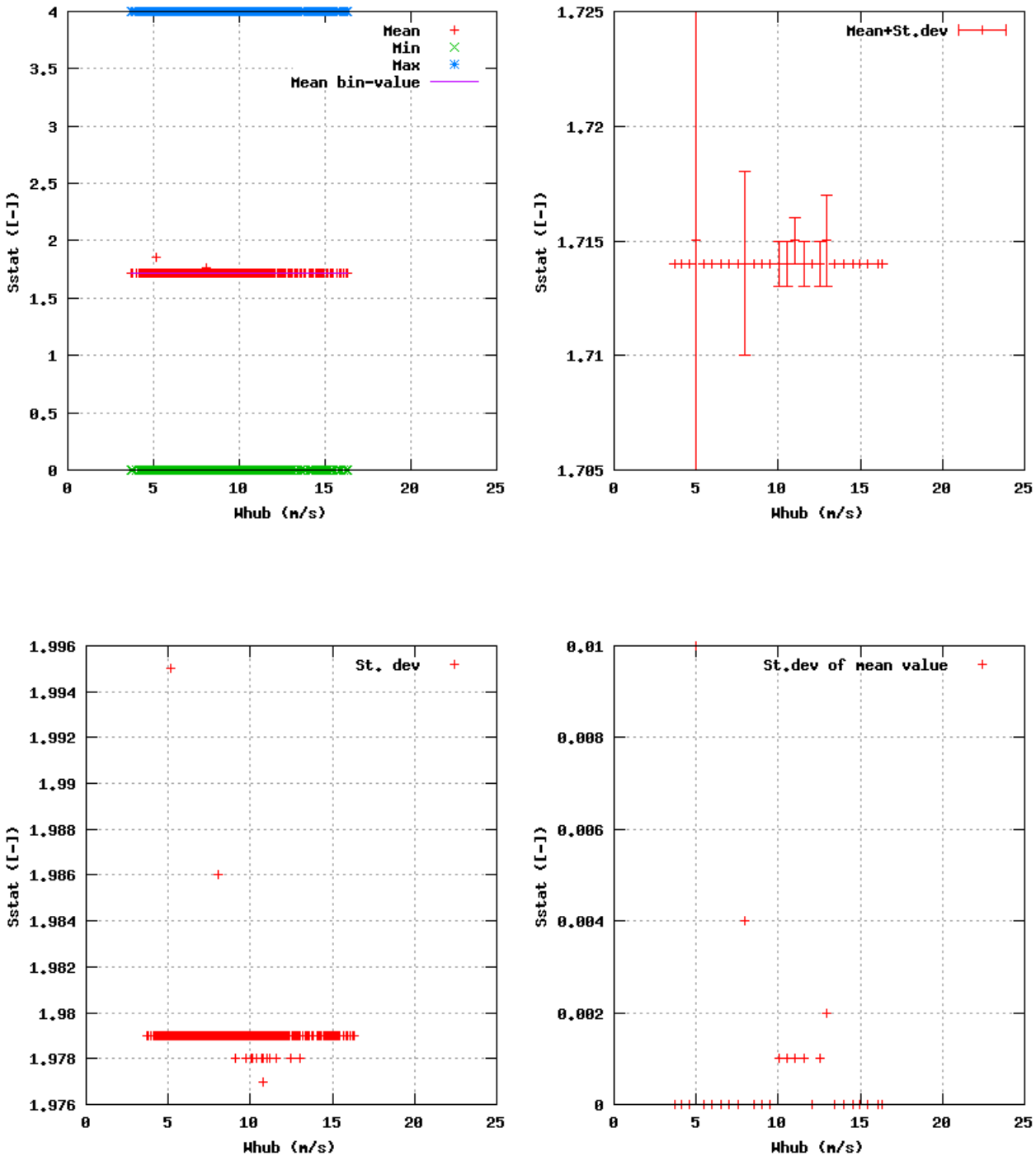

Figure 44a, Sensor 175: Sonic status Sstat,Nacelle versus wind speed
Input files: ntk500res.dat, stat_175.dat

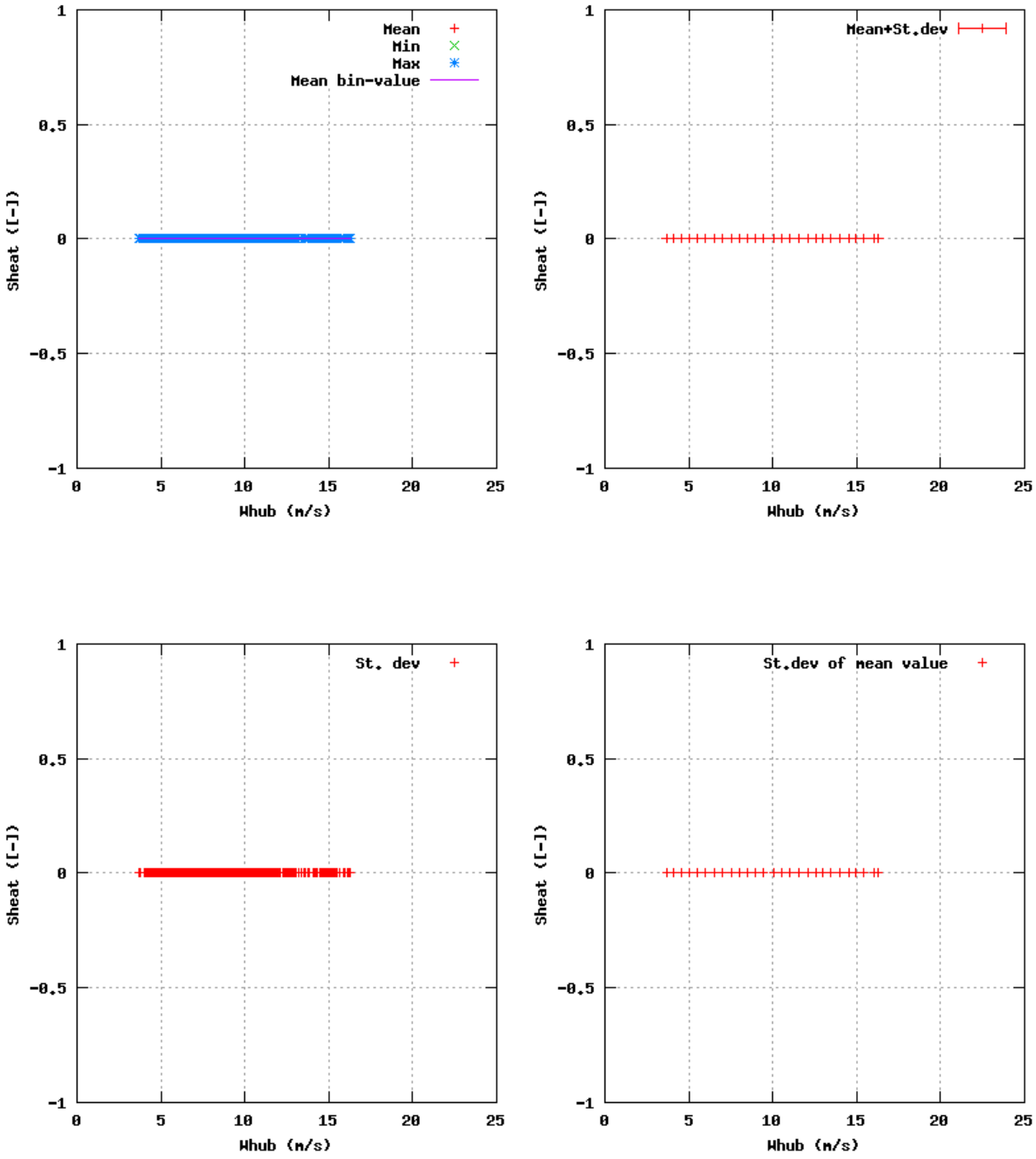

Figure 45a, Sensor 179: Sonic status Sheat,Nacelle versus wind speed
Input files: ntk500res.dat, stat_179.dat

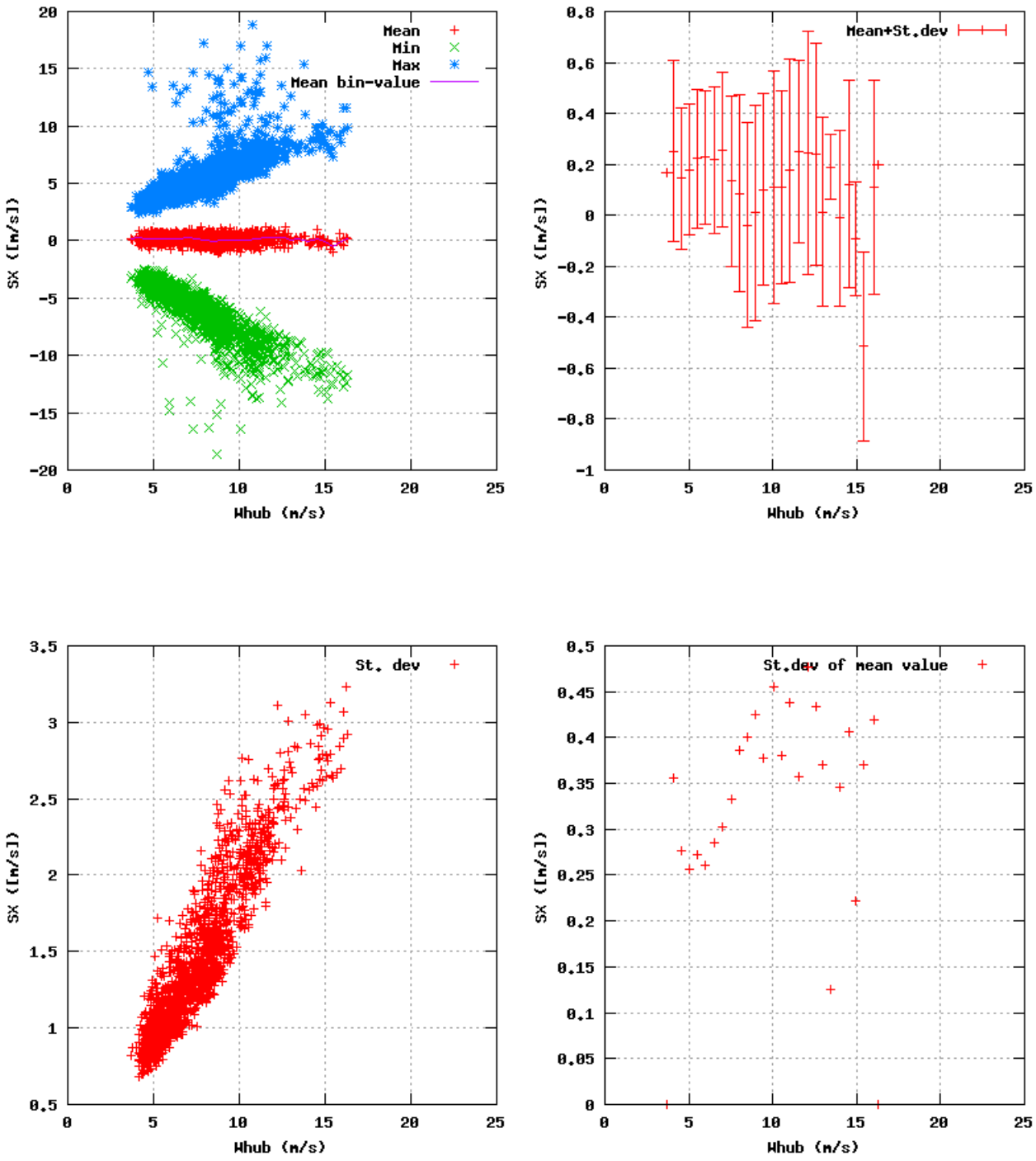

Figure 46a, Sensor 183: Sonic wind component SX,Nacelle versus wind speed
Input files: ntk500res.dat, stat_183.dat

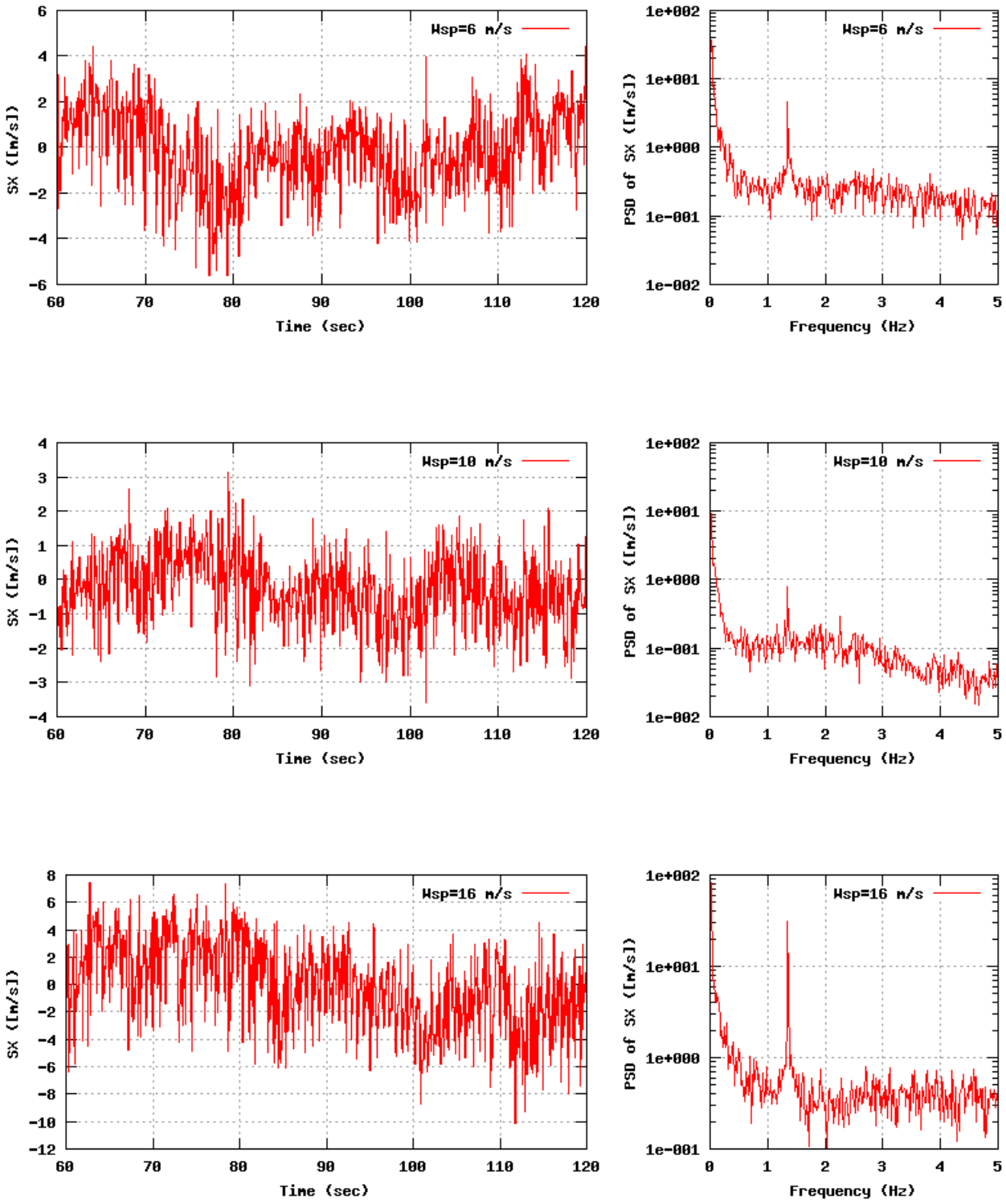

Figure 46b, Sensor 183: Sonic wind component SX,Nacelle versus time and frequency
Input files: m06.asc, m10.asc, m16.asc, m06.psd, m10.psd and m16.psd

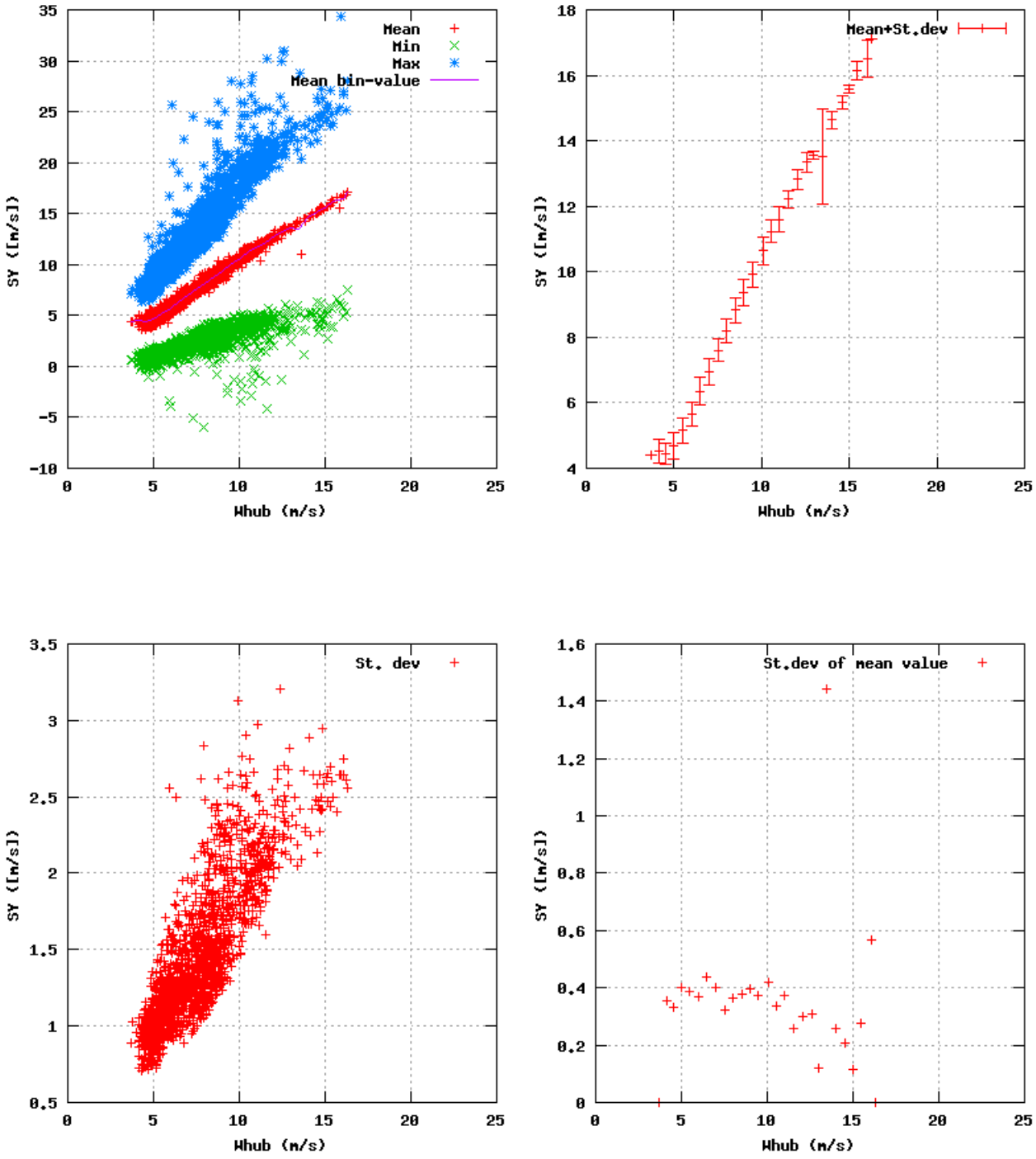

Figure 47a, Sensor 187: Sonic wind component SY,Nacelle versus wind speed
Input files: ntk500res.dat, stat_187.dat

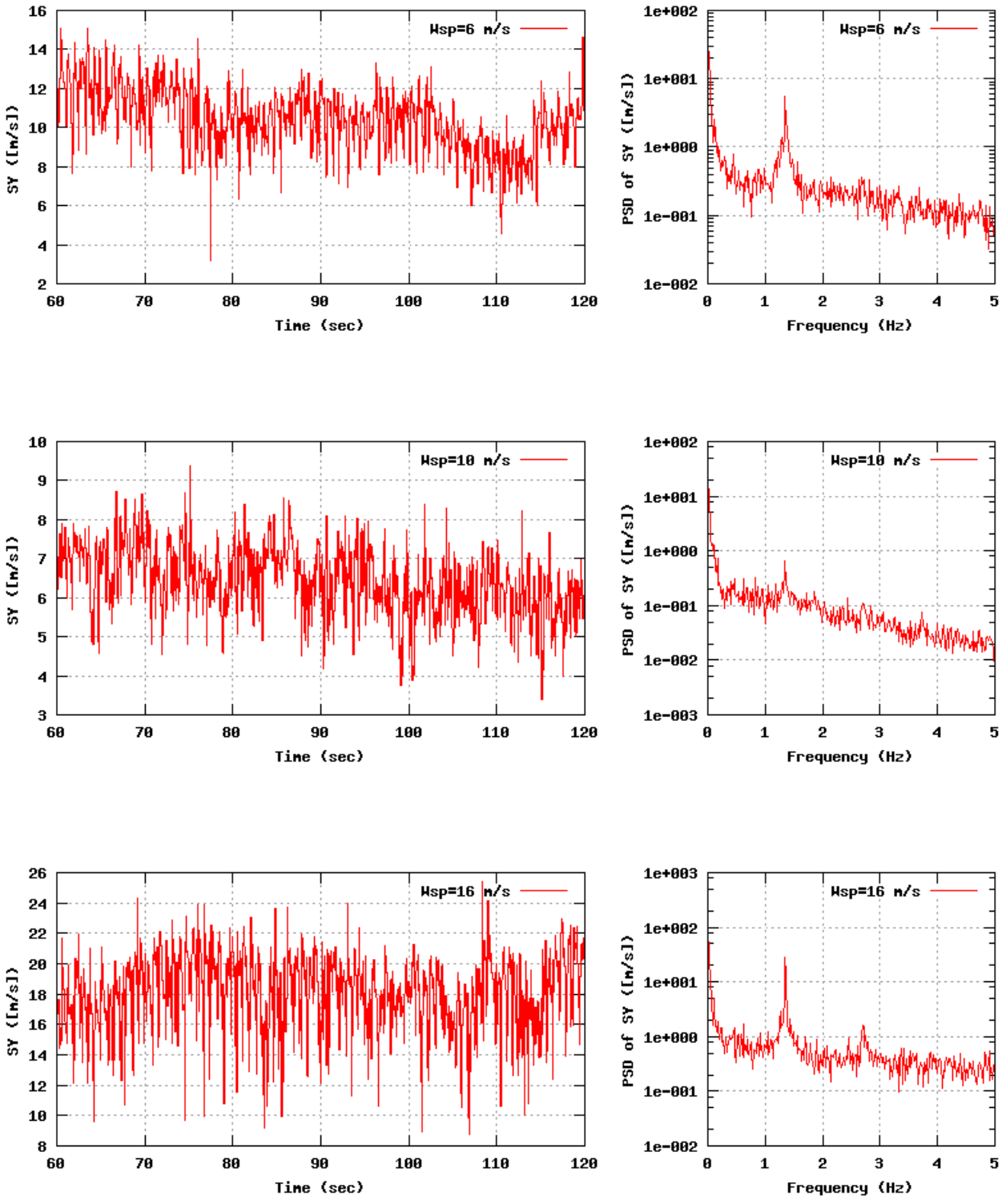

Figure 47b, Sensor 187: Sonic wind component SY,Nacelle versus time and frequency
Input files: m06.asc, m10.asc, m16.asc, m06.psd, m10.psd and m16.psd

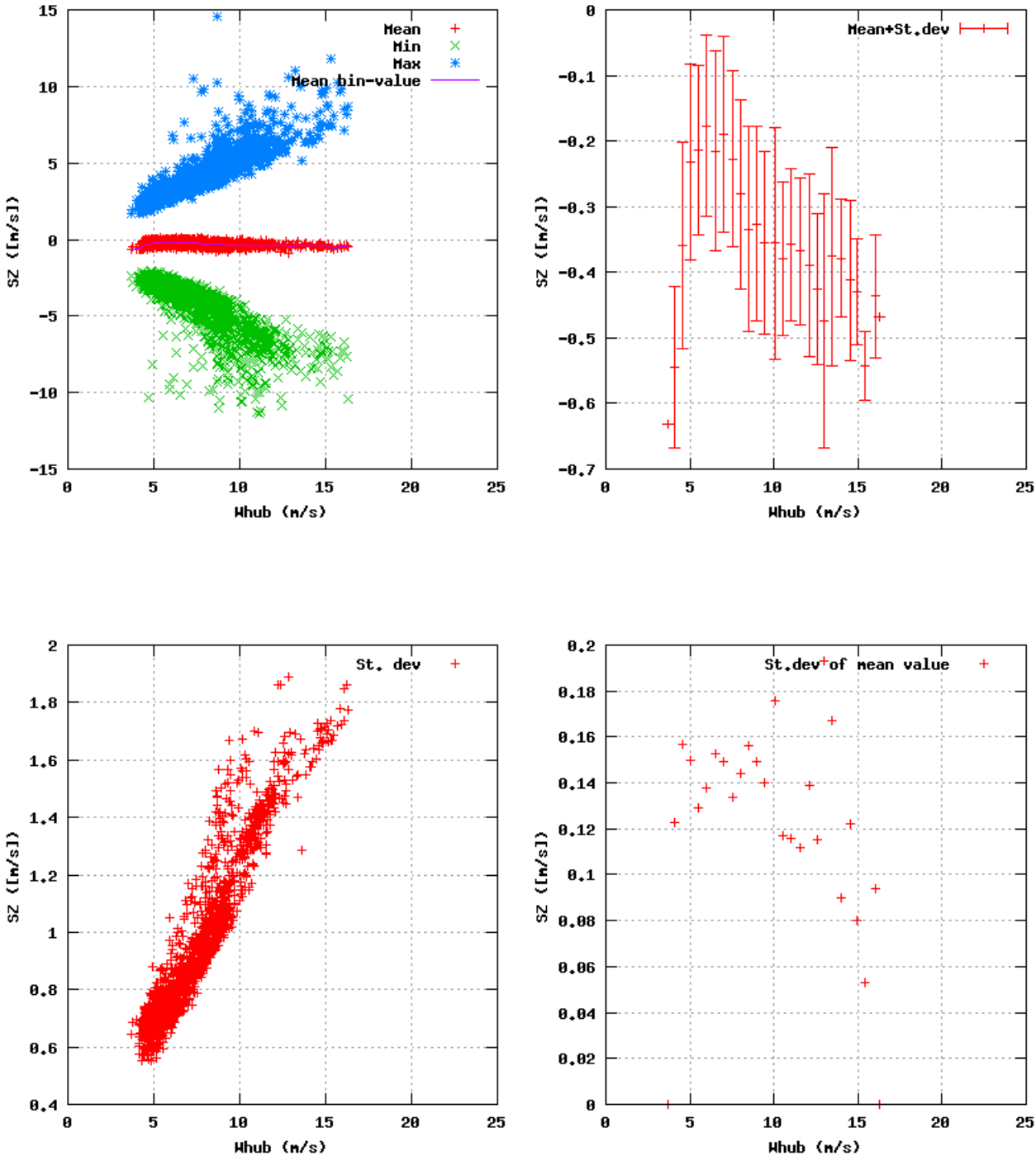

Figure 48a, Sensor 191: Sonic wind component SZ,Nacelle versus wind speed
Input files: ntk500res.dat, stat_191.dat

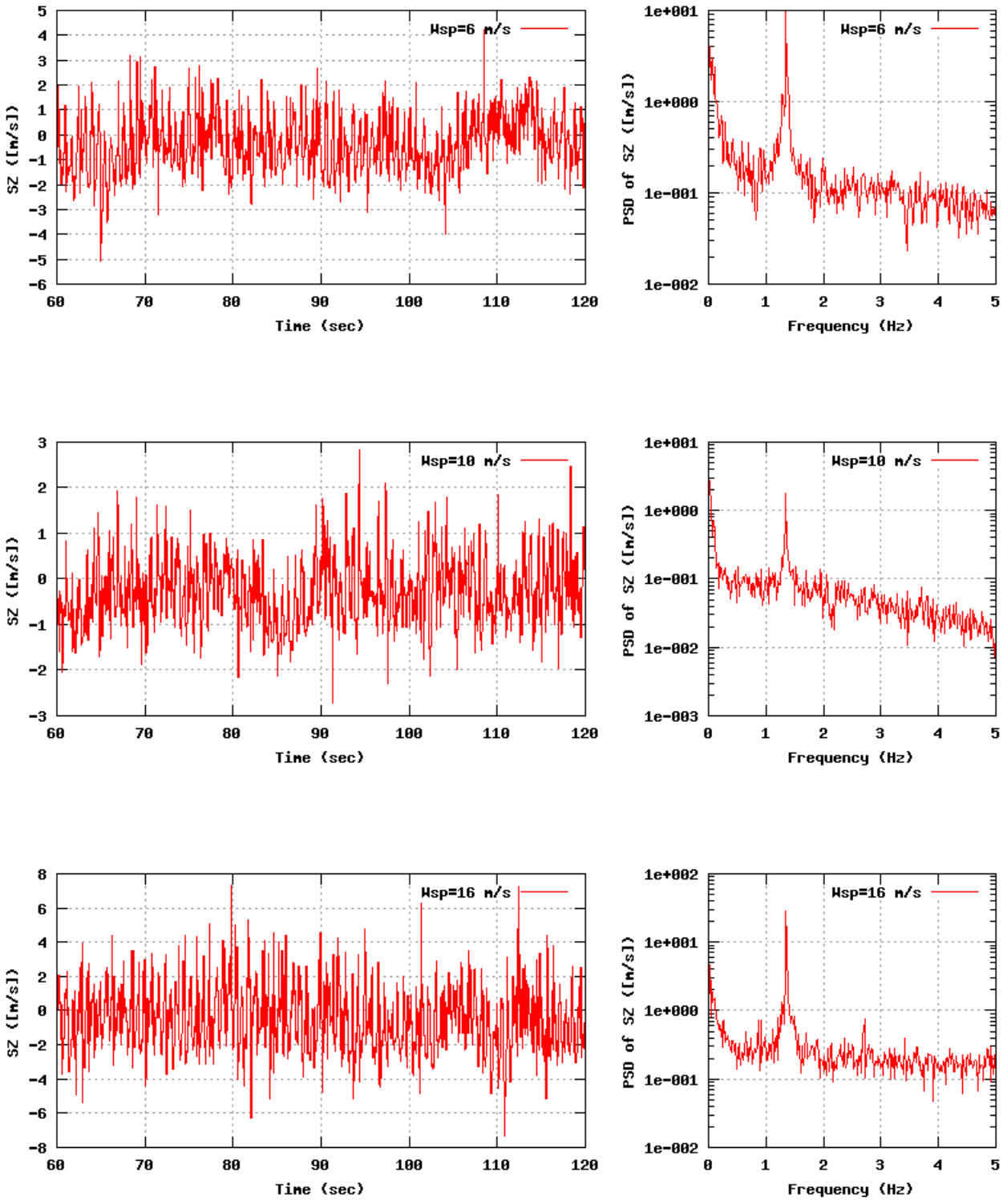

Figure 48b, Sensor 191: Sonic wind component SZ,Nacelle versus time and frequency
Input files: m06.asc, m10.asc, m16.asc, m06.psd, m10.psd and m16.psd

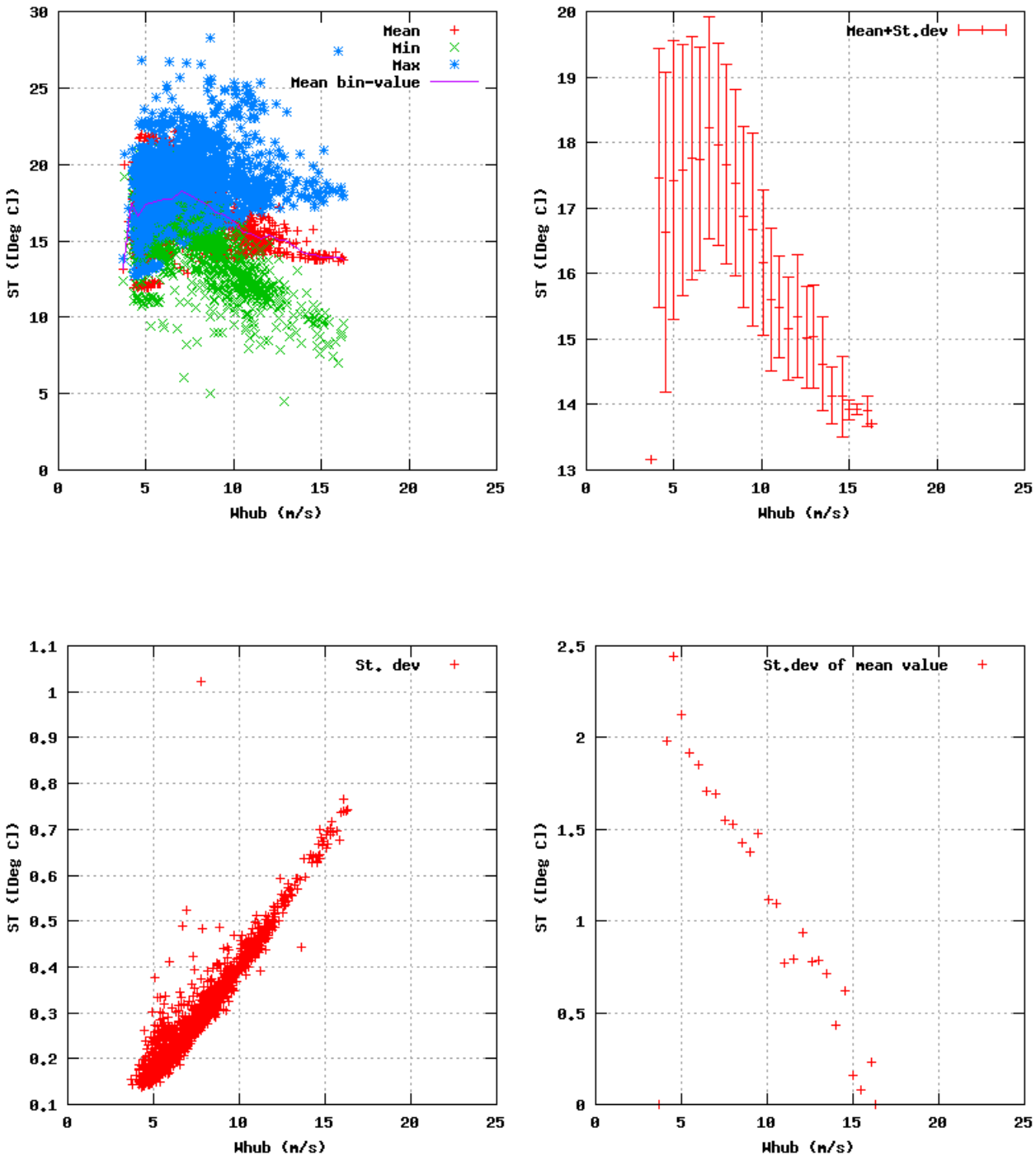

Figure 49a, Sensor 195: Sonic air temperature ST,Nacelle versus wind speed
Input files: ntk500res.dat, stat_195.dat

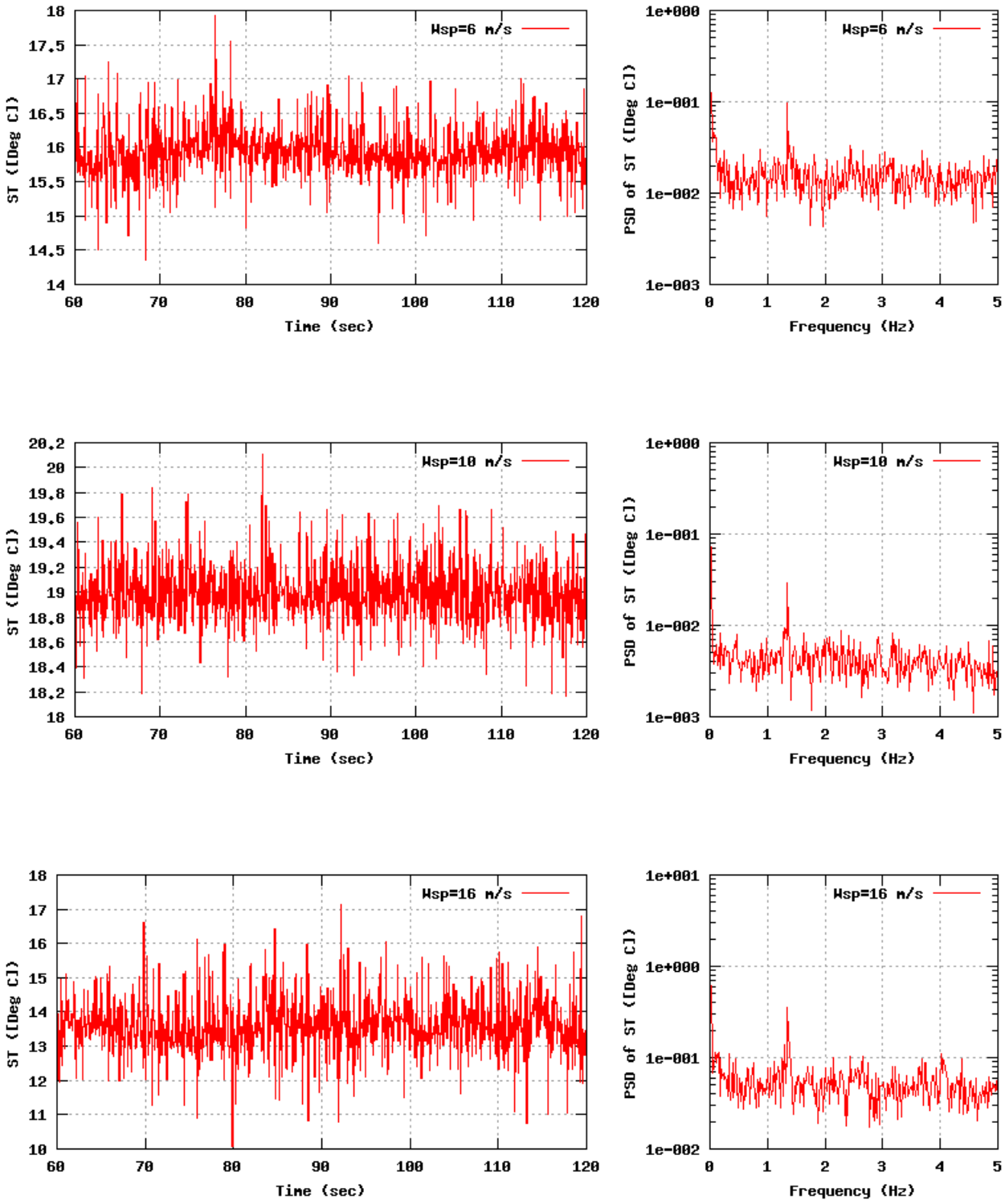

Figure 49b, Sensor 195: Sonic air temperature ST,Nacelle versus time and frequency
Input files: m06.asc, m10.asc, m16.asc, m06.psd, m10.psd and m16.psd

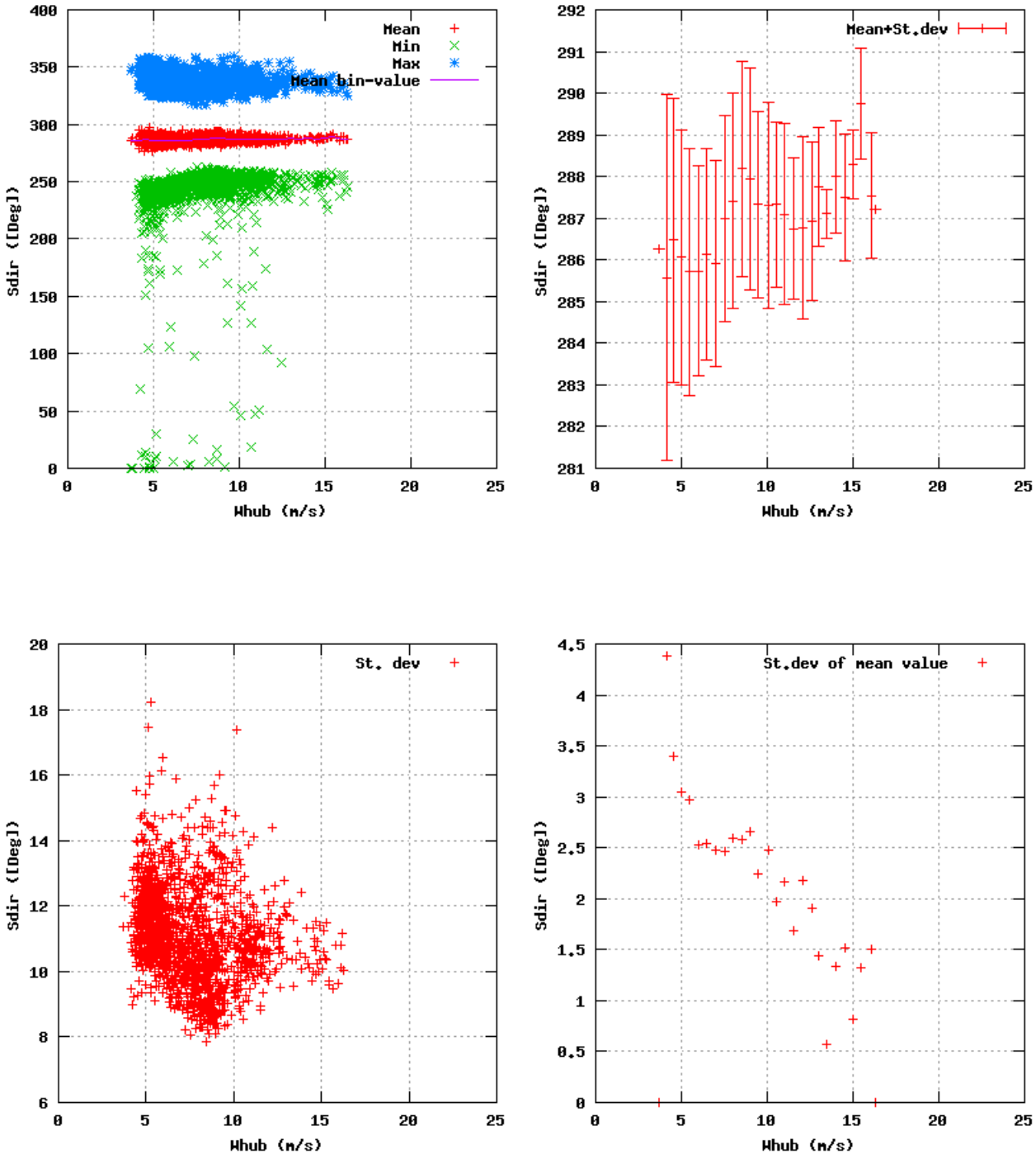

Figure 50a, Sensor 199: Sonic horisontal flow direction Sdir,Nacelle versus wind speed
Input files: ntk500res.dat, stat_199.dat

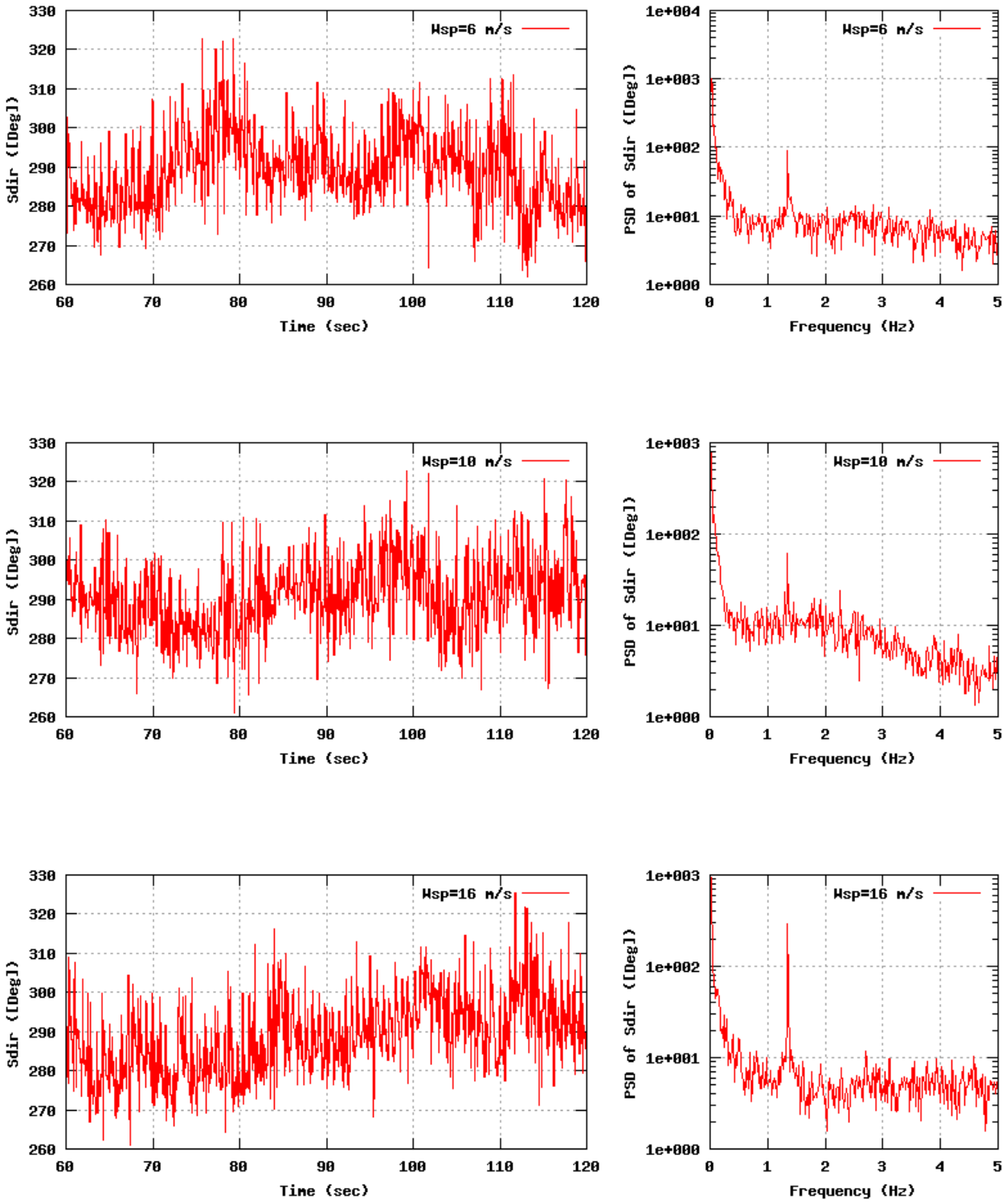

Figure 50b, Sensor 199: Sonic horisontal flow direction Sdir,Nacelle versus time and frequency
Input files: m06.asc, m10.asc, m16.asc, m06.psd, m10.psd and m16.psd

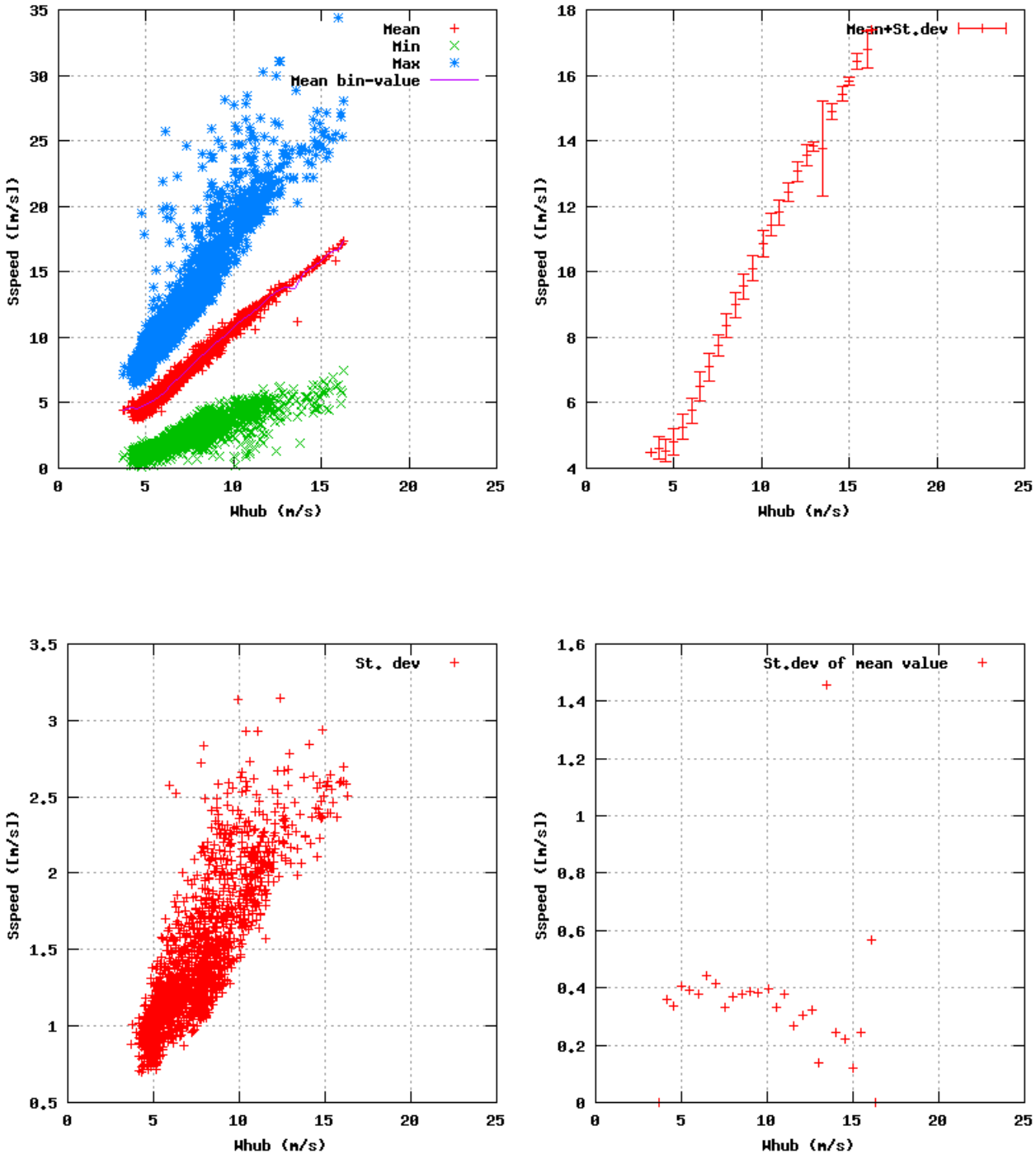

Figure 51a, Sensor 203: Sonic wind speed Sspeed,Nacelle versus wind speed
Input files: ntk500res.dat, stat_203.dat

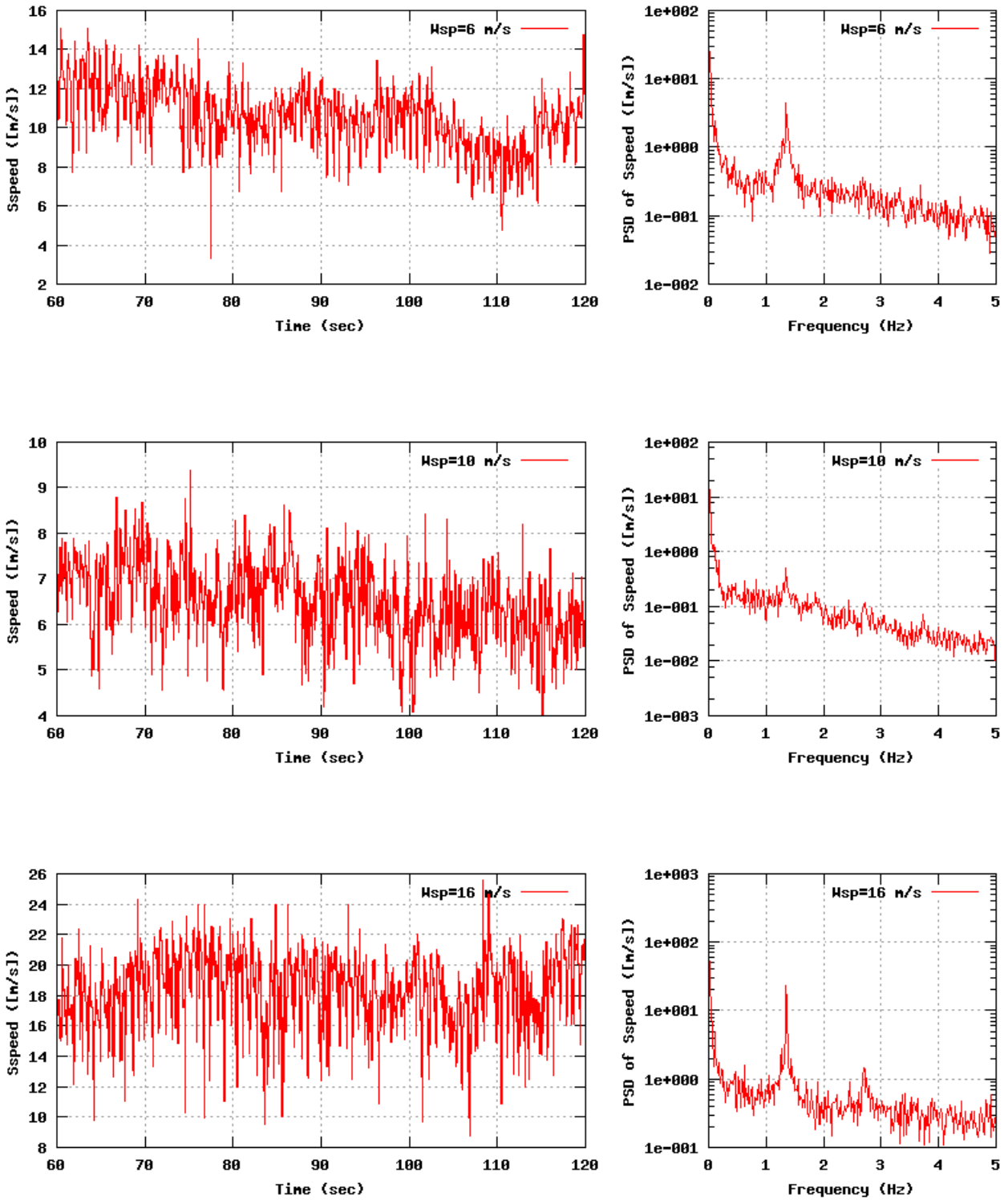

Figure 51b, Sensor 203: Sonic wind speed Sspeed,Nacelle versus time and frequency
Input files: m06.asc, m10.asc, m16.asc, m06.psd, m10.psd and m16.psd

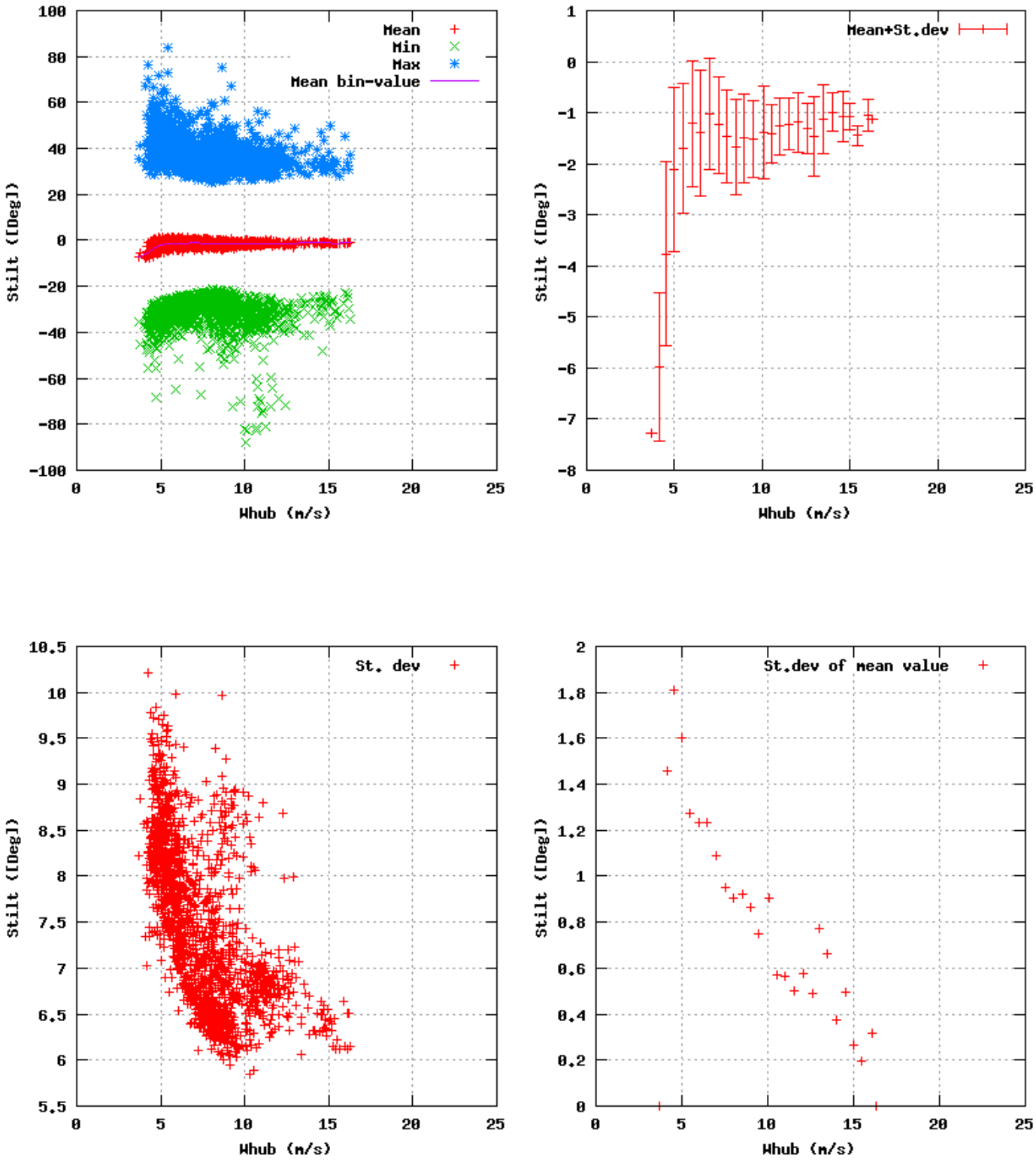

Figure 52a, Sensor 207: Sonic vertical flow angle Stilt,Nacelle versus wind speed
Input files: ntk500res.dat, stat_207.dat

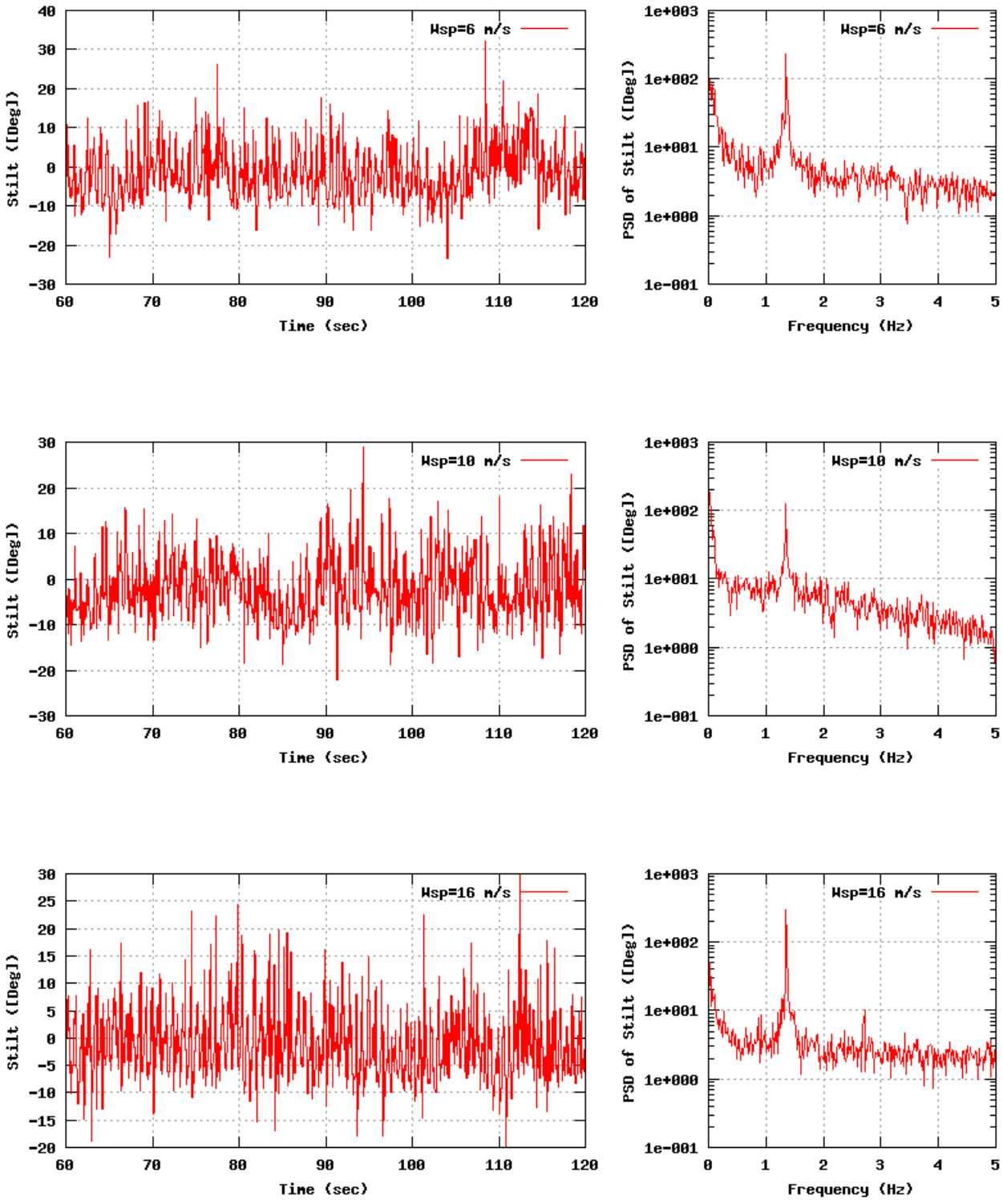

Figure 52b, Sensor 207: Sonic vertical flow angle Stilt,Nacelle versus time and frequency
Input files: m06.asc, m10.asc, m16.asc, m06.psd, m10.psd and m16.psd

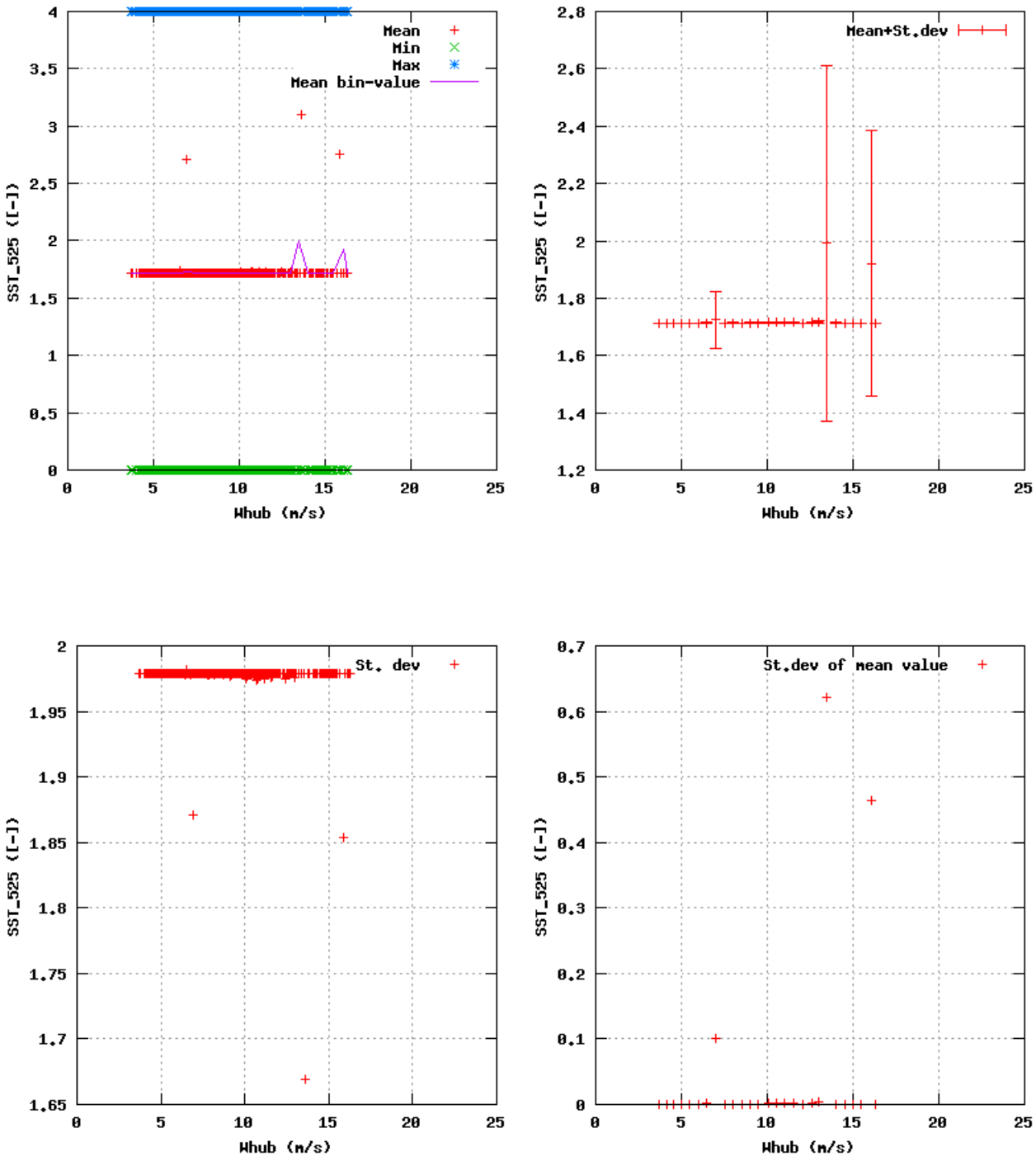

Figure 53a, Sensor 211: Sonic status Sstat,52.5m versus wind speed
Input files: ntk500res.dat, stat_211.dat

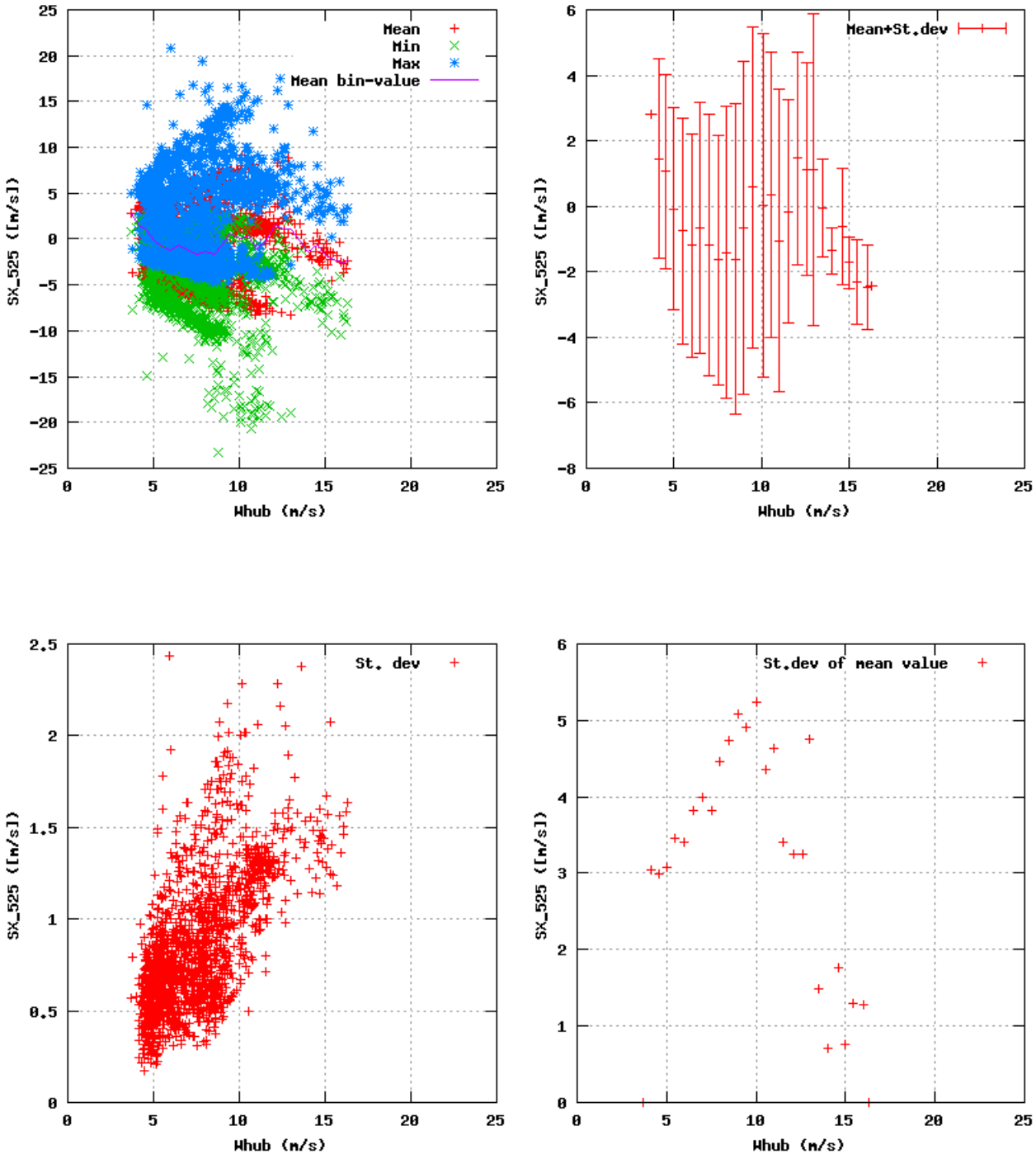

Figure 54a, Sensor 215: Sonic wind component SX,52.5m versus wind speed
Input files: ntk500res.dat, stat_215.dat

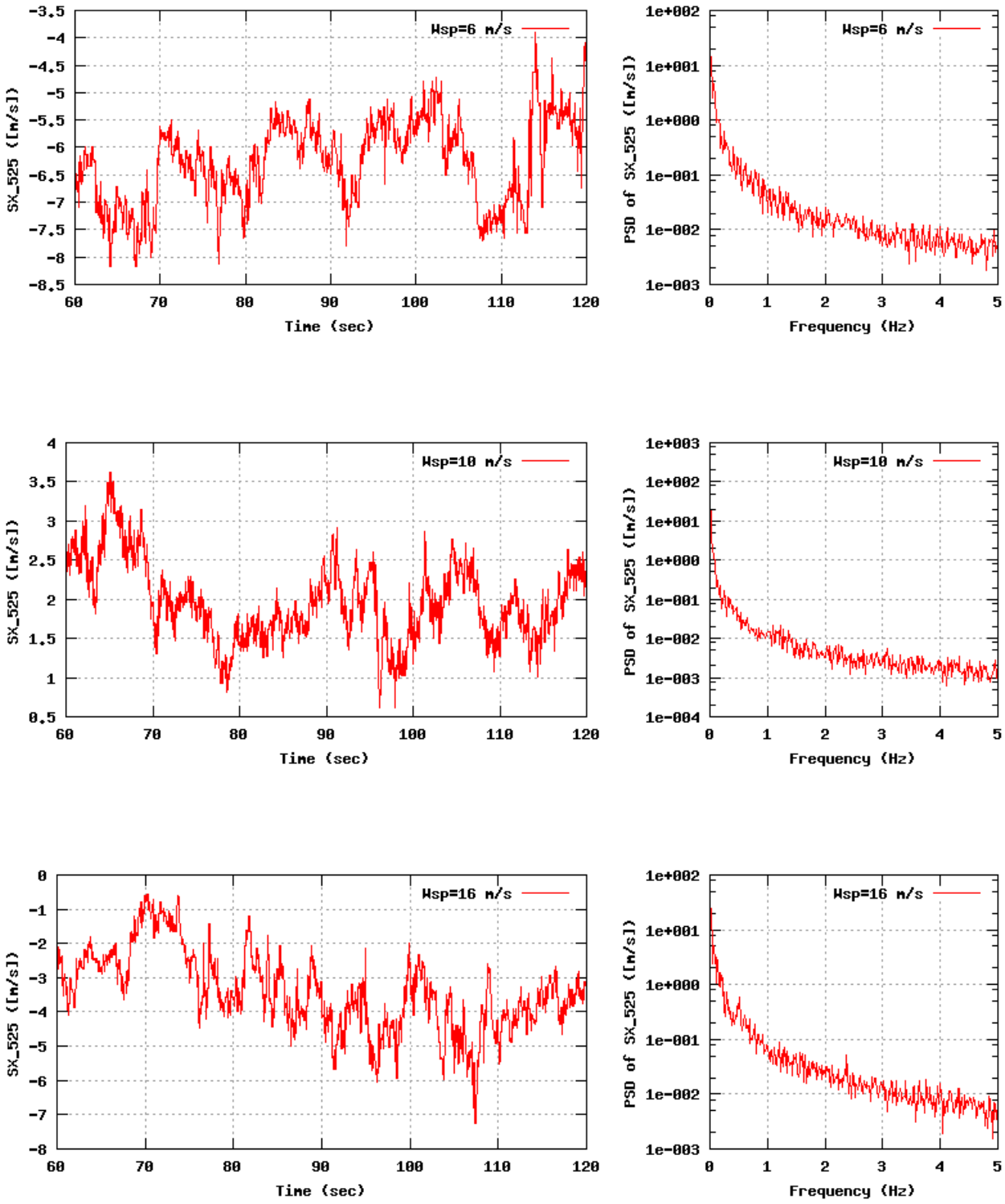

Figure 54b, Sensor 215: Sonic wind component SX,52.5m versus time and frequency
Input files: m06.asc, m10.asc, m16.asc, m06.psd, m10.psd and m16.psd

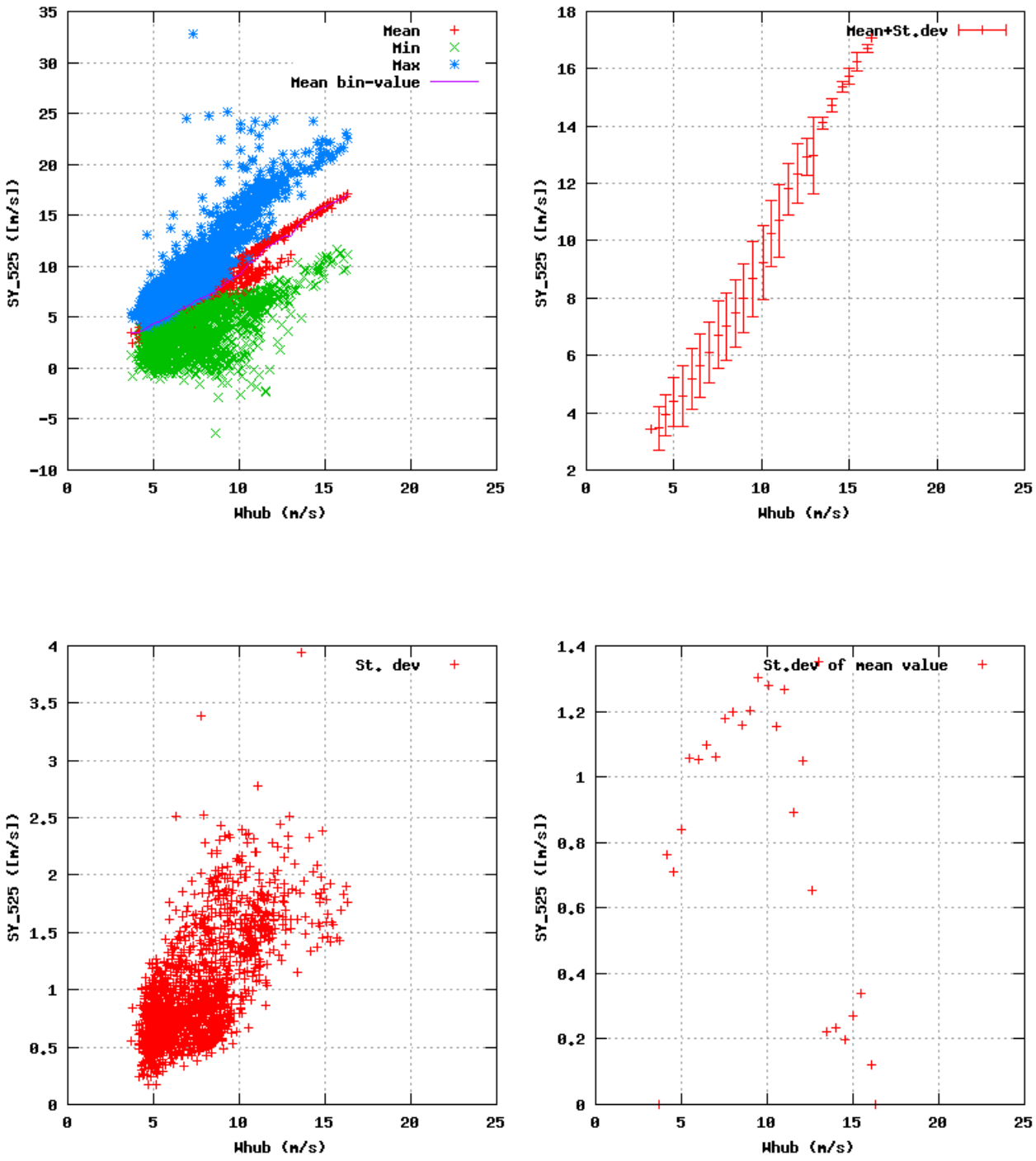

Figure 55a, Sensor 219: Sonic wind component SY,52.5m versus wind speed
Input files: ntk500res.dat, stat_219.dat

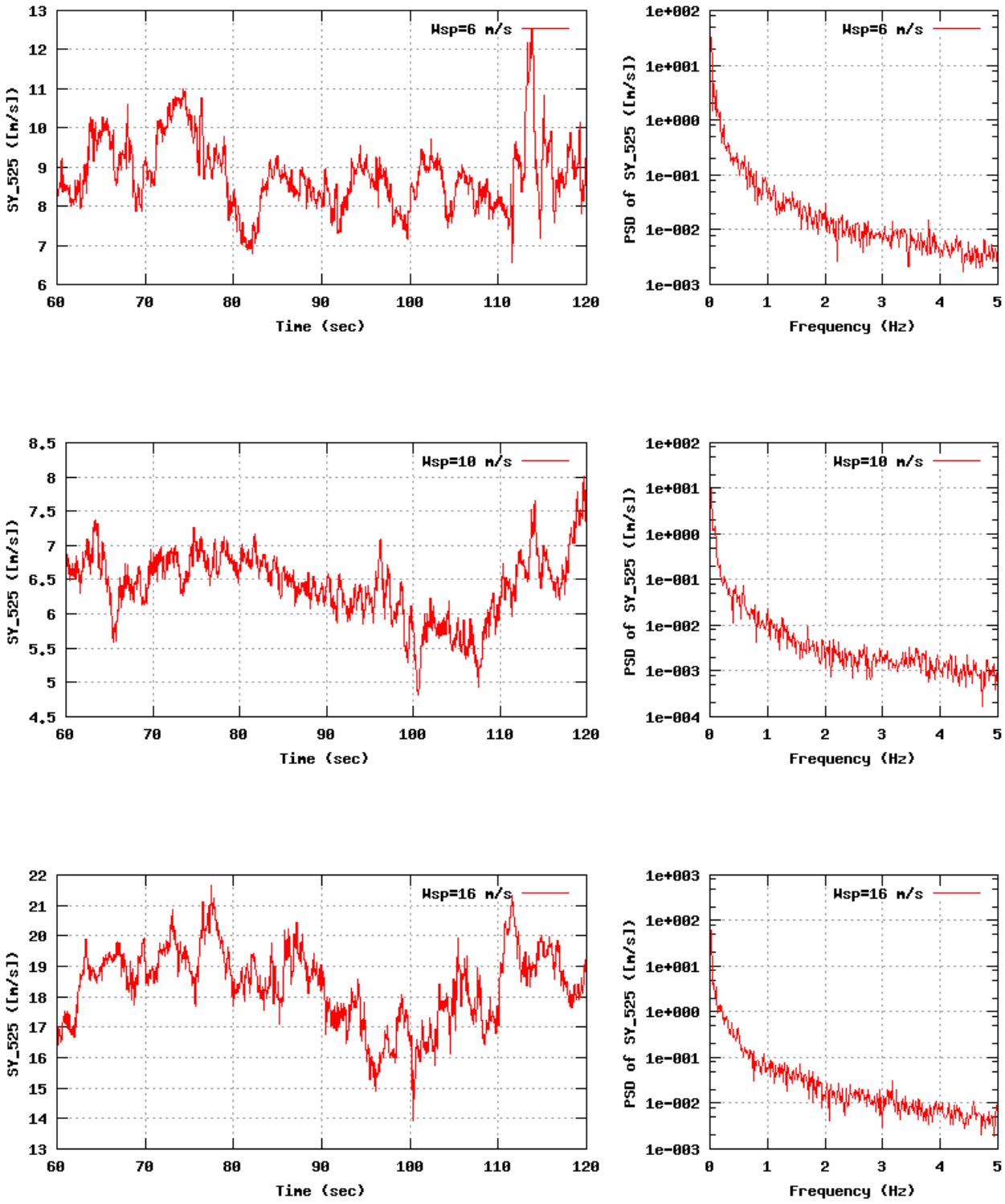

Figure 55b, Sensor 219: Sonic wind component SY,52.5m versus time and frequency
Input files: m06.asc, m10.asc, m16.asc, m06.psd, m10.psd and m16.psd

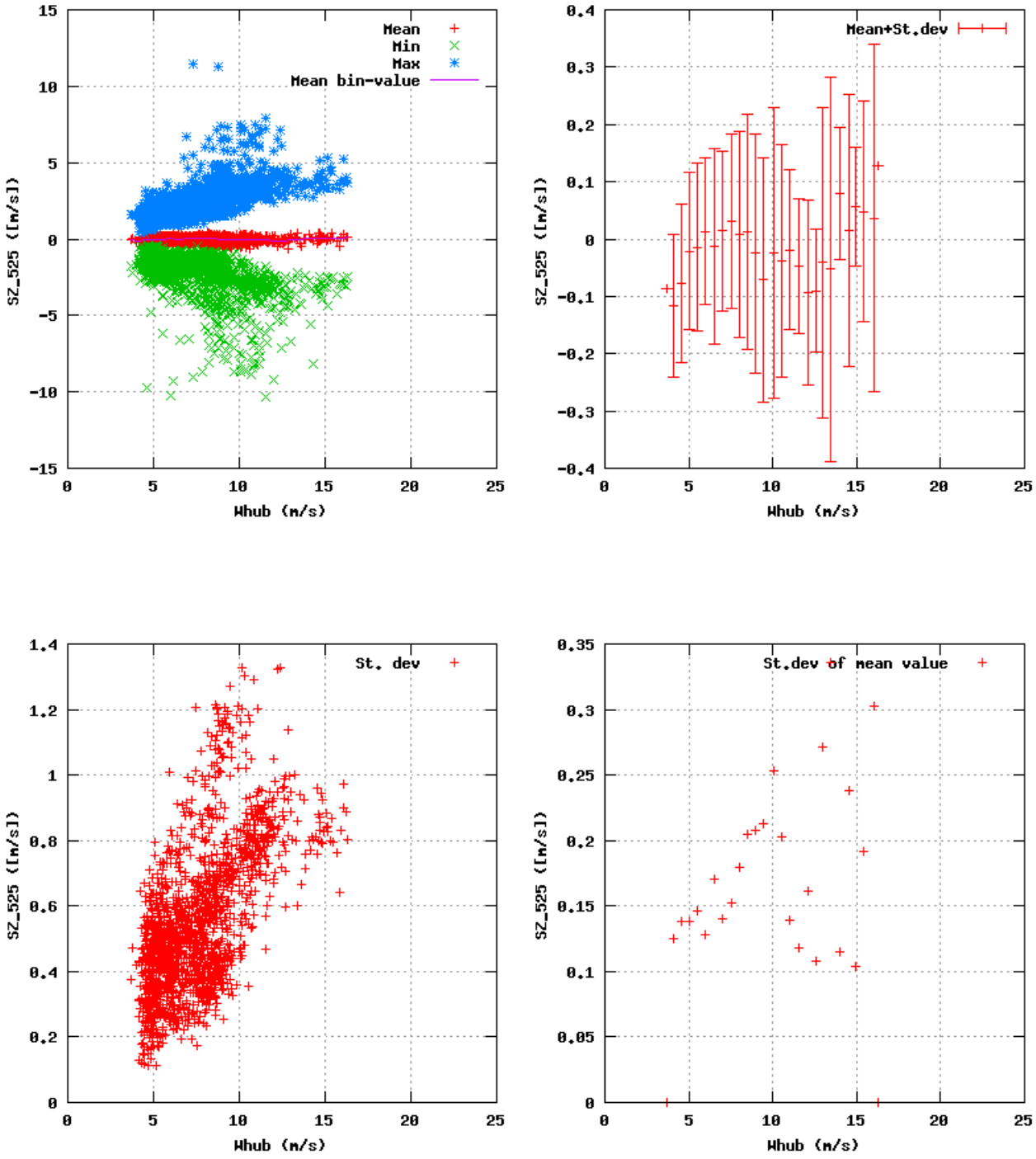

Figure 56a, Sensor 223: Sonic wind component SZ,52.5m versus wind speed
Input files: ntk500res.dat, stat_223.dat

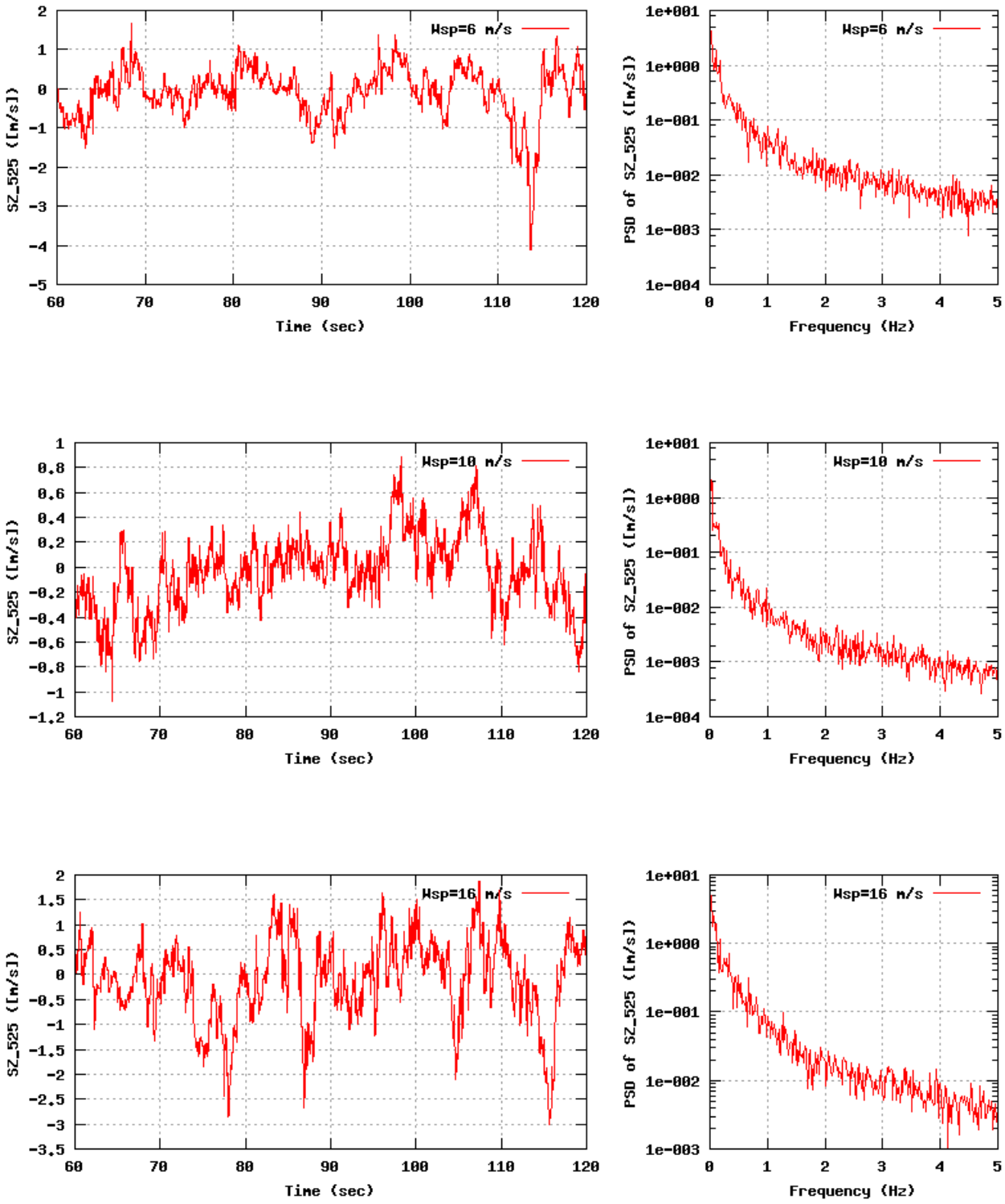

Figure 56b, Sensor 223: Sonic wind component SZ,52.5m versus time and frequency
Input files: m06.asc, m10.asc, m16.asc, m06.psd, m10.psd and m16.psd

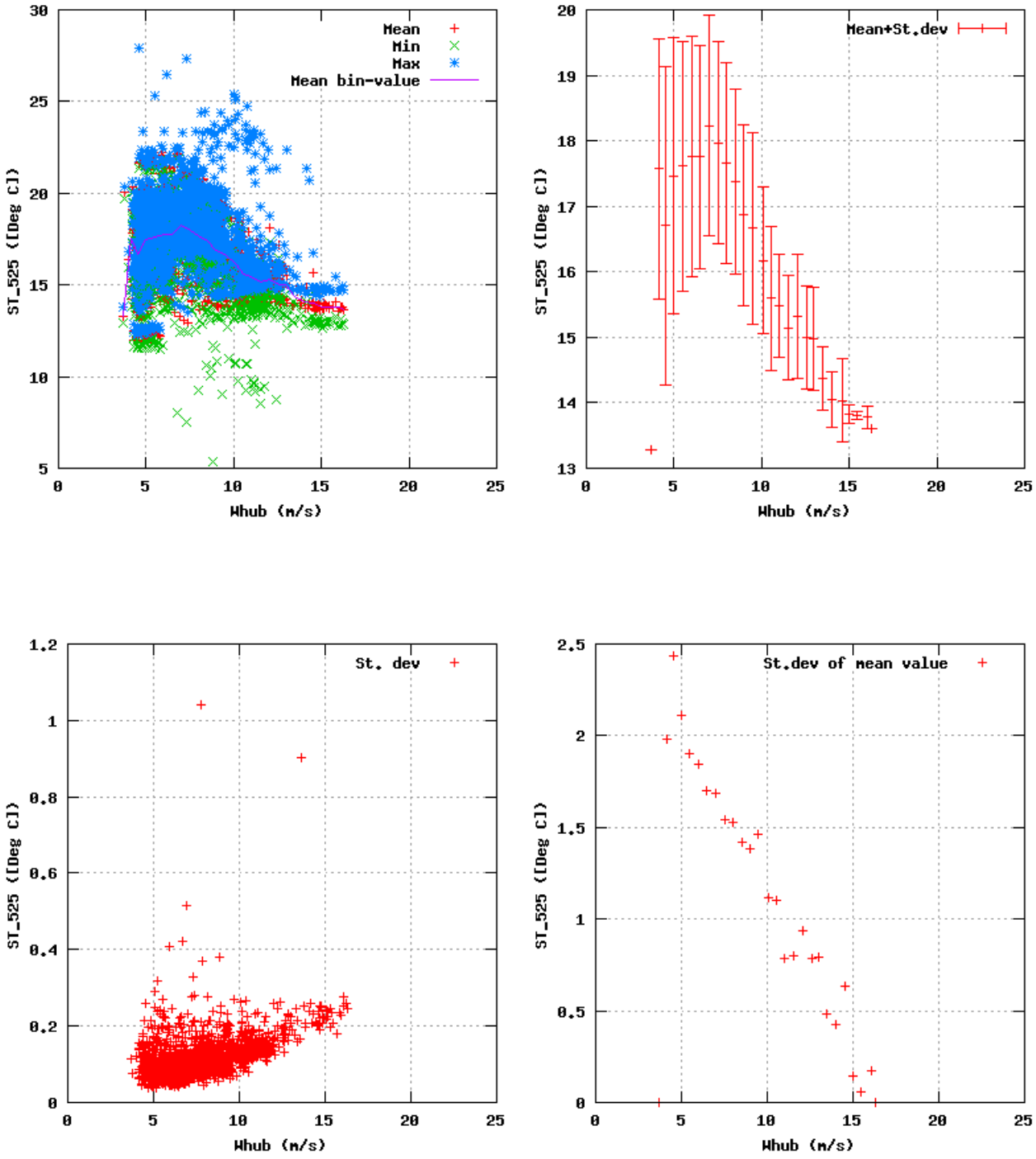

Figure 57a, Sensor 227: Sonic air temperature ST,52.5m versus wind speed
Input files: ntk500res.dat, stat_227.dat

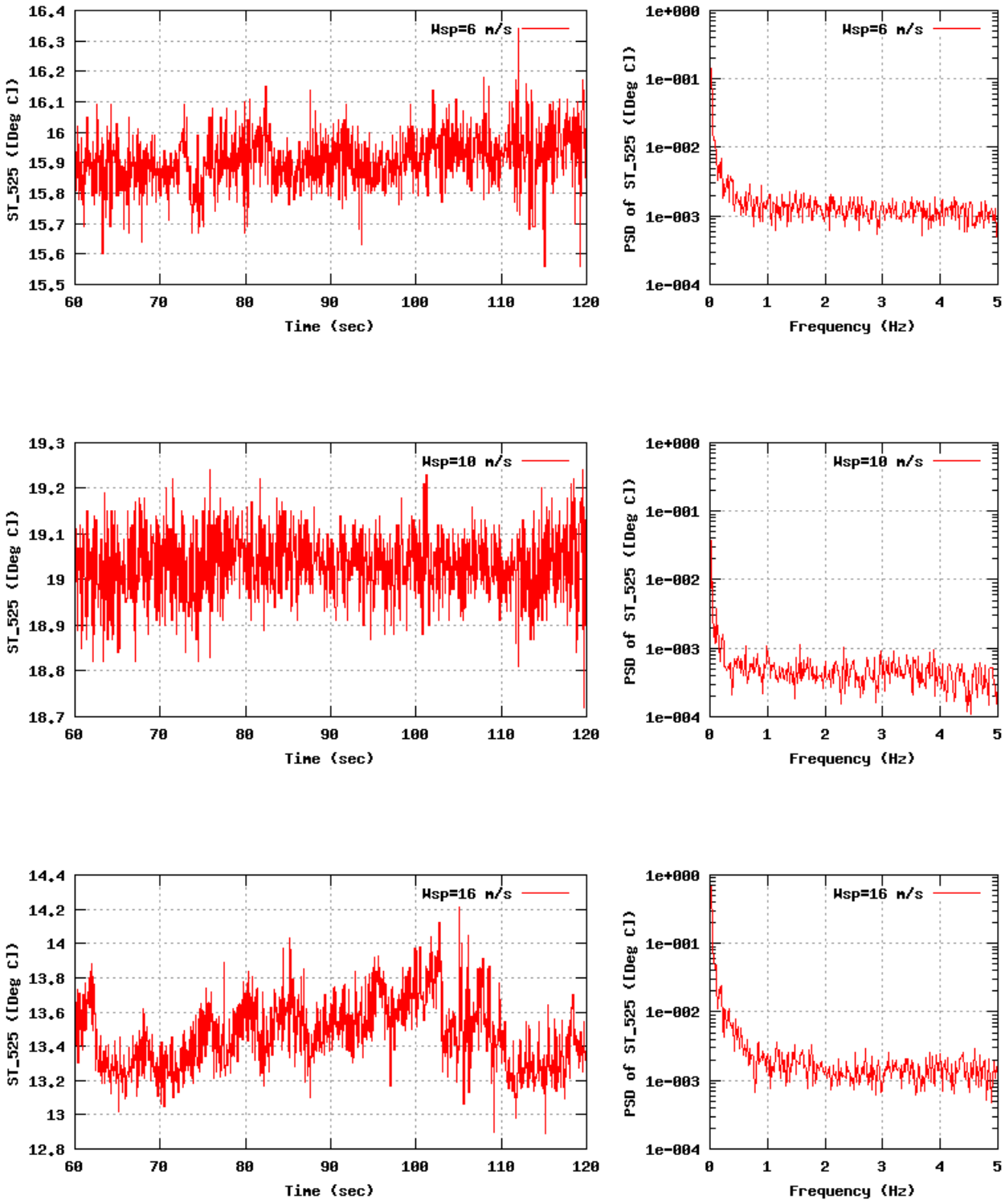

Figure 57b, Sensor 227: Sonic air temperature ST,52.5m versus time and frequency
Input files: m06.asc, m10.asc, m16.asc, m06.psd, m10.psd and m16.psd

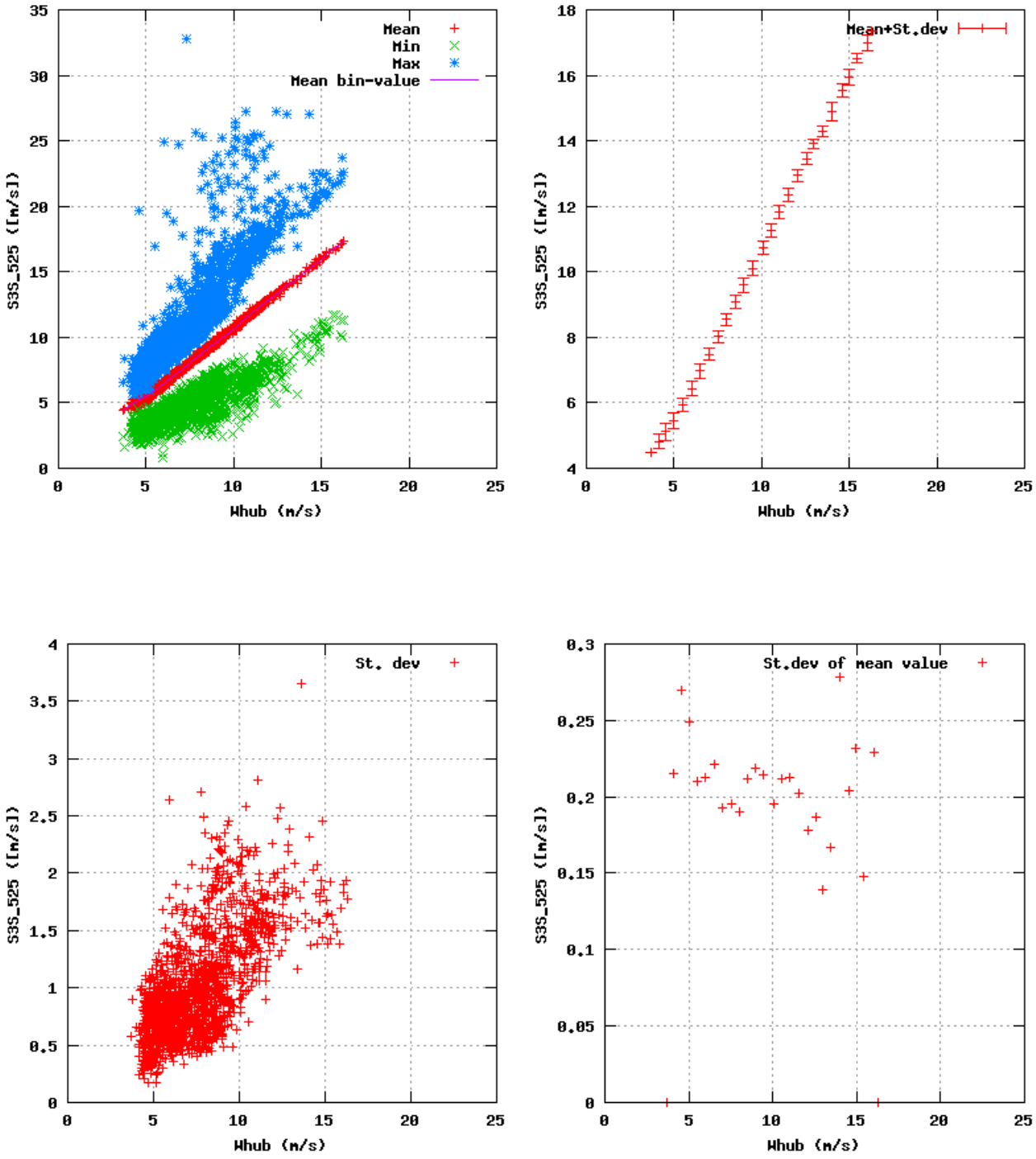

Figure 58a, Sensor 231: Sonic wind speed Sspeed,52.5m versus wind speed
Input files: ntk500res.dat, stat_231.dat

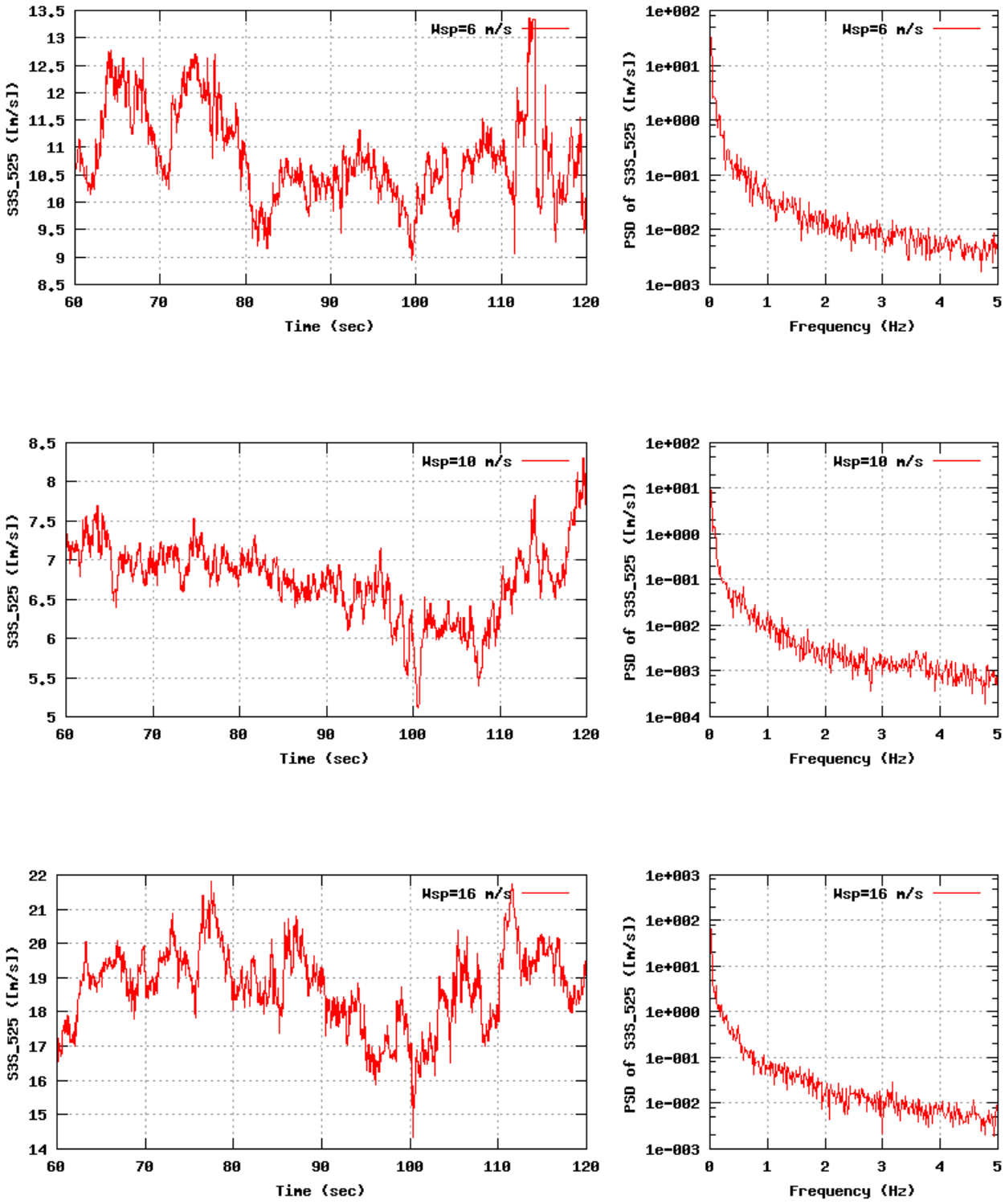

Figure 58b, Sensor 231: Sonic wind speed Sspeed,52.5m versus time and frequency
Input files: m06.asc, m10.asc, m16.asc, m06.psd, m10.psd and m16.psd

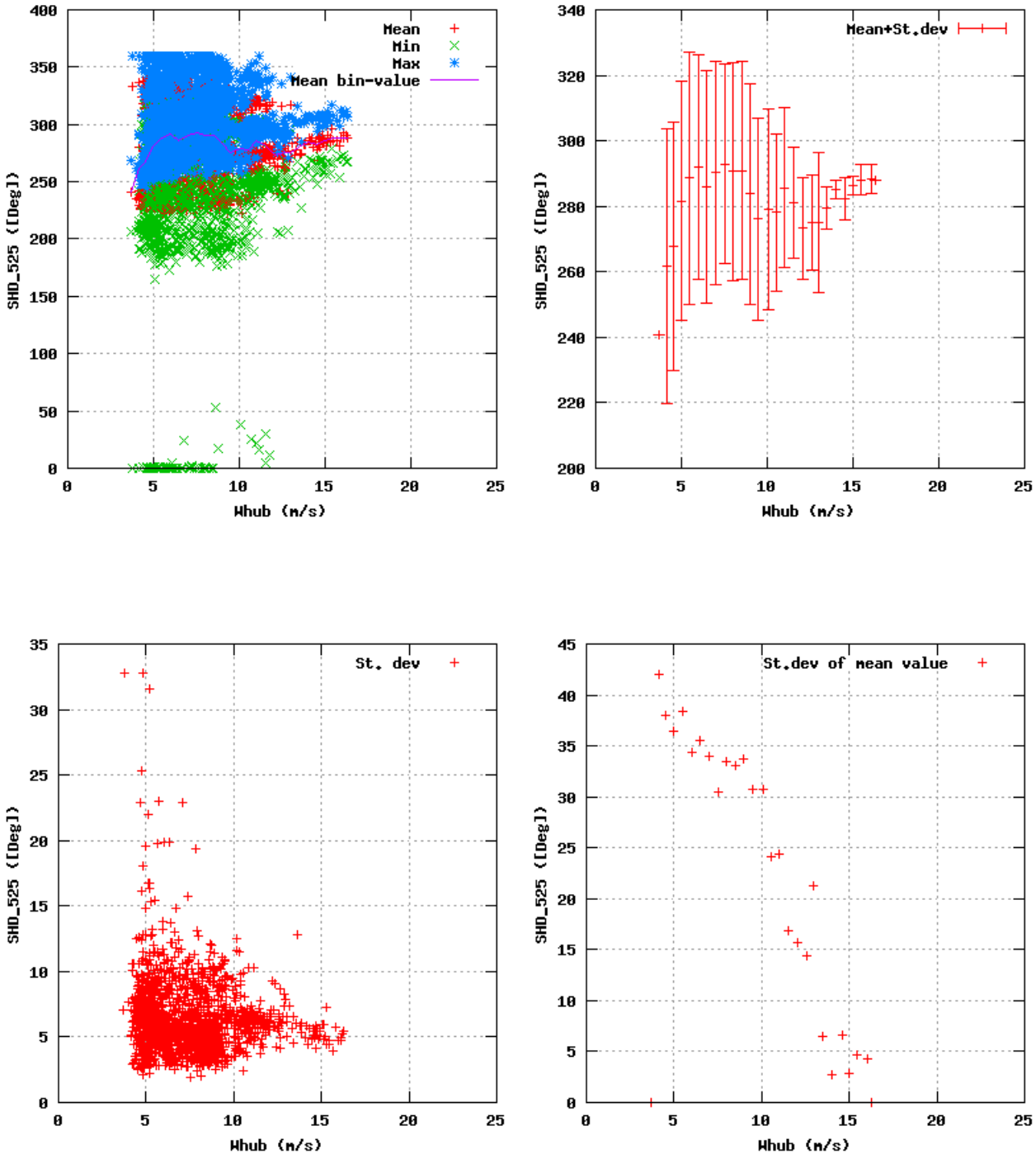

Figure 59a, Sensor 235: Sonic horisontal flow direction Sdir,52.5m versus wind speed
Input files: ntk500res.dat, stat_235.dat

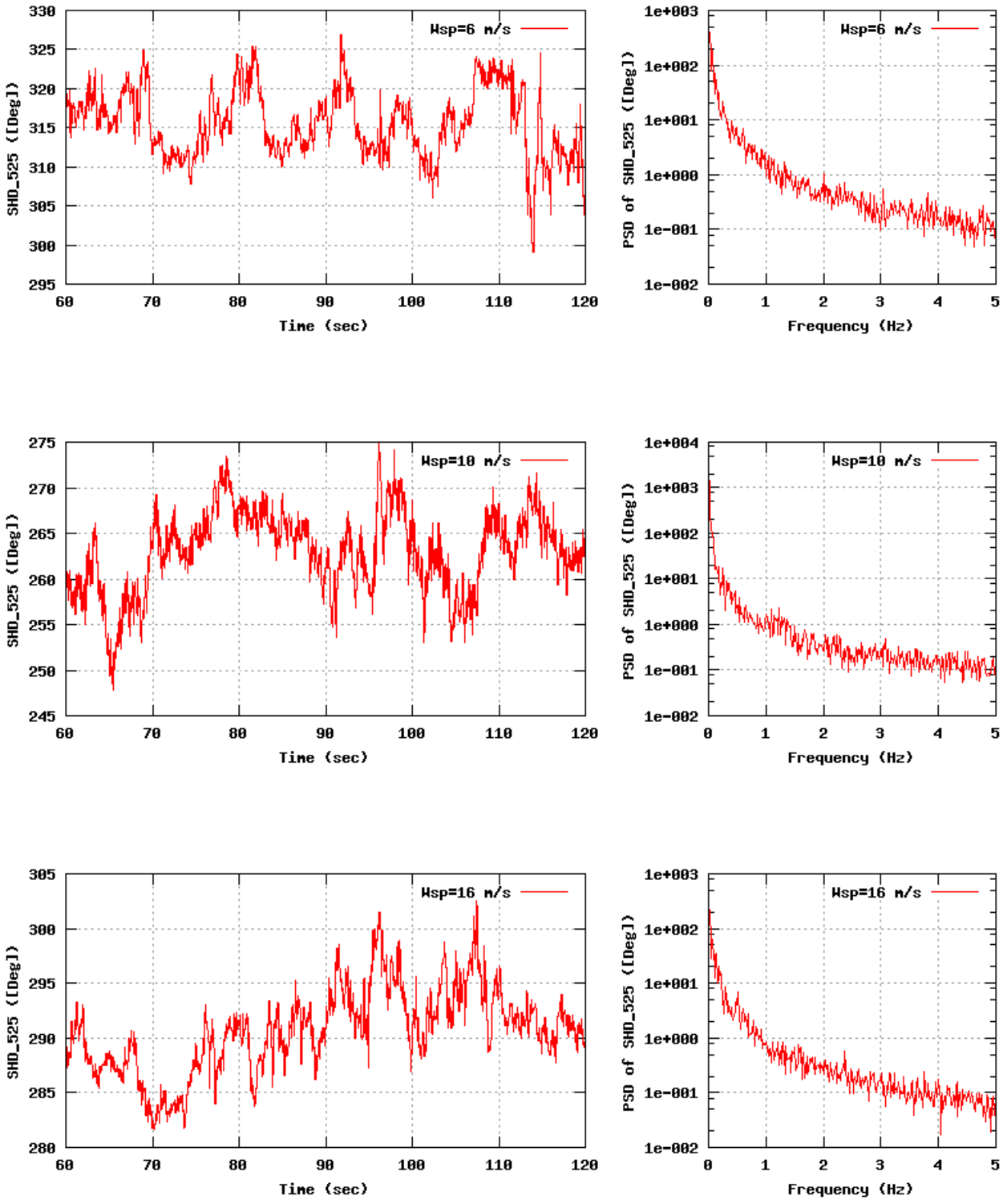

Figure 59b, Sensor 235: Sonic horisontal flow direction Sdir,52.5m versus time and frequency
Input files: m06.asc, m10.asc, m16.asc, m06.psd, m10.psd and m16.psd

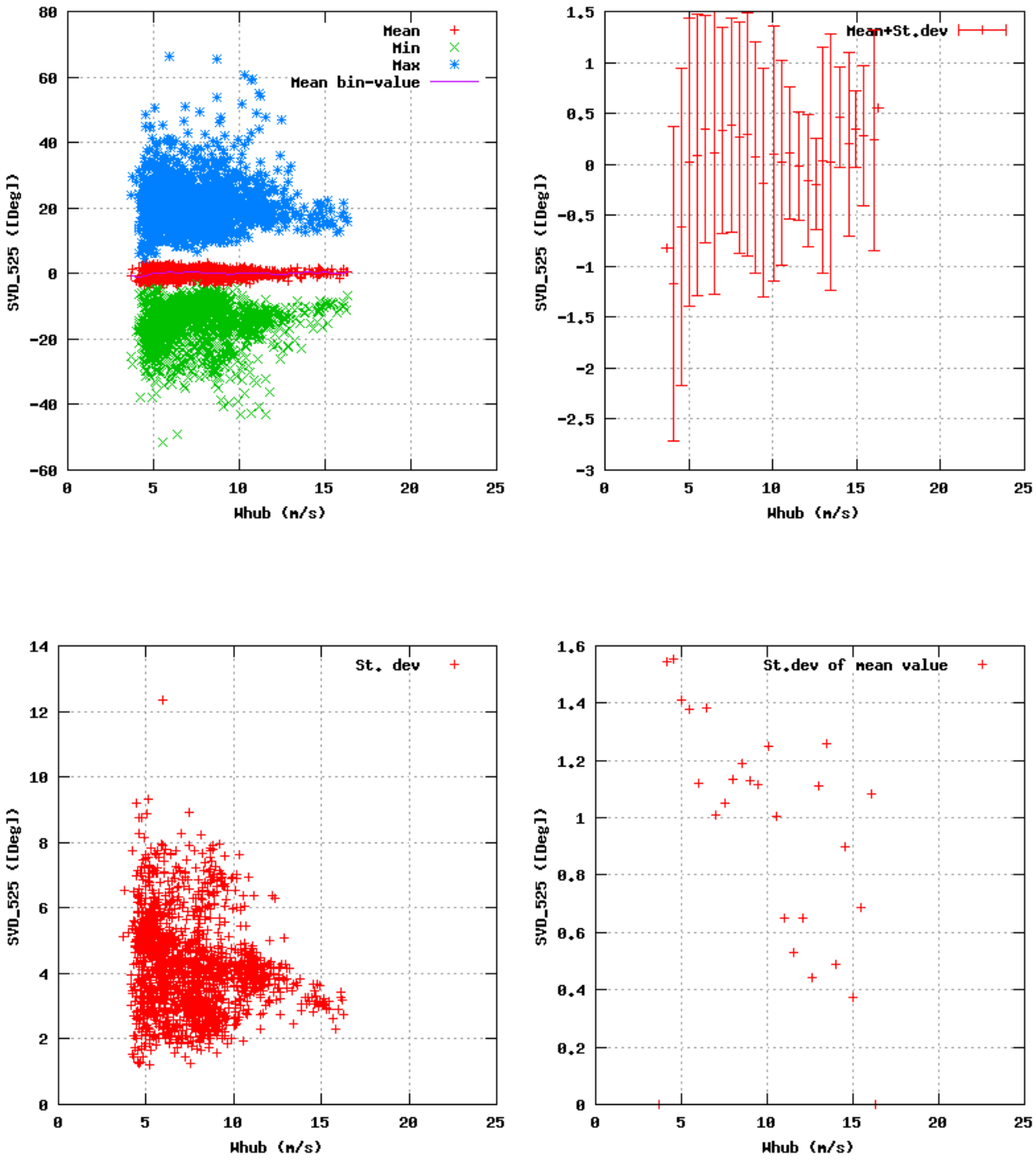

Figure 60a, Sensor 239: Sonic vertical flow angle Stilt,52.5m versus wind speed
Input files: ntk500res.dat, stat_239.dat

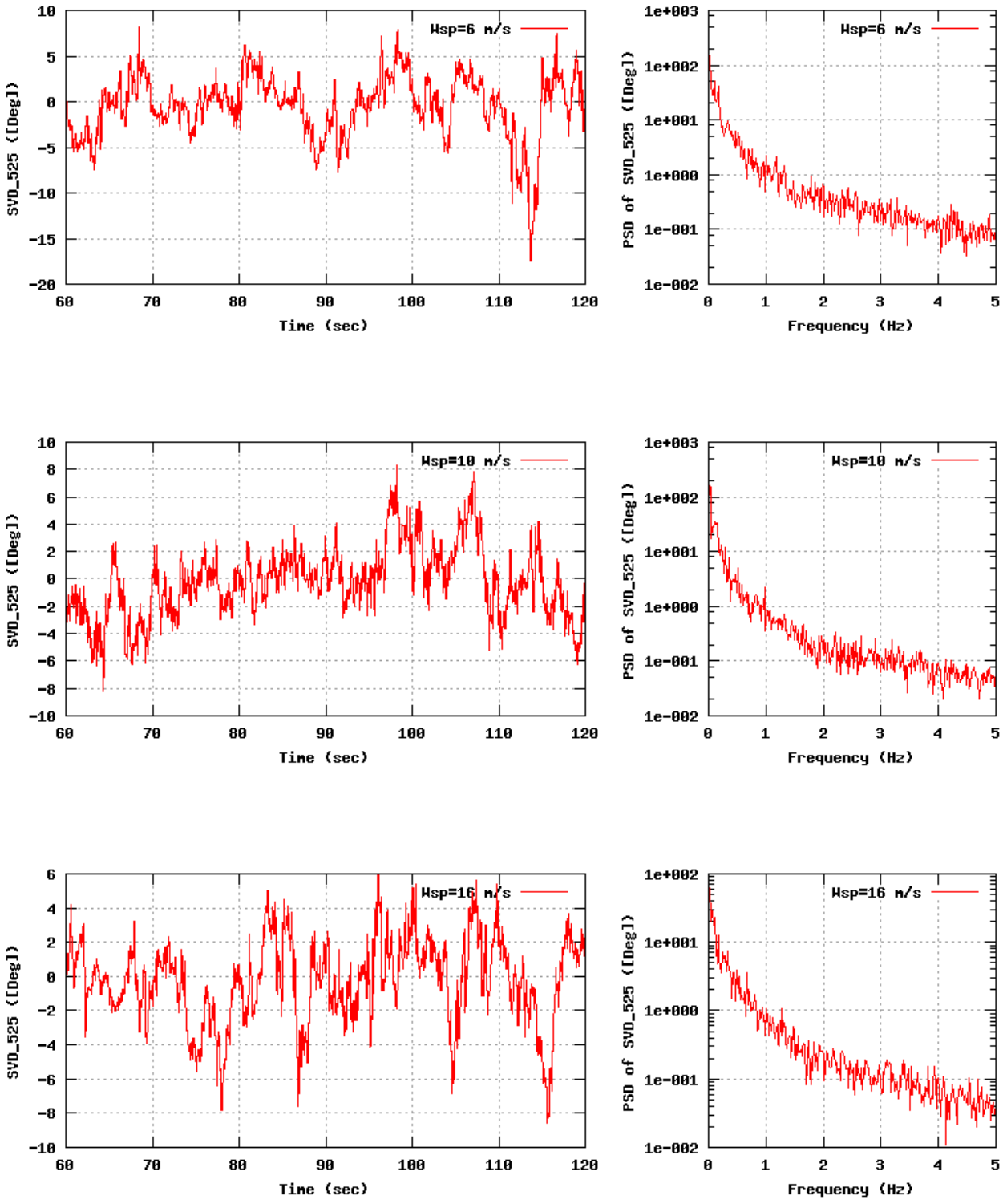

Figure 60b, Sensor 239: Sonic vertical flow angle Stilt,52.5m versus time and frequency
Input files: m06.asc, m10.asc, m16.asc, m06.psd, m10.psd and m16.psd

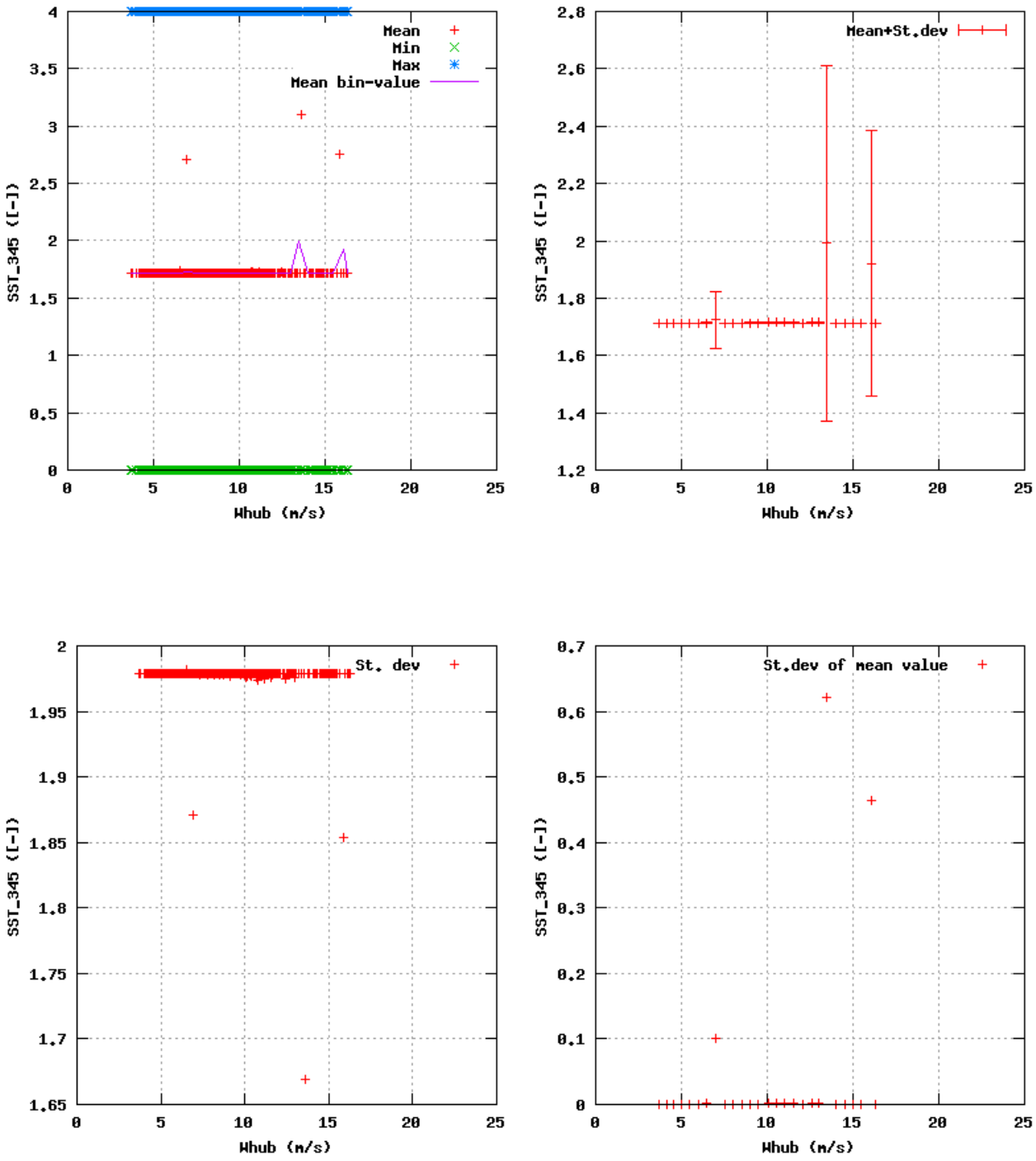

Figure 61a, Sensor 243: Sonic status Sstat,34.5m versus wind speed
Input files: ntk500res.dat, stat_243.dat

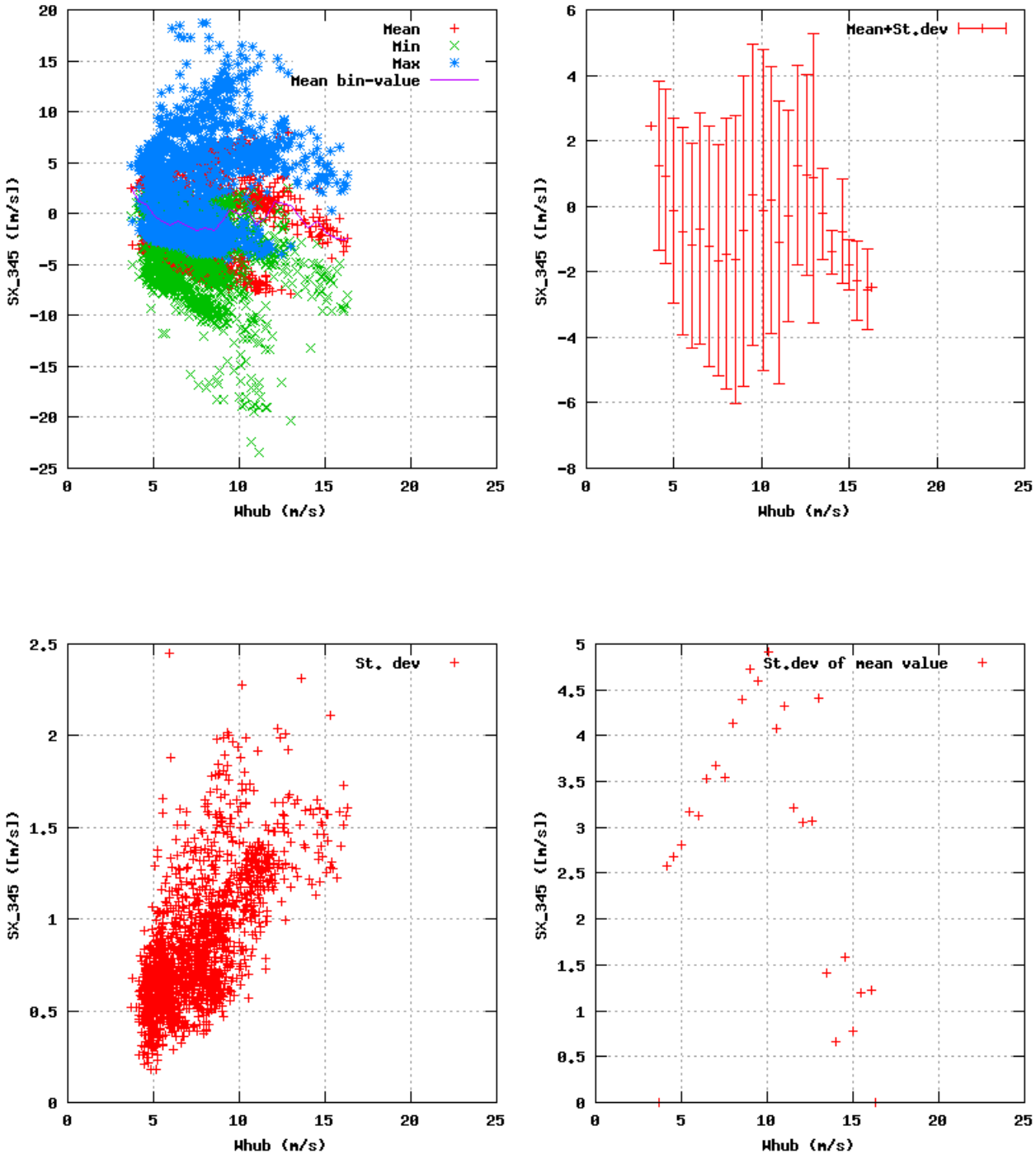

Figure 62a, Sensor 247: Sonic wind component SX,34.5m versus wind speed
Input files: ntk500res.dat, stat_247.dat

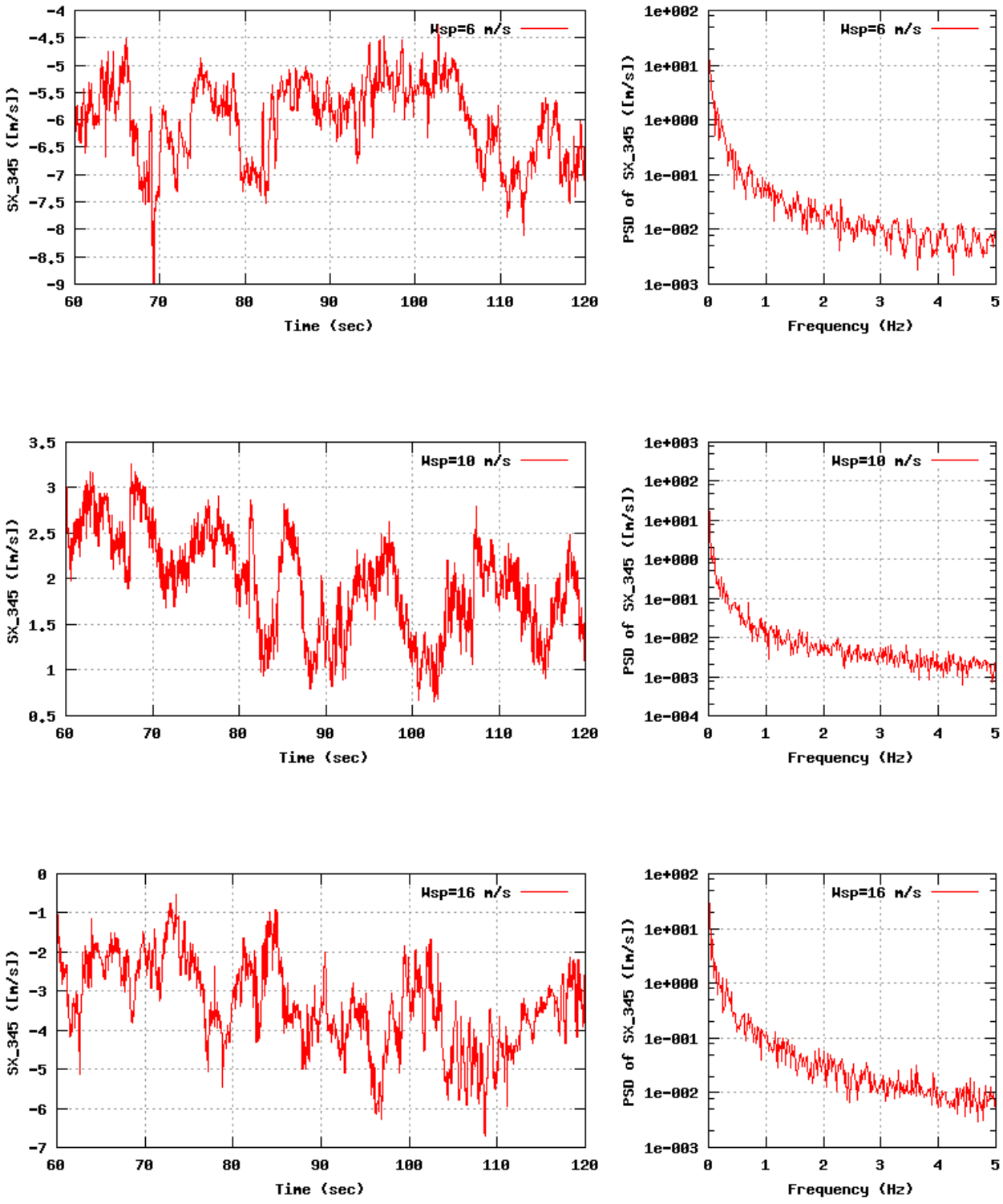

Figure 62b, Sensor 247: Sonic wind component SX,34.5m versus time and frequency
Input files: m06.asc, m10.asc, m16.asc, m06.psd, m10.psd and m16.psd

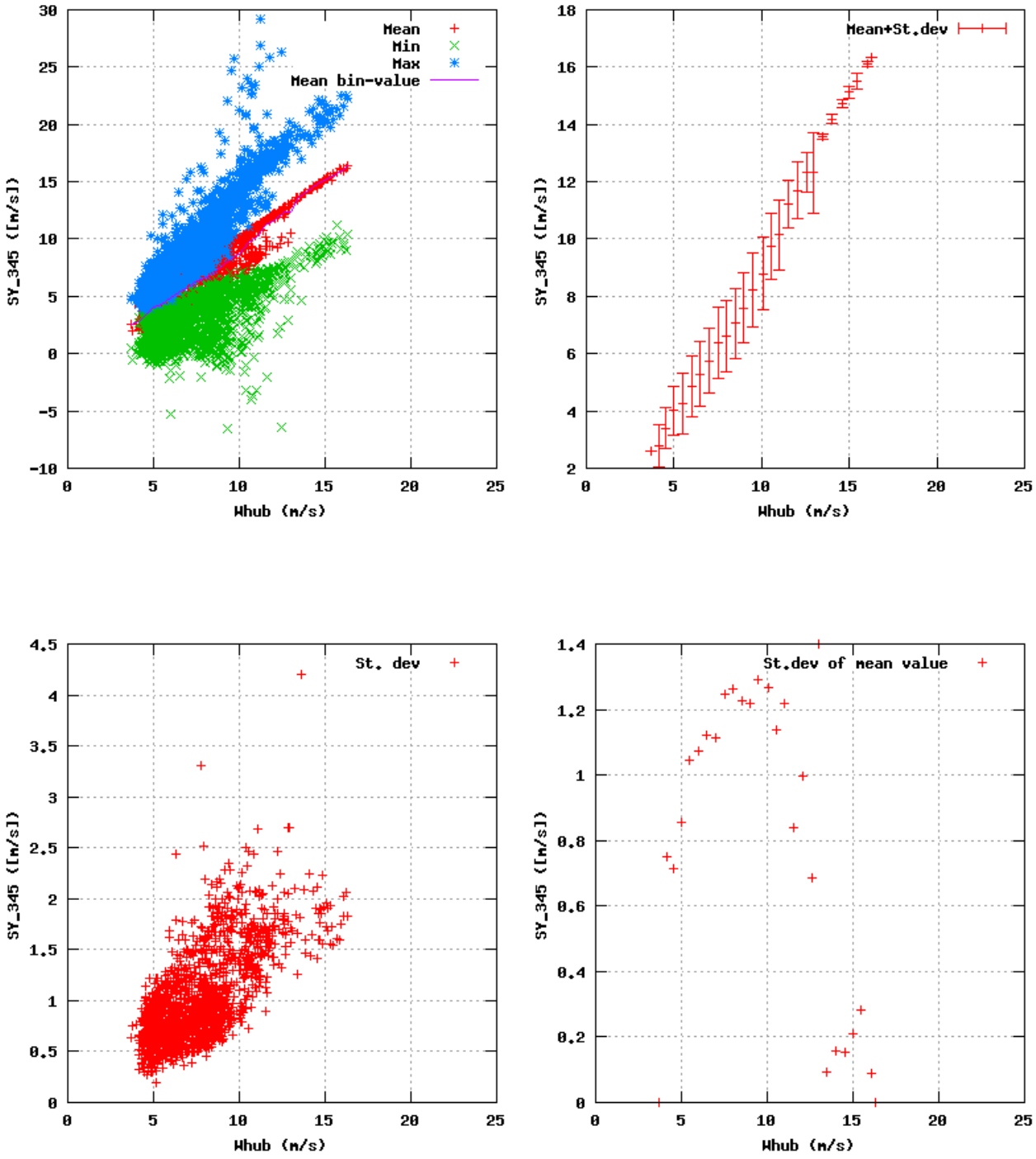

Figure 63a, Sensor 251: Sonic wind component SY,34.5m versus wind speed
Input files: ntk500res.dat, stat_251.dat

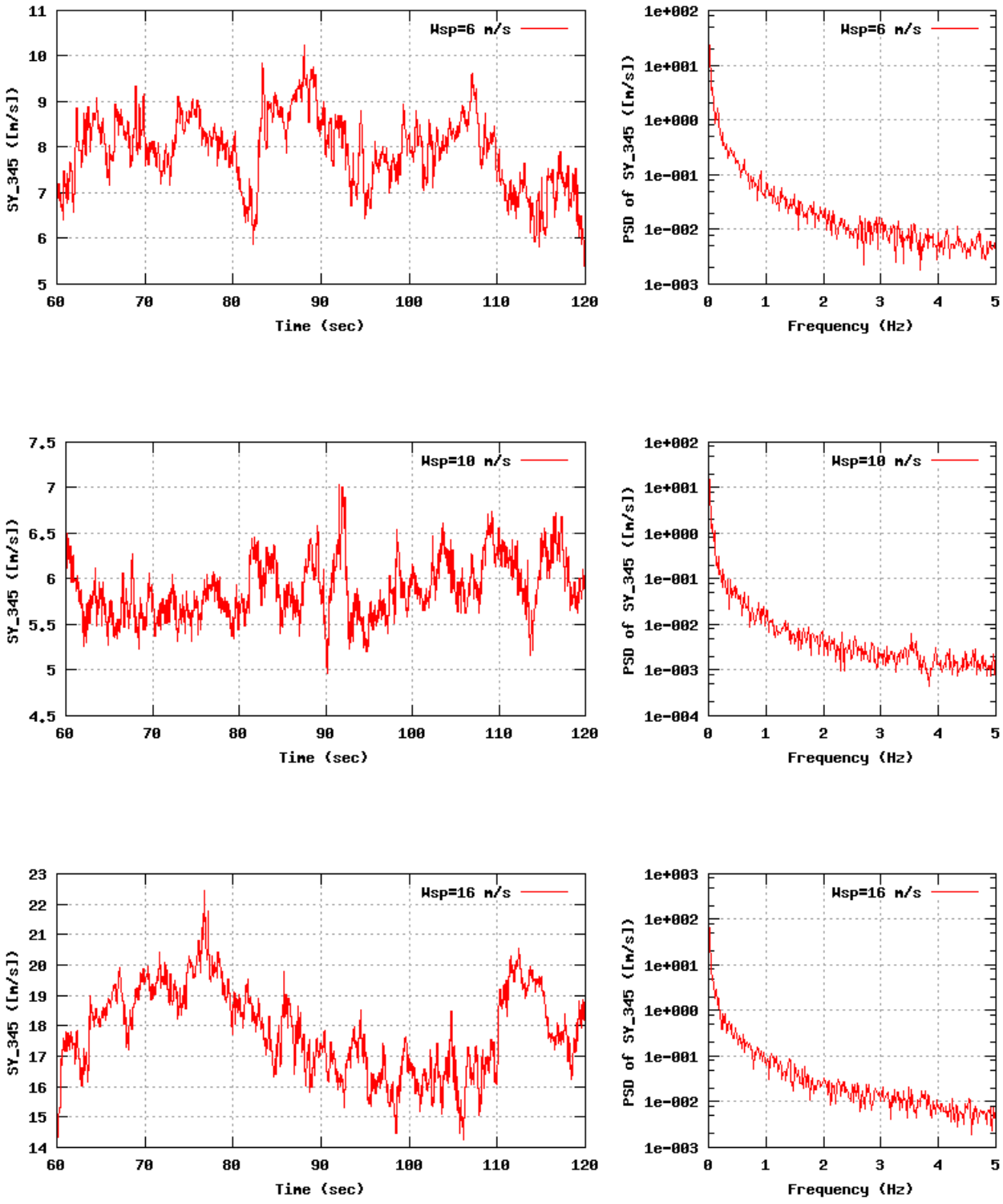

Figure 63b, Sensor 251: Sonic wind component SY,34.5m versus time and frequency
Input files: m06.asc, m10.asc, m16.asc, m06.psd, m10.psd and m16.psd

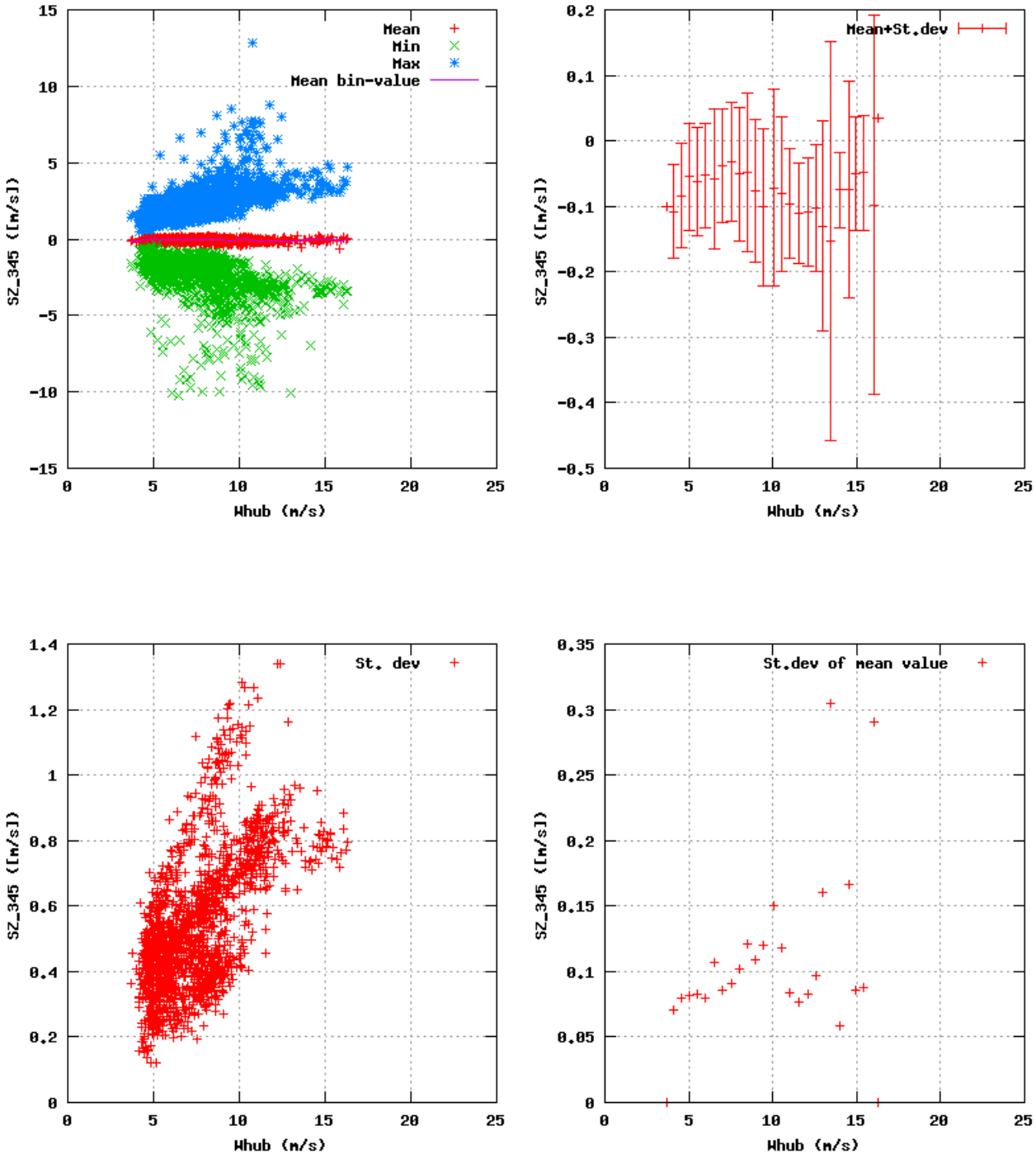

Figure 64a, Sensor 255: Sonic wind component SZ,34.5m versus wind speed
Input files: ntk500res.dat, stat_255.dat

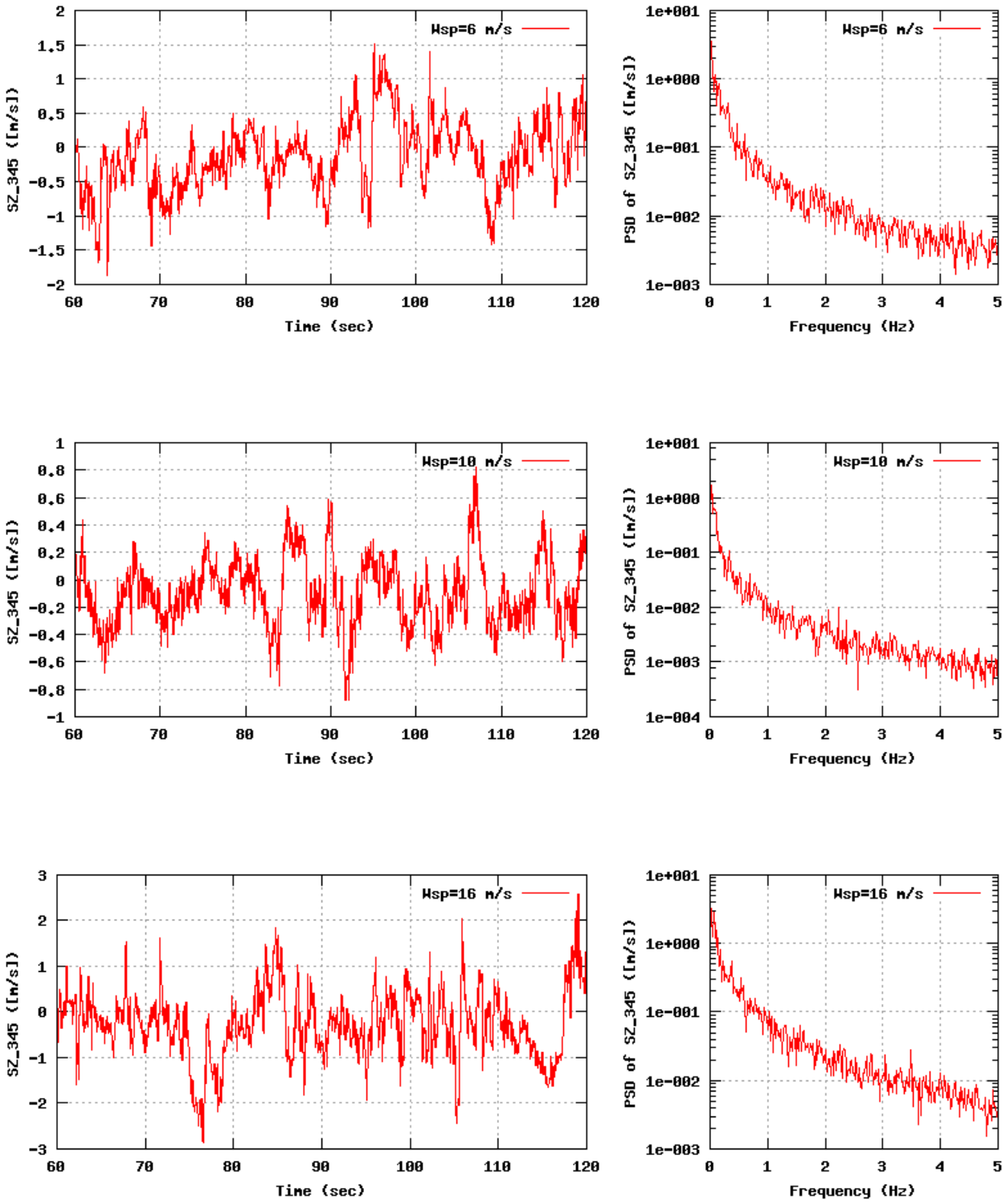

Figure 64b, Sensor 255: Sonic wind component SZ,34.5m versus time and frequency
Input files: m06.asc, m10.asc, m16.asc, m06.psd, m10.psd and m16.psd

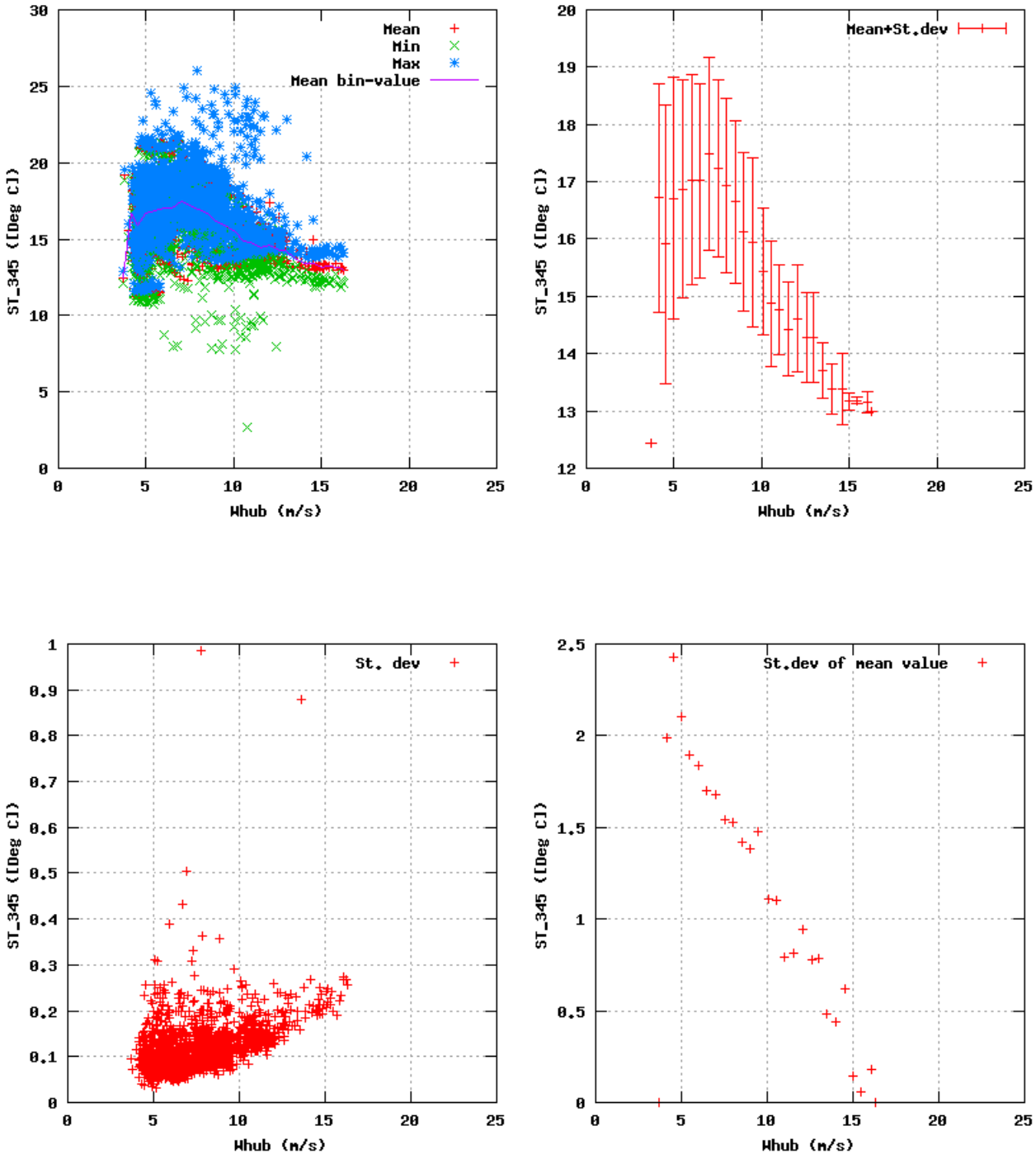

Figure 65a, Sensor 259: Sonic air temperature ST,34.5m versus wind speed
Input files: ntk500res.dat, stat_259.dat

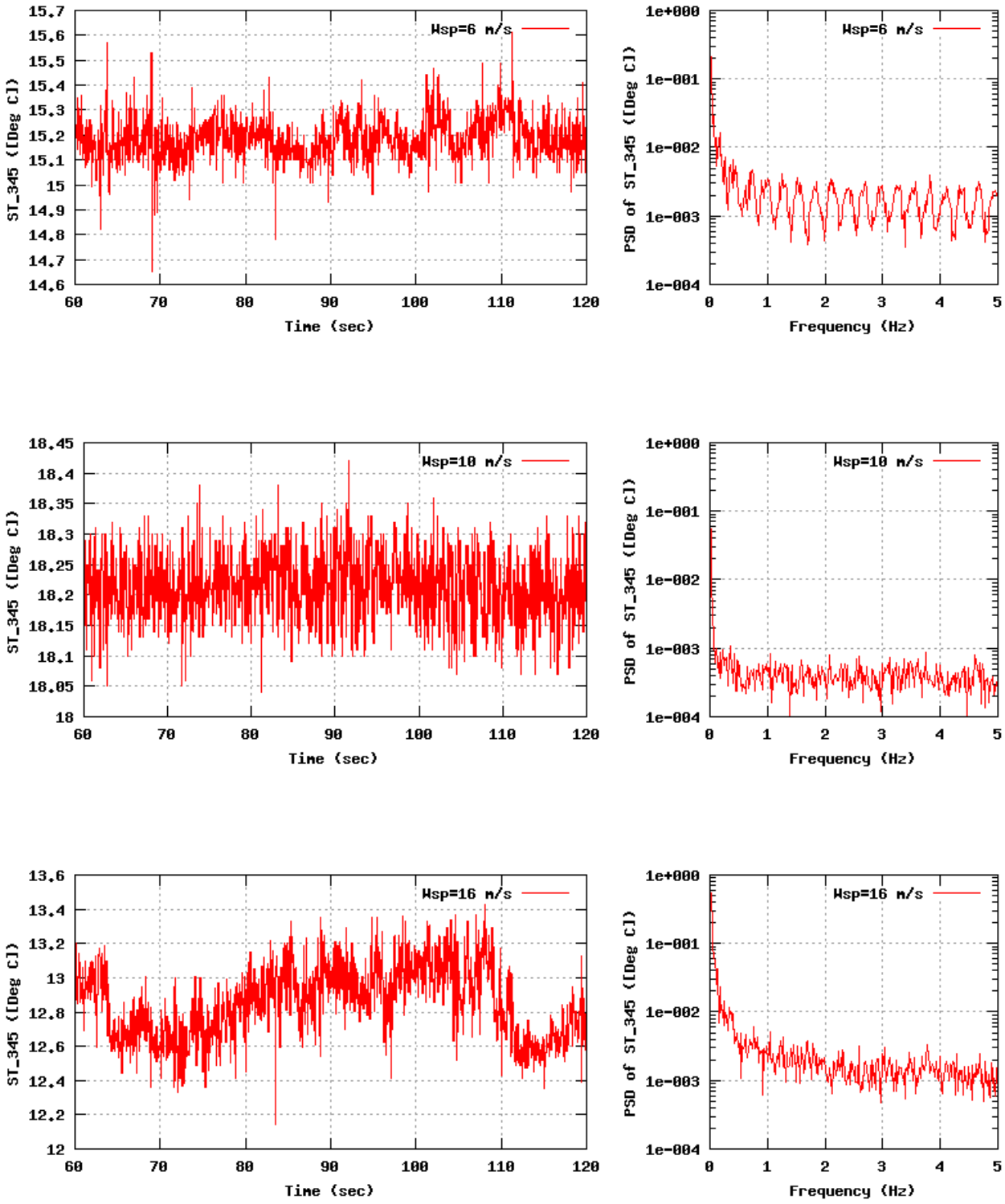

Figure 65b, Sensor 259: Sonic air temperature ST,34.5m versus time and frequency
Input files: m06.asc, m10.asc, m16.asc, m06.psd, m10.psd and m16.psd

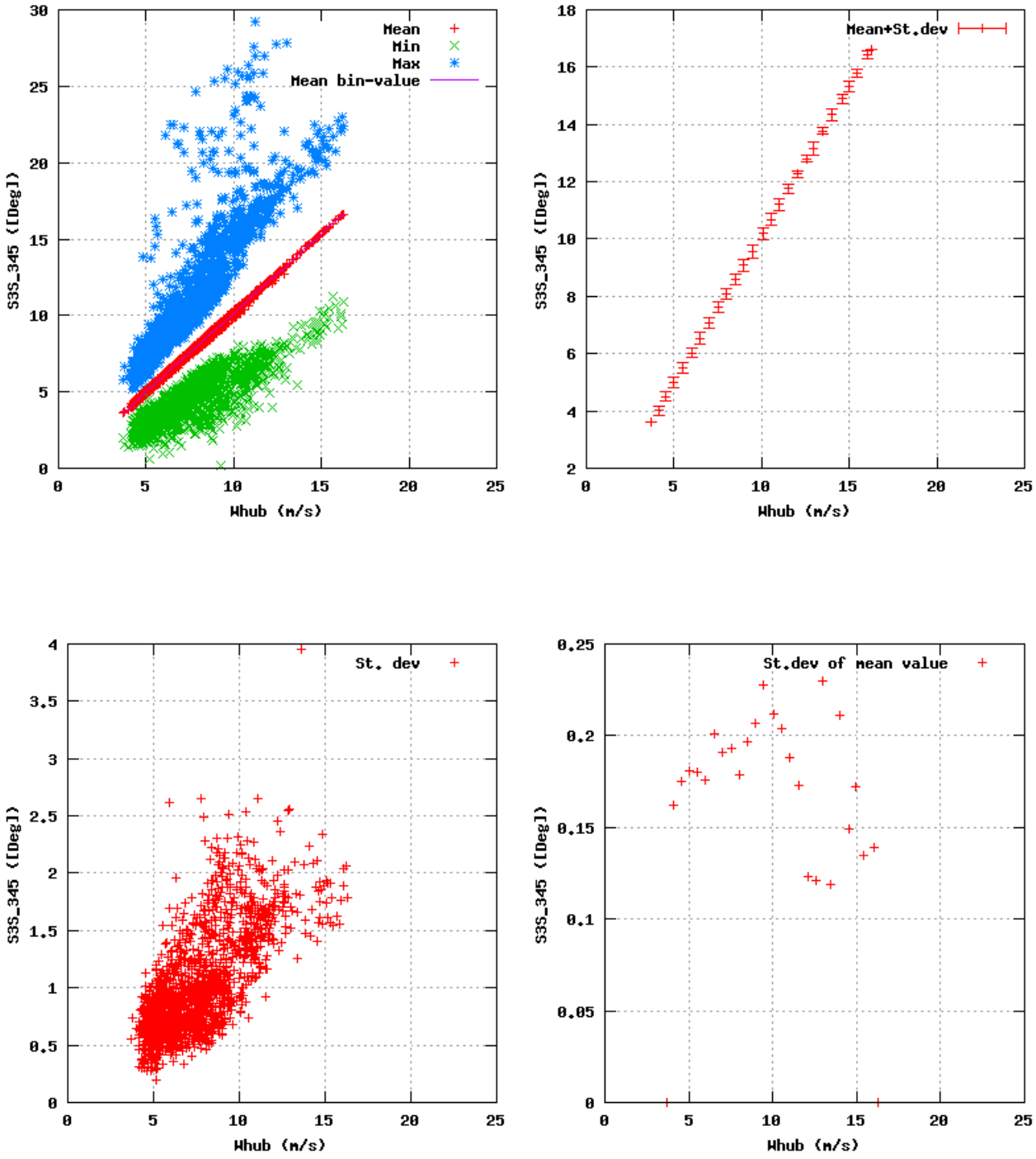

Figure 66a, Sensor 263: Sonic wind speed Sspeed,34.5m versus wind speed
Input files: ntk500res.dat, stat_263.dat

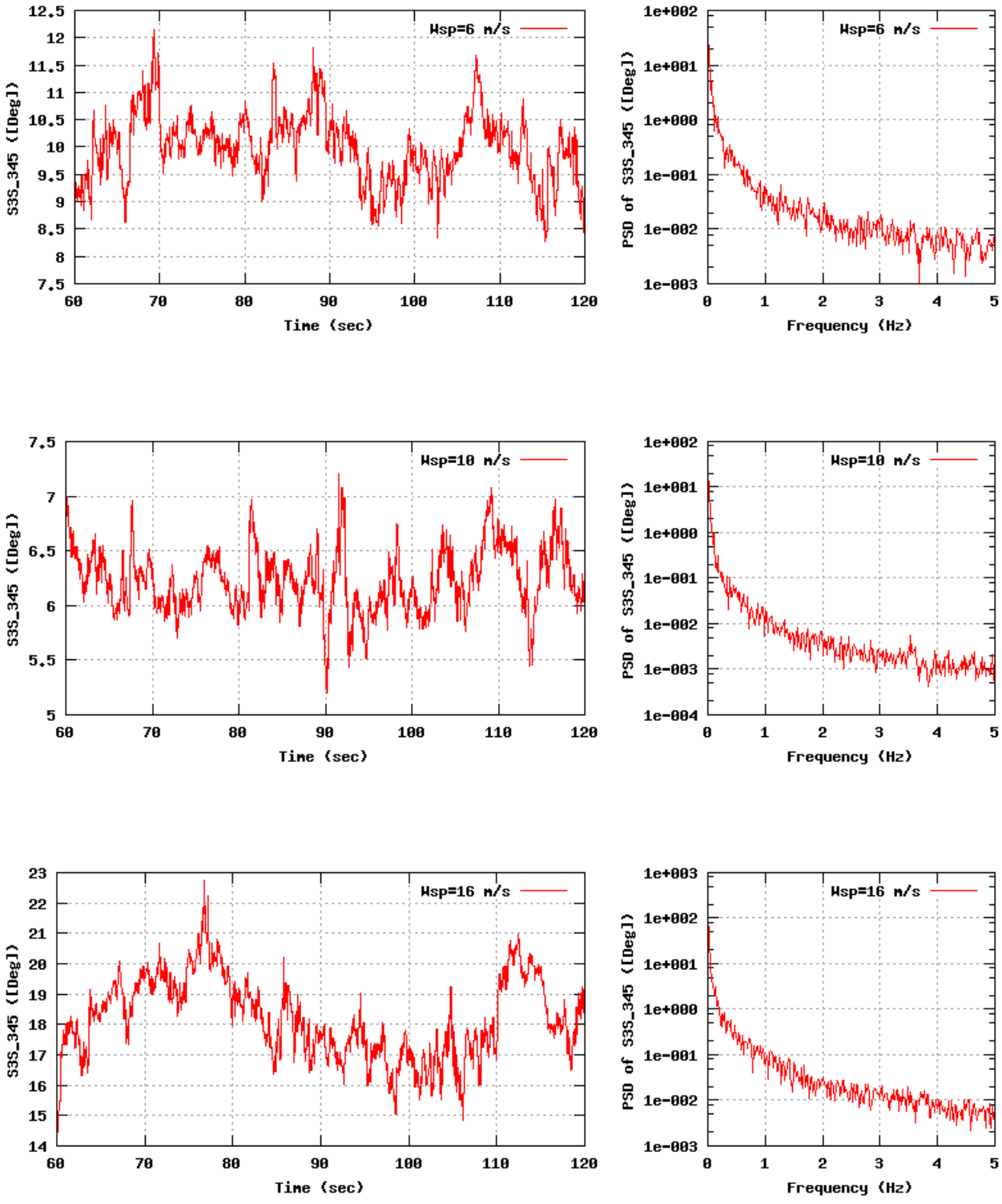

Figure 66b, Sensor 263: Sonic wind speed Sspeed,34.5m versus time and frequency
Input files: m06.asc, m10.asc, m16.asc, m06.psd, m10.psd and m16.psd

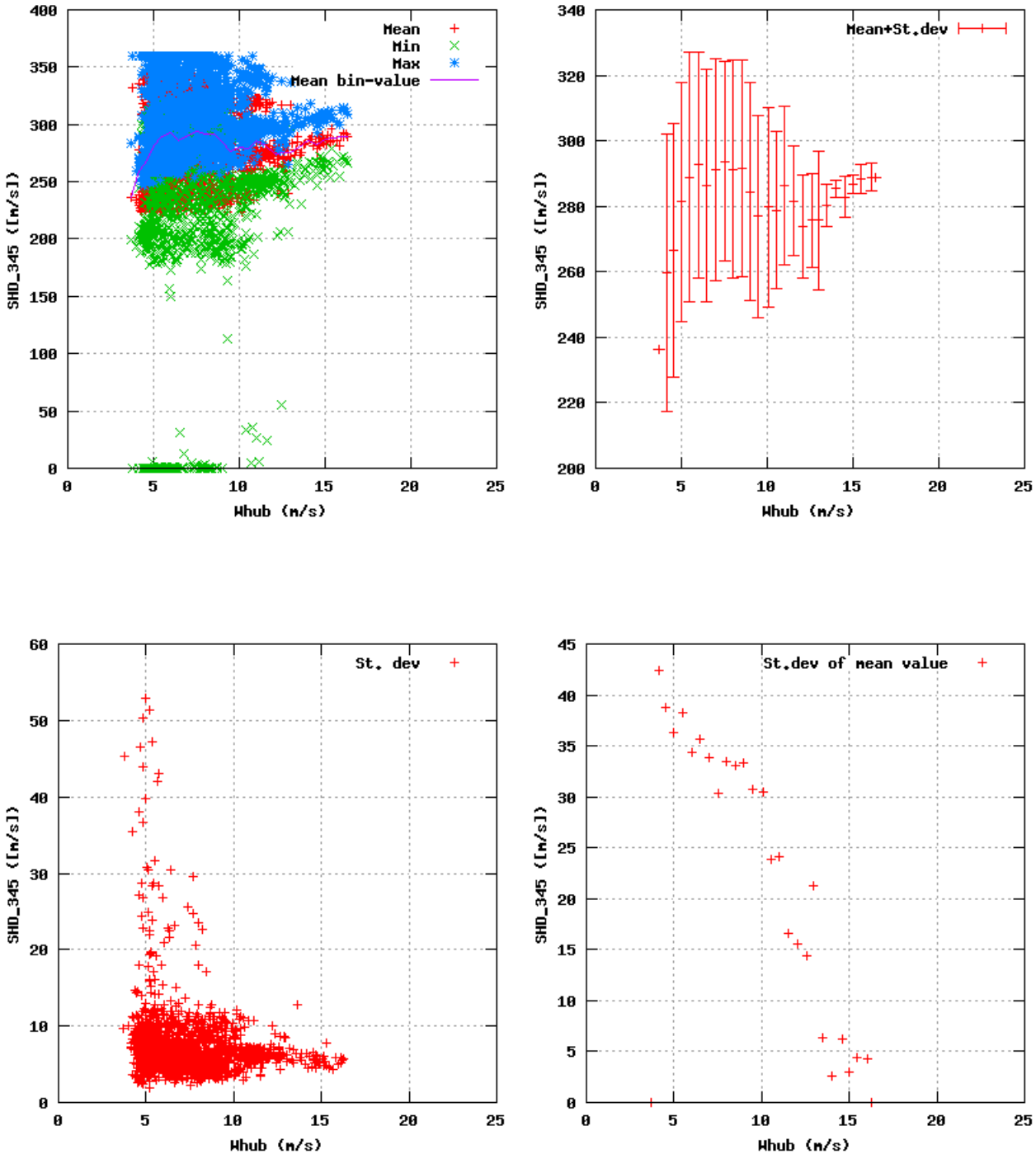

Figure 67a, Sensor 267: Sonic horisontal flow direction Sdir,34.5m versus wind speed
Input files: ntk500res.dat, stat_267.dat

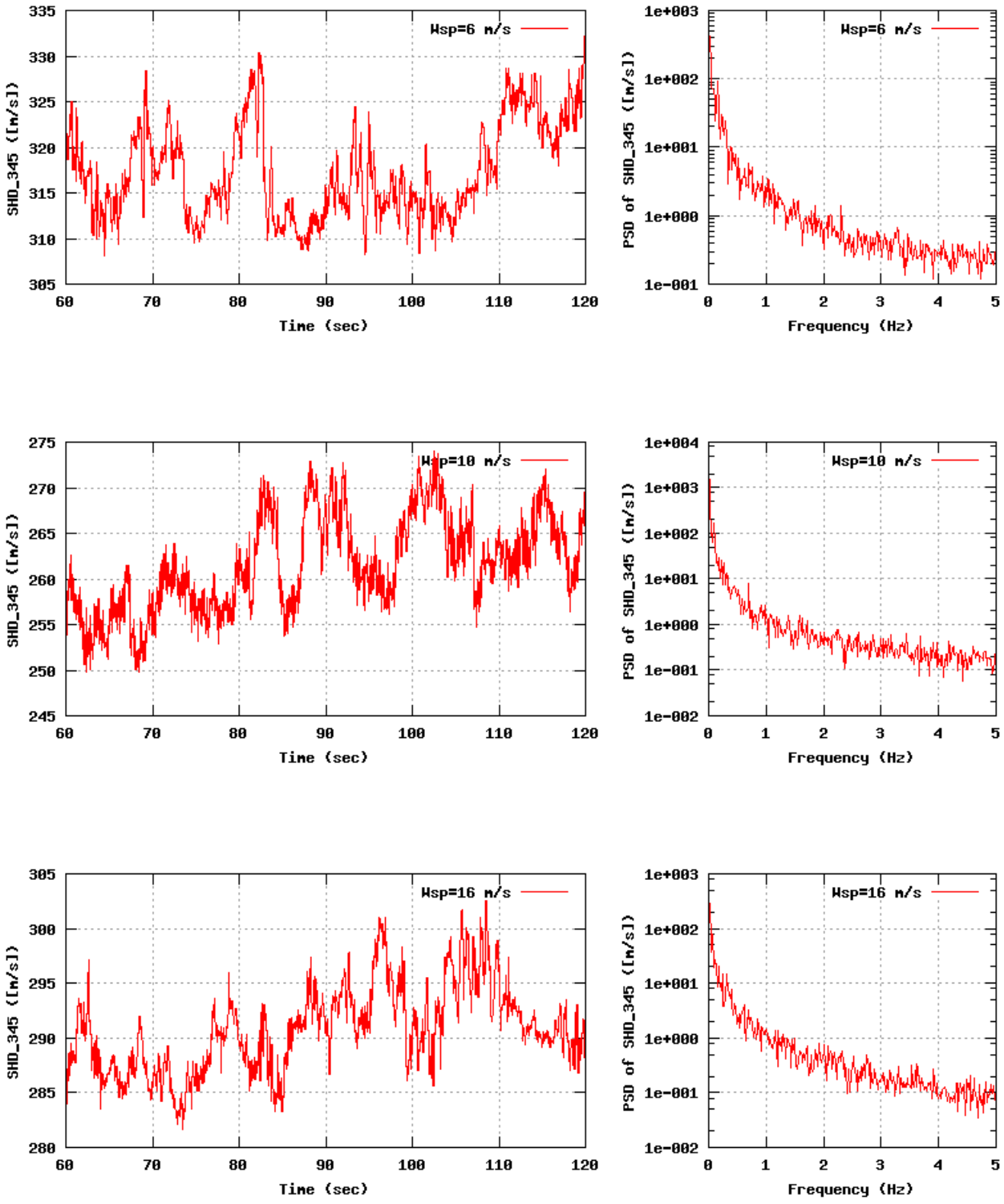

Figure 67b, Sensor 267: Sonic horisontal flow direction Sdir,34.5m versus time and frequency
Input files: m06.asc, m10.asc, m16.asc, m06.psd, m10.psd and m16.psd

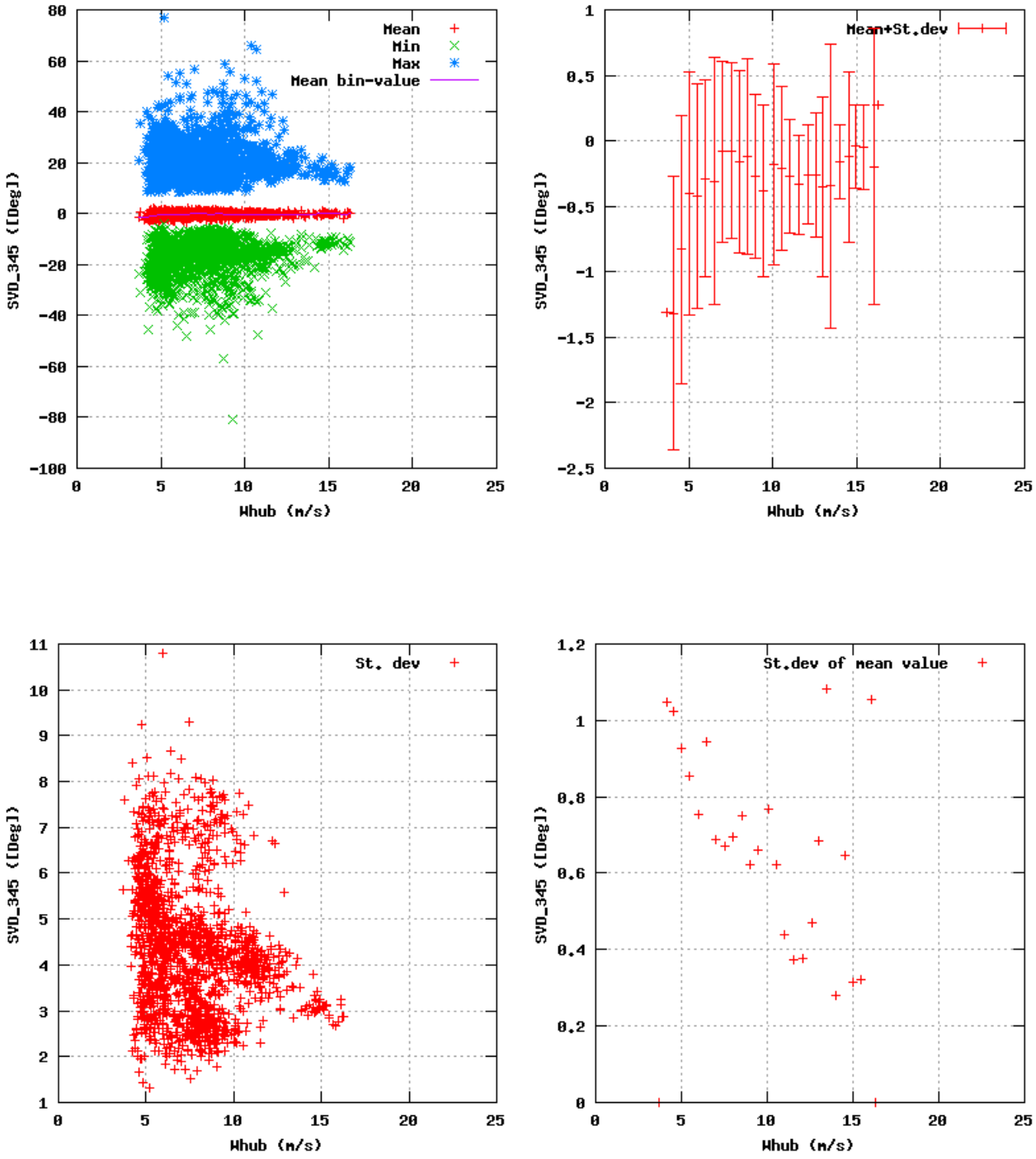

Figure 68a, Sensor 271: Sonic vertical flow angle Stilt,34.5m versus wind speed
Input files: ntk500res.dat, stat_271.dat

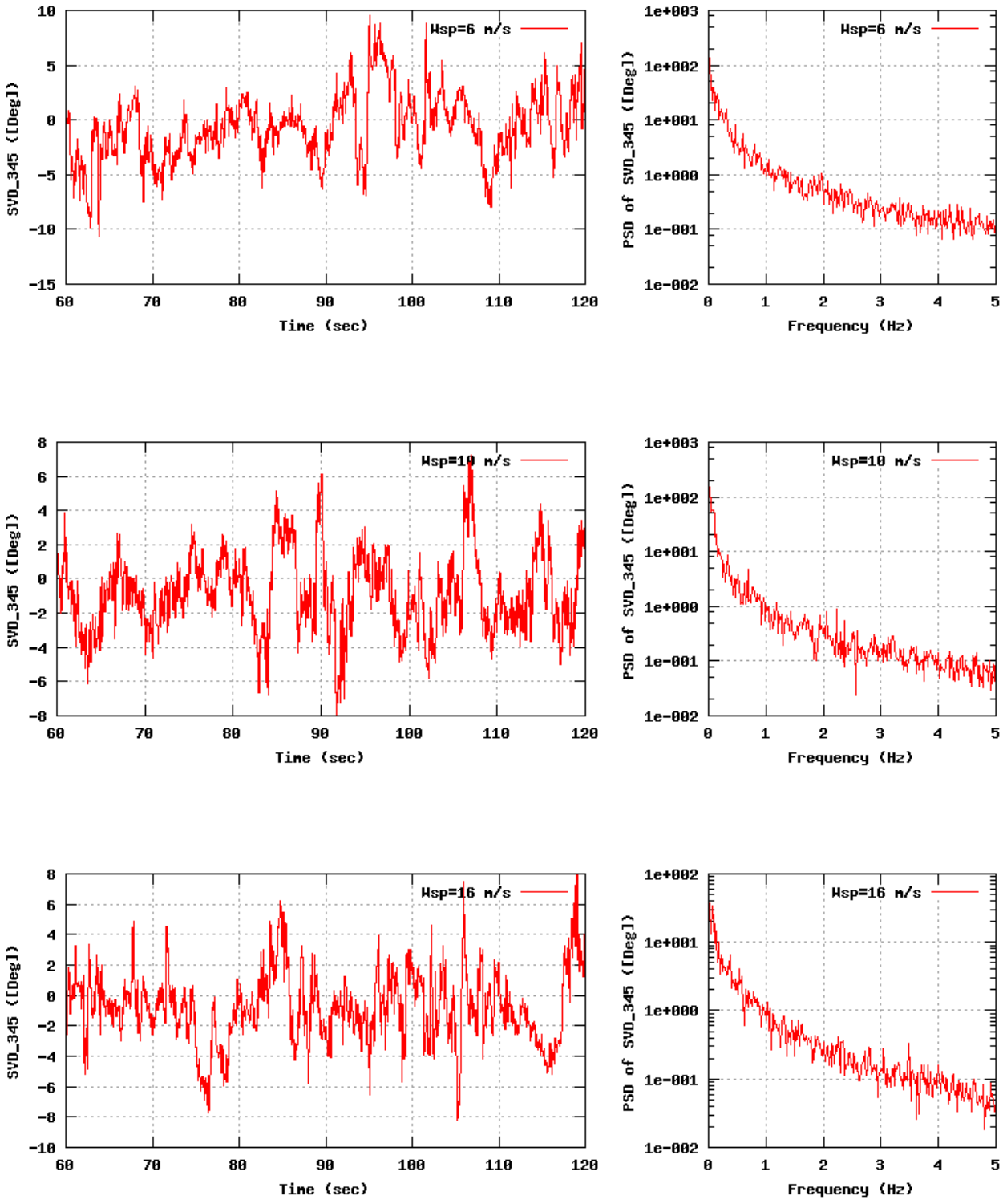

Figure 68b, Sensor 271: Sonic vertical flow angle Stilt,34.5m versus time and frequency
Input files: m06.asc, m10.asc, m16.asc, m06.psd, m10.psd and m16.psd

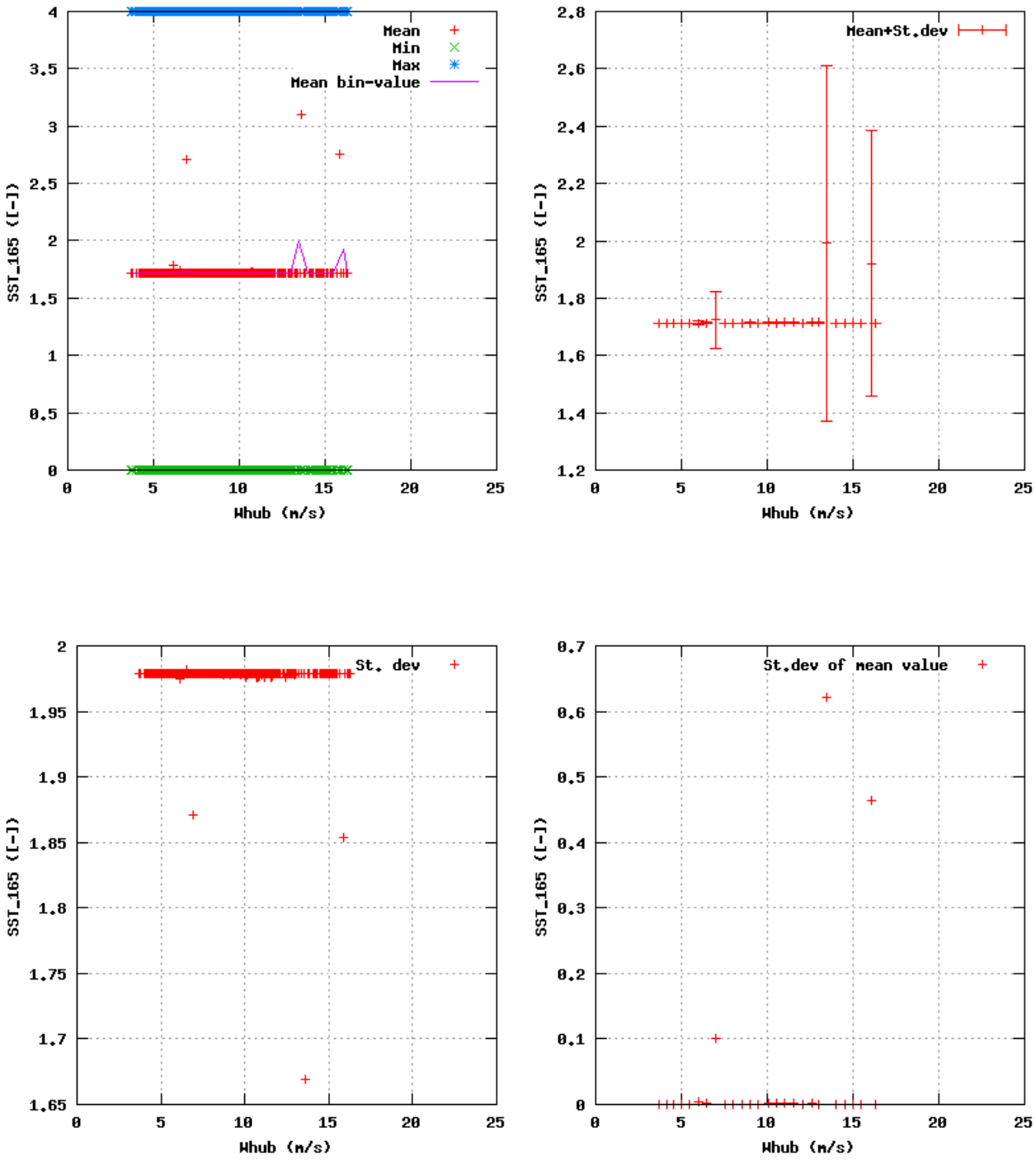

Figure 69a, Sensor 275: Sonic status Sstat,34.5m versus wind speed
Input files: ntk500res.dat, stat_275.dat

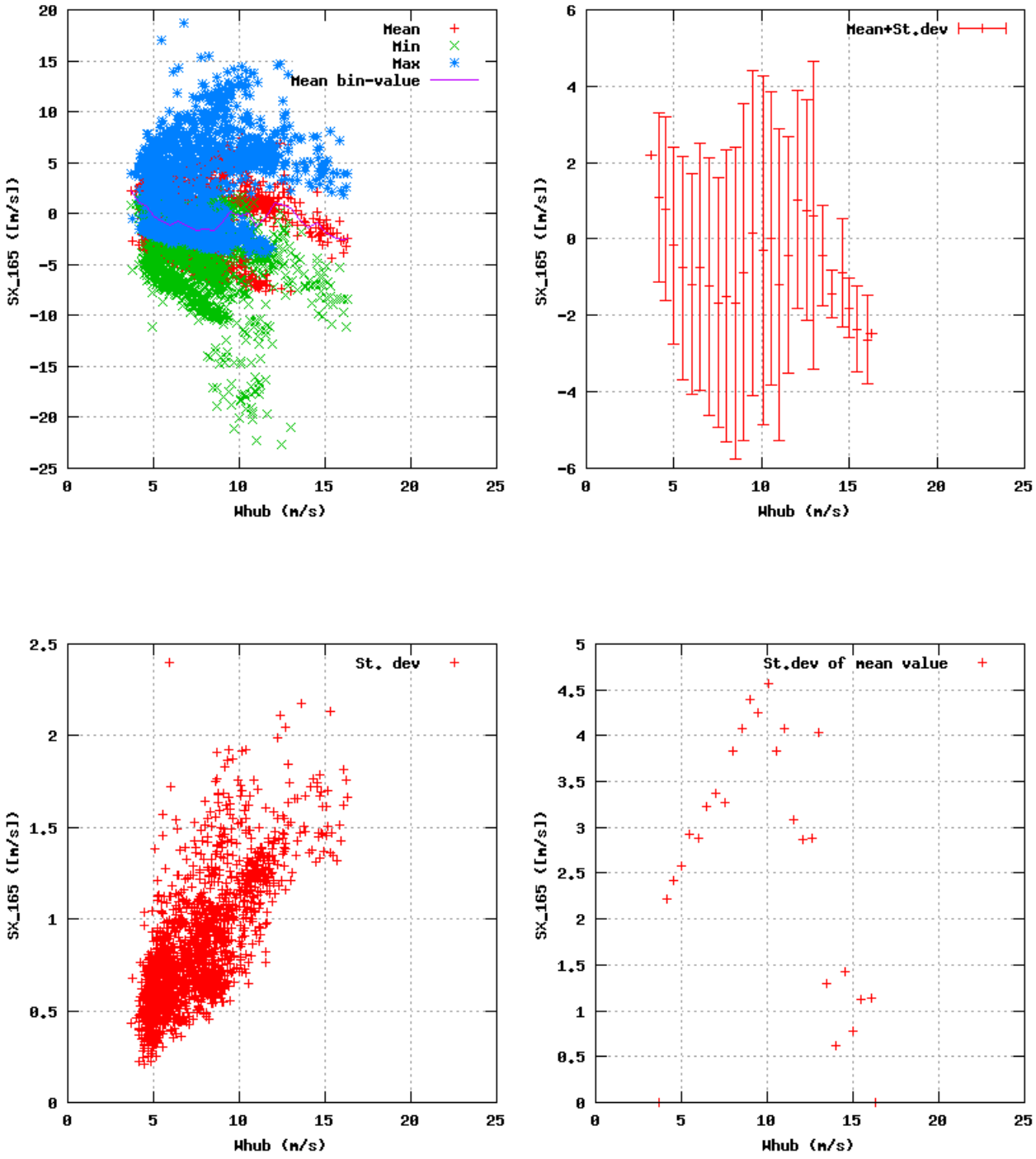

Figure 70a, Sensor 279: Sonic wind component SX,16.5m versus wind speed
Input files: ntk500res.dat, stat_279.dat

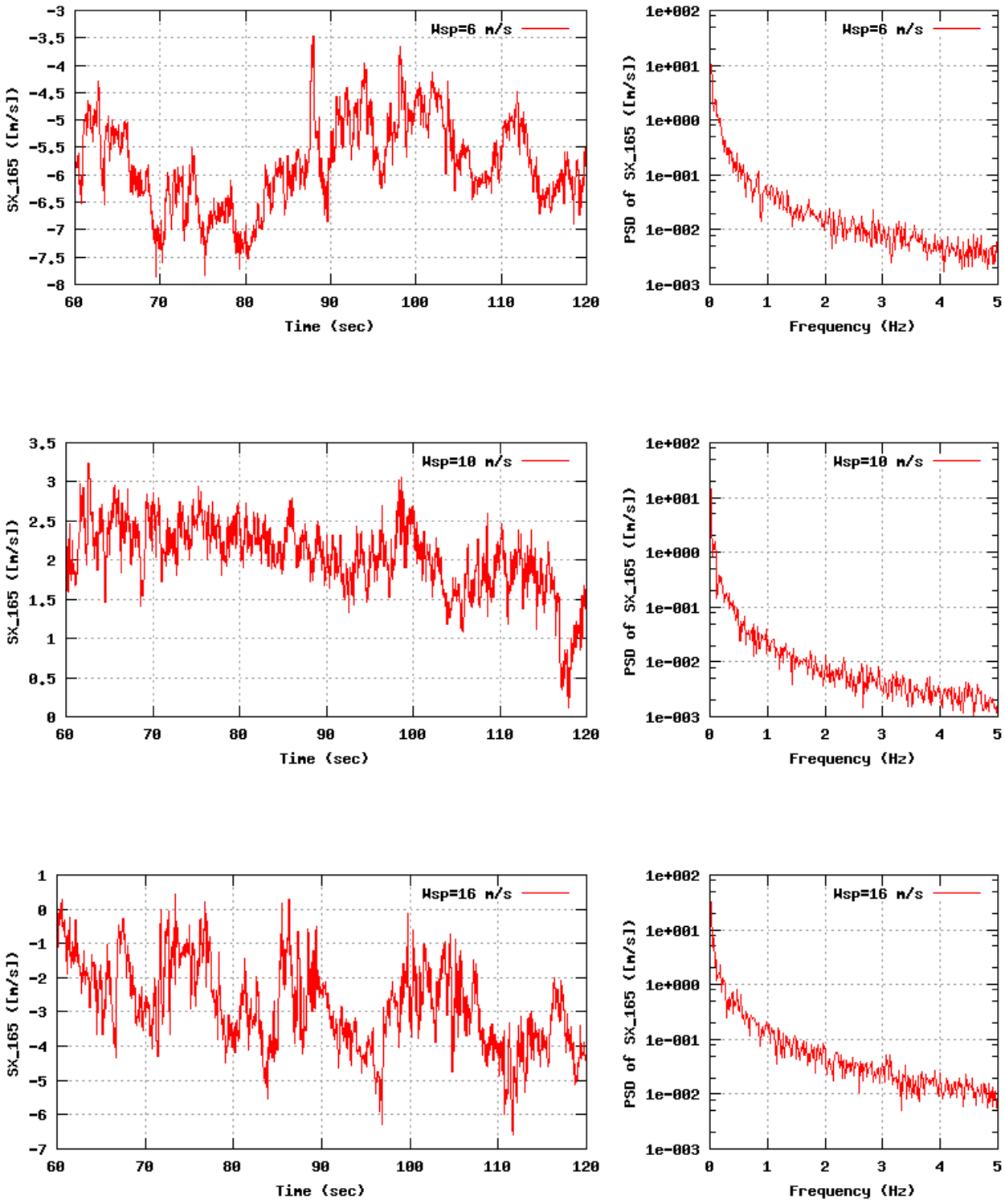

Figure 70b, Sensor 279: Sonic wind component SX,16.5m versus time and frequency
Input files: m06.asc, m10.asc, m16.asc, m06.psd, m10.psd and m16.psd

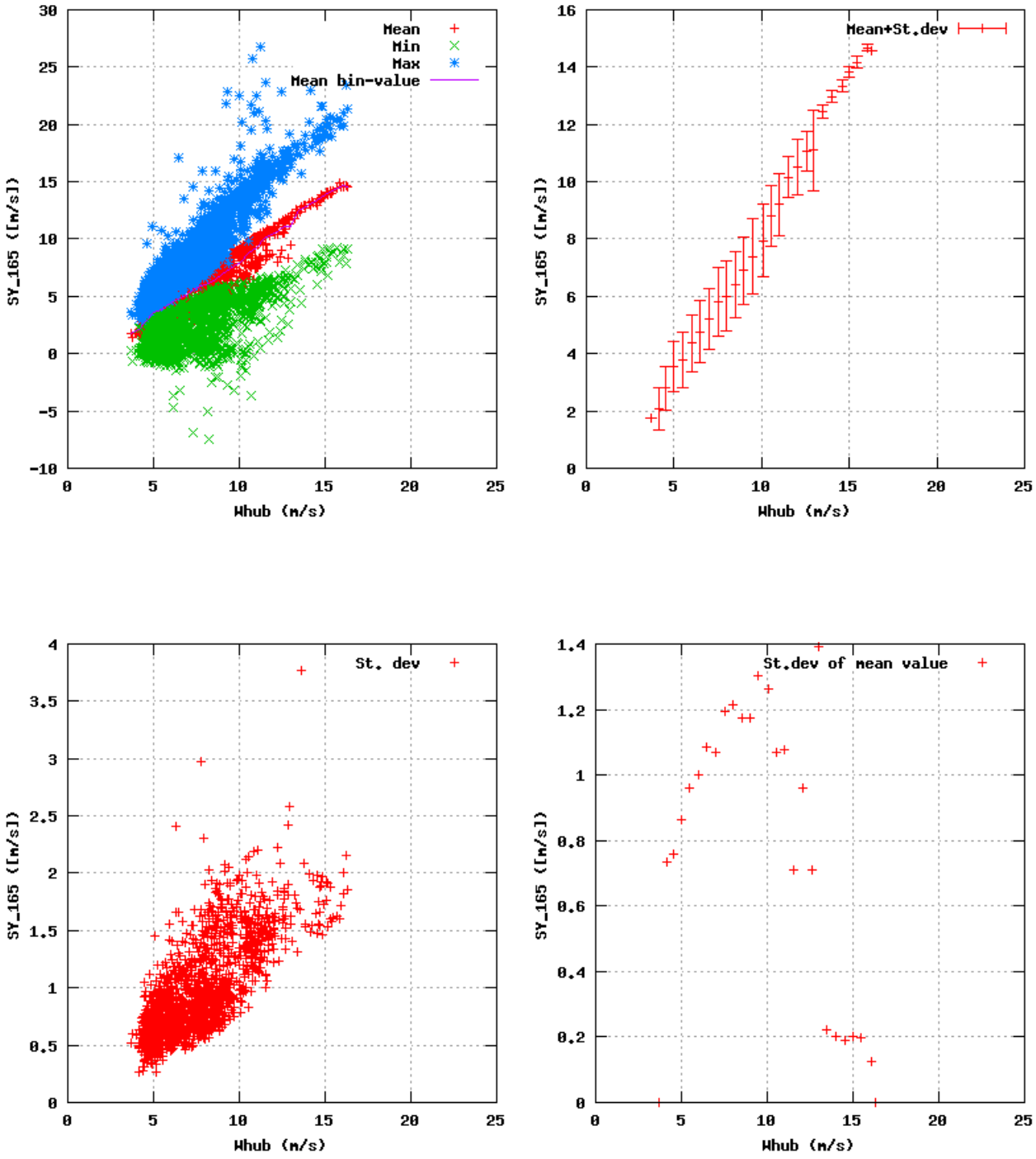

Figure 71a, Sensor 283: Sonic wind component SY,16.5m versus wind speed
Input files: ntk500res.dat, stat_283.dat

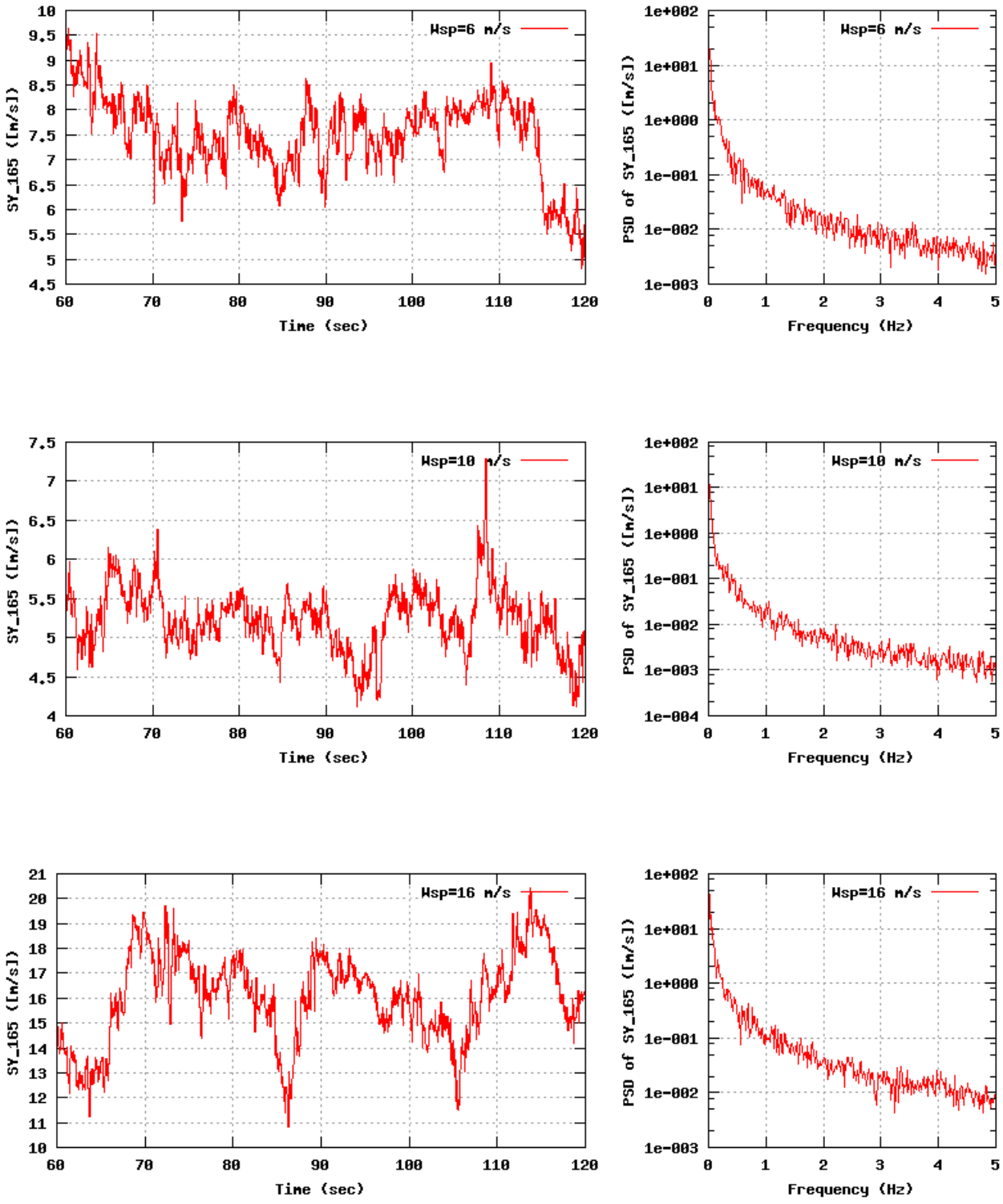

Figure 71b, Sensor 283: Sonic wind component SY,16.5m versus time and frequency
Input files: m06.asc, m10.asc, m16.asc, m06.psd, m10.psd and m16.psd

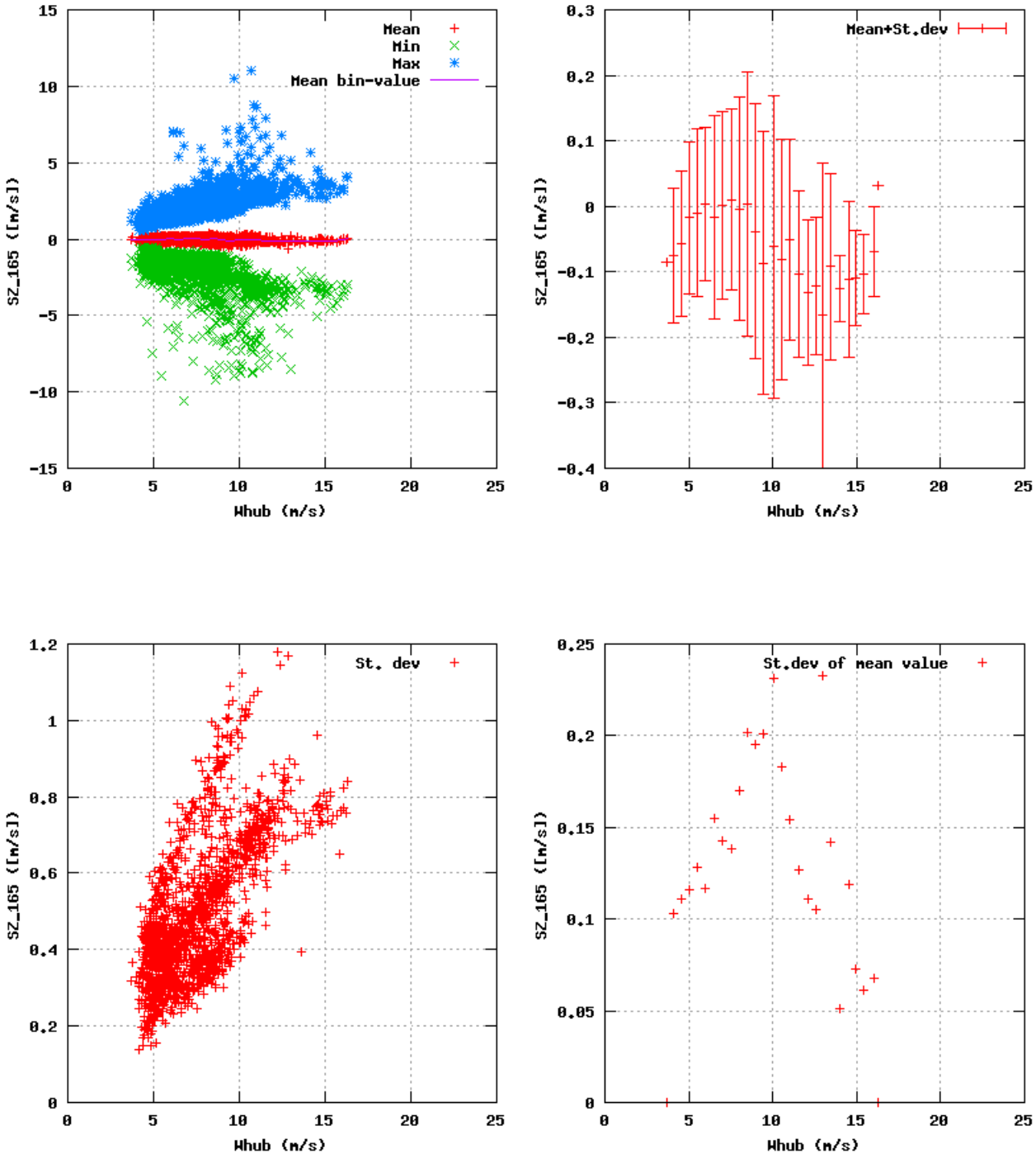

Figure 72a, Sensor 287: Sonic wind component SZ,16.5m versus wind speed
Input files: ntk500res.dat, stat_287.dat

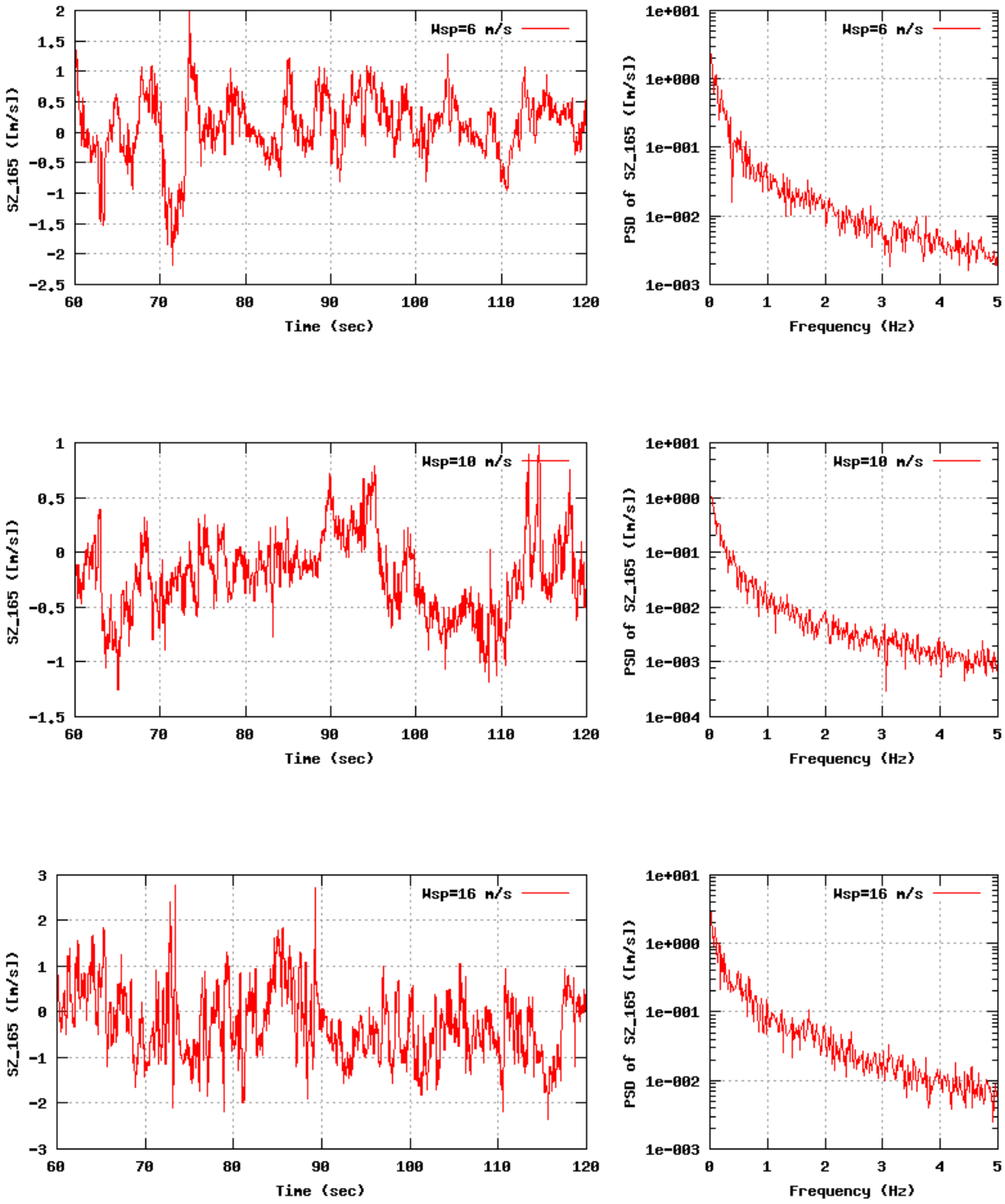

Figure 72b, Sensor 287: Sonic wind component SZ,16.5m versus time and frequency
Input files: m06.asc, m10.asc, m16.asc, m06.psd, m10.psd and m16.psd

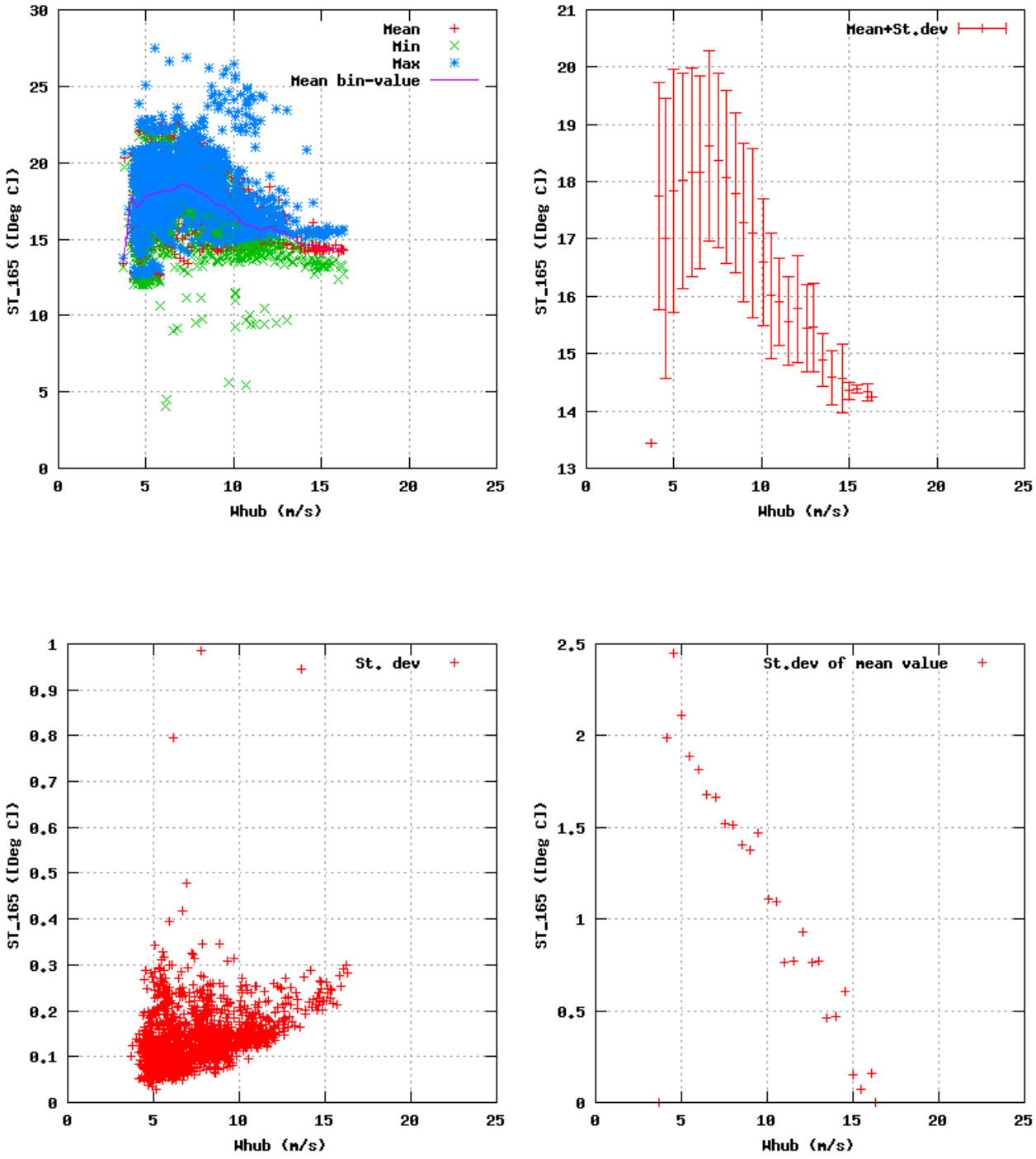

Figure 73a, Sensor 291: Sonic air temperature ST,16.5m versus wind speed
Input files: ntk500res.dat, stat_291.dat

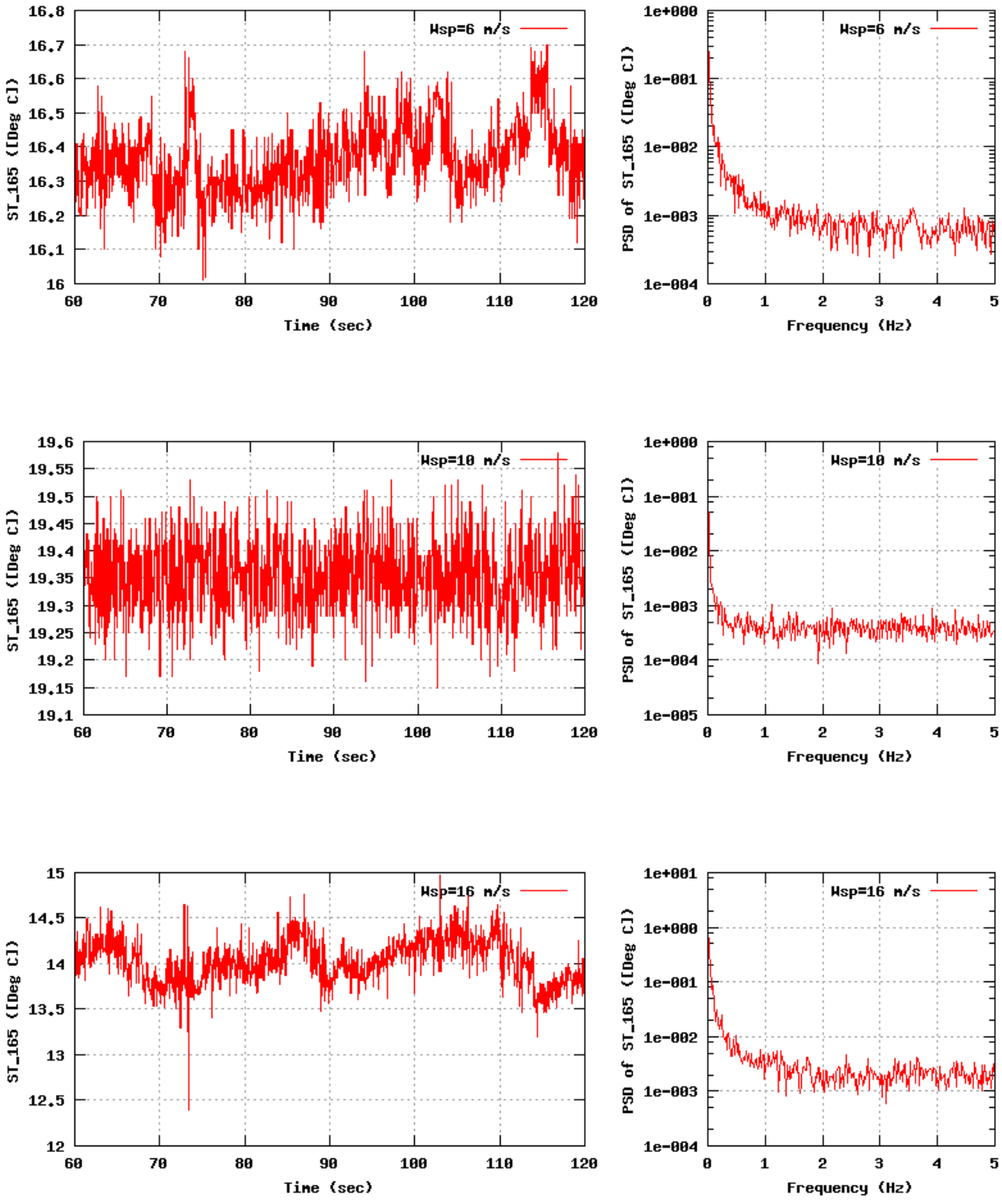

Figure 73b, Sensor 291: Sonic air temperature ST,16.5m versus time and frequency
Input files: m06.asc, m10.asc, m16.asc, m06.psd, m10.psd and m16.psd

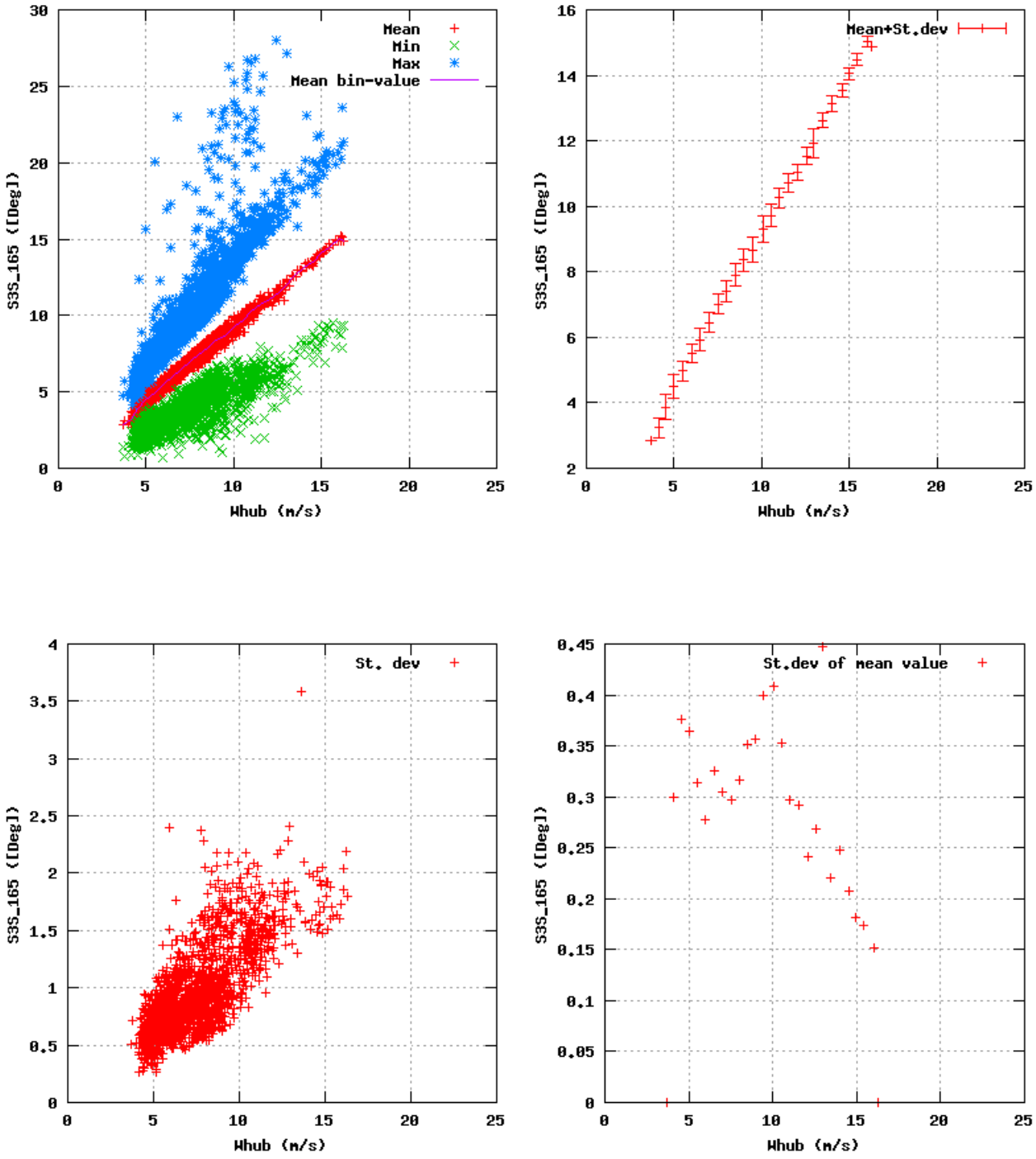

Figure 74a, Sensor 295: Sonic wind speed Sspeed,16.5m versus wind speed
Input files: ntk500res.dat, stat_295.dat

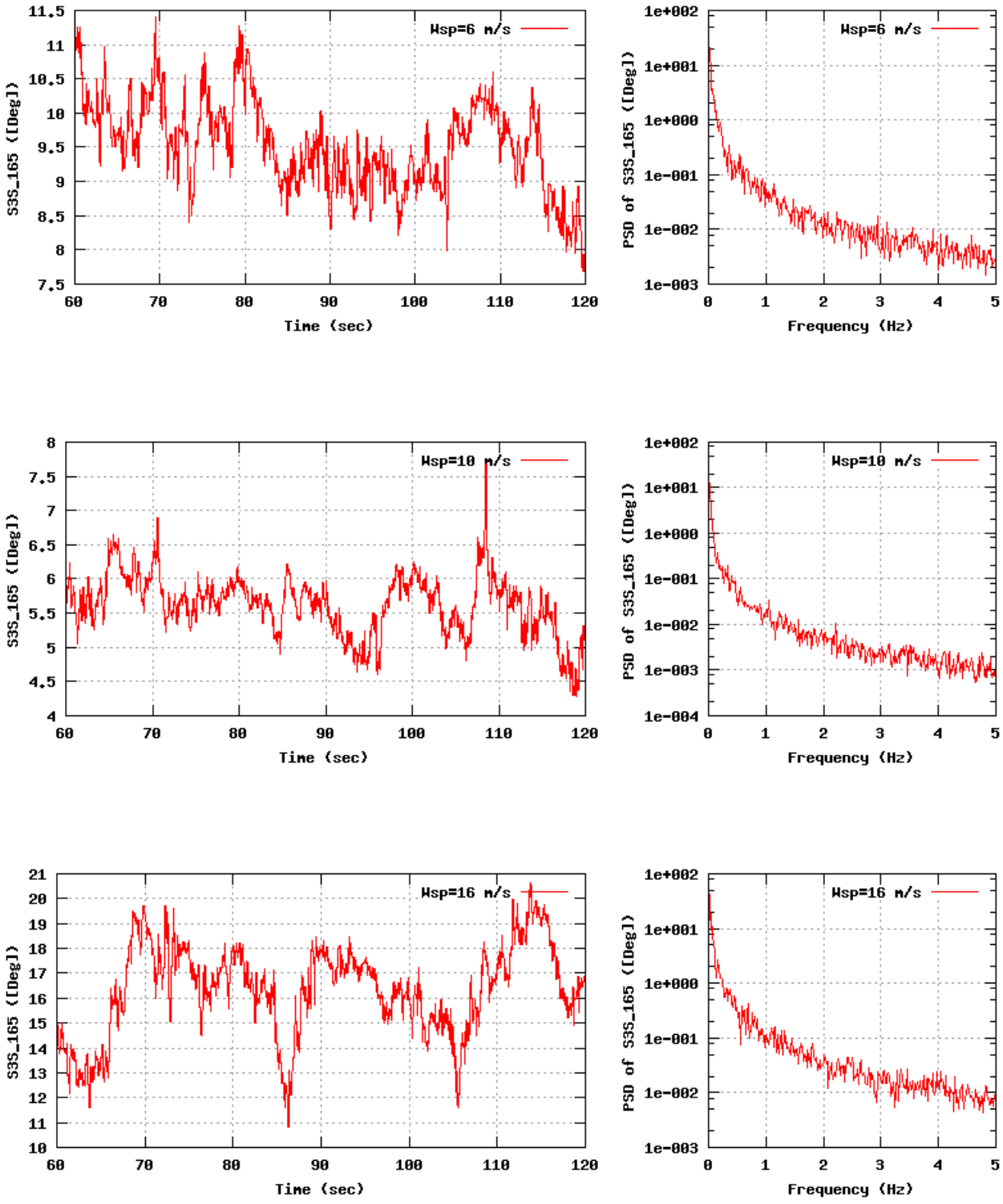

Figure 74b, Sensor 295: Sonic wind speed Sspeed,16.5m versus time and frequency
Input files: m06.asc, m10.asc, m16.asc, m06.psd, m10.psd and m16.psd

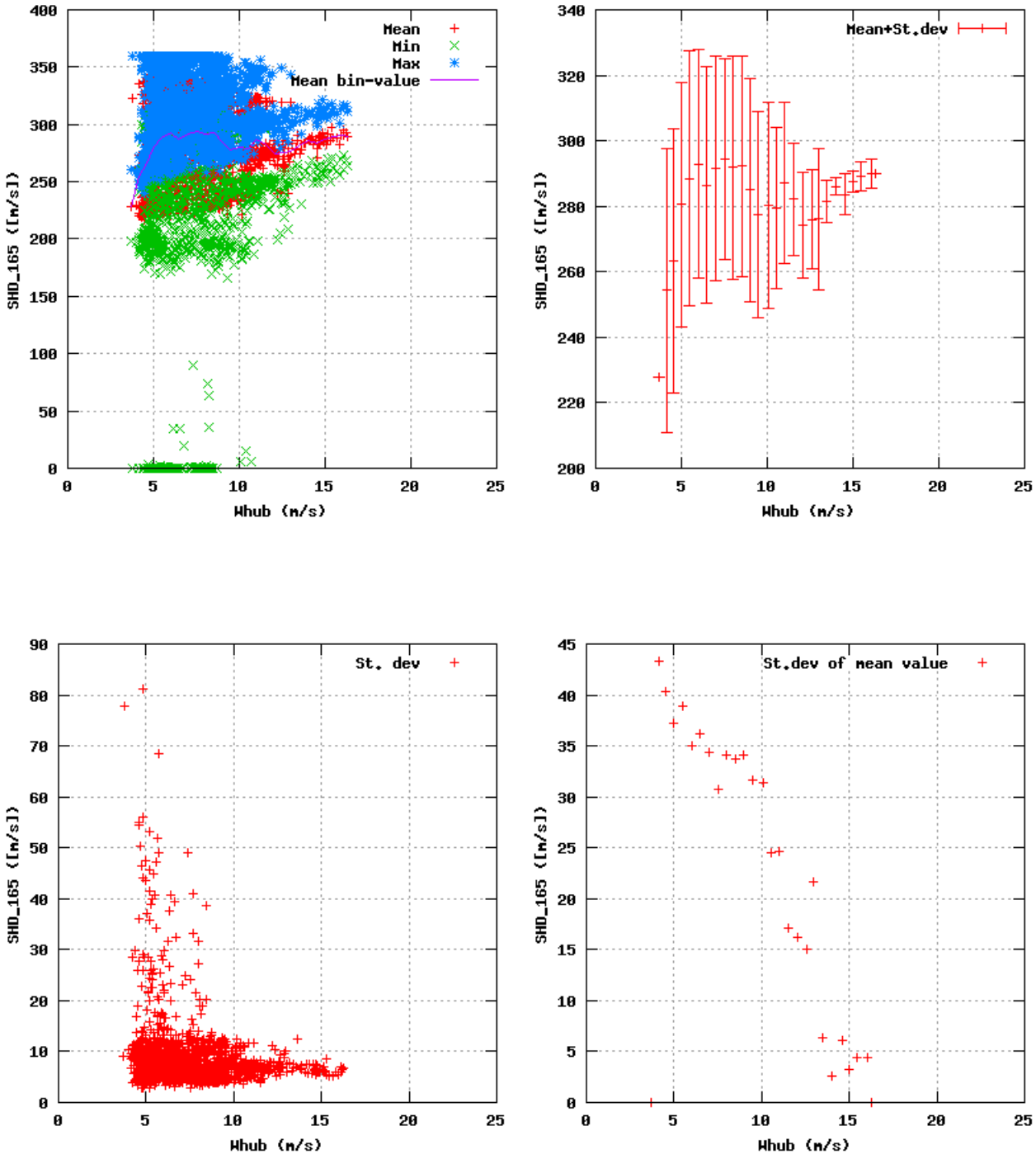

Figure 75a, Sensor 299: Sonic horisontal flow direction Sdir,16.5m versus wind speed
Input files: ntk500res.dat, stat_299.dat

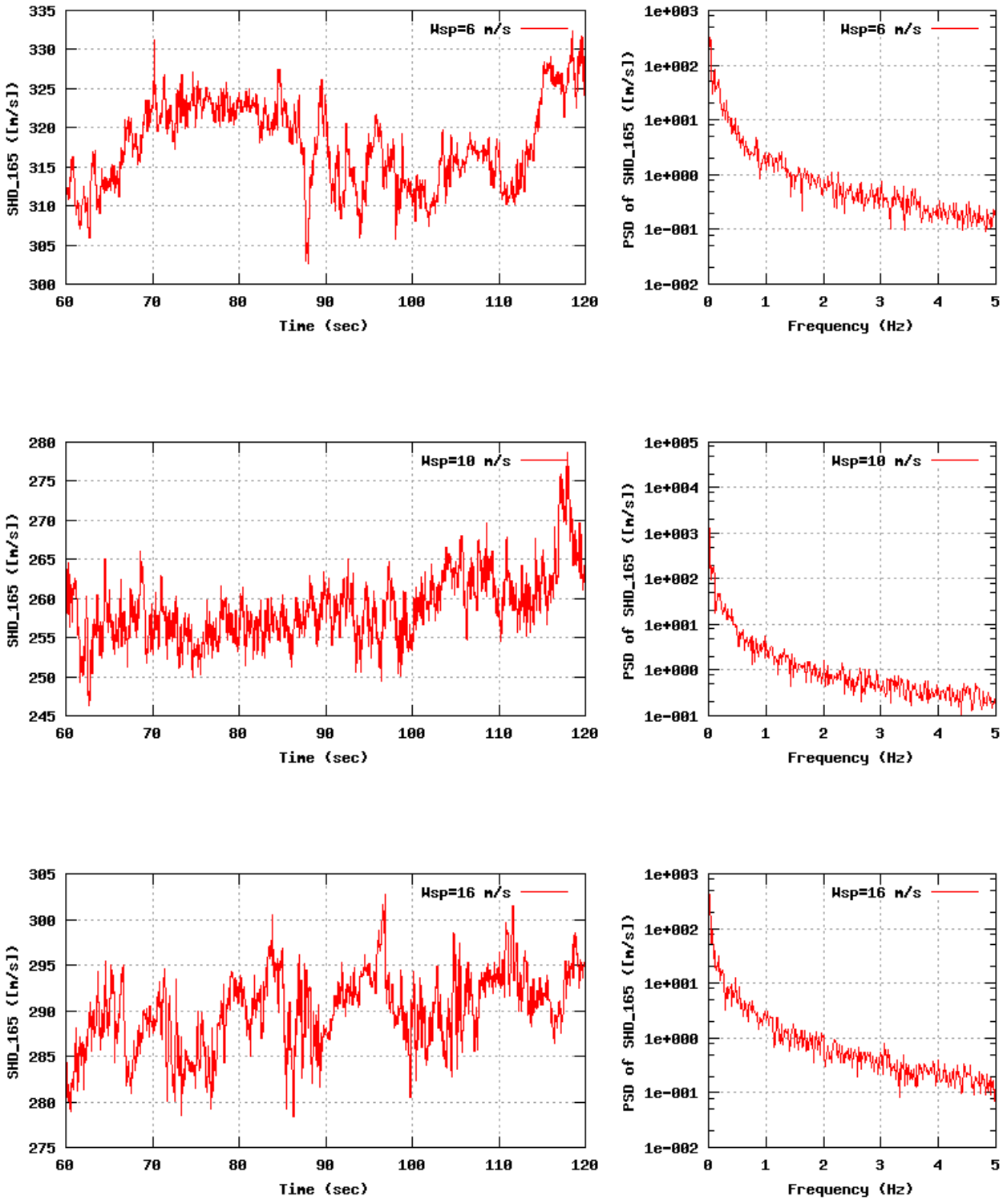

Figure 75b, Sensor 299: Sonic horisontal flow direction Sdir,16.5m versus time and frequency
Input files: m06.asc, m10.asc, m16.asc, m06.psd, m10.psd and m16.psd

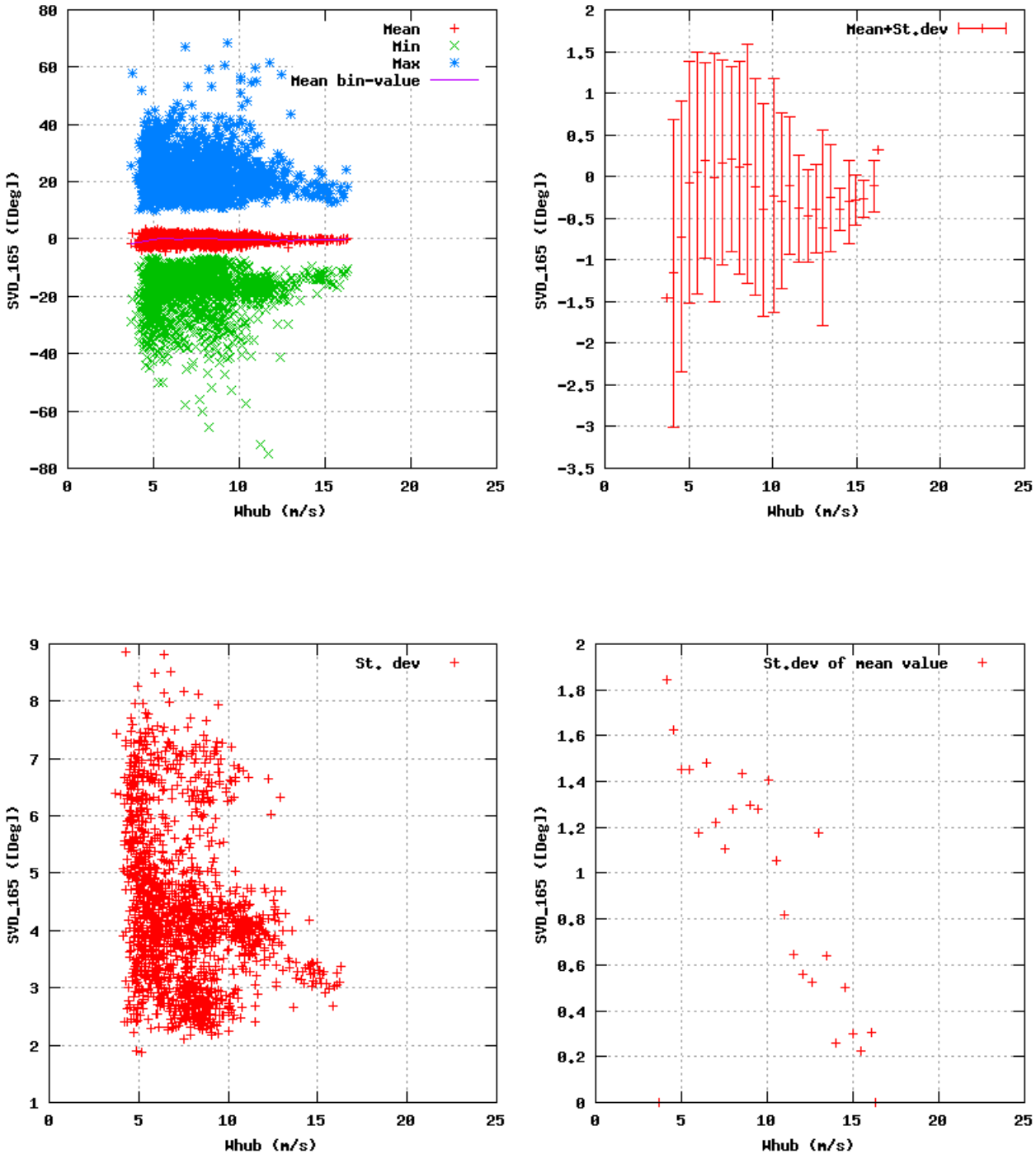

Figure 76a, Sensor 303: Sonic vertical flow angle Stilt,16.5m versus wind speed
Input files: ntk500res.dat, stat_303.dat

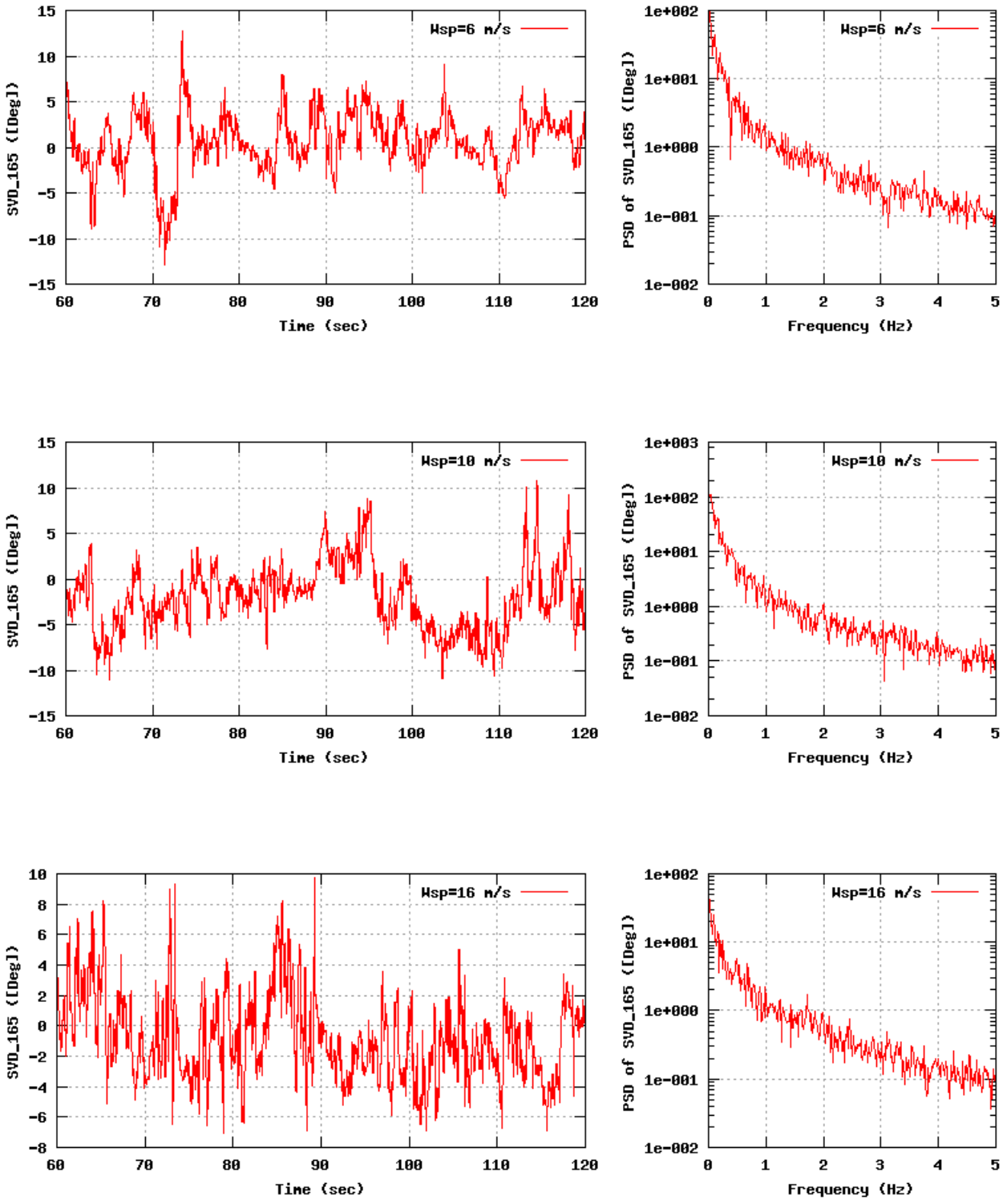

Figure 76b, Sensor 303: Sonic vertical flow angle Stilt,16.5m versus time and frequency
Input files: m06.asc, m10.asc, m16.asc, m06.psd, m10.psd and m16.psd

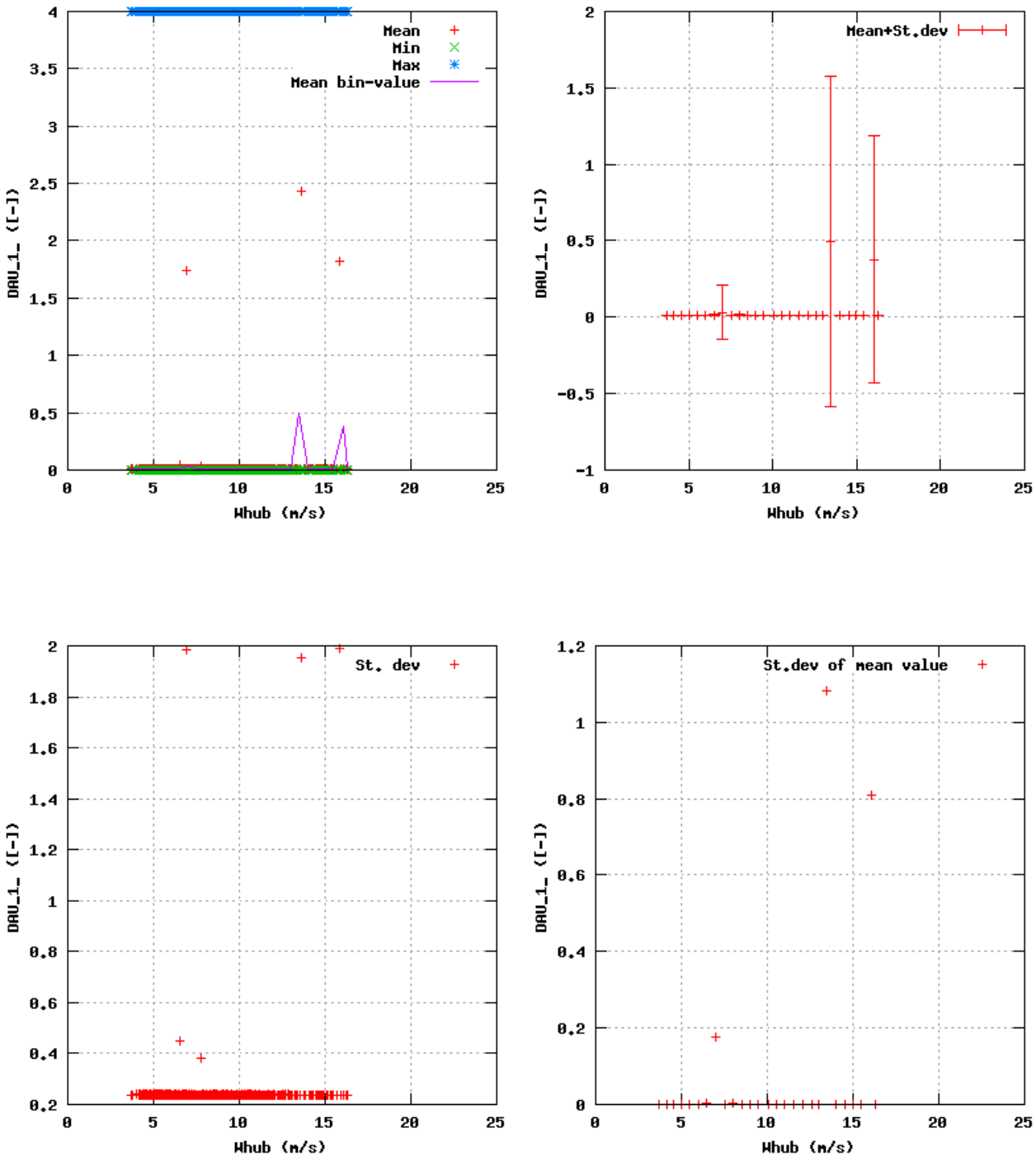

Figure 77a, Sensor 307: DAU_1_ versus wind speed
Input files: ntk500res.dat, stat_307.dat

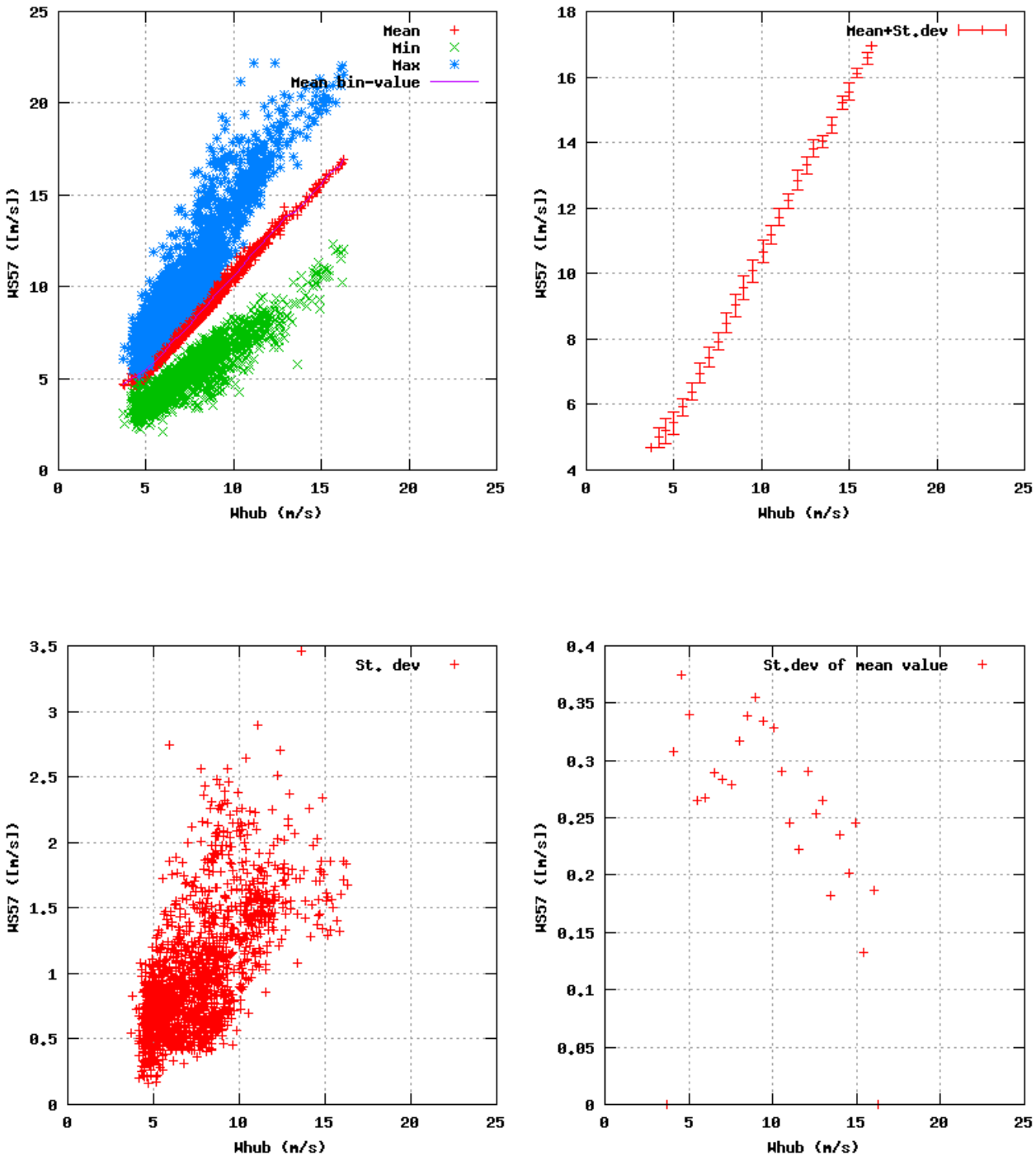

Figure 78a, Sensor 311: Wind speed Metmast @57m versus wind speed
Input files: ntk500res.dat, stat_311.dat

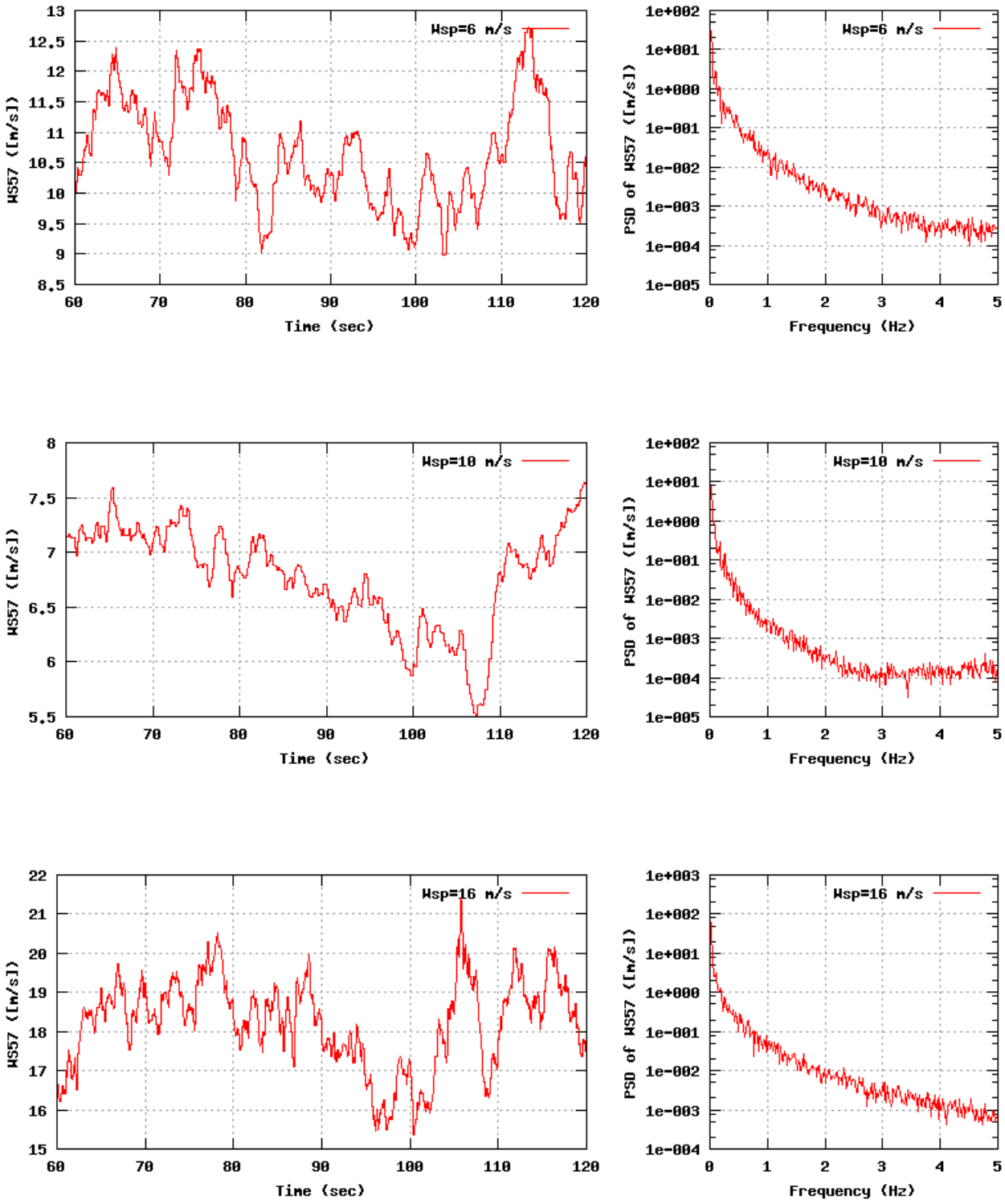

Figure 78b, Sensor 311: Wind speed Metmast @57m versus time and frequency
Input files: m06.asc, m10.asc, m16.asc, m06.psd, m10.psd and m16.psd

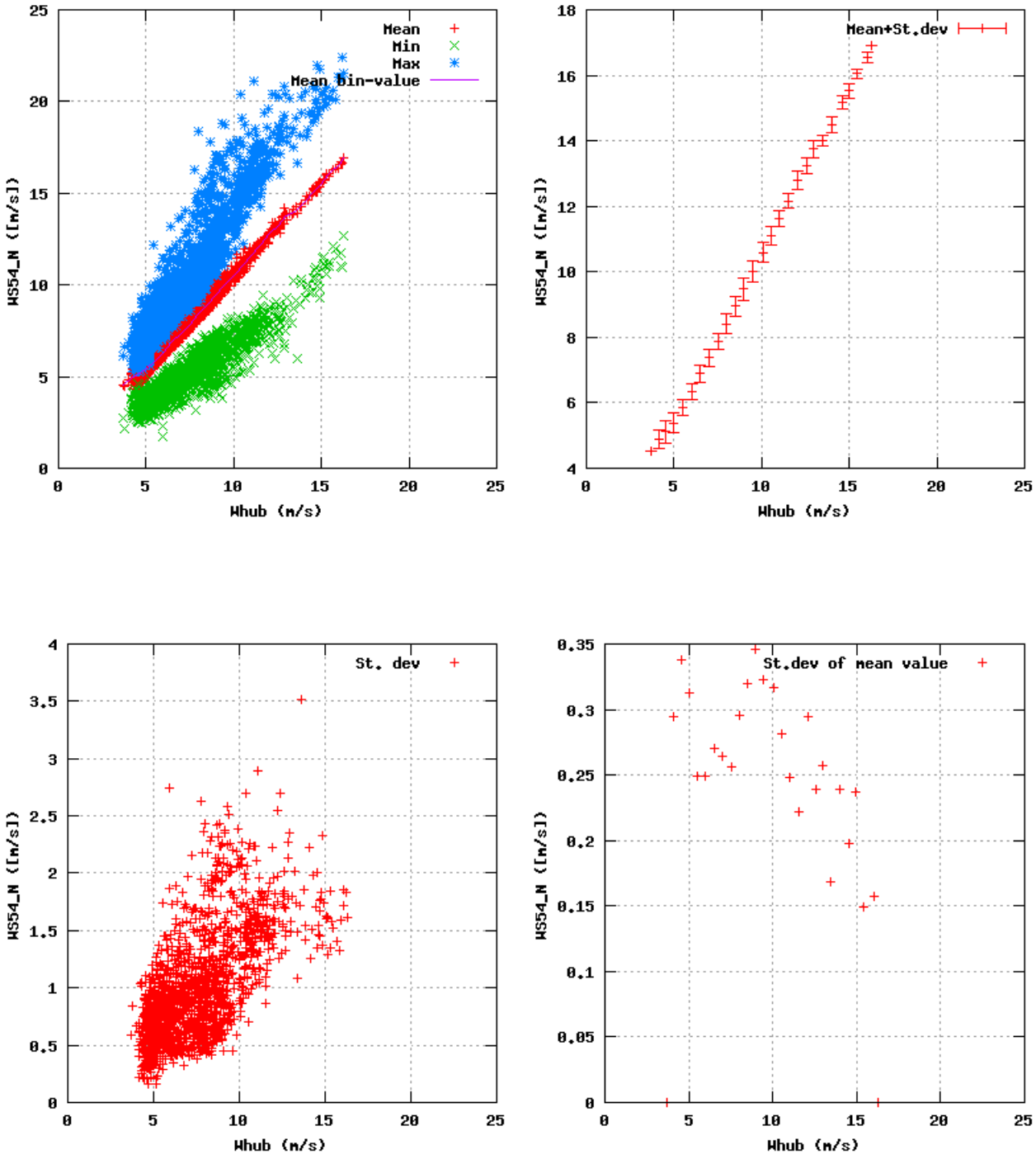

Figure 79a, Sensor 315: Wind speed Metmast @54m,North versus wind speed
Input files: ntk500res.dat, stat_315.dat

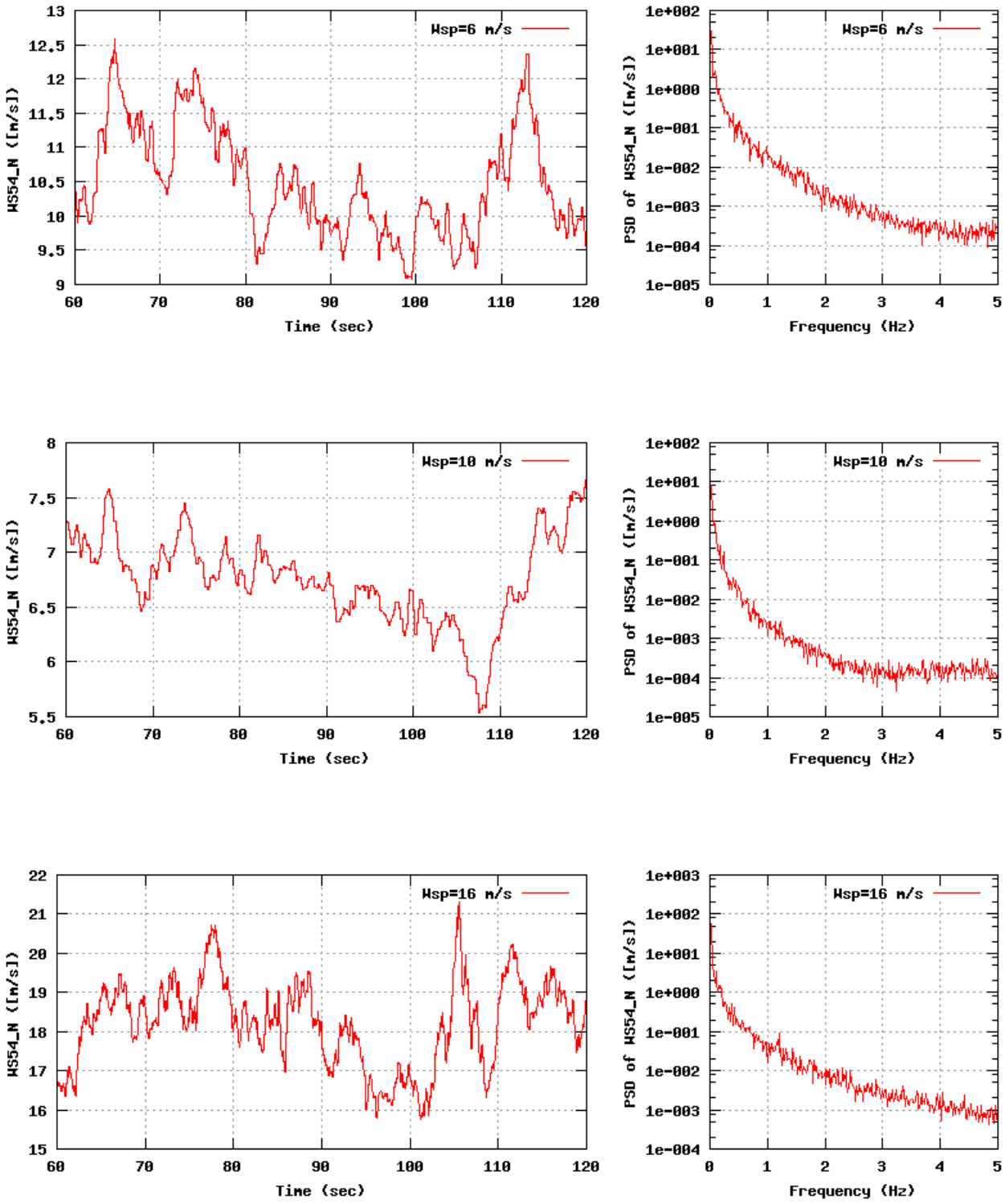

Figure 79b, Sensor 315: Wind speed Metmast @54m,North versus time and frequency
Input files: m06.asc, m10.asc, m16.asc, m06.psd, m10.psd and m16.psd

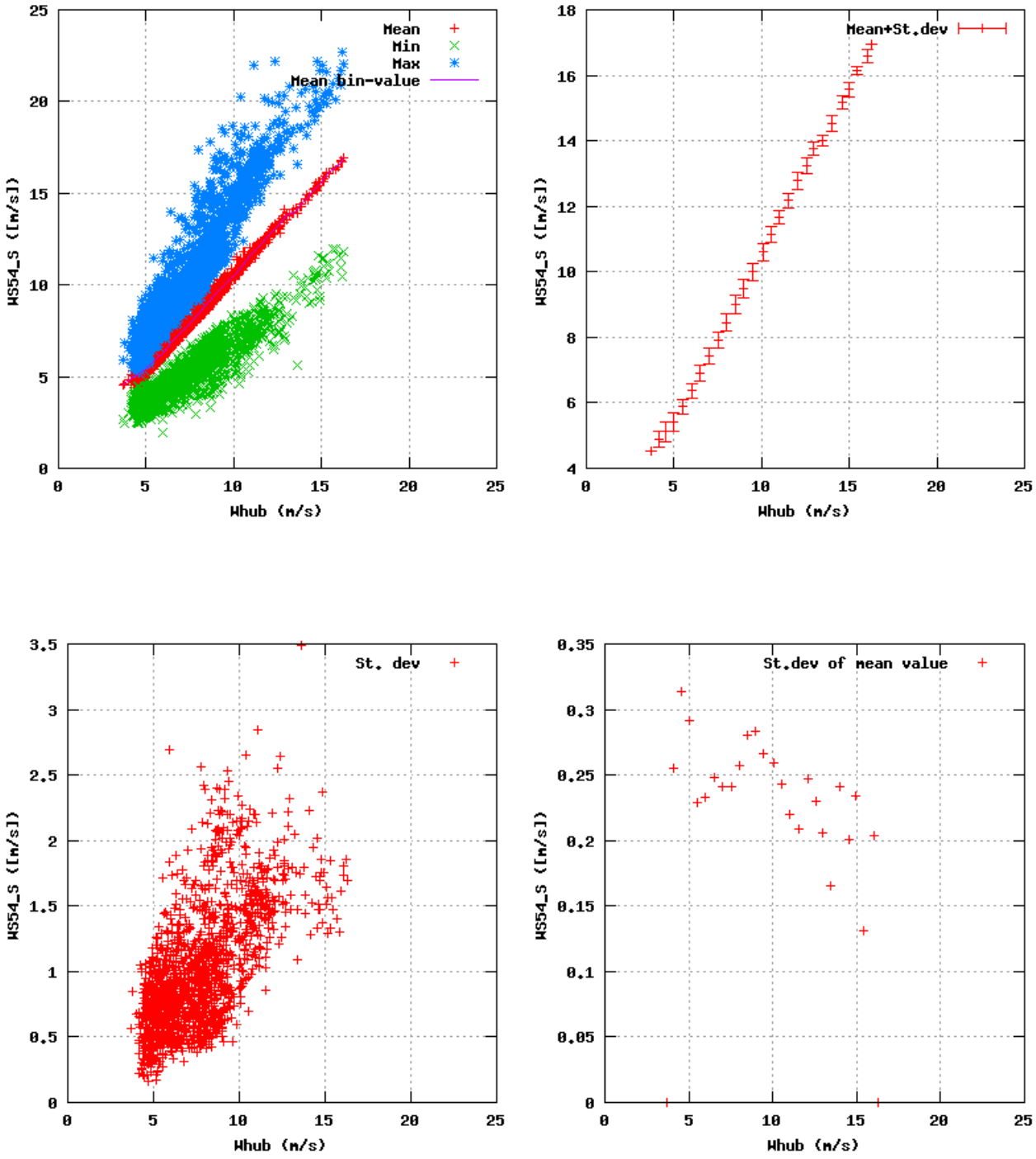

Figure 80a, Sensor 319: Wind speed Metmast @54m,South versus wind speed
Input files: ntk500res.dat, stat_319.dat

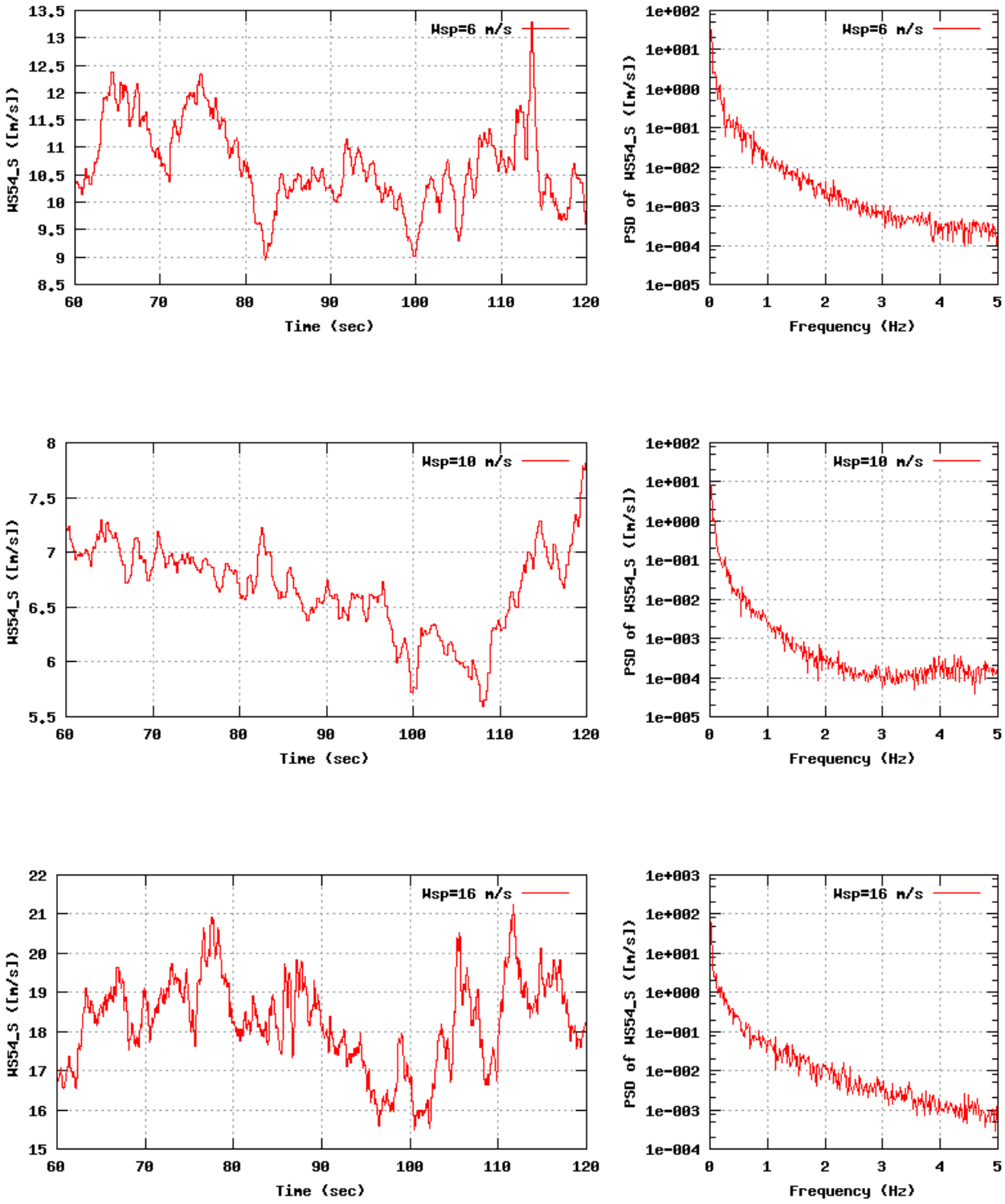

Figure 80b, Sensor 319: Wind speed Metmast @54m,South versus time and frequency
Input files: m06.asc, m10.asc, m16.asc, m06.psd, m10.psd and m16.psd

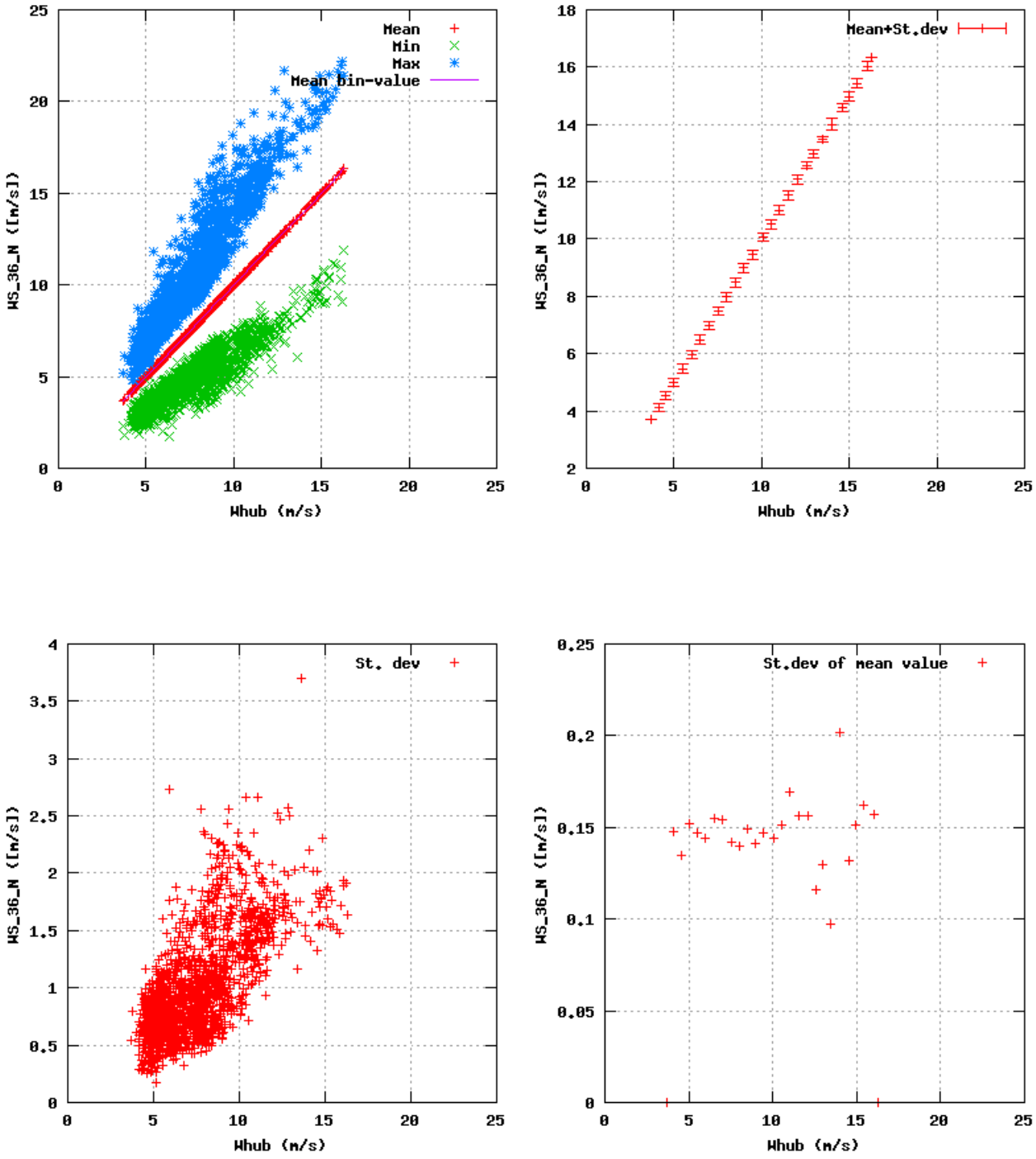

Figure 81a, Sensor 323: Wind speed Metmast @36m,North versus wind speed
Input files: ntk500res.dat, stat_323.dat

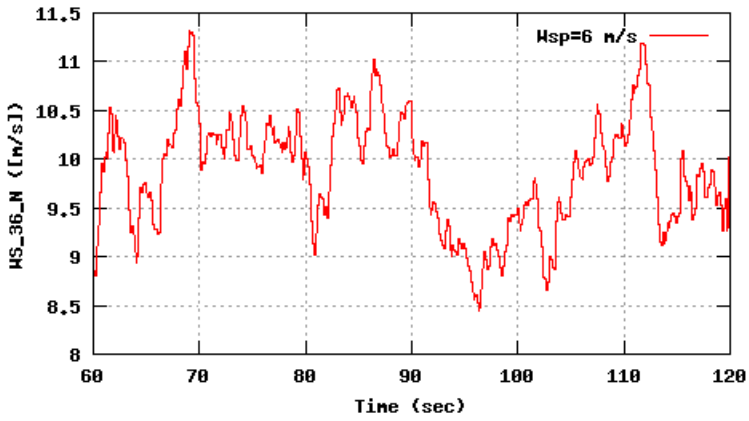

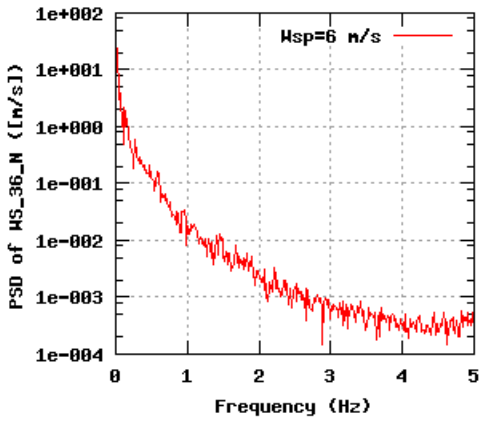

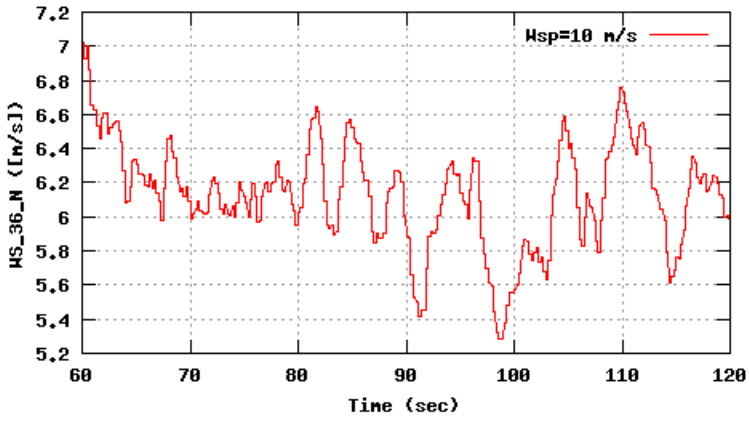

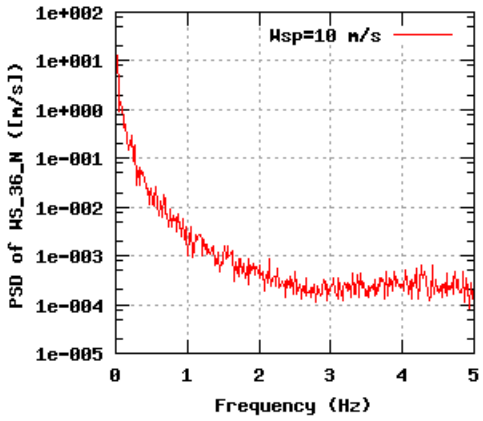

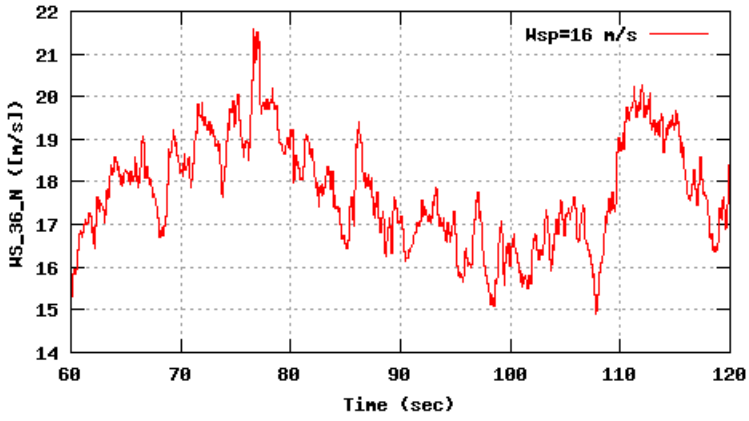

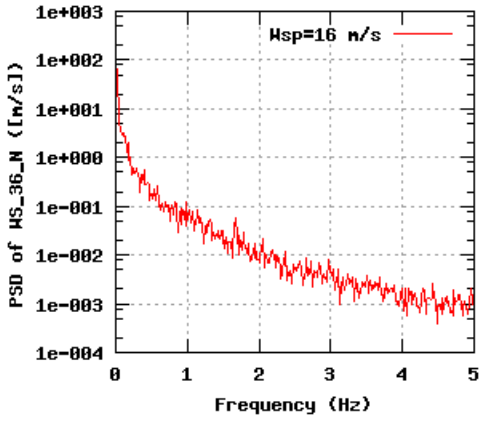

Figure 81b, Sensor 323: Wind speed Metmast @36m,North versus time and frequency
Input files: m06.asc, m10.asc, m16.asc, m06.psd, m10.psd and m16.psd

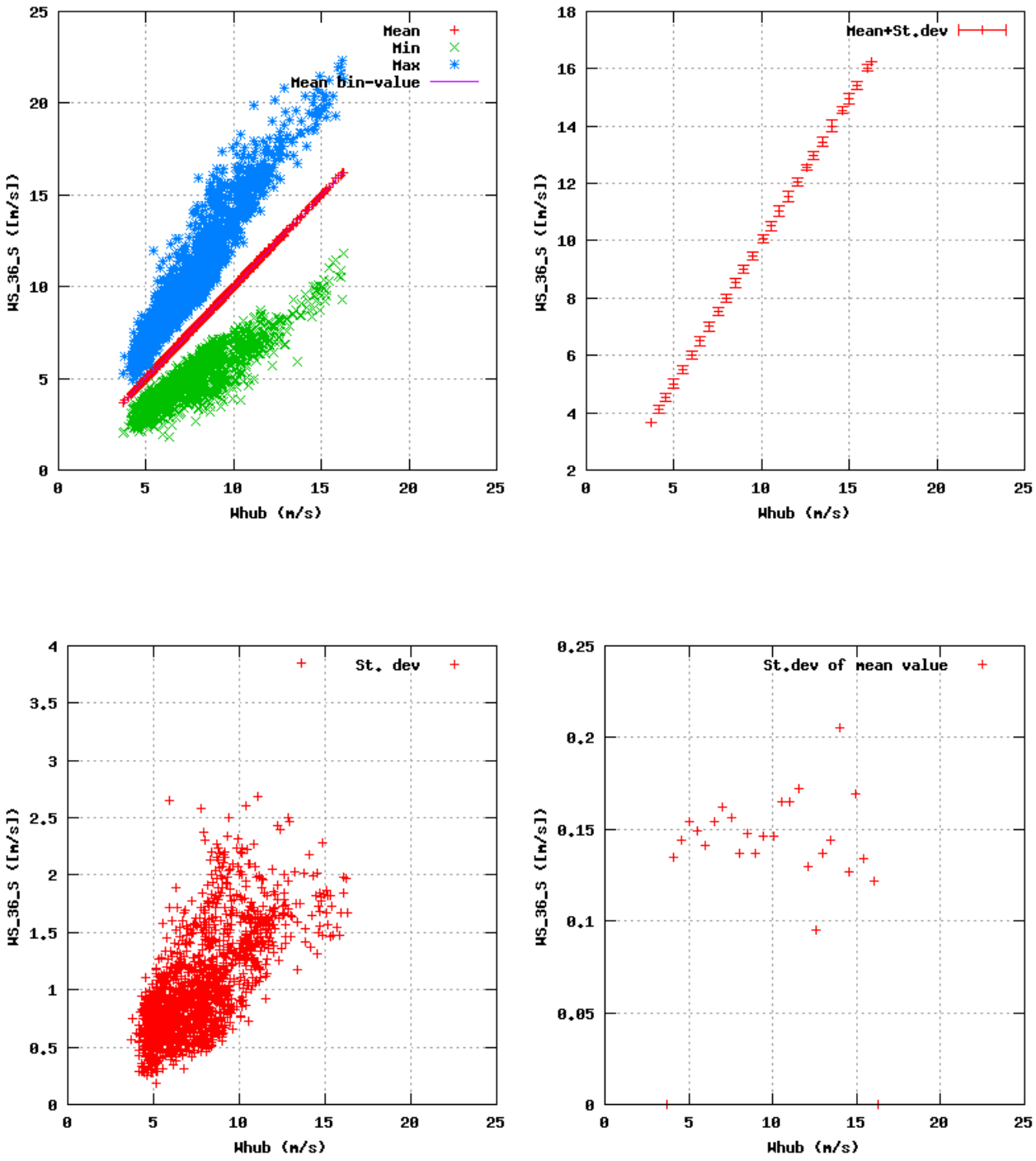

Figure 82a, Sensor 327: Wind speed Metmast @36m,South versus wind speed
Input files: ntk500res.dat, stat_327.dat

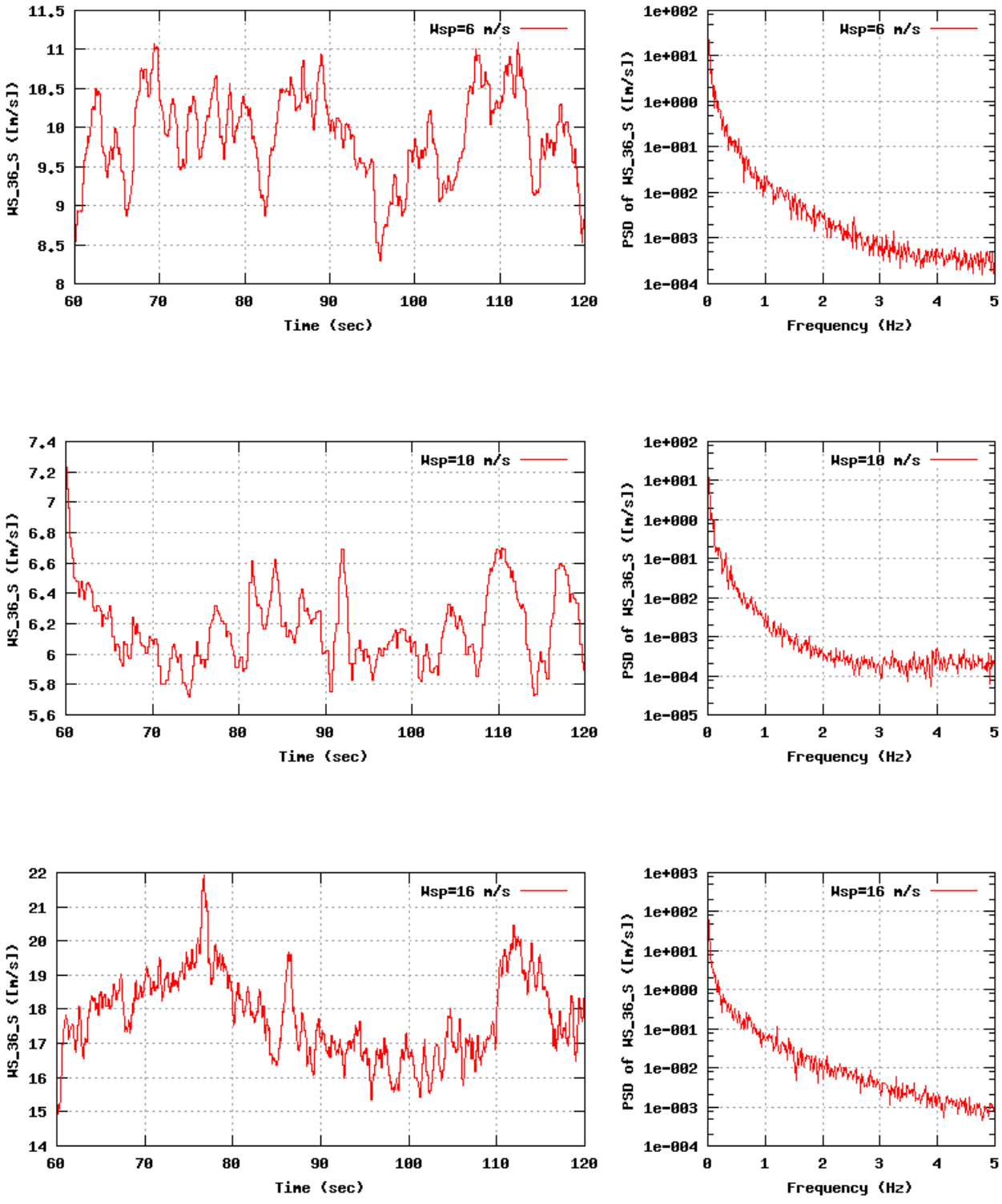

Figure 82b, Sensor 327: Wind speed Metmast @36m,South versus time and frequency
Input files: m06.asc, m10.asc, m16.asc, m06.psd, m10.psd and m16.psd

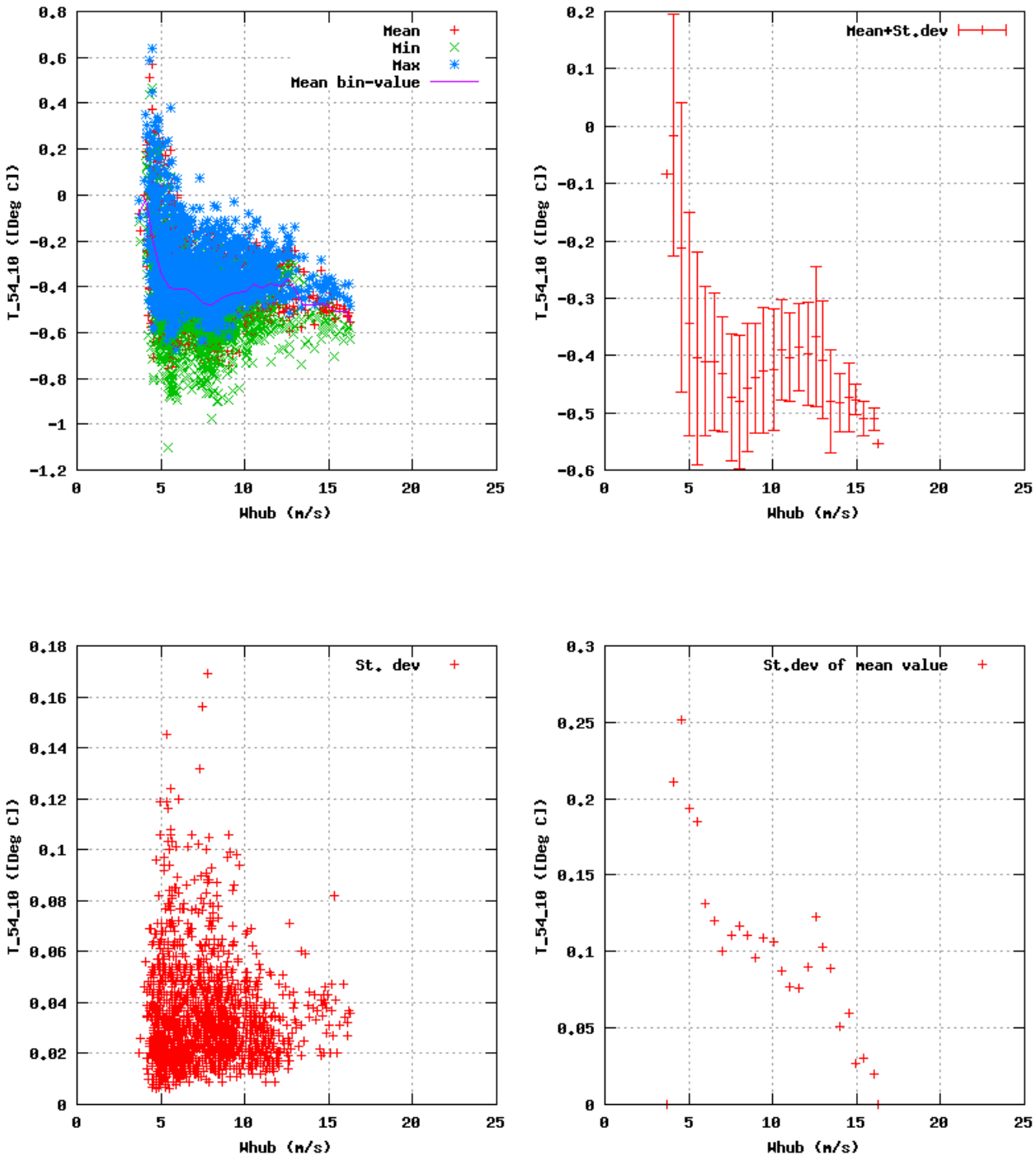

Figure 83a, Sensor 331: Difference Temperature 54-10 m versus wind speed
Input files: ntk500res.dat, stat_331.dat

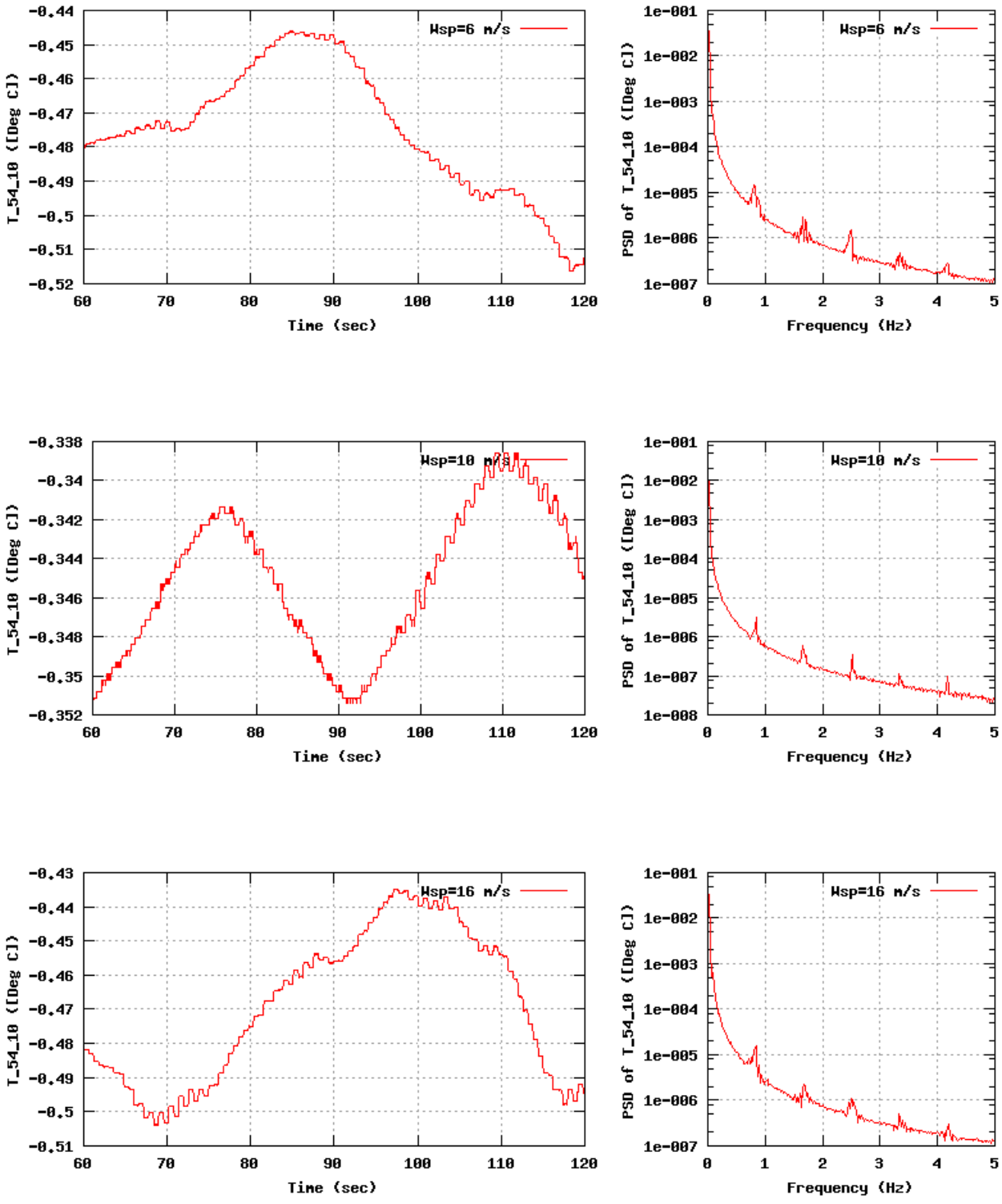

Figure 83b, Sensor 331: Difference Temperature 54-10 m versus time and frequency
Input files: m06.asc, m10.asc, m16.asc, m06.psd, m10.psd and m16.psd

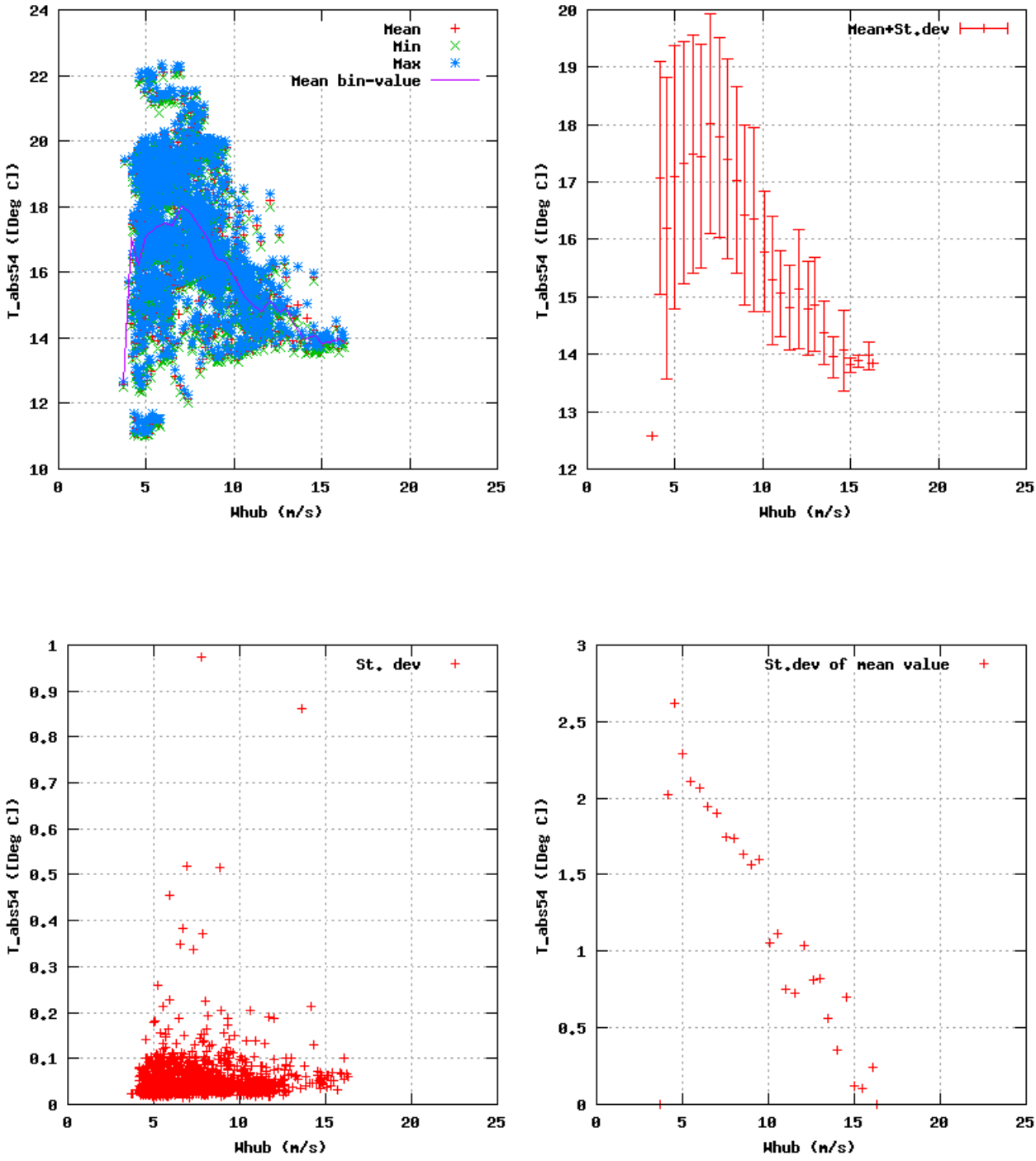

Figure 84a, Sensor 335: Temperature@54m versus wind speed
Input files: ntk500res.dat, stat_335.dat

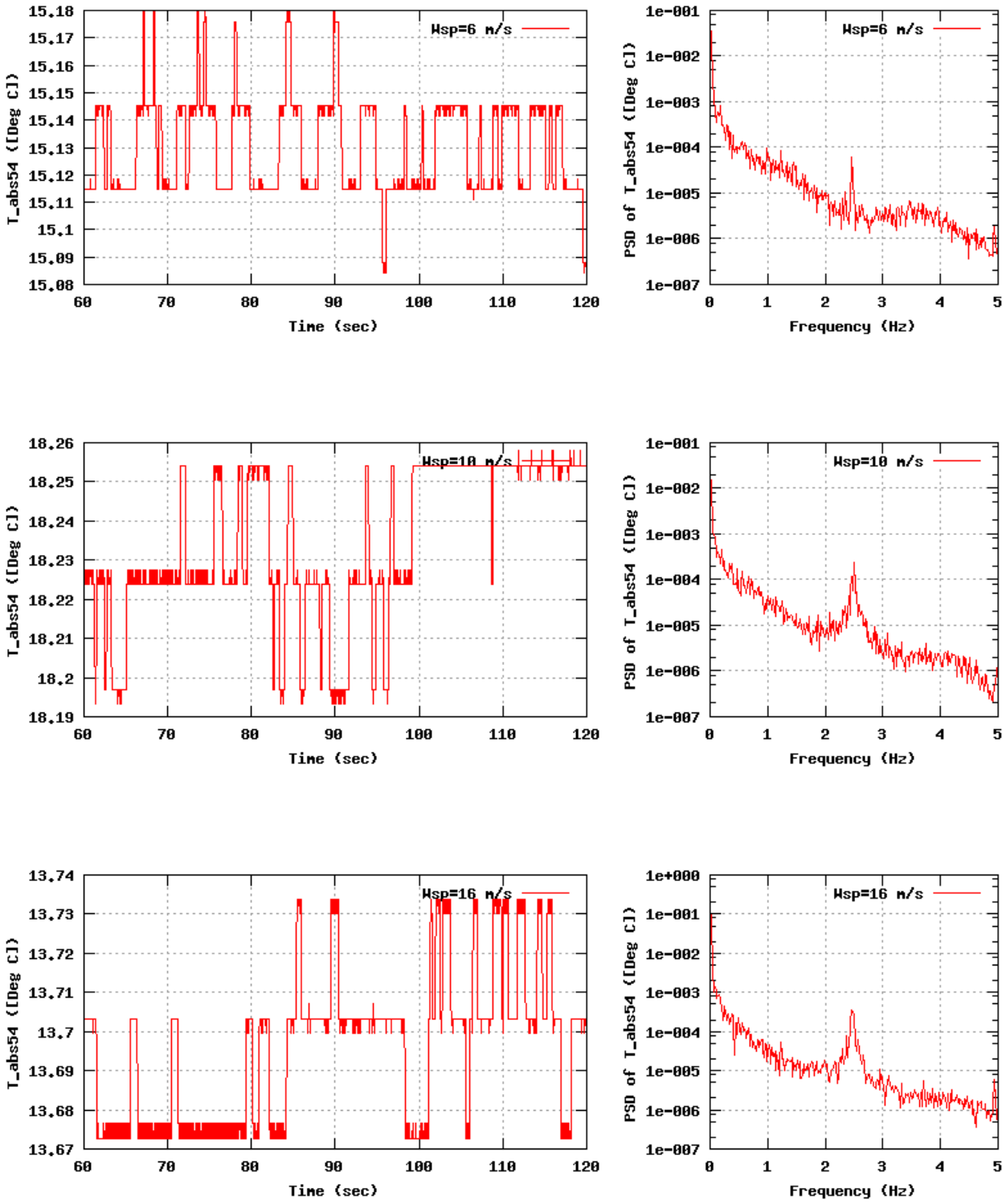

Figure 84b, Sensor 335: Temperature@54m versus time and frequency
Input files: m06.asc, m10.asc, m16.asc, m06.psd, m10.psd and m16.psd

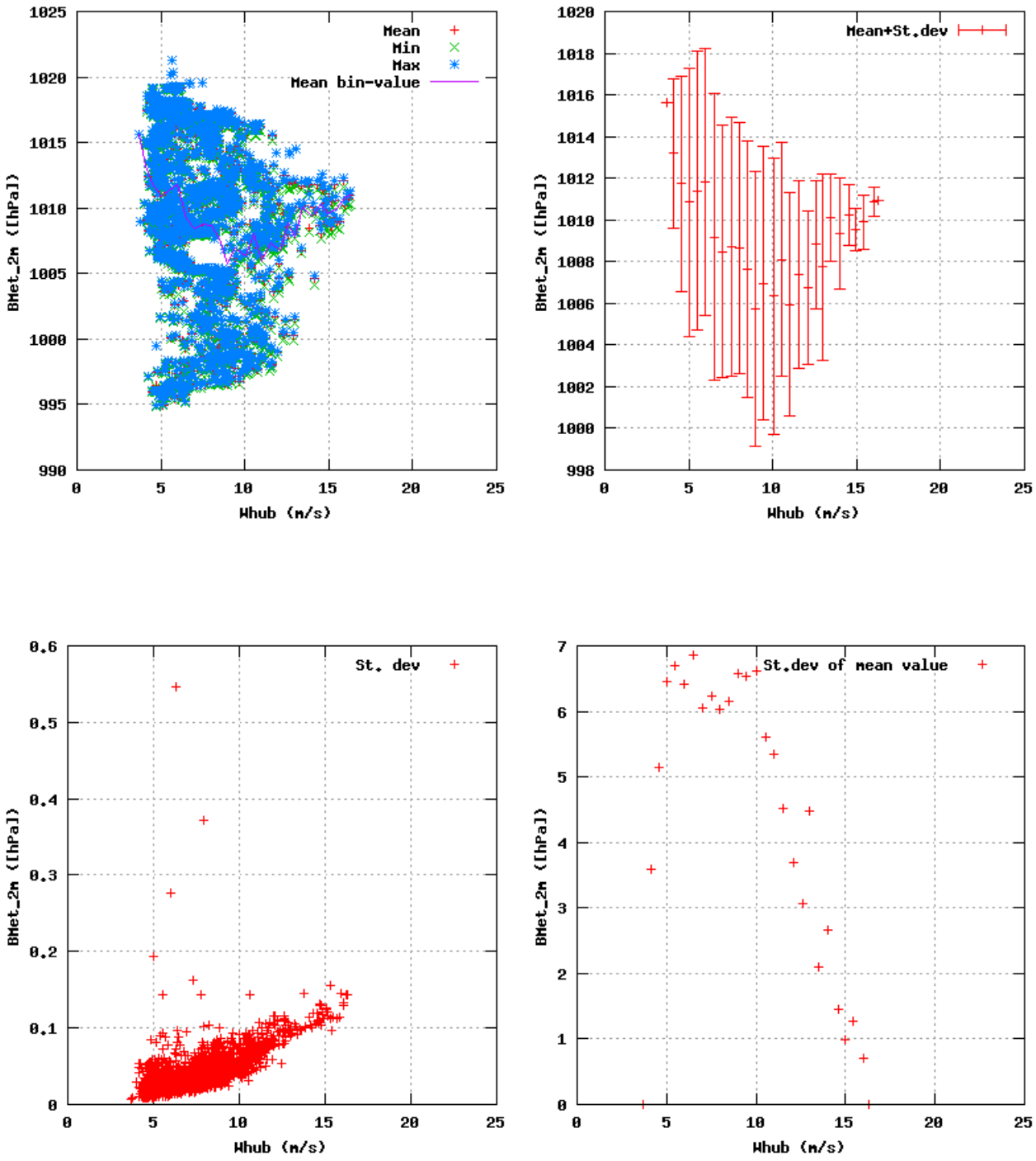

Figure 85a, Sensor 339: Air Barmetric Pressure@2m versus wind speed
Input files: ntk500res.dat, stat_339.dat

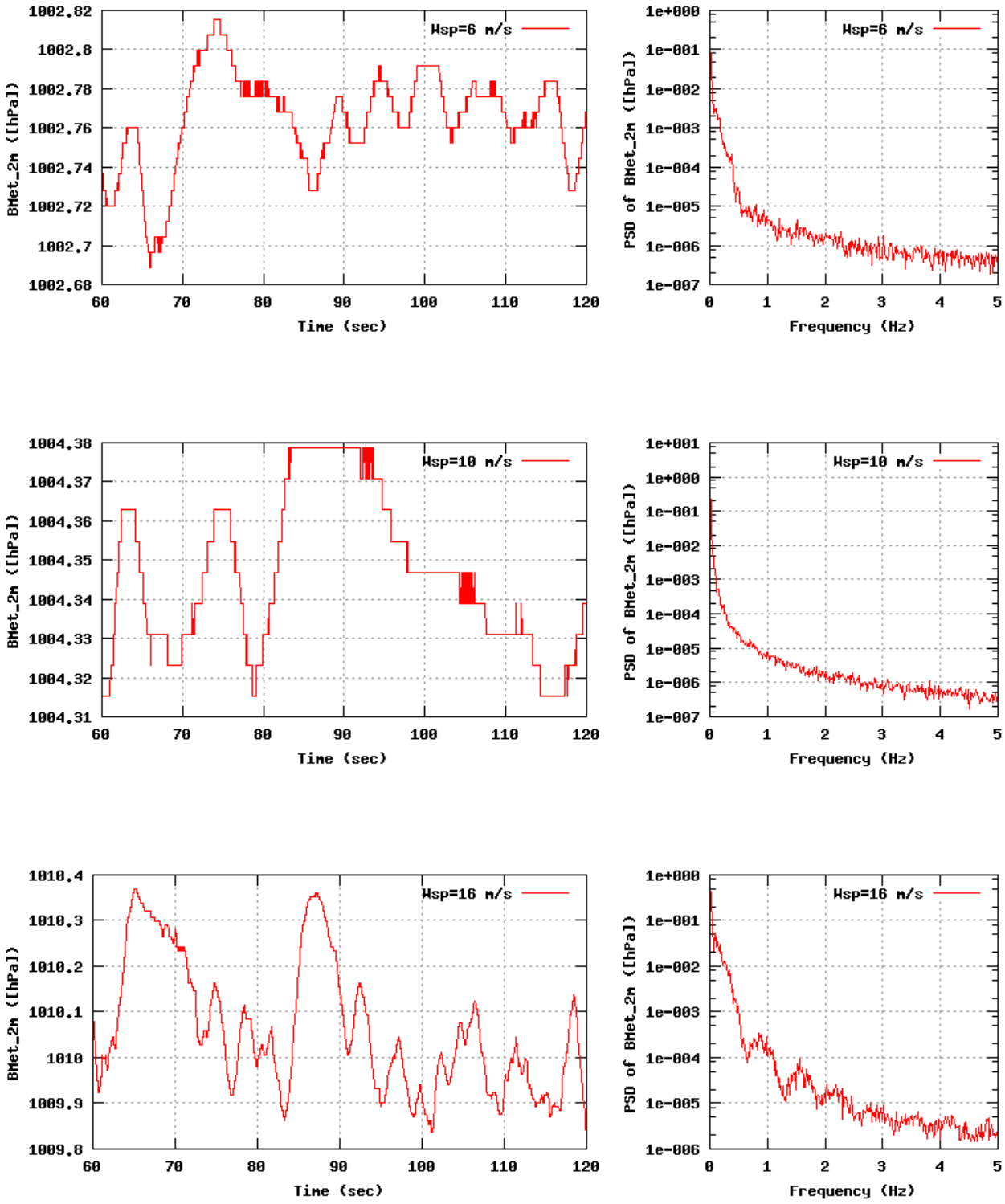

Figure 85b, Sensor 339: Air Barmetric Pressure@2m versus time and frequency
Input files: m06.asc, m10.asc, m16.asc, m06.psd, m10.psd and m16.psd

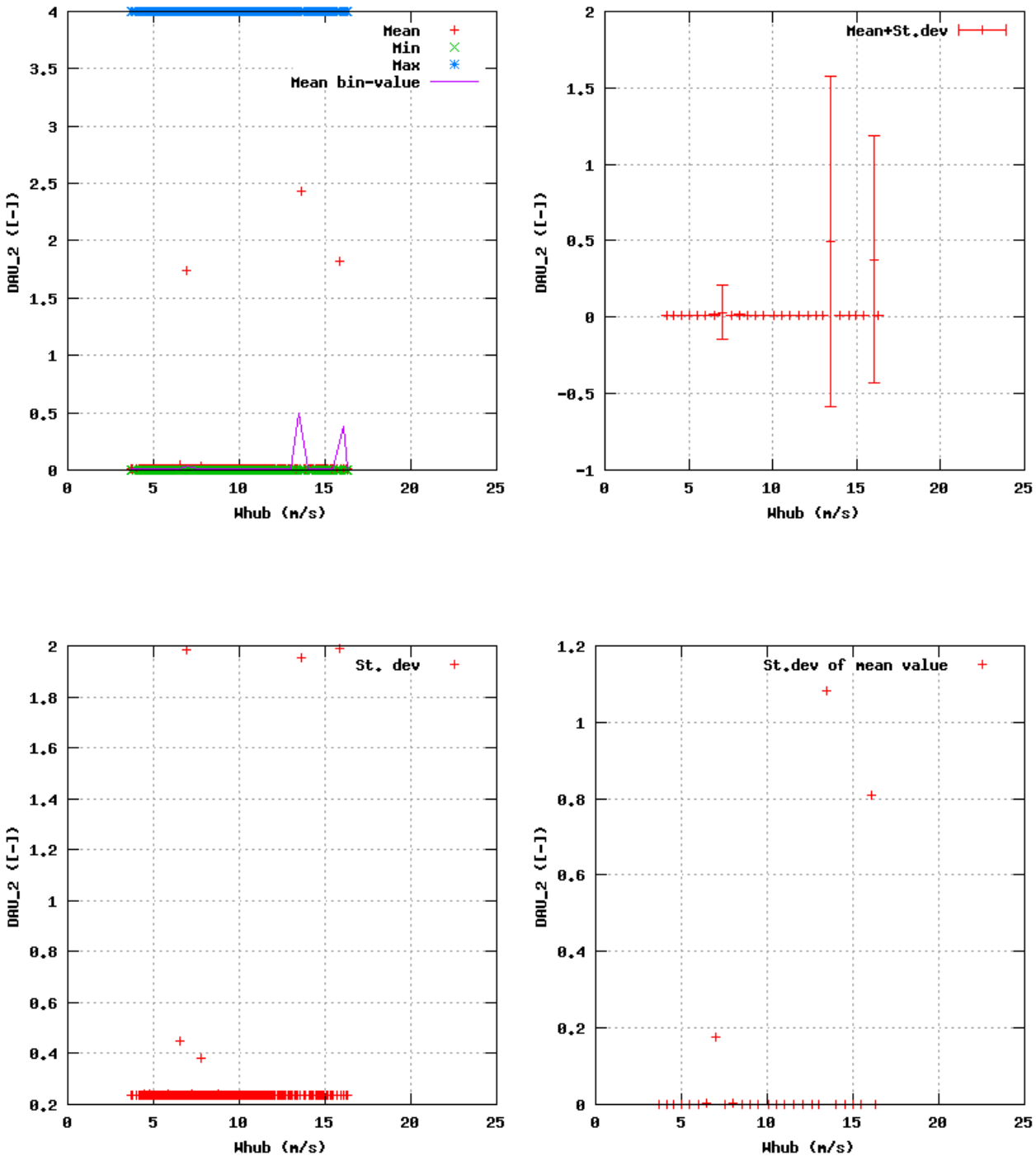

Figure 86a, Sensor 343: DAU_2 versus wind speed
Input files: ntk500res.dat, stat_343.dat

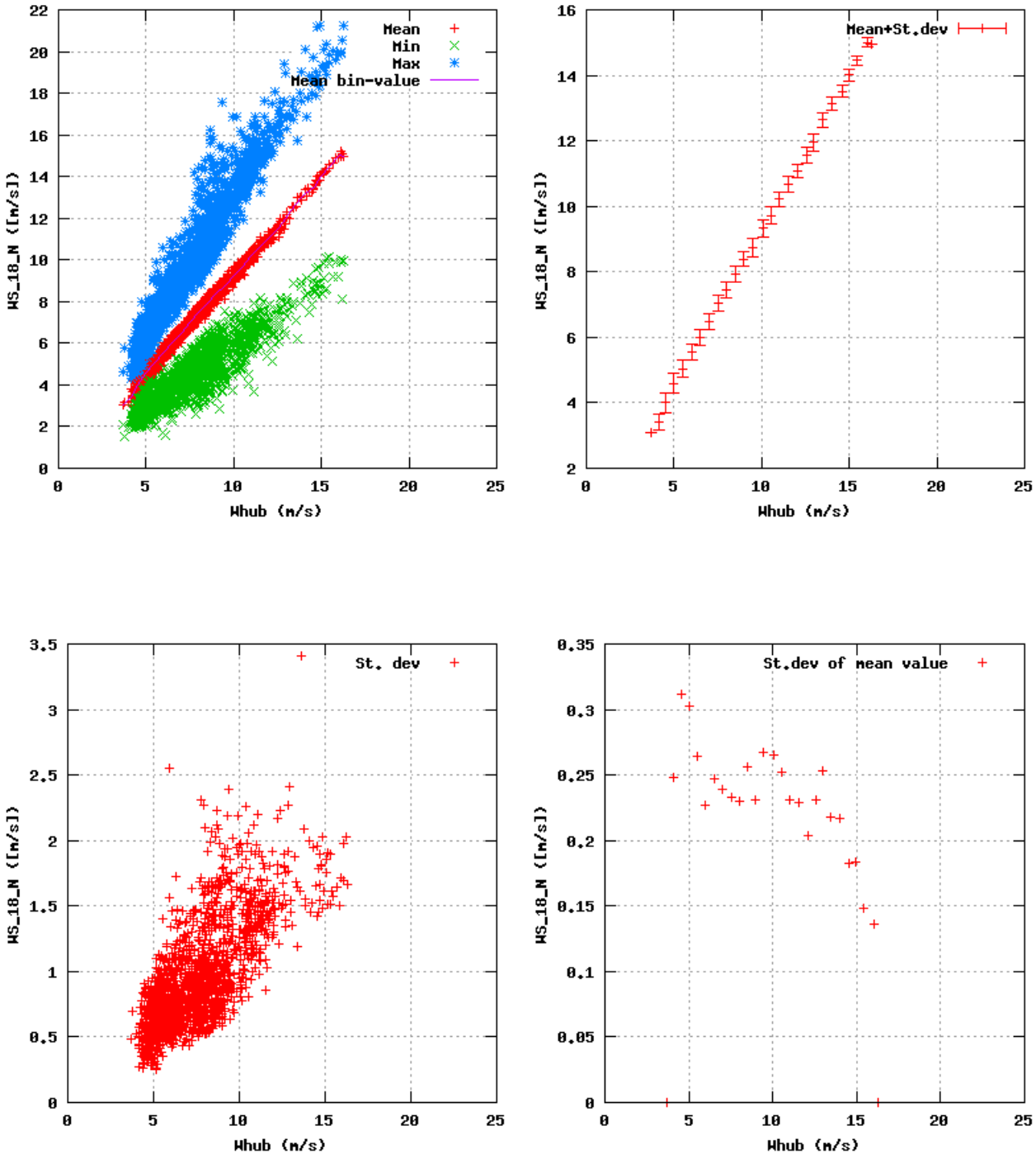

Figure 87a, Sensor 347: Wind speed Metmast @18m,North versus wind speed
Input files: ntk500res.dat, stat_347.dat

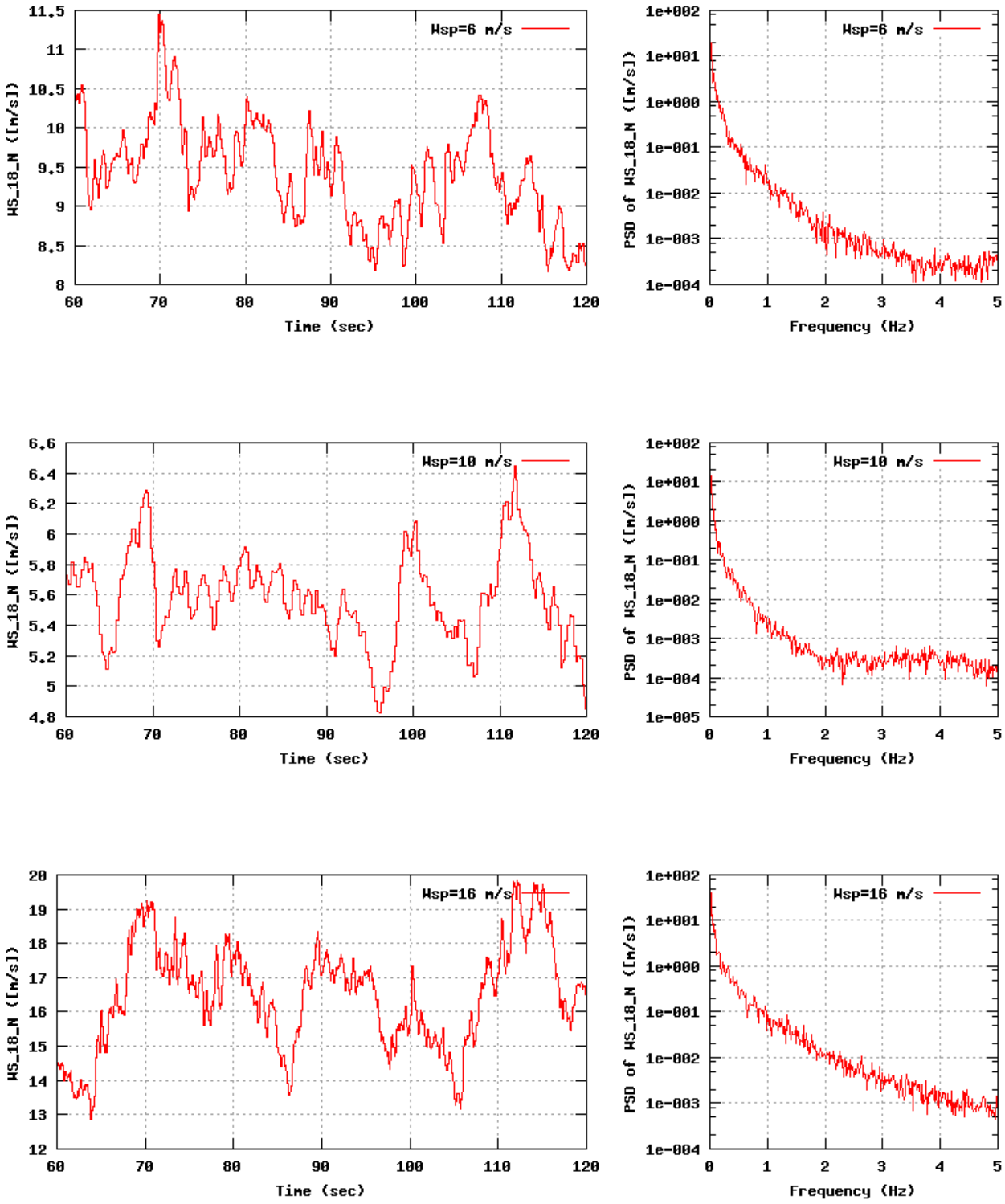

Figure 87b, Sensor 347: Wind speed Metmast @18m,North versus time and frequency
Input files: m06.asc, m10.asc, m16.asc, m06.psd, m10.psd and m16.psd

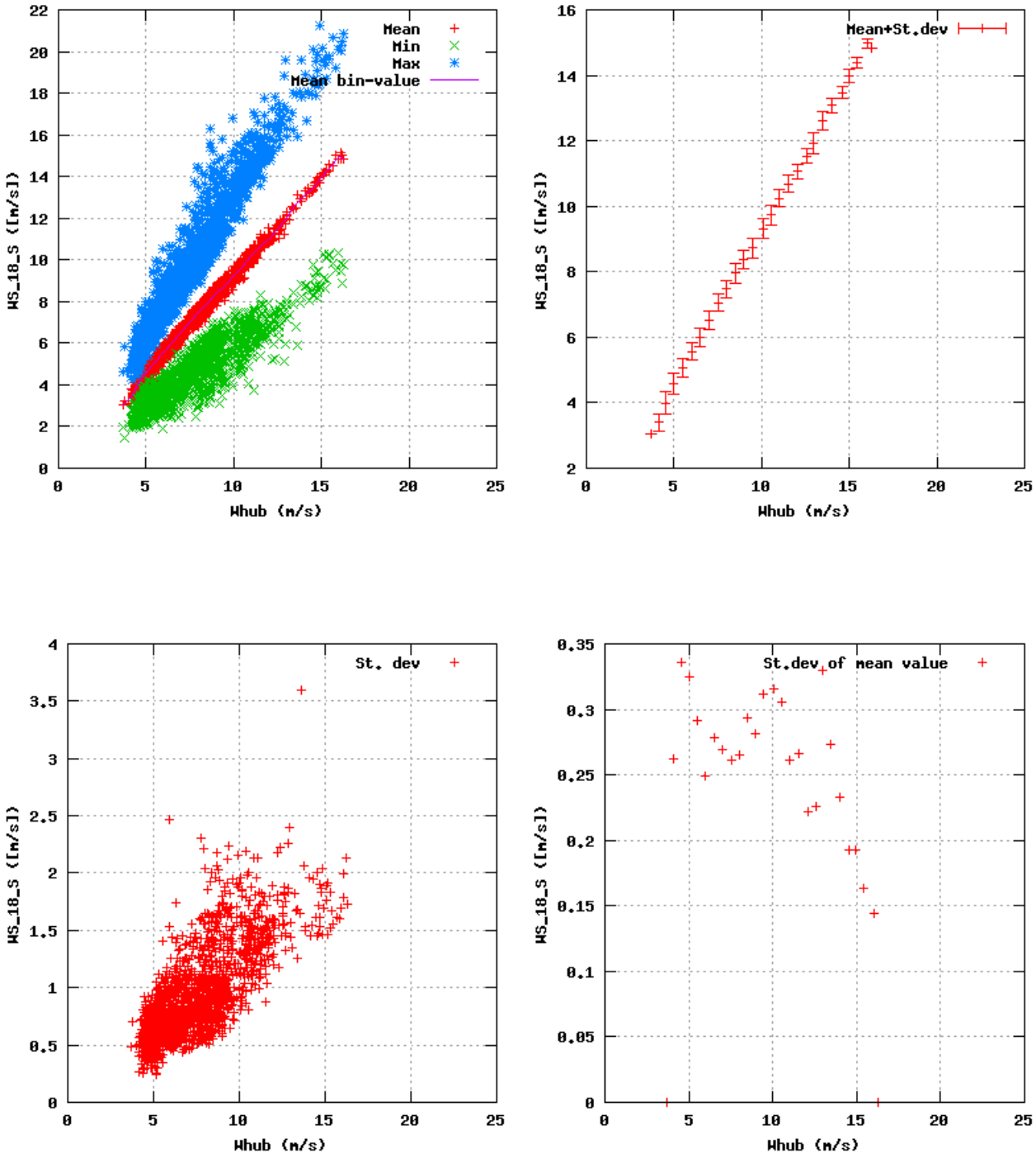

Figure 88a, Sensor 351: Wind speed Metmast @18m,South versus wind speed
Input files: ntk500res.dat, stat_351.dat

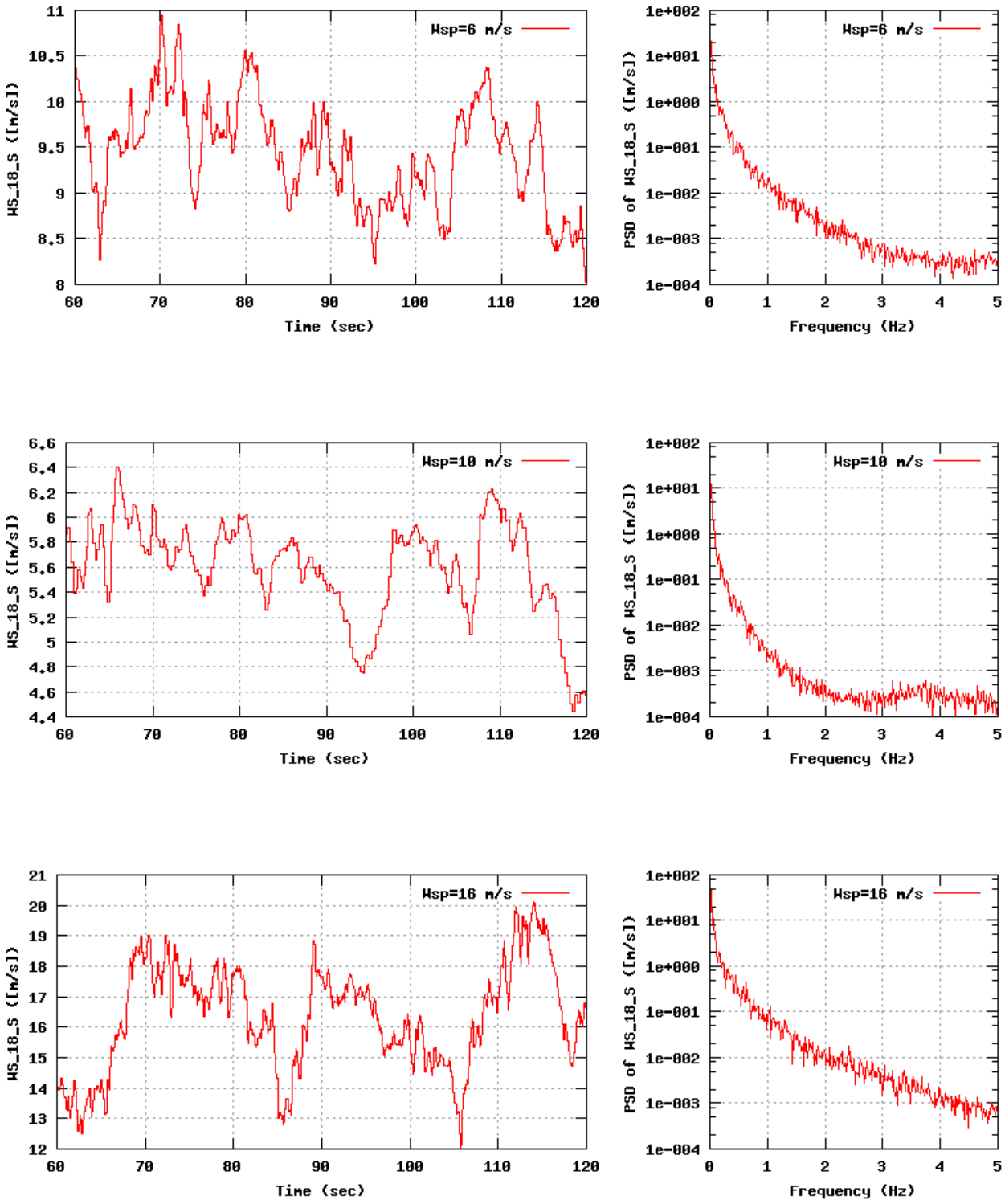

Figure 88b, Sensor 351: Wind speed Metmast @18m,South versus time and frequency
Input files: m06.asc, m10.asc, m16.asc, m06.psd, m10.psd and m16.psd

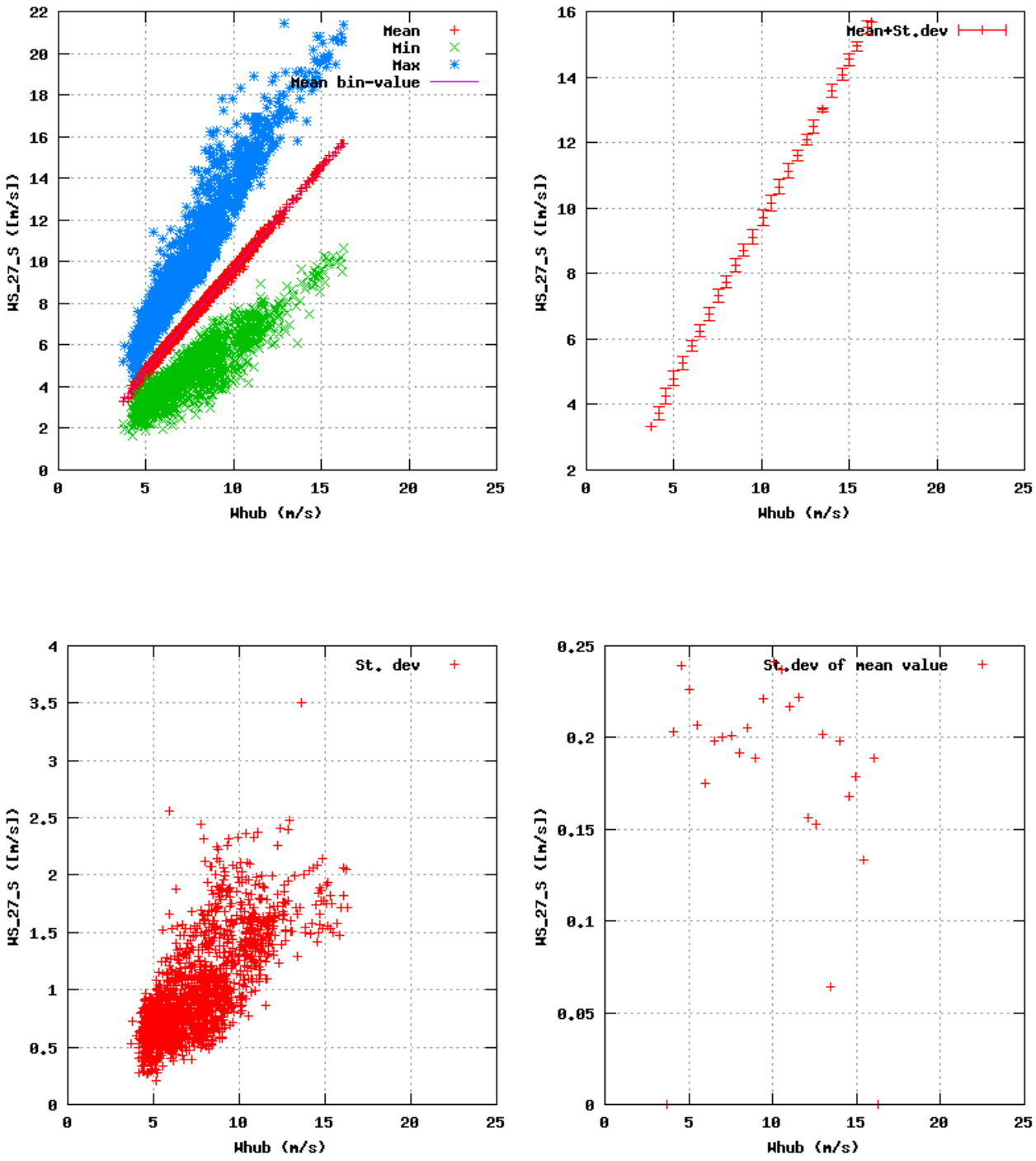

Figure 89a, Sensor 355: Wind speed Metmast @27m,South versus wind speed
Input files: ntk500res.dat, stat_355.dat

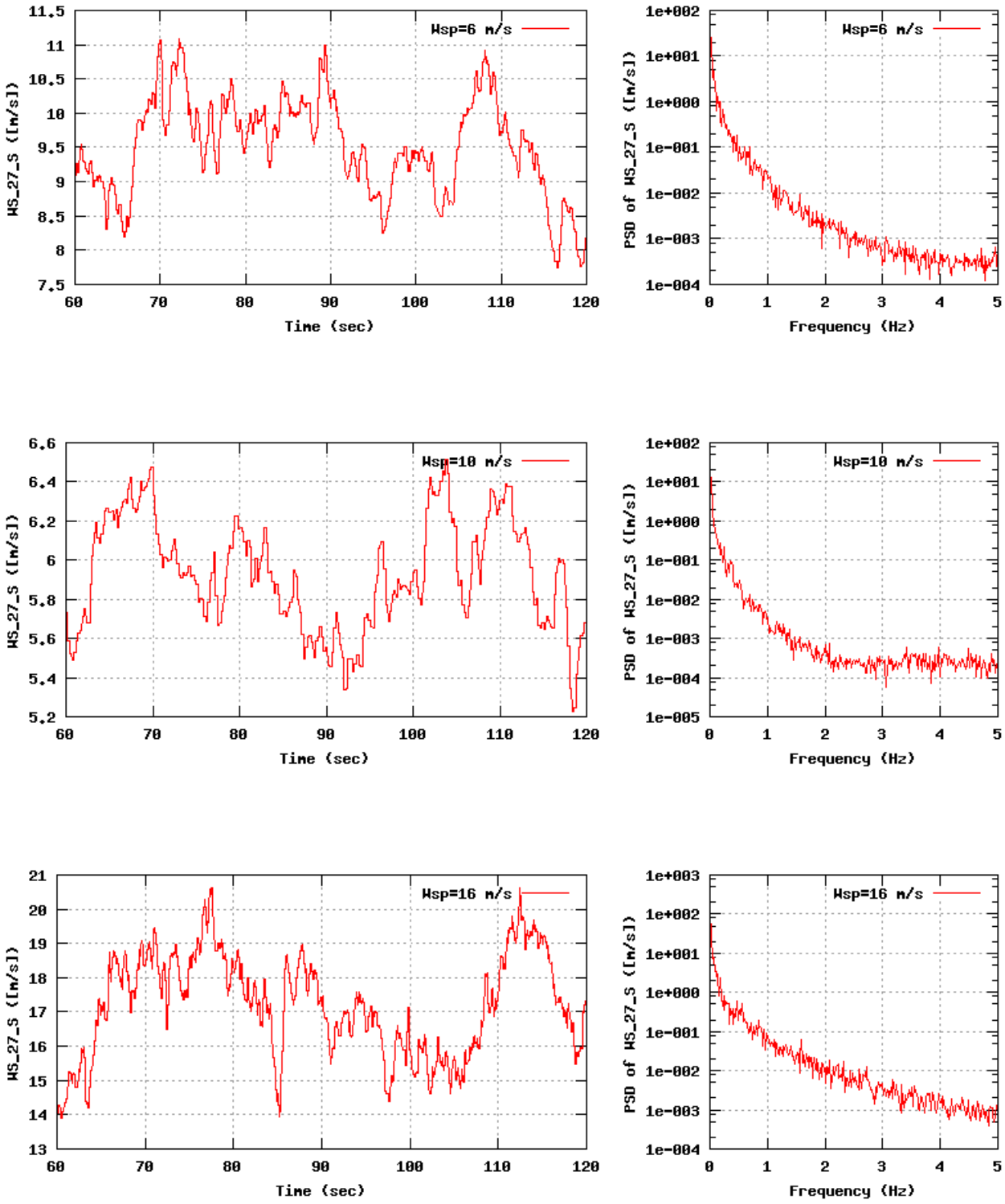

Figure 89b, Sensor 355: Wind speed Metmast @27m,South versus time and frequency
Input files: m06.asc, m10.asc, m16.asc, m06.psd, m10.psd and m16.psd

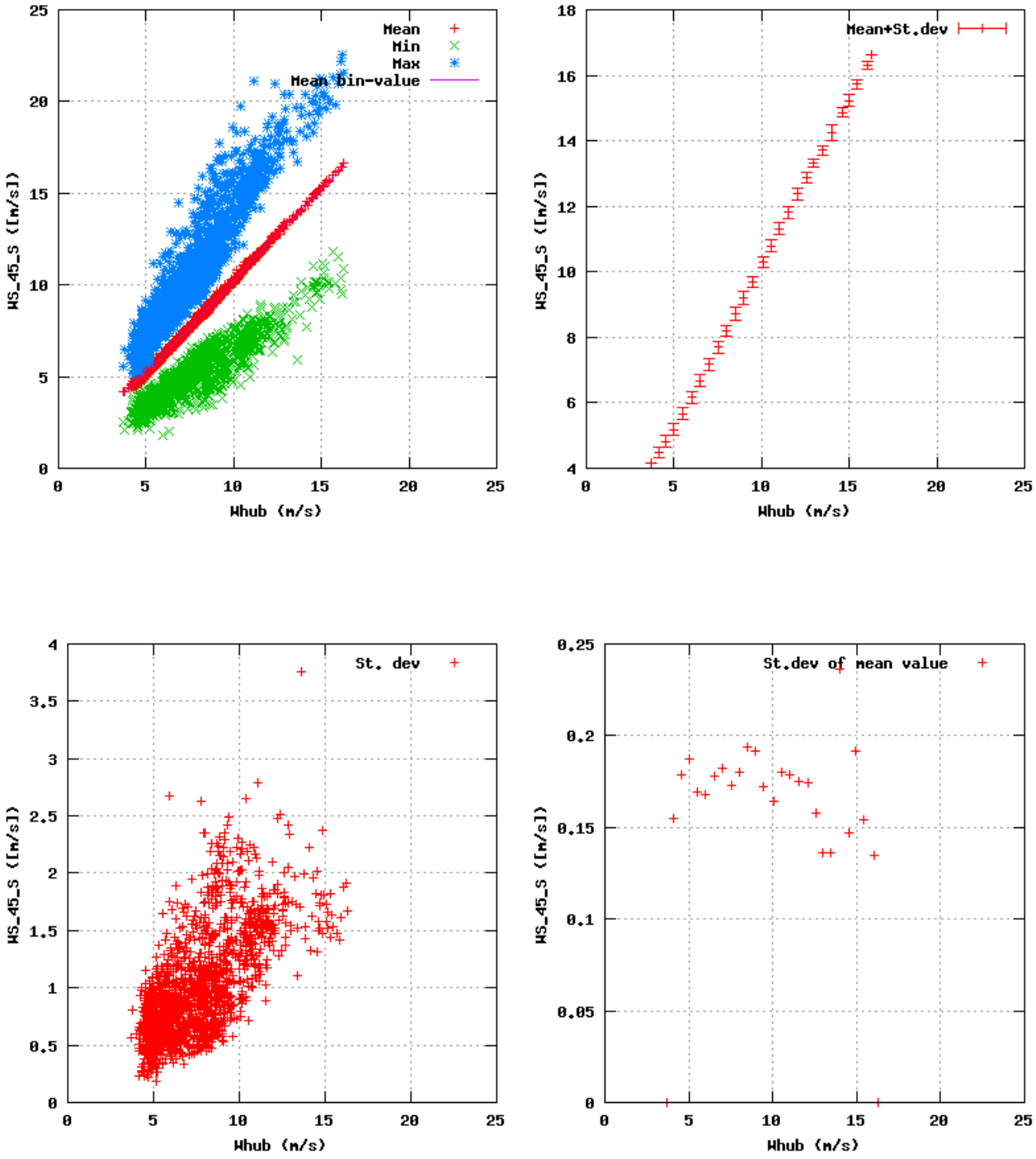

Figure 90a, Sensor 359: Wind speed Metmast @45m,South versus wind speed
Input files: ntk500res.dat, stat_359.dat

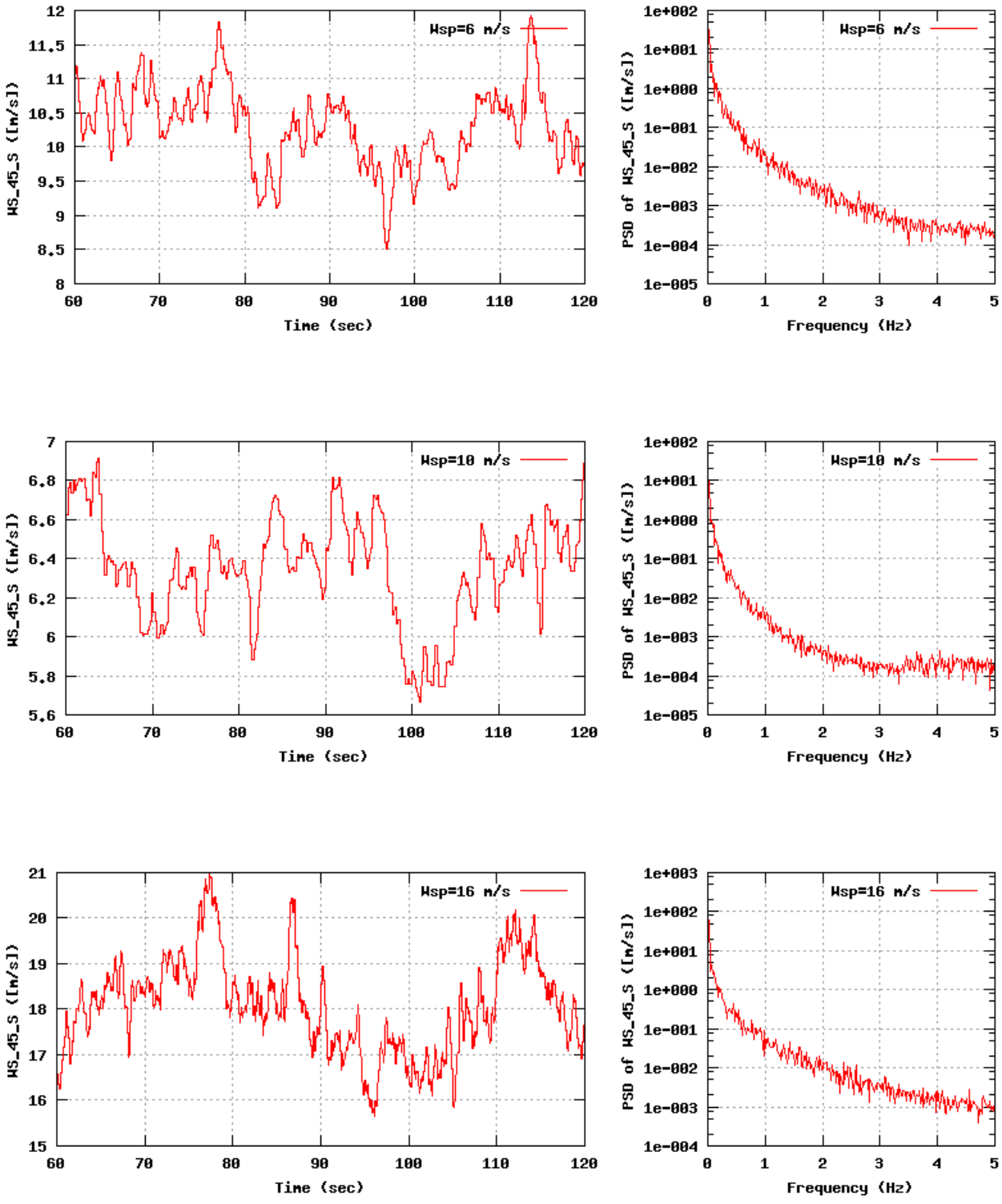

Figure 90b, Sensor 359: Wind speed Metmast @45m,South versus time and frequency
Input files: m06.asc, m10.asc, m16.asc, m06.psd, m10.psd and m16.psd

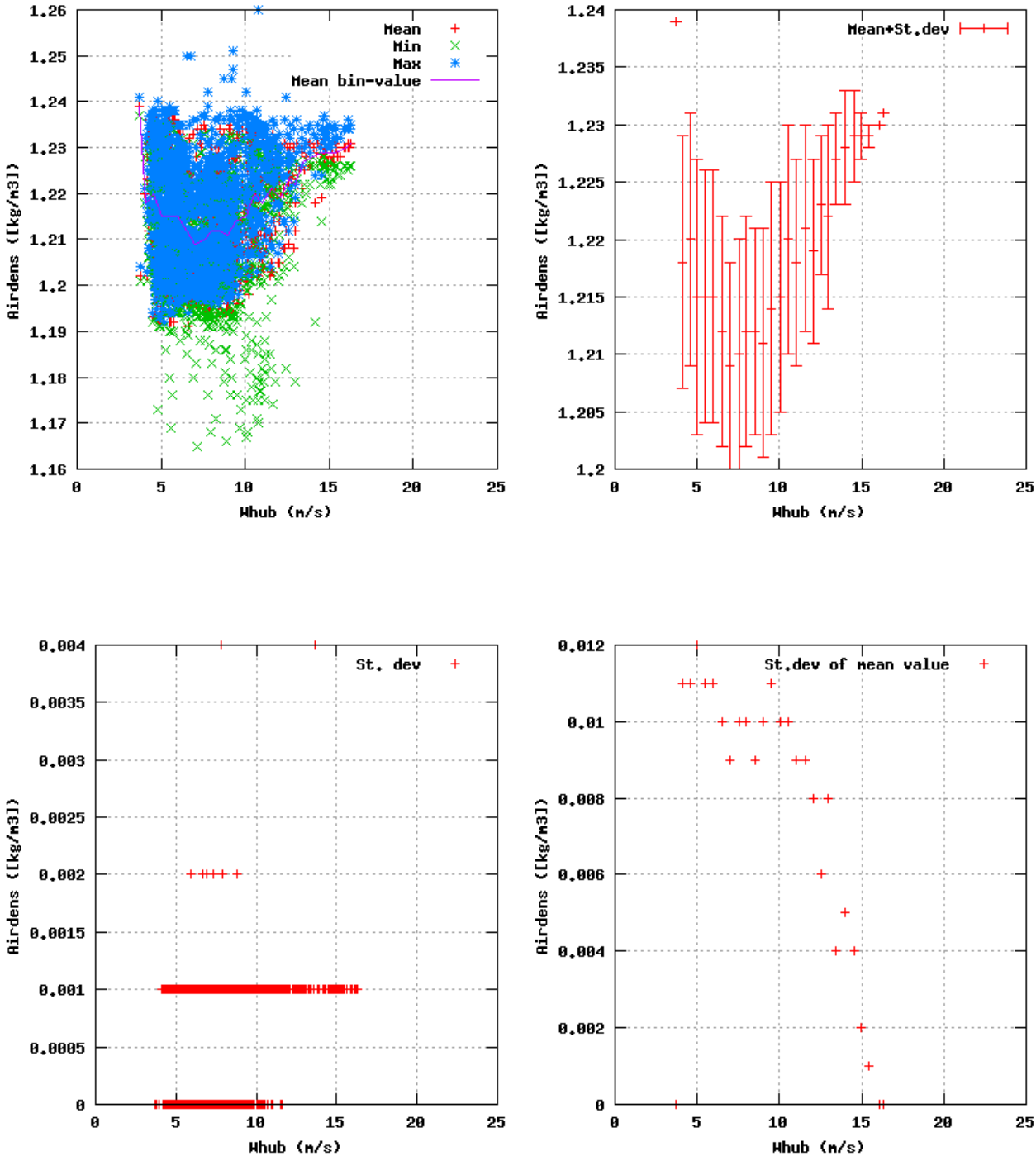

Figure 91a, Sensor 363: Air density versus wind speed
Input files: ntk500res.dat, stat_363.dat

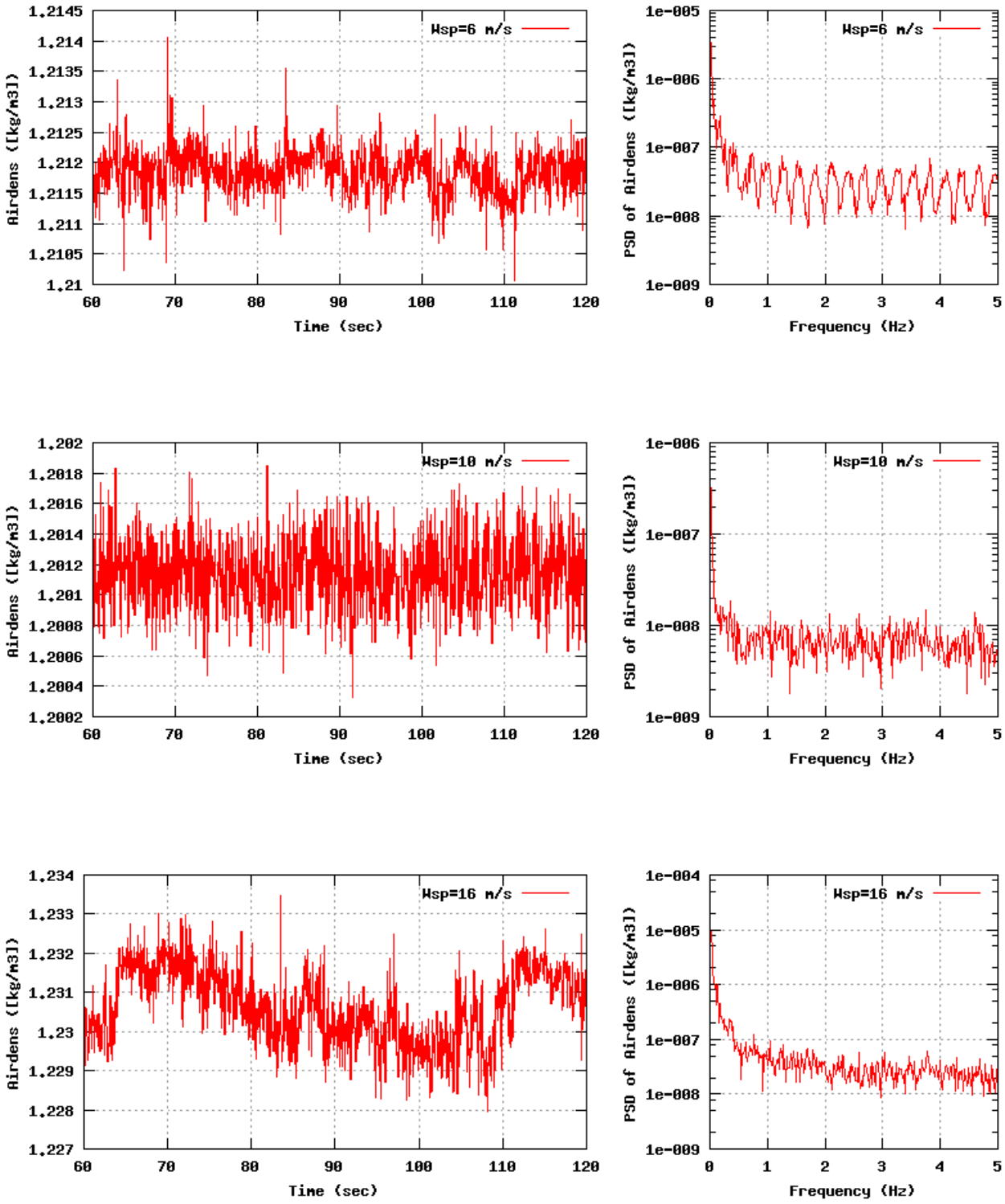

Figure 91b, Sensor 363: Air density versus time and frequency
Input files: m06.asc, m10.asc, m16.asc, m06.psd, m10.psd and m16.psd

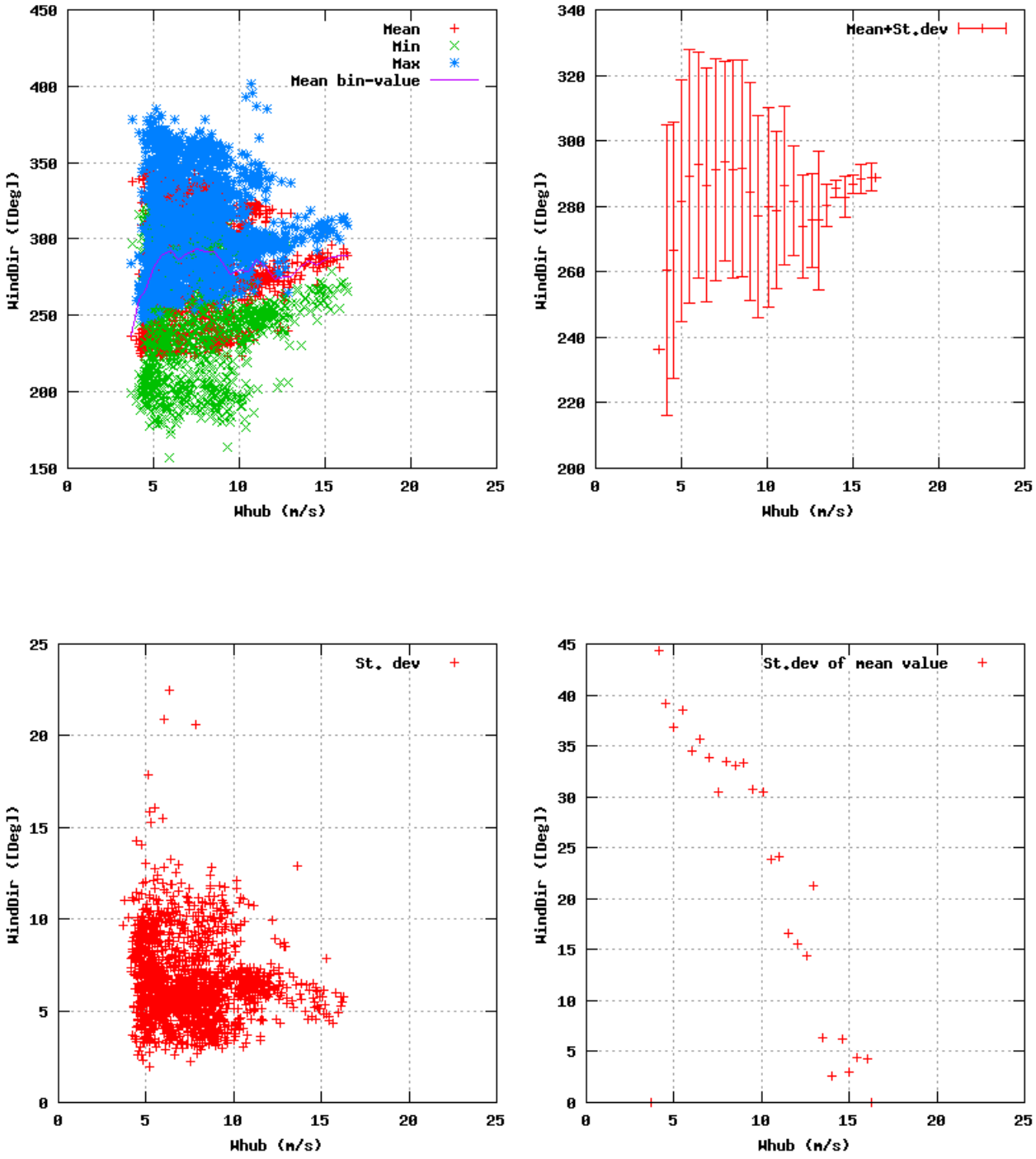

Figure 92a, Sensor 367: Wind Direction versus wind speed
Input files: ntk500res.dat, stat_367.dat

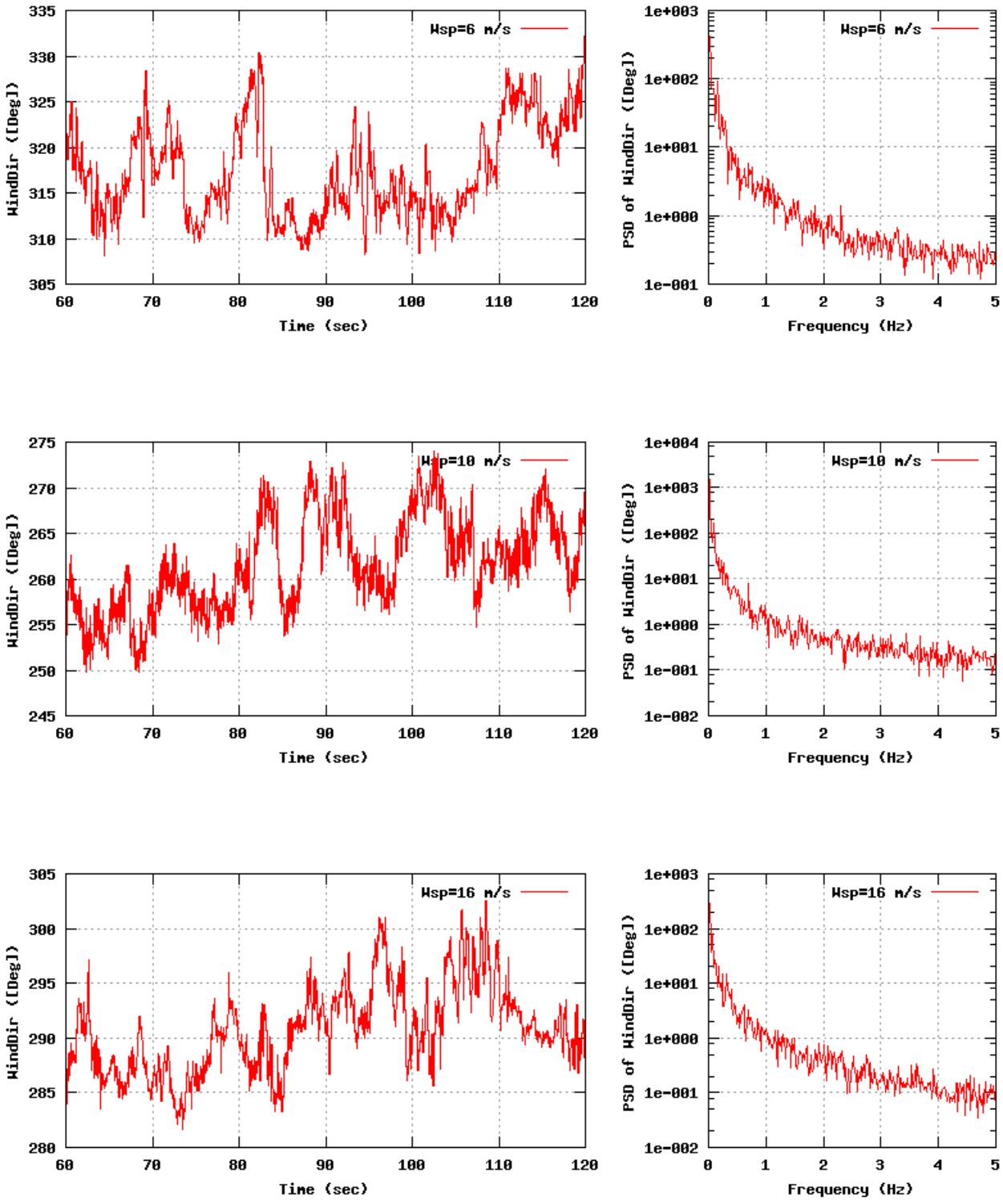

Figure 92b, Sensor 367: Wind Direction versus time and frequency
Input files: m06.asc, m10.asc, m16.asc, m06.psd, m10.psd and m16.psd

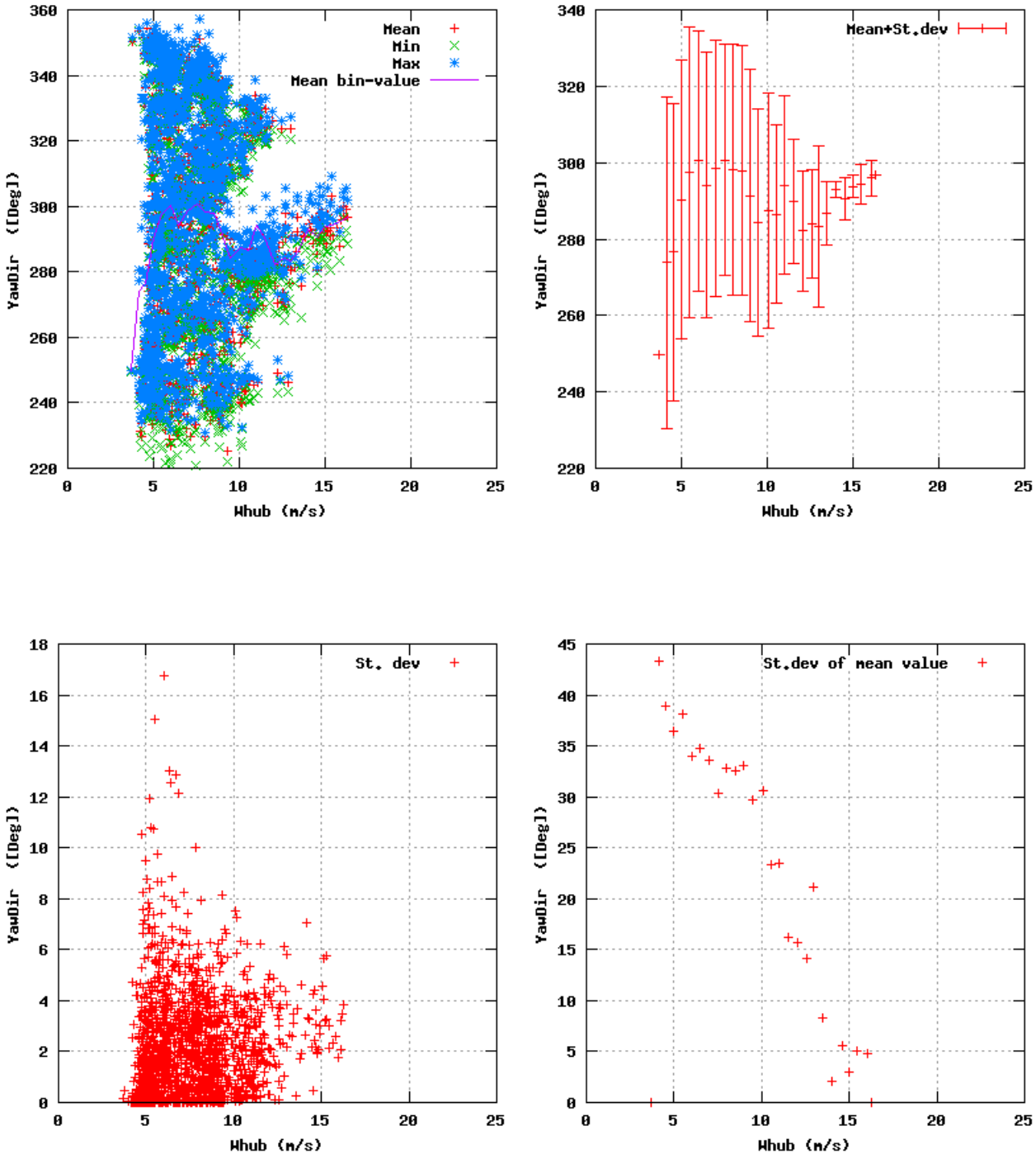

Figure 93a, Sensor 371: Yaw Position, nacelle versus wind speed
Input files: ntk500res.dat, stat_371.dat

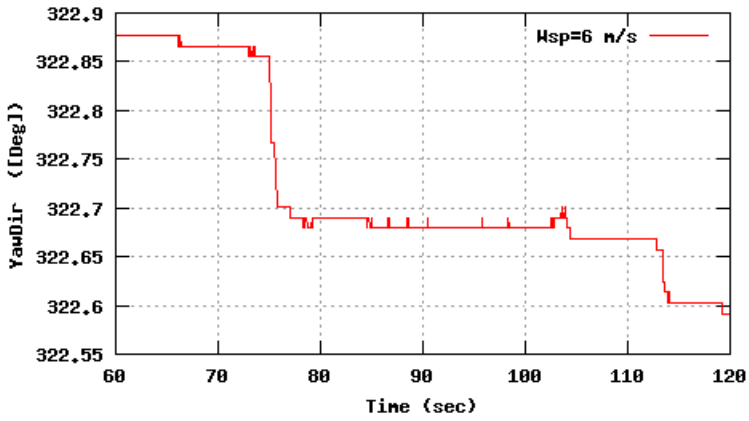

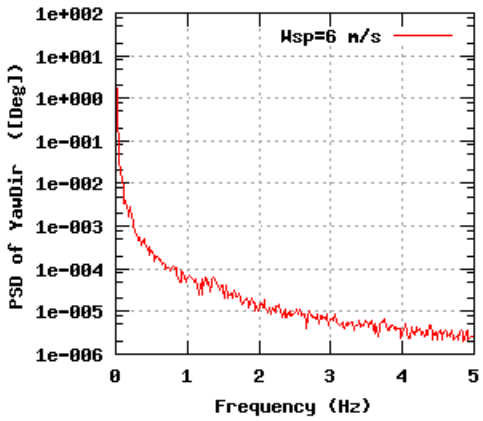

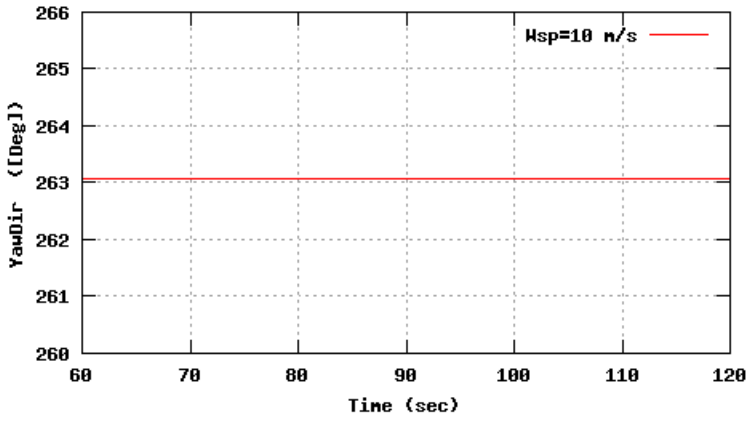

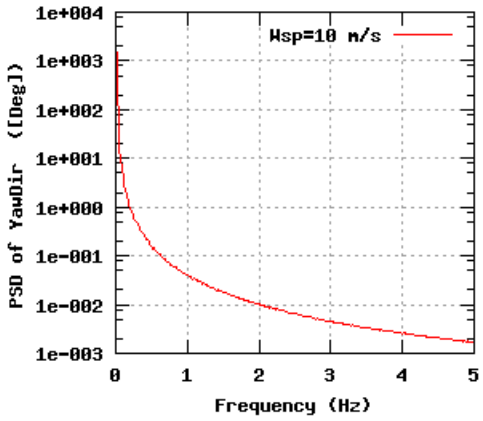

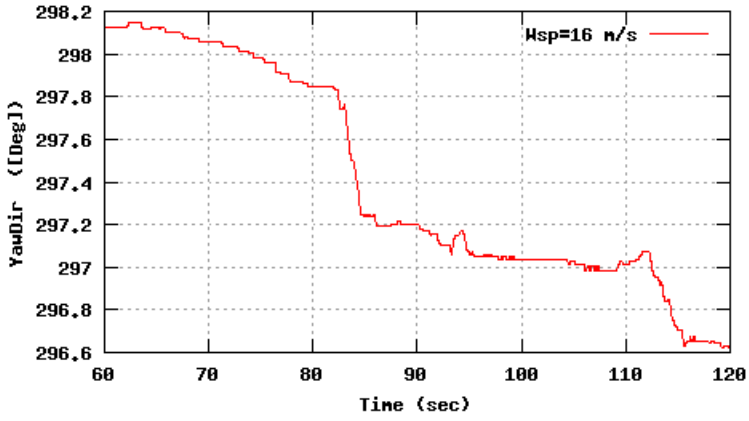

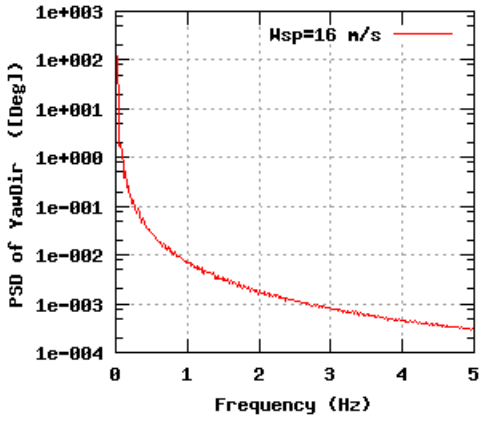

Figure 93b, Sensor 371: Yaw Position, nacelle versus time and frequency
Input files: m06.asc, m10.asc, m16.asc, m06.psd, m10.psd and m16.psd

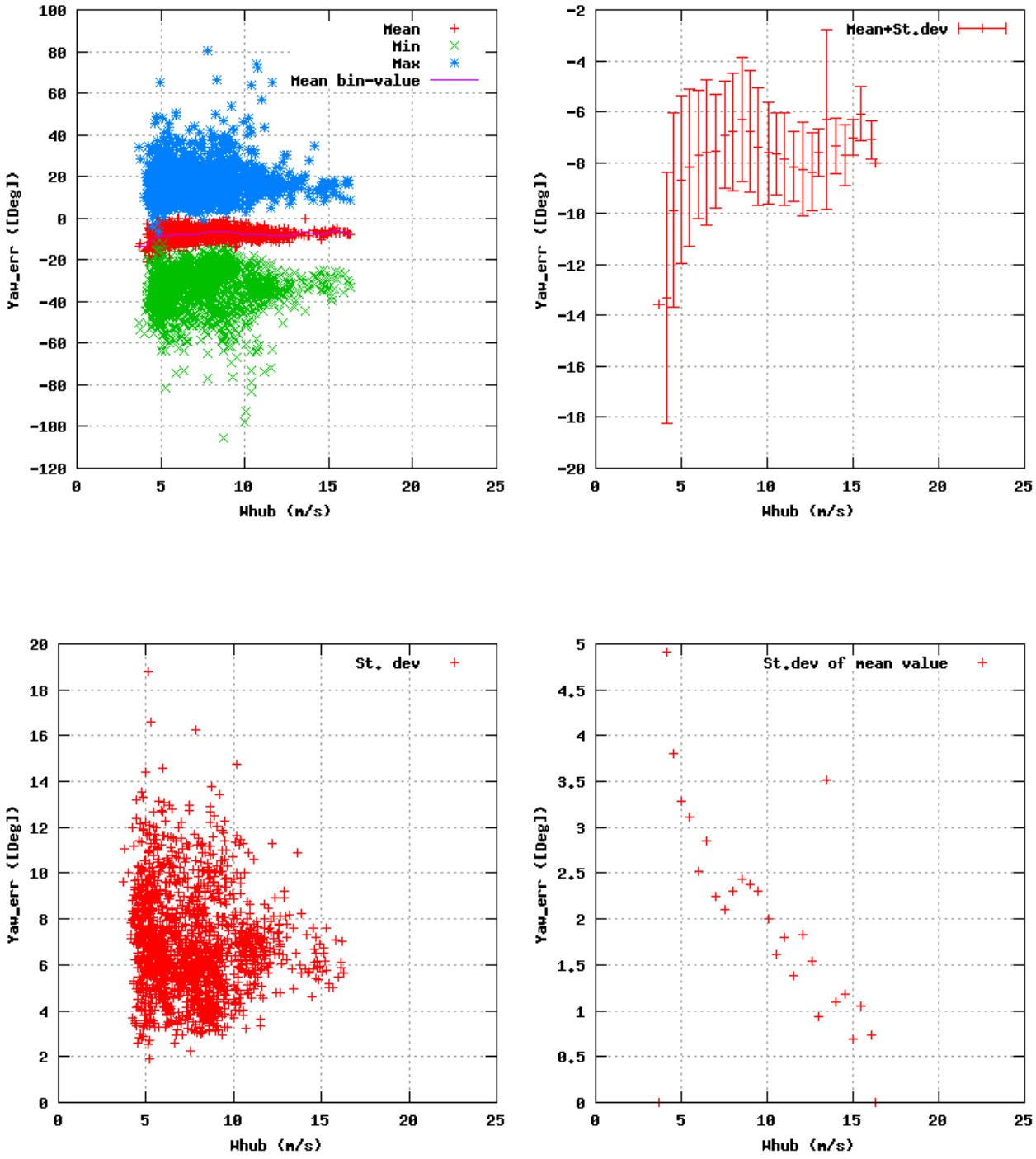

Figure 94a, Sensor 375: Yaw_err versus wind speed
Input files: ntk500res.dat, stat_375.dat

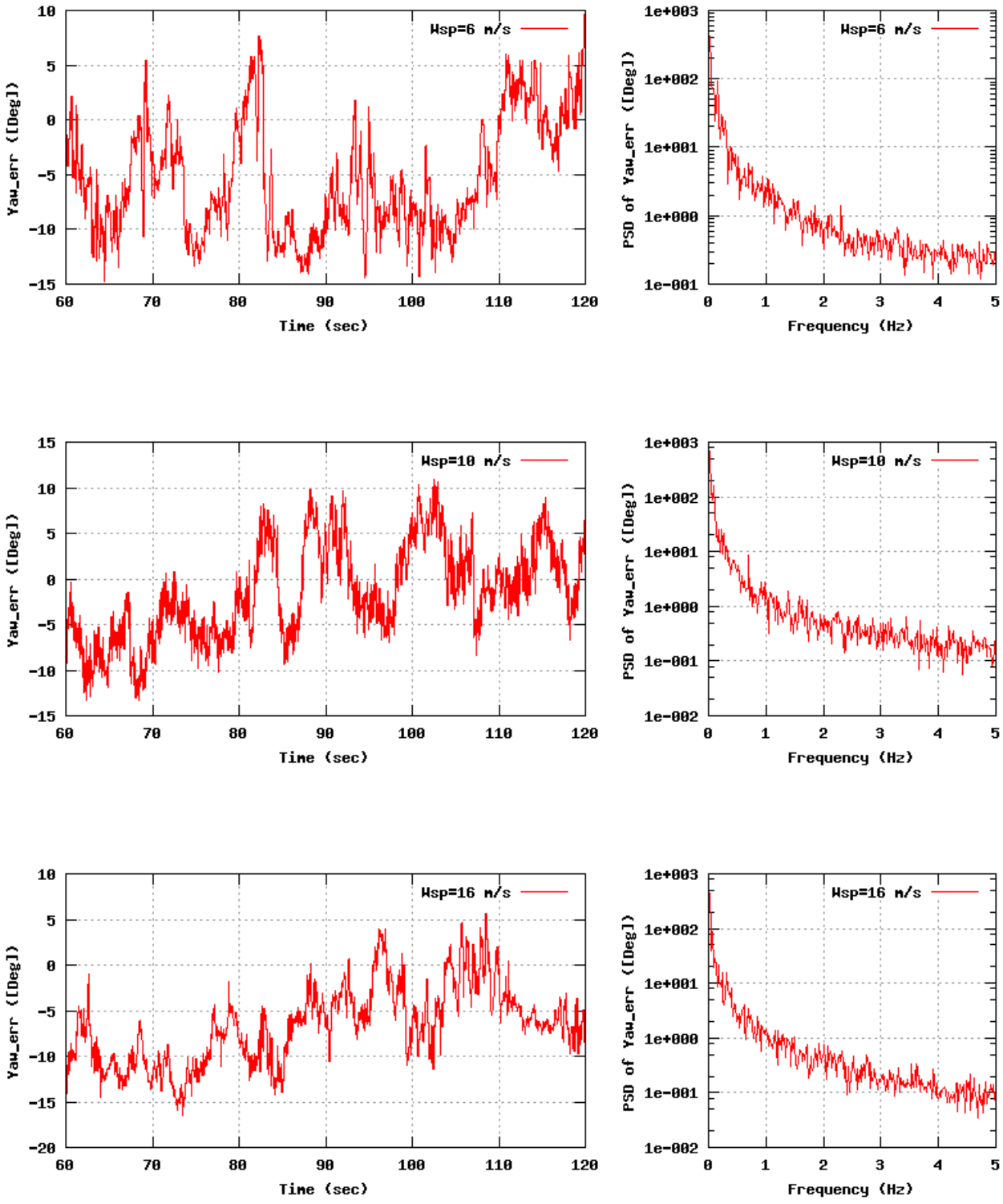

Figure 94b, Sensor 375: Yaw_err versus time and frequency
Input files: m06.asc, m10.asc, m16.asc, m06.psd, m10.psd and m16.psd

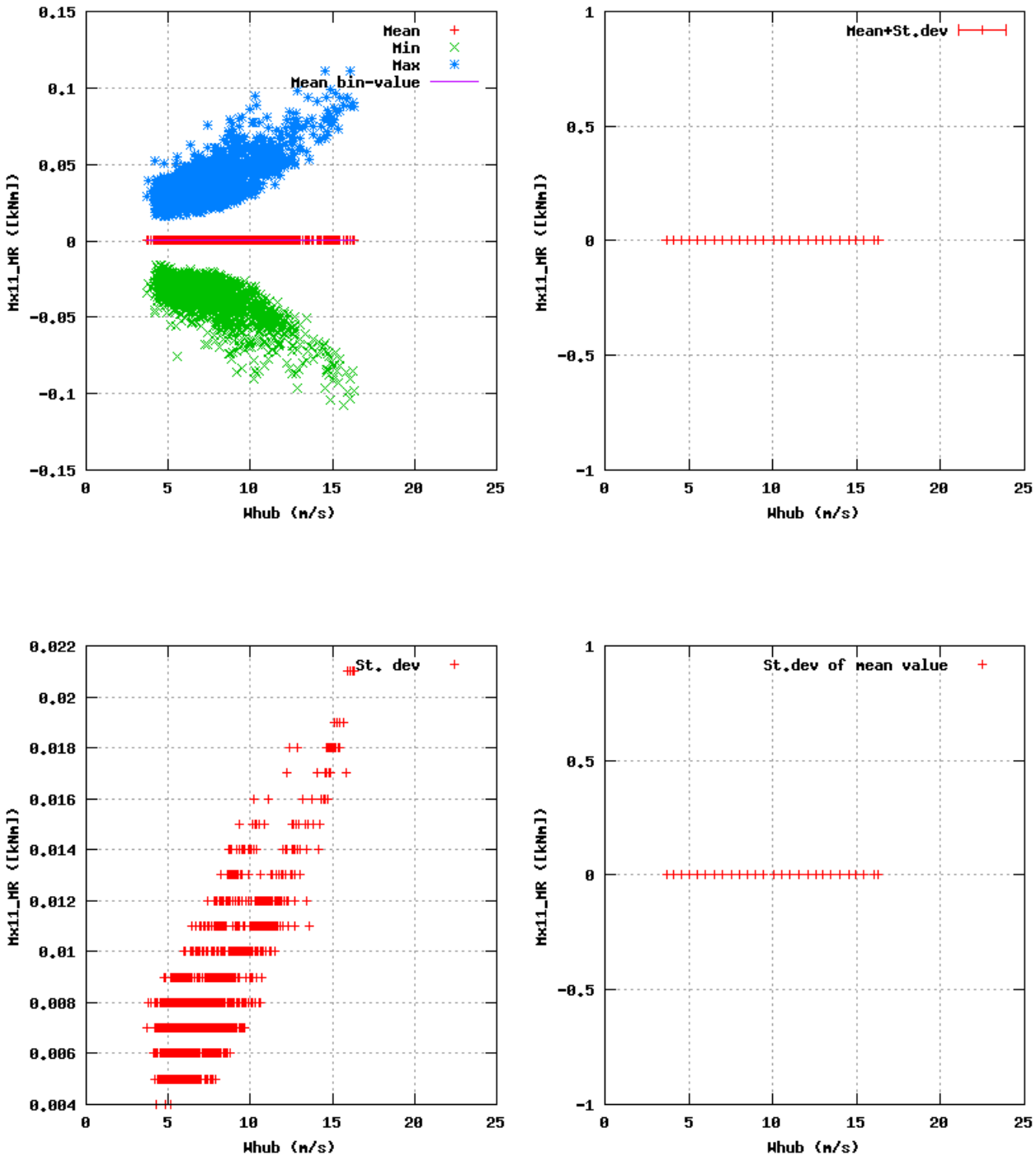

Figure 95a, Sensor 379: Edge bending mean removal Mx11_MR versus wind speed
Input files: ntk500res.dat, stat_379.dat

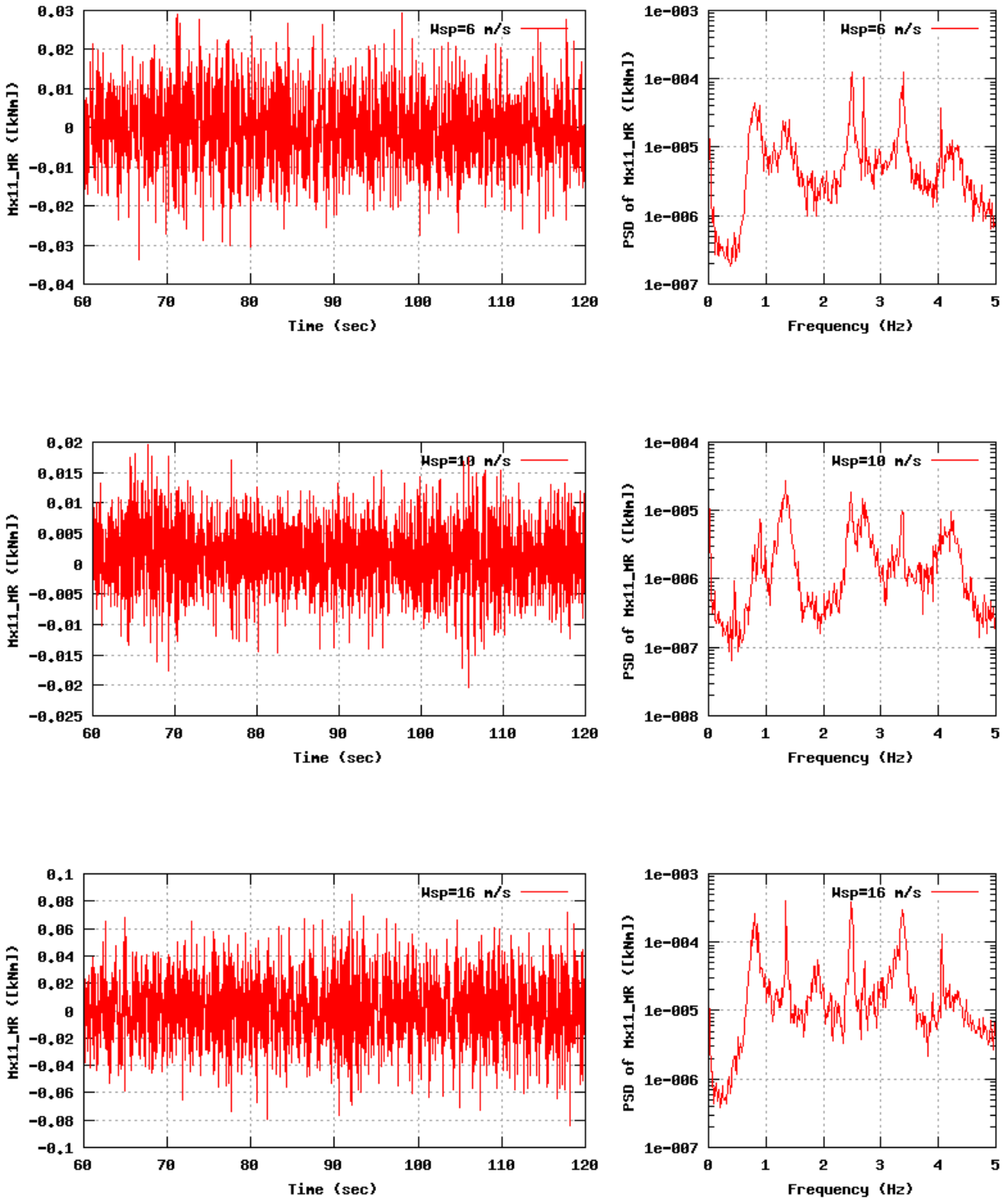

Figure 95b, Sensor 379: Edge bending mean removal Mx11_MR versus time and frequency
Input files: m06.asc, m10.asc, m16.asc, m06.psd, m10.psd and m16.psd

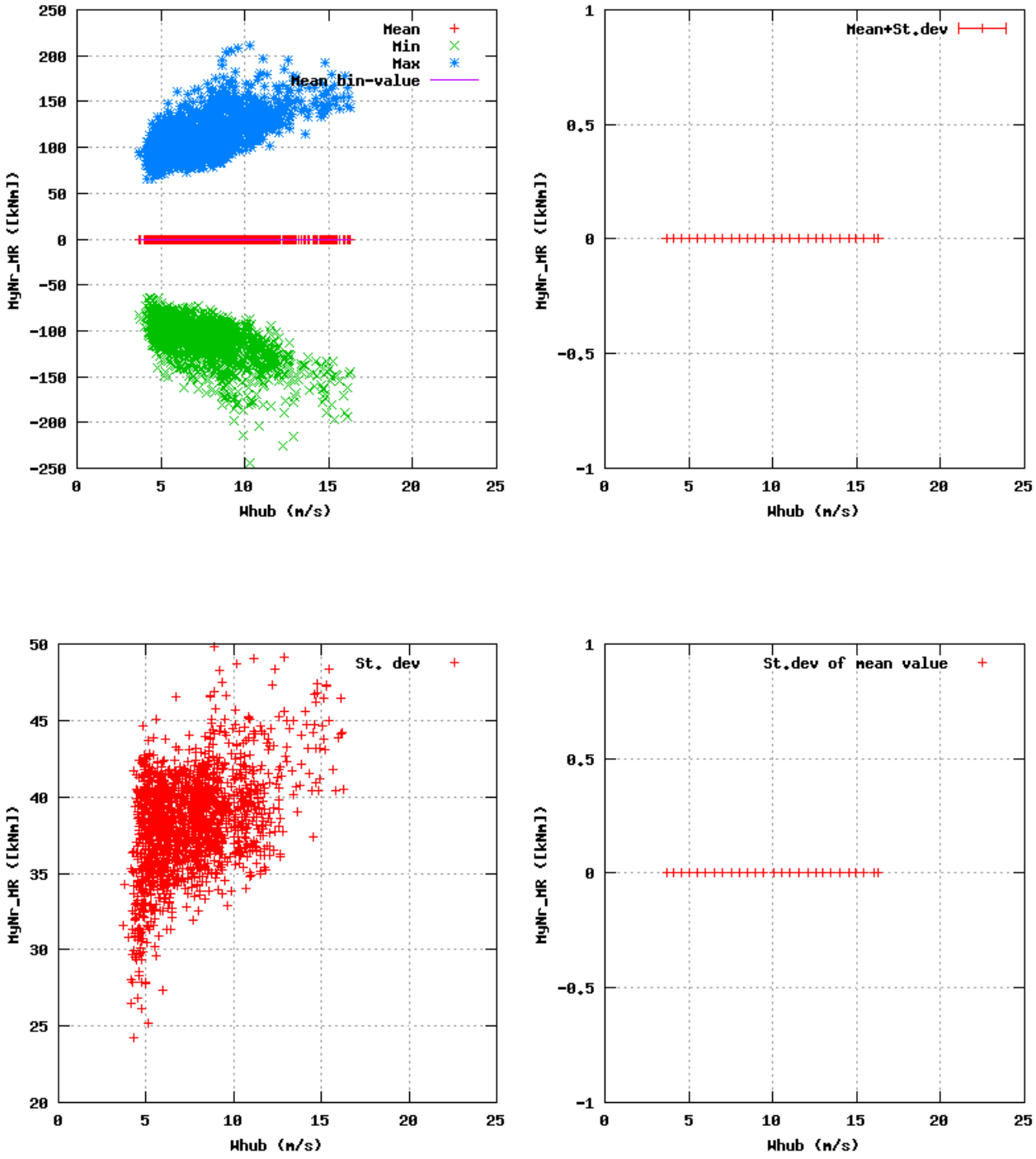

Figure 96a, Sensor 383: Rotor shaft moment mean removal MyNr_MR versus wind speed
Input files: ntk500res.dat, stat_383.dat

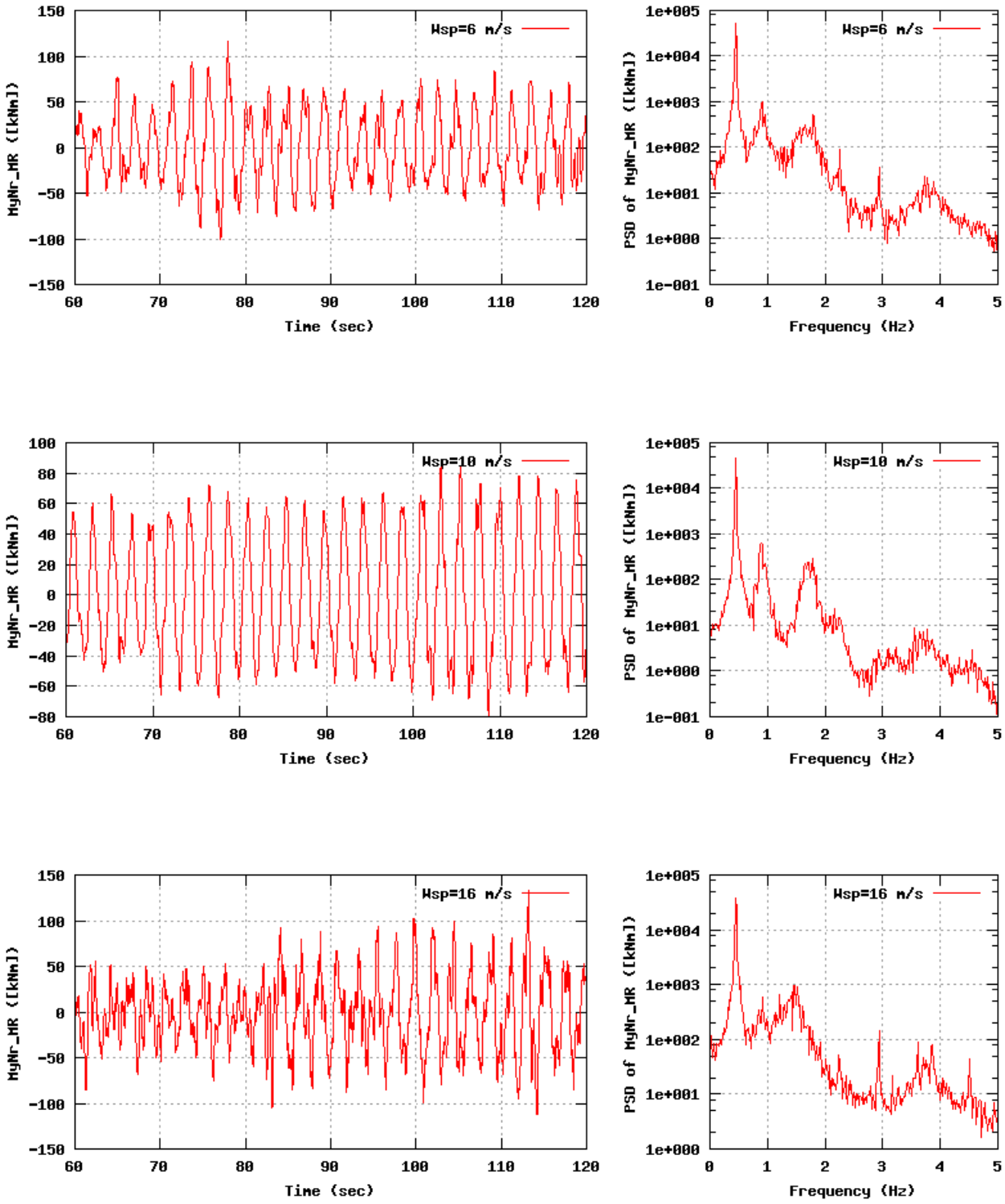

Figure 96b, Sensor 383: Rotor shaft moment mean removal MyNr_MR versus time and frequency
Input files: m06.asc, m10.asc, m16.asc, m06.psd, m10.psd and m16.psd

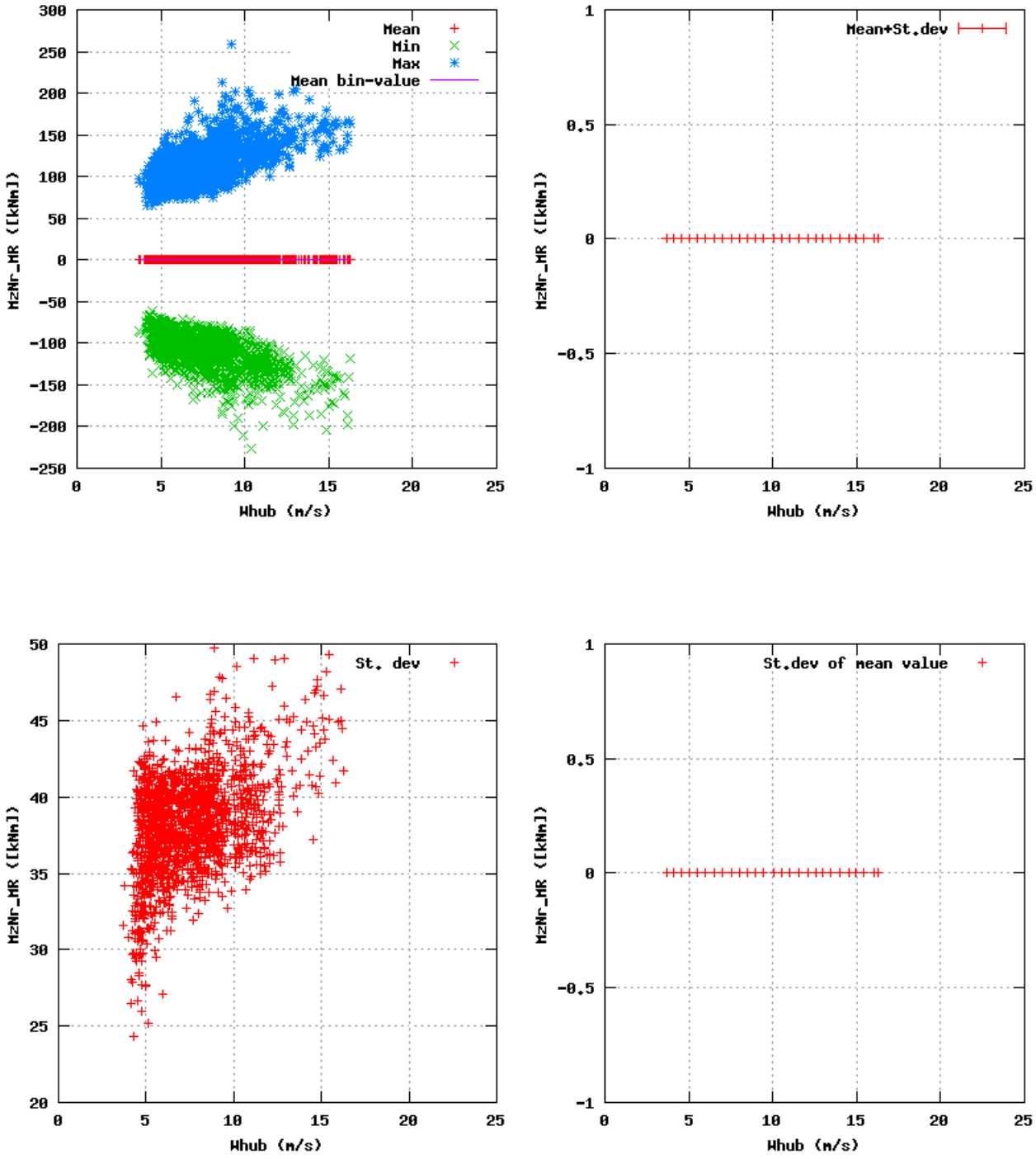

Figure 97a, Sensor 387: Rotor shaft moment mean removal MzNr_MR versus wind speed
Input files: ntk500res.dat, stat_387.dat

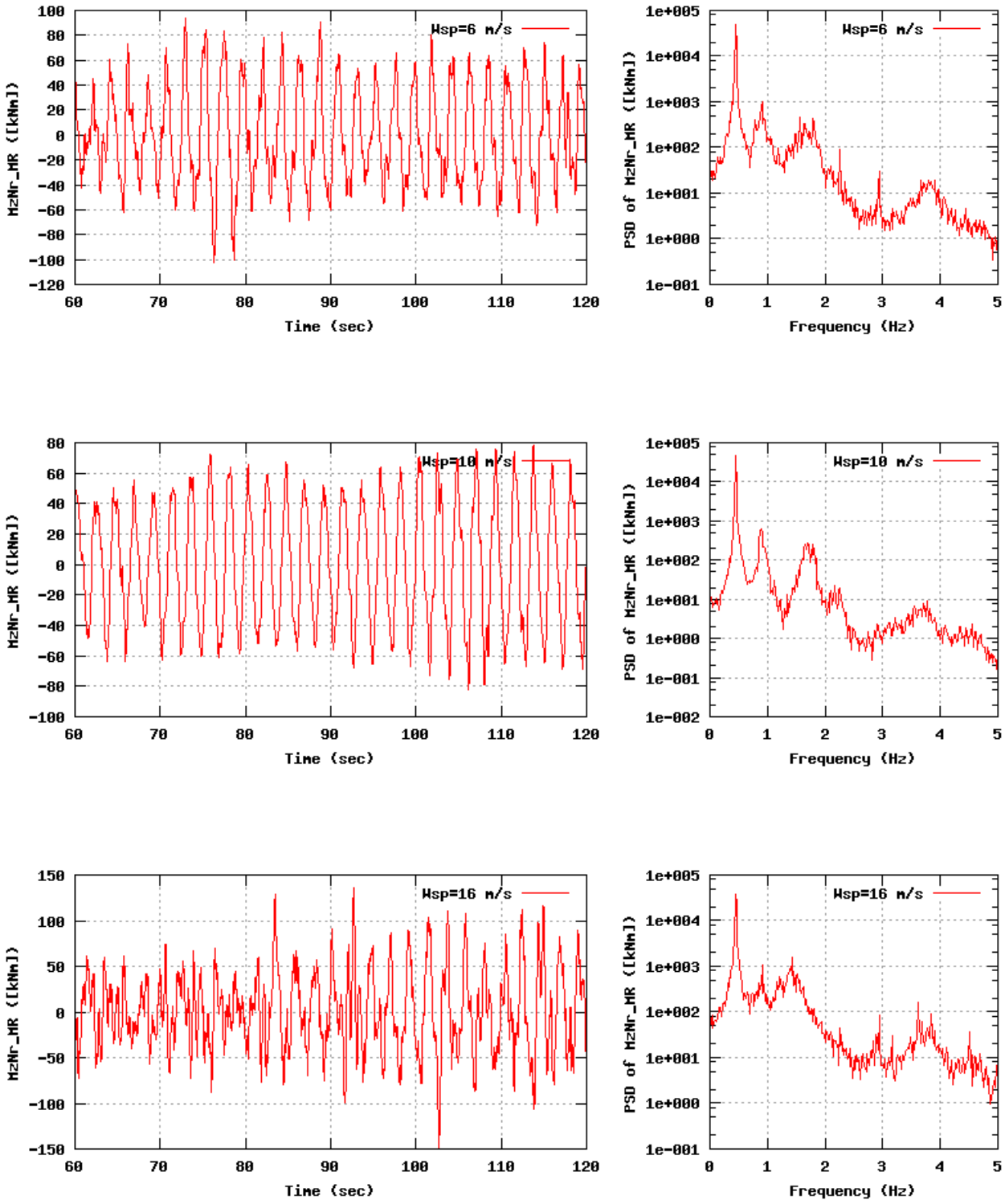

Figure 97b, Sensor 387: Rotor shaft moment mean removal MzNr_MR versus time and frequency
Input files: m06.asc, m10.asc, m16.asc, m06.psd, m10.psd and m16.psd

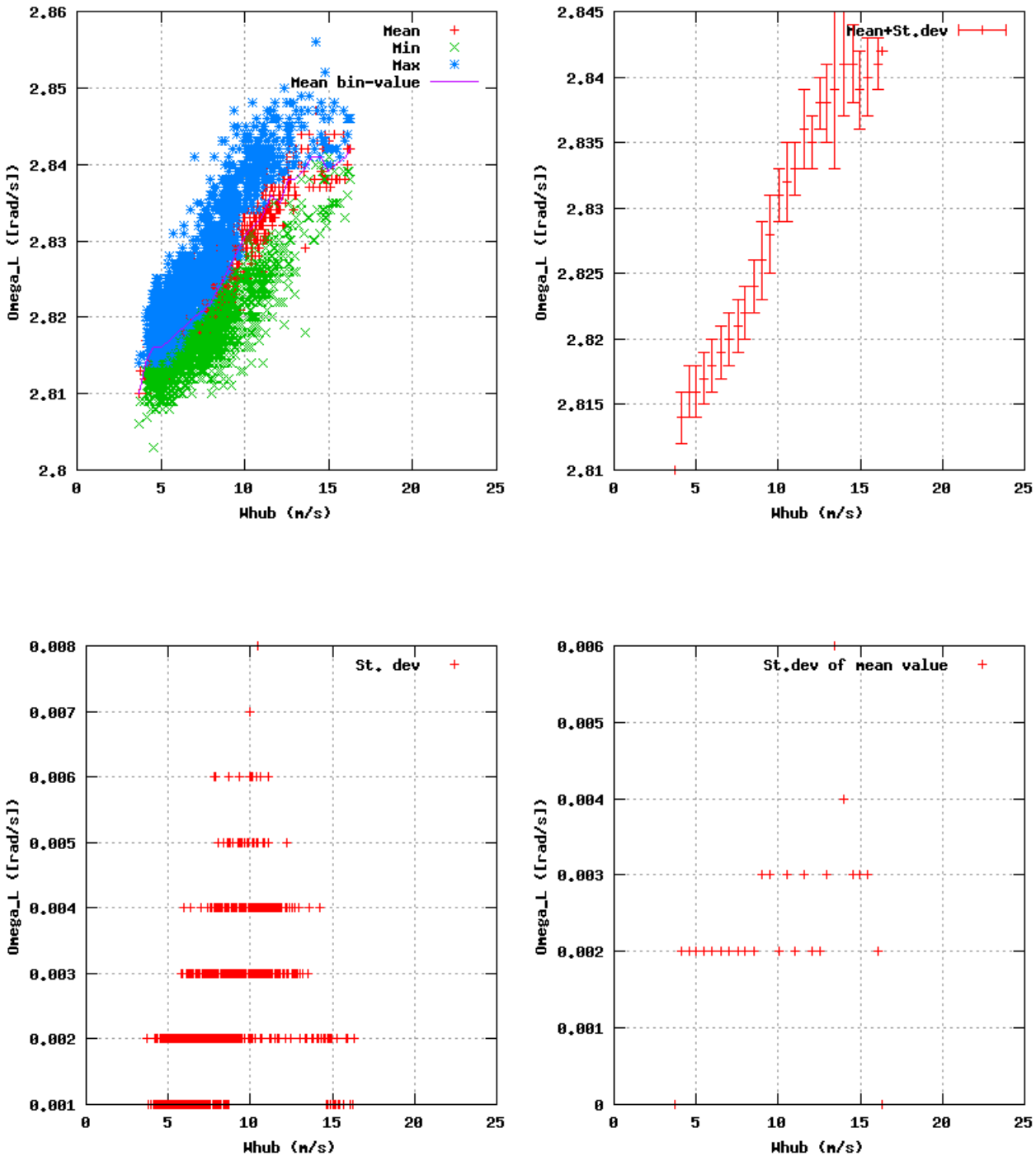

Figure 98a, Sensor 391: Rotor shaft speed LSS versus wind speed
Input files: ntk500res.dat, stat_391.dat

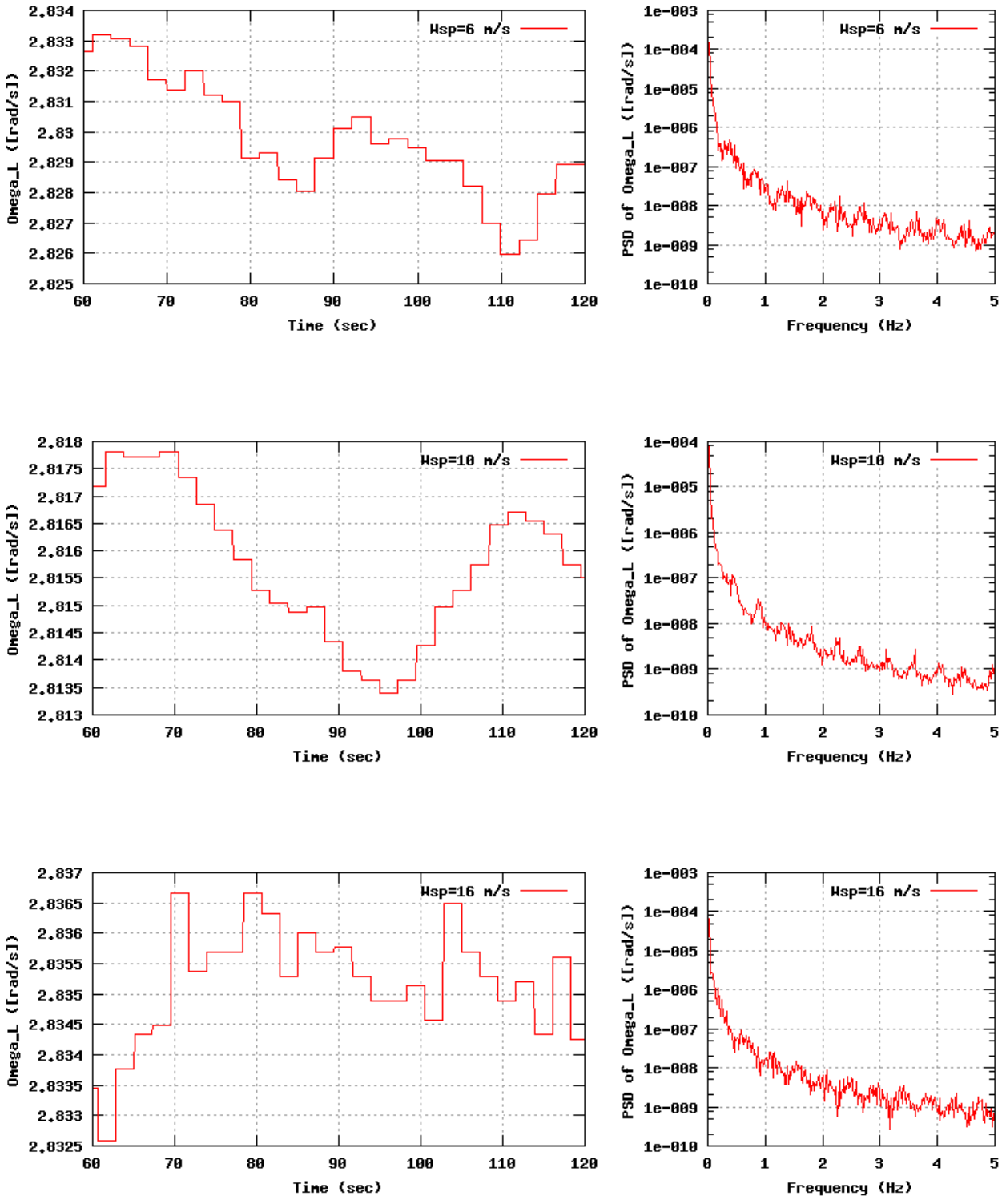

Figure 98b, Sensor 391: Rotor shaft speed LSS versus time and frequency
Input files: m06.asc, m10.asc, m16.asc, m06.psd, m10.psd and m16.psd

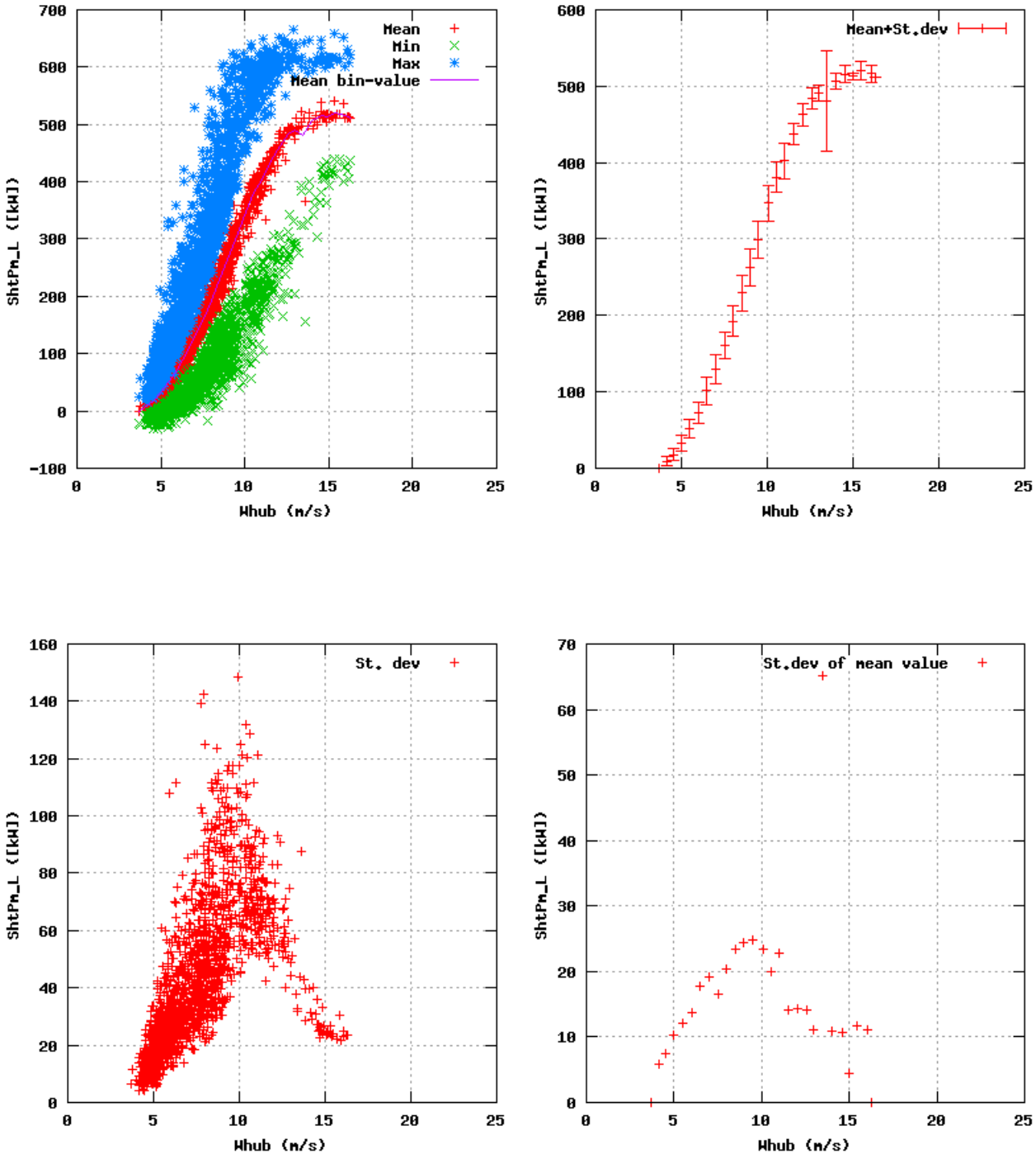

Figure 99a, Sensor 395: Mechanical shaft power LSS versus wind speed
Input files: ntk500res.dat, stat_395.dat

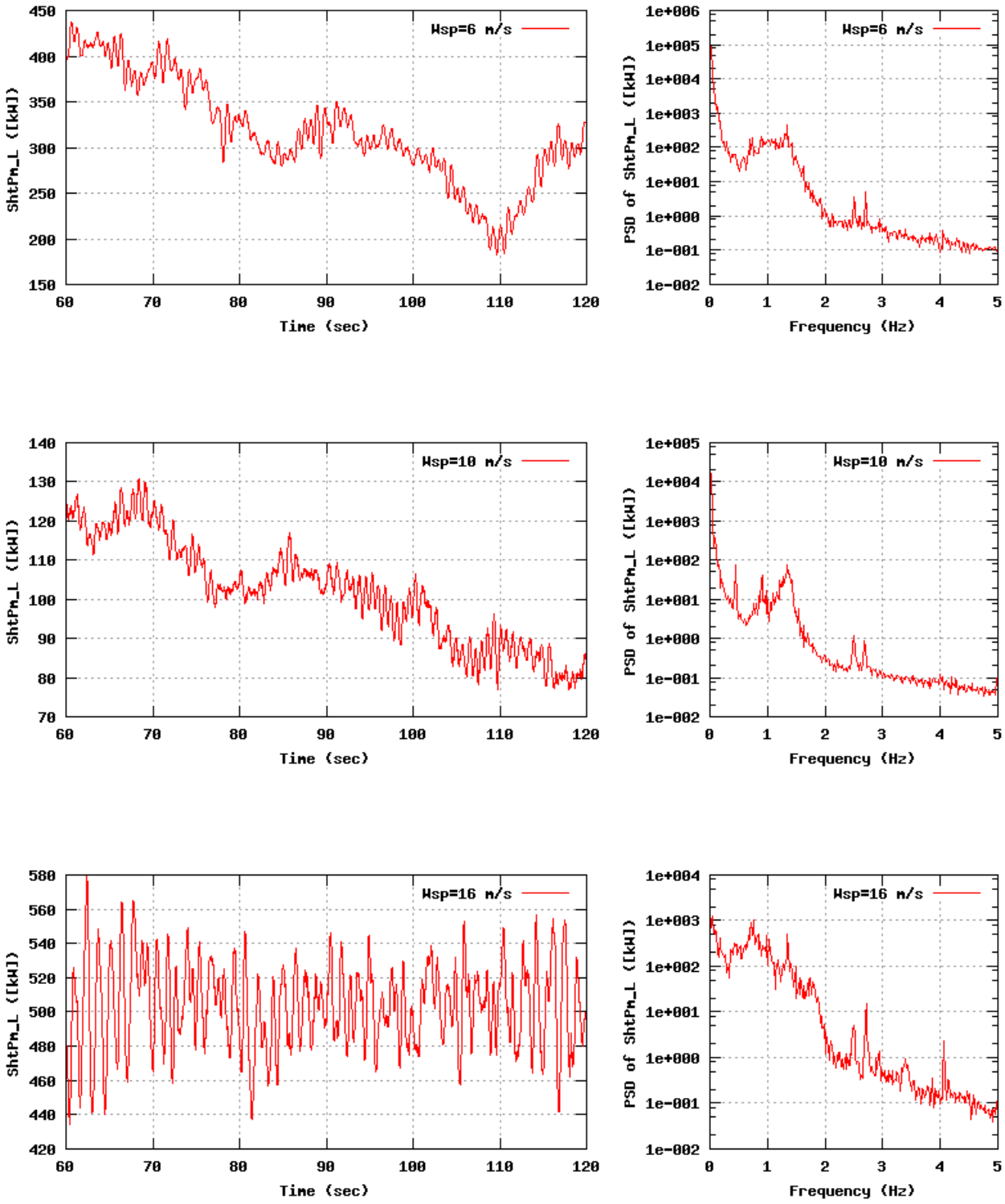

Figure 99b, Sensor 395: Mechanical shaft power LSS versus time and frequency
Input files: m06.asc, m10.asc, m16.asc, m06.psd, m10.psd and m16.psd

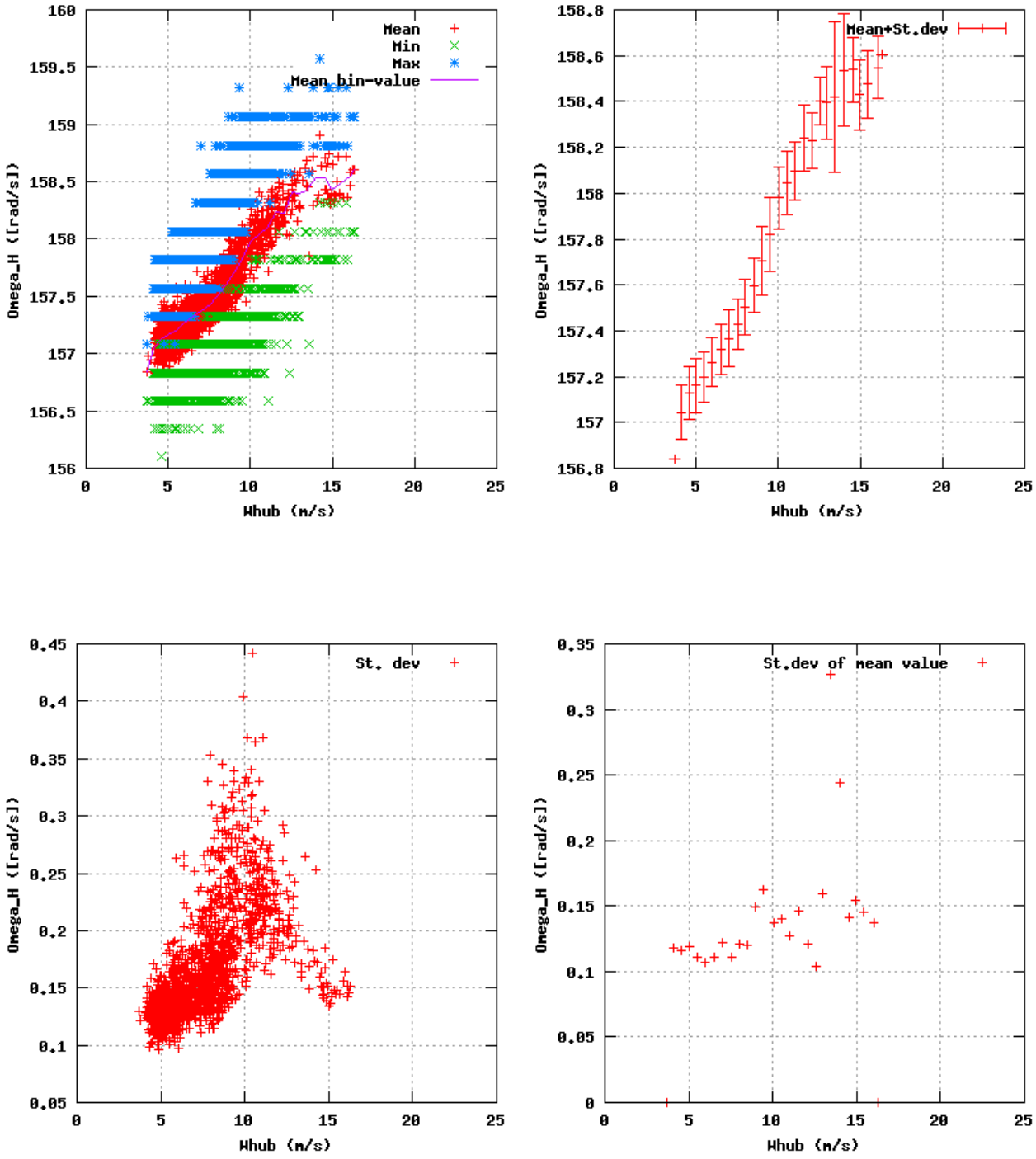

Figure 100a, Sensor 399: Rotor speed Omega_HSS versus wind speed
Input files: ntk500res.dat, stat_399.dat

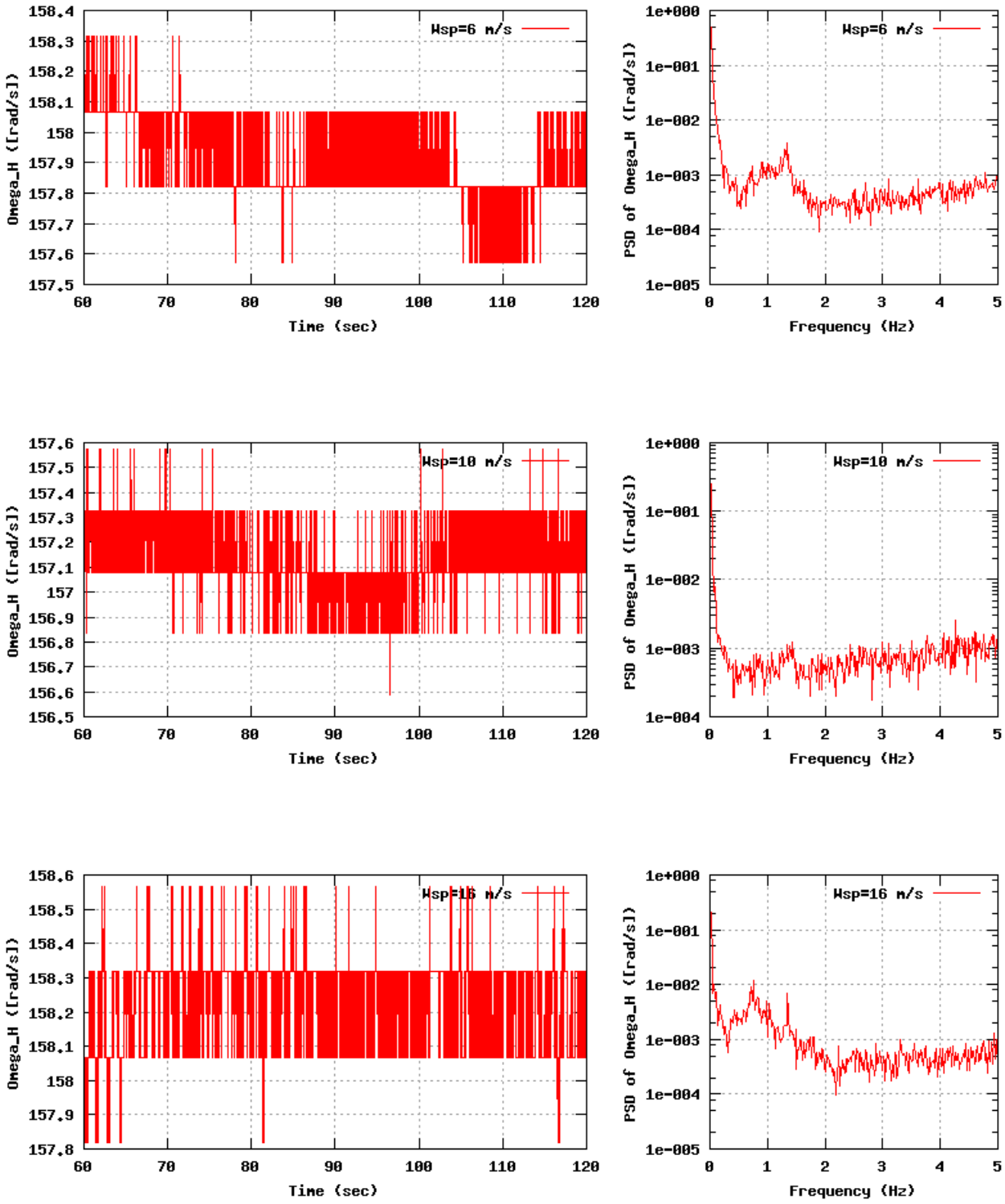

Figure 100b, Sensor 399: Rotor speed Omega_HSS versus time and frequency
Input files: m06.asc, m10.asc, m16.asc, m06.psd, m10.psd and m16.psd

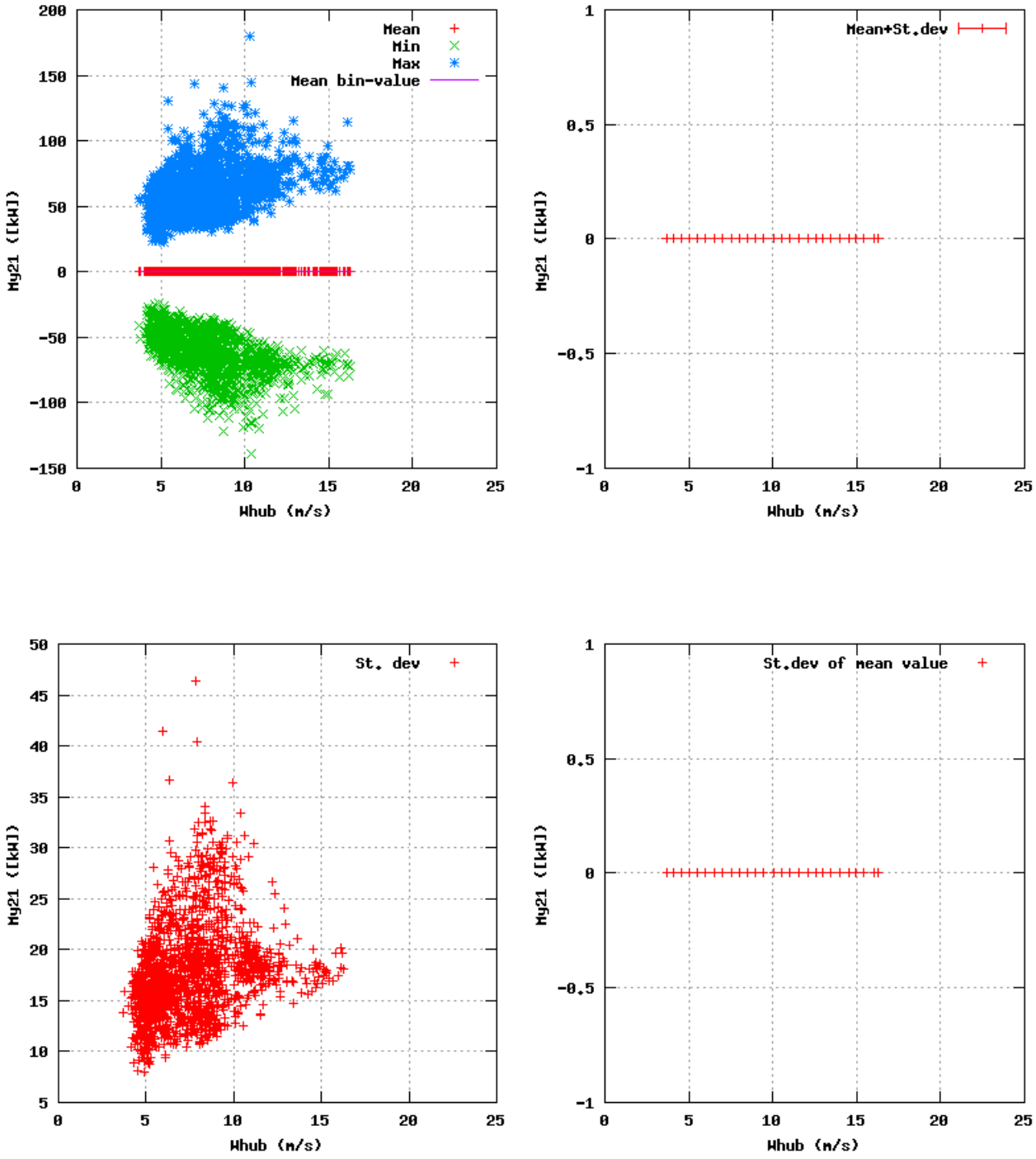

Figure 101a, Sensor 403: Flap bending moment B2 r=2.1m versus wind speed
Input files: ntk500res.dat, stat_403.dat

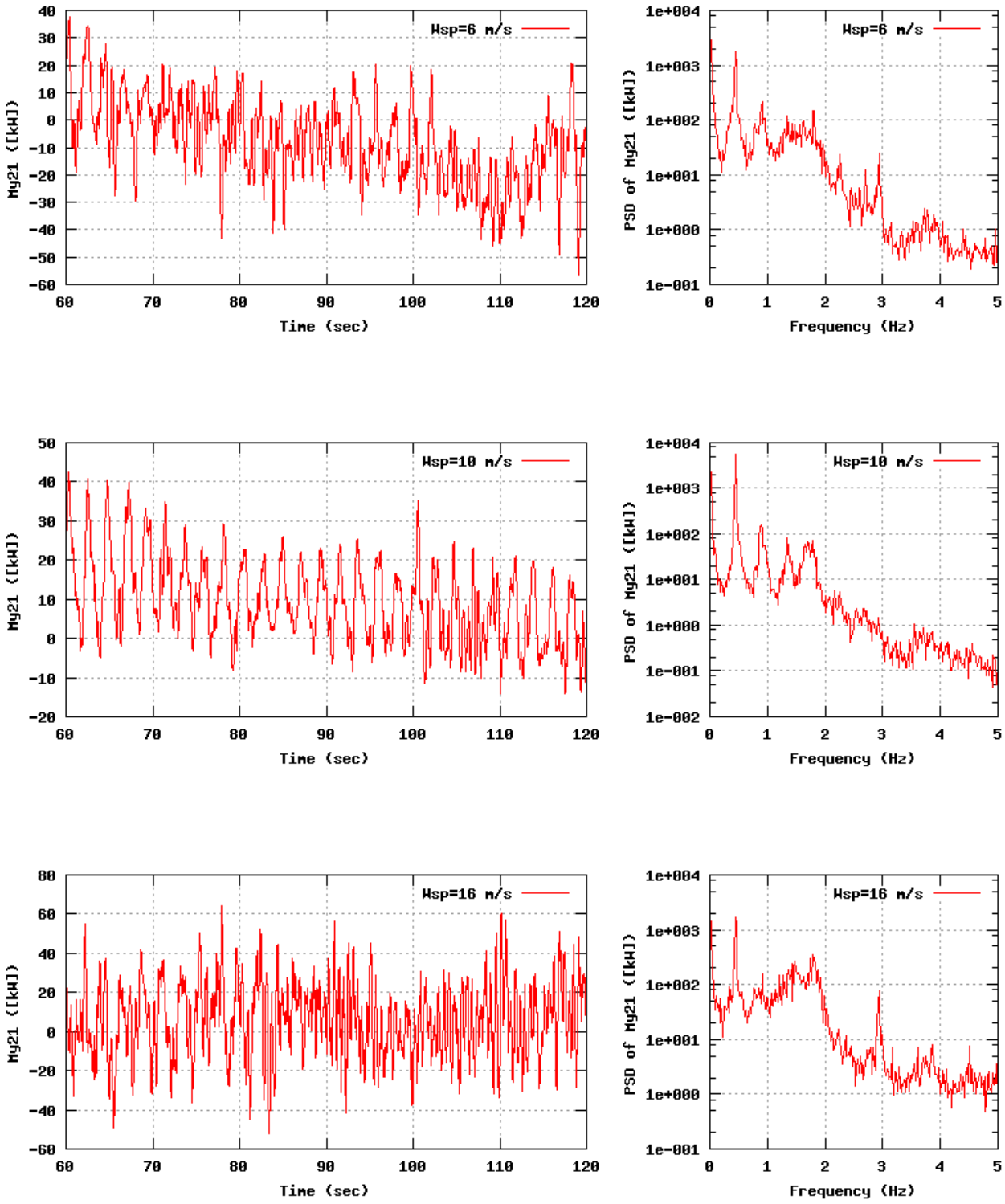

Figure 101b, Sensor 403: Flap bending moment B2 r=2.1m versus time and frequency
Input files: m06.asc, m10.asc, m16.asc, m06.psd, m10.psd and m16.psd

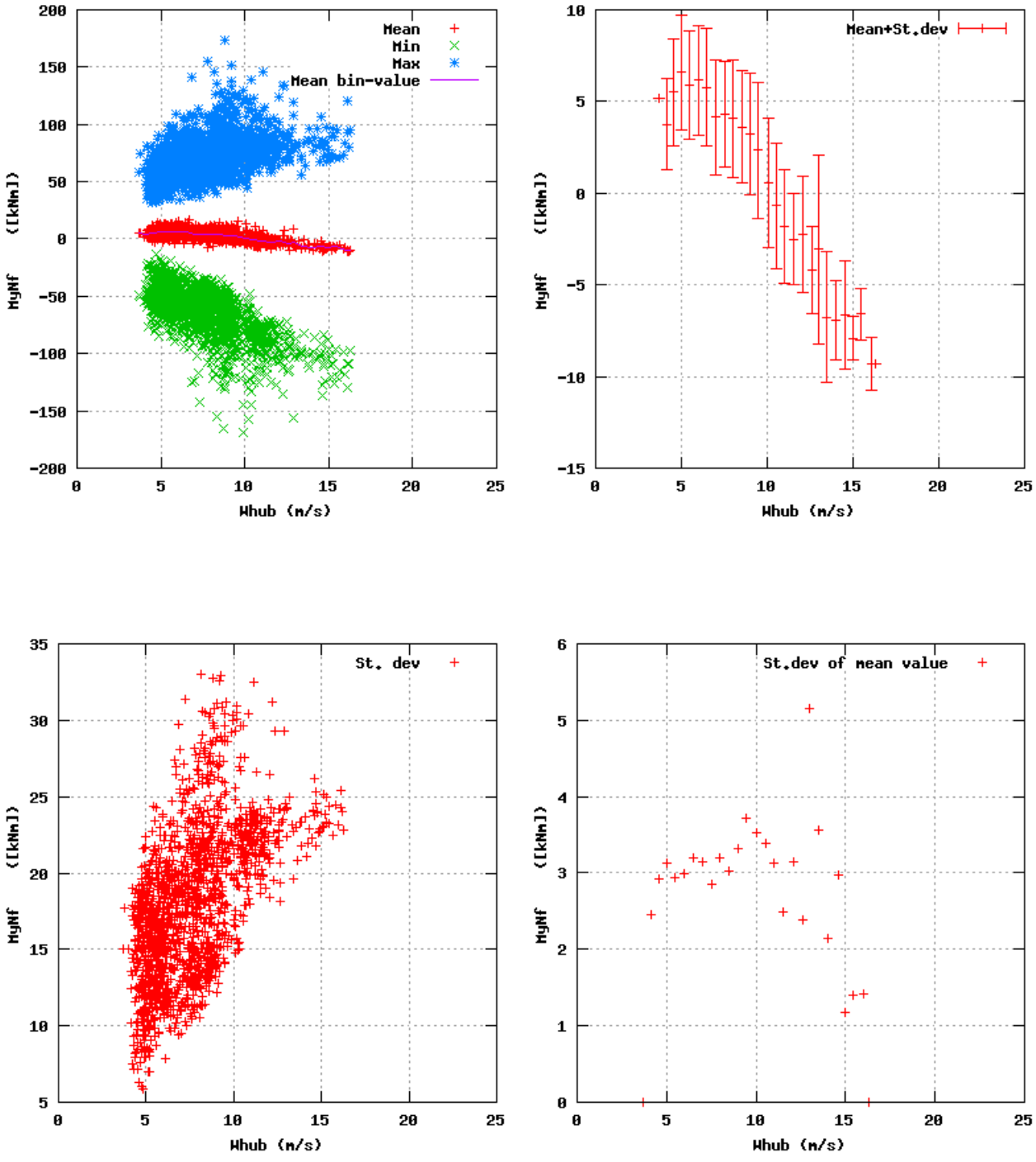

Figure 102a, Sensor 407: Rotor Tilt Moment versus wind speed
Input files: ntk500res.dat, stat_407.dat

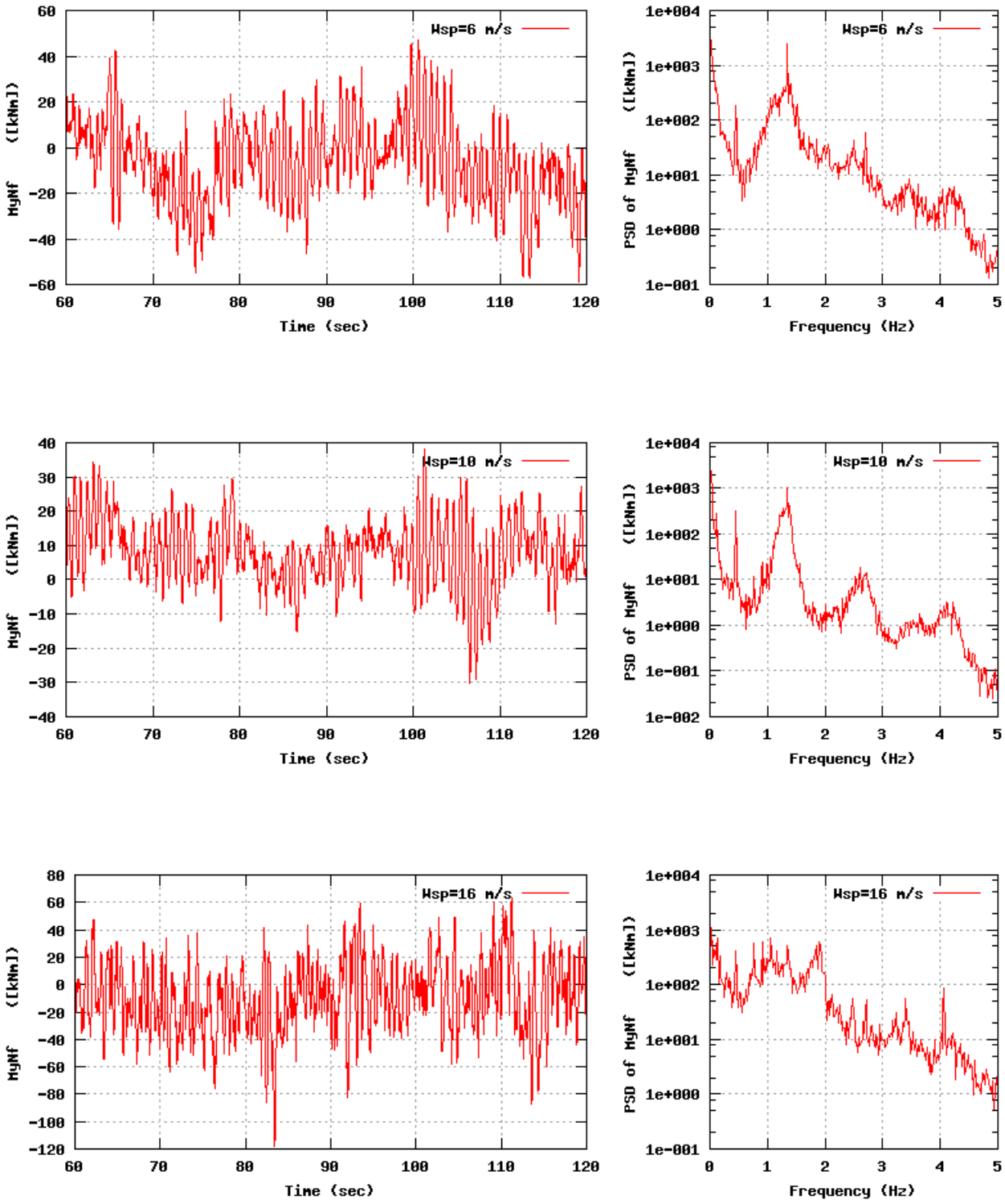

Figure 102b, Sensor 407: Rotor Tilt Moment versus time and frequency
Input files: m06.asc, m10.asc, m16.asc, m06.psd, m10.psd and m16.psd

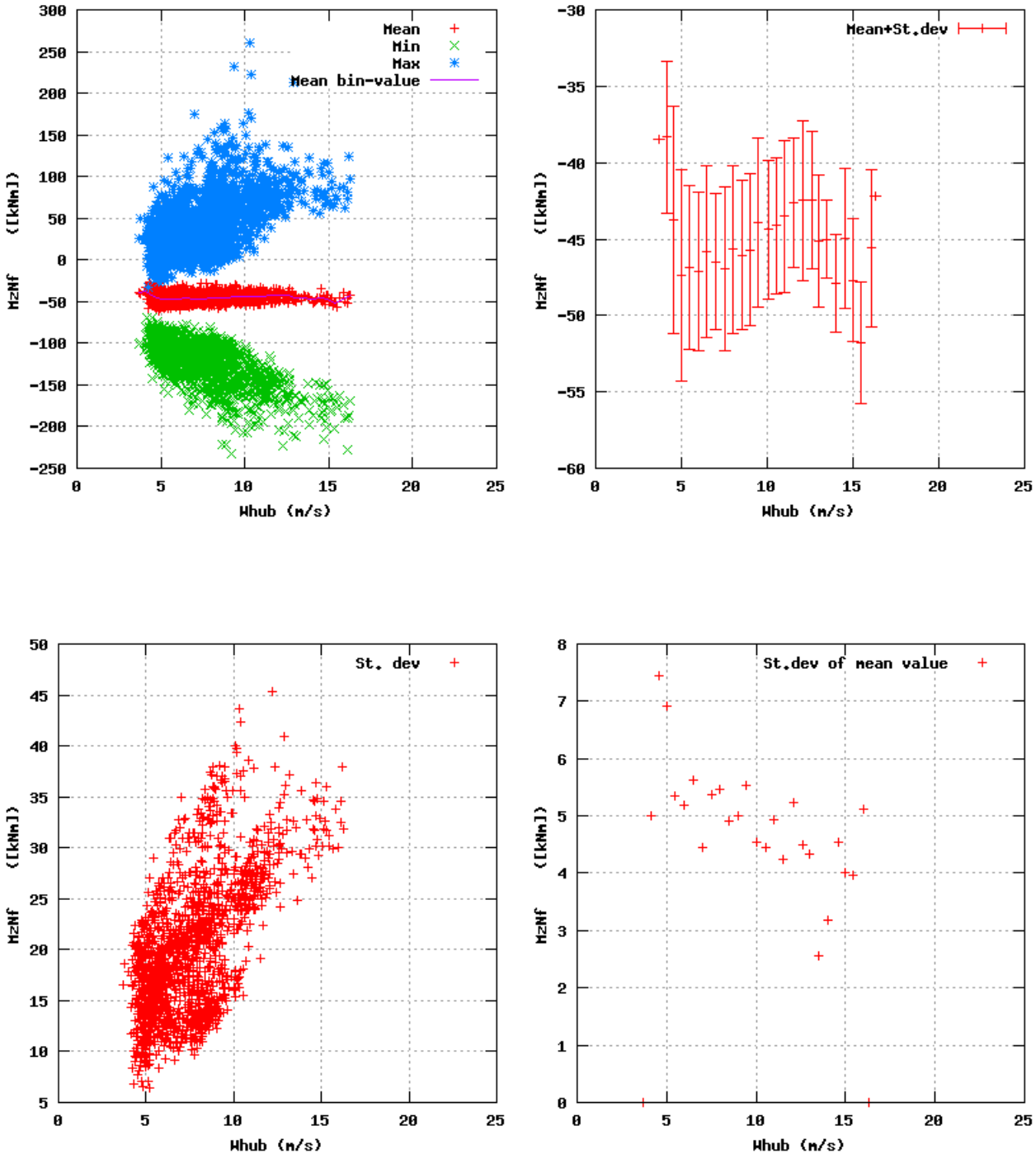

Figure 103a, Sensor 411: Rotor Yaw Moment versus wind speed
Input files: ntk500res.dat, stat_411.dat

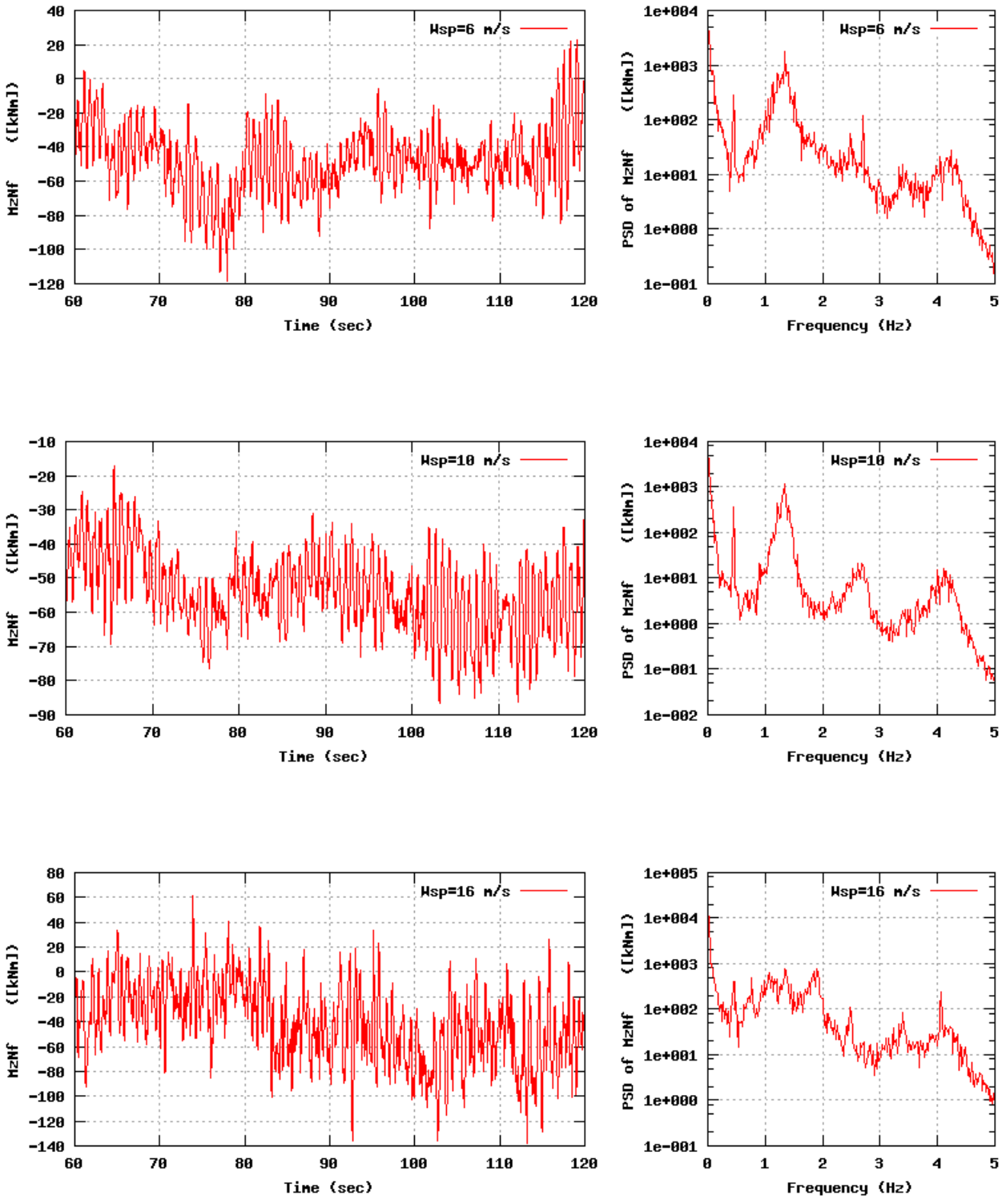

Figure 103b, Sensor 411: Rotor Yaw Moment versus time and frequency
Input files: m06.asc, m10.asc, m16.asc, m06.psd, m10.psd and m16.psd

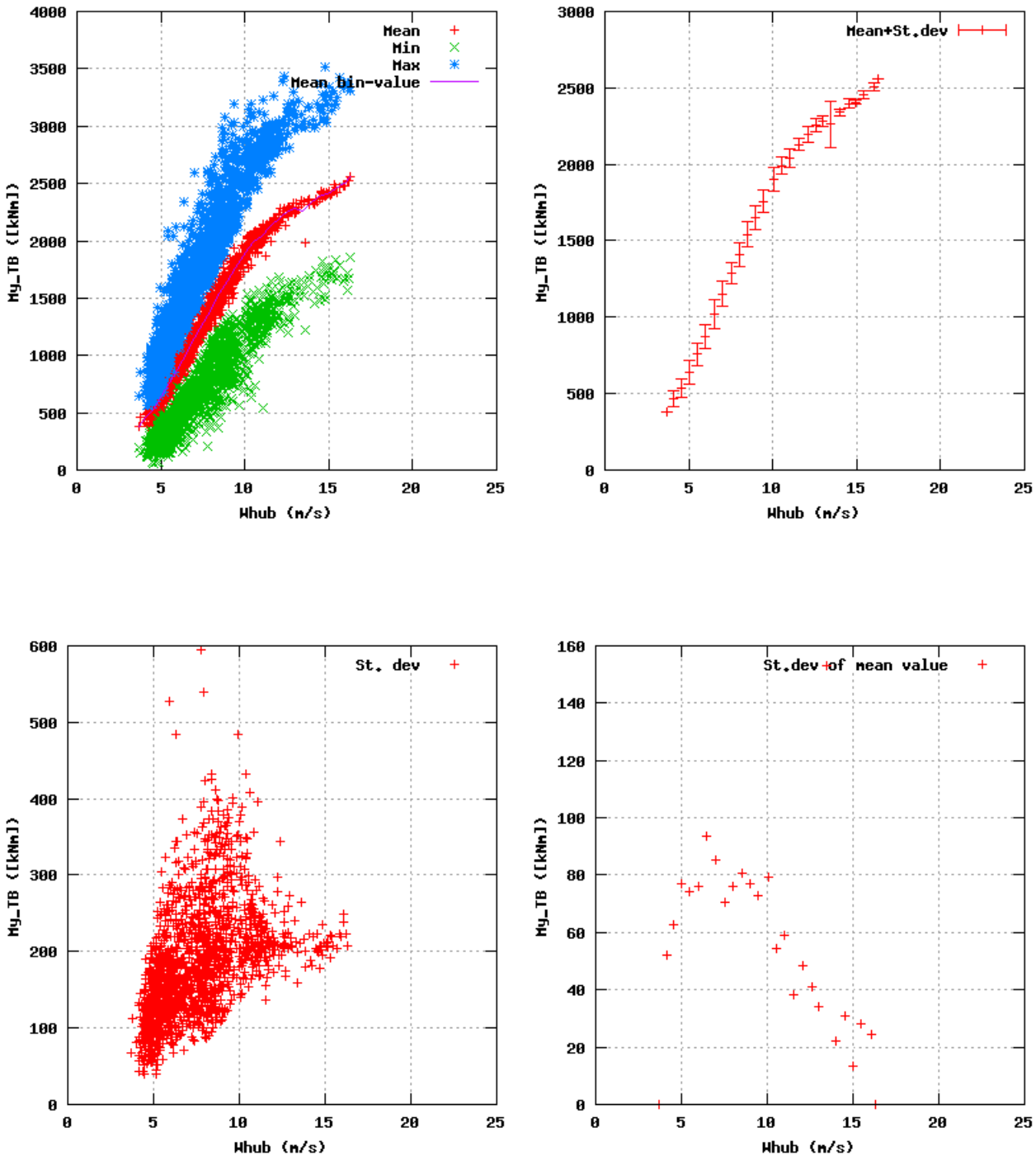

Figure 104a, Sensor 415: Tower Tilt bending moment versus wind speed
Input files: ntk500res.dat, stat_415.dat

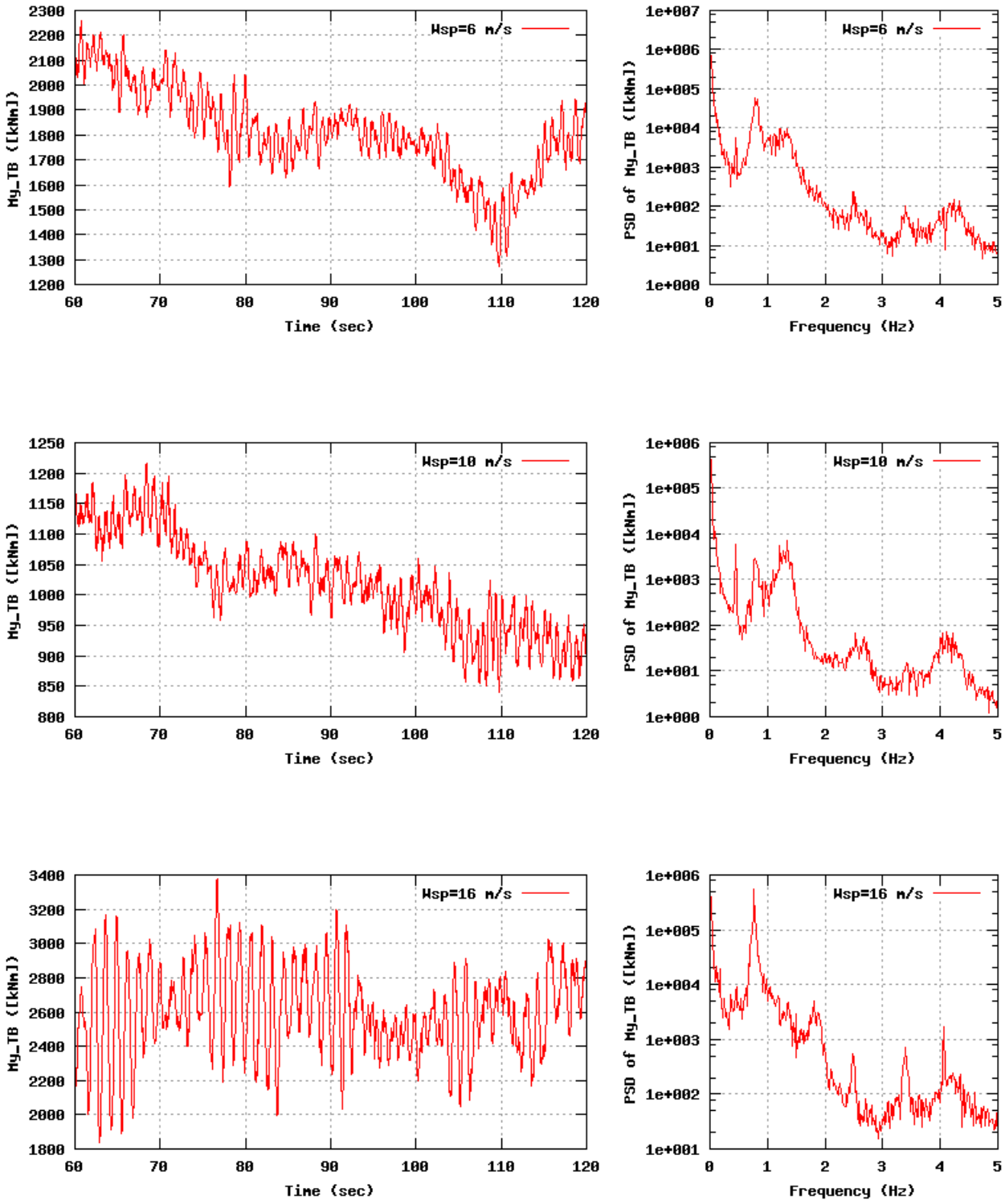

Figure 104b, Sensor 415: Tower Tilt bending moment versus time and frequency
Input files: m06.asc, m10.asc, m16.asc, m06.psd, m10.psd and m16.psd

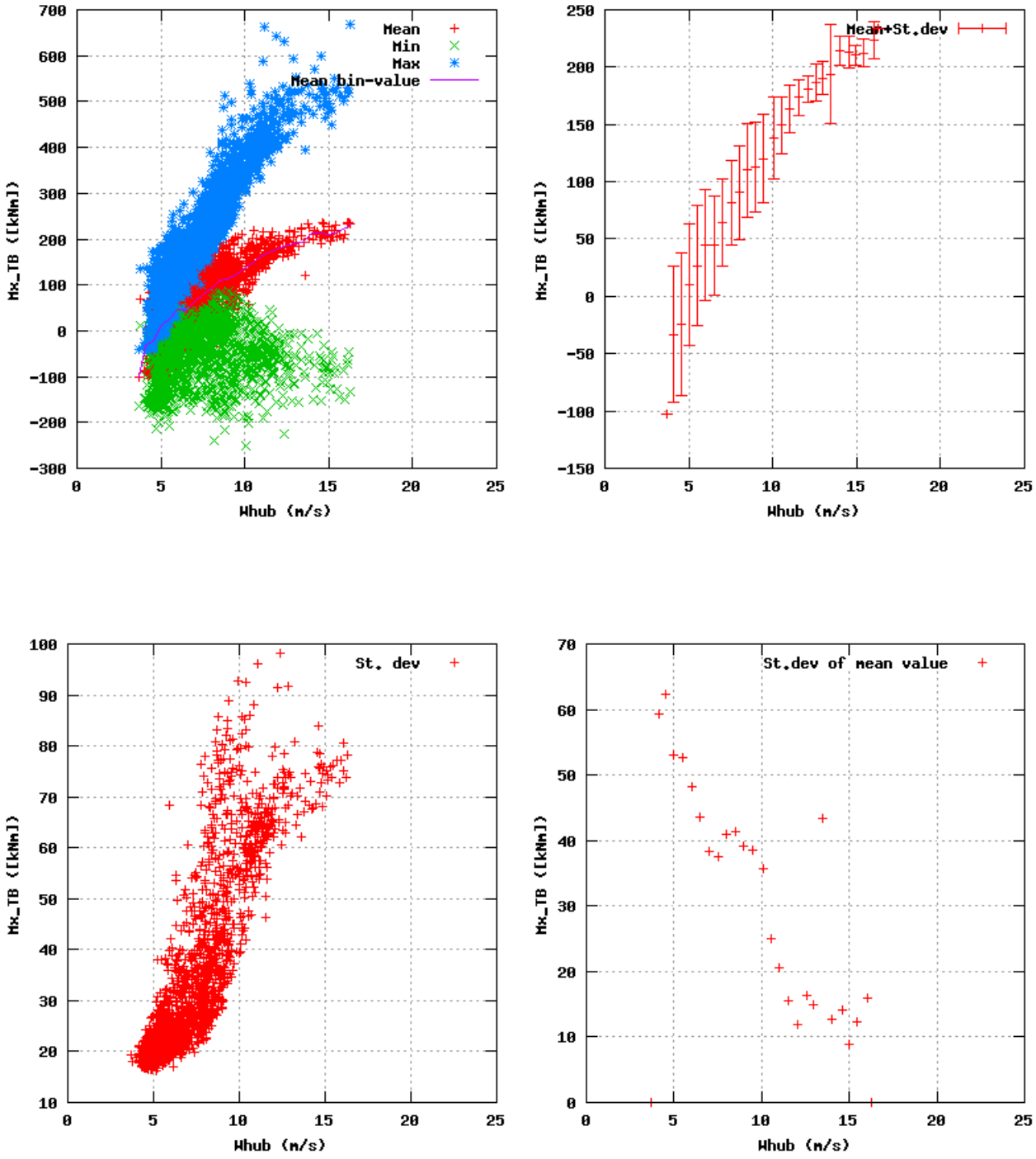

Figure 105a, Sensor 419: Tower Roll bending moment versus wind speed
Input files: ntk500res.dat, stat_419.dat

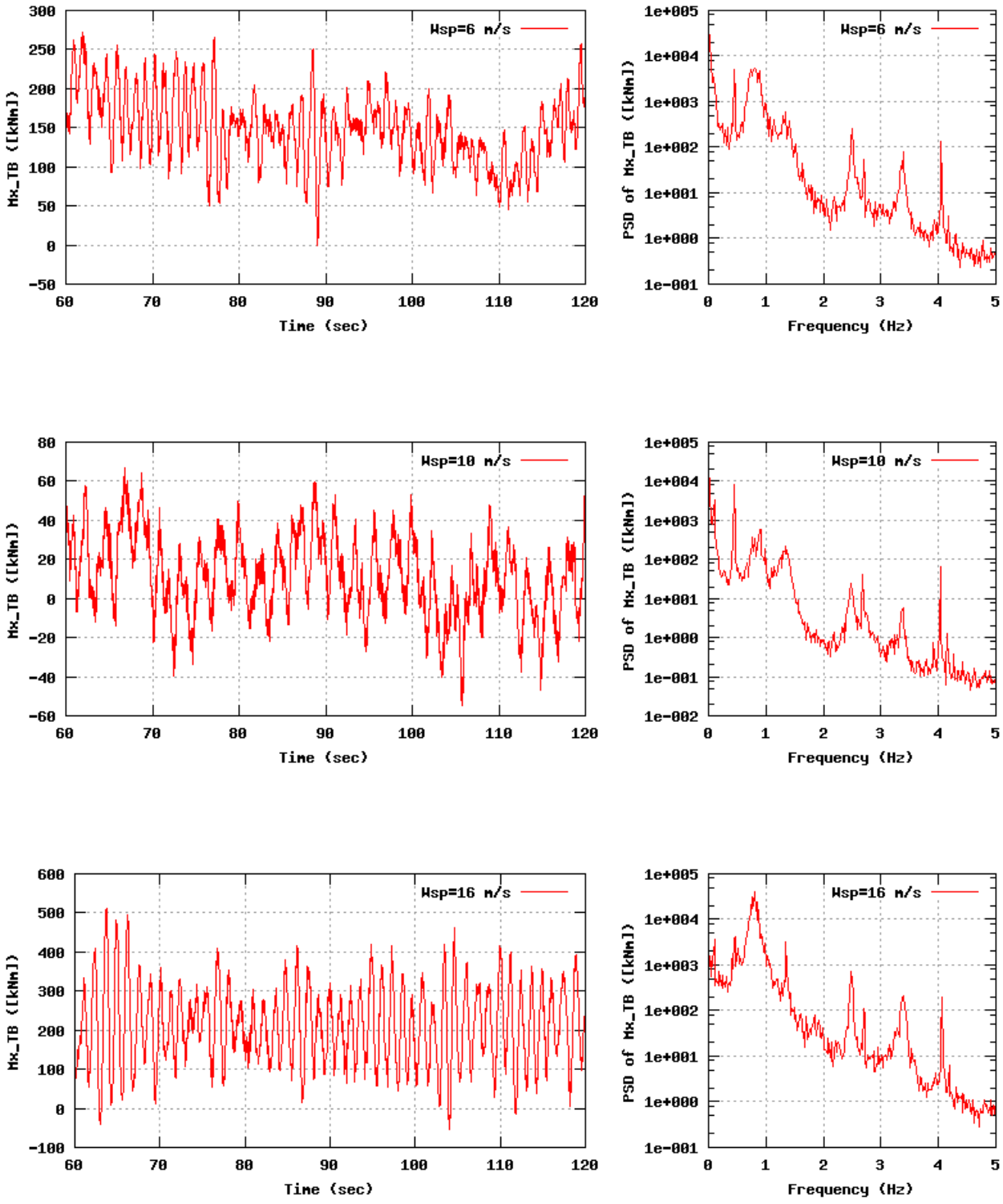

Figure 105b, Sensor 419: Tower Roll bending moment versus time and frequency
Input files: m06.asc, m10.asc, m16.asc, m06.psd, m10.psd and m16.psd

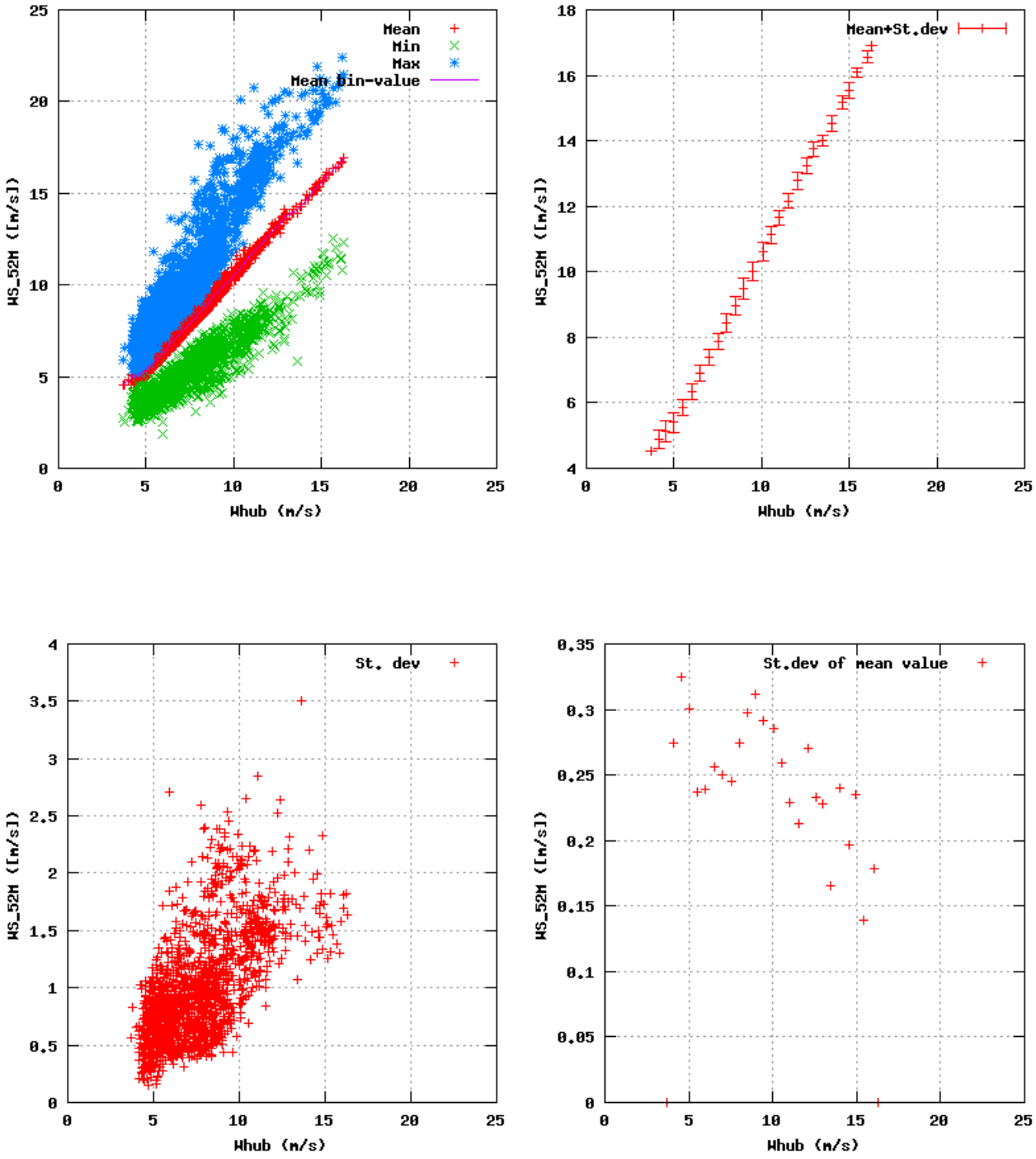

Figure 106a, Sensor 423: Wind speed Metmast @52m,(South+North)/2 versus wind speed
Input files: ntk500res.dat, stat_423.dat

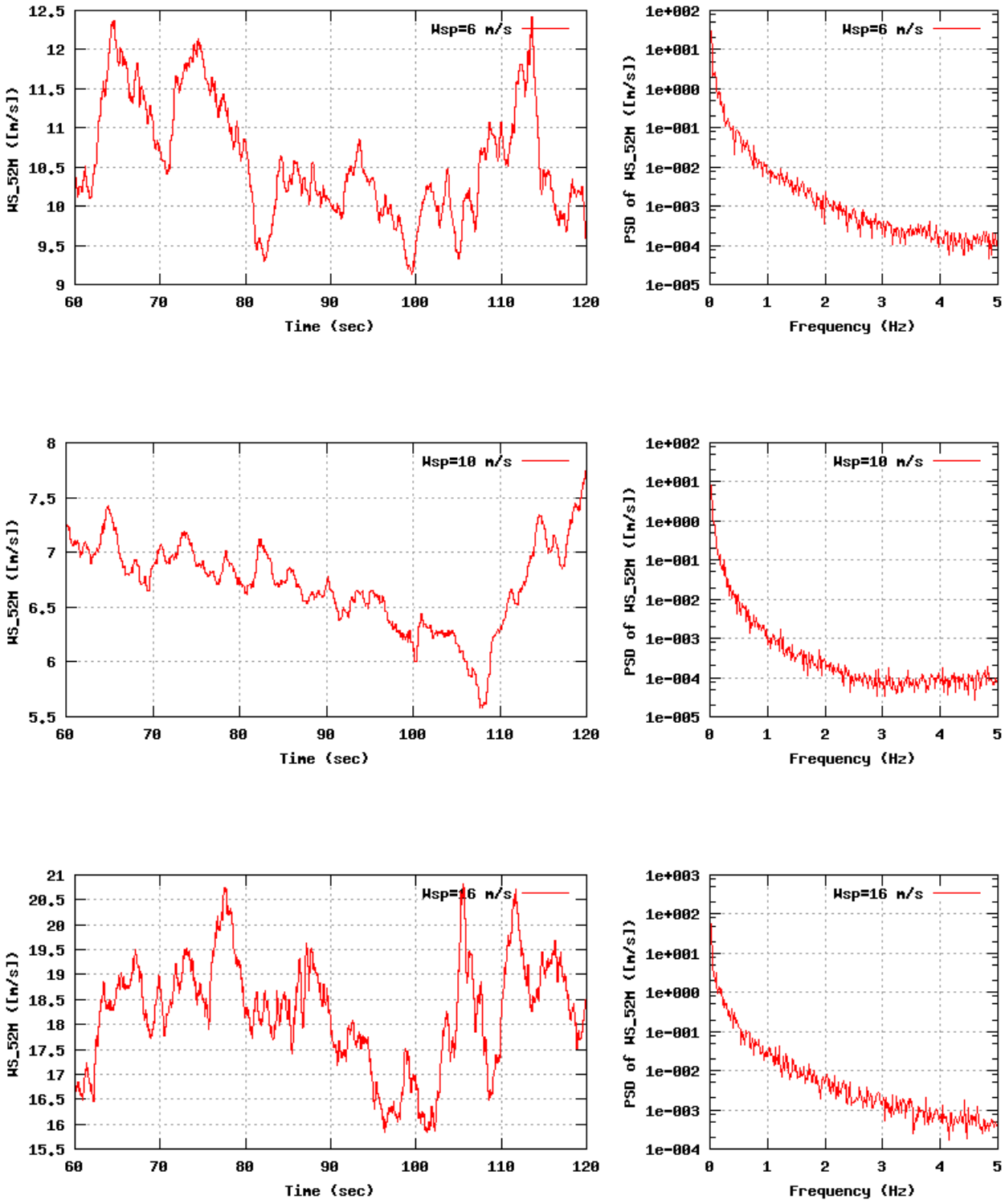

Figure 106b, Sensor 423: Wind speed Metmast @52m,(South+North)/2 versus time and frequency
Input files: m06.asc, m10.asc, m16.asc, m06.psd, m10.psd and m16.psd

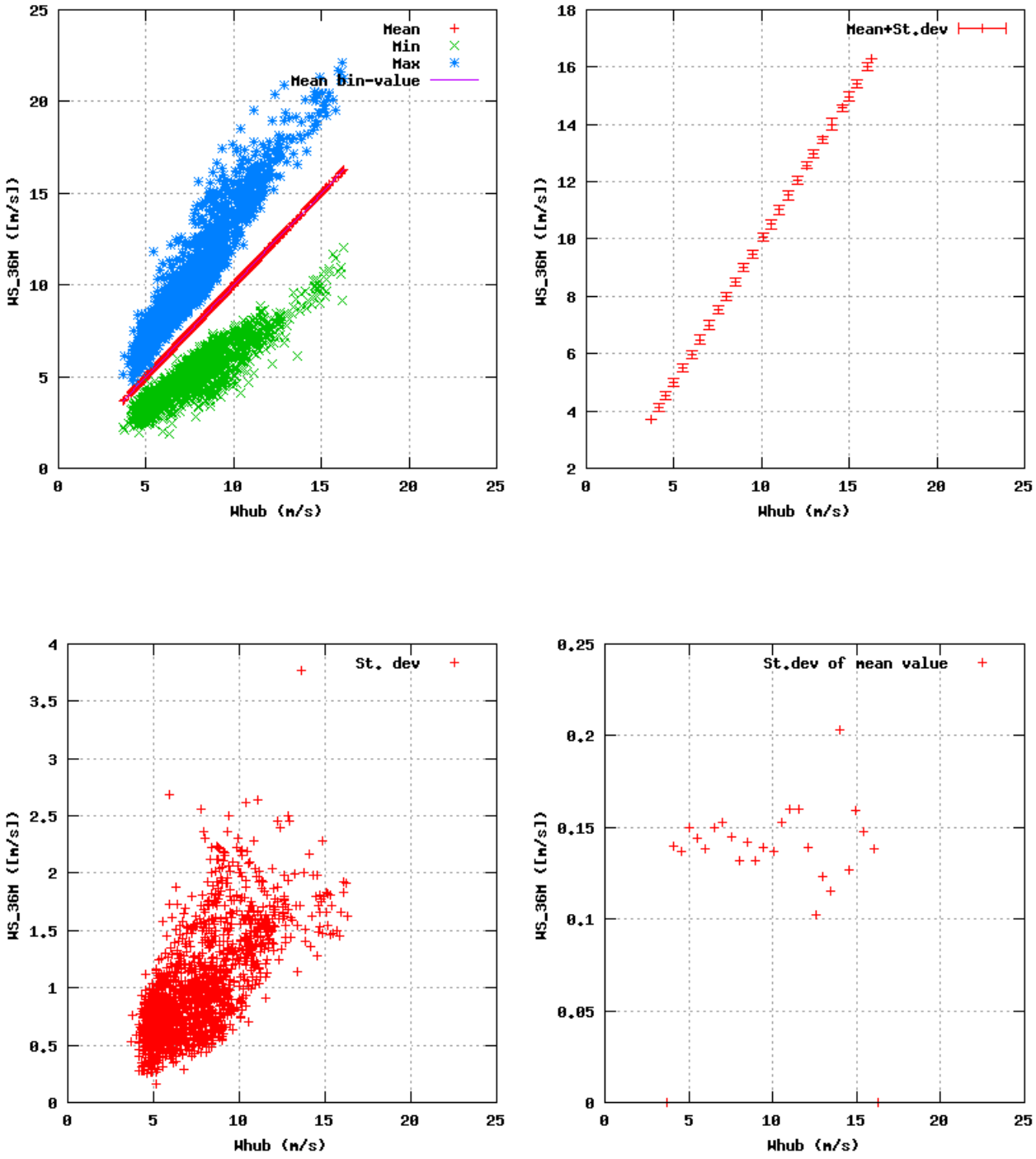

Figure 107a, Sensor 427: Wind speed Metmast @36m,(South+North)/2 versus wind speed
Input files: ntk500res.dat, stat_427.dat

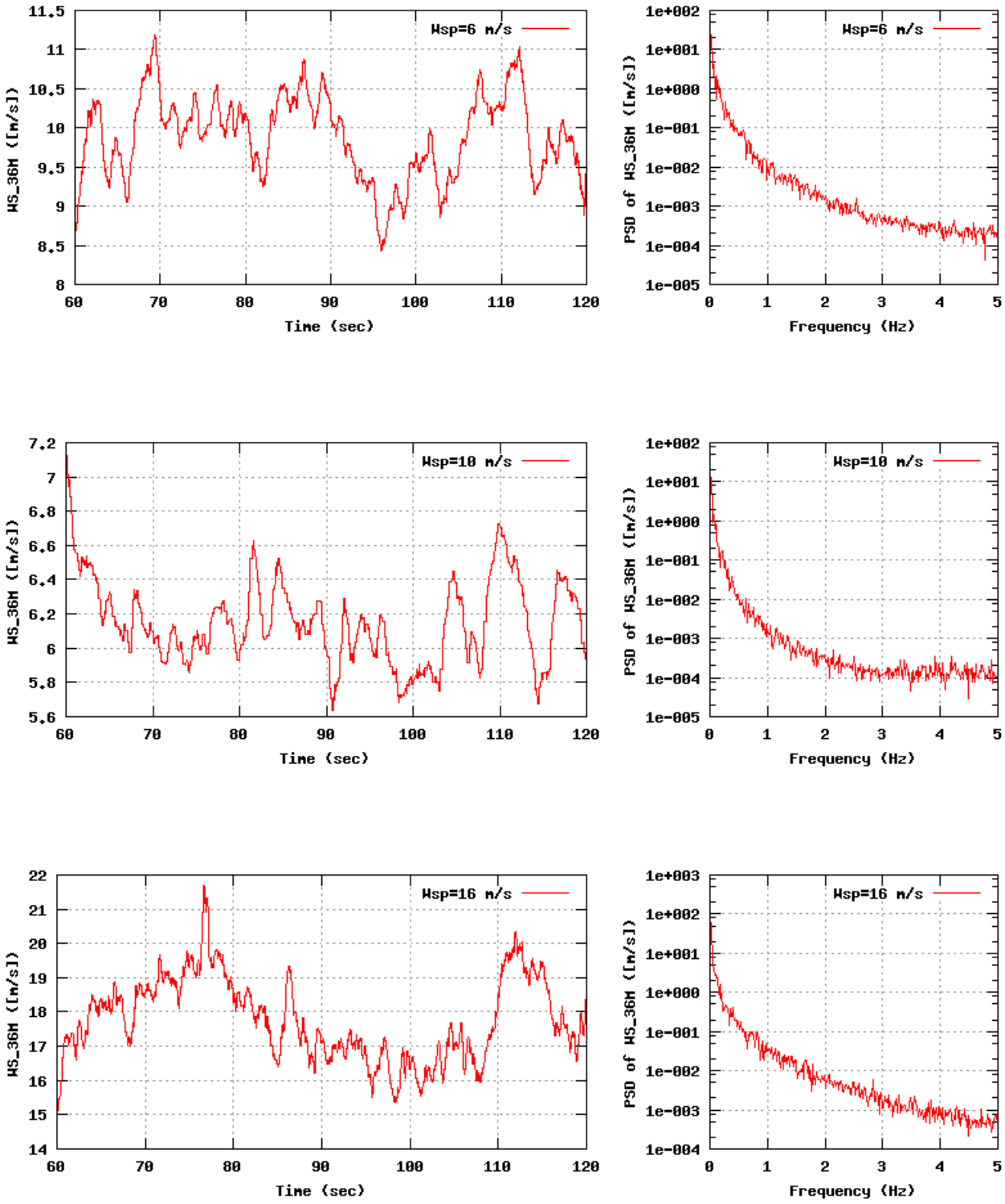

Figure 107b, Sensor 427: Wind speed Metmast @36m,(South+North)/2 versus time and frequency
Input files: m06.asc, m10.asc, m16.asc, m06.psd, m10.psd and m16.psd

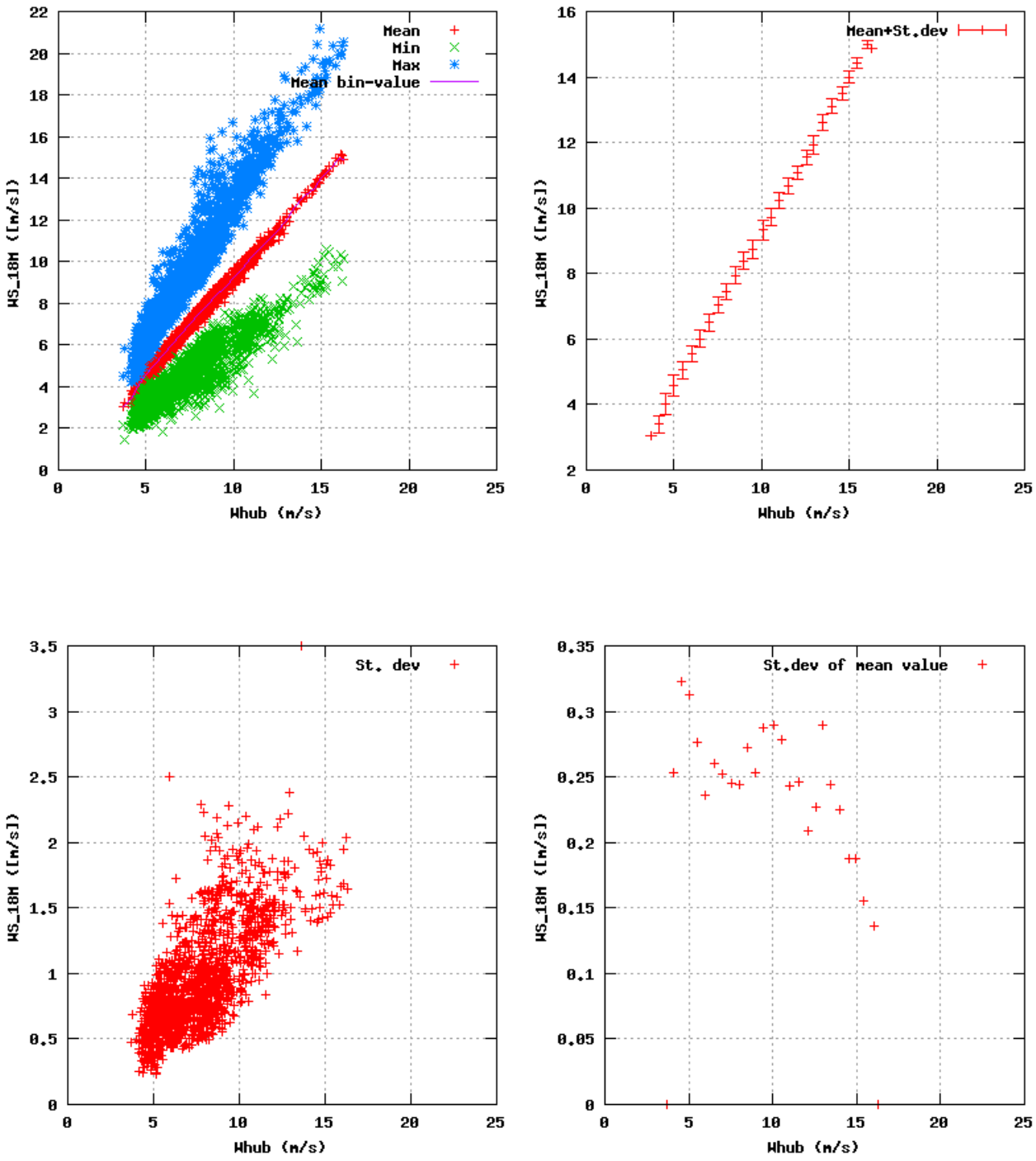

Figure 108a, Sensor 431: Wind speed Metmast @18m,(South+North)/2 versus wind speed
Input files: ntk500res.dat, stat_431.dat

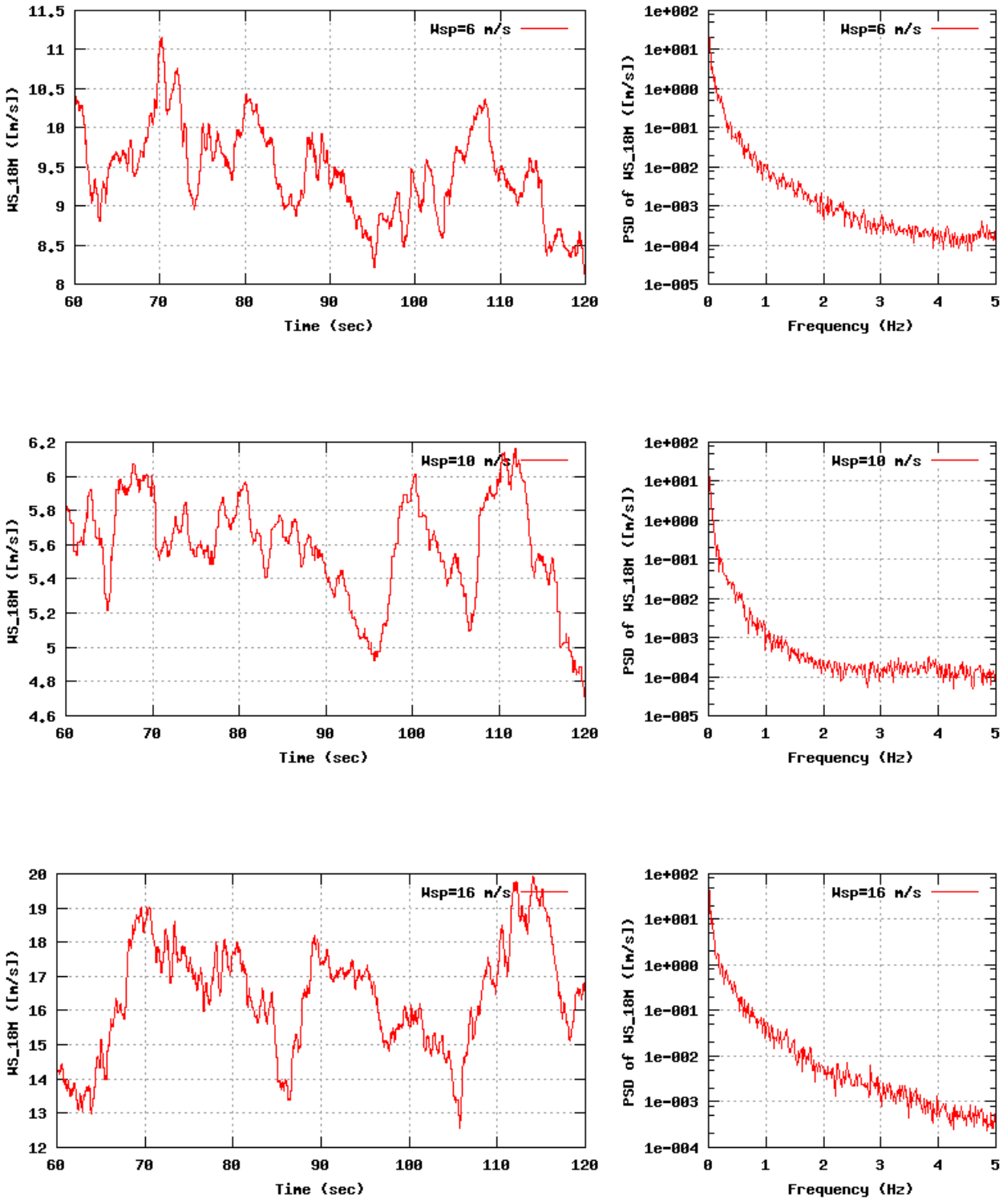

Figure 108b, Sensor 431: Wind speed Metmast @18m,(South+North)/2 versus time and frequency
Input files: m06.asc, m10.asc, m16.asc, m06.psd, m10.psd and m16.psd

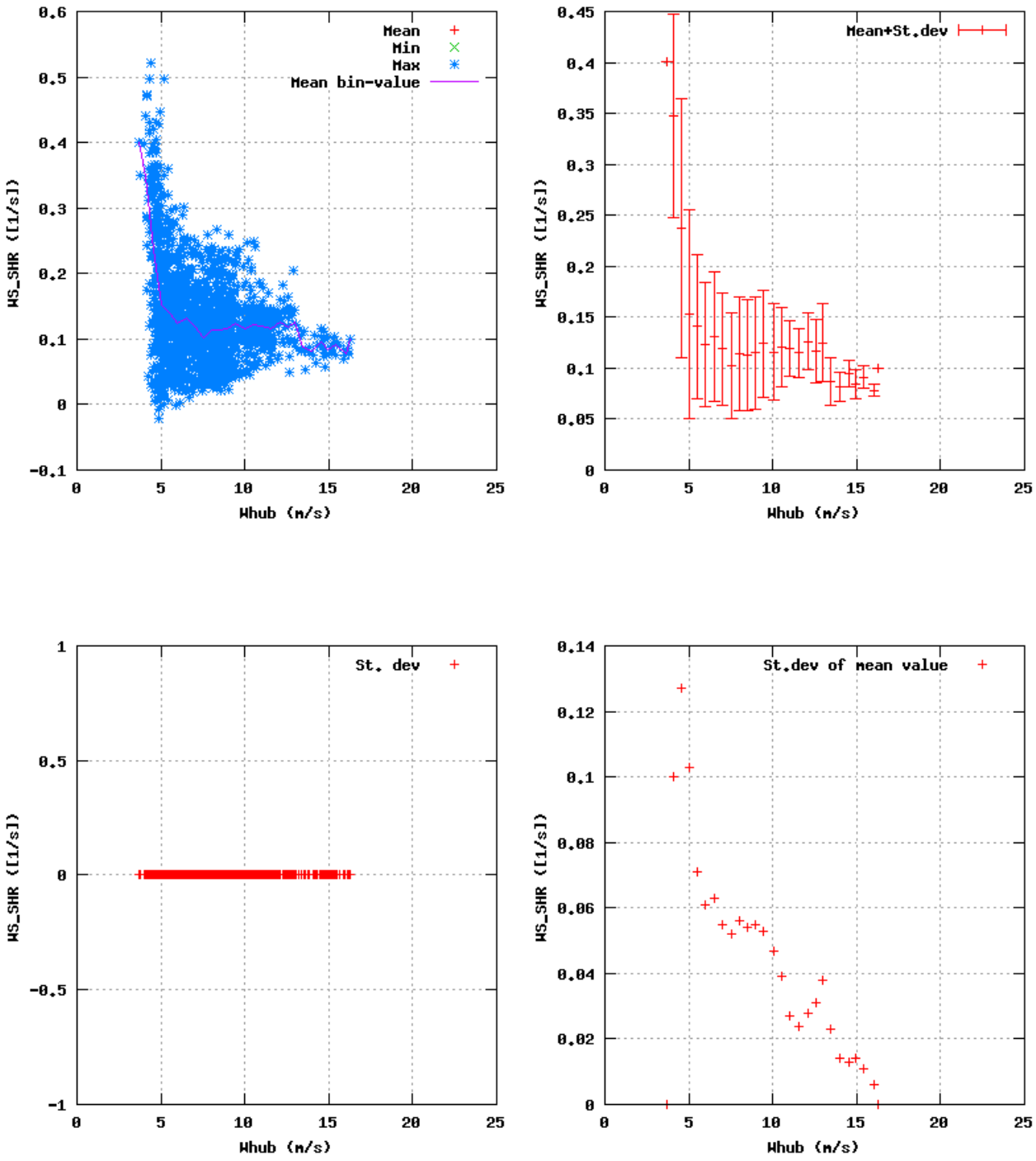

Figure 109a, Sensor 435: Wind Shear exponent coefficient versus wind speed
Input files: ntk500res.dat, stat_435.dat

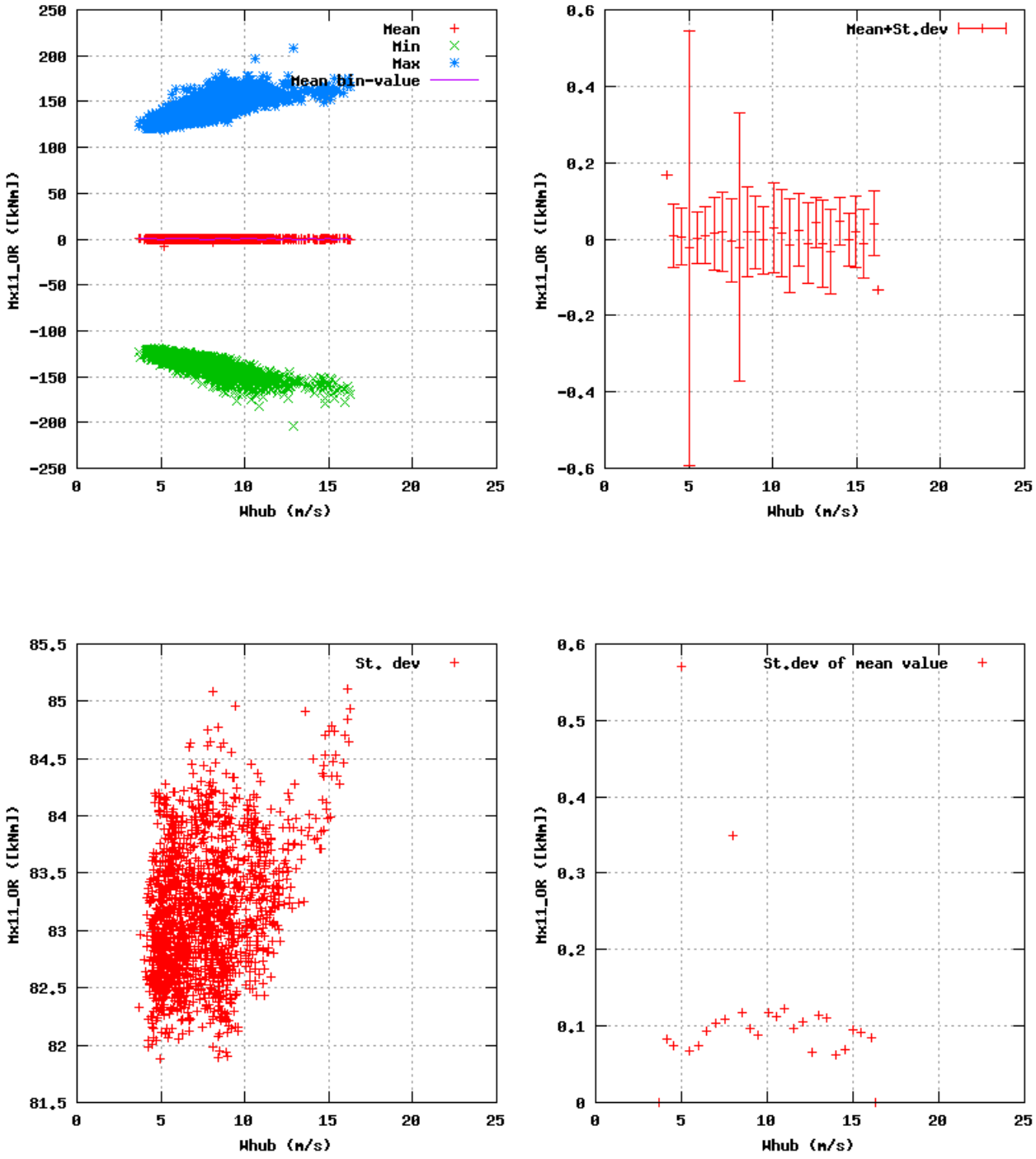

Figure 110a, Sensor 439: Edge bending moment B1 r=2.1m_OR versus wind speed
Input files: ntk500res.dat, stat_439.dat

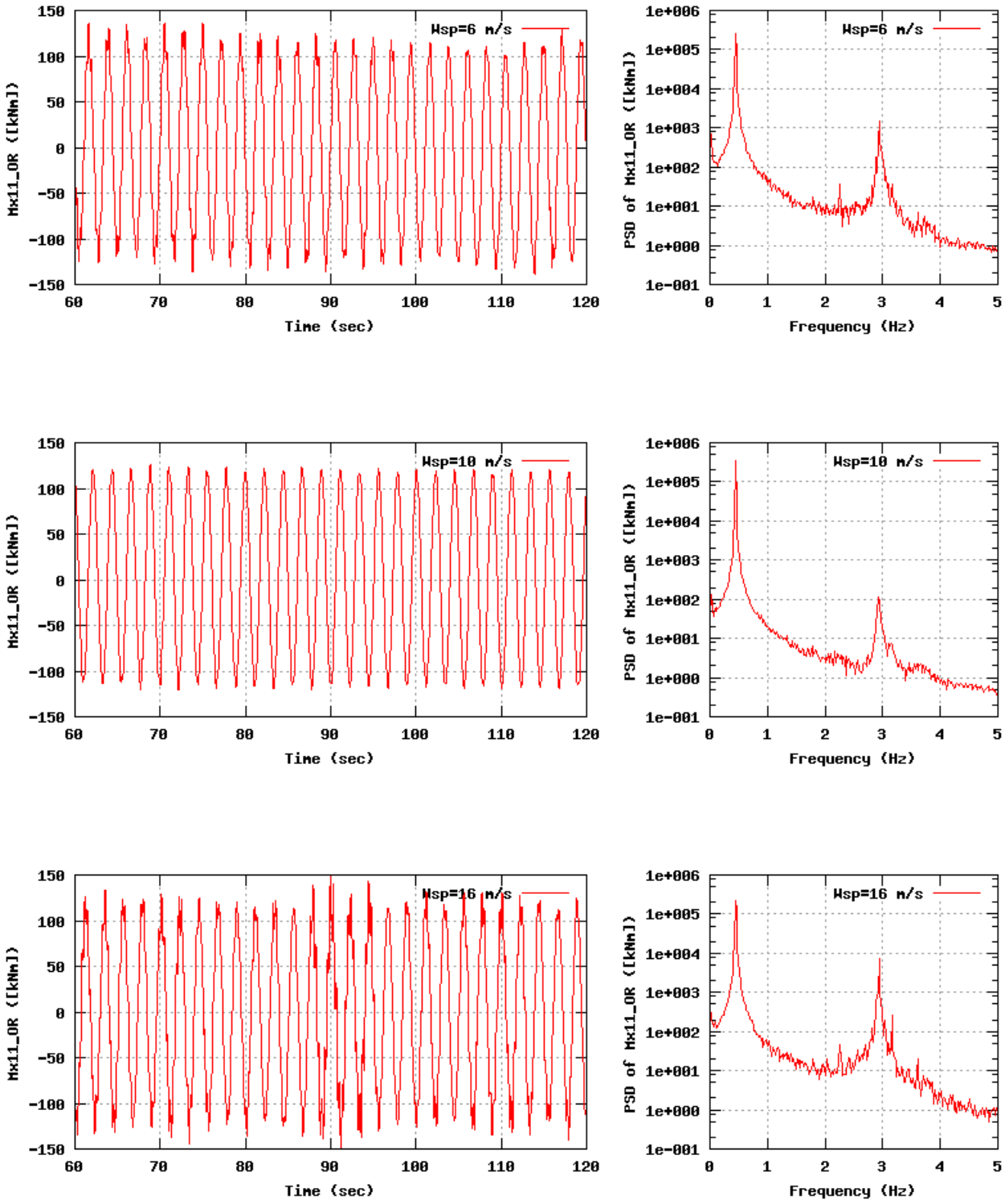

Figure 110b, Sensor 439: Edge bending moment B1 r=2.1m_OR versus time and frequency
Input files: m06.asc, m10.asc, m16.asc, m06.psd, m10.psd and m16.psd

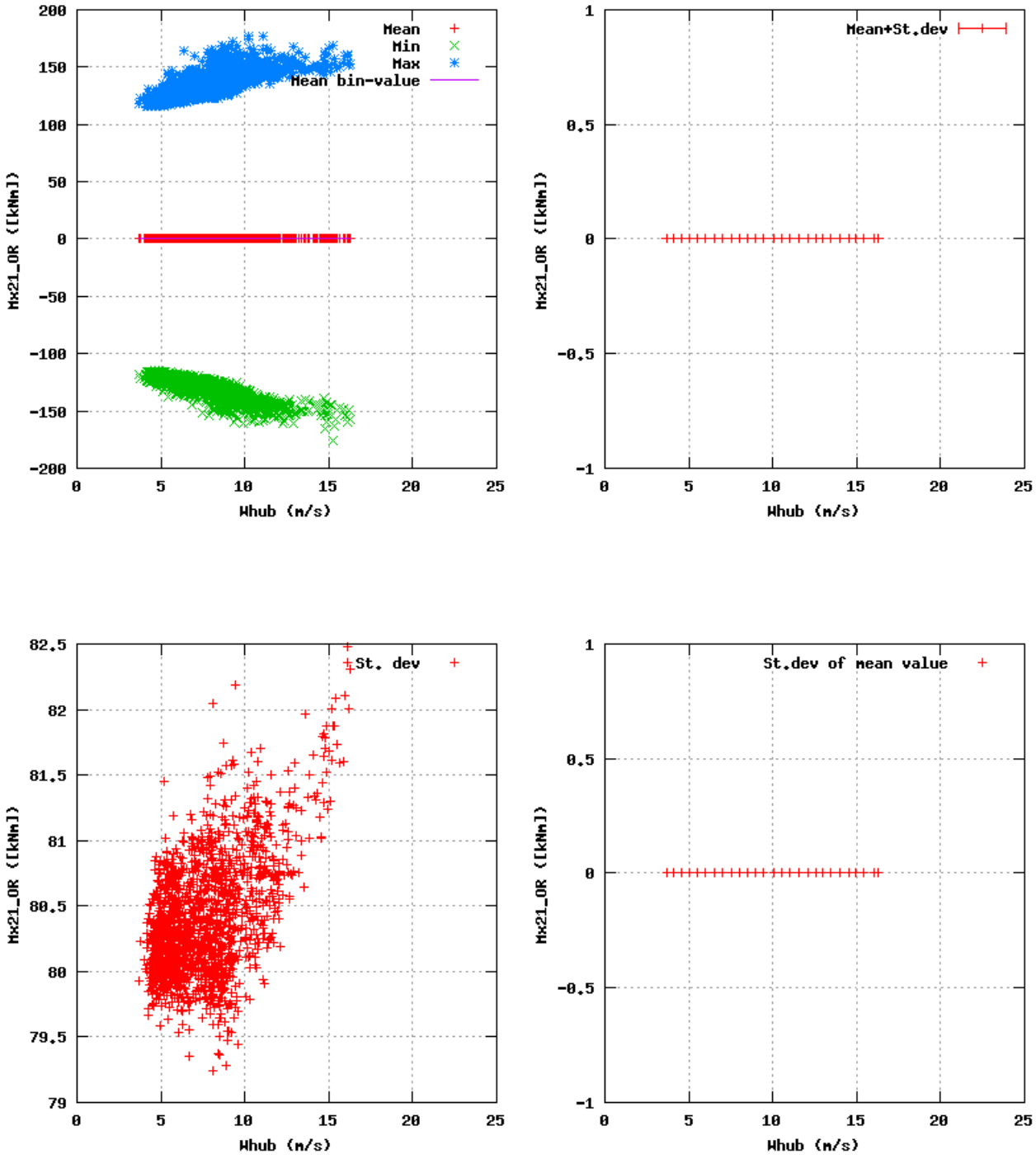

Figure 111a, Sensor 443: Edge bending moment B2 r=2.1m_OR versus wind speed
Input files: ntk500res.dat, stat_443.dat

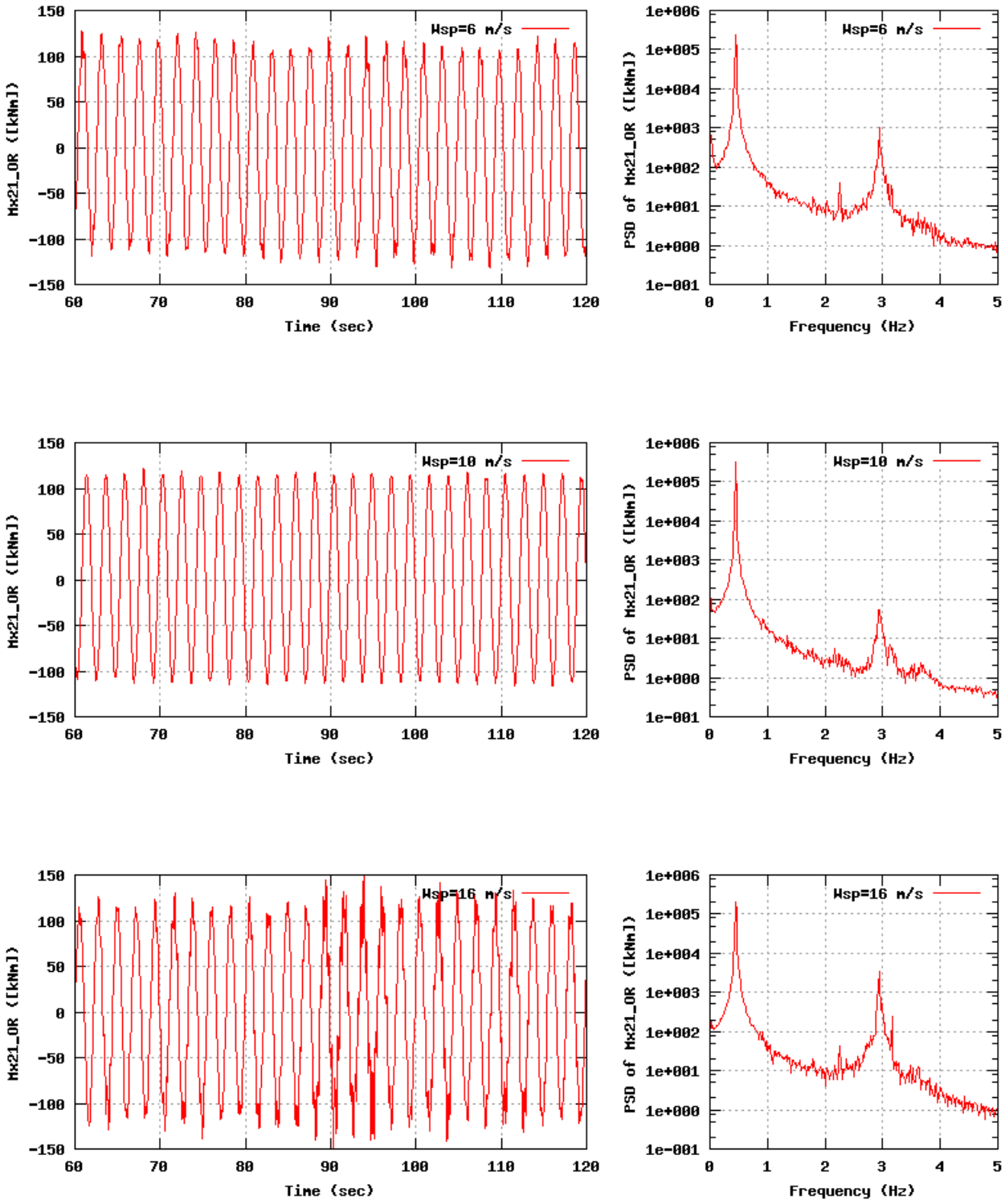

Figure 111b, Sensor 443: Edge bending moment B2 r=2.1m_OR versus time and frequency
Input files: m06.asc, m10.asc, m16.asc, m06.psd, m10.psd and m16.psd

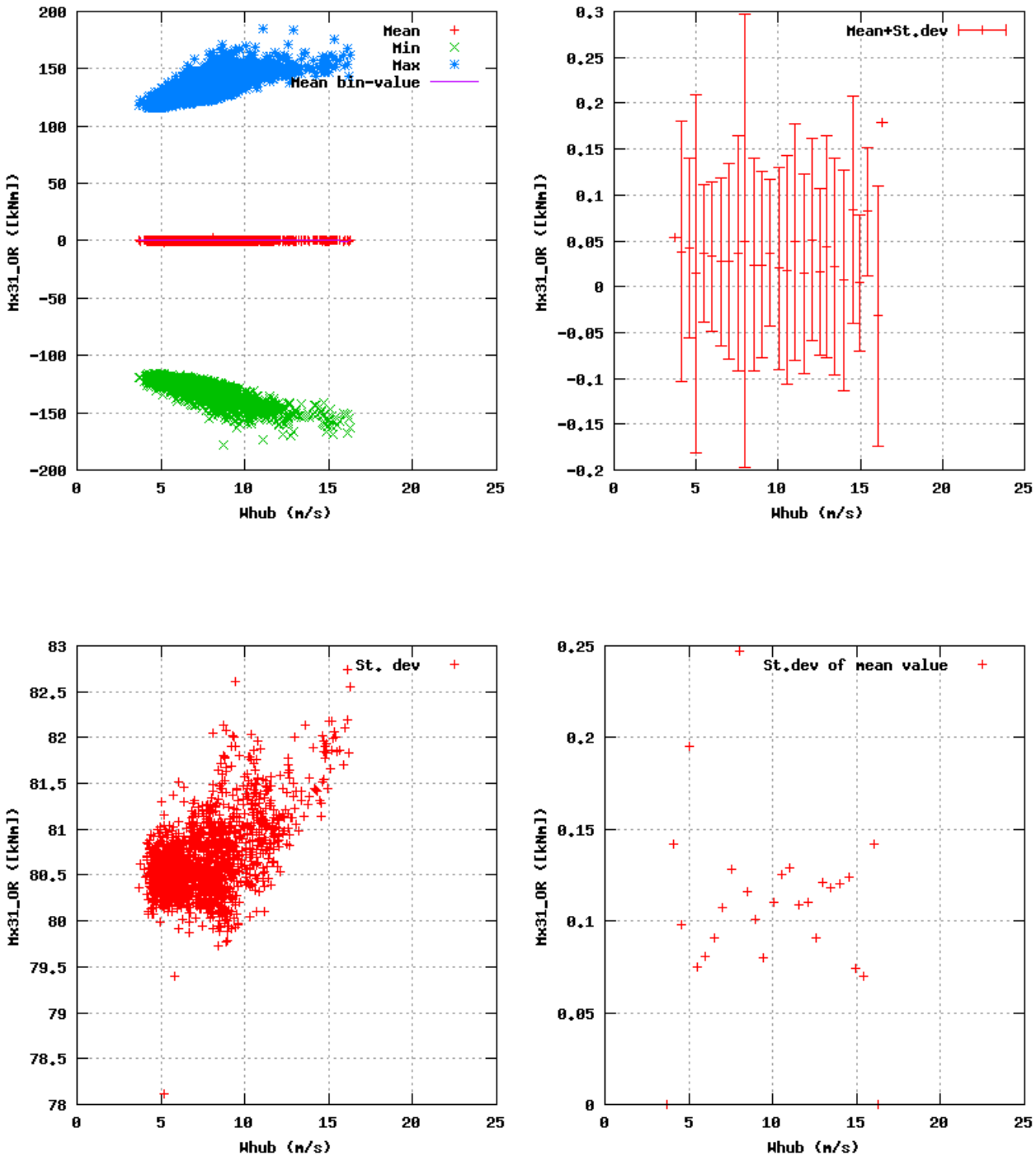

Figure 112a, Sensor 447: Edge bending moment B3 r=2.1m_OR versus wind speed
Input files: ntk500res.dat, stat_447.dat

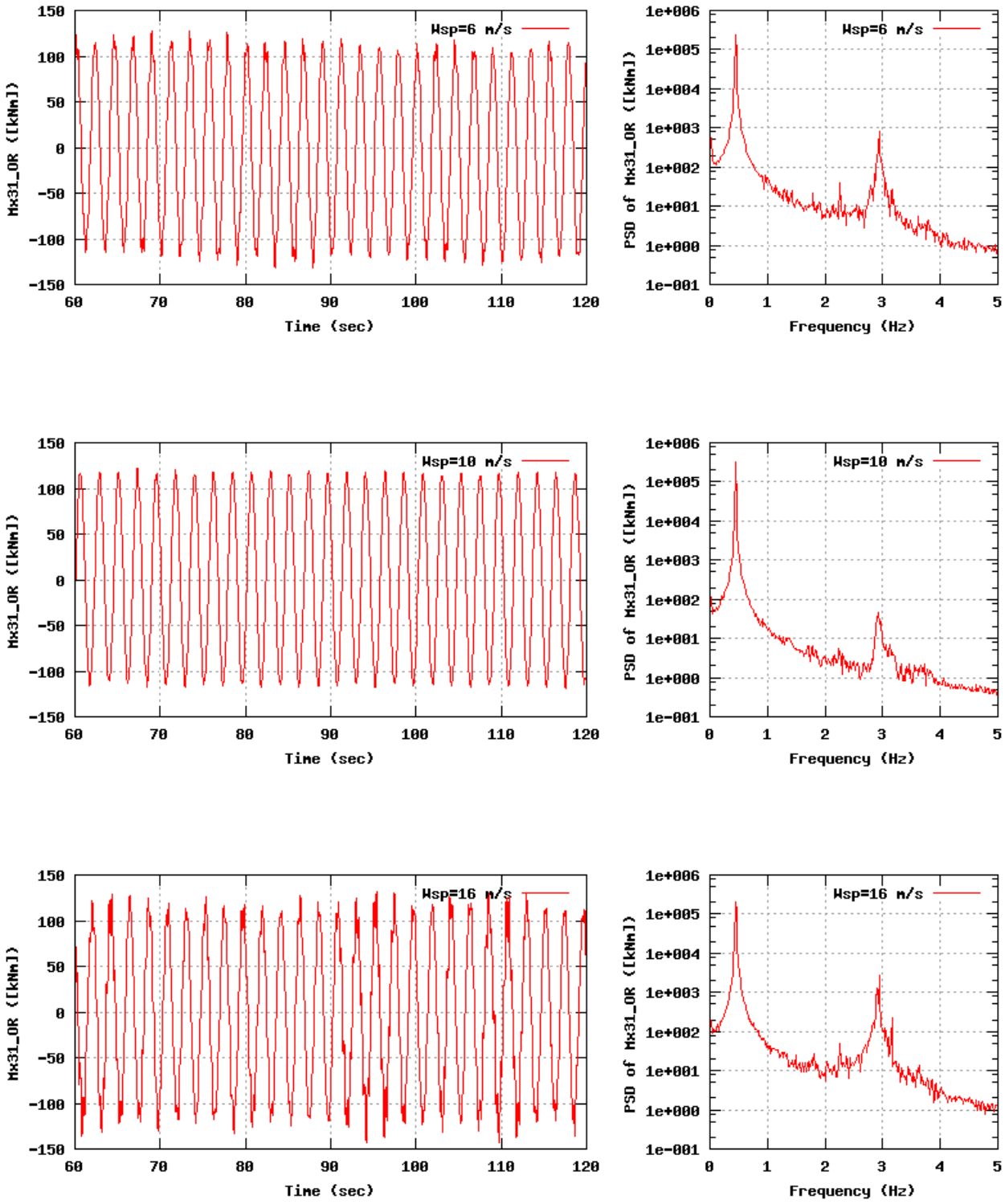

Figure 112b, Sensor 447: Edge bending moment B3 r=2.1m_OR versus time and frequency
Input files: m06.asc, m10.asc, m16.asc, m06.psd, m10.psd and m16.psd

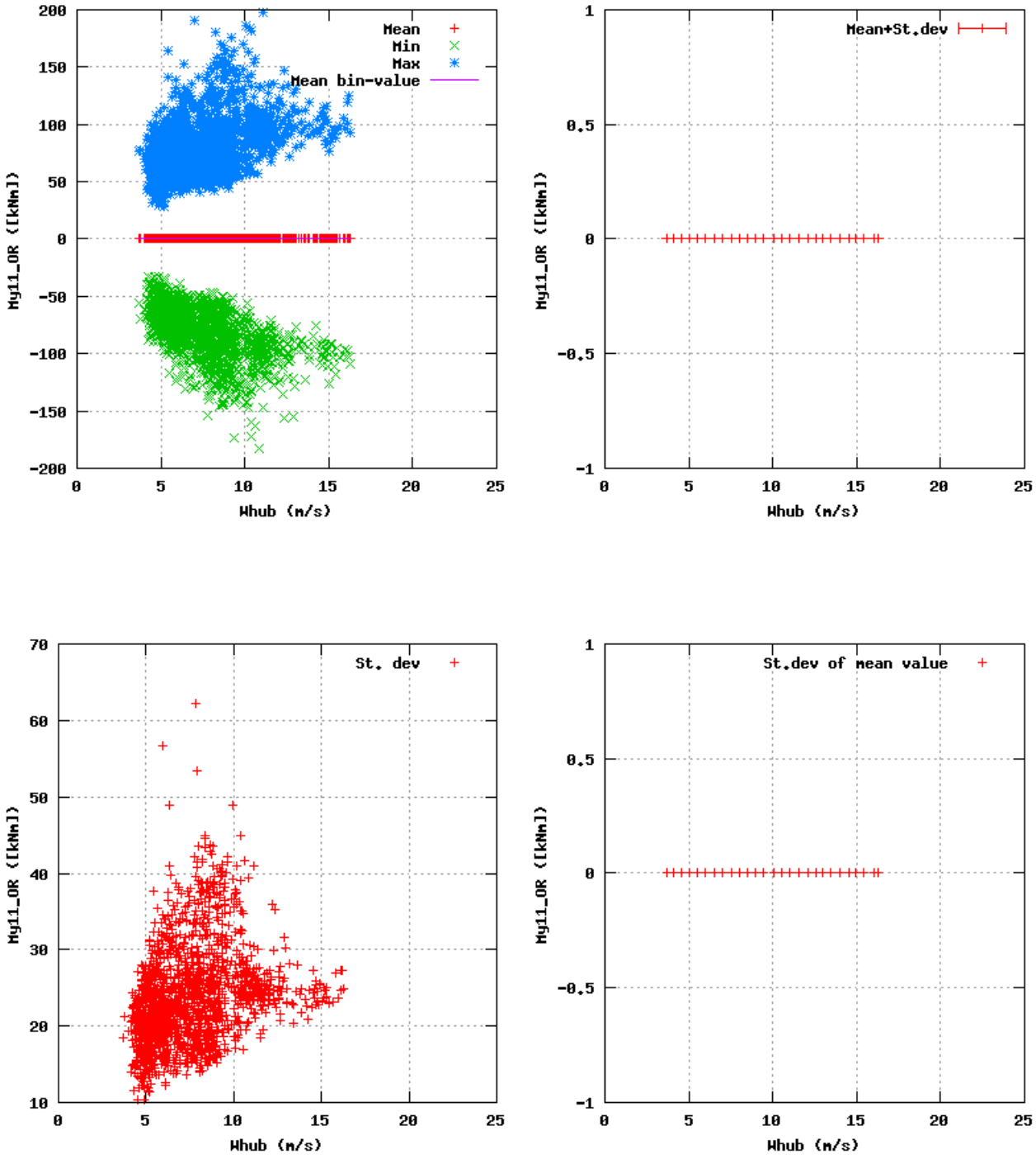

Figure 113a, Sensor 451: Flap bending moment B1 r=2.1m_OR versus wind speed
Input files: ntk500res.dat, stat_451.dat

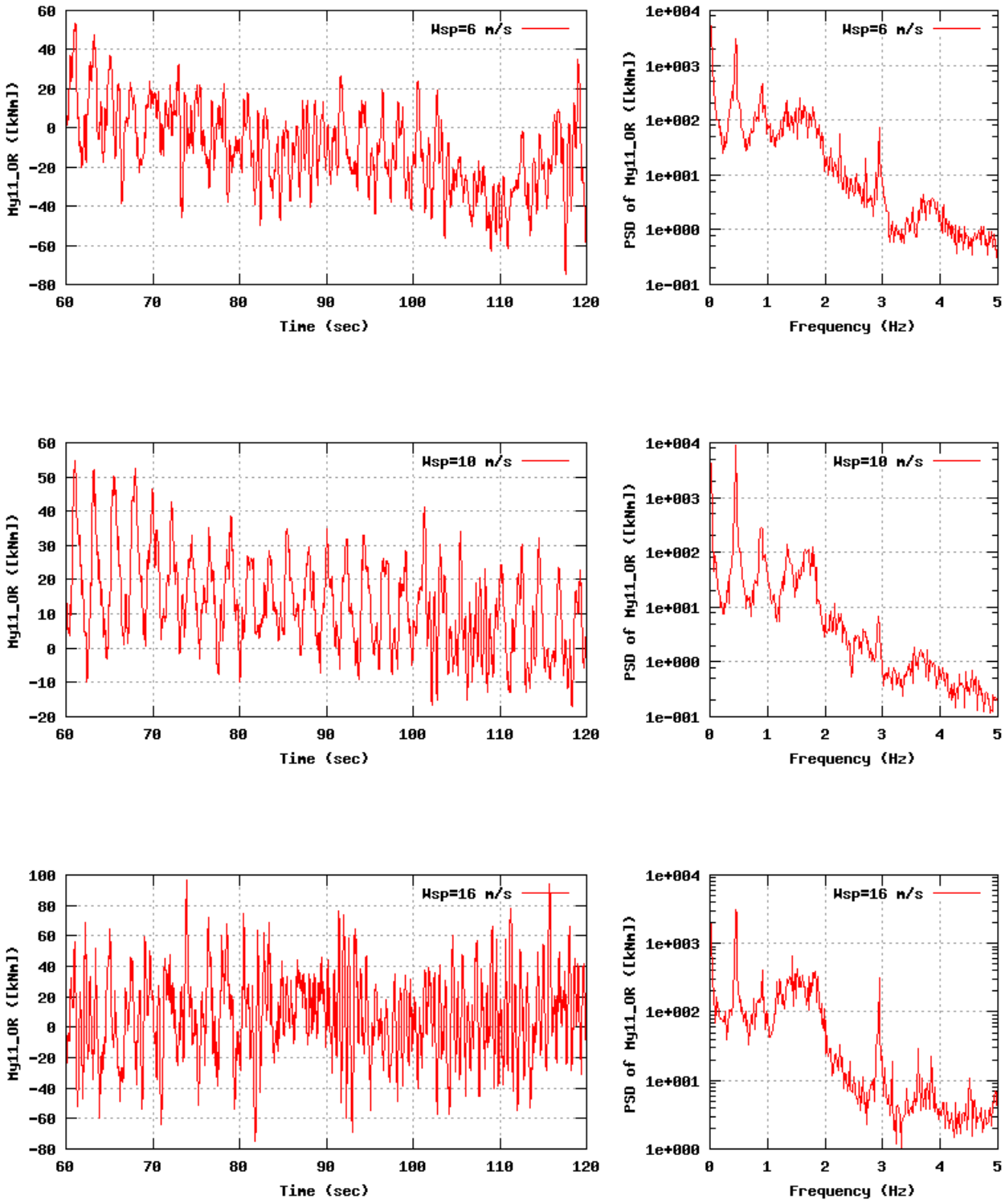

Figure 113b, Sensor 451: Flap bending moment B1 r=2.1m_OR versus time and frequency
Input files: m06.asc, m10.asc, m16.asc, m06.psd, m10.psd and m16.psd

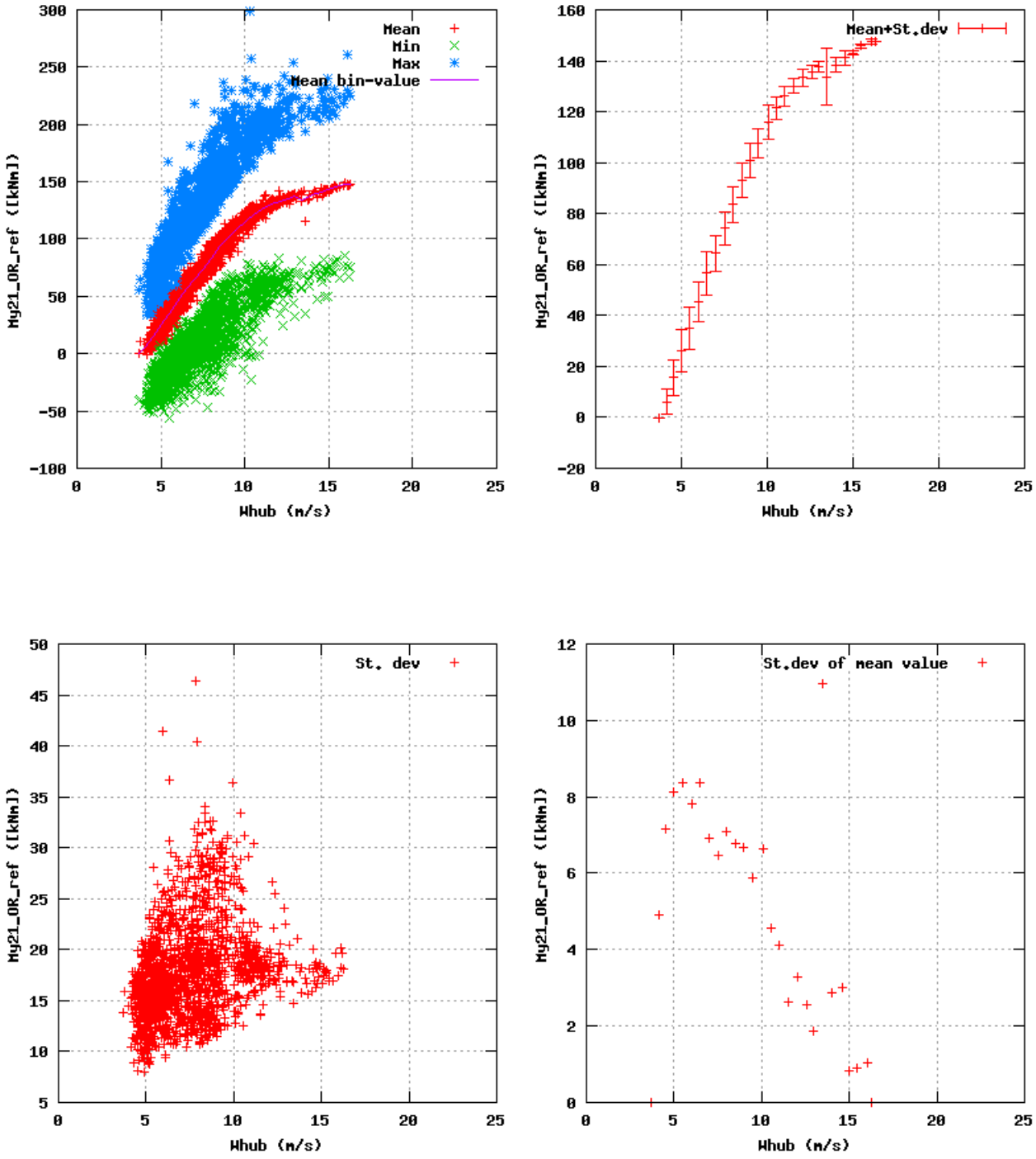

Figure 114a, Sensor 455: Flap bending moment B2 r=2.1m_OR versus wind speed
Input files: ntk500res.dat, stat_455.dat

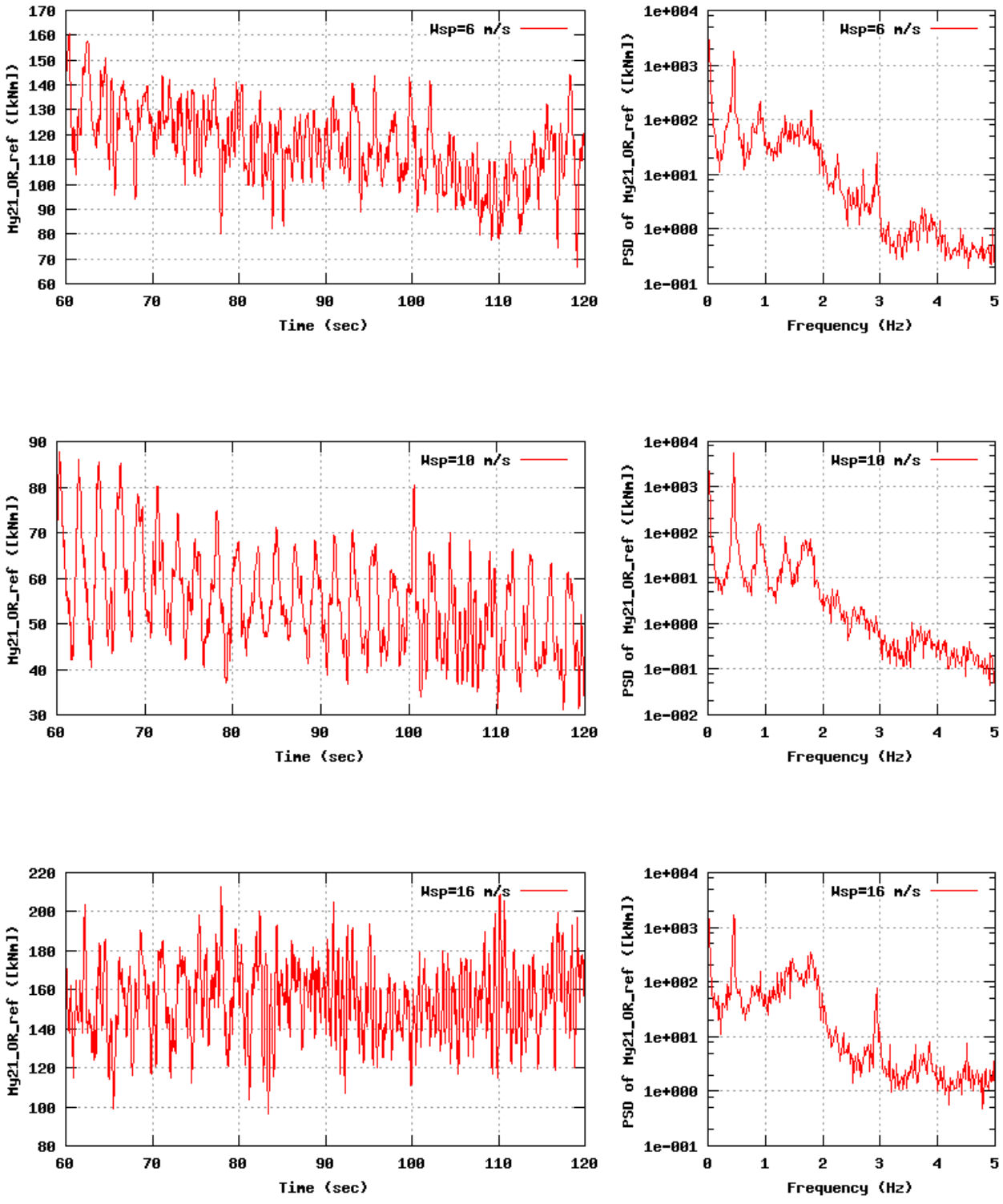

Figure 114b, Sensor 455: Flap bending moment B2 r=2.1m_OR versus time and frequency
Input files: m06.asc, m10.asc, m16.asc, m06.psd, m10.psd and m16.psd

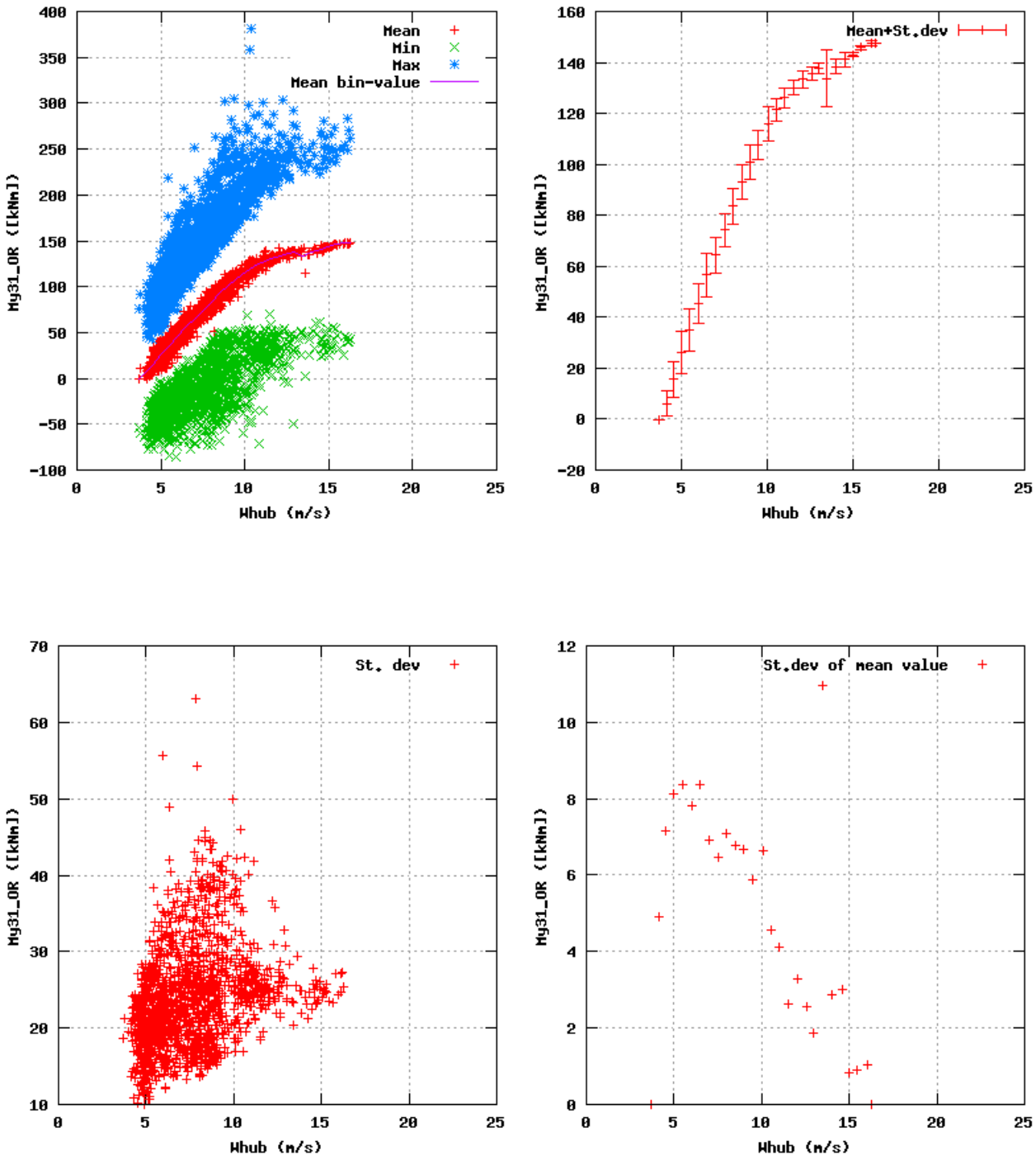

Figure 115a, Sensor 459: Flap bending moment B3 r=2.1m_OR versus wind speed
Input files: ntk500res.dat, stat_459.dat

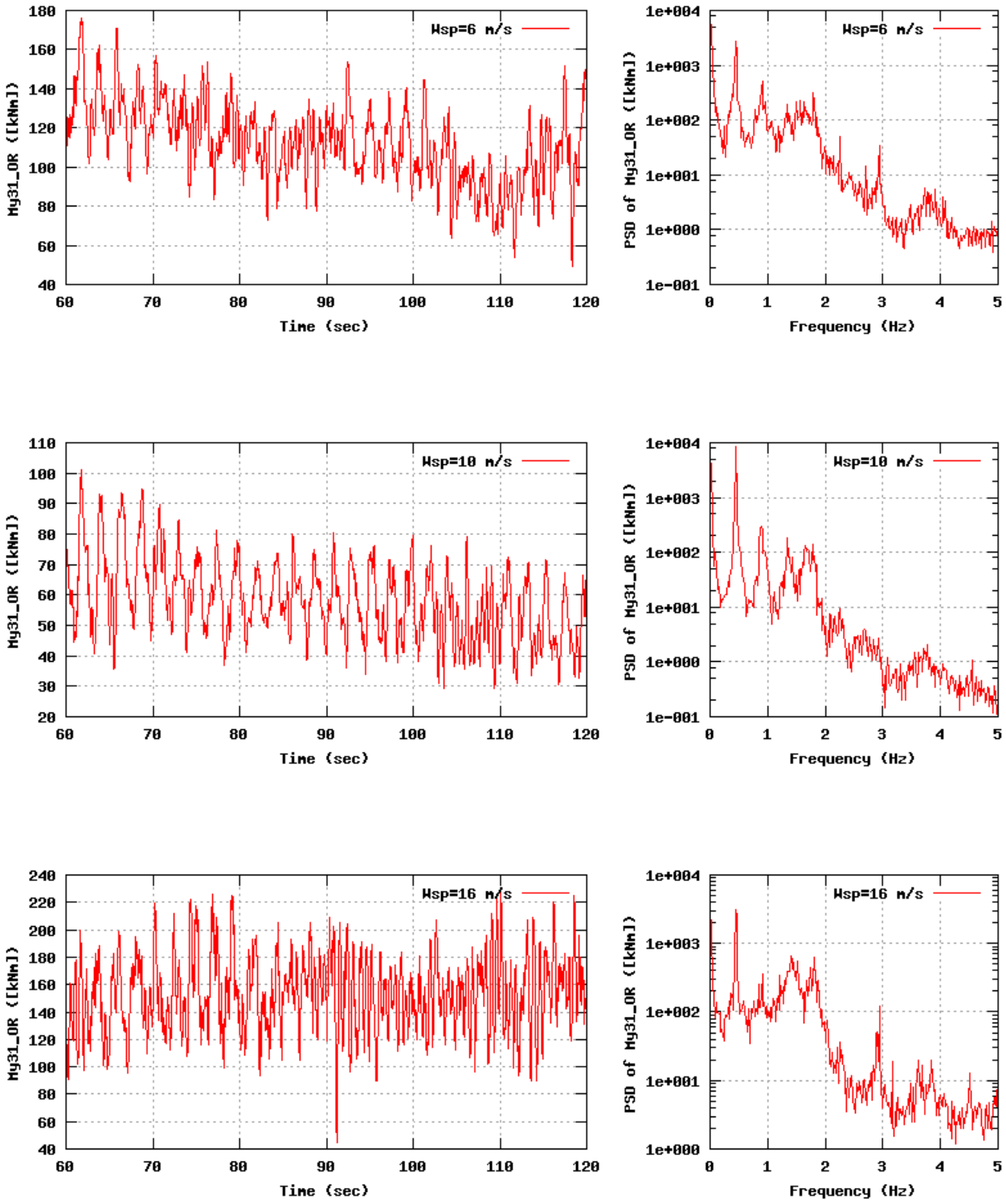

Figure 115b, Sensor 459: Flap bending moment B3 r=2.1m_OR versus time and frequency
Input files: m06.asc, m10.asc, m16.asc, m06.psd, m10.psd and m16.psd

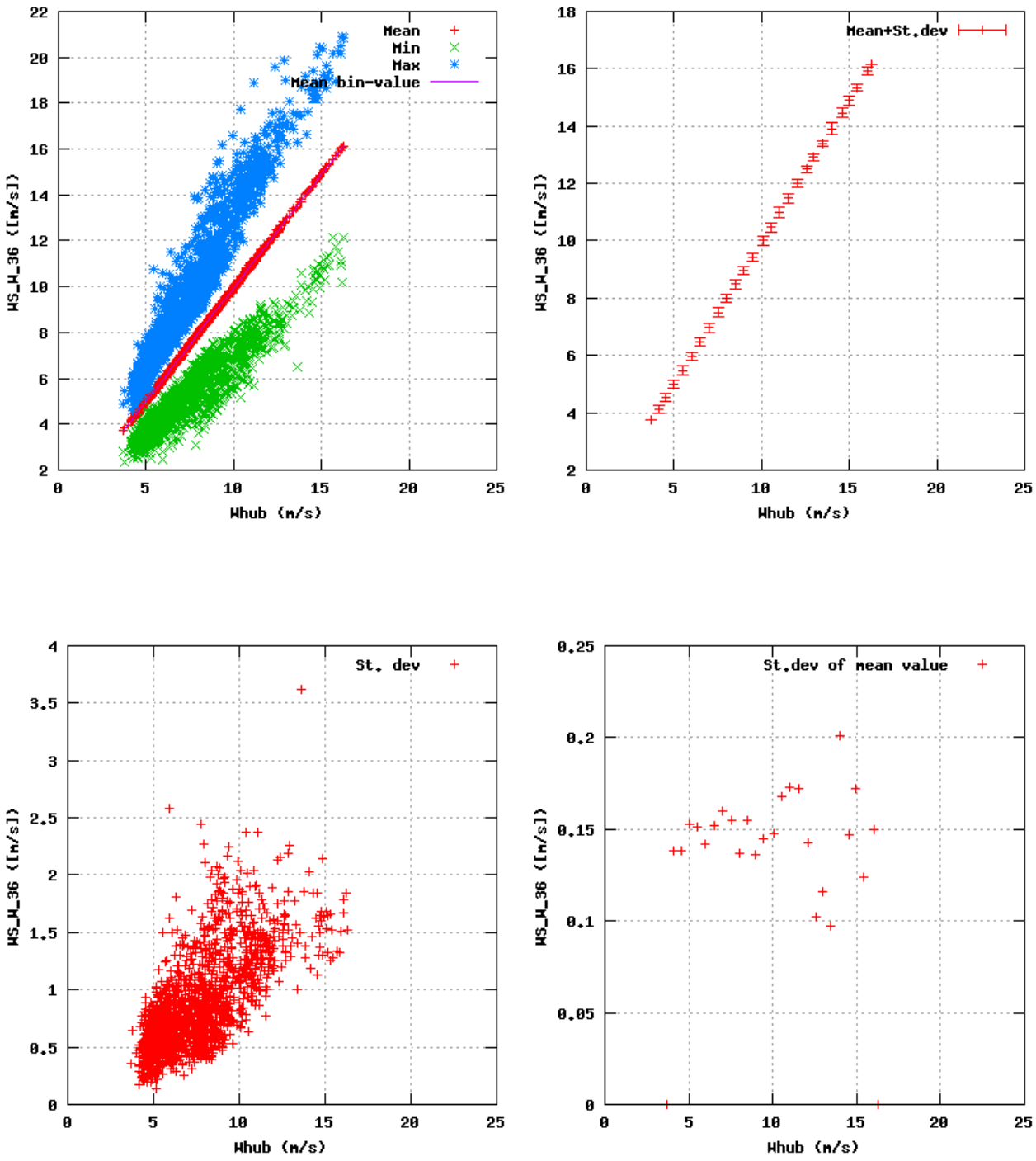

Figure 116a, Sensor 463: Wind speed Metmast @18m,(South+North)/2 versus wind speed
Input files: ntk500res.dat, stat_463.dat

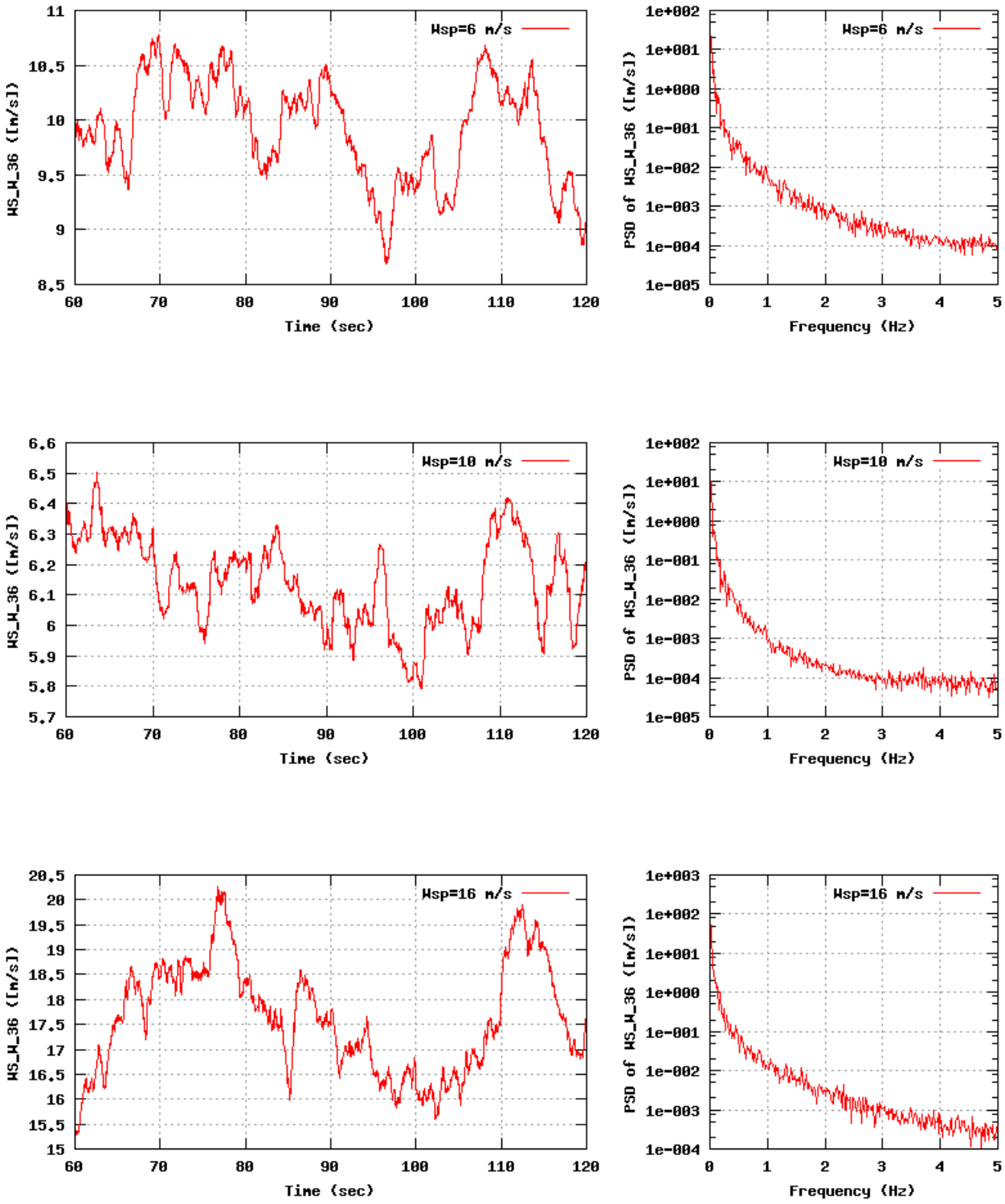

Figure 116b, Sensor 463: Wind speed Metmast @18m,(South+North)/2 versus time and frequency
Input files: m06.asc, m10.asc, m16.asc, m06.psd, m10.psd and m16.psd

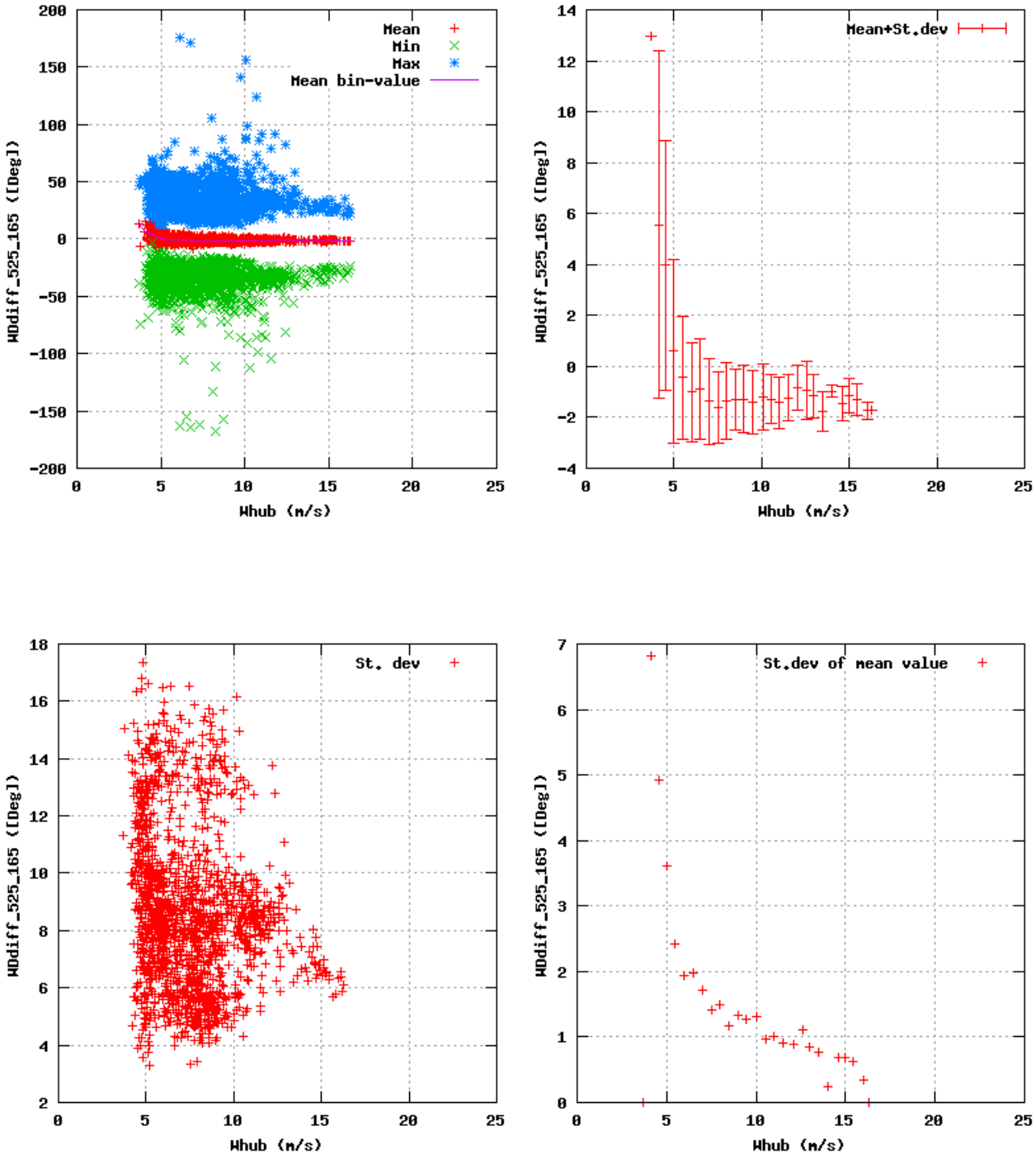

Figure 117a, Sensor 467: Wind Direction versus wind speed
Input files: ntk500res.dat, stat_467.dat

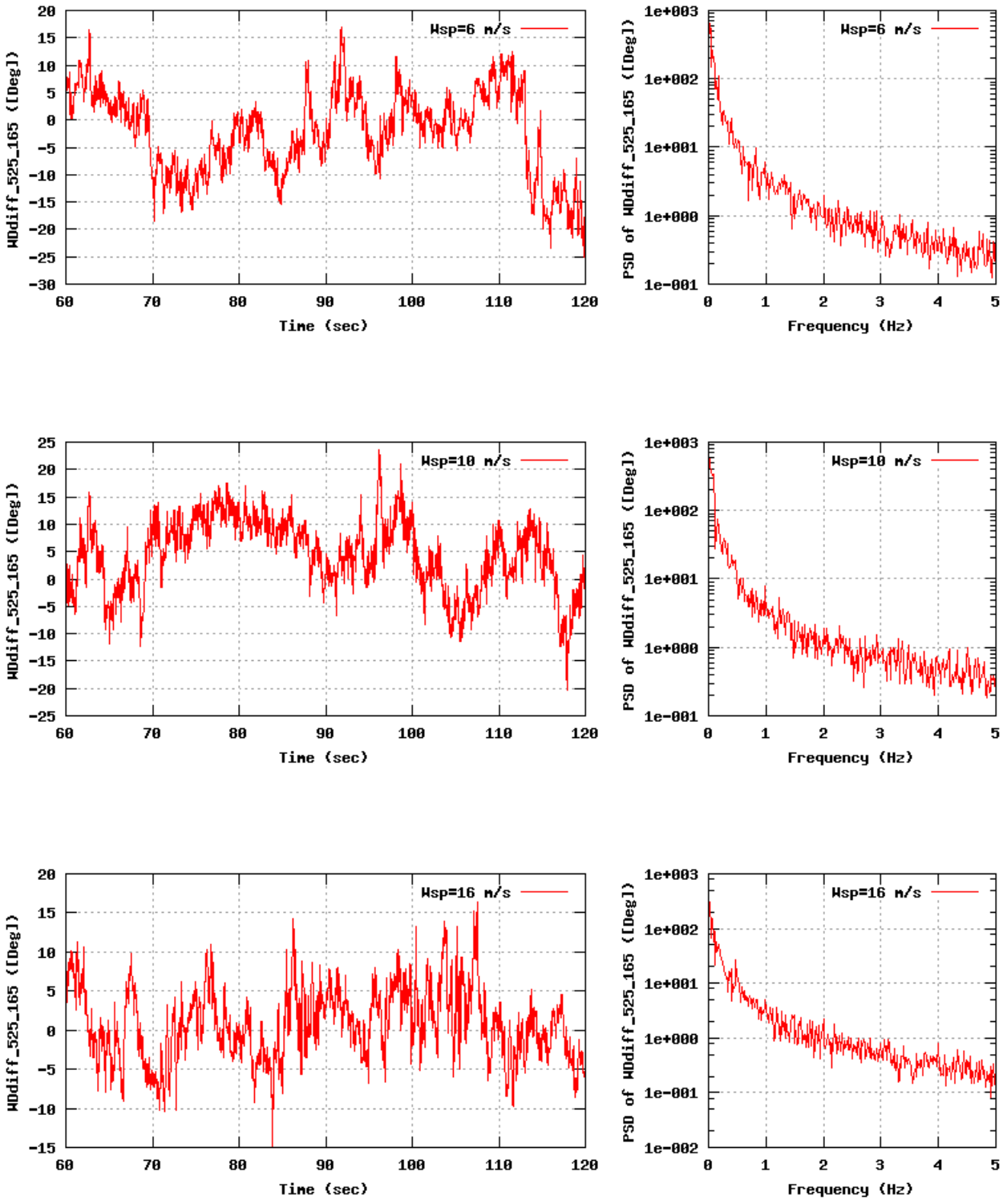

Figure 117b, Sensor 467: Wind Direction versus time and frequency
Input files: m06.asc, m10.asc, m16.asc, m06.psd, m10.psd and m16.psd

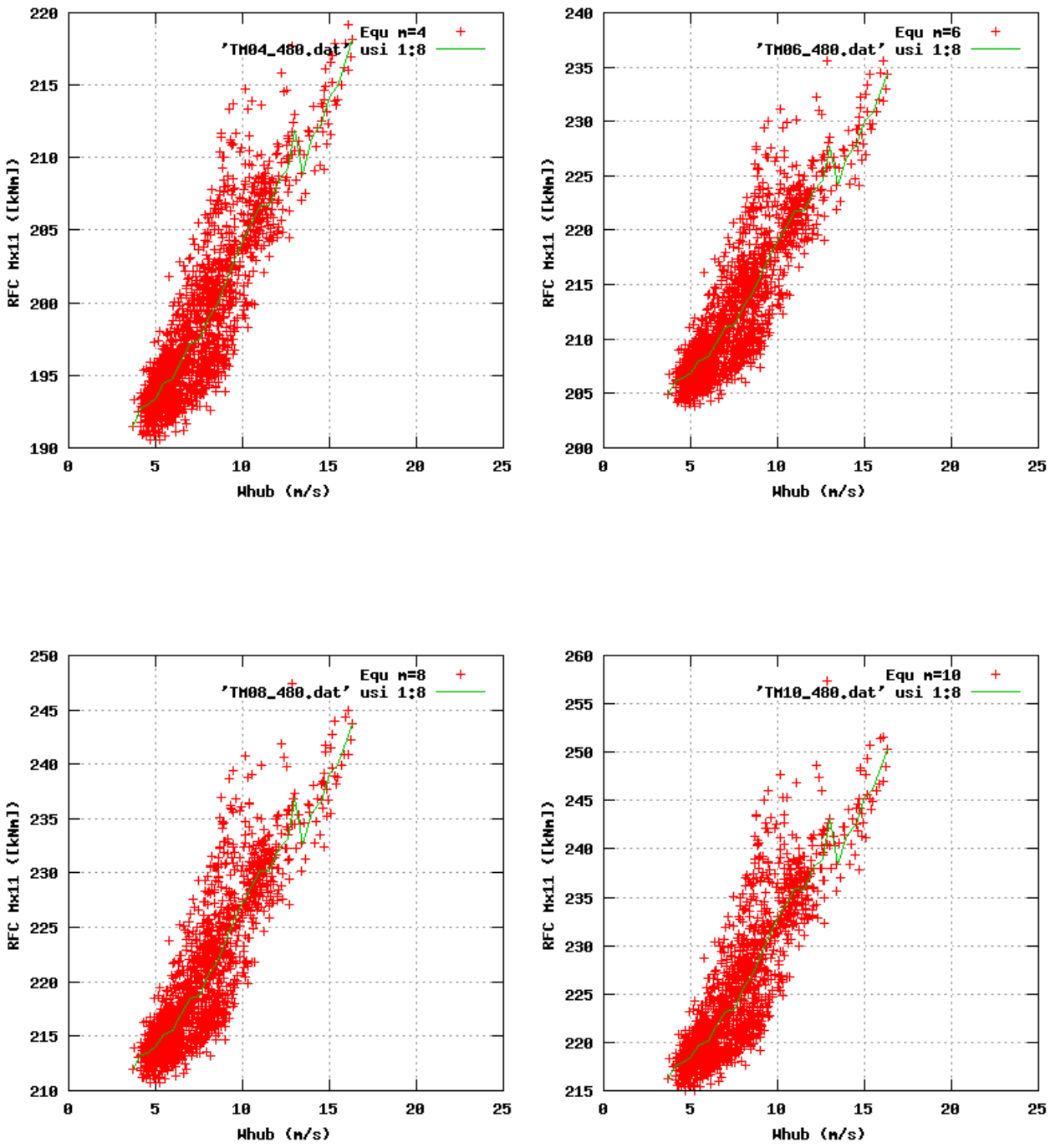

Figure 118a, Sensor 480: Rain Flow Count Mx11 versus wind speed
Input files: ntk500res.dat, TM04_480.dat, TM06_480.dat,TM08_480.dat,TM10_480.dat

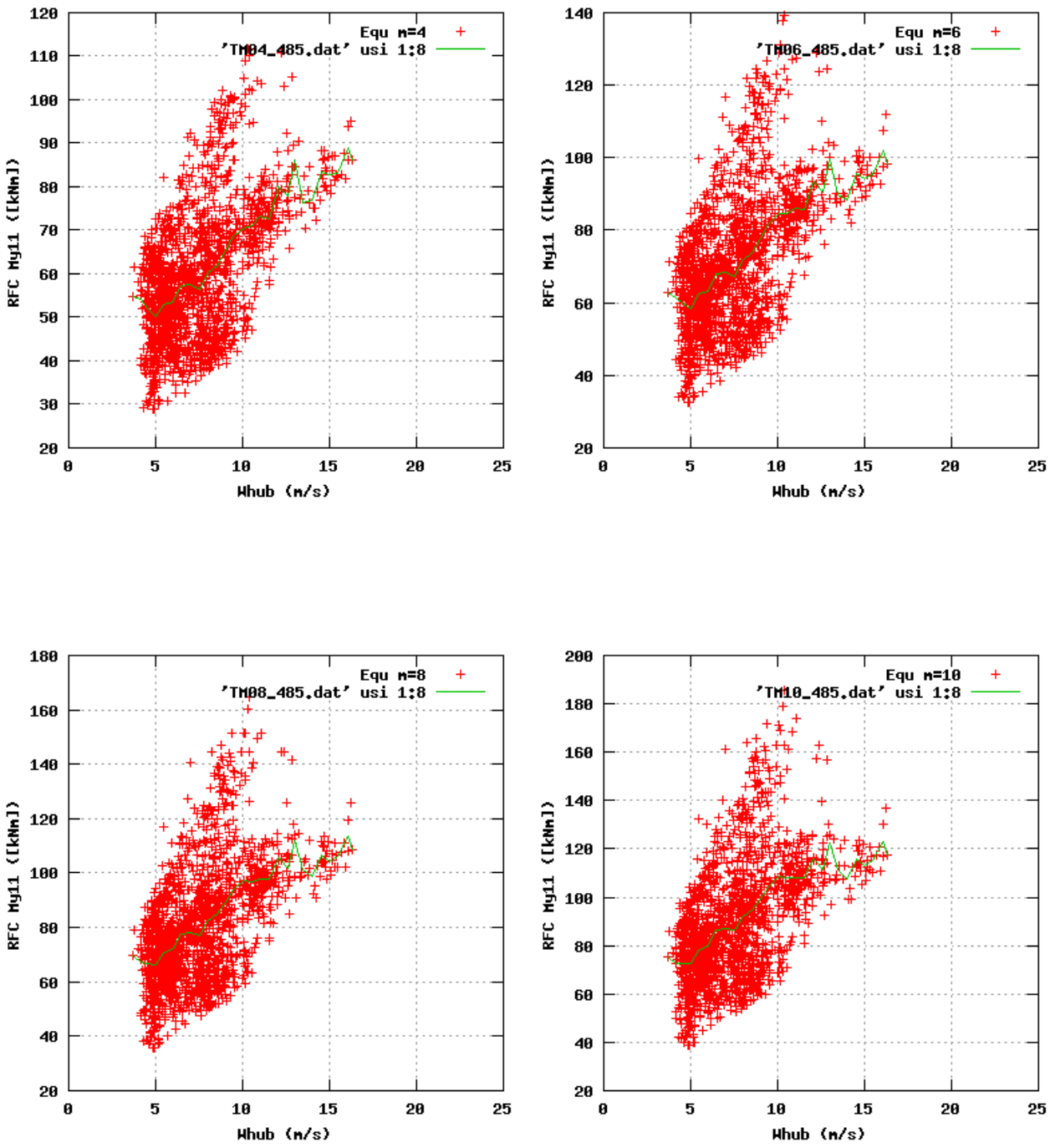

Figure 119a, Sensor 485: Rain Flow Count My11 versus wind speed
Input files: ntk500res.dat, TM04_485.dat, TM06_485.dat,TM08_485.dat,TM10_485.dat

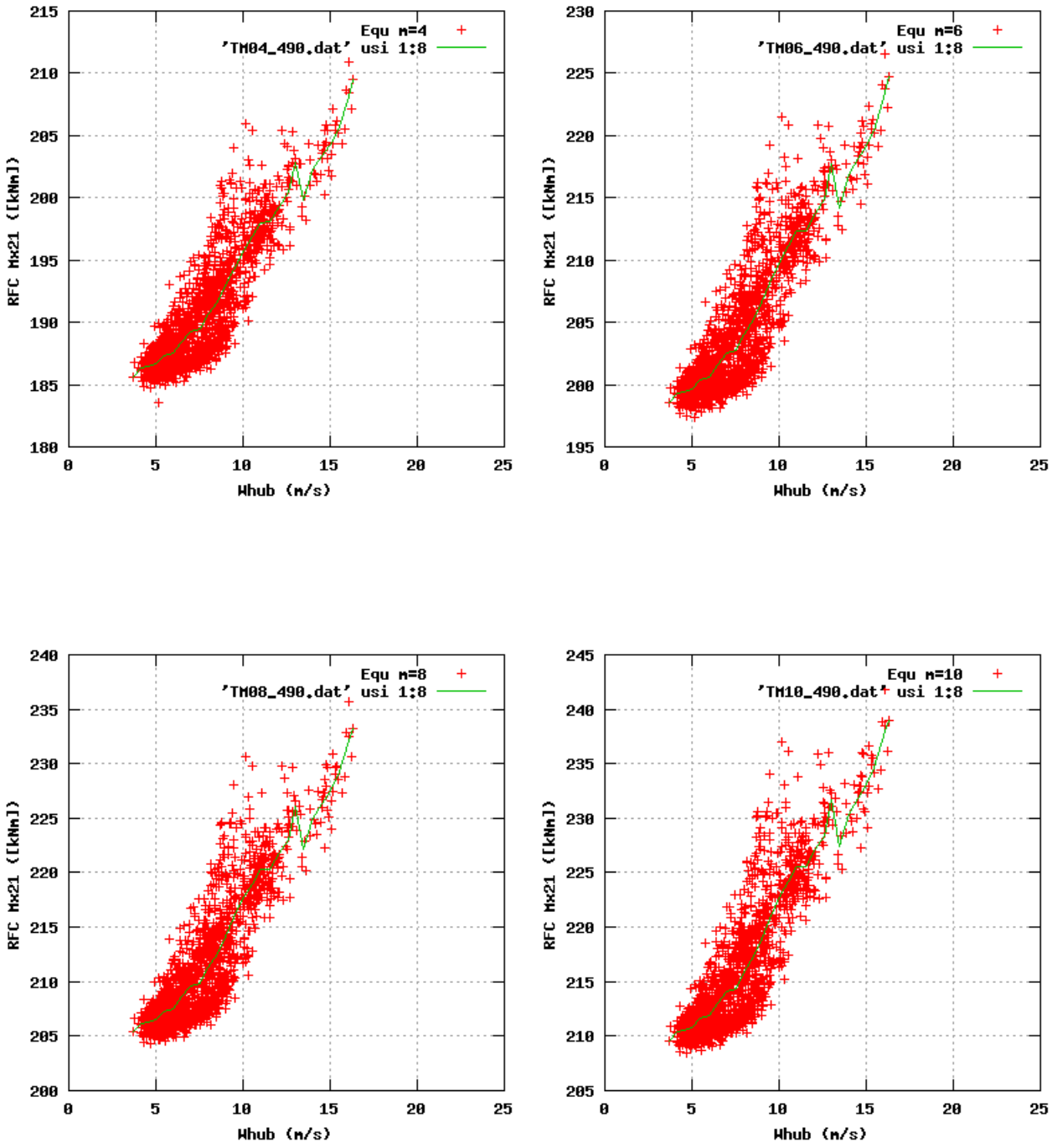

Figure 120a, Sensor 490: Rain Flow Count Mx21 versus wind speed
Input files: ntk500res.dat, TM04_490.dat, TM06_490.dat,TM08_490.dat,TM10_490.dat

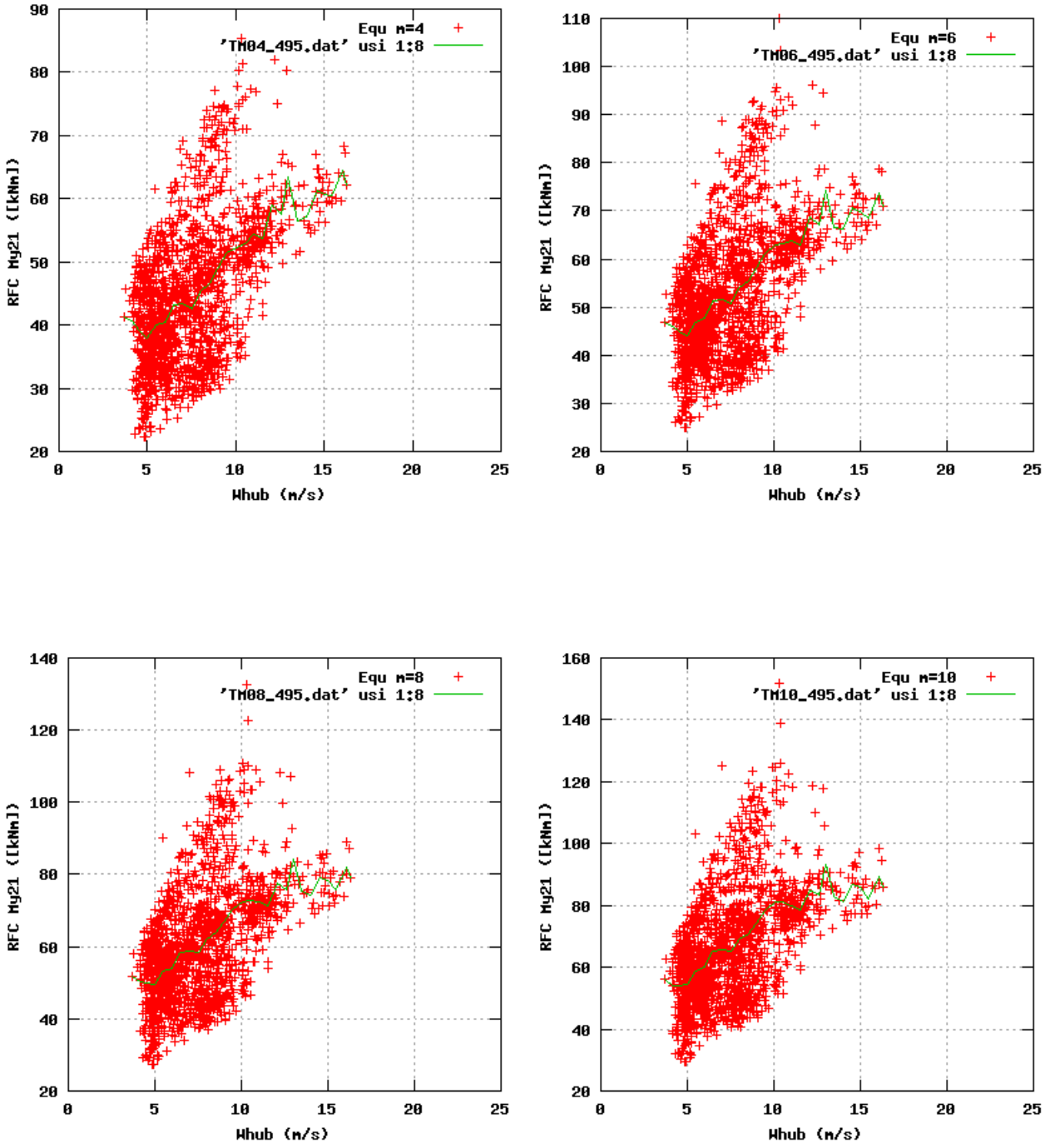

Figure 121a, Sensor 495: Rain Flow Count My21 versus wind speed
Input files: ntk500res.dat, TM04_495.dat, TM06_495.dat,TM08_495.dat,TM10_495.dat

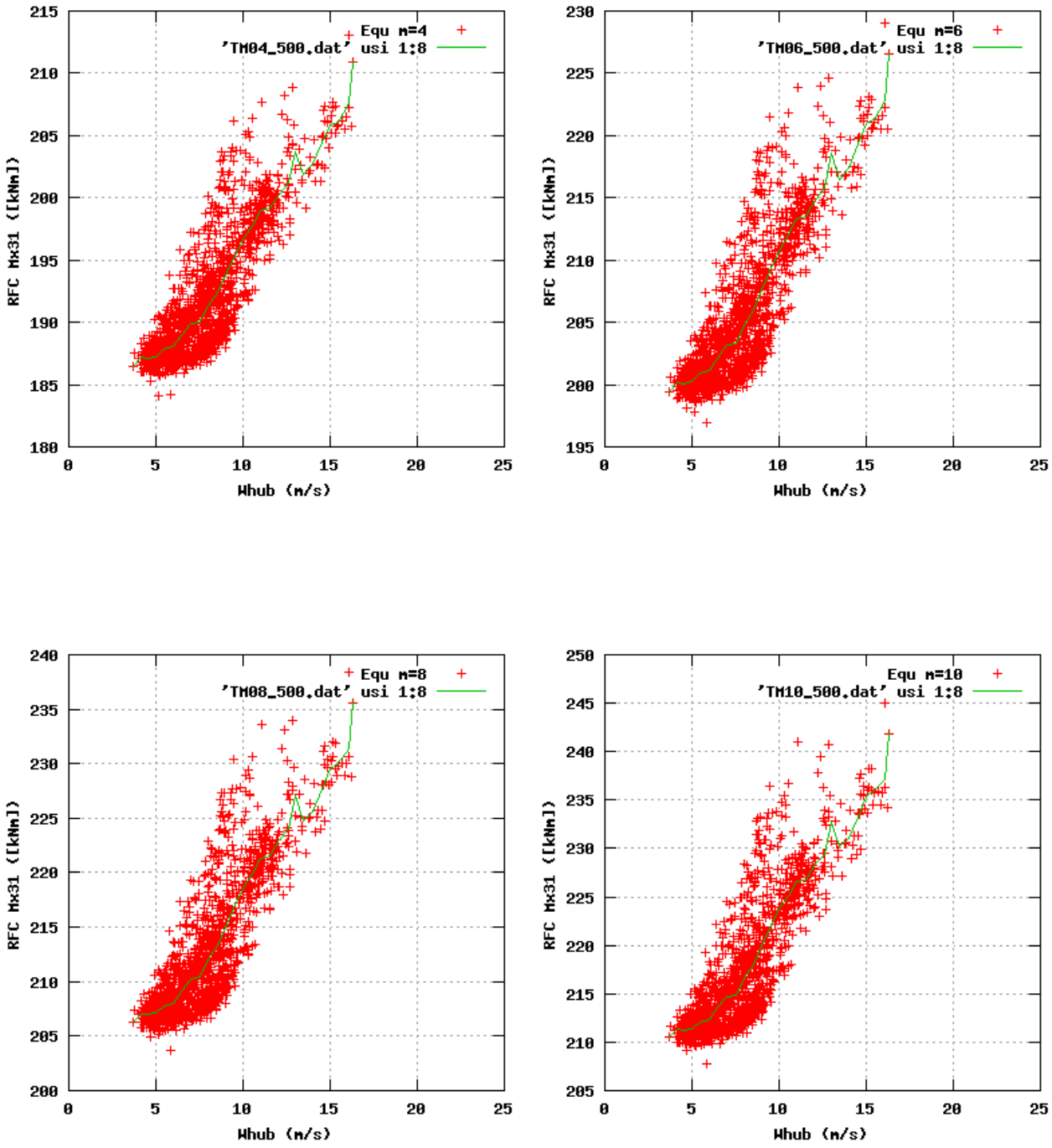

Figure 122a, Sensor 500: Rain Flow Count Mx31 versus wind speed
Input files: ntk500res.dat, TM04_500.dat, TM06_500.dat,TM08_500.dat,TM10_500.dat

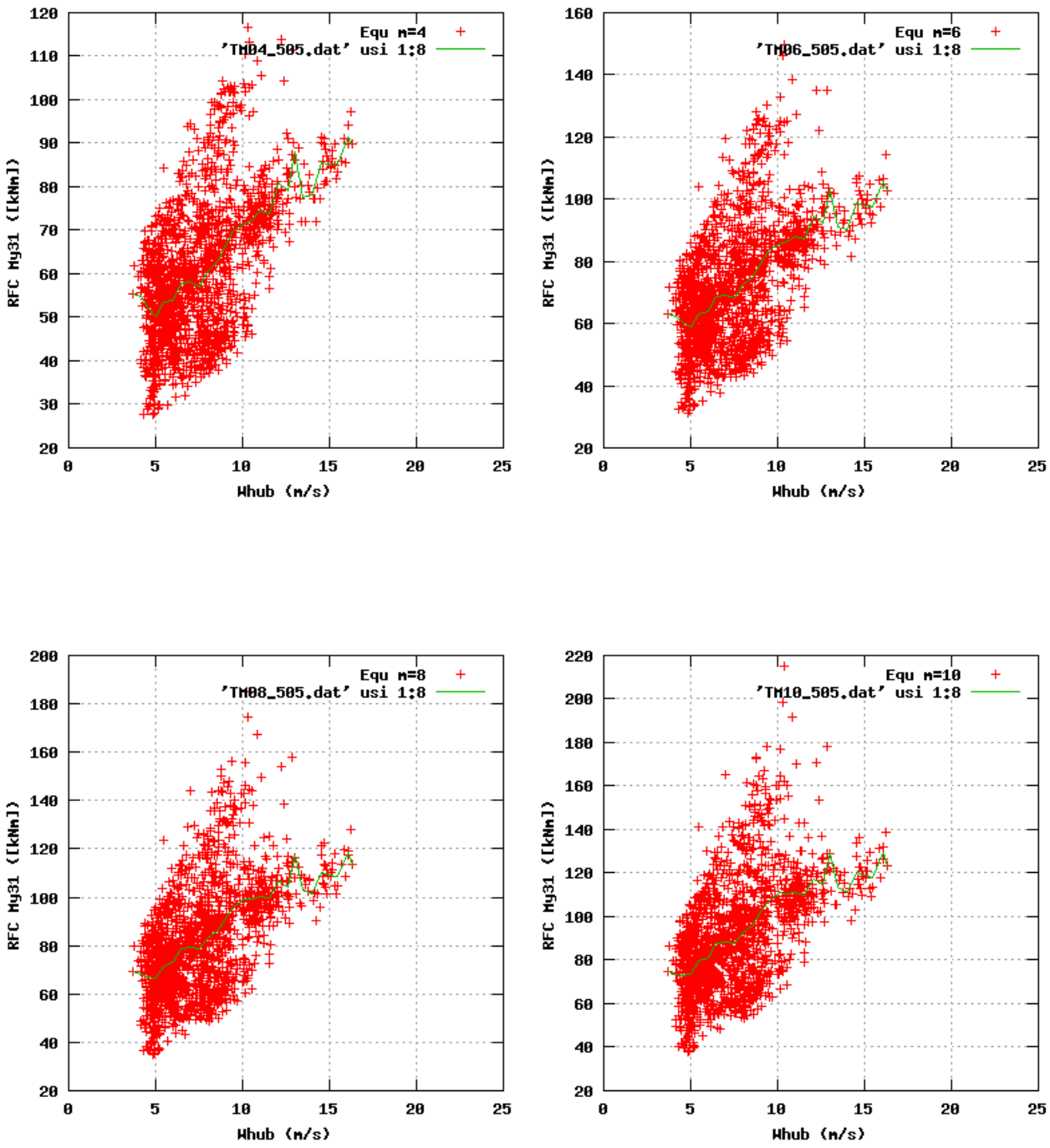

Figure 123a, Sensor 505: Rain Flow Count My31 versus wind speed
Input files: ntk500res.dat, TM04_505.dat, TM06_505.dat,TM08_505.dat,TM10_505.dat

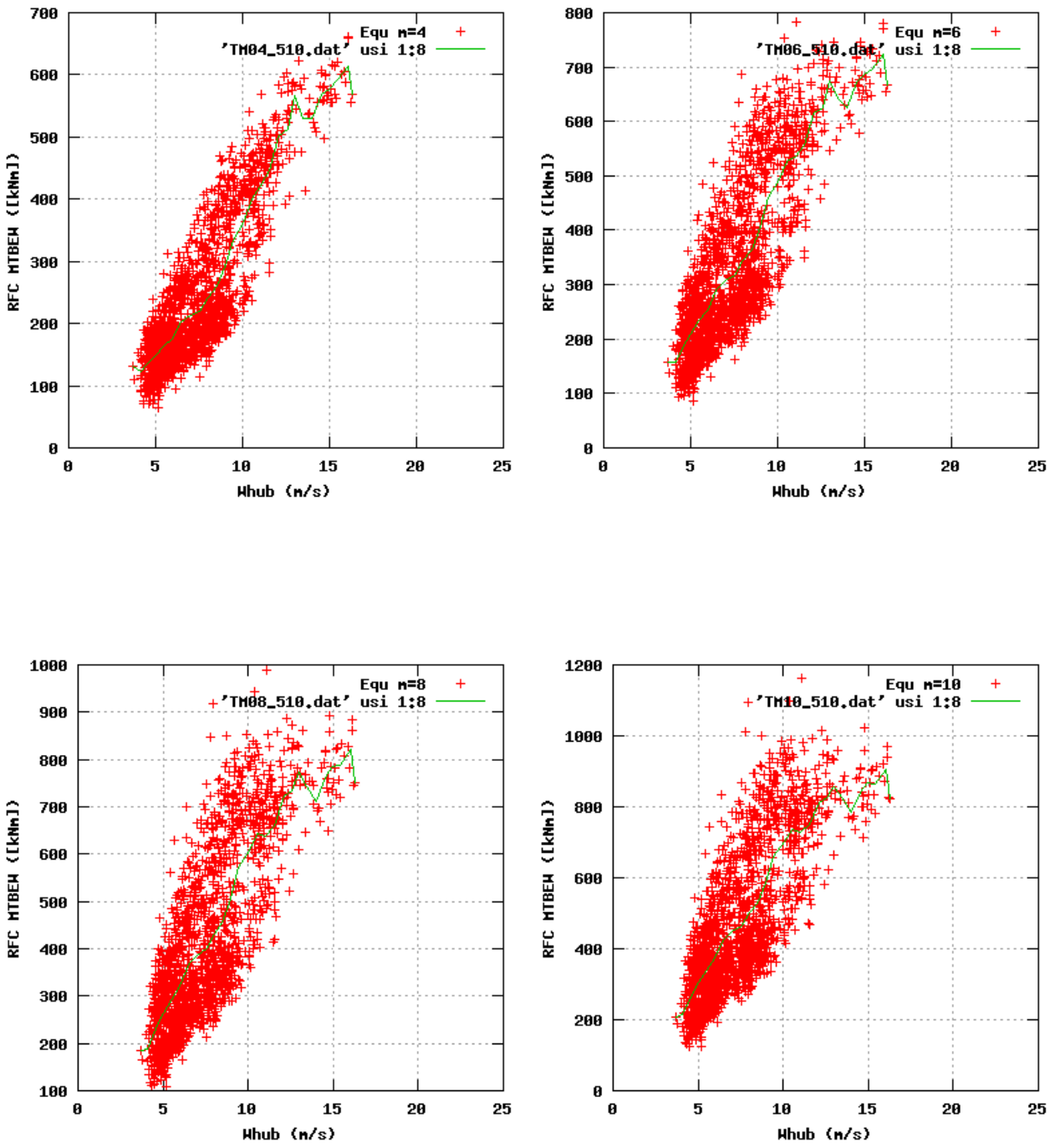

Figure 124a, Sensor 510: Rain Flow Count MTBEW versus wind speed
Input files: ntk500res.dat, TM04_510.dat, TM06_510.dat,TM08_510.dat,TM10_510.dat

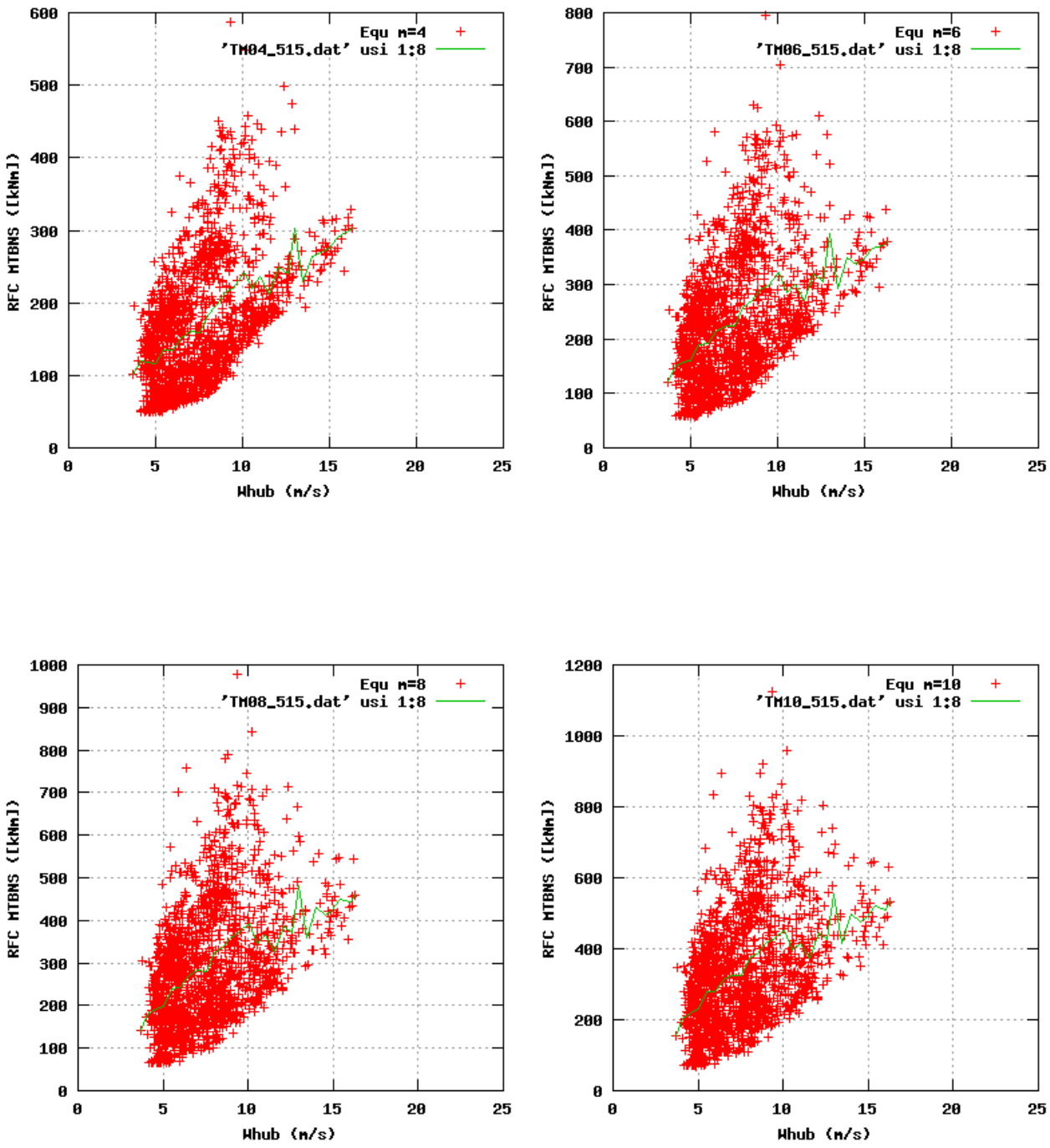

Figure 125a, Sensor 515: Rain Flow Count MTBNS versus wind speed
Input files: ntk500res.dat, TM04_515.dat, TM06_515.dat,TM08_515.dat,TM10_515.dat

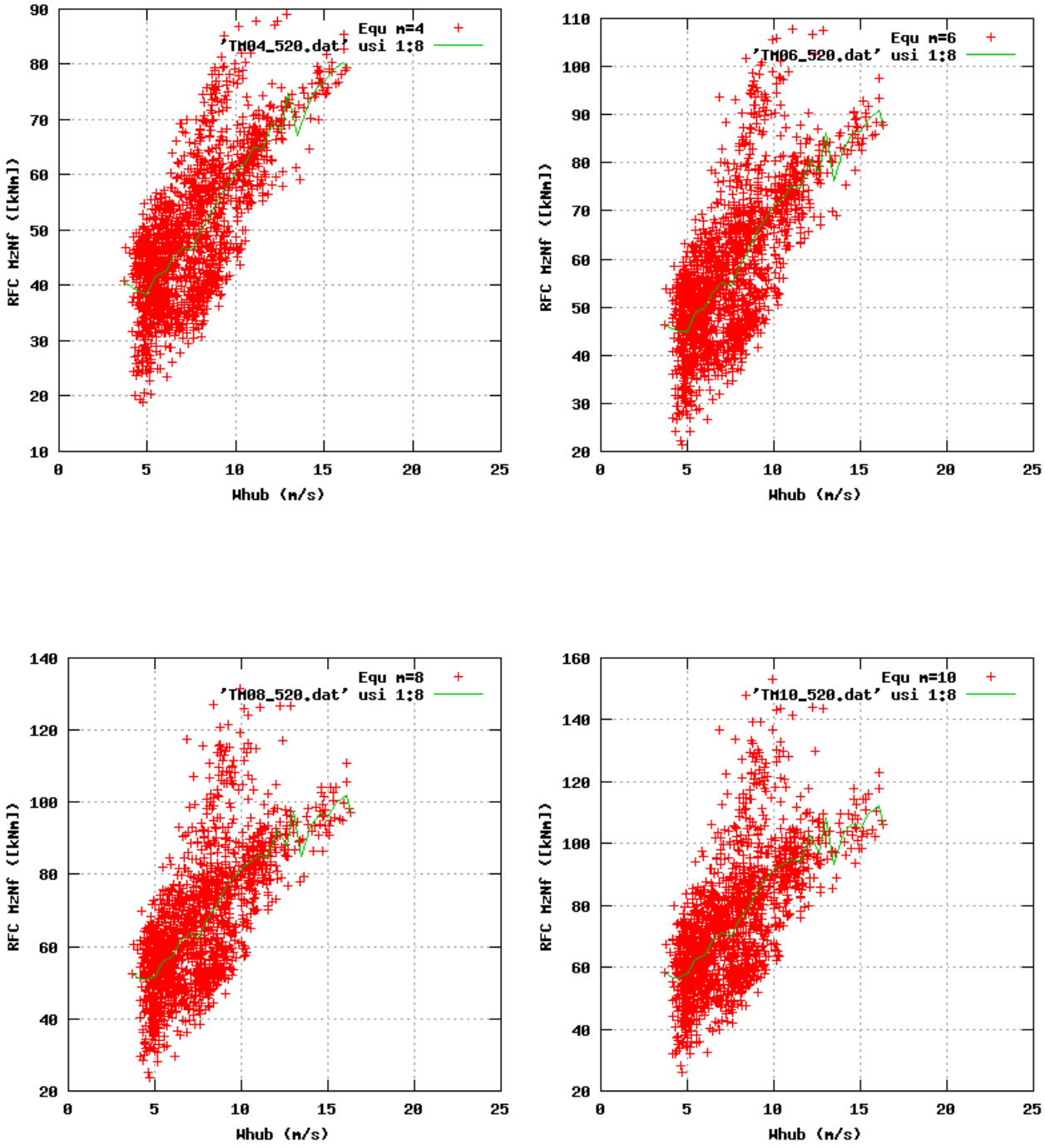

Figure 126a, Sensor 520: Rain Flow Count MzNf versus wind speed
Input files: ntk500res.dat, TM04_520.dat, TM06_520.dat,TM08_520.dat,TM10_520.dat

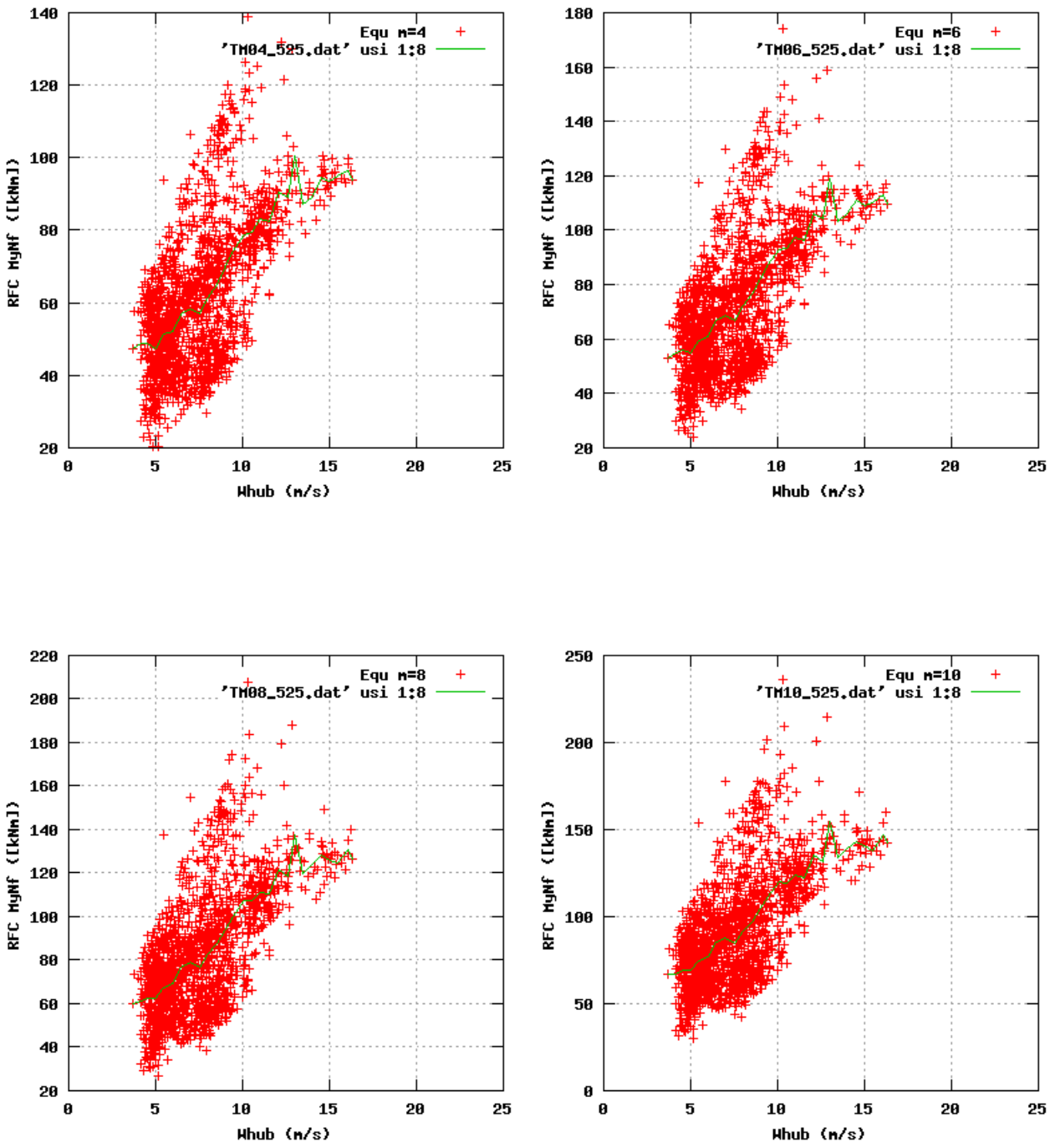

Figure 127a, Sensor 525: Rain Flow Count MyNf versus wind speed
Input files: ntk500res.dat, TM04_525.dat, TM06_525.dat,TM08_525.dat,TM10_525.dat

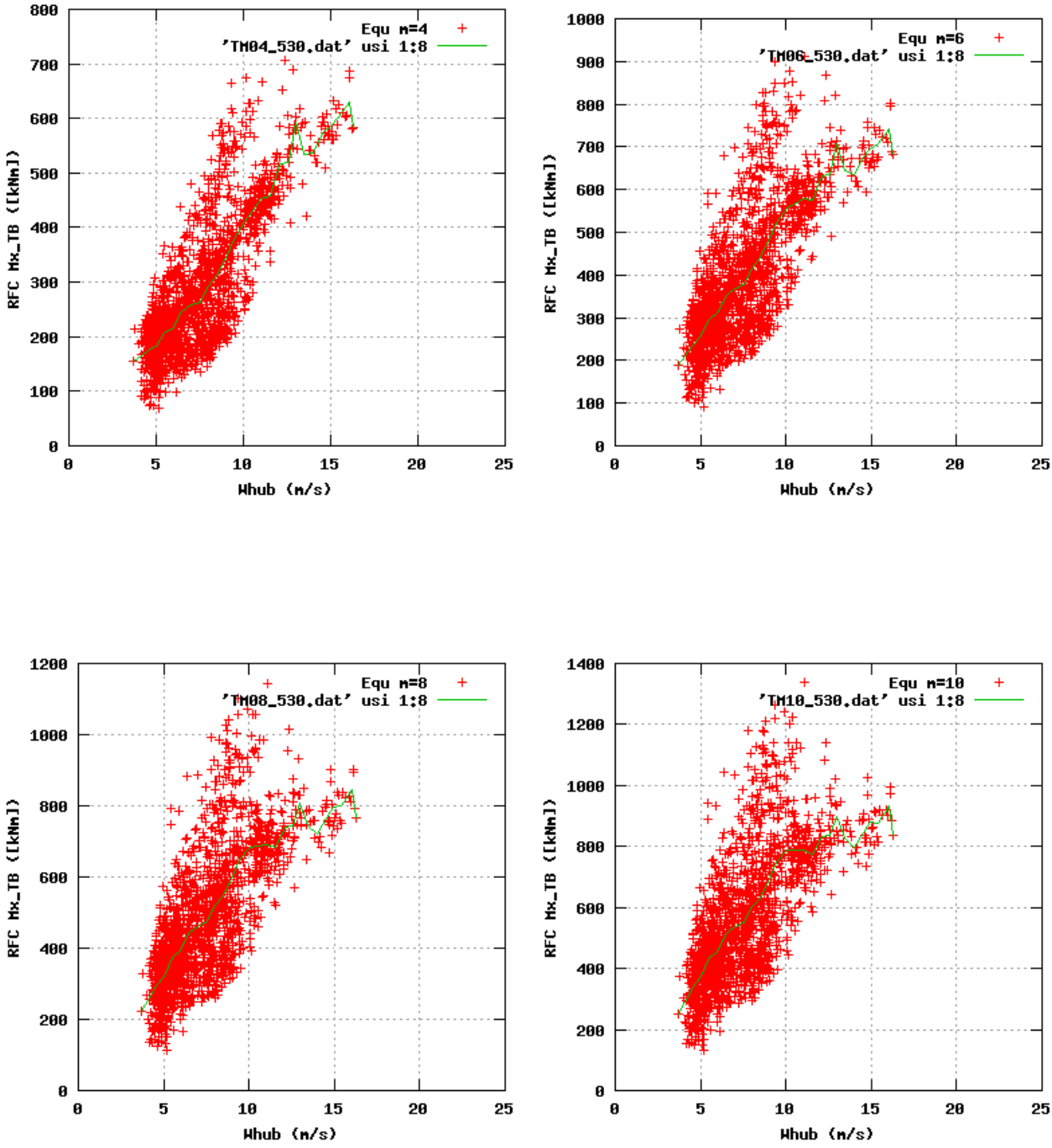

Figure 128a, Sensor 530: Rain Flow Count Mx_TB versus wind speed
Input files: ntk500res.dat, TM04_530.dat, TM06_530.dat,TM08_530.dat,TM10_530.dat

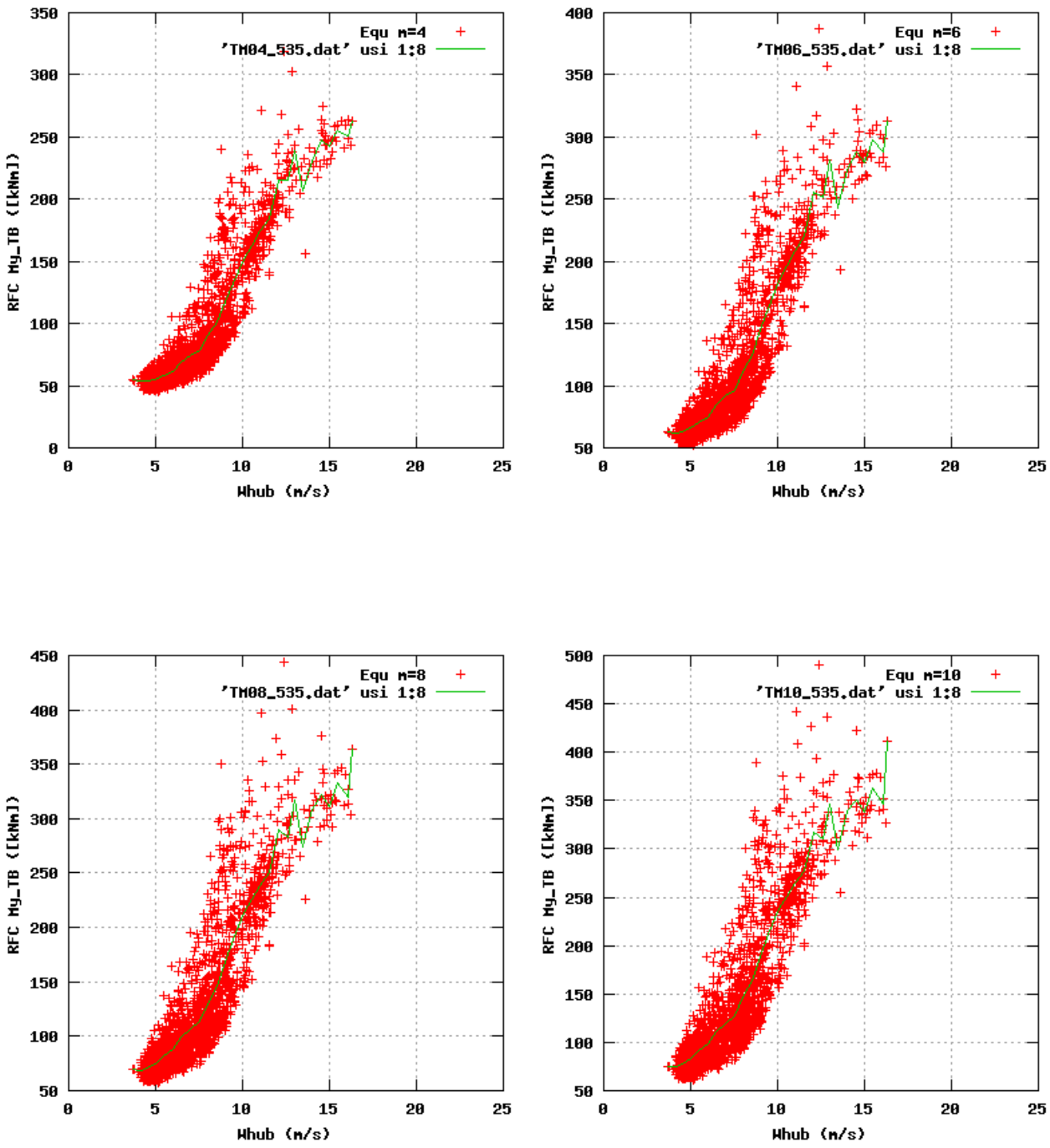

Figure 129a, Sensor 535: Rain Flow Count My_TB versus wind speed
Input files: ntk500res.dat, TM04_535.dat, TM06_535.dat,TM08_535.dat,TM10_535.dat

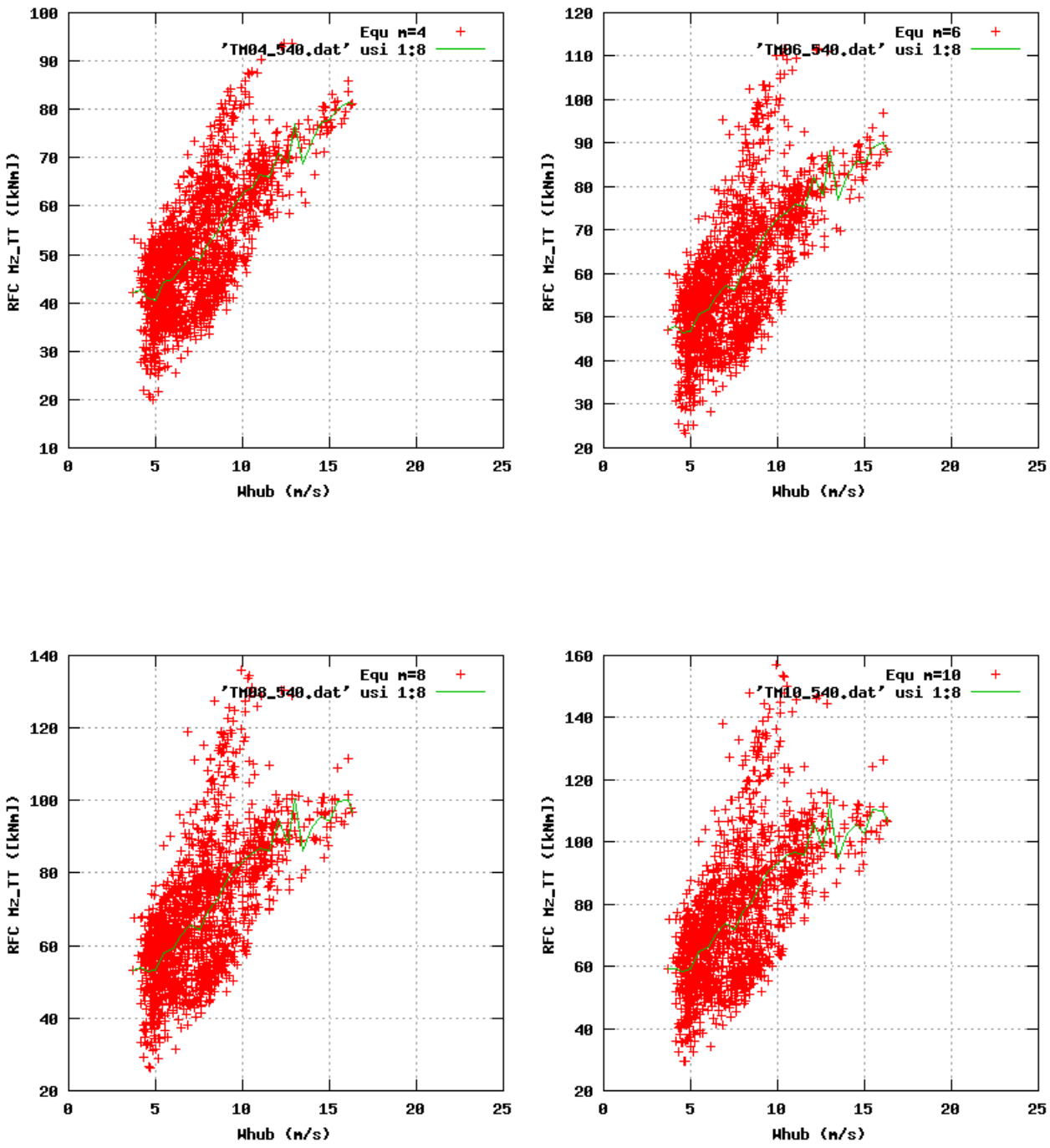

Figure 130a, Sensor 540: Rain Flow Count Mz_TT versus wind speed
Input files: ntk500res.dat, TM04_540.dat, TM06_540.dat,TM08_540.dat,TM10_540.dat

LIDAR results

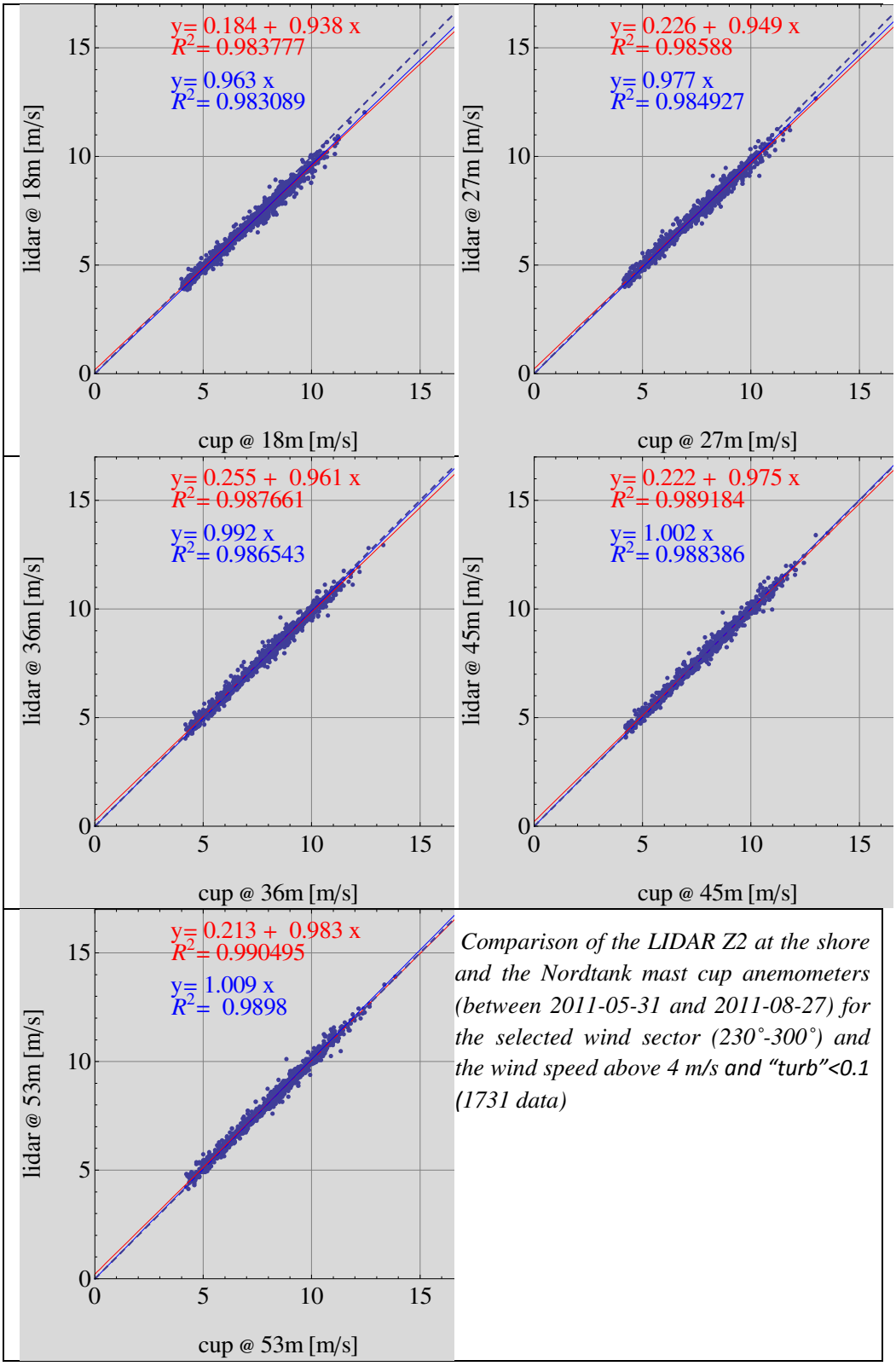

Comparison of the LIDAR Z2 at the shore and the Nordtank mast cup anemometers (between 2011-05-31 and 2011-08-27) for the selected wind sector (230°-300°) and the wind speed above 4 m/s and "turb"<0.1 (1731 data)

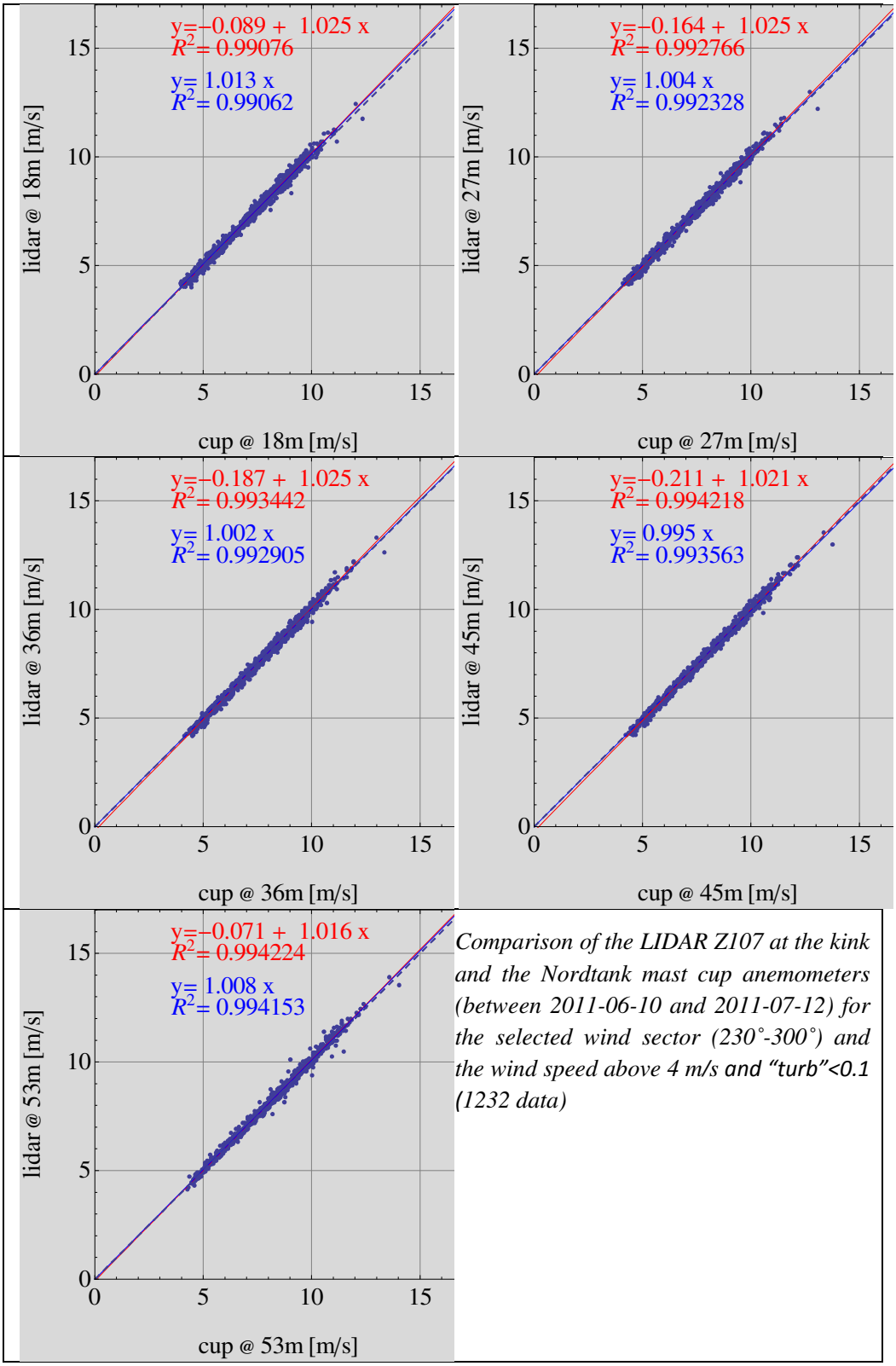

Comparison of the LIDAR Z107 at the kink and the Nordtank mast cup anemometers (between 2011-06-10 and 2011-07-12) for the selected wind sector (230°-300°) and the wind speed above 4 m/s and "turb"<0.1 (1232 data)

List of IMPER output

2011:

Wagner, R. et al., Accounting for the speed shear in wind turbine power performance measurement, Wind Energy, 2011; 14:993--1004

Cariou et al: Analysis of vertical wind direction and speed gradients for data from the metmast at Høvsøre Risø-R-1733, May 2011

2010:

Giebel, G., U.S. Paulsen, J. Reuder, A. la Cour-Harbo, C. Thomsen, J. Bange: Autonomous Aerial Sensors for Wind Power Meteorology. EWEC 2010, Warsaw (PL), 20-23 Apr 2010

Aagård H. et al. DAN-AERO MW: Detailed aerodynamic measurements on a full scale MW wind turbine, EWEC 2010, Warsaw (PL) 20-23 Apr 2010

R. Wagner, et al.: Improvement of power curve measurement with LIDAR wind speed profiles, EWEC March 2010, Polen

Wagner R. Accounting for the speed shear in wind turbine power performance measurement, Risø-PhD-58(EN), 155pp, 2010

Wagner R. et al: Simulation of shear and turbulence impact on wind turbine performance Risø-R-1722(EN) January 2010

Gottschall J., et al: Characterization and categorization of vertical wind shear, Risø DTU 16-02-2010, Memo

2009:

Wagner, R. et al. The Influence of the Wind Speed Profile on Wind Turbine Performance Measurements Wind Energy 2009; 12:348–362

Paulsen U. : Imper technical report 2009: journalnr 33032-0106 programområde vind og vand

Wagner R. and M.S. Courtney: Can we measure the performance of a wind turbine with a lidar?, Proc. of WINDPOWER, Chicago, Il. 2009

Wagner R. and M.S. Courtney, 2009: Multi-MW wind turbine power curve measurements using remote sensing instruments - the first Høvsøre campaign, Tech. report Risø-R-1679(EN).

Wagner R., Courtney M.S., Gottschall J. and P. Lindelöw-Marsden: MultiMW wind turbine power curve measurement using LIDAR (second Høvsøre campaign), Tech. report Risø-I-2954(EN), 2009

Wagner, R, Courtney, M, Results of the first measurement campaign using remote sensing instruments for multi MW wind turbine power curve measurement at Høvsøre, Draft report Jan 09

Anoniou I, Pedersen S M, The method uncertainty: Wind speed at hub height. Presentation at IEC symposium Seattle Jan- 09

2008:

Paulsen U.: Imper technical report 2008: journalnr 33032-0106 programområde vind og vand

Mikkelsen, T.: A forward looking LIDAR ZephIR CW

Wagner R, Antoniou I, Pedersen S M, Jørgensen H E, Wind profile influence on turbine performance, Wind Energy, online, 2008; 10.1002/we.297.
Courtney M, Wagner R, Lindelöw P, Testing and comparison of LiDARs for profile and turbulence measurements in wind energy, EWEC 2008. M. Courtney, R. Wagner and P. Lindelöw: Testing and comparison of lidars for profile and turbulence measurements in wind energy. Paper submitted at the Isars Conference, Risø DTU June 2008

Wagner R. et al: Remote sensing used for power curves Paper submitted at the Isars Conference, Risø DTU June 2008

2007:
Paulsen U.: Imper technical report 2007: journalnr 33032-0106 programområde vind og vand
Antoniou I, R. Wagner R., Petersen SM, Paulsen U, Jørgensen HE, Thomsen K., Enevoldsen P., Thesbjerg L: Influence of wind characteristics on turbine performance. Paper presented at the EWEC 2007 conference in Milan, Italy March 2007.
Wagner R.,. Jørgensen H.E, Paulsen U..: The influence of wind profiles on the wind turbine performance measurement. Paper submitted to Wind Energy Journal June 2007
Zhou Y., Antoniou I., Courtney M.: Preliminary sodar-cup comparisons and power curve results using the AQ500 sodar. Risoe-I-2603(EN) September 2007.
S. M. Pedersen, U. S. Paulsen, H. E. Jørgensen: Symposium on Wind profiles from Høvsøre. Held at Risø Dec 2007

2006:
Antoniou et al: Imper technical report 2006: journalnr 33032-0106 programområde vind og vand
Kick-off meeting 16-6-2006 at Risø

Overview of sensor and transmitter

Table 6: Sensor and transmitter description 35 Hz sampling

Measurement description	Sensor	Signal type	Conversion principle	Transmitter
Wind speed at hub height-18m	RISØ cup anemometer P2546A with Reed relay	Digital	Direct counting of pulses and pulse pr rpm	Risø P2858A DAU Configured to periodic time measurement
Wind speed at hub height -9m	RISØ cup anemometer P2546A with Reed relay	Digital	Direct counting of pulses and pulse pr rpm	Risø P2858A DAU Configured to periodic time measurement
Wind speed at hub height 36m	RISØ cup anemometer P2546A with Reed relay	Digital	Direct counting of pulses and pulse pr rpm	Risø P2858A DAU Configured to

				periodic time measurement
Wind speed at hub height +9m	RISØ cup anemometer P2546A with Reed relay	Digital	Direct counting of pulses and pulse pr rpm	Risø P2858A DAU Configured to periodic time measurement
Wind speed at hub height+18m	RISØ cup anemometer P2546A with Reed relay	Digital	Direct counting of pulses and pulse pr rpm	Risø P2858A DAU Configured to periodic time measurement
Wind speed at hub height+21m	RISØ cup anemometer P2546A with Reed relay	Digital	Direct counting of pulses and pulse pr rpm	Risø P2858A DAU Configured to periodic time measurement
Wind speed, direction and temperature at 16.5magl	Sonic METEK USA 1	Digital	Measuring speed of travel	RS485 to RS232 converter
Wind speed, direction and temperature at 34.5magl	Sonic METEK USA 1	Digital	Measuring speed of travel	RS485 to RS232 converter
Wind speed, direction and temperature at 52.5magl	Sonic METEK USA 1	Digital	Measuring speed of travel	RS485 to RS232 converter
Air barometric pressure 2 magl	VAISALA PTB100B Pressure sensitive vessel with position gauge	Analogue	Measuring of gauge position	
Precipitation	LED Light array	Digital	Blockage of light array path	LED circuit
Position of nacelle	Resistor with gearbox attached to yaw drive	Analogue	Measuring on resistive path	Voltage divider
Position of rotor	Inductive sensor on low speed shaft together with inductive sensor on high speed shaft with 6 holes	Digital	Dampening of transistor oscillations due to presence of metal provides pulse	Risø P2858A DAU Configured to position measurement
Rotor shaft speed low speed	Inductive sensor one pulse/rev	Digital	Dampening of transistor oscillations due to presence of metal provides pulse	Risø P2858A DAU Configured to periodic time measurement
Rotor shaft speed high speed	Inductive sensor with 6 pulses/rev	Digital	Dampening of transistor oscillations due to presence of metal provides pulse	Risø P2858A DAU Configured to periodic time measurement
Wind speed nacelle	Risø cup anemometer P2546A with Reed relay	Digital	2 magnets on turning shaft controls the contact closure timings of the relay per revolution	Risø P2858A DAU Configured to periodic time measurement
Wind Direction nacelle	Vector Wind vane F2819A	Analogue	Measuring on resistive viper path relative to one full turn	Voltage divider
Flap-wise bending root moment #1	Micro Measurement Strain Gauge CEA-06-250A-350	Analogue	Semiconductor foil subjected to resistive change due to bending	RisøP2912B SG amplifier
Edge-wise bending root moment #1	Micro Measurement Strain Gauge CEA-06-250A-350	Analogue	Semiconductor foil subjected to resistive change due to bending	Risø P2912B SG amplifier
Rotor shaft torque	Micro Measurement Strain Gauge CEA-06-W250C-350	Analogue	Semiconductor foil subjected to resistive change due to twisting	Risø P2912B SG amplifier
Main shaft bending moment X,	Micro Measurement Strain Gauge CEA-06-250A-350	Analogue	Semiconductor foil subjected to resistive change due to bending	Risø P2912B SG amplifier
Main shaft bending moment Y	Micro Measurement Strain Gauge CEA-06-250A-350	Analogue	Semiconductor foil subjected to resistive change due to bending	Risø P2912B SG amplifier
Tower top torsion,	Micro Measurement Strain Gauge CEA-06-W250C-350	Analogue	Semiconductor foil subjected to resistive change due to twisting	Risø P2912B SG amplifier
Tower bottom bending	Micro Measurement Strain Gauge CEA-06-250C-350	Analogue	Semiconductor foil subjected to resistive change due to	Risø P2912B SG amplifier

moment X			bending	
Tower bottom bending moment Y	Micro Measurement Strain Gauge CEA-06-250UW-350	Analogue	Semiconductor foil subjected to resistive change due to bending	Risø P2912B SG amplifier
Electrical Power	Camille Bauer 502-34F1 Z291 0090 61 Watt converter, cl 05	Analogue	Time division multiplier principle of 3 voltage and 3 current signals	3 Garre G30/20 cl. 01 Current transformers 500/1
Tip deployment indicator	Via Controller electronics	Digital	Non-potential hazardous NPN signal amplifier	Risø P2858A DAU Configured to status measurement
Brake activation indicator	Via Controller electronics	Digital	Non-potential hazardous NPN signal amplifier	Risø P2858A DAU Configured to status measurement
Generator mode indicator	Via Controller electronics	Digital	Non-potential hazardous NPN signal amplifier	Risø P2858A DAU Configured to status measurement
Operations mode indicator	Via Controller electronics	Digital	Non-potential hazardous NPN signal amplifier	Risø P2858A DAU Configured to status measurement

DTU Wind Energy is the largest research centre for wind energy worldwide with more than 230 staff members, including 150 academic staff members and nearly 60 PhD students. The department is composed of the former Wind Energy Division at Risø DTU, two groups from DTU Mechanical Engineering with focus on fluid dynamics and composite mechanics and two groups from the Materials Research Division at Risø DTU with focus on composite materials and metallic materials.

DTU Wind Energy
Technical University of Denmark

Frederiksborgvej 399
4000 Roskilde
Denmark
Phone +45 4677 5024

www.vindenergi.dtu.dk